Growth of Bismuth Oxide and Bismuth Ferrite Thin Films *via* CVD

This thesis is submitted in partial fulfilment of the requirements for the Degree of Doctor of Philosophy (Chemistry)

Savio Joseph Anthony Moniz

University College London

Supervised by Dr C S Blackman and Professor C J Carmalt

2012

Declaration

I, Savio Moniz, confirm that the work presented in this thesis is my own. Where information has been derived from other sources, I confirm this has been indicated in the thesis.

Abstract

This thesis describes the growth of bismuth oxide (Bi_2O_3) and multiferroic bismuth ferrite ($BiFeO_3$) films *via* chemical vapour deposition (CVD).

The synthesis of a range of bismuth(III) β-diketonate complexes was carried out *via* a ligand-exchange reaction between $[Bi(N(SiMe_3)_2)_3]$ and the respective free ligand, and crystal structures of $[Bi(dbm)_3]_2$ and $[Bi(acac)_3]_n$ are reported. The decomposition of these complexes was studied *via* DSC-TGA to assess their potential as single-source precursors to Bi_2O_3, and the mass transport characteristics of the volatile complexes $[Bi(mmp)_3]$, $[Bi(thd)_3]$ and $[Bi(O^tBu)_3]$ were studied.

Bi_2O_3 films were grown *via* the LPCVD reaction of the single-source precursor $[Bi(O^tBu)_3]$; the crystalline phase (and band-gap) of the resultant films depended strongly upon the reactor conditions. Films were tested for photo-oxidation of water under UV-light, revealing high activities comparable to those of TiO_2 films described previously. $[Bi(dbm)_3]_2$ was utilised as a single-source precursor to β-Bi_2O_3 films *via* AACVD, together with the growth of Pt(0) films using $H_2PtCl_6.6H_2O$ as a precursor. Pt-nanoparticle Bi_2O_3 films were grown *via* a 'one-pot' AACVD reaction of both precursors; composite Pt-Bi_2O_3 films were able to evolve hydrogen *via* the photo-reduction of water, a property not observed for films containing either Pt or Bi_2O_3 alone.

$BiFeO_3$ films were grown *via* a multi-source LPCVD reaction between $[Fe(acac)_3]$, $[Bi(O^tBu)_3]$ and air, as well as *via* the dual-source reaction of $[Bi(O^tBu)_3]$ and $[Fe(O^tBu)_3]_2$ without oxidising gas, and, furthermore, *via* the single-source precursor $[\{Cp(CO)_2Fe\}BiCl_2]$ using AACVD. Magnetometry revealed low temperature ferromagnetism and spin-glass behaviour, characteristic of larger particle sizes. Ferroelectric measurements revealed low polarisation but nevertheless indicated films were multiferroic at room temperature. A selection of these films were tested for photo-oxidation of water under visible-light; films displayed high photoactivities with rates in excess of those from optimised TiO_2 films measured under UV-light, highlighting the potential of $BiFeO_3$ films as strong visible-light active photocatalysts.

.

Acknowledgements

Firstly, I would like to thank my supervisors Dr Chris Blackman and Professor Claire Carmalt for allowing me to undertake this project, and for the knowledge, support, guidance and belief they have given me over the last three years. I would also like to thank Dr Paul Southern at the RI for carrying out the magnetometry measurements and for his ideas and suggestions. Thanks also go to Dr Ian Watts for all his efforts with the SQUID at UCL and for discussions on magnetometry. I am indebted to Dr Paul Weaver and Dr Melvin Vopson at the NPL who allowed me to visit and who enthusiastically conducted the ferroelectric measurements for me.

I would like to thank Dr Steve Firth for assistance with DSC and Raman measurements, and Kevin Reeves for his patience and expertise with SEM. Thanks must also go to Dave Knapp and Joe Nolan for fixing the LPCVD kit almost on a daily basis during my first year. For photocatalysis measurements, I would like to thank Dr Geoffrey Hyett, Dr Raul Quesada-Cabrera and Dr Sofia Elouali. I would like to thank Davinder Bhachu for AFM measurements, Dr Emily Smith at the University of Nottingham for XPS analysis and Dr David Pugh for single crystal X-ray diffraction and discussions regarding synthesis. Martin Vickers and Dr Jeremy Cockcroft are thanked for their help with X-ray diffraction analysis, advice, friendship and use of their facilities. I would especially like to thank my fellow group member Dr Stella Vallejos-Vargas for TEM analysis and for use of her prized AACVD apparatus.

Dr Hywel Davies, Dr Rajesh Odedra and Dr John Roberts of SAFC Hitech are thanked for carrying out precursor vapour pressure measurements. I acknowledge my sponsors, UCL and the EPSRC, for funding this studentship award and for providing travel assistance for the numerous conferences and meetings I have attended during the PhD.

Thanks must go to all those, past and present, who I have met and worked with in Lab 308 and the Stills Room, and to those in both offices for providing a friendly research environment and for their support and encouragement which will leave me with fond memories.

Lastly, I would like to thank my family, and especially my mother, for the undying patience and support you have given me since I began the project in 2008 – this work is dedicated to all of you. I hope this thesis goes some way in explaining where I have been and what I have been doing over the last three years.

Contents

List of Figures

Chapter 1 – Introduction

Chapter 2 - Synthesis of bismuth oxide and bismuth ferrite CVD precursors

Chapter 3 - Decomposition studies of potential bismuth oxide single-source precursors

Chapter 4 - Low pressure CVD of bismuth oxide utilising a single-source precursor

Chapter 5 - Aerosol-assisted CVD of platinum incorporated bismuth oxide films

Chapter 6 - Low pressure CVD of bismuth ferrite

Chapter 7 - Dual-source low pressure CVD of bismuth ferrite

Chapter 8 - Aerosol-assisted CVD of bismuth ferrite

List of Tables

Chapter 2 - Synthesis of bismuth oxide and bismuth ferrite CVD precursors

Chapter 4 - Low pressure CVD of bismuth oxide utilising a single-source precursor

Chapter 5 - Aerosol-assisted CVD of platinum incorporated bismuth oxide films

Chapter 6 - Low pressure CVD of bismuth ferrite

Chapter 7 - Dual-source low pressure CVD of bismuth ferrite

Chapter 8 - Aerosol-assisted CVD of bismuth ferrite

List of Abbreviations

AACVD	Aerosol-Assisted Chemical Vapour Deposition
Acac	Acetylacetone
AFM	Atomic Force Microscopy
ALD	Atomic Layer Deposition
APCVD	Atmospheric Pressure Chemical Vapour Deposition
A.U.	Arbitrary Units
BFO	$BiFeO_3$
Bzac	1-Benzoylacetone
CB	Conduction Band
CCDC	Cambridge Crystallographic Data Centre
CI^+	Positive Chemical Ionisation
Cp	Cyclopentadiene
Dbm	Dibenzoylmethane
DFT	Density Functional Theory
DLI-CVD	Direct Liquid Injection Chemical Vapour Deposition
EDX	Energy Dispersive Analysis of X-rays
E_g	Energy Gap (Band-gap)
Emu	Electromagnetic Units
eV	Electron volt
FT-IR	Fourier-Transform Infrared
GADDS	General Area Detector Diffraction System
Hfac	Hexafluoroacetylacetone
ICDD/ICSD	Inorganic Crystal Structure Database/International Centre for Diffraction Data

ITO	Indium Tin Oxide
JCPDS	Joint Committee on Powder Diffraction Standards
LPCVD	Low Pressure Chemical Vapour Deposition
ME	Magnetoelectric
M-H	Magnetisation (M) – Magnetic Field (H)
Mmp	1-Methoxy-2-Methyl-2-Propanol
MOCVD	Metalorganic Chemical Vapour Deposition
MS-DSC-TGA	Mass Spectrometry – Differential Scanning Calorimetry – Thermogravimetric Analysis
NHE	Normal Hydrogen Electrode
NMR	Nuclear Magnetic Resonance
Oe	Oersted
PDF	Powder Diffraction File
PLD	Pulsed Laser Deposition
PXRD	Powder X-ray diffraction
RMS	Root mean square
RSF	Relative Sensitivity Factor
SEM	Scanning Electron Microscopy
STO	Strontium Titanate
SRO	Strontium Ruthenate
T_B	Blocking Temperature
^{t}Bu	*tert*-Butyl
T_C	Curie Temperature or Critical Temperature
TEM	Transmission Electron Microscopy
T_F	Freezing Temperature

Tfac	1,1,1-Trifluoroacetylacetone
Thd	2,2-6,6-Tetramethyl-3,5-heptanedione
TM	Transition Metal
T_N	Neel Temperature
UV	Ultraviolet
UV-Vis	Ultraviolet-visible spectroscopy
VB	Valence Band
V_P	Vapour Pressure
WDX	Wavelength Dispersive Analysis of X-rays
XPS	X-ray Photoelectron Spectroscopy
XRD	X-ray Diffraction
ZFC-FC	Zero Field Cooled – Field Cooled

1 Introduction

Over the last thirty years, interest in the synthesis and functional properties of bismuth containing metal oxides has greatly increased, and was stimulated by the discovery of the high T_c superconductor oxides $Bi_2Sr_2Ca_{n-1}Cu_nO_{2n+4+x}$ during the late 1980s. Bismuth oxide itself is not without its own functionality - it has seen use in a wide variety of applications including gas sensors, solid oxide fuel cell electrolytes, and as active visible light photocatalysts. Details of the growth of thin films of bismuth oxide, mostly *via* solution methods such as sol-gel processing and dip-coating are already abundant in the literature, however details of the growth of bismuth oxide films *via* chemical vapour deposition (CVD) are extremely limited. This is due to the scarcity of suitably volatile precursors for CVD, and the lack of single-source precursors to such materials. This, in turn, has limited the research conducted on the synthesis of bismuth oxide and bismuth oxide based materials and their utility in critical everyday applications.

This introduction chapter is designed to set the theme with regard to research into the deposition of bismuth oxide containing films, principally using CVD. To begin with, a brief introduction to film growth *via* CVD, together with the importance of precursor design, will be given. Bismuth oxide and its uses will then be described, along with synthetic routes to bismuth oxide precursors, which will be followed by examples of deposition of bismuth oxide thin films. The introduction will then focus upon the fascinating and emergent field of multiferroics, including the synthesis of bulk and thin film multiferroics and then moving onto their characterisation and functional testing.

1.1 Film growth *via* chemical vapour deposition

Chemical vapour deposition has been used extensively for deposition of thin films of functional materials and is commonly used by industry for large-scale coatings and device manufacture. It has a number of advantages that include, but are not limited to the following: (a) excellent substrate coverage, (b) low-cost, (c) ease of scale-up, (d) control over thickness and morphology and finally, (e) high throughput capabilities, all of which the electronics and glazing industries rely upon. The definition of CVD allows it to be differentiated from other thin film deposition processes - CVD may be simply described as a chemical process by which a solid coating is deposited *via* the chemical transformation of gaseous precursors. Film deposition *via* CVD involves homogeneous gas phase reactions and/or heterogeneous chemical

reactions that occur on or near the vicinity of a heated surface (substrate) that possesses the required activation energy to lead to the formation of a thin film.

CVD has a number of variants, which will be discussed later; however the different surface processes in a CVD reaction will now be addressed.

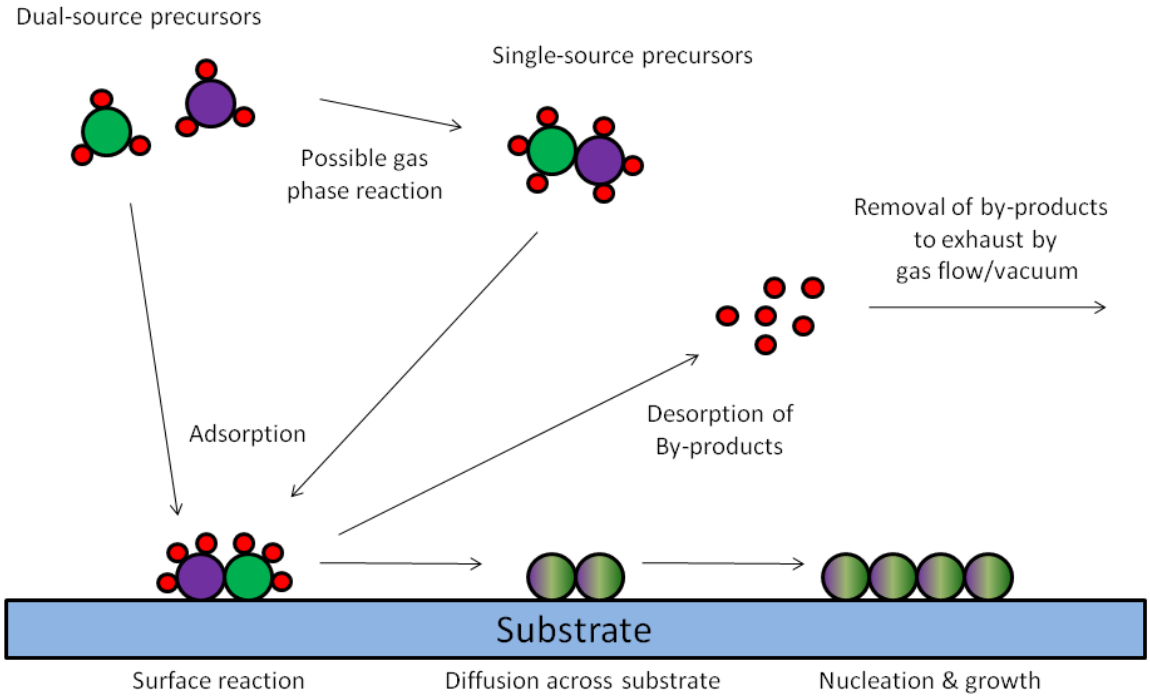

Figure 1: Schematic showing the individual stages of the CVD process.

A number of key steps are characteristic of a CVD process (Figure 1). The first step is the generation of a gaseous precursor species as a result of one or more of the following - heating, applying reduced pressure, a carrier gas flow or, in the case of AACVD, through an aerosol mist. The second step is the transport of the precursor(s) to the reaction chamber. Note that in a multi-source precursor CVD system, the individual precursors may meet in the gas phase through a mixing chamber and may undergo gas phase reactions here. The third step is therefore the gas phase reactions that form intermediate species. At quite elevated temperatures required for precursor decomposition, the gas phase intermediate species decompose to powders and other volatiles. The powders may deposit onto the substrate and act as crystallisation centres, whilst the volatiles are transported away as by-products of the reaction. Preferably, at not such high temperatures, the intermediate species diffuse across close to the surface of the substrate (boundary layer). A number of sub-processes are then initiated.[1]

1. Absorption of gaseous species onto substrate, leading to chemical reaction on the surface. Synthesis of deposit (film) and by-products.
2. Diffusion across substrate by deposit to form crystallisation centres.
3. By-products removed by convection or diffusion.
4. Removal of unreacted precursor molecules and by-products, usually *via* a carrier gas.

There are three main types of film growth associated with CVD – epitaxial growth, polycrystalline growth and amorphous growth. Clearly, amorphous growth leads to no crystallinity in the resultant film, and in polycrystalline growth the film contains micro-crystalline grains with randomly aligned lattice orientations. Epitaxial growth occurs when the lattice of the film tends to match that of the substrate, however in the case of $BiFeO_3$ and similar ferroelectrics, epitaxial strain induced by lattice mismatch may be an important factor for enhancement of polarisation and should not be ignored. Preferred orientation can also occur when the crystal lattice of the film is not matched to the substrate, but instead it is parallel or perpendicular to the substrate surface. The atoms on the substrate surface can be adsorbed to form clusters of adatoms that can then coalesce to form a continuous film *via* one of the mechanisms shown in Figures 2 - 4. Cluster growth tends to occur preferentially at defect sites (kinks, steps) on the surface of the substrate and is governed by kinetic and thermodynamic constraints.

1.1.1. Island growth (Volmer-Weber growth)

Island growth occurs as a result of stronger interactions between the atoms contained within the film compared to the interaction between the film and the substrate, and as cluster formation typically occurs in most CVD processes, island growth is by far the most common mechanism. The adatoms nucleate on the substrate, growing into islands that coalesce to form a continuous film (Figure 2).

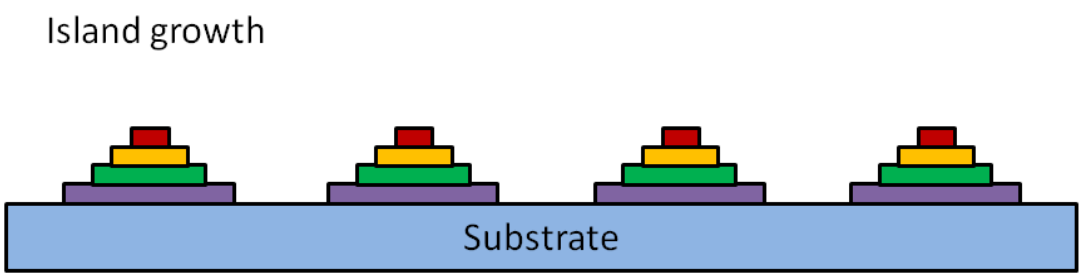

Figure 2: Island growth mode of film deposition and growth, commonly observed in most CVD processes.

1.1.2. Layer growth (Franck-van der Merwe growth)

Conversely, for a film to grow *via* a layer growth mechanism, layered islands of the film grow and eventually coalesce in order to form a continuous film (Figure 3). Here, the affinity between the atoms in the film and the atoms on the surface of the substrate are similar.

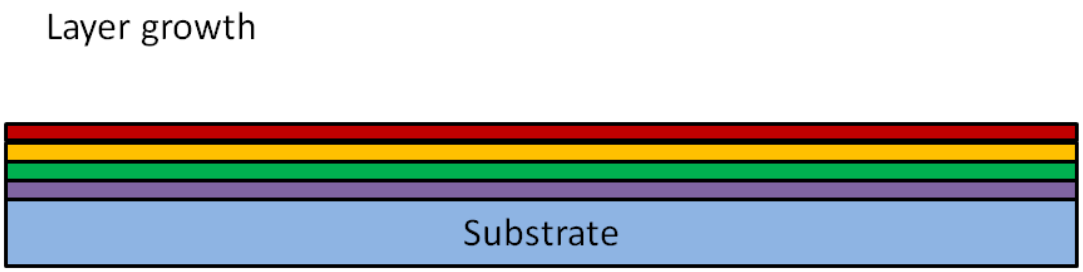

Figure 3: Layer growth mode of film deposition.

1.1.3. Intermediate growth (*Stranski-Krastanov)*

Quite simply, intermediate film growth is a combination of island and layer growth (Figure 4). The deposited atoms in the film are less weakly bound to each other than to the surface of the substrate, resulting in growth of a monolayer (Franck-Van der Meer type) first, followed by a columnar-style layer afterwards (Volmer-Weber type).

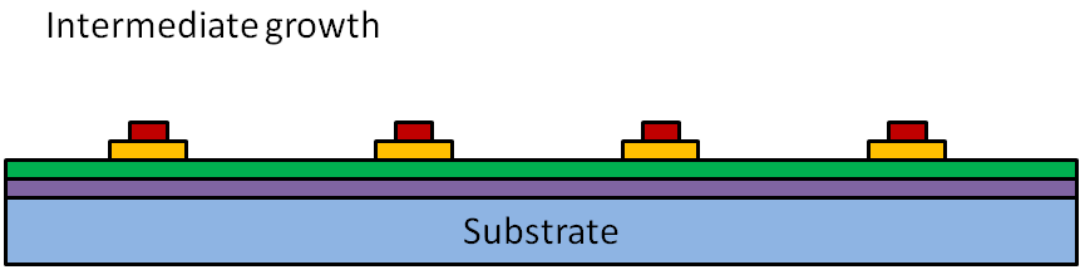

Figure 4: Intermediate film growth mechanism.

Indeed, the reaction kinetics for a CVD system are extremely complex, involving gas phase reactions and reactions upon the substrate, as well as chemisorption and desorption processes. Nevertheless, kinetic data of a particular CVD process may be obtained using the rate of deposition (film thickness as a function of time) so that process parameters such as the activation energy may be calculated and compared for different systems:

Deposition rate = A exp (-E_a/RT), where A is a pre-exponential factor, E_a is the activation energy, R is the molar gas constant and T is the substrate temperature in Kelvin.

An Arrhenius plot of the logarithm of deposition temperature against the reciprocal of substrate temperature can reveal whether the reaction is chemical kinetics or mass transport limited, whilst the gradient of the plot corresponds to the activation energy for the process.[1]

1.2 CVD Precursors

The CVD process has traditionally relied on the availability of volatile precursors with suitable decomposition characteristics. It is fair to say that the growth of the electronics and coatings industries during the last thirty years have catalysed research into precursor development, and armed with a better understanding of the processes involved, the range of commercially available precursors has increased rapidly. Recent advances in liquid-injection and aerosol techniques for precursor delivery have to some extent overcome some of the problems associated with lack of volatility or poor decomposition; however these processes are yet to be fully implemented on a large scale for commercial purposes and for growth of thin films in industry. Typically, metalorganics, metal hydrides and halides are often employed as precursors, with hydrides generally possessing the highest volatilities but lowest stabilities. Metal-organics are perhaps the most popular class of precursor as they are commonly liquids with high vapour pressures, and have appreciable stabilities and low decomposition/deposition temperatures. CVD is usually conducted using multiple precursors, for example, deposition of indium oxide may require an organoindium source in conjunction with an oxygen gas co-reactant. Similarly, deposition of strontium bismuth tantalate (SBT) films may rely on individual strontium, bismuth and tantalum sources, where each precursor could possess contrasting volatilities, mass transport and decomposition characteristics, not to mention the overall potential for additional, unwanted gas-phase reactions that could occur between the precursors during the deposition process. When multi-component films are sought, in, for example, mixed-metal oxides, single-source precursors that possess all necessary components with the desired bonds already preformed offer control of film stoichiometry, and in some cases lower decomposition temperatures, as well as the main advantage of fewer deposition parameters to control. An example is the use of the $[Me_2GaAs^tBu]_2$ dimer that contains a preformed Ga-As bond for the growth of GaAs films, which is believed to leave isobutene and methane as volatile by-products (Figure 5).[2]

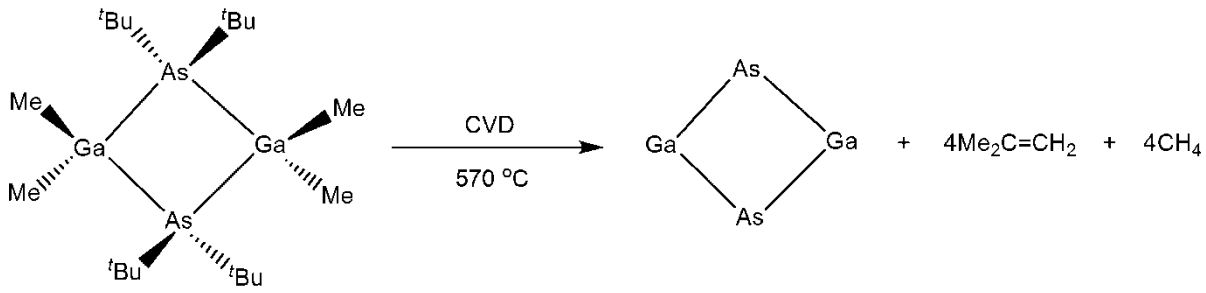

Figure 5: Decomposition of the single-source precursor $[Me_2GaAs^tBu]_2$ at temperatures > 570 °C results in deposition of GaAs, producing isobutene and methane as volatile by-products.

For deposition of bismuth oxide, an ideal precursor would have at least one pre-formed Bi-O bond, as this should theoretically lower the energy required for film formation. Ideally, saturation of the bismuth centre with oxygen atoms is preferred in order to obtain fully oxidised films, inhibit oligimerisation, as well as to avoid impurities if other atoms were coordinated to the metal centre. However, the availability of such single-source precursors is generally fairly limited and they tend to be less volatile and more air sensitive than dual-source precursors.

1.3 Precursor design

The mechanism of precursor decomposition is important as it can dictate its suitability for CVD; the nature of the ligand and the metal-ligand bond control the pathway of decomposition. There are generally two main methods of decomposition - β-hydride elimination (Figure 6) and C-C bond cleavage followed by hydrogen abstraction; however free radical processes are also thought to exist as well as α- and γ-H eliminations.[3] β-hydride elimination is prevalent in alkyl moieties such as ethyl, iso-propyl and *tert*-butyl groups because they contain β-hydrogen atoms. One could infer that smaller-sized ligands are therefore preferable as their contribution to film contamination would be limited. Precursors containing a weak adduct bond to a ligand (such as a bond to THF) are also sought-after, as the ligand helps inhibit oligimerisation, whilst the bond has a weak dissociation energy and will easily break during the CVD process. The use of donor- functionalised ligands aids in saturating the metal centre and reducing the polarising strength of the metal ion by charge transfer from donor ligands. The use of sterically demanding donor-functionalised ligands aids volatility by inhibiting oligimerisation. Such ligands that have at least two coordination sites may easily surround a metal centre; the alcoholate function provides charge neutralisation whilst the donor arm compensates for the steric and electronic demands of the metal centre whilst acting as a further coordination site to additional metals (in the case of heterometallic precursors). The chelate effect further improves the stability of the complex with respect to moisture.[4]

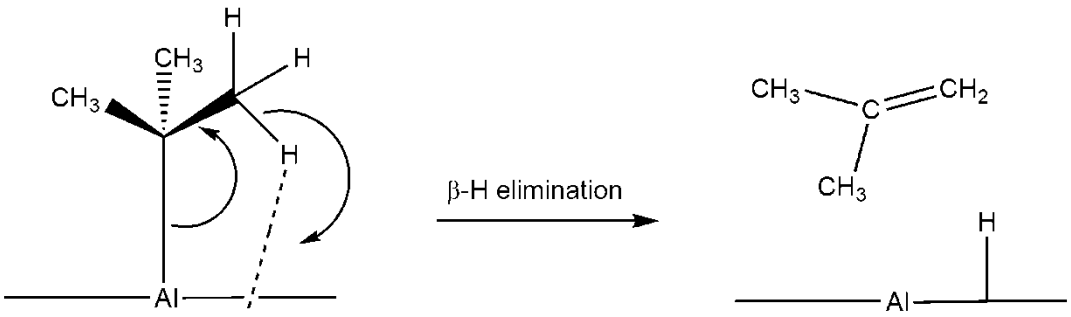

Figure 6: β-hydride elimination using [Al(^{t}Bu)$_3$] as an example. The tri-*tert*-butyl radical is eliminated from the surface *via* β-hydride elimination, leaving isobutene and surface bound hydrogen.[3]

In summary, the key properties for a good CVD precursor to possess would be as follows:

1. Good stability at ambient conditions.
2. Readily available or easy to synthesise.
3. Low-cost, low toxicity and flammability.
4. Volatile under mild conditions, and whose vapour is stable at ambient conditions.
5. Deposit films at a suitable rate and temperature.
6. Deposit films that are low in contamination (e.g. halides, carbon).

It is often difficult to obtain all such properties for a single precursor, for example a metal hydride may be suitably volatile but thermally explosive. Likewise a metal *β*-diketonate may be stable and inexpensive, but may require high reaction temperatures or lead to elevated levels of carbon contamination. In either case, a level of compromise is usually sought and the conditions carefully tailored in order to achieve optimal film growth.

1.4 The most common types of CVD

This section is intended to give an overview of the most common variants of CVD used today. More precise details concerning the CVD experimental set up and conditions employed will be given at the beginning of every chapter that contains film growth *via* CVD.

1.4.1 Low Pressure (LP)CVD

LPCVD relies on precursors that may be transferred into the gas phase *via* reduced pressure, as well as by resistive heating and *via* a carrier gas. This method is particularly suitable for air sensitive precursors and deposition of non-oxides because the vacuum should be able to remove

most of the air and moisture from the system. Likewise, unreacted precursor molecules and by-products are carried away by the vacuum to the exhaust. Film growth rates tend to be low at the rate of *ca.*100 nm/hr, however this slow growth rate can result in high quality, crystalline films and offers the possibility of epitaxial growth. Due to the requirement for low pressures and accurate monitoring of gas flow rates, high quality equipment is required and the cost of vacuum pumps and mass flow lines with controllers make this method initially more expensive to set up. Nevertheless, LPCVD is perhaps the most popular method of CVD and is typically used in device manufacture by the electronics industry, as it possesses the advantages of high film purity, epitaxial growth and reasonable film growth rates.

1.4.2 Atmospheric Pressure (AP)CVD

APCVD relies on precursors that are volatile at atmospheric pressure, and usually involves the use of precursors that are commercially available. Air sensitive precursors may also be used. Usually, resistive heating is required to transfer the precursor to the gas phase, in conjunction with an inert carrier gas for transport to the reaction chamber. Dual-source APCVD reactions are much more common than single-source reactions, and as the equipment is generally much more straightforward than that required for LPCVD, the process is relatively inexpensive and easy to scale up. Depositions are also extremely fast and optimisation of conditions can lead to good quality, reproducible films. Indeed, the large-scale industrial production of coatings on glass windows uses this method of CVD.

1.4.3 Aerosol-Assisted (AA)CVD

Aerosol-assisted CVD relies on precursors that have a good solubility in suitable solvents that can then transfer into an aerosol by use of a piezoelectric device. The traditional requirement of precursor volatility may be overcome if the precursor is soluble in a solvent that is easily "misted," of which typically toluene, THF and hexane are the best examples. The aerosol mist, usually consisting of droplets between 1-10 μm in diameter, is then carried into the reaction chamber by means of an inert gas supply. In AACVD, the choice of solvent is almost as important as the choice of precursor. The solvent itself should not have a boiling point lower than 60 °C otherwise it will rapidly evaporate and leave the precursor behind. The solvent should also have a low viscosity and should not adversely react with or affect the precursor dissolved within it. The other advantage of AACVD is that through the control of intensity of the piezoelectric humidifier and carrier gas flow, the aerosol droplet size, mist intensity and flow rate may be controlled. These advantages, coupled with the growing migration over to

solution-based deposition methods for growth of functional materials (including nanoparticle incorporated materials) makes AACVD a popular film deposition method at present. The process is a relatively low cost one and can be used for air sensitive compounds if suitable glassware and apparatus is available. Deposition rates are typically high and although it frequently utilises single-source precursors, the process may be optimised for controlled, multi-source depositions using appropriate equipment. It is possible, however, that the use of organic solvents could lead to high levels of carbon contamination in the resultant films.

1.4.4 Plasma-enhanced (PE)CVD

PECVD requires the use of a plasma to ionise and dissociate precursor gases, and also serves as the heating source for the substrate. Plasma, in this case, may be defined as a gas where the majority of the molecules are ionised. The plasma is produced *via* a DC discharge between two electrodes, between which lies the reacting precursor gases. The result is a lower deposition temperature together with a high deposition rate; however complex and expensive apparatus is required for generation of the plasma and is therefore not widely employed in research but has found application in the area of semiconductor wafer synthesis.

1.4.5 Direct-Liquid Injection (DLI-)CVD

Precursors that possess low volatilities or poor decomposition characteristics may be used for DLI-CVD if they are soluble in suitable solvents and are stable in such solvents for a reasonable length of time. The precursor is then delivered to the evaporator (through an "injector") at a precise rate and transported *via* a carrier gas to the reaction zone close by (see section on "CVD of $BiFeO_3$ films," Figure 18). The main advantage of DLI-CVD is the rapid, controlled evaporation of precursors coupled with the short delivery time of the precursor vapour into the reaction zone, and it has been commented that high growth rates can be achieved.[5] For multi-component materials, the individual precursors may be mixed in the appropriate ratios and then dissolved in a single solution. The evaporator is usually held at a fixed temperature, so it is important that all components of the precursor mixture evaporate at similar temperatures and that they are stable in solution at room temperature for extended periods.

1.5 Bismuth (III) Oxide (Bi_2O_3)

There are a number of formal oxidation states displayed by bismuth in its oxides, notably 3^+ (Bi_2O_3) and 5^+ (Bi_2O_5) (and mixed valent states $3/5^+$ (Bi_2O_4, Bi_4O_7)), of which the 3^+ state is the most common and occurs naturally as the mineral bismite, however the 5^+ oxidation state in bismuth oxides is doubtful and therefore the references to bismuth oxide from hereon in this thesis will correspond to bismuth(III) oxide. Bi_2O_3 is the most basic of the heavy pnictogen oxides and easily dissolves in mineral acids to form salts. Compounds purporting to be composed of Bi_2O_5 are extremely rare in comparison to its Group 15 relatives arsenic (As_2O_5) and antimony (Sb_2O_5), and almost always contain impurity phases.[6]

Indeed, the chemistry of bismuth oxide is almost entirely dominated by the stable 3^+ oxidation state, which has five fully crystallographically characterised polymorphs: α, β, γ, δ and ε phases, along with a triclinic ω- phase that was reported to have been grown on a BeO susbtrate.[7] These phases may be interconverted *via* heat treatment and cooling. The low temperature monoclinic α-phase together with the high temperature face centred cubic (fcc) δ-phase are stable, whereas the other phases are metastable.[8] The α-phase converts to the δ-form upon heating at T = 729 °C, which itself, is stable up to the melting point at 824 °C. Upon controlled cooling, the δ-phase forms first, followed by the tetragonal β-phase around 650 °C and then the body centred cubic (bcc) γ-phase closer to 640 °C, however this phase selectivity process is often difficult to control. The β-phase can then be transformed to the stable α-phase upon cooling below 650 °C, whilst the γ-phase also converts to the α-phase *via* cooling but has been reported to persist even as low as room temperature.[9] At temperatures of 400 °C and lower, the metastable orthorhombic ε- phase irreversibly converts to the α- phase.[10] The α- and γ-bcc forms are semiconductors, whereas the β- and δ-fcc forms are oxide ion conductors; the highest conductivity occurring with the δ-phase (see later). The phase diagram of Bi_2O_3 is shown in Figure 7.

In addition to those phases mentioned in Figure 7, substoichiometric phases BiO, $Bi_2O_{2.33}$ and $Bi_2O_{2.75}$ have also been isolated but usually as impurity phases in Bi_2O_3.

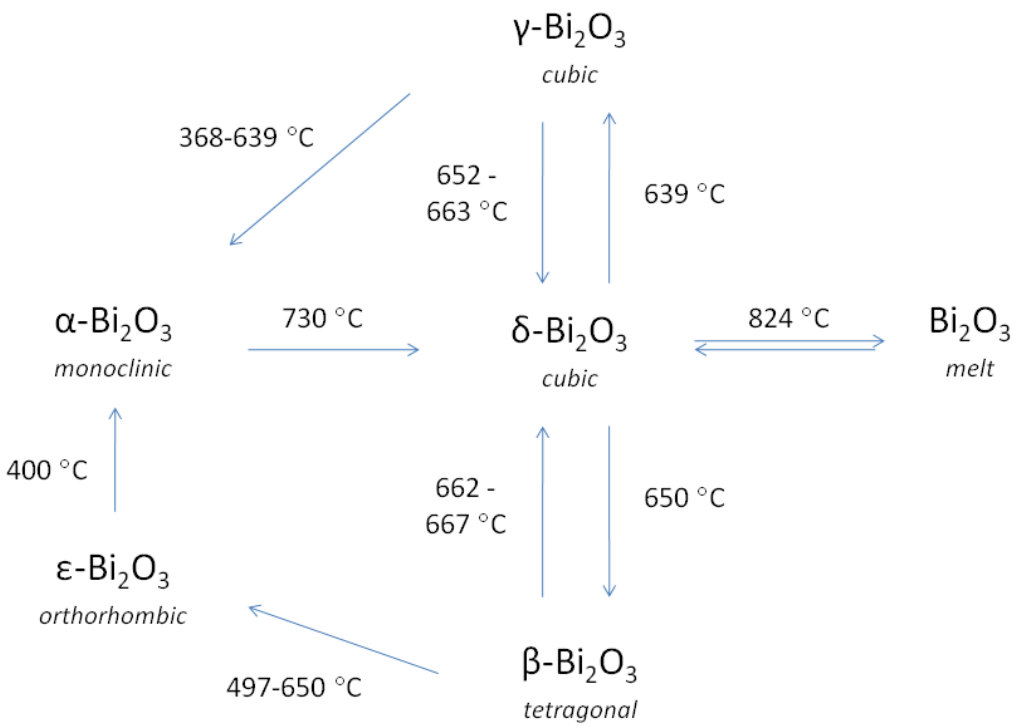

Figure 7: Transformations according to temperature for the different structurally characterised phases of Bi_2O_3.[9]

1.6 Applications of Bismuth Oxide

The suggested applications of bismuth oxide are currently restricted to its use as a photocatalyst for degradation of organic pollutants and as the electrolyte material in solid oxide fuel cells. The drive to develop cheap, portable and renewable energy sources led to the discovery in 1949[11] that δ-Bi_2O_3, with the fluorite structure, possessed the highest oxide ion conductivity of any material known at that time. There are a number of reasons put forward to explain the high oxide ion conductivity of this phase. Firstly, it is known that a quarter of the oxygen sites are vacant in the fluorite structure lattice; the $6s^2$ lone pair on the bismuth(III) leads to a high polarisability of the network of cations (giving rise to oxide ion mobility), coupled with the ability of the bismuth atom to accommodate highly disordered surroundings.[12] Since this discovery, δ-Bi_2O_3 has been doped with metal oxides La_2O_3, Gd_2O_3, Y_2O_3 and Er_2O_3 as solid solutions in order to stabilise this phase at lower temperatures and improve conductivity.[13] The unit cell packing of the most commonly observed bismuth oxide structures are displayed in Figure 8.

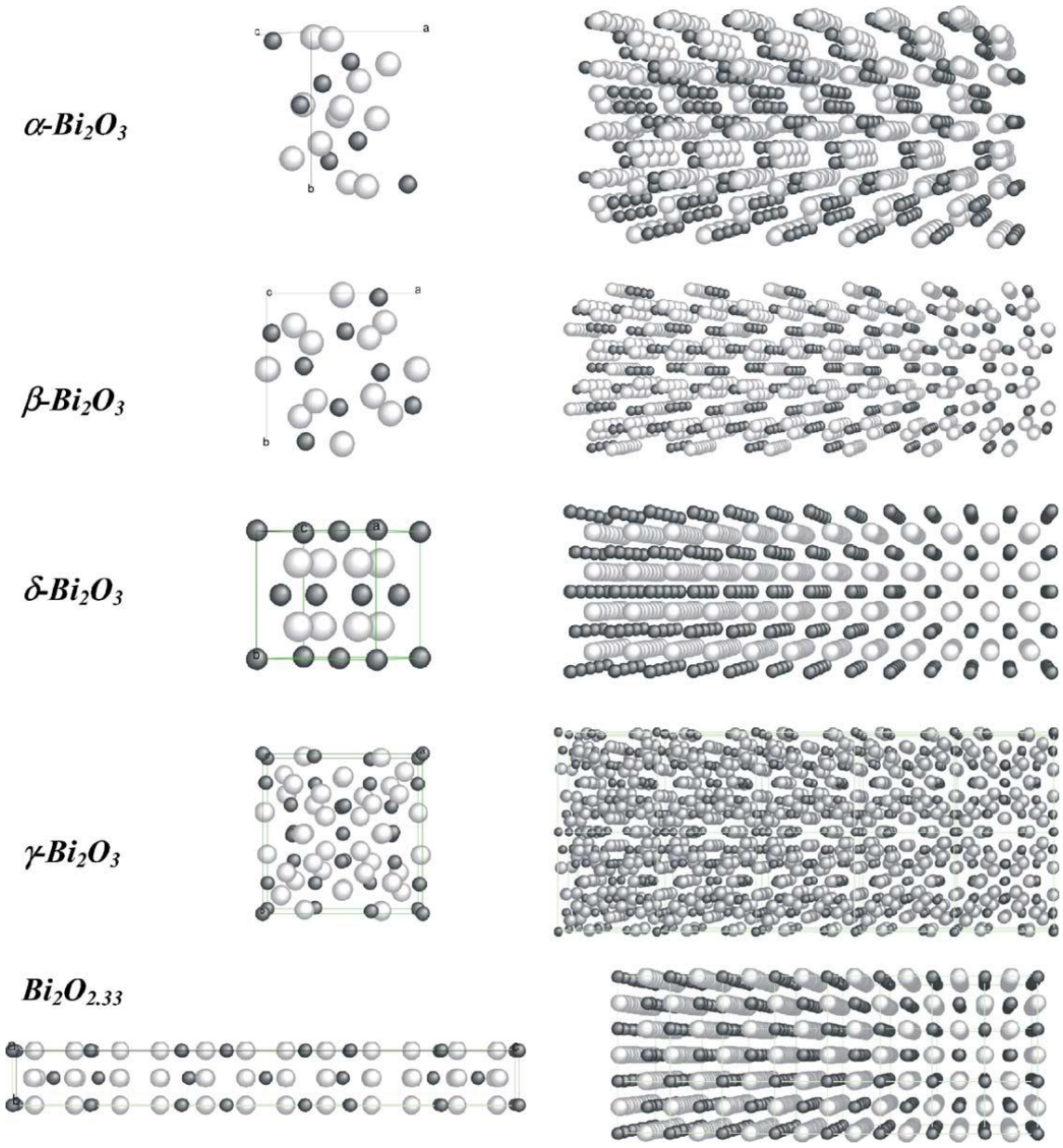

Figure 8: Unit cells and crystal structures of the various crystallographically characterised Bi_2O_3 phases. The oxygen deficient $Bi_2O_{2.33}$ phase is included. The dark spheres represent the bismuth cations and the lighter spheres correspond to the oxygen anions. Image reproduced from the paper by Cabot *et al.*[14]

1.6.1 Bi_2O_3 photocatalysts

Given that the band-gap of bismuth oxide is usually considered to be in the visible range of the spectrum (2.29 – 3.31 eV), there have been many reports on the photocatalytic activity of bismuth oxide for removal of organic pollutants and degradation of organic dyes.[15] Bismuth oxide has also been used as a photo-sensitizer in conjunction with other metal oxides, such as TiO_2, whose band-gaps are too high to serve as serve as efficient photocatalyts under visible light. Hierarchical δ-Bi_2O_3 nanostructures were synthesised *via* an aqueous route using

$Bi(NO_3)_3.5H_2O$ and NH_4VO_3 and were found to possess high photocatalytic activity under visible light – the activity was between six to ten times higher than that of commercial samples for degradation of Rhodamine B dye.[16] Wang *et al.*[17] synthesised nanocrystalline α-Bi_2O_3 powders *via* a sonochemical route and observed an 86% photocatalytic destruction of methyl orange dye in 100 minutes under visible light irradiation. Thin films of α- and β-Bi_2O_3 were synthesised *via* a sol-gel route on glass substrates, followed by annealing, with films displaying appreciable photocatalytic activity for degradation of Rhodamine B dye under 365 nm UV-light irradiation, and it was found that the tetragonal β- phase was more photocatalytically active than the α- phase.[15]

Gurunathan *et al.* observed that doping γ-Bi_2O_3 powders with transition metal ions (Fe, Cr, Pd, Ru, Co, Ni) led to photocatalytic hydrogen production under visible light irradiation ($\lambda > 350$ nm) when using methyl viologen as an electron relay, resulting in quantum yields as high as 1.28%.[18] The incorporation of transition metal ions, particularly ruthenium, was believed to increase photosensitisation in comparison to the undoped sample; however no explanation was given for the formation of hydrogen, albeit in small amounts, from the undoped sample.

Recently, platinum nanoparticle loaded Bi_2O_3 was found to exhibit improved photocatalytic activity for oxidation of acetaldehyde and methanol which was ascribed to the positive conduction band level of Bi_2O_3 being able to transfer plasmon induced electrons from the platinum nanoparticles.[19] Somewhat surprisingly, it appears that very little work has been conducted on the ability of undoped bismuth oxide (films or powders) to photo-oxidise water given the relatively positive valence and conduction band potentials of bismuth oxide.[20]

1.6.2 Gas Sensing

The accurate detection and quantification of trace exhaust gases from internal combustion engines in motor vehicles is currently of importance as part of the government's ambitions to limit greenhouse gas emissions. It has recently been demonstrated that undoped bismuth oxide exhibits promising gas sensing properties, with nanopowder α-Bi_2O_3, γ-Bi_2O_3 and $Bi_2O_{2.33}$ based sensors found to be suitable for detection of NO, more importantly in the presence of NO_2 in oxidising environments at temperatures between 200 – 500 °C.[14] However, they were reported to be ineffective in sensing for CO, CO_2 and hydrocarbon gases.

β-Bi_2O_3 nanosheet based sensors were shown to be effective for detection of CO_2 at operating temperatures as low as 150 °C, with response and recovery times of 40 and 50 seconds, and a saturation level of up to 11000 ppm.[21] Bismuth oxide film-based gas sensors grown *via* electron beam evaporation have also been demonstrated to be highly effective in the detection of smoke at room temperature and exhibited low response and recovery times.[22]

Bismuth oxide has also been used in conjunction with tin oxide (SnO_2) in gas sensor applications. It was found that the selectivity of SnO_2 gas sensors toward CO detection was significantly improved by doping with Bi_2O_3, which resulted in the formation of bismuth stannate ($Bi_2Sn_2O_7$) above 800 °C.[23] Bismuth stannate acts as a molecular sieve, only allowing CO molecules to adsorb on the surface of the sensor, therefore imparting a high degree of selectivity to CO in the device. Similarly, Bi:Sn oxide sensors were found to be effective for NO detection at 250 °C and displayed increasing sensitivity toward C_2H_5OH and CH_4 at temperatures around 400 °C at the expense of NO detection.[24]

1.7 Applications of bismuth oxide based materials

The very high abundance and low toxicity of elemental bismuth and its oxides have played fundamental roles in driving research and development into bismuth oxide containing materials for a variety of applications. Heterometallic bismuth oxide based materials have displayed potential to be used in applications as diverse as superconductors, gas sensors, data storage, catalysis and solid oxide fuel cells; the most common examples of which will now be discussed.

1.7.1 Heterometallic bismuth oxide based ferroelectrics

Before beginning a description of the different types of bismuth oxide containing ferroelectric oxides, it is important to begin with a description of the structures they tend to adopt. The vast majority of heterometallic bismuth oxide based materials adopt the perovskite ($CaTiO_3$) structure with general structure ABO_3, where the 'A' and 'B' atoms correspond to cations of two different sizes – 'A' being much larger than 'B'. In these cases, the bismuth ion would correspond to cation 'A' and the transition metal to cation 'B', with the O anion taking the role of the counter anion for charge neutralisation, and therefore corresponding to oxygen in oxide materials. Traditionally, the perovskite lattice consists of these small 'B' cations within the oxygen octahedra with the larger 'A' cations in a 12-fold coordination. For the $A^{3+}B^{3+}O_3$ type of perovskites, which include the multiferroics $BiFeO_3$ and $BiMnO_3$, the most symmetric structure observed is rhombohedral (space group *R*3*c*), and involves rotation of the BO_6 octahedra with respect to the cubic structure. A typical cubic perovskite structure is shown in Figure 9. The blue spheres in the corners of the cube represent the 'B' cations, the green sphere located in the centre represents the 'A' cation and the face-centred positions are occupied by the oxygen ions (red).

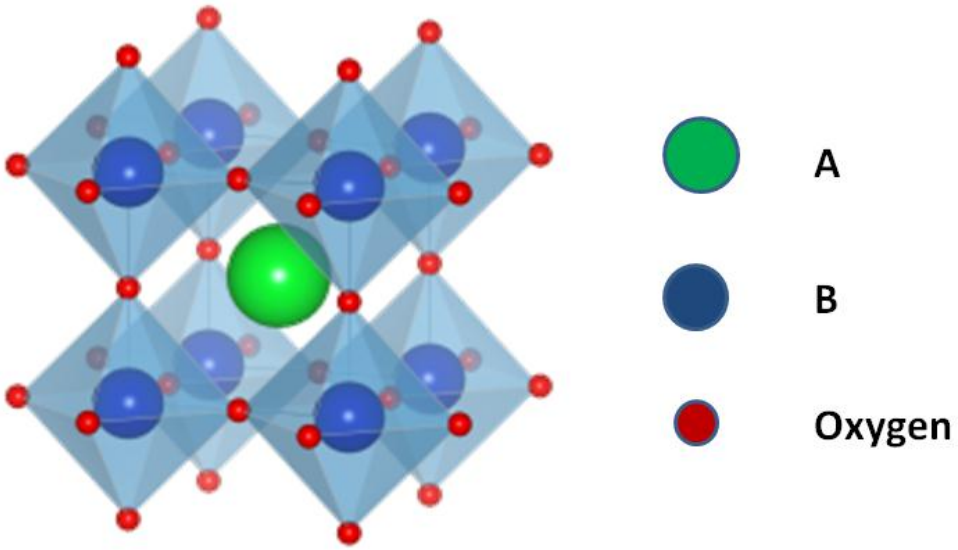

Figure 9: Typical cubic perovskite unit cell, where the green sphere represents the 'A' cations in the cuboctahedral sites, the blue spheres represent the 'B' cations which are located at the centre of the octahedral sites formed by the oxygen anions (red spheres).

As the relative ion size requirements for stability of the cubic structure are quite stringent, any slight buckling and distortion can produce several lower symmetry distorted versions, whereby the coordination numbers of 'A' cations, 'B' cations or both are reduced. Indeed, there are many ABO_3 compounds for which the ideal cubic structure is distorted to a lower symmetry such as tetragonal or orthorhombic. Layered perovskites (Ruddlesdon-Popper and Aurivillius type) still contain the same ABO_3 structure but each is separated by a particular motif; the differentiating characteristics of which are the type of motif separating the layers and the offsetting of the layers from each other. Further description of the structures of bismuth oxide containing Aurivillius perovskites together with their applications will be given in the following sub-sections.

1.7.1.1 Bismuth Titanate

Ferroelectric materials have been widely investigated for applications in non-volatile random access memory (NVRAM) and dynamic random access memory (DRAM) devices. Bismuth titanate, $Bi_4Ti_3O_{12}$, discovered in 1949 and found to be ferroelectric in 1961,[25] has been known to exhibit a strong ferroelectric polarisation since 1968, when a high spontaneous polarisation of 50 $\mu C/cm^2$ was recorded at room temperature on single crystals of the material in the monoclinic *a*-*c* direction.[26] The perovskite structure of $Bi_4Ti_3O_{12}$ belongs to the Aurivillius family of perovskite compounds that contain the general formula $(Bi_2O_2)^{2+}(A_{m-1}B_mO_{3m+1})^{2-}$, consisting of '*m*' perovskite units sandwiched between bismuth oxide layers, where A and B are the two types of metal cation (m = 3 for $Bi_4Ti_3O_{12}$). It has an orthorhombic (pseudotetragonal) structure with lattice parameters a = 5.448 Å, b =5.411 Å and c = 32.83 Å.[27] The explanation

for its ferroelectric property stems from the relatively small amplitude displacive perturbations away from a high symmetry prototype parent structure, whereby there is an *a*-axis displacement of A-site Bi atoms with respect to the chains of TiO_6 octahedra, and *not* the movement of B-site Ti atoms moving to the edges of the octahedron (unit cell displayed in Figure 10).[28] Problems such as high leakage current and a decrease in remnant polarisation (due to fatigue) have limited the practical use of $Bi_4Ti_3O_{12}$ in lead-free ferroelectric devices, however, lanthanum substituted bismuth titanate has emerged as a viable alternative.[29]

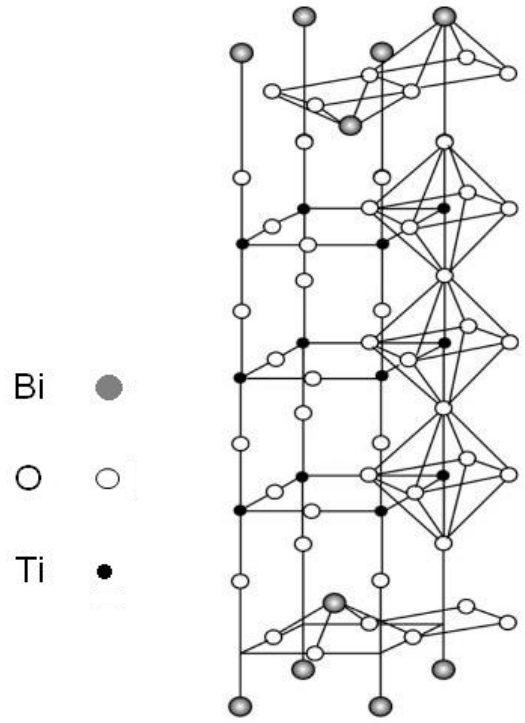

Figure 10: Structure of the unit cell of $Bi_3Ti_4O_{12}$, containing three layers of Ti-O octahedra in between the $(Bi_2O_2)^{2+}$ layers.[29]

Bi_2TiO_7, although not ferroelectric nor piezoelectric, has a large dielectric constant and thin films of Bi_2TiO_7 have displayed low leakage currents, making them a potential candidate for use in buffer layers or in storage capacitors.[30]

1.7.1.2 Strontium Bismuth Tantalate (SBT)

Strontium bismuth tantalate ($SrBi_2Ta_2O_9$, SBT) has been demonstrated to be a viable option for robust, fatigue–free ferroelectric capacitors. The structure of SBT is composed of pseudoperovskite $(SrTa_2O_7)^{2-}$ blocks, which are comprised of double TaO_6 octahedra,[31] where the strontium occupies the A site, and these blocks are interleaved with $(Bi_2O_2)^{2+}$ insulating layers. These are reported to help prevent degradation from the use of high electric fields. The ferroelectric distortion is attributed to the displacement of Ta ions as well as the tilting of the

TaO_6 octahedra.[32] Films of lanthanum-substituted bismuth titanate ($Bi_{3.25}La_{0.75}Ti_3O_{12}$), grown *via* PLD, have been demonstrated to have higher resistance to fatigue, have larger remnant polarisation values (P_r = 16-20 μC/cm^2) and possess lower processing temperatures than those of SBT films, however leakage current still remained high.[29] Similarly, the related materials strontium bismuth niobate ($SrBi_2Nb_2O_9$) and $SrBi_2NbTaO_9$[31] have also been shown to have adequate ferroelectric polarisations at room temperature, together with low fatigue and low processing temperatures which are crucial for device manufacture.[33]

1.7.1.3 Bi_2WO_6 and $BiMO_4$ (M = Nb, Ta)

The ferroelectric oxide, bismuth tungstate (Bi_2WO_6), has also been the subject of numerous investigations into the relationship between its structure and its temperature-dependent ferroelectric properties. It is also a member of the Aurivillius family of perovskites with general formula $[Bi_2O_2][A_{n-1}B_nO_{3n+1}]$.[34] At 660 °C a phase transition occurs whereby the space group switches from $P2_1ab$ to $B2cb$, however at 960 °C (Curie Temperature, T_c) an additional phase change takes place that results in the WO_4 layers being transformed from corner-sharing octahedral sheets to edge-sharing octahedral chains.[35] Thin films of $BiNbO_4$ deposited on silicon substrates *via* pulsed laser ablation possessed electrical properties which varied according to film thickness; films below 250 nm thickness were ferroelectric whilst those above 250 nm were antiferroelectric.[36] Films of $BiTaO_4$ grown *via* sol-gel processing were shown to have typical dielectric behaviour with a very low capacitance of 2.4 fF/μm^2, compared to films of $SrBi_2Ta_2O_9$ formed in the same manner that had a capacitance of 5-7 fF/μm^2.[37]

1.7.1.4 Multiferroic Oxides $BiMO_3$ (M = Fe, Cr, Mn)

Multiferroics are an emerging class of materials that display at least two of the fundamental "ferroic" properties - ferroelectricity, ferromagnetism, ferroelasticity and ferrotoroidicity in the same phase (these properties are highlighted later in Figure 14). Those that simultaneously exhibit coupled ferromagnetic and ferroelectric properties are known as magnetoelectrics and offer the potential to control electrical and magnetic functionalities within a single device.[38] Multiferroics will be covered in more detail later, however several bismuth based multiferroic oxides will now be discussed. The most widely studied of these, $BiFeO_3$ (T_c = 1143 K), has been the subject of increased scientific study, that has accelerated largely since the discovery of an enhanced spontaneous polarisation (an order of magnitude increase) in epitaxially grown films of $BiFeO_3$ at room temperature compared with the bulk material.[39] Thickness dependence magnetism and a rhombohedral to monoclinic distortion were also observed in these films grown on $SrTiO_3$ substrates. The perovskite $BiMnO_3$ displays ferromagnetic ordering below 105 K, however it has been found to be strongly electrically conducting, making measurement of polarisation difficult at typical operating temperatures. Epitaxially grown thin films of

$BiMnO_3$ have been shown to be insulating, allowing for room temperature dielectric measurements to be conducted.[40] The comparatively least studied bismuth-containing, candidate multiferroic $BiCrO_3$, has been shown to be antiferromagnetic,[41] albeit with a weak ferromagnetic moment below 125 K, and has been predicted to be ferroelectric as well.[42]

1.7.2 Bismuth oxide based superconductors

Research into precursors and deposition of bismuth oxide-based materials enjoyed a renaissance in the late 1980s with the discovery of a family of high critical temperature (T_c) Bi-Sr-Ca-Cu-O superconductors, which contain two BiO layers sandwiched between SrO, CuO_2 and Ca layers and furthermore, in light of previous research, did not contain a rare earth element.[43] The T_c of $BiSrCaCu_2O_x$ was observed to be 105 K, which was 10 K higher than those of the previously studied high T_c superconducting $YBa_2Cu_3O_7$ family. Prior to this discovery, Michel and co-workers obtained oxides with stoichiometries close to $Sr_2Bi_2Cu_2O_{7+a}$ which possessed critical temperatures between 7 and 22 K.[44] Phase identification of the Bi-Sr-Ca-Cu-O superconductors revealed the stoichiometry of the high T_c phase to be $Bi_2Sr_2CaCu_2O_{9-x}$, which had an onset temperature nearer 120 K and was similar to the layered structure to proposed by Michel.[44,45] The layered structure of $Bi_2Sr_2CaCu_2O_8$ is shown in Figure 11.[46]

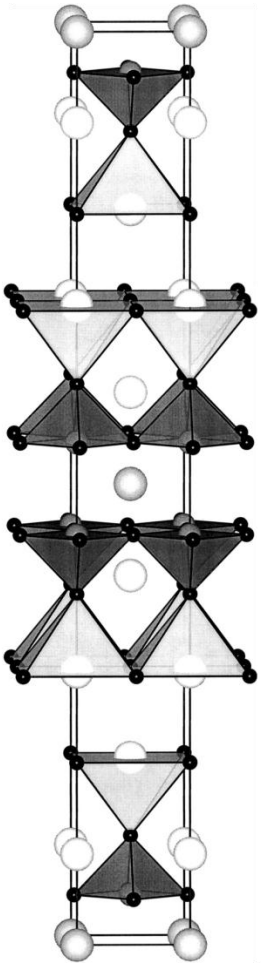

Figure 11: Structure of $Bi_2Sr_2CaCu_2O_8$. Copper atoms are represented by small grey circles, oxygen by small black circles, bismuth atoms connected by the framework polyhedra, strontium and calcium represented by large circles not connected by coordination polyhedra (taken from the review article by Cava).[46]

1.7.3 Heterometallic bismuth oxide based catalysts

Aurivillius type bismuth molybdates Bi_2MoO_6, $Bi_2Mo_2O_9$ and $Bi_2Mo_3O_{12}$ have attracted considerable attention as potent olefination catalysts in the petrochemicals industry. The $Bi_2O_3.MoO_3$ based family of catalysts have played an important part in the SOHIO (Standard Oil of Ohio Company) process through the industrially important conversion of propene to acrolein and acrylonitrile.[47] There are numerous reports on the visible light photocatalytic properties of Bi_2MoO_6 (koechlinite, band-gap 2.5 – 2.8 eV) for degradation of organic pollutants[48] and it, along with the other similar structured heterometallic oxides Bi_3TiNbO_9, Bi_2WO_6 and $Bi_2W_2O_9$, have been reported to be potent photocatalysts for oxygen evolution from an aqueous $AgNO_3$ sacrificial solution.[49,50] Similarly, $Bi_2Fe_4O_9$ has been demonstrated to be an active photocatalyst for methyl orange degradation under both UV and visible light; however the photocatalytic activity differed between nanosheets and microplatelets of the material.[51] Additionally, α-$Bi_2Sn_2O_7$, with and without the addition of MoO_3, has been

investigated for the selective oxidation of isobutene into methacrolein.[52,53] The solid-state reaction between PbO, Bi_2O_3 and Nb_2O_5 at 1473 K yielded the Aurivillius oxide $PbBi_2Nb_2O_9$, which when loaded with 1% Pt co-catalyst, displayed appreciable photocatalytic activity for oxygen and hydrogen evolution from an aqueous methanol solution under visible light irradiation.[54] Similarly, the photocatalytic properties of $BiVO_4$ (possessing the scheelite structure) have been investigated *via* the evolution of oxygen from an aqueous $AgNO_3$ solution using both UV and visible light.[55,56] Bismuth-copper-vanadate ($BiCu_2VO_4$) has also been investigated as a potent photocatalyst for oxygen evolution from aqueous $AgNO_3$ and $FeCl_3$ solutions, and displayed higher photocatalytic activity than $BiVO_4$ under visible light irradiation.[57]

1.8 CVD of bismuth oxide films – precursors and deposition conditions

There are many techniques that have been reported to deposit thin films of bismuth oxide. These include CVD – LPCVD, AACVD, DLI-CVD, APCVD and ALD, sputtering, sol-gel processes, spray pyrolysis, dip coating, screen printing and spin coating. In this section an overview of the film deposition experiments that have utilized single-source precursors will be given as well as a discussion of the well-known dual-source CVD routes to bismuth oxide films. It will become apparent that although there are a wide variety of methods (DLI-CVD, LPCVD, APCVD, sol-gel, sputtering etc.) to deposit such films and a similarly large collection of well-defined molecular compounds to choose from, the number of suitable single-source precursors is in fact extremely limited, and the reasons for this will be discussed. This is despite the fact that volatile single-source precursors containing a pre-formed Bi-O bond would be ideal for deposition of bismuth oxide as this would provide a much simpler route to obtain such materials, eliminating any possibility of complex side reactions in the gas phase together with the reduction in the use of oxygen gas at high substrate temperatures.

There are numerous examples of dual source CVD routes to bismuth oxide, most of which require a bismuth source and oxygen gas or plasma as the reactive gas. Bismuth halides together with oxygen gas have been shown to deposit amorphous bismuth oxide films on glass substrates using APCVD at a variety of substrate temperatures.[58] As predicted, the use of BiI_3 as the bismuth source led to an impurity BiOI phase observed in the XRD pattern at substrate temperatures between 600 - 800 °C. Similarly, Schuisky and Hårsta[59] demonstrated the use of BiI_3 and oxygen to deposit oxygen deficient bismuth oxide ($Bi_2O_{2.33}$) and β-Bi_2O_3 films on $SrTiO_3$(100) and MgO(100) substrates *via* LPCVD. Only at substrate temperatures above 600 °C was the deposition of iodine-free bismuth oxide films achieved. The solid precursor, BiI_3, was maintained at 200 °C during deposition. Kim *et al.* used the extremely pyrophoric alkylbismuth liquid precursor, trimethylbismuth $BiMe_3$, to deposit one-dimensional

nanostructured α-Bi_2O_3 films at 450 °C using an oxygen reactive gas.[60] Due to its high volatility and pyrophoricity, the precursor was maintained at -5 °C during deposition.

As a consequence of its low air and moisture sensitivity triphenylbismuth, $BiPh_3$, is the most commonly used dual-source CVD precursor to bismuth oxide films.[61] Similarly, [Bi(*o*-tol)$_3$] and [Bi(*p*-tol)$_3$] have been shown to be useful bismuth precursors and their gas phase transport mechanisms have been studied extensively.[62] Tondello *et al*. deposited phase selective Bi_2O_3 films on SiO_2 and Al_2O_3 substrates at 420 °C using $BiPh_3$ and oxygen gas *via* LPCVD.[63] At a system pressure of 6 mbar and at low gas flow rates, the β-phase was deposited, whereas mixed α- and β-phase films were grown at higher flow rates. The crystalline phase obtained was found to depend strongly upon the oxygen flow rate and the nature of the substrate. Recently, Caussat[64] used a fluidized bed MOCVD procedure at atmospheric pressure to deposit mixed phase bismuth oxide films on the surface of alumina particles.

There are numerous examples of potential single-source precursors whose syntheses and structures have been described in some detail by Mehring in his comprehensive review in 2007,[9] and therefore for an in-depth analysis of the synthesis of single-source precursors to bismuth oxide one should refer to that review. In order not to replicate such a detailed text, what follows is a brief overview covering the main classes of precursors to bismuth oxide. The basic requirements for incorporation of oxygen into a molecule using sterically bulky ligands to inhibit oligomerization have led to the development of three main types of potential single-source precursors to bismuth oxide:

1. Alkoxides, [M(OR)$_3$], R = alkyl, aryl, OR (donor functionalized), CX_3 (X = halogen).

2. *β*-Diketonates, [M($R_1COCHCOR_2$)$_3$], R = alkyl, aryl, CX_3 (X = halogen).

3. Carboxylates, [M(O_2CR)$_3$], R = alkyl, aryl, CX_3 (X = halogen).

1.8.1 Bismuth alkoxides

The first synthesis of bismuth alkoxides of the type [Bi(OR)$_3$] was reported in 1960 by Mehrotra and Rai,[65] however structural characterization of a bismuth alkoxide was only reported in 1990 by Buhro with the synthesis of the polymeric bismuth methoxyethoxide [Bi(μ-OCH_2CH_2OMe)$_2$(OCH_2CH_2OMe)]$_\infty$ *via* alcoholysis of the highly unstable bismuth amide [Bi(NMe_2)$_3$].[66] A further study by Hubert-Pfalzgraf and co-workers in 1991[67] investigated the synthesis of bismuth alkoxides, first *via* the alcoholysis of the less sensitive bismuth silylamide [Bi{N($SiMe_3$)$_2$}$_3$], and secondly, from the metathesis reaction between bismuth halides and sodium alkoxides. [Bi(μ-OCH_2CH_2OMe)$_2$(OCH_2CH_2OMe)]$_\infty$was found to be polymeric and

therefore not volatile, whereas bismuth *tert*-butoxide, $[Bi(O^tBu)_3]$, was volatile but at the time predicted to be polymeric in the solid state. The use of $[Bi(O^tBu)_3]$ as a CVD precursor has had very little investigation due to the perceived problems concerning its air and moisture stability.[5] Hanna *et al*. recently prepared several bismuth aryl alkoxides *via* the alcoholysis of $[Bi\{N(SiMe_3)_2\}_3]$,[68] whereas Knispel *et al.* synthesized a range of bismuth allyl oxides *via* alcoholysis of $[Bi(O^tBu)_3]$ and also *via* salt metathesis reactions starting from $BiCl_3$ and sodium allylates.[69] Highly fluorinated alkoxides, of the type $[Bi(OCH(CF_3)_2)_3]$, were synthesized *via* the reaction of $BiCl_3$ with the *in situ* generated $NaOCH(CF_3)_2$,[70,71] however these compounds decomposed upon heating to yield BiOF. The reaction of $BiPh_3$ and pentafluorophenol (C_6F_5OH) in refluxing toluene also yielded the dimeric bismuth pentafluorophenoxide complex $[Bi(OC_6F_5)_3.C_7H_8]_2$. The various common synthetic routes to bismuth(III) alkoxides are summarized in Scheme 1.

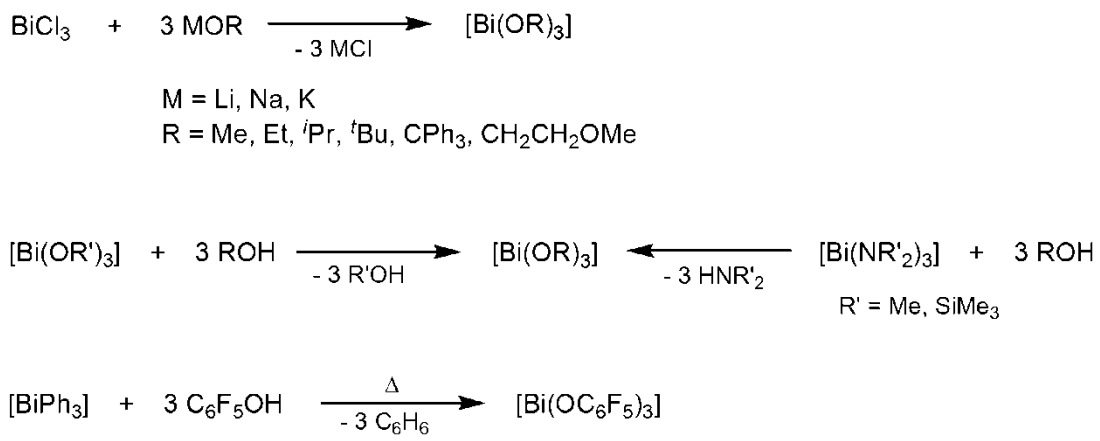

Scheme 1: Common synthetic routes to bismuth(III) alkoxides.

Alkoxides of bismuth typically exhibit poor solubility, poor volatility and high air and moisture sensitivity, however in general metal alkoxides have always been the subject of investigation as metal oxide CVD precursors as they tend to decompose cleanly at low substrate temperatures. Jones and co-workers[72] synthesized the donor-functionalized monomeric bismuth alkoxide $[Bi(mmp)_3]$, (mmp = 1-methoxy-2-methyl-2-propanol; Figure 12) *via* the reaction of $[Bi\{N(SiMe_3)_2\}_3]$ and three molar equivalents of the free alcohol in diethyl ether solvent. Although its synthesis was first reported in 1993 by Hermann,[73] the molecular structure and use in thin film deposition was only confirmed in 2001. These studies confirmed that $[Bi(mmp)_3]$ was particularly volatile, and when dissolved in heptane was shown to deposit bismuth oxide films in conjunction with oxygen gas on silicon substrates at temperatures between 250 - 550 °C. Jones and co-workers described one deposition using $[Bi(mmp)_3]$ as a single-source precursor, whereby no reactive gas was added to obtain a film, however details regarding the

crystallinity of the films were not mentioned. The resulting bismuth oxide films were low in carbon contamination and growth rates appeared to be constant over a wide temperature range. It was noted that the decomposition properties of $[Bi(mmp)_3]$ suggest it would have excellent compatibility for use as a co-precursor with strontium and tantalum alkoxides for the deposition of ferroelectric strontium bismuth tantalate (SBT) films.[5]

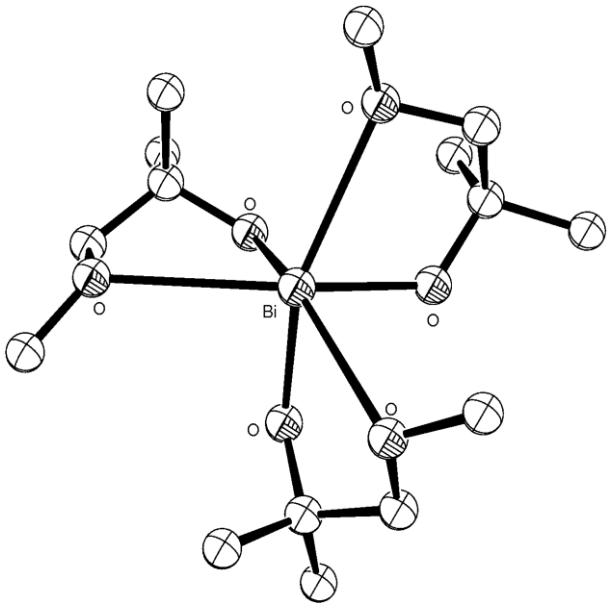

Figure 12: Molecular structure of $[Bi(mmp)_3]$, hydrogen atoms omitted for clarity.

1.8.2 Bismuth *β*-diketonates

The range of structurally characterized bismuth(III) *β*-diketonates of the type $[Bi(R_1COCHCOR_2)_3]$ found in the literature that do not contain bulky aromatic substituents are relatively low in comparison to the alkoxides, and as a result, only one such molecule has been used as a CVD precursor to Bi_2O_3 films. Bismuth tetramethylheptanedionate ($[Bi(thd)_3]$), despite containing an excess of oxygen within the coordination sphere of bismuth, has been used in conjunction with oxygen to deposit amorphous bismuth oxide films on silicon substrates at temperatures between 240 - 435 °C.[74] Although $[Bi(thd)_3]$ possesses a lower decomposition temperature in comparison to bismuth halides and alkylbismuth compounds, it has poor thermal stability, undergoing premature weight loss according to numerous TGA studies which limits its use principally to DLI-CVD apparatus.[62] The first reported synthesis of a bismuth(III) *β*-diketonate was indeed $[Bi(thd)_3]$, published by Hubert-Pfalzgraf in 1991.[67] The compound was synthesised *via* a salt metathesis reaction between $BiCl_3$ and Na(thd) and the volatile product was purified by sublimation (110 °C, 10^{-4} mmHg), although attempts to grow single crystals *via* sublimation led to decomposition. The crystal structure of $[Bi(thd)_3]$ was solved in 1997 and reported to be dimeric.[75]

Brooks *et al.*[76] synthesized a number of volatile bismuth diketonates intended for MOCVD application. The reaction of the free ligand with $BiPh_3$ in refluxing toluene yielded $[Bi(fod)_3]$ (fod = 6,6,7,7,8,8,8-heptafuoro-2,2-dimethyl-3,5-octanedione) and $[Bi(hfac)_3]$ (hfac = 1,1,1,5,5,5-hexafluoro-2,4-pentanedione). It was reported that the same synthetic procedure when using the "thd" ligand yielded no reaction due to its lower acidity, whereas the reaction with l,l,l-trifluoro-2,4-pentanedione (Tfac)) produced a mixed phenyl/diketonate complex. The authors went on to utilise $[Bi(fod)_3]$ in a hot-wall LPCVD reactor to produce bismuth films which deposited on the walls of the reactor and on pyrex substrates. No carrier or oxidizing gas was used. Analysis of the resulting brown coloured film revealed that it consisted of 73% bismuth, 15% carbon and 12% oxygen, with carbon levels increasing towards the hottest area of the reaction chamber; however all the films had surprisingly low levels of fluorine contamination (below detector limit). The crystal structure of $[Bi(hfac)_3]$ was reported by Dikarev *et al.* in 2005 as a dimer and was described as a useful reagent for the synthesis of heterobimetallic bismuth-transition metal complexes, which are potential single-source precursors for mixed-metal oxides.[77] Pisarevsky[78] attempted to synthesise a range of bismuth(III) *β*-diketonates *via* a reflux of $BiPh_3$ and the free ligand, however the synthesis of $[Bi(acac)_3]$ (acac = acetylacetonate) was said to be unsuccessful due to the low acidity and boiling point of acetylacetone. Using this methodology, Armelao *et al.* observed the formation of 1-(2-hydroxy-4,6-dimethylphenyl)-ethanone *via* the intramolecular cyclisation of two acetylacetone molecules, catalysed by $BiPh_3$, instead of the desired $[Bi(acac)_3]$ molecule.[79] The molecular structure of $[Bi(acac)_3]$ is yet to be reported. Dikarev *et al.* synthesized a range of phenyl bismuth *β*-diketonate complexes of the type $[BiPh(hfac)_2(L)]$ from refluxing $BiPh_3$ with two equivalents of hexafluoroacetylacetone, but were only able to grow single crystals with the addition of coordinating solvents MeCN, Me_2CO, THF, DMA, DMSO and PhCN (L).[80]

The mixed alkoxide-diketonate polymer $[Bi_2(\mu\text{-}O^iPr)_2(O^iPr)_2(acac)_2]_\infty$ was synthesised unexpectedly by Hubert-Pfalzgraf *via* a reaction of $[Bi(acac)_3]$ with $[Ti(O^iPr)_4]$ in toluene, and is held together *via* isopropoxide bridging groups.[81] The complex has an improved solubility in polar solvents compared to $[Bi(O^iPr)_3]$. The common synthetic routes to bismuth *β*-diketonates are summarized in Scheme 2.

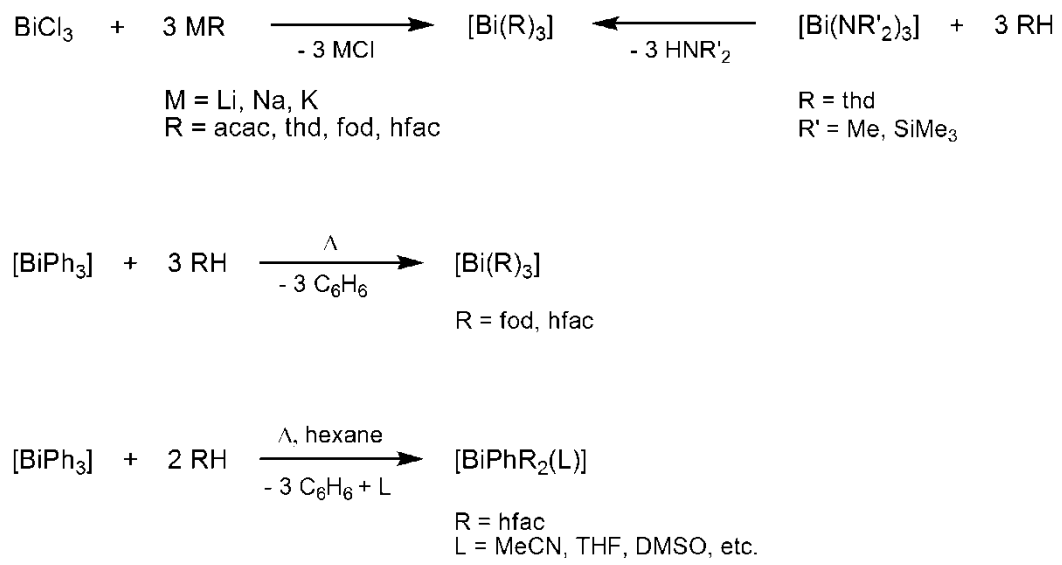

Scheme 2: Common synthetic routes to bismuth(III) *β*-diketonates.

1.8.3 Bismuth Carboxylates

The synthesis and decomposition study of a number of bismuth(III) carboxylates was carried out by Pisarevsky to find suitable precursors to bismuth containing superconductors.[78,82] Bismuth acetate $[Bi(O_2CCH_3)_3]$ was prepared *via* reaction of bismuth oxide (Bi_2O_3) with acetic acid in the presence of acetic anhydride. Detailed experimental procedures were not given, however, it was reported that the compound can then go on further to react with a variety of carboxylic acids to yield other bismuth carboxylates. Indeed, bismuth(III) 2,2-dimethylpropanoate, $[\{Bi(O_2CCMe_3)_3\}_4]$, was synthesized *via* a ligand exchange reaction between $[Bi(O_2CCH_3)_3]$ and 2,2-dimethylpropanoic acid and purified *via* sublimation in a sealed ampoule possessing a temperature gradient between 120 - 160 °C. The structure of $[\{Bi(O_2CCMe_3)_3\}_4]$ was found to be composed of isolated tetrameric $[Bi(O_2CCMe_3)_3]_4$ groups.[83] Andrews and co-workers have also synthesised a range of bismuth(III) carboxylates utilising solvent-free conditions.[84] The volatilities of the bismuth carboxylate complexes are extremely low in comparison to the aforementioned alkoxide and *β*-diketonate compounds, and any vaporization is usually accompanied by some decomposition, which has made these complexes unsuitable for most CVD processes. There appears to be no references in the literature to the use of bismuth carboxylates as single or dual-source precursors to bismuth oxide films, however their use in binary and ternary oxide materials synthesized *via* solution based deposition techniques are more commonplace.

1.9 Atomic Layer Deposition (ALD) of bismuth oxide films

There are only a few examples of the growth of bismuth oxide films by ALD, owing to the general trend of poor thermal stabilities of bismuth precursors which such a deposition process seeks to avoid. ALD itself requires the use of two precursors – one bismuth, the other an oxygen source, usually water (H_2O), which are fed into the reaction chamber through a sequence of individual purge cycles, and so is considered a dual-source approach. The ALD reaction of $BiPh_3$ and O_3 resulted in deposition of dark and patchy films, possibly composed of metallic bismuth,[85] and the use of H_2O_2 (instead of O_3) also proved unsuccessful.[86] Vehkamaki *et al.*[87] synthesized a range of bismuth(III) amido and thioamido complexes to assess their suitability for the growth of ferroelectric Bi-Ti-O films in conjunction with suitable titanium precursors. The bismuth silylamide $[Bi\{N(SiMe_3)_2\}_3]$ was chosen for further study due to its high volatility and thermal stability, resulting in deposition of BiO_x films using H_2O as a reactant. However, poor reproducibility in forming the binary bismuth oxide phase was encountered and the use of O_3 as a more reactive oxygen source was predicted to yield bismuth silicates. The same group has also demonstrated the growth of bismuth silicate films using $[Bi(CH_2SiMe_3)_3]$ in conjunction with an ozone oxidising gas at substrate temperatures between 200 – 400 °C, which was then followed by post-deposition annealing in order to improve film crystallinity.[88] Single-source precursors to bismuth silicates would typically include bismuth siloxides of the type $[Bi(OSiR_3)_3]$, (R = alkyl) and may be synthesised in the same manner as bismuth alkoxides[9,89] and can yield interesting cluster-type structures not yet observed for the alkoxides.[90]

Ritala and co-workers recently reported the syntheses and structures of a number of bismuth(III) alkoxides as potential ALD precursors for bismuth oxide.[91] The use of $[Bi(O^tBu)_3]$ was unsuccessful in this methodology due to premature aging of the precursor. The structures of $[Bi(O^tBu)_3]$ (formed of loose polymeric chains) and $[Bi(OC^iPr_3)_3]$ were finally solved *via* single crystal X-ray diffraction, however only the alkoxide $[Bi(OCMe_2{}^iPr)_3]$, when used in conjunction with an H_2O co-reactant, was suitable for ALD of bismuth oxide films due to its higher thermal stability (an evaporator temperature of 85 °C was employed). Films grown at 150 °C were amorphous, whereas those grown above 200 °C contained an unidentified Bi_2O_3 phase from time-of-flight energy recoil detector analysis (TOF-ERDA). On crystallization from toluene, single crystal XRD revealed that tetrameric $[Bi_2O(OCMe_2{}^iPr)_4]_2$ was actually formed in the solid state (Figure 13).

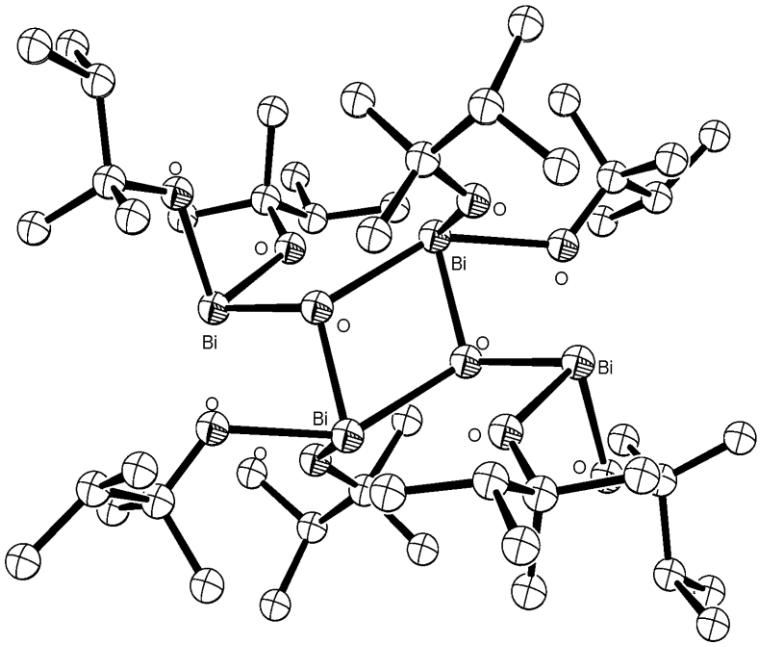

Figure 13: Molecular structure of $[Bi_2O(OCMe_2{}^iPr)_4]_2$. Hydrogen atoms omitted for clarity.

1.10 $BiFeO_3$: Introduction to multiferroics – bulk to thin films

Multiferroics, which, in this case, describes materials that display simultaneous coupling between ferromagnetic and ferroelectric ordering, have enjoyed a considerable amount of research and attention during the last ten years. Researchers have continually tried to understand and then build devices that could efficiently couple electrical and magnetic ordering, wherein a magnetic field could control the polarisation and *vice versa*, yielding a multifunctional device. The brief stint of research into such materials appeared to run out of momentum during the late 1960s and 1970s, mainly because of the lack of success in finding single-phased materials, as well as a lack of materials which exhibited appreciably strong magnetoelectric coupling to warrant further research. Ramesh and Hill[92] correctly pinpoint that the main reason for the previously limited research into multiferroics stemmed from an insufficient understanding of the physics behind the properties of such materials. However, this was overcome to an extent by recent technological advances in nanoscale materials synthesis and thin film growth, coupled with the emergence and increased availability of high performance computing resources, as well as interests driven by long-term technological aspirations for the next generation of computer memory devices. This has enabled physicists, chemists, earth and materials scientists, engineers and computer scientists to predict and synthesise fascinating materials with enhanced magnetoelectric properties, and, just as importantly, propose rational theories for the physics that govern it all.

The magnetoelectric (ME) effect applied to antiferromagnetic materials was first described by Rado and Folen in 1961 using bulk Cr_2O_3 as an example.[93,94] These papers sought to rationalise how the magnetic polarisation was proportional to the applied electric field (and *vice versa*), as well as investigating temperature and mechanistic effects. Shortly after, Hornreich[95] predicted a range of materials to possess ME coupling based upon symmetry (removal of the centre of symmetry to allow electric polarisation) and point group effects, and these all happened to be either tri-rutile or perovskite structured mixed metal oxides. In 1966, the first electric field polarisation hysteresis loops were recorded (at 64 K) of a ferroelectric ferromagnetic material, in this case, nickel boracite ($Ni_3B_7O_{13}I$) and were soon published.[96] The major classes of multiferroics were thereafter classified as perovskites, boracites, hexagonal rare-earth manganites and $BaMF_4$ (M = Mg, Mn, Fe, Co, Ni, Zn) compounds. The relationship between multiferroic and magnetoelectric materials are shown in Figure 14.[97]

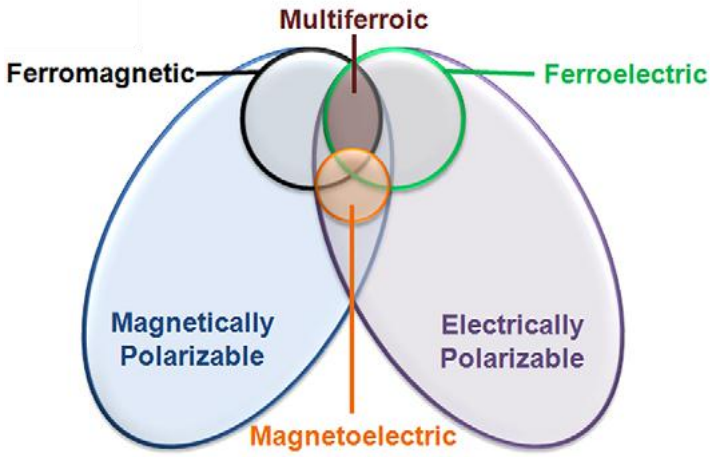

Figure 14: Diagram illustrating the relationship between multiferroic and magnetoelectric materials, illustrating the requirements to achieve both properties in a material. Taken from L. W. Martin, S. P. Crane, Y.-H. Chu, M. B. Holcomb, M. Gajek, M. Huijben, C.-H. Yang, N. Balke, and R. Ramesh, *Journal of Physics: Condensed Matter*, 2008, 20, 1–12,[97] adapted from Eerenstein *et al*., *Nature*, 442, 759-765[111]).

One of the first bismuth containing multiferroic materials, $Bi_5Bi_4Ti_3Fe_5O_{27}$, was reported in 1971.[98] The material (T_C = 830 °C) was observed to be antiferromagnetic (T_C = 130 °C) but did display weak ferromagnetic ordering, and the application of a (very low) external magnetic field (10^{-3} A/m) resulted in an electric current which depended upon the direction of the applied magnetic field. There then followed a significant period of almost three decades when research into ME materials was scarce, likely to have not been helped by the surge of interest in high T_C superconductors in the late 1980s and 1990s. Typically, the majority of (proper) ferroelectrics are transition metal (TM) oxides whereby the TM ion possesses unoccupied d-orbitals (d^0 state). Here, the TM ion would appear to form a covalent bond with neighbouring oxygen ions, resulting in a collective shift of anions and cations within the crystal, leading to a bulk electric polarisation as the TM shifts away from the centre of the unit cell (second-order Jahn-Teller effect)[99] - the mechanism of which can be described as hopping of electrons from the filled oxygen shell to the vacant TM d-orbital.[100] In contrast, magnetism relies on occupied d- or f-orbitals with unpaired electrons, and therefore it could be said that the filling of the d-orbitals for both magnetism and ferroelectricity are mutually exclusive. In the case of the multiferroics $BiFeO_3$ and $BiMnO_3$, the stereochemically active $6s^2$ lone pair on the bismuth atom has been shown to drive the off-centre distortion, whilst the B-site cation induces magnetism, giving rise to their multiferroic properties.[101,102] Such compounds are named Type I multiferroics because the magnetic and ferroelectric ordering arises from two unrelated mechanisms, and hence the magnetoelectric coupling is not particularly strong compared to Type II multiferroics such as $TbMnO_3$, where magnetism actually causes ferroelectricity. The reasoning for this is the

presence of a lower symmetry, non centrosymmetric magnetic ground state which leads to polarisation.[99]

In 2000, Nicola Spaldin (previously Nicola Hill) published a handful of papers that asked the question many had asked at the time magnetoelectric materials were first discovered forty years prior to this – Why are there so few magnetic ferroelectrics? The requirements for such coupling were highlighted:[103]

1. Transition from high to low symmetry
2. Electrical properties – insulator characteristics (low conductivity)
3. D-orbital occupancy: Jahn-Teller or other associated distortions

As stated earlier, symmetry properties were fundamental to the understanding of the first magnetoelectric materials discovered over forty years ago. The transition from high to low symmetry enables ferroelectric polarisation through structural distortion, with 31 point groups that allow this ascribed with the letter "P." There are also 31 point groups that allow magnetic polarisation, "M," of which there are 13 point groups that overlap both sets - *1, 2, 2', m, m', 3, 3m', 4, 4m'm', m'm2', mm'2', 6,* and *6m'm* which would "allow" ferroelectric and magnetic polarisation to co-exist within the same material. Nevertheless, Hill states that despite the existence of so many possible permutations, there are numerous materials that are neither ferroelectric nor ferromagnetic but still exist in one of the "allowed" symmetry groups. The answer to why there are so few magnetic ferroelectrics was never answered definitively. D-orbital occupancy on the transition metal cation appeared to be a key factor amongst the numerous contributing factors just mentioned. Calculations based on prototypical distorted perovskite multiferroics $LaMnO_3$, $YMnO_3$ and $BiMnO_3$ revealed few clues to the origin of the simultaneous existence between ferroelectricity and ferromagnetism; however in the case of $BiMnO_3$, the ferroelectricity was believed to originate not only from the stereochemically active lone pair on the bismuth ion, but also as a result of the structure containing an additional contribution from the adjacent oxygen 2p states (i.e. Bi-O covalency), that created a Bi-O dipole moment.[101] Perhaps more crucially, such an effect was also predicted to exist in other bismuth A-site perovskites such as $BiFeO_3$.

1.11 $BiFeO_3$

$BiFeO_3$, a compound discovered as far back as 1960,[104] is perhaps the most studied single-phase multiferroic, and due to its high Curie Temperature (T_C = 1143 K) and Neel Temperature (T_N = 640 K) it could make an ideal material for room temperature non-volatile random access memory devices that should survive at elevated temperatures. The material is also free of lead

and other toxic elements which gives it an advantage over the current lead-based ferroelectric and piezoelectric materials. The ferroelectric properties of $BiFeO_3$ remained in question until important measurements were conducted at 77 K in 1970, which resulted in the observation of a spontaneous polarisation of 6.1 μC/cm^2 in the 111-direction.[105]

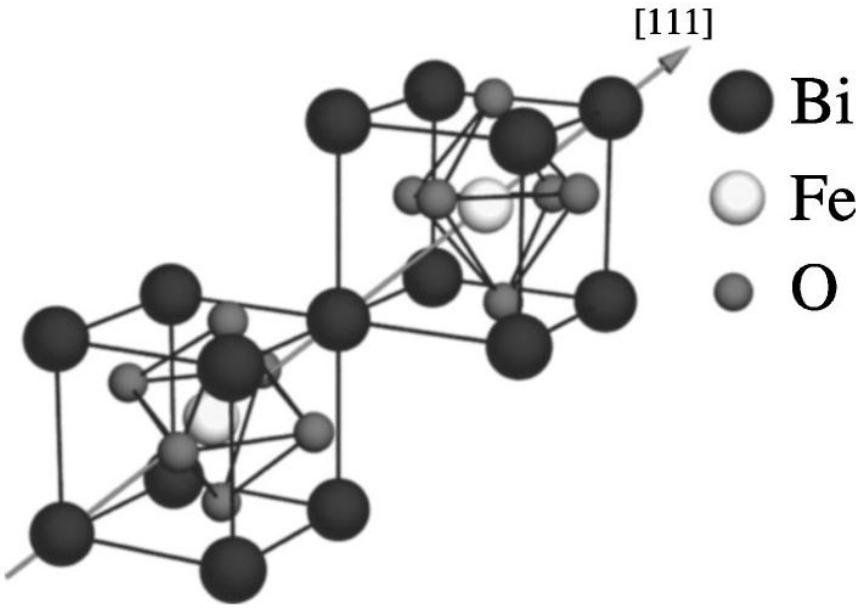

Figure 15: Schematic view of the R3c structure built up from two cubic perovskite unit cells. The cations are displaced along the [111] direction relative to the anions, and the oxygen octahedra rotate around the [111] axis. Image taken from C. Ederer and N. Spaldin, *Physical Review B*, 71, 2005, 1–4. Copyright (2005) by the American Physical Society.[102]

The structure of single crystal (bulk) $BiFeO_3$ (Figure 15) was found to be a rhombohedrally distorted cubic perovskite (space group *R*3*c*), where the bismuth atom is shifted with respect to two neighbouring octahedron centres by about 0.540 Å along the three-fold axis, and the iron atom is shifted by about 0.134 Å from the centre of the deformed oxygen octahedron.[106] In a hexagonal frame of reference (hexagonal *c*-axis parallel to the diagonals of the perovskite cube), the hexagonal lattice parameters were found to be a = 5.58 Å and c = 13.90 Å. The magnetism of $BiFeO_3$ is somewhat complex. Its magnetic structure may be described as a "G-type" antiferromagnet; this so-called "G-type" antiferromagnetism arises as a result of ferromagnetic coupling of the Fe moments within the pseudcubic [111] planes and antiferromagnetic coupling between adjacent planes.[102] Each Fe^{3+} ion is surrounded by 6 antiparallel spins on the neighbouring Fe atoms, but as these spins are not perfectly parallel, there is a weak canting moment due to magnetoelectric coupling with the polarisation. It was also noted that if the moments were oriented perpendicular to the <111> polarization direction, the symmetry would also permit a small canting of the moments in the structure, leading to a small magnetisation and a weak ferromagnetic moment of the Dzyaloshinskii–Moriya type.[99]

However, in addition to this, the presence of a spin cycloid (64 nm in length) consisting of individually antiferromagnetically aligned sublattices spatially averages out the net magnetic moment to zero due to rotation of the cycloid (Figure 16).[107]

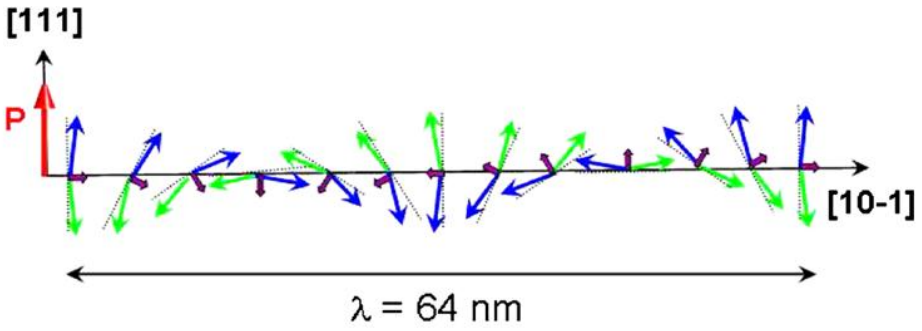

Figure 16: Diagram of the 64 nm spin cycloid in $BiFeO_3$, where the canted anti- ferromagnetic spins (blue and green) result in a net magnetic moment (purple) which is spacially averaged out to zero due to rotation of the cycloid. The spins are contained within the plane defined by the polarization vector (red) and the cycloidal propagation vector (black). Image reproduced from D. Lebeugle, D. Colson, A. Forget, M. Viret, A. M. Bataille, and A. Gukasov, *Physical Review Letters*, 100, 2008, 1–4. Copyright (2008) by the American Physical Society.[108]

At room temperature the spins in $BiFeO_3$ are antiferromagnetically aligned, but despite this weak local canting moment being cancelled out by the spin cycloid, there have been reports that at low temperatures a weak ferromagnetic state may still exist. Synthesis of phase-pure $BiFeO_3$ is difficult. Questions over the purity of such samples have been raised, as a small percentage of Fe^{2+} and the presence of parasitic phases such as $Bi_{25}FeO_{39}$ have been shown to affect the magnetic state of $BiFeO_3$. There are also many arguments supporting spin-glass behaviour in $BiFeO_3$ as evidenced by numerous reports that show a large difference between the zero field cooled – field cooled (ZFC-FC) data, along with a peak at 50 K in the magnetic susceptibility data, which could be due to magnetic frustration brought about by the numerous competing forces.[109] For an overview of the debate surrounding the magnetic and domain structure of $BiFeO_3$, readers are pointed toward J.F. Scott's comprehensive review paper.[107]

The big breakthrough for $BiFeO_3$, and for that matter for the field of multiferroics came in 2003, with the observation of an enhancement of polarisation at up to 60 $\mu C/cm^2$ at room temperature (an order of magnitude increase compared to the bulk) along with thickness dependent magnetism in heteroepitaxially grown films of $BiFeO_3$ (Figure 17).[39] The films were grown *via* pulsed laser deposition (PLD) onto (100) $SrTiO_3$ with a conducting $SrRuO_3$ bottom electrode. The major breakthrough from this lead paper was the observation of the decrease in symmetry and change in crystal structure from rhombohedral (found in bulk $BiFeO_3$) to monoclinic, which

was said to be induced by the compressive stress imposed by the $SrRuO_3$ electrode and appears to decrease with increasing thickness. Computational calculations on monoclinic $BiFeO_3$ confirmed the enhancement of polarisation and agreed with the results obtained by experiment. The reproducibility of this experiment, the possible incorporation of impurity Fe^{2+} in non-fully oxygenated samples, and both the observation of epitaxial enhancement of magnetisation and polarisation were brought into question soon after,[110,111,112] and it now appears widely accepted that the poor quality of bulk samples used for earlier measurements inhibited researchers from observing such high polarisation. Furthermore, the high magnetic moment measured by Wang (~70 emu/cm^3) has been debated as it is higher than the expected canted moment (~ 7 emu/cm^3) for $BiFeO_3$.[102]

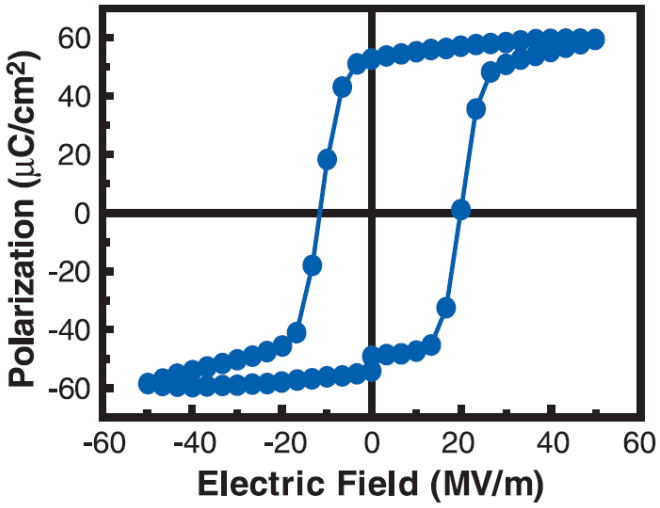

Figure 17: P-E hysteresis loop measured by Wang *et al.*[39] of an epitaxially strained $BiFeO_3$ thin film, exhibiting a large remnant polarisation of 55 μC/cm^2.

Since this initial discovery, problems associated with high leakage and poor insulating properties have made valid ferroelectric measurements difficult (because mobile charges screen out the ferroelectric polarisation) and have thus hampered the potential application of $BiFeO_3$ in magnetic storage devices. Efforts to grow multi-component films or films doped on the B-site with Cr and Ti^{4+} (giving rise to charge compensation) have sought to decrease leakage currents, induce well-saturated polarisation hysteresis loops and maintain high remnant polarisation.[113,114] A-site alloying with alkaline and rare earth metals and lanthanides have also received much interest, and for an overview of the progress made *via* this methodology readers are directed to Martin's recent review.[99]

1.12 $BiFeO_3$ - Thin film growth

There are numerous examples of the growth of thin films of $BiFeO_3$ *via* a variety of routes, of which physical methods such as PLD are the most popular to grow epitaxial films. The problem with the use of PLD is that it is an expensive and extremely time consuming process (growth rates as low as 5 Å/min) and is therefore not suitable for mass production of thin films for device applications. As such, the development of solution-based synthetic approaches with the intention of producing high quality, phase-pure films have been the focus for many researchers investigating $BiFeO_3$ films for a variety of applications. For example, Liu grew $BiFeO_3$ films on ITO/glass substrates *via* a sol-gel technique using bismuth(III) nitrate and iron(III) nitrate as precursors dissolved in 2-methoxyethanol.[115] The films were formed through spin-coating and were annealed at 600 °C in air for 3 h. Films displayed low ferroelectric polarisation at room temperature (5 $\mu C/cm^2$) and a small amount of impurity $Bi_{46}Fe_2O_{72}$ was identified. Wang also used these precursors but first deposited a seed layer using bismuth nitrate and citric acid onto silicon substrates, followed by spin coating the $BiFeO_3$ layer.[116] Annealing at 600 °C resulted in some reaction with the substrate, leading to the formation of a $BiFeO_3/Bi_2SiO_5/Si$ heterostructure; furthermore the deposition of platinum electrodes on top of the $BiFeO_3$ layer led to the formation of a metal/ferroelectric/insulator/semiconductor heterostructure. Ishiwara[117] used a solution of stoichiometric $BiFeO_3$ to deposit films onto $Pt/Ti/TiO_2/Si$ substrates. The films displayed low leakage and remnant polarisation values as high as 90 $\mu C/cm^2$ at room temperature and 80 K. Similarly, pure $BiFeO_3$ films were grown on $LaAlO_3$ substrates *via* chemical solution deposition using bismuth nitrate and iron(III) nitrate precursors followed by annealing at 500 °C.[118]

Deposition of $BiFeO_3$ films *via* rf sputtering has also been investigated. Films were grown onto miscut $SrTiO_3$ substrates using high-rate off axis sputtering, which resulted in high remnant polarisations of up to 98 $\mu C/cm^2$.[119] Even higher remnant polarisation values were obtained from $BiFeO_3$ films deposited *via* rf sputtering onto $Pt/TiO_2/Si/SiO_2$ substrates that had been pre-deposited with a 100 nm thick $SrRuO_3$ buffer layer.[119] Clearly some of these papers reinforce the claims by Eerenstein *et. al*[110] that heteroepitaxial strain may not be the main reason for enhancement of both polarisation and magnetism in contrast to what was originally suggested by Wang in 2003. An overview of the variety of deposition methods and metalorganic precursors used so far for thin films of multiferroic materials are given in a recent review.[38]

1.13 CVD of $BiFeO_3$ films – precursors and deposition conditions

More recently, in an effort to scale up its synthesis, the growth of $BiFeO_3$ films has shifted away from physical methods and instead, has focussed upon the use of CVD; the advantages of which were discussed earlier in this chapter. Currently there are several reports of the use of CVD to deposit $BiFeO_3$ in the literature, and in most of these examples the authors have used direct liquid injection (DLI) apparatus or similar techniques for precursor delivery (Figure 18). Aito *et al*. used [2-[(dimethylamino-N)methyl]phenylbismuth(III)], $[Bi((CH_3)_2(2\text{-}(CH_3)_2NCH_2C_6H_4))]$, together with $[Fe(EtCp)_2]$ (where EtCp = ethylcyclopentadiene) in conjunction with an oxygen reactive gas to deposit epitaxially strained $BiFeO_3$ films at 620 °C on $SrTiO_3/SrRuO_3$ substrates.[120] Remnant polarisation values of ~ 51 μC/cm^2 were obtained from well-saturated hysteresis loops measured at 80 K, but due to high leakage, measurements at ambient temperature were not obtained. Yang used the ligand-matched metalorganic precursors $[Bi(thd)_3]$ and $[Fe(thd)_3]$ to grow $BiFeO_3$ films on $SrTiO_3/SrRuO_3/Si$ substrates at 650 °C, using a showerhead system for precursor delivery.[121] Excess bismuth precursor was required due to the significantly poorer volatility and decomposition characteristics of $[Bi(thd)_3]$ compared to $[Fe(thd)_3]$. A very narrow growth window for $BiFeO_3$ was noticed and the secondary phases α-Fe_2O_3 and β-Bi_2O_3 were obtained at non-ideal precursor mixing ratios, however a post-deposition oxygen "flush" appeared to remove excess bismuth from the film surface.

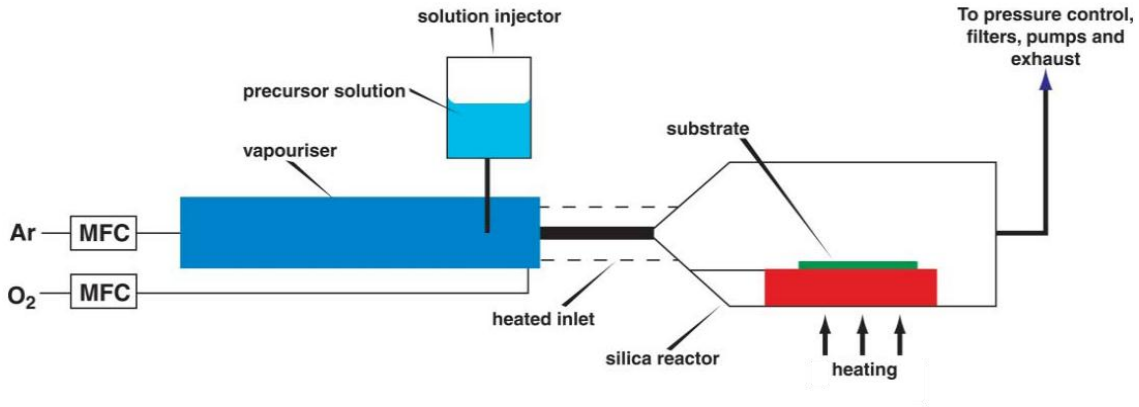

Figure 18: Schematic diagram of a typical DLI-CVD system used to deposit metal oxides, adapted from Jones.[5] Reproduced by permission of The Royal Society of Chemistry.

Tasaki grew films of $BiFeO_3$ on silicon substrates using a variety of iron and bismuth precursors *via* DLI-CVD.[122] Bismuth precursors tri-orthotolyl bismuth [Bi(*o*-tol)$_3$] and tri-paratolyl bismuth [Bi(*p*-tol)$_3$] were used in conjunction with several iron(III) *β*-diketonates $[Fe(thd)_3]$, $[Fe(tmod)_3]$, $[Fe(dibm)_3]$ and $[Fe(ibpm)_3]$ (where tmod = tetramethyl-3,5-octanedione, dibm =

diisobutyrylmethane, and ibpm = isobutyrylpivaloylmethane). Iron cyclopentadienes [$Fe(Cp)_2$] and [$Fe(MeCp)_2$] were also investigated. Oxygen was used as the reactive gas and the substrate temperature varied between 450 and 625 °C. It was found that iron *β*-diketonates were more suitable precursors as they displayed constant deposition rates with temperature. Using [$Bi(p\text{-}tol)_3$] together with [$Fe(ibpm)_3$], mixed in a 2:1 ratio, resulted in stoichiometric $BiFeO_3$ films on $Pt/Ti/SiO_2/Si$ substrates at 500 and 525 °C, albeit with some additional Bi_2O_3 phase observed at 550 °C. Ferroelectric measurements revealed a low remnant polarisation of <1 μC/cm^2. Bismuth precursors [$Bi(mmp)_3$] and [$Bi(thd)_3$] were used in conjunction with [$Fe(thd)_3$] by Dubourdieu *et al.* to grow $BiFeO_3$ films on (001) $SrTiO_3$ substrates using oxygen as the reactive gas at a variety of substrate temperatures, again *via* DLI-CVD.[123] Better control over film stoichiometry was achieved using [$Bi(mmp)_3$] as the bismuth source and a growth temperature of 550 °C proved to be the most suitable. The clear presence of Fe^{2+} and Fe^{3+} states was observed *via* XPS, and was postulated to be the reason for the larger than expected saturation magnetisation recorded (70 emu/cm^3). The authors commented that single-source, heterometallic precursors should be explored in order to improve stoichiometry control in the films.

Kartavsteva used [$BiPh_3$] and [$Fe(thd)_3$] together with an oxygen reactive gas to grow $BiFeO_3$ films on a variety of substrates using LPCVD.[124] [$Bi(thd)_3$] and [$Bi(CH_3COO)_3$] were also evaluated as bismuth precursors due to their better evaporation characteristics and lower thermal stability compared to [$BiPh_3$], however they were observed to be more susceptible to hydrolysis due to their higher air and moisture sensitivity. Films were grown at 700 °C but contained a small amount of impurity phase $Bi_{26-x}FeO_{39}$. Takoudis[125] utilised the liquid precursor *n*-butylferrocene in conjunction with [$BiPh_3$] and oxygen gas to deposit $BiFeO_3$ on $Pt(111)/TiO_2/SiO_2/Si$ substrates using a hot-wall quartz tube LPCVD reactor. Polycrystalline films were obtained at 550 °C and they possessed a saturation magnetisation of 8 emu/cm^3 at 300 K. As stated earlier, the recent developments in the use of metalorganic precursors (as well as measurements of their vapour pressures) for growth of different multiferroic materials are summarised by Takoudis in his review, and readers are directed to this article.[38] At the time of writing, the growth of $BiFeO_3$ films *via* ALD has not been conducted, which is somewhat surprising seeing as films grown *via* this method have the advantage of strict control over morphology and thickness (for even ultra-thin films), they would be highly strained as a result of epitaxial growth with a crystal structure more akin to a monoclinic phase rather than the bulk rhombohedral structure, and have the potential to display interesting properties similar to the finite size effects observed for nanoparticulate $BiFeO_3$ powders with varying diameters,[126] and excitingly could reveal a dependence of the ferroelectric domain structure upon film growth rate.[127]

1.14 Single-source molecular precursors to $BiFeO_3$

To date, very little work has been carried out on the synthesis of single-source precursors to $BiFeO_3$ films, which is again surprising, given firstly the difficulties in synthesising phase-pure $BiFeO_3$ and the advantage of film stoichiometry control gained by using such precursors, and secondly because of the large volume of work that has already focussed on the synthesis of heterometallic precursors for ternary metal oxides such as bismuth molybdates,[128,129] titanates[81,130] and vanadates.[131]

The Lewis acidity of the bismuth atom in the *in situ* formed bismuth salicylate $[Bi(HSal)_3]$ allowed for easy formation of bimetallic bismuth-transition metal species *via* its reaction with first row TM acetylacetonates.[132] The complexes $[Bi_2(Hsal)_6.M(acac)_3]$ (M = Al, V, Cr, Fe, Co) were synthesized under mild conditions and all contain a 2:1 bismuth to metal ratio, which is advantageous because of the likelihood of bismuth evaporation at the high temperatures used for their conversion to metal oxides. A range of stable complexes, of the type $[Bi_2M(\beta\text{-diketonate})_8]$ (M = Mn, Fe, Co, Ni, Cu, Zn), were synthesized using $[Bi(hfac)_3]$ and either $[M(hfac)_2]$ or finely divided metals.[77] The reactions were carried out in a sealed ampoule containing a temperature gradient along its length, and resulted in crystals of the desired product at the colder end of the ampoule after a few days. Their crystal structures simply contain two $[Bi(hfac)_3]$ units that sandwich a $[M(hfac)_2]$ molecule and are held together *via* Lewis acid-base interactions between one oxygen atom of $[Bi(hfac)_3]$ and the TM(II) centre. It is not yet known whether the complexes decompose to the desired mixed-metal oxides. A somewhat unexpected, but beautiful paddle-wheel structure was obtained for the bimetallic complexes $[BiM(O_2CCF_3)_4]$ (M = Rh, Ru) which contain a metal–bismuth single bond (Figure 19) and may be isolated *via* the equimolar reaction of $[Bi_2(O_2CCF_3)_4]$ and $[M_2(O_2CCF_3)_4]$ in a sealed ampoule.[133] Again, thermal decomposition studies of these complexes have not been carried out so it is not clear whether they may be suitable molecular precursors to mixed-metal oxides.

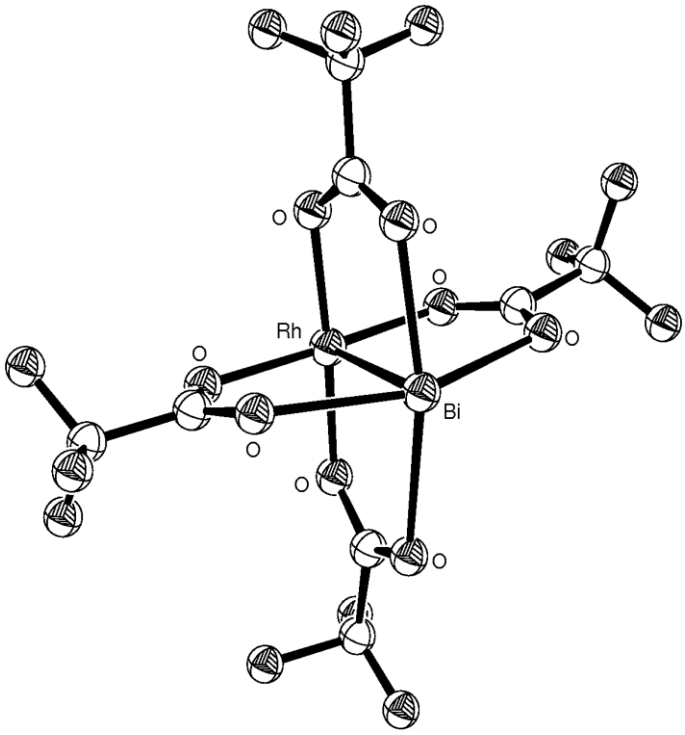

Figure 19: Molecular structure of [BiRh(O_2CCF_3)$_4$], hydrogen atoms omitted for clarity.

More recently, Wójcik *et al.* reacted Fe_2CO_9 with the bismuth alkoxides [Bi(OSiMe$_2$^{t}Bu)$_3$] and [BiO^tBu)$_3$], resulting in the formation of bismuth-iron carbonyl clusters [(CO)$_4$FeBi(OSiMe$_2$^{t}Bu)]$_2$ and [(CO)$_3$FeBi$_3$(O^tBu)$_4${OCO(O^tBu)}]$_2$.[134] The former compound undergoes thermal decomposition in air to yield [$Bi_4(SiO_4)_3$] and $Bi_2Fe_4O_9$ powders as revealed *via* PXRD and TGA of the residual material, whereas, in contrast, the latter compound decomposes in a helium atmosphere to afford bulk $BiFeO_3$ with a minimal $Bi_{25}FeO_{39}$ impurity phase. Farhady *et al.*[135] recently synthesised the bimetallic bismuth hexacyanoferrate complex [BiFe(CN)$_6$.5H$_2$O] and demonstrated that it decomposes at 600 °C in ambient air to yield well-defined, single-phase $BiFeO_3$ nanoparticles. Similarly, Navarro *et al.* synthesised pure $BiFeO_3$ powders *via* the decomposition of the analogous [BiFe(CN)$_6$.4H$_2$O] complex in air at 600 °C.[136]

1.15 Applications of $BiFeO_3$

As stated previously, multiferroics such as $BiFeO_3$ have the potential to be used in magnetically controlled ferroelectric data storage, and because they do not contain toxic elements such as lead, many companies are investigating its use for a variety of applications. This, coupled with the fact that $BiFeO_3$ exhibits reasonably strong multiferroic coupling at room temperature (unlike, for example, $YMnO_3$) makes it an exciting candidate material for a variety of applications. There are, however, many obstacles that have to be overcome before integration

of $BiFeO_3$ into devices. A main problem is high conductivity, and therefore high leakage current and large dielectric loss. Another issue is the lifetime and stability (fatigue) of $BiFeO_3$ for continuous use in storage applications that use high voltages which would ultimately cause breakdown. Scott has described many potential uses for $BiFeO_3$ in tetrahertz radiation and piezoelectric applications in his recent review, and Ramesh highlights the use of $BiFeO_3$ in microwave applications and in electrically tuneable magnetic devices *via* magnetic exchange.[92,94] For its application in spintronics, Barthelemy[137] first demonstrated the use of $BiFeO_3$ films as tunnel junctions for tunnel magnetoresistance, as well as their ability to induce an exchange bias upon a ferromagnetic film of CoFeB with low fatigue. A big breakthrough for the use of $BiFeO_3$ for spintronic applications came in 2006 with the visual evidence for electrical control of antiferromagnetic domain structures,[138] thus confirming the previously anticipated strong magnetoelectrical coupling. In 2008, the same group reported the control of ferromagnetism *via* an applied electric field of a multi-layered $CoFe/BiFeO_3$ material *via* exchange bias.[139] In 2009, the observation of a switchable ferroelectric diode and photovoltaic effect in $BiFeO_3$ led to the expectation that switchable devices combining ferroelectric, electric and optical properties could be constructed in the future.[140] This was rapidly followed by the observation of a novel mechanism for photovoltaic charge separation in the ferroelectric domain structure of $BiFeO_3$, which was said to produce voltages much higher than the band-gap of the material.[141] This could be switched on or off *via* an applied electrical field and could lead to application in optoelectronic devices.

1.15.1 $BiFeO_3$ for photocatalysis applications

The visible light photocatalytic activity of $BiFeO_3$ has also been investigated in numerous reports because it possesses an optical band-gap of approximately 2.2 eV. Maggard used bulk $BiFeO_3$ as a photosensitizer which was hydrothermally coated with $SrTiO_3$ particles in conjunction with a Pt co-catalyst for photocatalytic water splitting.[142] Appreciable hydrogen production was detected for the $SrTiO_3$-$BiFeO_3$ system (surpassing that of the Fe_2O_3-$SrTiO_3$ system) under visible light irradiation, compared to zero activity for $SrTiO_3$ alone using methanol as a hole scavenger (which precluded measurement of oxygen formation). $SrTiO_3$ itself has a very high photoactivity and possesses the required overpotential to photo-reduce water, albeit only under UV-light, whereas $BiFeO_3$ only possesses an overpotential to photo-oxidise water[143] (Figure 20; no hydrogen was produced from $BiFeO_3$ alone), and therefore only the $SrTiO_3$ was functioning as the photocatalyst in this example. $BiFeO_3$ nanowires have been demonstrated to be promising oxygen evolution catalysts from an $AgNO_3/H_2O$ system under UV-light irradiation, exhibiting high efficiencies,[144] and $BiFeO_3$ nanocubes have been shown to photocatalytically produce small volumes of oxygen (~ 0.5 μmol h^{-1}) using an aqueous $FeCl_3$ sacrificial electron acceptor solution under visible light irradiation.[145] Much work has also

focussed upon the use of $BiFeO_3$ to photocatalytically degrade organic pollutants under visible light[146,147,148] and also its use as a photosensitiser in conjunction with an ALD–grown TiO_2 surface layer, where it has been observed that electrons generated in $BiFeO_3$ migrate to the TiO_2 and can photochemically reduce silver ions on the surface in patterns that mimic the ferroelectric domain structure of the $BiFeO_3$ substrate, implying that the domains aid charge-carrier separation.[149,150]

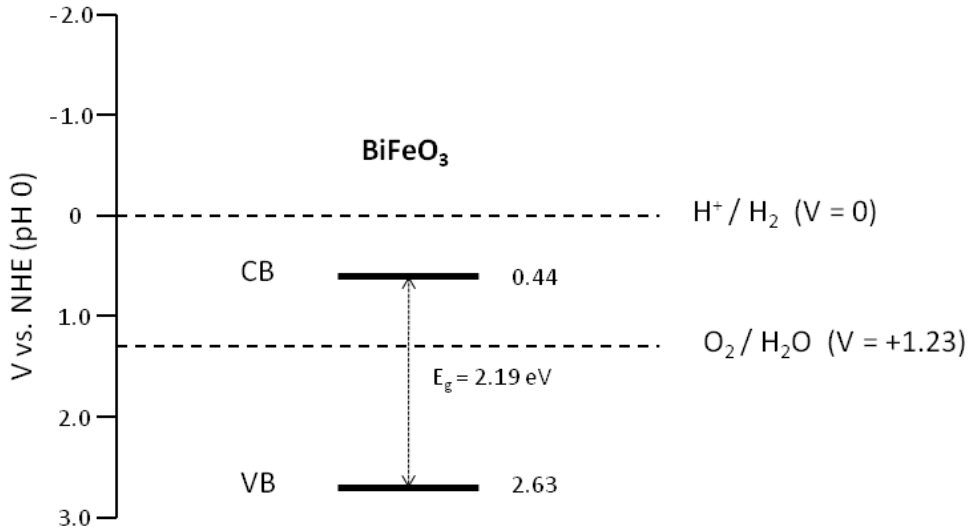

Figure 20: Energy level diagram calculated for $BiFeO_3$, showing the locations of the conduction (CB) and valence bands (VB) with respect to the redox potentials of water at pH 0.[143]

1.16 Photocatalytic water splitting

Photocatalytic water splitting for hydrogen production has the potential to make a sizeable impact in alleviating the environmental problems caused by continued burning of unsustainable fossil fuels in conjunction with meeting the world's ever increasing energy demands. Current investment in renewable and alternative fuel sources have concentrated on wind, solar and nuclear energy for electricity generation, however a viable alternative for propulsion for the automotive industry is the use of a chemical fuel source such as hydrogen in either hydrogen fuel cells or through direct combustion, whereby the only emission would be water. Solar energy, in conjunction with a suitable semiconductor photocatalyst, may be used in order to generate this hydrogen *via* photochemical reduction of water, instead of the current method, encompassing steam reforming of natural gas.

The most common materials used for photochemical water splitting are transition metal oxides with d^0 electron configurations, i.e. TiO_2,[151] whose band-gaps (typically 3.0 eV and above) are

too high to serve as efficient water splitting photocatalysts under solar/visible light irradiation. There are a number of mechanisms involved in such a process. Photons that are of energies higher than that of the band-gap of the semiconductor are absorbed by the photocatalyst, resulting in formation of electron-hole pairs in the conduction (CB) and valence bands (VB), so that the holes may go on to oxidise water to O_2 and the electrons to reduce water into H_2. This may sound simple; however there are firstly some fundamental properties that the band-gap of the photocatalyst must possess, mainly concerning its position and width.

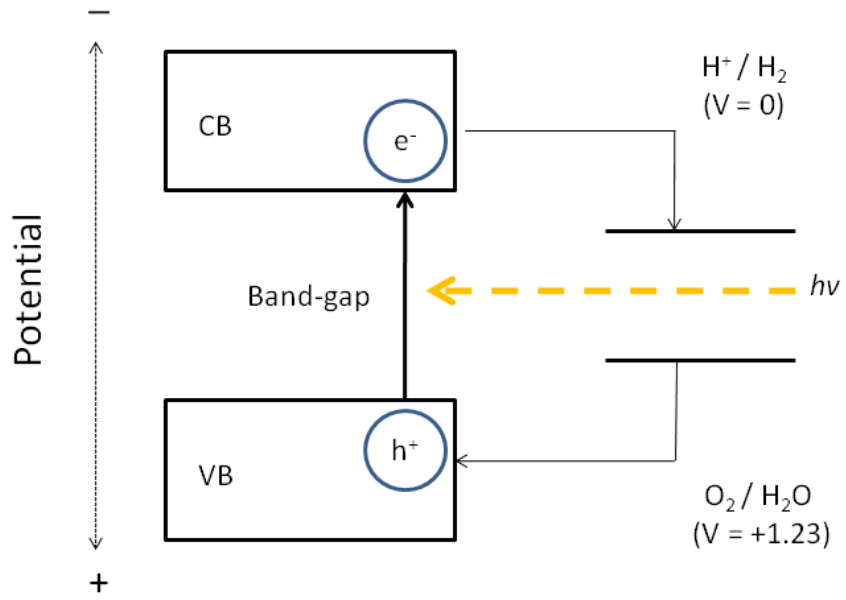

Figure 21: Diagram illustrating the principles of water splitting using semiconductor photocatalysts.[152]

The bottom level of the CB has to be more negative than the redox potential of H^+/H_2 at 0 V *vs.* NHE, whilst the top level of the VB has to be more positive than the redox potential of O_2/H_2O (+1.23 V), giving a theoretical minimum band-gap of 1.23 eV for the photocatalyst (Figure 21). However, in order for the reaction to be kinetically and thermodynamically feasible, sufficient overpotential is required. Following creation of electron-hole pairs, their separation is a key requirement as otherwise they would recombine and lower the efficiency of the material. Loading with co-catalysts such as Pt, Ni, Rh are often required for H_2 generation as the conduction bands of most catalysts are not high enough or do not possess sufficient overpotential to reduce water. Aqueous solutions of sacrificial reagents that include electron acceptors or donors are commonly used in order to test photocatalytic activity for water splitting and can measure oxidation and reduction in isolation, and therefore may reveal whether a potential photocatalyst satisfies the kinetic and thermodynamic requirements for the reaction. For example, oxygen evolution reactions may be carried out in a solution that contains Ag^+ ions

which may be reduced by the photo-generated electrons to Ag metal, whilst hydrogen evolution may be tested in solutions containing methanol which is irreversibly oxidised.[153] Kudo and Miseki have recently covered the field of photocatalytic water splitting in some detail in their comprehensive review, and readers are directed to this for an overview of the vast array of materials investigated and current state of the art.[152]

1.17 Thesis overview

The first part of this thesis therefore describes the synthesis of novel single-source molecular precursors, with the aim of using them to grow films of bismuth oxide *via* CVD. In order to identify their suitability for CVD their mass transport and thermal decomposition profiles were assessed. Thin films of bismuth oxide were grown using LPCVD and AACVD using single-source precursors, and platinum nanoparticle incorporated bismuth oxide films were grown *via* AACVD. The photocatalytic properties of these materials were tested *via* photo-oxidation and photo-reduction of water.

The second part of this thesis describes the synthesis of multiferroic $BiFeO_3$ films *via* LPCVD using a dual-source approach and AACVD using a single-source precursor. The $BiFeO_3$ films were characterised fully and their photocatalytic properties tested *via* the photo-oxidation of water under visible light irradiation.

Chapter 1: An introduction to bismuth oxide and bismuth ferrite

Chapter 2: Synthesis of precursors for deposition of bismuth oxide, iron oxide and $BiFeO_3$ films

This chapter describes the synthesis and characterisation of several bismuth(III) alkoxide and *β*-diketonate complexes. A universal route to the synthesis of these *β*-diketonates was achieved *via* the reaction of $[Bi(N(SiMe_3)_2)_3]$ and the respective free ligand. The main aim was to find an overall synthetic route to such complexes and to rationalise their volatility by comparing their structures. Additionally, volatile bismuth(III) alkoxide complexes were synthesised for deposition of bismuth oxide films *via* LPCVD. $[Fe(O^tBu)_3]_2$ was synthesised in order to be used as a precursor, in conjunction with $[Bi(O^tBu)_3]$, for growth of $BiFeO_3$ *via* dual-source LPCVD. The synthesis of the bimetallic complex $[\{Cp(CO)_2Fe\}BiCl_2]$ was described in order to be used as a single-source precursor to $BiFeO_3$ films.

Chapter 3: Thermal decomposition studies of potential single-source bismuth oxide CVD precursors

The thermal decomposition of the novel bismuth *β*-diketonate complexes that were described in Chapter 2 were investigated using DSC-TGA in order to identify suitable precursors and

deposition conditions for film growth. Similarly, the thermal decomposition of the volatile bismuth alkoxides [Bi(mmp)$_3$] and [Bi(O^{t}Bu)$_3$] were investigated in addition to the *β*-diketonate [Bi(thd)$_3$] in order to identify suitable deposition conditions for their use in the growth of bismuth oxide films *via* LPCVD.

Chapter 4: LPCVD of Bi_2O_3 films and their use in photo-oxidation of water

The thermal and mass transport characteristics of several volatile bismuth oxide single-source precursors were investigated *via* DSC-TGA and vapour pressure charts to identify suitable conditions for film growth *via* LPCVD. The use of a single-source alkoxide precursor for phase-selective deposition of Bi_2O_3 films, along with the films' potential to photo-oxidise water were studied. Growth of Bi_2O_3 films has not previously been undertaken *via* a single-source precursor route, nor have undoped Bi_2O_3 been used for photo-oxidation of water and these were the main aims for this work.

Chapter 5: AACVD of Pt-Bi_2O_3 films

β-Bi_2O_3 films were grown using the single-source precursor [Bi(dbm)$_3$]$_2$ in toluene solvent *via* AACVD. Platinum(0) films were grown from the AACVD reaction of $H_2PtCl_6.6H_2O$ in methanol solvent, and subsequently platinum-nanoparticle incorporated *β*-Bi_2O_3 films were grown *via* a one-pot AACVD procedure using [Bi(dbm)$_3$]$_2$ and $H_2PtCl_6.6H_2O$ as precursors. The resultant films were investigated for photo-reduction of water using a sacrificial solution. The aim was to show how Pt-nanoparticle incorporated Bi_2O_3 films may be grown *via* AACVD and to highlight the ability of the *composite* material to produce hydrogen from water under solar illumination.

Chapter 6: Dual-source LPCVD of $BiFeO_3$ films with an oxidising source

The growth of $BiFeO_3$ films using a commercially available iron precursor, a bismuth alkoxide and an oxidising gas, are described. Film characterisation, including magnetism studies will be described, along with an investigation of the films' potential to photo-oxidise water under visible light irradiation. The aim was to demonstrate that multiferroic $BiFeO_3$ films could be grown using these three sources *via* careful adjustment of the deposition conditions.

Chapter 7: Dual-source LPCVD of $BiFeO_3$ films

The dual-source CVD reaction of an iron and bismuth precursor containing matching ligands to deposit $BiFeO_3$ films will be described. Film characterisation using SQUID magnetometry and ferroelectric measurements, along with their potential to photo-oxidise water under visible light will also be investigated. The benefit of using matched precursors without the use of an oxidising gas will therefore be demonstrated.

Chapter 8: AACVD of $BiFeO_3$ films from a bimetallic Bi-Fe single-source precursor

The growth of $BiFeO_3$ films using a single-source precursor through use of the AACVD technique will be described. Conditions for growth of phase-pure films will be covered, along with details of their magnetoelectric characterisation. Similarly, their use in the photo-oxidation of water under visible light irradiation will be compared and contrasted with those films synthesised *via* LPCVD. The aim was to illustrate how solution-based techniques, together with the use of single-source precursors, are more beneficial for controlled growth of mixed-metal oxides rather than employing dual-source precursors. The use of $BiFeO_3$ as a strong visible light photo-oxidiser will be discussed.

Chapter 9: Conclusions.

The overall conclusions of the work described in this thesis will be summarised.

1.18 Film analysis techniques

1.18.1 Powder X-ray diffraction (PXRD)

PXRD is a rapid analytical technique used to investigate the structures of crystalline materials, and can provide information on the unit cell dimensions, and if of sufficient quality, the arrangement of the atoms within the unit cell. The technique is based on the constructive interference (diffraction) of X-rays by correctly orientated planes present within the sample according to Bragg's Law: $n\lambda = 2d\sin\theta$. Here, λ is the wavelength of the incident X-ray radiation, d corresponds to the interplanar spacing, *n* is an integer, referred to as the order of diffraction (usually 1), and θ is the angle between the diffracted beam and the crystal planes. For powder diffraction, the crystallites must be randomly oriented and be small enough in size to statistically represent all possible orientations for diffraction to occur. In this thesis, PXRD in reflection (flat-plate) geometry will be used for film analysis (Figure 22). The anode is usually fixed (at approximately 5°) and the sample is rotated by θ and the detector rotated by 2θ, however it is possible to fix the sample position and rotate the detector, depending on the setup available.

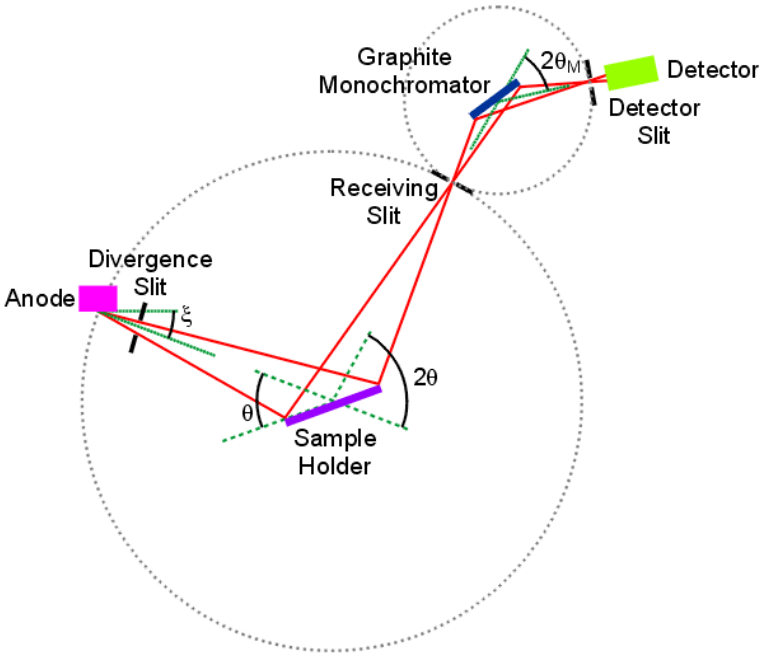

Figure 22: PXRD set up in reflection geometry. $2\theta_M$ is the diffracted angle of the X-ray after diffraction through the post sample monochromator, which is used to limit beam divergence and results in narrower diffraction peaks (Bruker D4 diffractometer).[154]

PXRD may be used for phase identification of crystalline materials within a sample, or for complete structural solution in the field of new materials discovery. For this study, PXRD will only be used for phase identification *via* a comparison with database powder diffraction patterns

as well as for the estimation of average particle sizes using the Scherrer Equation (see Chapter 4 for more details).

1.18.2 Scanning Electron Microscopy (SEM)

SEM is a useful tool for imaging the morphology of a film's surface as well as the composition (*via* EDX), and the orientation of the crystallites that the film is composed of. A high energy electron beam interacts with the sample and as a result, secondary electrons, backscattered electrons and X-rays are produced. The X-rays are produced by excitation of electrons in the inner shells of the sample, leading to their ejection, and creating holes. Higher energy electrons fill these holes and release energy in the form of X-rays which are characteristic of the energy levels and atomic structure of the element(s) present. The secondary electrons are ejected from the K-orbitals of the atoms through inelastic scattering, after which the signal is amplified and displayed as an intensity distribution upon a display screen. Wavelength dispersive analysis of X-rays (WDX) is a form of electron microscopy used for compositional analysis of samples. The X-rays emitted by the sample after interaction from the incident electron beam are focussed to irradiate a known single crystal standard of the material thought to be present within the sample. Diffraction occurs according to Bragg's Law, however only X-ray wavelengths of the desired material are allowed to pass through to the detector. This technique is more suitable for samples containing light elements and is more accurate for both qualitative and quantitative analysis in comparison to EDX, where peak overlap between neighbouring elements is a common problem.

1.18.3 X-ray photoelectron spectroscopy (XPS)

XPS is a powerful technique for obtaining quantitative analysis of the composition of a thin film but requires UHV conditions. The sample is irradiated with monochromatic X-rays (in this case Al K_α X-rays with an energy of 1486.6 eV) which cause the ejection of electrons from the core shells of the atoms within the sample. The kinetic energy (KE) distribution of the escaping photoelectrons may be measured using an electron analyser, and, through conservation of momentum, $KE = h\nu + BE$. The binding energy (BE) of the escaping photoelectron may therefore be calculated, and as each element possesses a characteristic BE associated with each core atomic orbital, not only the presence but also the oxidation state of the element within that sample may be found, as peak shifting arises from the chemical state an element may be present in. XPS is primarily a surface technique but etching experiments can be undertaken which probe deeper into a sample, however preferential sputtering of lighter elements becomes likely.

Furthermore, the intensities of the peaks are directly proportional to the concentration of that element within the sample, allowing for elemental quantification. Appropriate software is required (e.g. CasaXPS) in order to fit peaks from the background signal and determine peak areas and shifts.

1.18.4 Atomic Force Microscopy (AFM)

AFM in was used in this study in order to investigate the surface morphology and roughness of the films. The mode of use was intermittent contact mode (or "tapping mode") whereby the cantilever oscillates at a height of approximately 200 nm above the film surface at its resonant frequency through the use of a piezoelectric within the AFM tip. The effects of surface forces such as dipole-dople interactions, Van der Waals forces and electrostatics cause shifts in the oscillations of the AFM tip, and therefore an image of the surface morphology may be visualised. In addition to imaging, an estimation of the root mean squared roughness (rms) along with other parameters may be obtained by the use of appropriate statistical software (e.g. Gwyddion freeware).

1.18.5 SQUID Magnetometry

The second half of this thesis focuses on the growth and characterisation of $BiFeO_3$ films, and as a result, magnetism measurements were required in order to investigate the magnetic behaviour of $BiFeO_3$ at room temperature and low temperature (5 K). Magnetism measurements were carried out using a Vibrating Sample Magnetometer, where a linear motor vibrates the sample mounted on a quartz rod into the magnetometer. The magnetic field (up to 7 Tesla) is generated *via* a liquid helium cooled superconducting magnet. The sample is oscillated at a frequency of 40 Hz near a detector coil where the induced voltage is amplified and detected. In simplistic terms the induced voltage in the detector coil is proportional to the magnetic moment of the sample. In this thesis the hysteresis loops (M-H curves) will be measured in order to provide information on the saturation magnetisation and coercivity of the samples. This is carried out by measuring the magnetisation (M) of a sample as a function of the applied magnetic field strength (H) at a fixed temperature. Removal of the field followed by its reversal will give information as to the remnance and coercivity of the sample. As $BiFeO_3$ has been known to show low temperature ferromagnetic behaviour by exhibiting hysteresis, one way to test this observation is to conduct a zero field cooled-field cooled (ZFC-FC) measurement. For zero field cooling, the sample is cooled in the absence of a magnetic field to 5 K, and once stabilised, the magnetisation is measured as a function of temperature whilst

employing a constant field strength. For field cooling, the sample is cooled back to 5 K and the measurement conducted again as a function of decreasing temperature. The difference in the shapes of these curves can be used to explain the irreversibility of ferromagnetic materials and magnetic phase transitions may be observed experimentally.

1.18.6 Ferroelectric measurements

Measurement of the polarisation, (P), per unit area as a function of electric field strength, (E), for films of $BiFeO_3$ were carried out in collaboration with the National Physical Laboratory, Teddington, UK. Films had to be deposited on conducting substrates (silicon) and have platinum top electrodes sputtered on top of the film in order to contact the two analyser electrodes to the material in the form of a capacitor. For an ideal capacitor, the P-E loop is a straight line whose gradient is proportional to its capacitance due to the fact that as the current leads the voltage by 90°, this results in the charge being in phase with the voltage. Conversely a resistor has the voltage and current in phase so the resultant loop is circular in shape. A ferroelectric hysteresis loop is therefore a combination of the two. When charging a capacitor, the increase in voltage with charge is given by $dQ = C(V)\,dV$, where C(V) is dependent upon the applied electric field. The polarisation 'P' (C/m^2) that is induced in a polarisable material (a dielectric) by the applied electric field 'E' (V/m) is given by $P = \chi e$, where χ (F/m) is the dielectric susceptibility of the material. An excellent description of the ferroelectric, dielectric and piezoelectric properties of ferroelectric thin films is given in an article by Damjanovic.[155]

For measurements, an electric field at a constant frequency (1 kHz) is applied to the sample from zero to 150 kV/cm. The polarisation (charge) is measured as a function of increasing electric field strength. At saturation, the field is switched off and then reversed. The process is cycled continuously and allows for measurement of saturation polarisation, remnance and coercivity, analogous to an M-H loop. A typical setup for a P-E measurement device is shown in Figure 23.

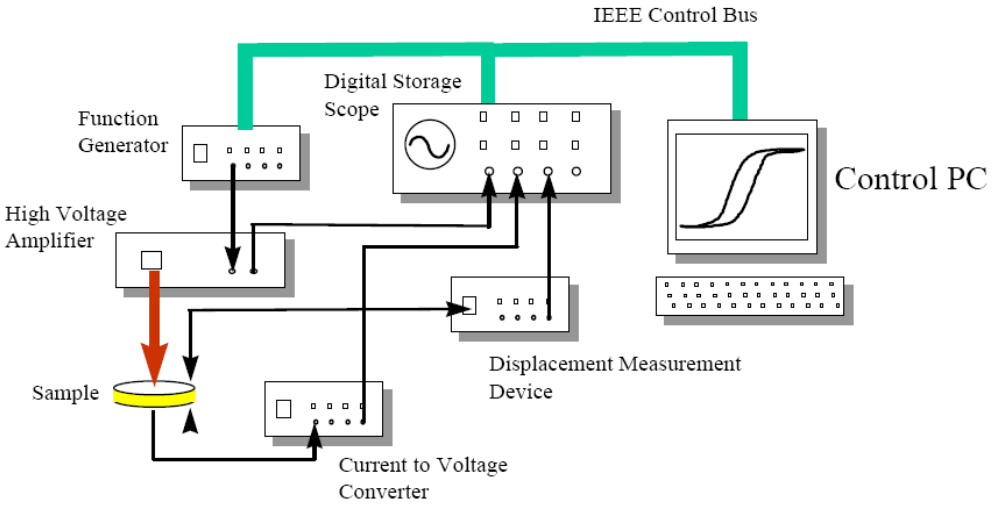

Figure 23: Typical set-up of a device for carrying out ferroelectric measurements, taken from M. Stewart and M.G. Cain, NPL.[156]

2 Synthesis of bismuth oxide and bismuth ferrite CVD precursors

2.1 Introduction

As described in the introduction, single-source precursors for the deposition of bismuth oxide and bismuth ferrite ($BiFeO_3$) thin films have previously not been employed, which is surprising given the advantages of single-source precursors for controlling deposition and film stoichiometry. This chapter describes the synthesis of potential single-source molecular precursors for the deposition of bismuth oxide and bismuth ferrite thin films *via* chemical vapour deposition (CVD). The precursors were fully characterised *via* NMR, IR, mass spectrometry, elemental analysis, and where applicable, single crystal X-ray diffraction.

2.2 Experimental – General Procedures

All reactions were performed under a dry, oxygen-free nitrogen atmosphere using standard Schlenk techniques and an MBraun Unilab glove box. Nitrogen (99.96%) was obtained from BOC and used as supplied. All solvents were stored in alumina columns and dried with anhydrous engineering equipment, such that the water concentration was 5-15 ppm. All reagents (apart from acetylacetone, which was distilled over calcium hydride) were used without further purification and were procured from Sigma-Aldrich, Alfa Aesar or Strem Chemicals Ltd.

2.3 Physical Measurements

NMR spectra were recorded on Bruker AMX300, AMX400 and AMX500 machines using C_6D_6 as solvent (unless otherwise stated), distilled over sodium/benzophenone ketyl. ^1H and $^{13}C\{^1H\}$ chemical shifts are reported relative to $SiMe_4$ (δ = 0.00 ppm). FT-IR spectra were recorded on a Perkin Elmer Spectrum RX I instrument, over the range 4000-400 cm^{-1} in nujol mulls. CI^+ mass spectra were recorded on a Micromass ZABSE instrument, and the letter "L" utilised for the results corresponds to each ligand. Microanalytical data were obtained at University College London (UCL) using an EA-440 horizontal load analyser supplied by Exeter Analytical.

For crystal structures recorded at UCL, crystals were mounted on a glass fibre using silicon grease and Fomblin vacuum oil. Geometric and intensity data were obtained on a Bruker SMART APEX CCD diffractometer using graphite-monochromated Mo-K_α radiation (λ_1 =

0.71073 Å) at 150(2) K. Data reduction and integration were carried out with SAINT+, absorption corrections were applied using SADABS, refinements and solutions were performed using PLATON, the WinGX package and all software packages within.[157] All non-hydrogen atoms were refined using anisotropic thermal parameters. Hydrogen atoms were placed in geometrically assigned positions with fixed bond lengths of 0.95 Å (aromatic CH) and 0.98 Å (CH_3). These were refined using a riding model with a $U_{iso}(H)$ value of 1.2 U_{eq} (CH) or 1.5 U_{eq} (CH_3) of the parent atom.

2.4 Synthesis of single-source bismuth oxide precursors

2.4.1 Synthesis of bismuth amido complexes

2.4.1.1 Synthesis of $[LiN(SiMe_3)_2]$ (1)

A solution of *n*-butyl lithium in hexane (1.60 M, 9.30 ml, 14.8 mmol) was added slowly *via* cannula to a separate flask containing hexamethyldisilazane (2.40 g, 14.8 mmol) that was immersed in liquid nitrogen. The solution was stirred overnight, resulting in a colourless solution of **(1)**. The solvent and volatile by-products were removed *in vacuo* leaving a white crystalline powder of $LiN(SiMe_3)_2$, (1.9 g, 77%). **^{1}H NMR**, δ/ppm (C_6D_6, 300MHz): (s, 18H, (CH_3)$_2$). **^{13}C{^{1}H} NMR**, δ/ppm (C_6D_6, 300MHz): 4.97 (SiCH_3). **Mass Spec**: m/z (CI^+, methane): 162 $[HN(SiMe_3)_2]^+$

2.4.1.2 Synthesis of $[Bi(N(SiMe_3)_2)_3]$ (2)

Compound **(2)** synthesised according to a literature method.[87] Bismuth(III) chloride (3.76 g, 11.9 mmol) dissolved in THF (40 ml) was added drop wise *via* cannula to a stirred solution of $LiN(SiMe_3)_2$ (6.0 g, 35.9 mmol) in hexane at -78 °C. Upon addition, the solution slowly changed in appearance from colourless to bright yellow and was stirred at room temperature for 24 h. The solvents were removed *in vacuo*, and the residue dissolved in hexane. The yellow solution was filtered leaving undissolved lithium chloride which was discarded. The solvent was removed *in vacuo*, leaving a bright yellow crystalline powder (7.67 g, 93%). **Anal. Calc** for $C_{18}H_{54}N_3Si_6Bi$: C 31.3%, H 7.9%, N 6.1% **Found:** C 29.0%, H 7.6%, N 4.6%. **^{1}H NMR**, δ/ppm (C_6D_6, 300MHz): 0.39 (s, 54H, (CH_3)). **^{13}C{^{1}H} NMR**, δ/ppm (C_6D_6, 75.4 MHz): 6.58 ($SiCH_3$). **FT-IR** cm^{-1} (KBr disc, nujol mull): 2957 s, 2924 m, 2851 m, 2728 w, 2677 vw, 2361 w, 2330 w, 1460 vs, 1377 vs, 1297 w, 1250 m, 1152 w, 1090 m, 1020 m, 907 s, 850 vs, 777 s, 755 w, 722 m, 692 w, 666 s, 610 m. **Mass Spec**: m/z (CI^+, methane): 529 $[Bi(N(SiMe_3)_2]^+$, 161 $[HN(SiMe_3)_2]^+$

2.4.1.3 Synthesis of [Bi(NMe$_2$)$_3$] (3)

Bismuth(III) chloride (3.0 g, 9.5 mmol) dissolved in THF (40 ml) and was added drop wise *via* cannula to a stirred solution of $LiNMe_2$ (1.46 g, 28.5 mmol) in hexane (60 ml) at -78 °C. Upon addition, the solution slowly changed in appearance from colourless to pale yellow-green and was stirred at room temperature for 24 h. The solvents were removed *in vacuo* and the residue dissolved in hexane. The green solution was filtered leaving undissolved lithium chloride which was discarded. The solvent was evaporated to dryness, leaving behind a green oily residue. The residue was sublimed, using a heat gun, across to a separate Schlenk flask immersed in liquid nitrogen, resulting in a pale yellow-green oily solid (2.4 g, 73%). The extreme sensitivity of this compound toward light, air and moisture should be noted. Despite its subsequent storage under in a freezer at -30 °C, its gradual decomposition into metallic bismuth was clearly evident. Unfortunately due to its highly air and light sensitivity, no additional characterisation, apart from ^{1}H NMR spectroscopy, could be obtained. **^{1}H NMR**, δ/ppm (C_6D_6, 400MHz): 3.46 (s, 6H, $(CH_3)_2$).

2.4.2 Synthesis of bismuth alkoxides

2.4.2.1 Synthesis of [Bi(O^{t}Bu)$_3$] (4)

Bismuth(III) chloride (1.0 g, 3.2 mmol) dissolved in THF (40 ml) and was added drop wise *via* cannula to a solution of sodium *tert*-butoxide (0.9 g, 9.5 mmol) in THF (40 ml) whilst stirring at -78 °C. Upon addition, the solution slowly changed in appearance and a white precipitate formed almost immediately. The reaction was stirred at room temperature for 24 h. The solvent was removed *in vacuo*, leaving an oily residue containing sodium chloride and the desired product in the bottom of the flask. The bismuth *tert*-butoxide was then sublimed onto a water cooled cold finger (85 °C, 2 mmHg) which resulted in the deposition of long white needles (1.12 g, 82%). The single crystal datasets obtained from the needles were of poor quality due to twinning of the crystals, but unit cell parameters obtained were in agreement with the literature.[67] **Anal. Calc** for $C_{12}H_{27}O_3Bi$: C 33.6%, H 6.4%. **Found:** C 33.4%, H 6.4%. **^{1}H NMR**, δ/ppm (C_6D_6, 300MHz): 1.43 (s, 27H, $(CH_3)_3$). **^{13}C{^{1}H} NMR**, δ/ppm (C_6D_6, 75.4 MHz): 35.4 (CH_3), 74.2 (*C*-O). **FT-IR** cm^{-1} (KBr disc, nujol mull): 3182 w, 2952 s, 2918 s, 2853 s, 2727 w, 1463 vs, 1377 vs, 1304 w, 1260 m, 1235 w, 1174 br s, 1089 br m, 1022 w, 923 s, 903 s, 800 m, 758 m, 722 s, 571 s, 545 w, 452 m. **Mass Spec:** m/z (CI$^+$, methane): 209 $[HBi]^+$, 239 $[BiOCH_3]^+$. 254 $[BiO(CH_3)_2]^+$.

2.4.2.2 Synthesis of [Bi(OCMe$_2$CH$_2$OMe)$_3$] (5)

1-methoxy-2-methyl-2-propanol (0.45 g, 4.4 mmol) was added carefully drop-wise *via* syringe to a Schlenk flask containing compound **(2)**, (1.0 g, 1.45 mmol) in diethyl ether (30 ml). The bright yellow solution changed colour to a very light yellow, almost colourless appearance, and was allowed to stir for 24 h at room temperature, after which the solvent and volatile by-products were removed, resulting in a light yellow oily solid which was pumped under vacuum for 72 h to dryness. The resulting yellow solid was washed with hexane three times, filtered and dried to leave a light yellow solid (0.56 g, 75%). **Anal. Calc** for $C_{15}H_{33}O_6Bi$: C 34.81%, H 6.39%. **Found:** C 31.94%, H 5.98%. **^{1}H NMR**, δ/ppm (C_6D_6, 500MHz): 1.39 (s, 6H, C(CH_3)$_2$), 3.09 (s, 3H (OCH_3)), 3.23 (s, 2H, CH_2). **^{13}C NMR**, δ/ppm (C_6D_6, 125 MHz): 31.1 (C(*C*H$_3$)$_2$), 58.6 (O*C*H$_3$), 71.4 (*C*(CH$_3$)$_2$), 85.9 (CH_2). **FT-IR** cm^{-1} (KBr disc, nujol mull): 2952 s, 2918 s, 2855 s, 2727 w, 1464 vs, 1377 vs, 1365 vw, 1354 m, 1260 s, 1228 m, 1172 s, 1151 m, 1102 br s, 1020 vw, 995 w, 955 s, 936 w, 914 w, 895 w, 847 w, 792 vs, 722 m, 599 s, 491 m, 469 w, 450 w. **Mass Spec:** m/z (CI$^+$, methane): 415 [BiL$_2$]$^+$, 1080 2[BiL$_3$]$^+$

2.4.3 Synthesis of bismuth *β*-diketonates

2.4.3.1 Synthesis of [Bi(thd)$_3$] (6)

2.4.3.1.1 Method 1:

2,2-6,6-tetramethylheptanedione (0.63 g, 3.4 mmol) was added drop wise to triphenylbismuth (0.5 g, 1.14 mmol) that had been dissolved in dry toluene (30 ml). The light yellow mixture was heated under reflux for 24h resulting in a slightly darker yellow coloured solution. The toluene and benzene produced from the reaction were removed under vacuum and the resulting solid washed with dichloromethane, filtered and dried under vacuum, leaving behind a sticky white solid. The excess tetramethylheptanedione was removed *via* sublimation (50 °C, 2.4 mmHg) onto a liquid nitrogen cooled cold finger, leaving the final product, consisting of a white crystalline solid (0.54 g, 62%) in the bottom of the flask. **Anal. Calc** for $C_{33}H_{57}O_6Bi$: C 52.2%, H 7.6%. **Found:** C 47.6%, H 7.1%. **^{1}H NMR**, δ/ppm (C_6D_6, 500MHz): 1.19 (s, 18H, (6C*H*$_3$)), 5.7 (s, 1H, (C=C*H*)), 17.1 (s, 1H, (C-O*H*)). **^{13}C{^{1}H} NMR**, δ/ppm (C_6D_6, 125 MHz): 28.6 (*C*H$_3$), 90.7 (C=*C*H), 197.5 (*C*-OH). **FT-IR** cm^{-1} (KBr disc, nujol mull): 2959 s, 2924 s, 2853 s, 1588 vw, 1567 m, 1552 w, 1499 m, 1463 s, 1377 s, 1359 vw, 1260 vs, 1222 w, 1092 br s, 1019 br s, 869 m, 798 vs, 735 vw, 722 w, 601 w, 475 w**. Mass Spec:** m/z (CI+, methane): 184 [L]$^+$, 241 [BiOCH$_3$]$^+$, 575 [BiL$_2$]$^+$, 757 [BiL$_3$]$^+$.

2.4.3.1.2 Method 2:

2,2-6,6-tetramethylheptanedione (0.24 g, 1.3 mmol) was added drop wise to a flask containing compound **(2)**, (0.3 g, 0.44 mmol) in hexane (40 ml). A white precipitate formed almost immediately upon addition of the diketone to the amide. The solution was allowed to stir for 24h at room temperature after which the hexane was removed. The white solid was washed with hexane, filtered and dried to leave a white crystalline solid (0.25 g, 76%) which had identical ^{1}H NMR, ^{13}C NMR and infrared data to the method above, apart from the disappearance of the OH proton peak at approximately 17 ppm in the ^{1}H NMR spectrum, indicating isolation of a cleaner product, free from the starting ligand.

2.4.3.2 Attempted synthesis of $[Bi(acac)_3]_n$ (7)

2.4.3.2.1 Method 1:

Acetylacetone, (1.36 g, 13.6 mmol) was added drop wise to triphenylbismuth (2.0 g, 4.5 mmol) that had been dissolved in dry toluene (30 ml). The light yellow mixture was heated under reflux for 24 h resulting in a slightly darker yellow solution along with some fine grey deposit on the flask walls (elemental bismuth). The toluene and benzene produced from the reaction was removed under vacuum, and the resulting solid washed with dry dichloromethane, filtered and removed under vacuum, leaving behind a white crystalline solid. Due to the relatively high volatility of triphenylbismuth, a large amount of the material evaporated with the solvent and recrystallised in the glass tubing as white needles as well as in the cold trap. The ^{1}H NMR spectrum of the solid remaining in the flask displayed only aromatic protons at 7.56 ppm, hence no reaction between triphenylbismuth and acetylacetone had taken place.

2.4.3.2.2 Method 2:

Acetylacetone (0.22 g, 2.17 mmol) was added carefully dropwise to a schlenk flask containing compound **(2)**, (0.5 g, 0.72 mmol) in hexane (50 ml). A white precipitate formed almost immediately upon addition of the ligand to compound **(2)**. The solution was allowed to stir for 24 h at room temperature after which the hexane was removed *via* filtration. The white solid was twice washed with hexane, filtered and dried to leave a free-flowing white crystalline solid (0.29 g, 80%). Single crystals suitable for single crystal X-ray diffraction were grown by dissolving the solid in the minimum amount of dry toluene and placing in a freezer at -18 °C for seven months. **Anal. Calc** for $C_{15}H_{21}O_6Bi$: C 35.6%, H 4.2%. **Found:** C 33.6%, H 4.0%. **^{1}H NMR**, δ/ppm (C_6D_6, 500MHz): 1.83 (s, 6H, (CH_3)), 5.1 (s, 1H (C=C*H*)), **^{13}C{^{1}H} NMR**, δ/ppm (C_6D_6, 125 MHz): 28.4 (*C*H_3), 104.9 (OC=*C*H), 188.5 (*C*=O/*C*-O). **FT-IR** cm^{-1} (KBr disc): 2957 s, 2924 m, 2854 m, 2728 w, 2671 vw, 2341 m, 1596 w, 1515 m, 1458 vs, 1375 vs, 1245

w, 1150 w, 1102 br w, 1016 m, 918 m, 800 w, 775 m, 721 s, 660 w, 590 w, 540 w. **Mass Spec:** m/z (CI^+, methane): 209 $[Bi]^+$, 239 $[BiOCH_3]^+$, 408 $[BiL_2]^+$.

2.4.3.3 Synthesis of $[Bi(dbm)_3]_2$ (8)

2.4.3.3.1 Method 1:

Dibenzoylmethane, (1.53 g, 6.8 mmol) was dissolved in toluene (50 ml) and added to triphenylbismuth (1.0 g, 2.3 mmol) that had been dissolved in toluene (20 ml). The light yellow mixture was heated under reflux for 24 h resulting in a deep yellow solution. The toluene and benzene produced from the reaction were removed under vacuum, and the resulting yellow oily solid washed with dry dichloromethane, filtered and solvents removed under vacuum, leaving behind a yellow crystalline solid (1.57 g, 79%). **Anal. Calc** for $C_{45}H_{33}O_6Bi$: C 61.5%, H 3.8%. **Found:** C 57.5%, H 3.6%. **^{1}H NMR**, δ/ppm (C_6D_6, 500MHz): 6.60 (s, 1H, (C*H*)), 7.6 (m, 10H, C_6H_5). **^{13}C{^{1}H} NMR**, δ/ppm (C_6D_6, 125 MHz): 93.0 (*C*-C=O), 127.8 (2-C_6H_5), 132.3 (3-C_6H_5), 133.2 (1-C_6H_5), 137 (4-C_6H_5). **FT-IR** cm^{-1} (KBr disc, nujol mull): 2924 s, 2957 s, 2857 s, 2722 w, 1806 w, 1599 s, 1588 w, 1538 m, 1510 m, 1463 br s, 1377 vs, 1301 m, 1261 m, 1223 m, 1180 m, 1156 w, 1096 br m, 1056 br m, 1021 s, 967 w, 926 m, 800 s, 751 s, 723 vs, 693 w, 684 m, 618 m, 608 s, 494 w, 447 s. **Mass Spec** (CI^+, methane): 225 $[L]^+$, 433 $[BiL]^+$, 650 $[BiL_2]^+$, 870 $[BiL_3]^+$.

2.4.3.3.2 Method 2:

A solution of dibenzoylmethane (0.3 g, 1.3 mmol) in dry hexane (40 ml) was added by cannula to a separate Schlenk flask containing compound **(2)**, (0.3 g, 0.44 mmol) in dry hexane (30 ml). A yellow precipitate formed almost immediately upon addition of the ligand to the silylamide. The solution was allowed to stir for 24 h at room temperature after which the solvent was removed *via* filtration. The yellow solid was washed with hexane (2 x 30 ml), filtered and dried to leave a free-flowing bright yellow solid (0.32 g, 84%) that had identical NMR and IR results to those obtained *via* the above route. Recrystallisation from a concentrated dry dichloromethane solution at -18 °C yielded X-ray quality single crystals after two days.

2.4.3.4 Synthesis of $[Bi(tfac)_3]$ (9)

1,1,1-trifluoro-2,4-pentanedione (0.67 g, 4.4 mmol) was added carefully drop wise *via* a syringe into a Schlenk flask containing compound **(2)**, (1.0 g, 1.45 mmol) dissolved in dry hexane (40 ml). In a similar manner to that described for the synthesis of compounds **(7)** and **(8)**, a white precipitate of the desired compound formed almost immediately upon addition of the ligand to the silylamide. The solution was allowed to stir for 24 h at room temperature after which time the excess hexane and hexamethyldisilazane were removed *via* filtration. The white solid was

twice washed with hexane, filtered and dried to leave a white crystalline solid (0.82 g, 85%). Despite numerous attempts crystals suitable for single crystal X-ray diffraction could not be obtained. **Anal. Calc** for $F_9C_{15}H_{12}O_6Bi$: C 27.0%, H 1.80%. **Found:** C 25.8%, H 1.8%. **^{1}H NMR**, δ/ppm (C_6D_6, 300 MHz): 1.64 (s, 3H, (CH_3)), 5.54 (s, 1H (C=CH)). **^{13}C{^{1}H} NMR**, δ/ppm (C_6D_6, 75.4 MHz): 23.4 (CH_3), no other peaks observed. **^{19}F NMR**, δ/ppm (C_6D_6, 282.1 MHz): -76.22 (s, 3F, CF_3). **FT-IR** cm^{-1} (KBr disc, nujol mull): 3170 w, 2957 s, 2918 s, 2854 s, 2727 w, 1618 br s, 1591 vw, 1530 s, 1460 br s, 1377 s, 1276 s, 1225 m, 1191 m, 1143 br s, 1088 vw, 1018 w, 940 w, 925 w, 858 m, 797 s, 724 s, 601 w, 577 m, 560 s, 461 vw. **Mass Spec:** m/z (CI^+, methane): 154 $[L]^+$, 239 $[BiOCH_3]^+$, 515 $[BiL_2]^+$.

2.4.3.5 Synthesis of [Bi(bzac)$_3$] (10)

1-phenylbutane-1,3-dione (0.35 g, 2.16 mmol) was dissolved in hexane (50 ml). This was added dropwise *via* cannula into a solution of compound **(2)**, (0.5 g, 0.72 mmol) dissolved in hexane (50 ml). A light yellow precipitate of the desired compound formed almost immediately upon addition of the ligand to the bismuth silylamide. The solution was allowed to stir for 24 h at room temperature after which the hexane and hexamethyldisilazane were removed *via* filtration. The light yellow solid was washed with hexane, filtered and dried to leave a yellow crystalline solid (0.38 g, 76%). Despite numerous attempts crystals suitable for single crystal X-ray diffraction could not be obtained. **Anal. Calc** for $C_{30}H_{27}O_6Bi$: C 52.03%, H 3.90%. **Found:** C 50.5%, H 3.9%. **^{1}H NMR**, δ/ppm (C_6D_6, 500MHz): 2.03 (s, 3H, (CH_3)), 5.88 (s, 1H (C*H*)), 7.06 (m, 3H, (o- & p-C_6H_5-)), 7.91 (m, 2H, (o-C_6H_5-)). **^{13}C NMR**, δ/ppm (C_6D_6, 125 MHz): 29.2 (CH_3), 101.86 (*C*=C), 127.8 (o-C_6H_5), 127.9 (m-C_6H_5-), 180.8 (1-C_6H_5-C=O), 191.9 (CH_3-*C*=O). **FT-IR** cm^{-1} (KBr disc, nujol mull): 2854 s, 1654 w, 1590 s, 1560 s, 1522 w, 1508 vw, 1458 br s, 1376 s, 1299 m, 1261 s, 1092 br, 1021 w, 799 s, 721 m, 702 w, 635 vw, 611 w, 560 vw, 515 vw. **Mass Spec:** m/z (CI^+, methane): 163 $[L]^+$, 370 $[BiL]^+$, 535 $[BiL_2]^+$.

2.4.4 Synthesis of Iron oxide precursors

2.4.4.1 Synthesis of [Fe(O^{t}Bu)$_3$]$_2$ (11)

A modified literature preparation was carried out for the synthesis of this compound.[158] Sodium *tert*-butoxide (1.8 g, 19.0 mmol) was dissolved in dry THF (60 ml). Anhydrous iron(III) chloride (1.0 g, 6.2 mmol) was dissolved in dry THF (40 ml) and added *via* cannula to the sodium *tert*-butoxide solution at -78 °C with continuous stirring. The solution turned a dark green-brown colour within 15 minutes. The solution was left to stir overnight, which was followed by gentle heating to 60 °C for 5 h. The THF solvent was removed *in vacuo* and the

$[Fe(O^tBu)_3]_2$ product was sublimed from the sodium chloride by-product onto a water-cooled cold finger at 120 °C, 0.1 mbar (1.6 g, 76%). **Anal. Calc** for $C_{24}H_{54}O_6Fe_2$: C 52.4%, H 9.8%. **Found:** C 52.9%, H 10.2%. **^{1}H NMR**, δ/ppm (C_6D_6, 125 MHz): 1.39 (s, 54H, ((CH_3)$_3$)), no other peaks observed. **^{13}C{^{1}H} NMR**, δ/ppm (C_6D_6, 500MHz): 35.53 ((CH_3)$_3$), no other peaks observed. **FT-IR** cm^{-1} (KBr disc, nujol mull): 2726 br s, 2671 vw, 1560 w, 1542 m, 1458 vs, 1365 m, 1377 m, 1356 w, 1299 m, 1245 w, 1224 w, 1193 vw, 1182 s, 1082 br, 992 br s, 910 s, 799 m, 782 m, 763 m, 722 s, 596 br s, 488 s, 465 m. **Mass Spec:** m/z (CI$^+$, methane): 202 $[FeL_2]^+$, 551 2$[FeL_3]^+$.

2.4.5 Synthesis of heterobimetallic bismuth-iron complexes

2.4.5.1 Synthesis of [{Cp(CO)$_2$Fe}BiCl$_2$] (12)

$[\{Cp(CO)_2Fe\}BiCl_2]$ was synthesised according to the literature.[159] A slurry of bismuth(III) chloride (1.0 g, 3.2 mmol) in dry dichloromethane (40 ml) was added dropwise with rapid stirring to a solution of the cyclopentadienyliron dicarbonyl dimer, $[Fe(CO)_2Cp]_2$ (1.12 g, 3.2 mmol) in dry dichloromethane (50 ml). The solution slowly changed colour from dark purple to orange with the evolution of an orange precipitate. The solution was left to stir overnight until all the bismuth chloride had dissolved, after which the residual solution was filtered off. The orange precipitate was washed three times with diethyl ether and dried to leave $[\{Cp(CO)_2Fe\}BiCl_2]$ as a free flowing crystalline powder (1.12 g, 77.4%). Unfortunately, crystals that were grown *via* solvent diffusion (THF/diethyl ether) could not be solved *via* single crystal X-ray diffraction. **Anal. Calc** for $C_7H_5O_2FeBiCl_2$: C 18.40%, H 1.10%. **Found:** C 18.20%, H 1.10%. **^{1}H NMR**, δ/ppm (((CD_3)$_2$CO), 500MHz): 5.29 (s, 5H (C_5H_5)). **^{13}C NMR**, δ/ppm (((CD_3)$_2$CO), 125 MHz): 85.5 (C_5H_5), 211.1 (*C*O). **FT-IR** cm^{-1} (KBr disc, nujol mull): 2854 br s, 2012 s, 1960 m, 1927 w, 1459 s, 1377 s, 1301 w, 1260 m, 1089 br s, 1021 w, 861w, 844 m, 799 s, 722 w, 617 m, 596 vw, 569 w, 558 w, 506 vw. **Mass Spec:** m/z (CI$^+$, methane): 154 $[M - BiCl_2]^+$, 421 $[M - CO]^+$.

2.5 Results and Discussion

2.5.1 Synthesis of bismuth amido compounds

2.5.1.1 Synthesis of $[Bi(N(SiMe_3)_2)_3]$ (2)

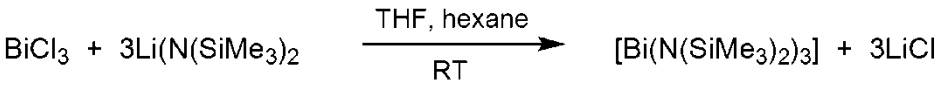

Equation 1

Compound **(2)** was synthesised by the well-known literature method,[87] from the reaction of bismuth(III) chloride and three equivalents of lithium bis-(trimethylsilylamide), shown in Equation 1. The bismuth silylamide was produced in excellent yield (93%) as a deep yellow crystalline solid, and displayed near identical NMR and mass spec data to those previously reported. The elemental analysis for measured for carbon content was 2.3% lower than calculated, which is most likely to be due to partial decomposition of **(2)** during the measurement, resulting in a lower carbon content. The ^{1}H NMR singlet peak ($Si(CH_3)_3$) was observed at 0.59 ppm where a trimethylsilyl resonance would be expected. The yield may be further increased if the lithium chloride by-product is washed at least four times with hexane, and then filtered to separate it from the highly soluble product (soluble in almost all aromatic and aliphatic solvents.) However, due to the high temperature sensitivity of this compound, heating the reaction to reflux quickly led to decomposition to elemental bismuth. The compound is extremely air and moisture sensitive, turning white and hydrolysing on exposure to air, but can be wrapped in aluminium foil (it is moderately light sensitive) and stored for several months in a glovebox. Due to its high volatility, it has displayed some potential use as a precursor for ALD of BiO_x films (oxygen deficient) using water as a co-reactant, as well as a precursor for ALD/CVD of bismuth silicate films in the presence of oxygen gas.[87] The compound was synthesised in order to be used as a reactant to form bismuth(III) alkoxides and β-diketonates that could be then used as single-source precursors to bismuth oxide films.[67]

2.5.1.2 Synthesis of $[Bi(NMe_2)_3]$ (3)

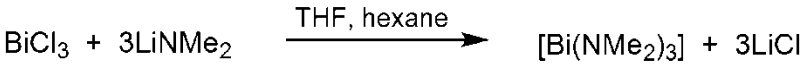

Equation 2

The bismuth amido complex, **(3)**, was synthesised according to the literature method,[160] from the reaction of bismuth(III) chloride and three equivalents of lithium dimethylamide (Equation 2). The method relies upon the distillation of a green oily residue of $[Bi(NMe_2)_3]$ into a Schlenk

flask submerged in liquid nitrogen (trap-to-trap distillation) and hence the yield (73%) was not very high. The contents of the flask had a yellow-green appearance, and slowly transformed into darker green needles a few hours after sublimation, despite being covered in aluminium foil and placed in a freezer at –18 °C. Due to its high air and light sensitivity, only ^{1}H NMR spectroscopy could be obtained on the sample, which showed the expected singlet peak at 3.46 ppm. The high photosensitivity of this material was realised after just a few days due to the appearance of metallic bismuth around the flask walls. The extreme sensitivity of this compound would render it troublesome in evaluating its synthetic potential to produce bismuth alkoxides and *β*-diketonates. It was decided therefore that this compound would be unsuitable for any further investigation. Nevertheless, its high volatility could be exploited for CVD purposes for deposition of bismuth containing films once problems concerning its storage are addressed.

2.5.2 Synthesis of bismuth alkoxides

2.5.2.1 Synthesis of [Bi(O^{t}Bu)$_3$] (4)

$$[Bi(N(SiMe_3)_2)_3] + 3\,{}^{t}BuOH \xrightarrow{Et_2O,\ RT} [Bi(O{}^{t}Bu)_3] + 3HN(SiMe_3)_2$$

Equation 3

The synthesis of this compound was firstly attempted *via* a ligand exchange reaction between [Bi(N(SiMe$_3$)$_2$)$_3$] **(2)** and three equivalents of distilled *tert*-butanol in diethyl ether solvent, as shown in Equation 3. However, regeneration of *tert*-butanol crystals along with compound **(2)** suggested that no reaction had taken place. There are a number of possible reasons for this observation. Firstly, this may be due to the relatively high *p*Ka of *tert*-butanol (approximately 19), indicative of a relatively strong RO-H bond, however the *p*Ka of hexamethyldisilazane is ~ 26, albeit measured in water. It is possible that the pKa value of *tert*-butanol is altered enough so that the reaction is no longer favourable – such bulky alcohols do not dissociate as easily in non-polar solvents, such as diethylether or hexane. It is also possible that the sterically bulky SiMe$_3$ and ^{t}Bu groups make the ligand-exchange reaction kinetically slow or thermodynamically unfavourable (analogous to the chelate effect); an attempt to reflux the reagents led to decomposition of **(2)** to grey, metallic bismuth. Given that the reaction of the donor-functionalised alcohol 1-methoxy-2-methyl-2-propanol (mmp) with [Bi(N(SiMe$_3$)$_2$)$_3$] successfully yielded the desired product ([Bi(mmp)$_3$], see below), it is likely that not only the acidity but also the mode of binding of the ligands (monodentate *vs*. bidentate) has an effect on

the likelihood for the reaction to take place. Cleavage of the Bi-N bond in compound **(2)** was successful using 'mmp' but unsuccessful with *tert*-butanol.

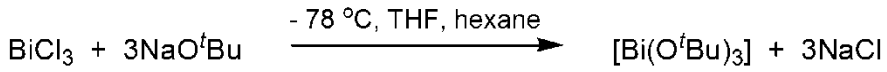

Equation 4

Bismuth *tert*-butoxide was therefore synthesised *via* the metathesis reaction between $BiCl_3$ and three equivalents of sodium *tert*-butoxide in THF, as shown in Equation 4. Following removal of the solvent, the product was sublimed onto a cold finger under relatively mild conditions, resulting in large white needles in high yield. Owing to the limited capacity of the cold finger, it was necessary to repeat the sublimation process at least five times to ensure the entire product had been captured. Unfortunately, an initial sample of crystals placed under the microscope was twinned. At the time of synthesis, the solid-state structure of **(4)** had not been obtained *via* single crystal X-ray diffraction; only the unit cell and heavy atom positions were found in an attempt in 1990.[67] Coincidentally, shortly after our synthesis in 2010 the crystal structure of **(4)** was published, revealing it to be composed of loosely bound polymeric chains.[91] A gas phase electron diffraction study of this compound revealed it to be monomeric in the gas phase.[161] Infrared analysis obtained for compound **(4)** show excellent agreement with the literature,[67] with a peak at 1174 cm^{-1} assigned to a C-O vibration and Bi-O vibrations at 571, 545 and 472 cm^{-1} . So far there appears to be no use of this compound to produce bismuth containing films *via* CVD, possibly due to the difficulty of synthesis, its instability in air and its poor solubility in solvents that are commonly used for *liquid injection* CVD. Nevertheless, its distinct advantages include its high volatility under mild conditions (Chapter 4) and its reported monomeric structure in the gas phase, both of which are advantageous for thermal CVD purposes. The TGA profile of this compound is described in Chapter 3.

2.5.2.2 Synthesis of $[Bi(OCMe_2CH_2OMe)_3]$ - $[Bi(mmp)_3]$ (5)

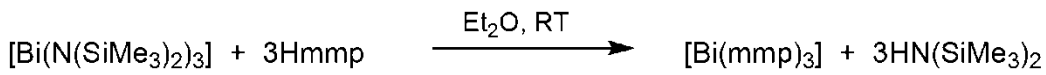

Equation 5

Tris(1-methoxy-2-methyl-2-propoxy)bismuth, was synthesised according to published procedures from the reaction of compound **(2)** with three equivalents of the donor functionalised alcohol in diethyl ether solvent, shown in Equation 5.[162] The yellow-brown oily solid required intense drying to form a creamy-white solid that displayed identical NMR results to those in the

literature.[72] In an attempt to improve the yield from 75%, refluxing the reagents in hexane or toluene resulted in decomposition to bismuth metal, again highlighting the thermal instability of the bismuth silylamide **(2)**. The product **(5)** is extremely air and light sensitive, and despite being stored in a glovebox wrapped in aluminium foil, decomposition to metallic bismuth was observed after a period of three months. Infrared analysis of the compound showed excellent agreement with the literature, with vibrations at 1228, 1172, 1151, 1102, 995, 955, 936, 914, 895, 792, 599 (C-O and C-C vibrations), and 491, 469 cm^{-1} being almost identical to those previously published.[162] Bi-O vibrations can be assigned to peaks at 491, 469 and 450 cm^{-1}. The crystal structure of **(5)** has been found to be monomeric, and has been identified as a suitable precursor for MOCVD of bismuth oxide and bismuth containing films using *liquid injection* MOCVD reactors. This compound was synthesised in order to compare its volatility and decomposition characteristics with other bismuth precursors. The TGA trace of this compound is described in Chapter 3.

2.5.3 Synthesis of bismuth *β*-diketonates

As described in the introductory chapter, there are a number of routes commonly used to synthesise bismuth(III) *β*-diketonates; these are summarised in Scheme 2, Chapter 1. The present study has made use of the amine-ligand exchange reaction as well as the reaction of the ligand with triphenylbismuth under reflux conditions. The metathesis reaction involving the use of alkali-metallated ligands was not pursued due to problems with isolating the desired product from the metal halide by-product.[67]

2.5.3.1 Synthesis of $[Bi(thd)_3]$ (6)

$$[Bi(Ph_3)] + 3Hthd \xrightarrow[toluene]{\Delta} [Bi(thd)_3] + 3C_6H_6$$

Equation 6

$[Bi(thd)_3]$ **(6)** was synthesised *via* two routes. The first was *via* the reflux of triphenylbismuth with three molar equivalents of the free ligand, Hthd, in toluene following a literature procedure (Equation 6).[75] The solvents were removed under vacuum and the excess free ligand was sublimed under reduced pressure to leave **(6)** as a free flowing, white crystalline powder in 63% yield. Despite the sublimation, some excess free ligand was still present in the final product with a small resonance observed at 17.1 ppm (C-O*H*) in the ^1H NMR spectrum. Nevertheless, the ^1H NMR spectrum displayed, as expected, the backbone proton resonance at 5.7 ppm along

with the *tert*-butyl resonance at 1.19 ppm, shifted slightly compared to the free ligand which suggests successful coordination to the metal centre.

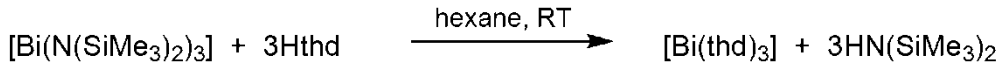

Equation 7

An alternative synthetic route to prepare **(6)** was *via* the ligand-exchange reaction between bismuth silylamide **(2)** with Hthd using hexane as a solvent (Equation 7). The reaction was complete in a matter of minutes with the product precipitating out of hexane as a white solid in higher yield (76%) compared to the reaction using $BiPh_3$ described above, and significantly higher than the metathesis route[67] (41%) which requires sublimation of the product. Compound **(6)** is soluble in most polar organic solvents. The NMR spectra of the product were almost identical using either route; however the disappearance of the OH peak at 17.1 ppm in the ^1H NMR spectrum suggests the ligand-exchange reaction went to completion and that, encouragingly, no free ligand was present in the final product. Infrared analysis revealed that vibrations at 1588, 1567, 1552 cm^{-1} (C-O/C=C) were in good agreement with the literature.[82] Peaks were also observed at 1499, 1377, 1359, 1222, 798, 735, 722, 601, 475 cm^{-1} that could be matched to those already published, with those at 601 and 475 cm^{-1} assigned to Bi-O vibrations. $[Bi(thd)_3]$ has been the subject of several investigations regarding its decomposition in order to be used as a bismuth oxide CVD precursor,[62,74] and here it was synthesised in order to make a comparison between other bismuth oxide precursors, with this new synthetic route allowing its isolation with minimal impurity. The TGA profile for this compound appeared to be in agreement with these reports and is described in Chapter 3.

2.5.3.2 Synthesis of $[Bi(acac)_3]_n$ (7)

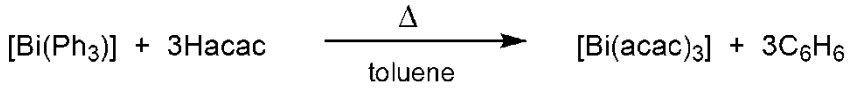

Equation 8

The synthesis of bismuth acetylacetonate was attempted *via* two routes, according to Equation 8 and Equation 9. Similar to the synthesis of $[Bi(thd)_3]$, one route attempted was *via* the reflux of triphenylbismuth with three equivalents of acetylacetone using toluene as the solvent. Unfortunately, the product obtained after removal of solvent was identified as triphenylbismuth from NMR spectroscopy and therefore no reaction had taken place. This was most likely to be due to the low thermal stability and relatively low acidity of the acetylacetone ligand.[82,78]

Another attempt to synthesise $[Bi(acac)_3]_n$ was attempted by Armelao[79] *via* the same method. This resulted in the apparent intramolecular cyclisation of acetylacetone to form 1-(2-hydroxy-4,6-dimethylphenyl)ethanone instead of the intended $[Bi(acac)_3]_n$ molecule.

$$[Bi(N(SiMe_3)_2)_3] + 3Hacac \xrightarrow{\text{hexane, RT}} [Bi(acac)_3] + 3HN(SiMe_3)_2$$

Equation 9

The other method utilised was *via* the reaction of the bismuth silylamide **(2)** with Hacac using hexane as the solvent (Equation 9). Again, the reaction appeared complete within a matter of minutes with the product precipitating out of hexane as a white solid in fairly good yield (79%). The ^{1}H NMR spectrum of **(7)** showed a slight downfield shift of resonances compared with free Hacac, suggesting successful coordination of the ligand to the metal centre. The backbone proton singlet was observed at 5.1 ppm and the CH_3 resonance at 1.83 ppm. Elemental analysis results were within reasonable agreement of the calculated values; however the 2% discrepancy between the observed and calculated values for the carbon analysis may be due to partial decomposition of **(7)** to bismuth oxide or other species as a consequence of the measurement procedure. The infrared spectrum displayed clear peaks at 1596 (C=C), 1515 and 1458 cm^{-1} (C-O), with vibrations at 721, 660, 590, 540 cm^{-1} attributed to the presence of Bi-O bonds. The mass spectrometry data did not reveal the expected molecular ion peak $[ML]H^+$ at *m/z* = 507, which may be due to decomposition of the compound during the analysis. Sublimation under reduced pressure onto a water cooled cold finger within the temperature range 50-150 °C led to gradual decomposition of the compound to yellow bismuth oxide, followed by decomposition to metallic bismuth towards the higher end of the temperature range, which suggests that this compound may not be suitable for low pressure CVD. TGA analysis for this compound is described in Chapter 3. Single crystals suitable for single crystal X-ray diffraction were eventually grown by dissolving the material in the minimum amount of dry toluene and placing in a freezer at -18 °C for seven months.

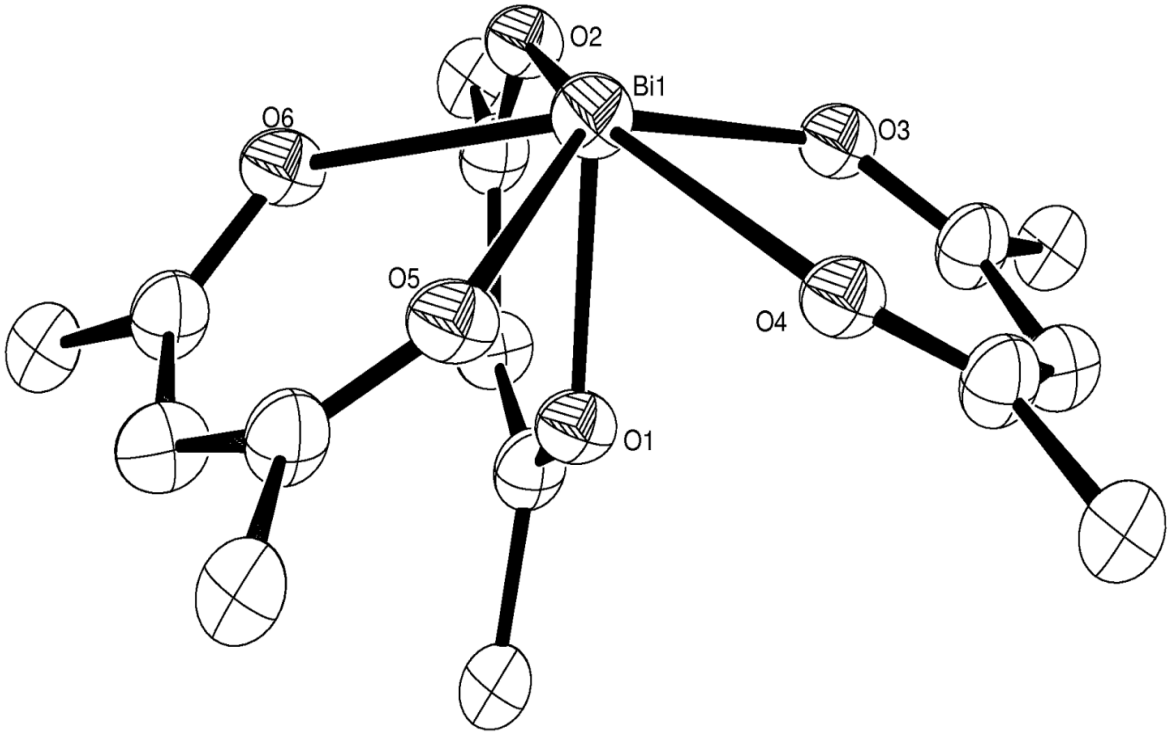

Figure 24: Structure of the asymmetric unit of $[Bi(acac)_3]_n$.

$[Bi(acac)_3]_n$ crystallises in the monoclinic $P2_1/c$ space group, and unlike many of the previously crystallographically characterised bismuth β-diketonates, it forms an extended 1-D polymer in the solid state with three oxygen atoms bridging to adjacent bismuth ions. The asymmetric unit of $[Bi(acac)_3]_n$ is shown in Figure 24, where the three "acac" ligands are shown surrounding the metal centre, giving the impression that the bismuth centre is based on a 7 electron pair coordinate geometry, (including the stereochemically active lone pair). Selected bond lengths and bond angles are given in Table 1.

Table 1: Selected bond lengths and angles for $[Bi(acac)_3]_n$.

Bond Lengths		Bond Angles	
Bond	**Bond length (Å)**	**Bond**	**Bond angle (°)**
Bi(1)-O(1)	2.193(14)		
Bi(1)-O(3)	2.296(15)	O(1)-Bi(1)-O(3)	77.4(5)
Bi(1)-O(2)	2.333(12)	O(1)-Bi(1)-O(2)	83.0(5)
Bi(1)-O(6)	2.347(12)	O(1)-Bi(1)-O(6)	75.5(5)
Bi(1)-O(4)	2.436(12)	O(1)-Bi(1)-O(4)	78.3(4)
Bi(1)-O(5)	2.499(13)	O(1)-Bi(1)-O(5)	77.8(5)

$[Bi(acac)_3]_n$ contains Bi-O bond lengths in the range 2.193(14) – 2.499(13) Å. The Bi-O bond lengths are shorter than those observed for the bridging Bi-O bonds in dimeric bismuth tris-*β*-diketonate complexes $[Bi(thd)_3]$ and $[Bi(hfac)_3]$, that possess Bi-O bridging bond lengths of 3.007(9) Å and 2.937(2) Å respectively. This can be attributed to less steric hindrance of the methyl groups on the acac ligand in comparison to the thd and hfac ligands which contain *tert*-butyl and trifluoro moieties respectively at either end of the ligand. This allows the repeat units of the polymer in $[Bi(acac)_3]_n$ to pack much closer together than in $[Bi(thd)_3]$ and $[Bi(hfac)_3]$. There is a large void or gap around one half of the coordination sphere which is too large to be explained by a stereochemically active lone pair.

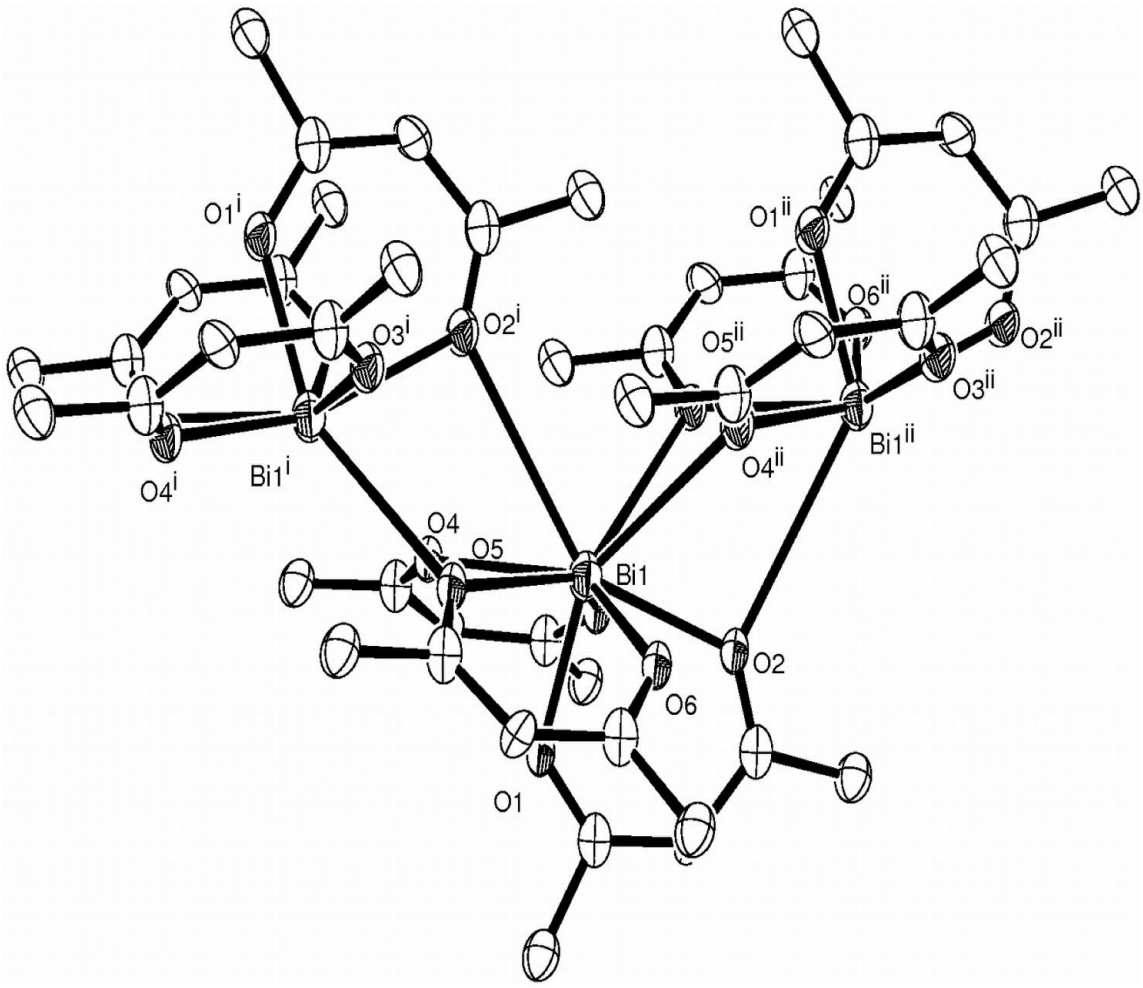

Figure 25: Diagram showing the polymeric nature of $[Bi(acac)_3]_n$. Thermal ellipsoids are at the 50% probability level and hydrogen atoms were omitted for clarity. Atoms labelled 'i' are related by the symmetry code – x, 0.5 + y, 1.5 – z and atoms marked 'ii' by the symmetry code – x, y – 0.5, 1.5 – z.

Figure 25 depicts the structure of $[Bi(acac)_3]_n$ as a 1-D polymer. The large gap is now filled in and shows the arrangement of the bridging Bi-O bonds to the adjacent molecule. The bismuth centre is crowded and is now based on a 10-coordinate geometry, when taking into account the stereochemically active lone pair on bismuth. Similar to other bismuth β-diketonates, there appears to be no Bi-Bi interaction as the Bi-Bi distance is 4.337 Å, and the approximate van der Waals radius of bismuth is 2.0 Å. As detailed in Table 1, there are three long-range Bi-O interactions present in the molecule, one to the neighbouring left bismuth centre, and two to the right. The polymeric structure of $[Bi(acac)_3]_n$ in the solid state is perhaps the most important reason why this complex possesses such low volatility, decomposing to metallic bismuth upon heating.

2.5.3.3 Synthesis of $[Bi(dbm)_3]_2$ (8)

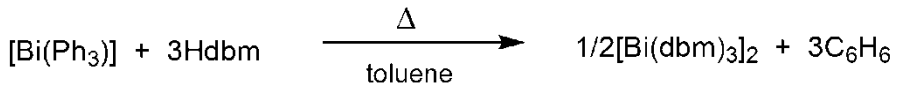

Equation 10

$[Bi(dbm)_3]_2$ **(8)** was synthesised in a similar fashion to that of compound **(7)** as shown in Equation 10. Firstly from a direct reflux of three equivalents of Hdbm with triphenylbismuth, and secondly from a direct ligand exchange reaction between the silylamide **(2)** and Hdbm in hexane (Equation 11). The yield was slightly greater from the latter route and the visual appearance of the product was found to be a more intense yellow colour than that obtained from the reflux reaction. A possible reason for this could be due to some unreacted cream-coloured free ligand being present after the reflux, which may be difficult to distinguish in NMR spectroscopy.

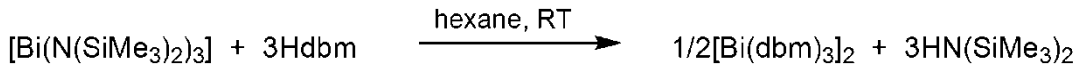

Equation 11

The second method to synthesise this compound requires the addition of the free diketone to the bismuth silylamide **(2)**, which allows the product to be isolated easily from the solvent *via* filtration, followed by drying under vacuum. ^{1}H NMR spectroscopy of **(8)** revealed the presence of the backbone proton at 6.60 ppm, along with the multiplet at 7.60 ppm corresponding to the aromatic protons. An infrared analysis for **(8)** revealed peaks at 1599, 1588, 1538 and 1510 cm^{-1} that can be assigned to C=C and C-O vibrations, with those at 494 and 447 cm^{-1} arising from the Bi-O bonds present. From the mass spectrometry data, the molecular ion peak $[ML_3]^+$ was observed at m/z = 870. It should be noted that there appeared to be some discrepancy between the observed and calculated values for carbon content (4.6%), of which there may be several reasons for. Firstly, the elemental analysis procedure at UCL involved a very brief exposure of the complex to air, which could lead to partial decomposition of the complex. Secondly, any residual solvent remaining in the sample could trigger decomposition of the complex into bismuth oxide or similar species, thus lowering the carbon value.

Recrystallisation from a concentrated dichloromethane solution at -30 °C yielded X-ray quality yellow prismatic crystals after three days. The crystal did not decompose despite being left in air for over 72 h after the study, indicating that the product possesses a degree of stability in air.

$[Bi(dbm)_3]_2$ crystallized in the triclinic space group *P*-1 as an oxygen-bridged centrosymmetric dimer (Figure 26).

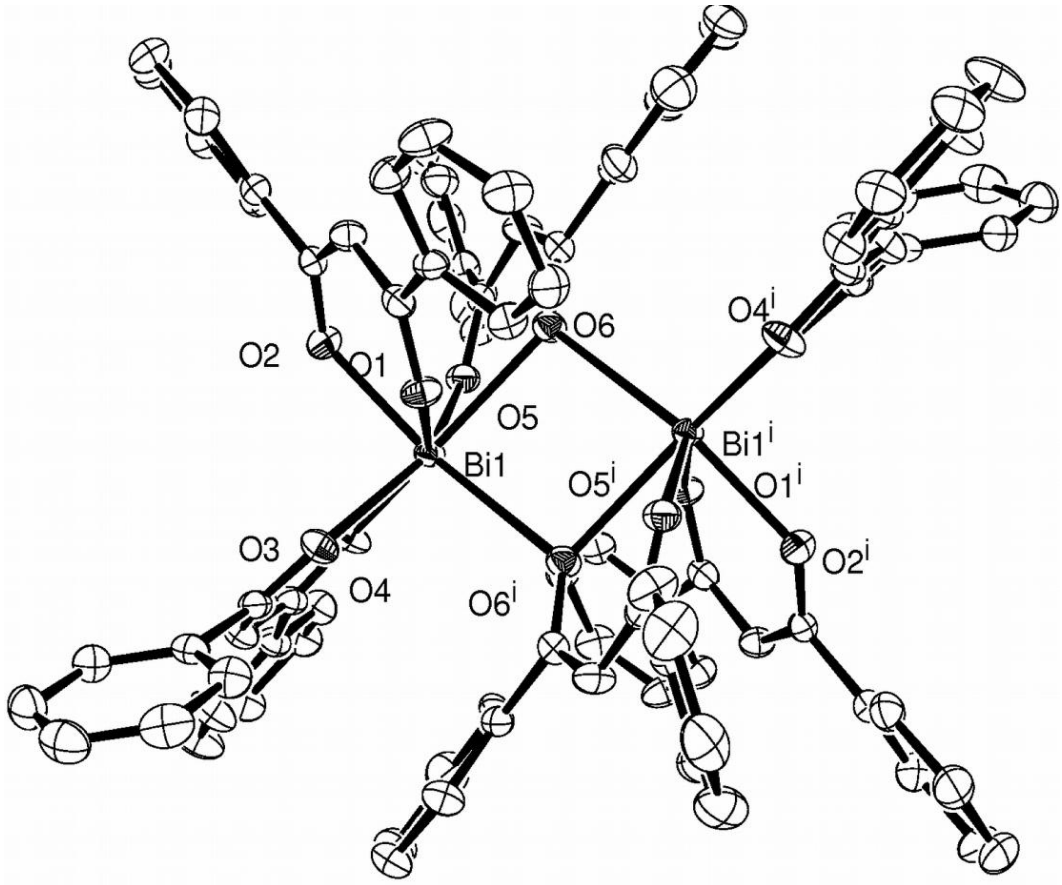

Figure 26: ORTEP diagram showing the dimeric nature of $[Bi(dbm)_3]_2$. Thermal ellipsoids at 50% probability, phenyl rings (bar ipso carbons), one CH_2Cl_2 solvent of crystallization and hydrogen atoms omitted for clarity. Atoms labelled 'i' are related by the symmetry code 1-x, 1-y, 1-z.

The inversion point lies at the heart of the Bi_2O_2 ring at the centre of the molecule. Each bismuth centre is formally 7-coordinate however, with the lone pair on bismuth, there are 8 valence pairs of electrons thus the coordination geometry of $[Bi(dbm)_3]_2$ is based on an 8 valence pair compound. The arrangement of electron pairs best fits a square antiprism, with the degree of distortion away from an ideal square antiprism, shown in Figure 27.

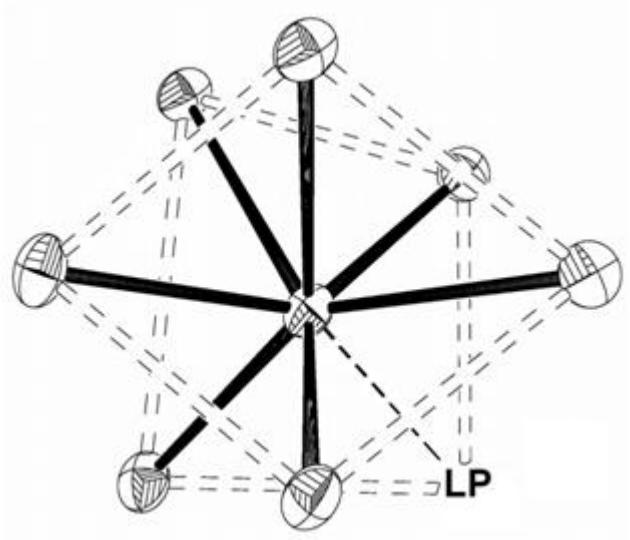

Figure 27: Diagram representing the 8 valence pairs of electrons around bismuth in a distorted square antiprismatic geometry. LP = stereochemically active lone pair.

The six Bi–O bonds to symmetry-independent oxygen atoms are in the range 2.177(3) Å to 2.477(3) Å, with one Bi–O bond being significantly shorter than the rest (Table 3). Whilst there is a wide disparity within that range, it is notable that the Bi–O(1) and Bi–O(2) bonds to the same *β*-diketonate (bdk) ligand greatly differ. The same effect, although less pronounced, is also noted for the Bi–O bonds to the other two *β*-diketonate ligands. This is probably due to packing effects as three sterically encumbered *β*-diketonate ligands attempt to minimise the interaction between themselves, the Bi lone pair and the second half of the dimer. The Bi–O(6) bond is the longest of the non-bridging bonds (apart from complex $[Bi(thd)_3]_2 \cdot H_2O$), as is expected owing to the fact that O(6) is involved in bridging to the second Bi centre. Selected bond angles for $[Bi(dbm)_3]_2$ are given in Table 2.

Table 2: Selected bond angles for $[Bi(dbm)_3]_2$.

Bond	Bond angle (°)
O(2)-Bi(1)-O(1)	78.75(11)
O(3)-Bi(1)-O(4)	75.78(10)
O(5)-Bi(1)-O(6)	70.73(10)
O(2)-Bi(1)-O(3)	87.98(11)
O(6)-Bi(1)-O(6)^{i}	80.15(10)
Bi(1)-O(6)-Bi(1)^{i}	99.85(10)

The same packing effect is also noted in other homoleptic *β*-diketonate complexes of Bi, namely $[Bi(thd)_3]_2$, $[Bi(thd)_3]_2 \cdot H_2O$, $[Bi(thd)_3]_2 \cdot 3H_2O$ and $[Bi(hfac)_3]_2$ (Table 3). In each case, there is one extremely short Bi–O(2) bond which is significantly different to the other bond [Bi–O(1)] to the same *β*-diketonate ligand. In the better-quality datasets, it is possible to see that there is a difference in Bi–O bond lengths for the other *β*-diketonate ligands [O(3) and O(4) are from the same ligand, as are O(5) and O(6)].

The Bi–O distance corresponding to the 'bridging' Bi–O bond is much longer than the non-bridging interactions in $[Bi(dbm)_3]_2$ at 2.760(3) Å. This is expected from bridging bonds and is replicated in all other $[Bi(bdk)_3]_2$ complexes (Table 3). However, it is by some distance the shortest bridging bond yet observed in dimeric $[Bi(bdk)_3]_2$ complexes with the next longest bridging Bi–O bond *ca.* 0.2 Å longer in $[Bi(hfac)_3]_2$. The $[Bi(acac)_3]_n$ molecule, where three Bi-O bonds bridge to adjacent bismuth centres has much shorter Bi-O bond lengths due to the comparatively lower steric bulk of the acetylacetone ligand in comparison to dibenzoylmethane (Table 1).

Table 3: Selected bond distances (Å) for $[Bi(dbm)_3]_2$ and comparison to other structurally characterized $[Bi(bdk)_3]_2$ complexes from the literature.

Bond	$[Bi(dbm)_3]_2$	$[Bi(thd)_3]_2$	$[Bi(thd)_3]_2 \cdot H_2O$	$[Bi(thd)_3]_2 \cdot 3H_2O$	$[Bi(hfac)_3]_2$
Bi–O(1)	2.337(3)	2.399(7)	2.38(2)	2.34(1)	2.376(3)
Bi–O(2)	2.177(3)	2.132(10)	2.26(2)	2.13(1)	2.159(3)
Bi–O(3)	2.326(3)	2.295(8)	2.30(2)	2.36(1)	2.370(3)
Bi–O(4)	2.345(3)	2.344(8)	2.36(2)	2.38(1)	2.396(2)
Bi–O(5)	2.458(3)	2.293(8)	2.47(2)	2.39(1)	2.357(3)
Bi–O(6)	2.477(3)	2.455(9)	2.32(2)	2.41(1)	2.394(3)
Bi–O(6^{i})	2.760(3)	3.007(9)	3.03(2)	3.05(1)	2.937(2)
Bi–Bi	4.0112(7)	3.968(4)	3.853(3)	3.987(3)	4.1908(3)

The Bi–Bi distance of $[Bi(dbm)_3]_2$ is the second-longest noted for $[Bi(bdk)_3]_2$ complexes. However, there is no reliable data available for the van der Waals (vdW) radius of bismuth - the often-quoted distance of 2.00 Å is an assumption on the part of the CCDC. By looking at the known vdW radii of neighbouring 6p elements (Tl 1.96 Å, Pb 2.02 Å) and the trends for lighter

main group elements (group 14 vdW radii are larger than both groups 13 and 15), it is possible to approximate an upper limit for the vdW radius of *ca.* 2.0 Å. Whilst this level of certainty is unsuitable for determining whether any kind of Bi–Bi interaction is present in $[Bi(dbm)_3]_2$, it does at least indicate that for this compound any interaction is unlikely to be present.

2.5.3.4 Synthesis of $[Bi(tfac)_3]$ (9)

$[Bi(tfac)_3]$ was synthesised as it is likely that the presence of fluorine atoms will aid its volatility and make it a more suitable CVD precursor. Additionally, the lower percentage of fluorine in the compound compared with $[Bi(hfac)_3]$ should lead to lower fluorine contamination in films deposited using this precursor. Brooks and co-workers[76] attempted to synthesise $[Bi(tfac)_3)]$ from the reaction of triphenylbismuth and three equivalents of Htfac in toluene under reflux, but without conclusive results. Perhaps unsurprisingly, this preparative route did not prove at all successful during our attempts to synthesise $[Bi(tfac)_3]$. They found that the reaction did not go to completion as the ^{1}H NMR spectrum displayed intense resonances in the aromatic region (from triphenylbismuth), and whilst mass spectrometry suggested that some of the bismuth *β*-diketonate had formed, phenyl groups were also attached to the bismuth atom, giving a mixed-ligand complex.

$$[Bi(N(SiMe_3)_2)_3] + 3Htfac \xrightarrow{\text{hexane, RT}} [Bi(tfac)_3] + 3HN(SiMe_3)_2$$

Equation 12

Therefore, $[Bi(tfac)_3]$ **(9)** was synthesised *via* a ligand-exchange reaction of bismuth silylamide **(2)** in hexane with 1,1,1-trifluoropentane-2,4-dione (Equation 12). In similar fashion to the other *β*-diketonates, the product precipitated rapidly out of the solvent, leaving a yellow-white powder in good yield (85%). ^{1}H NMR of **(9)** revealed the expected singlet at 5.54 ppm corresponding to the backbone proton. ^{19}F NMR spectroscopy of **(9)** showed the presence of equivalent fluorine atoms (CF_3) with the singlet at -75.6 ppm. The absence of the molecular ion peak $[ML_3]^+$ at *m/z* = 669 may suggest that either the compound had decomposed or perhaps fragmentation of the CF_3 moiety had occurred.[82] Infrared analysis of this compound resulted in peaks at 1618, 1591, 1530 and 1460cm^{-1} corresponding to C=C and C-O vibrations. The presence of fluorine atoms leads to bands at higher frequencies when compared to those of $[Bi(acac)_3]_n$. Similarly, Bi-O vibrations at 724, 601, 577, 560, and 461 cm^{-1} were observed and shifted to higher frequencies compared with $[Bi(acac)_3]_n$. In comparison with $[Bi(thd)_3]$ **(6)**, whose IR peaks were observed at 1588, 1567, 1552, 1499, 1377, 1359, 1222, 798, 735, 722, 601, 475 cm^{-1} respectively, the inductive effect of the *tert*-butyl groups at either end of the

ligand exert a positive inductive effect, donating electron density into the core and shifting the IR bands to lower frequencies.[82]

Despite numerous attempts utilising a variety of solvents and methods, X-ray quality single crystals of $[Bi(tfac)_3]$ could not be grown as they were too small. The TGA decomposition profile for this compound is described in Chapter 4.

2.5.3.5 Synthesis of $[Bi(bzac)_3]$ (10)

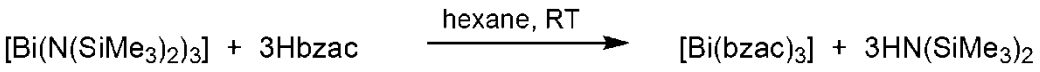

Equation 13

The bismuth β-diketonate complex $[Bi(bzac)_3]$ **(10)**, containing an asymmetric β-diketonate ligand was synthesised *via* the direct addition of 1-benzoylacetone to a solution of **(2)** in hexane solvent (Equation 13). The light yellow product precipitated from solution immediately upon addition of the ligand to the amide and was isolated in 76% yield. Similarly to $[Bi(tfac)_3]$, single crystals suitable for diffraction could not be grown, however NMR spectroscopy reveals that the intended product was obtained. From ^{1}H NMR analysis of **(10)**, the backbone (CH) resonance was observed at 5.88 ppm and the methyl (CH_3) protons were observed at 2.03 ppm. The aromatic protons were observed between 7.06 – 7.91 ppm. Elemental analysis results were also in good agreement with the calculated values. The IR spectrum of **(10)** revealed peaks ascribed to Bi-O vibrations at 721, 635, 611, 560 and, 515 cm^{-1}, along with peaks at 1590, 1560, 1522 and 1508 cm^{-1} that can be assigned to C=C and C-O vibrations, and these appear intermediate between those observed for $[Bi(acac)_3]_n$ and $[Bi(dbm)_3]_2$. From the mass spectrometry data for **(10)**, the molecular ion peak was not observed, however peaks corresponding to the free ligand at *m/z* = 163, BiL at *m/z* = 370 and BiL_2 at *m/z* = 535 were observed.

Attempts to sublime $[Bi(bzac)_3]$ between 50 - 150 °C under reduced pressure led to decomposition, forming a yellow powder in the bottom of the flask which was likely to be composed of bismuth oxide, and indicates the poor volatility of this complex. This would appear to be in agreement with the decomposition of related β-diketonates, $[Bi(acac)_3]_n$ and $[Bi(dbm)_3]_2$, which also possessed poor volatilities partly due to the structures they adopt in the solid state. Unfortunately crystals of this compound suitable for single crystal X-ray diffraction could be not obtained. The TGA profile of $[Bi(bzac)_3]$ is described in Chapter 3.

2.5.3.6 Synthesis of $[Fe(O^tBu)_3]_2$ (11)

$$2FeCl_3 + 6NaO^tBu \xrightarrow[60\ ^\circ C,\ 5\ h]{-78\ ^\circ C,\ THF,\ hexane} [Fe(O^tBu)_3]_2 + 6NaCl$$

Equation 14

The iron alkoxide complex $[Fe(O^tBu)_3]_2$ was synthesised in good yield (76%) *via* a salt metathesis reaction between anhydrous iron(III) chloride and three molar equivalents of sodium *tert*-butoxide according to Equation 14. The dark green product **(11)** was sublimed under relatively mild conditions (120 °C, 0.2 mbar) onto a water cooled cold finger. The crystal structure of **(11)** has previously been reported as a dimer, with *tert*-butoxide ligands forming the oxygen bridge to adjacent iron centres. However, ^1H NMR spectroscopy of **(11)** revealed only one broad singlet resonance at 1.39 ppm (the molecule is paramagnetic) and no other peaks for the bridging *tert*-butyl groups were observed, either suggesting that the molecule adopts a monomeric structure in solution, or that the paramagnetic nature of the molecule results in sufficient broadening of the lines to merge the two signals together. Compound **(11)** is very air sensitive and visually oxidises upon exposure to air in a matter of seconds. $[Fe(O^tBu)_3]_2$ has already been utilised as a single-source precursor to iron oxide films *via* LPCVD;[158] it also possesses a high degree of volatility which could be advantageous for CVD purposes if it were to be used in conjunction with the ligand-matched bismuth precursor $[Bi(O^tBu)_3]$ for growth of $BiFeO_3$ films. The TGA profile of $[Fe(O^tBu)_3]_2$ is discussed in Chapter 7.

2.5.3.7 Synthesis of $[\{Cp(CO)_2Fe\}BiCl_2]$ (12)

$$[CpFe(CO)_2]_2 + BiCl_3 \xrightarrow{CH_2Cl_2} [\{Cp(CO)_2Fe\}BiCl_2] + [Cp(CO)_2FeCl]$$

Equation 15

The bimetallic bismuth-transition metal compound $[\{Cp(CO)_2Fe\}BiCl_2]$ **(12)** was synthesised *via* the published reaction route[159] between $BiCl_3$ and $[Fe(CO)_2Cp]_2$ using dichloromethane as the solvent, as shown in Equation 15. The product was isolated as a bright orange powder in good yield (77%) after washing repeatedly with diethyl ether. Compound **(12)** was found to be soluble in THF only. Recrystallisation *via* solvent diffusion using a THF/diethyl ether combination resulted in large dark red crystals, however due to disorder the structure could not

be solved *via* single crystal diffraction. Nevertheless, a polymeric chlorine-bridged structure is expected similar to that obtained for the analogous compound [{Cp''$(CO)_2$Fe}$BiCl_2$], where Cp'' = n^5-$CH_5H_3{}^tBu_2$ (Figure 28).[159] The ^{1}H NMR spectrum of **(12)** recorded in $(CD_3)_2CO$ revealed a singlet at 5.29 ppm representing the cyclopentadienyl protons (C_5H_5), and from the ^{13}C NMR spectrum a peak at 85.5 ppm representing the same moiety was observed along with a peak at 211.1 ppm representing the carbonyl groups. IR analysis of **(12)** revealed carbonyl vibrations at 2012, 1960 and 1927 cm^{-1} consistent with the literature. The bismuth : iron ratio in the compound is 1:1, matching that of the target material $BiFeO_3$, and the high synthetic yield of **(12)** makes it attractive as a potential single-source precursor to $BiFeO_3$ films *via* CVD (a process that would require large amounts of precursor). The TGA trace of this compound is discussed in Chapter 8.

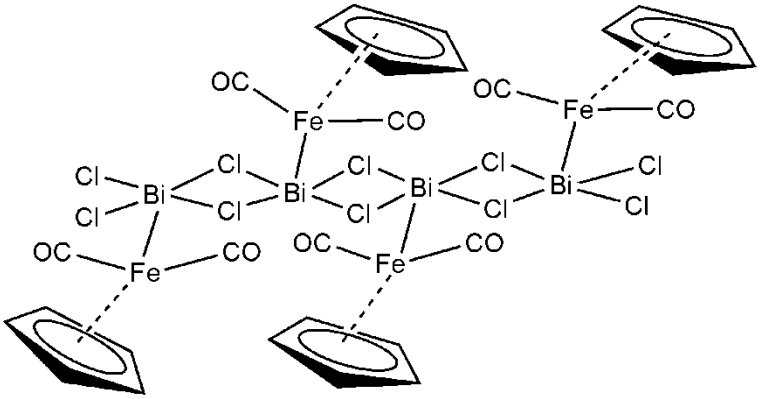

Figure 28: Structure likely to be adopted for [{Cp$(CO)_2$Fe}$BiCl_2$], following the reported structure of [{Cp''$(CO)_2$Fe}$BiCl_2$].

2.6 Conclusions

Two bismuth(III) alkoxides, $[Bi(O^tBu)_3]$ and $[Bi(mmp)_3]$, were synthesised according to the literature in good yield, either *via* metathesis or ligand-exchange reactions, for use as potential single-source precursors to bismuth oxide films. $[Bi(mmp)_3]$ has already been utilised as a precursor, in conjunction with oxygen, for deposition of bismuth oxide films (*via* DLI-CVD) and was synthesised in order to compare its thermal and mass transport characteristics with the other precursors. The complex is extremely moisture and light sensitive, making storage difficult over prolonged periods. $[Bi(O^tBu)_3]$ has so far not been used as a CVD precursor due to its perceived high moisture sensitivity. Sublimation experiments revealed that it is volatile under extremely mild conditions and could be a viable precursor for LPCVD of bismuth oxide films. The complex is light stable and may be stored for prolonged periods without decomposition. The potential use of bismuth alkoxides as single-source bismuth oxide precursors required an analysis of their decomposition and mass transport characteristics; these are described in Chapters 3 and 4.

A number of homoleptic bismuth(III) β-diketonate complexes were also synthesised for use as potential single-source precursors to CVD of bismuth oxide films. $[Bi(thd)_3]$ and $[Bi(dbm)_3]_2$ were synthesised *via* the reaction of the free diketone ligand with triphenylbismuth in refluxing toluene or *via* an amine-ligand exchange with $[Bi(N(SiMe_3)_2)_3]$. Contrastingly, $[Bi(acac)_3]_n$, $[Bi(tfac)_3]$ and $[Bi(bzac)_3]$ could only by synthesised *via* the amine-ligand exchange reaction due to the low acidities of the free ligands. The crystal structures of $[Bi(acac)_3]_n$ and $[Bi(dbm)_3]_2$ were solved, revealing a 1-D polymeric structure for $[Bi(acac)_3]_n$ and an oxygen-bridged dimer for $[Bi(dbm)_3]_2$. In order to determine the suitability of these β-diketonate complexes as potential single-source precursors to bismuth oxide, their decompositions were studied *via* TGA (Chapter 3).

Additionally, the synthesis of $[Fe(O^tBu)_3]_2$ was carried out in order for it to be used in conjunction with $[Bi(O^tBu)_3]$ for dual-source LPCVD of $BiFeO_3$ films. The decomposition and mass transport properties of $[Fe(O^tBu)_3]_2$ are described in Chapter 7.

The synthesis of $[\{Cp(CO)_2Fe\}BiCl_2]$, which contains a 1:1 ratio of bismuth and iron atoms, was carried out *via* the literature route in good yield in order to be used as a potential single-source precursor to $BiFeO_3$ films. The complex is not volatile for thermal CVD (it could not be sublimed); however its solubility in THF indicates potential use for AACVD of $BiFeO_3$ films. Its decomposition characteristics are described in Chapter 8.

.

3 Decomposition studies of potential bismuth oxide single-source precursors

3.1 Introduction

Chapter 2 described the synthesis of a variety of precursors to deposit bismuth oxide films *via* CVD. In this chapter, the decomposition profiles of several novel, synthesised bismuth(III) *β*-diketonate complexes were investigated *via* DSC-TGA in order to assess their suitability to serve as potential single-source precursors to bismuth oxide. In addition to these complexes, the decomposition of the commercially available and previously used, volatile bismuth oxide precursors [Bi(mmp)$_3$] and [Bi(thd)$_3$] were investigated for their use as single-source precursors in LPCVD. [Bi(O^{t}Bu)$_3$], despite possessing appreciable volatility, has not previously been employed as a CVD precursor to bismuth oxide, and therefore its decomposition characteristics were also analysed *via* TGA, and its potential to serve as a single-source precursor was highlighted.

3.2 Physical Measurements

TGA studies were conducted using a Netzsch 449 C Instrument under a flow of helium gas (50 ccm) with a heating rate of 10 °C min^{-1}. TGA samples were sealed in the glovebox into aluminium pans and pierced with a hole in the lid prior to analysis. X-ray diffraction was carried out using a Bruker-AXS D8 powder diffractometer equipped with a GADDS Hi-Star area detector, using Cu-K$_\alpha$ radiation (λ = 1.54056 Å) in the range 10 – 65° 2θ. X-ray diffraction was carried also out using a Bruker-AXS D4 powder diffractometer in reflection geometry using Cu-K$_\alpha$ radiation (λ = 1.54056 Å) on a rotating sample holder in the range 10 – 70° 2θ, 0.05° step size, with 2 s per step. Phase information was obtained from the Diffrac^{plus} EVA program suite (Version 2) and ICSD.

3.3 Results and discussion

3.3.1 DSC-TGA trace of [Bi(acac)$_3$]$_n$

The decomposition profile of [Bi(acac)$_3$]$_n$ is shown in Figure 29. There appears to be a total of six weight loss steps, of which three are quite large. From the TGA trace, there is an initial small mass loss of 1.2% up to the melting temperature which was observed in the DSC trace at

106 °C. There then follows a steep mass loss of 12% up to approximately 160 °C, accompanied by several small peaks in the DSC trace, which could potentially be ascribed to volatilisation of the material. There then follows a continuation of this steep mass loss (14%) up to 200 °C, followed by a more gradual mass loss of 8% to 355 °C. Between 355 °C and 380 °C there is one more steep mass loss of 4.1%, accompanied by a peak in the DSC trace which may be due to crystallisation to metallic bismuth or bismuth oxide; this is eventually followed by a gradual mass change of 2.6% up to 600 °C. In total, the weight loss of the precursor during the experiment was 41.9%, however the fraction of weight loss observed during decomposition was 34% (29.9% mass lost from a total of 88%, corrected for volatilisation).

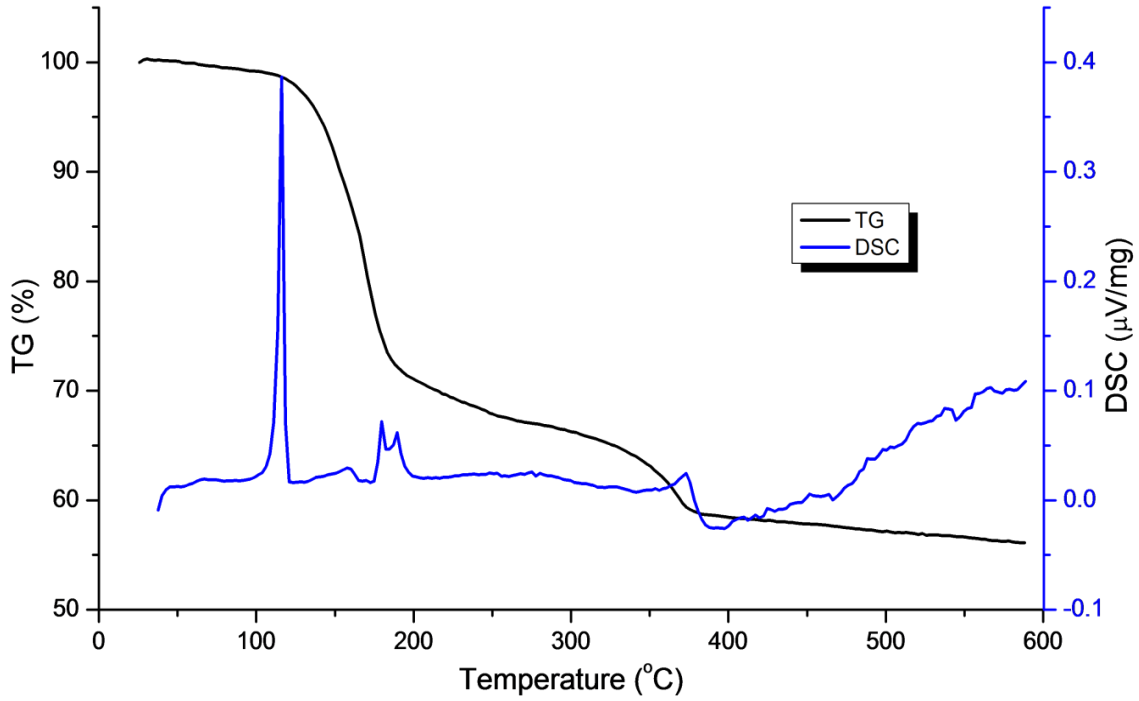

Figure 29: DSC-TGA trace for $[Bi(acac)_3]_n$. The heating rate was 10 °C min^{-1}.

In order to form stoichiometric Bi_2O_3, the calculated mass loss required would be 54%, and this figure is clearly much higher than that observed in the TGA trace. This might be somewhat surprising, given that attempts to sublime $[Bi(acac)_3]_n$ at a pressure of 10^{-2} mbar resulted in decomposition to a grey solid, possibly metallic bismuth, perhaps ruling out any possible volatilisation seen in the TGA. PXRD analysis of the residue remaining in the TGA pan after heating (Figure 30) revealed the presence of metallic bismuth in agreement with observations during sublimation experiments. Given that the conditions of the TGA experiment are much different to a laboratory sublimation experiment, such discrepancies can exist, however its use for LPCVD was discounted based on the latter observation.

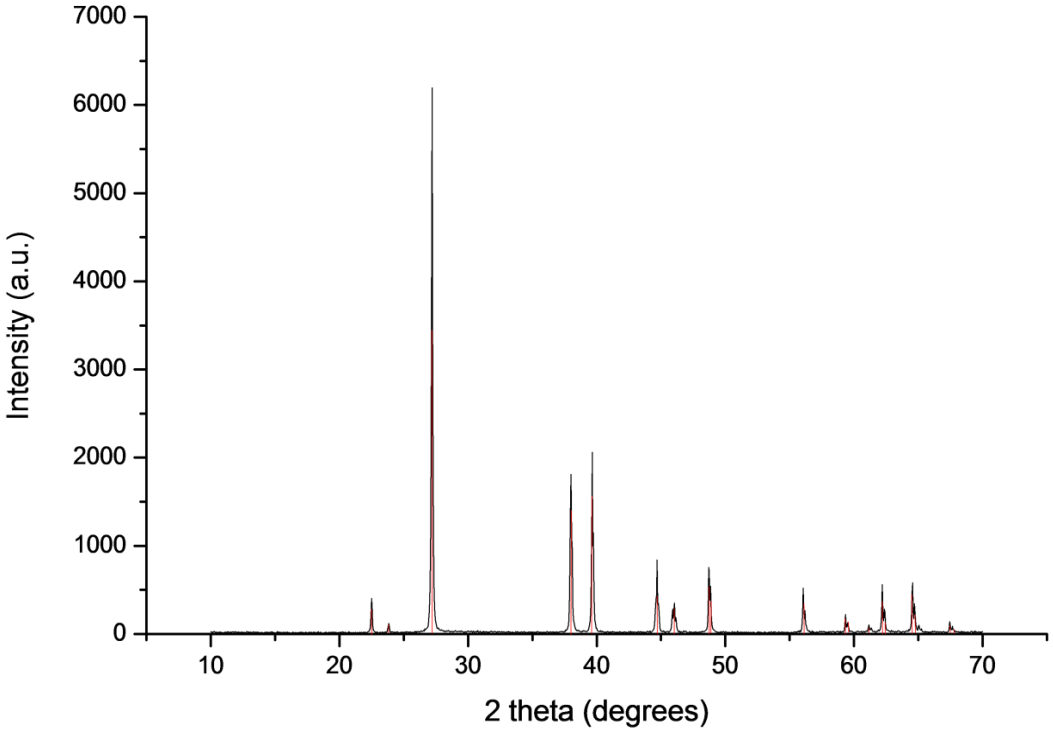

Figure 30: XRD pattern of the residue remaining in the TGA pan from the thermal decomposition of $[Bi(acac)_3]_n$. Lines in red correspond to the diffraction peaks of bismuth (PDF = 044-1246).

3.3.2 DSC-TGA trace of $[Bi(dbm)_3]_2$

The TGA trace of $[Bi(dbm)_3]_2$ is shown in Figure 31. The precursor decomposition pathway is composed of three main steps up to 500 °C, after which a continuing weight loss is observed, albeit at a very low rate. The first mass loss of 13.1% up to 225 °C coincides with the melt of the precursor (192 – 198 °C) supported by the weak signal observed in the DSC trace. This melting temperature was verified by filling a sealed glass capillary in the glovebox with the compound and using standard melting point apparatus. There then follows another mass loss of 18.9% up to 330 °C, followed by the steepest mass loss of 31.7% to 485 °C. The TGA trace reveals that the precursor is still losing mass by the end of the experiment, albeit at a very slow rate; nevertheless, by 600 °C the precursor had lost a total of 67.9 % weight, but the mass loss required for complete conversion to Bi_2O_3 was 73.5% {$[Bi(dbm)_3]_2$ to Bi_2O_3)}.

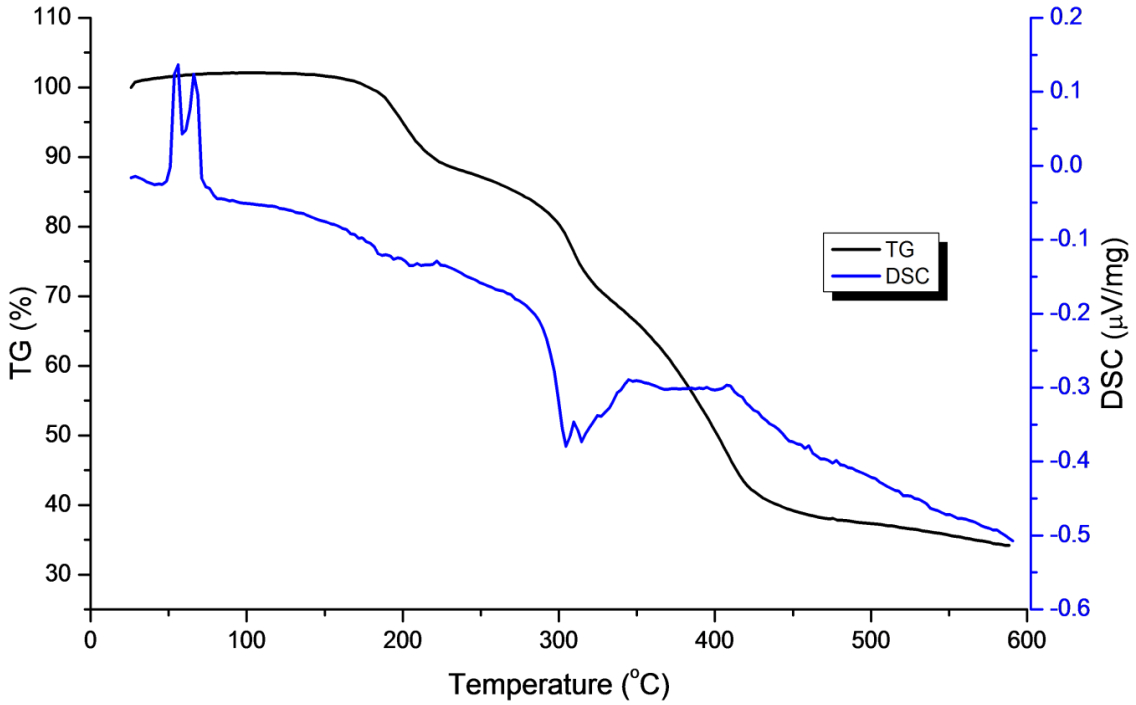

Figure 31: DSC-TGA trace of $[Bi(dbm)_3]_2$. The heating rate was 10 °C min^{-1}.

PXRD analysis of the residue remaining after the TGA experiment revealed the presence of β-Bi_2O_3 as the predominant crystalline phase present (Figure 32). Although the decomposition profile of the precursor is complex, the difference in observed and expected residual masses is relatively low at 5.6%, hence the thermal analysis has indicated that $[Bi(dbm)_3]_2$ could be suitable for use as a bismuth oxide single-source precursor. Attempts to sublime $[Bi(dbm)_3]_2$ between 50 – 200 °C onto a cold finger at 10^{-2} mbar resulted in decomposition without evaporation. In comparison to the TGA analysis of $[Bi(thd)_3]_2$ (m.p. 113-117 °C, see later), no volatilisation of $[Bi(dbm)_3]_2$ or any premature decomposition was observed, however the decomposition profiles of both precursors are composed of three distinct steps, albeit at a lower temperature for $[Bi(thd)_3]_2$.

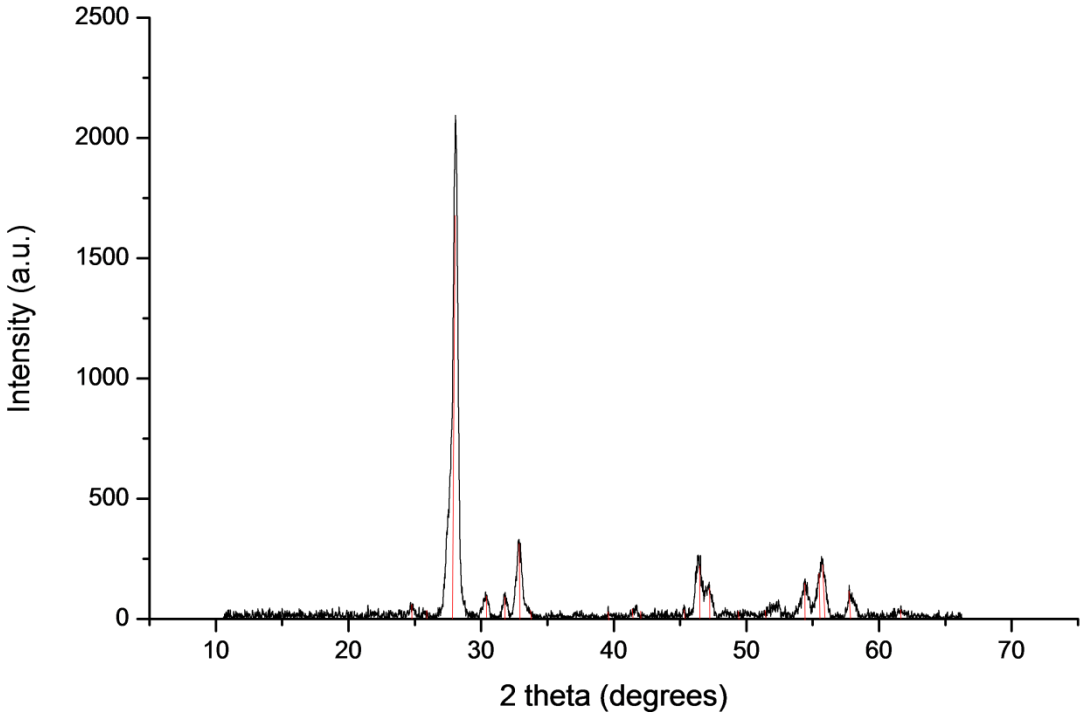

Figure 32: XRD pattern of the residue remaining in the TGA pan from the thermal decomposition of $[Bi(dbm)_3]_2$. Lines in red correspond to the stick pattern of β-Bi_2O_3 (PDF = 027-0050).

3.3.3 DSC-TGA trace of $[Bi(tfac)_3]$

The TGA trace of $[Bi(tfac)_3]$ is shown in Figure 33. The decomposition was composed of three main steps up to 600 °C. There is an initial small weight loss of 5.4% up to the melting temperature of 124 °C, observed by the peak in the DSC trace. Following the melt, there is an initial steep weight loss that occurs up to 170 °C, corresponding to a loss of 17.7%, and given that there is a simultaneous reading from the DSC, albeit fairly weak, this weight loss could be ascribed to volatilisation of the precursor. There then follows another steep mass loss of 21% up to 208 °C. This is followed by a more gradual mass loss of 16.4% up to 335 °C. Between this temperature and 600 °C there appears to be one more gradual mass loss of 8.5%, which is accompanied by a trough in the DSC trace which could be ascribed to crystallisation. In total, the weight loss of the precursor during the experiment was 69%, however the fraction of weight loss observed during decomposition was 62.3% (51.3% mass loss from a total of 82.3%, corrected for volatilisation).

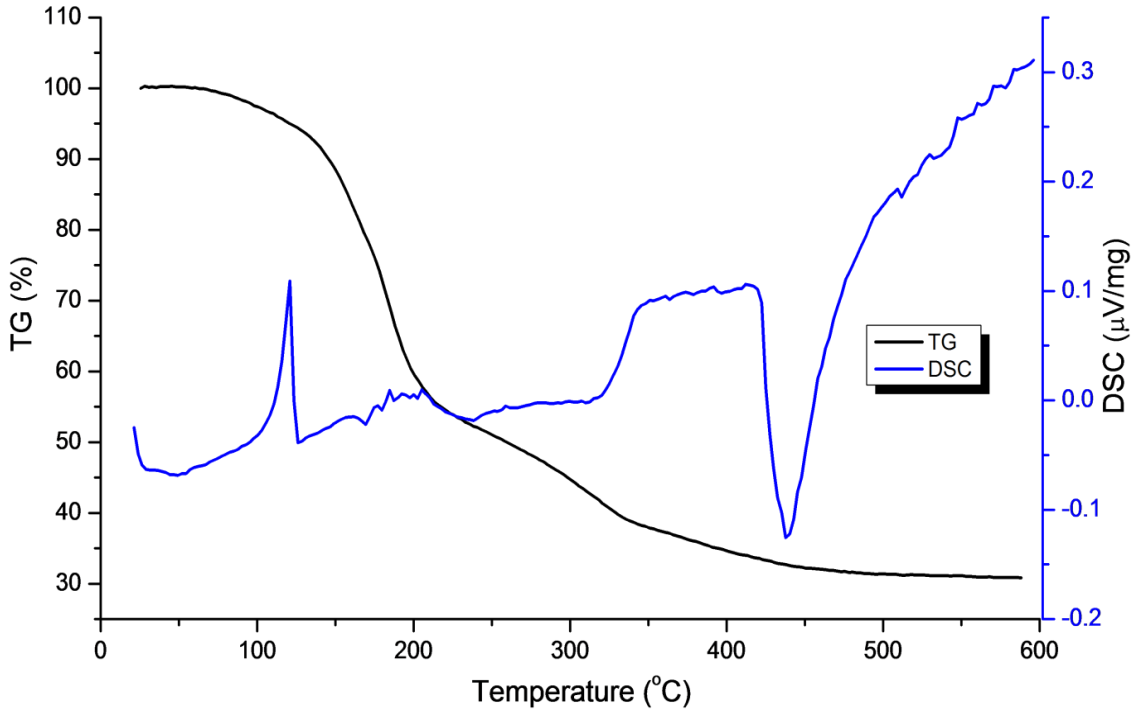

Figure 33: DSC-TGA trace of [Bi(tfac)$_3$]. The heating rate was 10 °C min^{-1}.

In order to form stoichiometric Bi_2O_3, a total mass loss of 65.1% would be required. The difference between the observed and calculated mass losses is comparatively low at 2.8%, and this may be considered as a reasonable match when accounting for experimental error. Sublimation experiments to test the volatility of [Bi(tfac)$_3$] resulted in decomposition in the flask to a light yellow solid with the appearance of yellow bismuth oxide, and PXRD analysis of the residue remaining in the pan after the DSC measurement was in agreement with this observation; the X-ray diffraction pattern of the residue was matched to α-Bi_2O_3 and is displayed in Figure 34. Although the volatility of [Bi(tfac)$_3$] proved to be low despite containing fluorine atoms, its decomposition to bismuth oxide and not BiOF is encouraging as it demonstrates that the compound could deposit bismuth oxide films using deposition techniques which do not rely on precursor volatility.

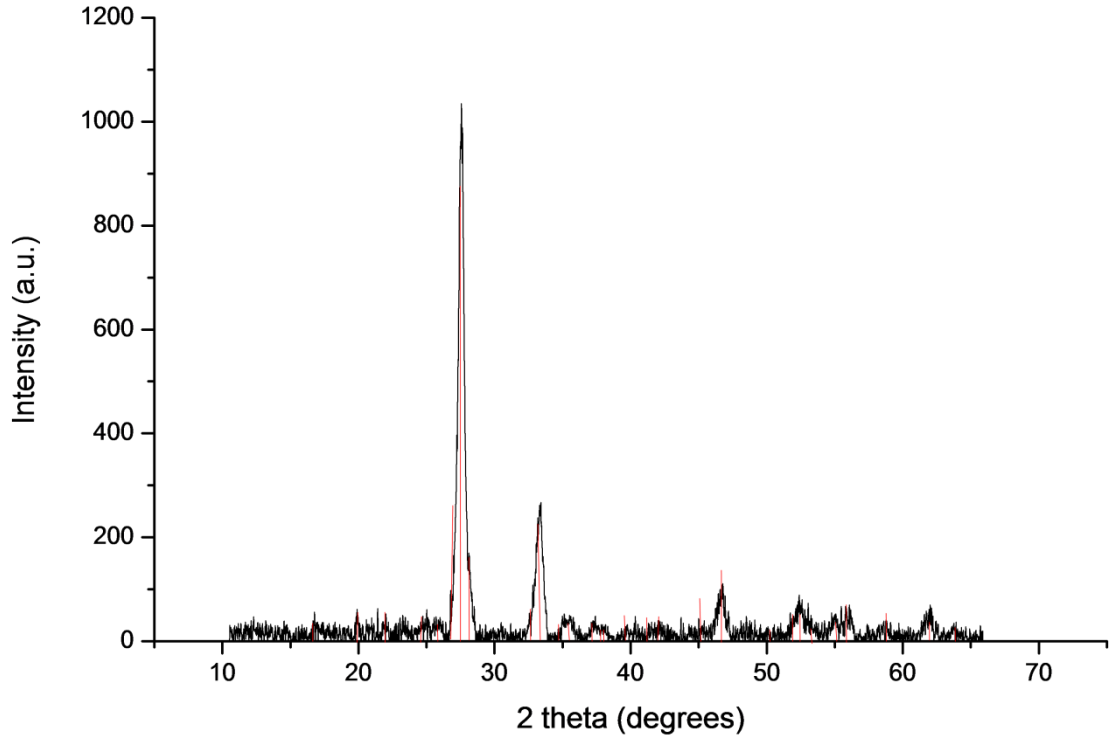

Figure 34: XRD pattern of the residue remaining in the TGA pan from the thermal decomposition of [Bi(tfac)$_3$]. Lines in red correspond to the stick pattern of α-Bi$_2$O$_3$ (PDF = 71-2274).

3.3.4 DSC-TGA trace of [Bi(bzac)$_3$]

The TGA trace of [Bi(bzac)$_3$] is shown in Figure 35. The decomposition is composed of one main weight loss step that begins at 160 °C. Initially, there is a small weight loss of 3.1% at the start of the experiment up to 160 °C, which is followed by a steep weight loss of 49.6% that stops at 260 °C. There is a very faint signal in the DSC trace at 169 °C that may represent the melting point of the compound. From 260 °C until the end of the experiment at 600 °C, there is a very small mass loss of approximately 2.6% with no peaks in the DSC trace. The flat nature of the DSC signal suggests that volatilisation of the compound did not occur, in line with experimental observations during sublimation attempts.

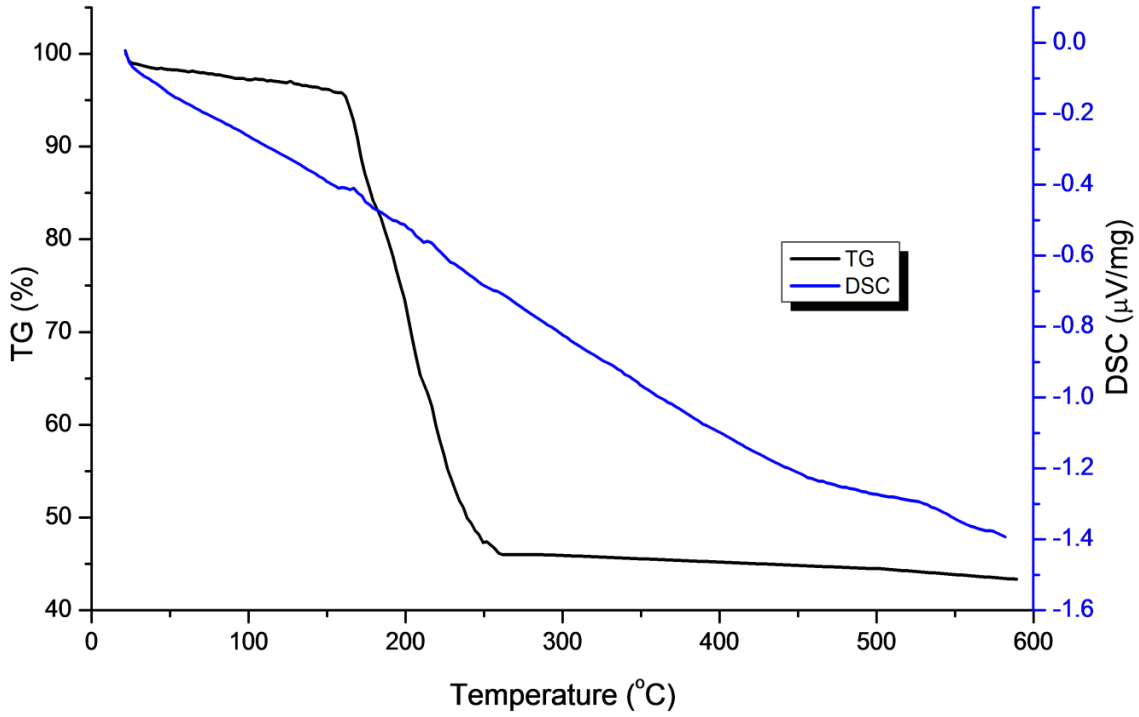

Figure 35: DSC-TGA trace of [Bi(bzac)$_3$]. The heating rate was 10 °C min^{-1}.

The total mass loss observed in the experiment was 55.3%, and the mass loss required to form stoichiometric Bi_2O_3 was calculated to be 66.3%, leaving a difference of 11.0%. PXRD analysis of the residue remaining in the TGA pan revealed the presence of both metallic bismuth and β-Bi_2O_3 (Figure 36). The fairly large difference between observed and calculated mass changes, coupled with the presence of metallic bismuth in the TGA residue demonstrates that [Bi(bzac)$_3$] may not be a suitable single-source precursor to Bi_2O_3 films.

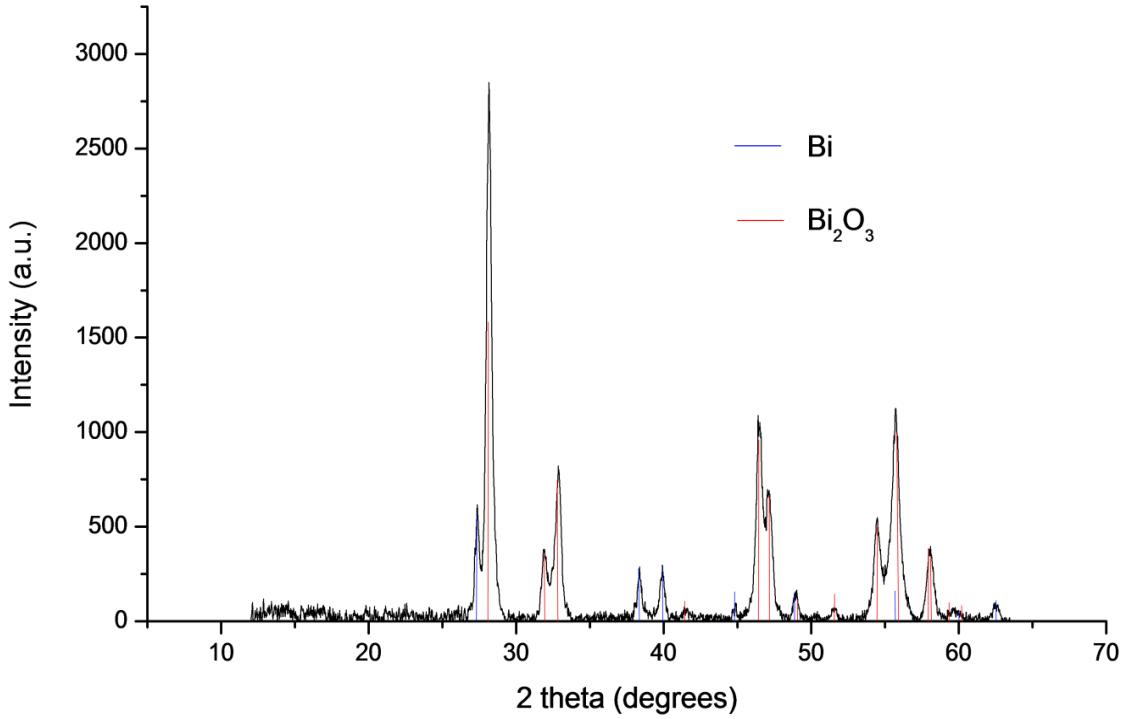

Figure 36: XRD pattern of the residue remaining in the TGA pan from the decomposition of [Bi(bzac)$_3$].

3.4 Thermal decomposition of [Bi(O^{t}Bu)$_3$], Bi(mmp)$_3$] and [Bi(thd)$_3$]

The decomposition profiles of the previously used bismuth oxide precursors [Bi(mmp)$_3$] and [Bi(thd)$_3$] were investigated *via* DSC-TGA under a helium atmosphere in order to assess their suitability as *single-source* precursors to bismuth oxide films. In addition to these complexes, the TGA profile of [Bi(O^{t}Bu)$_3$], which has not previously been used as a CVD precursor to bismuth oxide, was plotted in order to compare and contrast the decomposition characteristics of all three complexes for use in LPCVD.

3.4.1 DSC-TGA trace of [Bi(O^{t}Bu)$_3$]

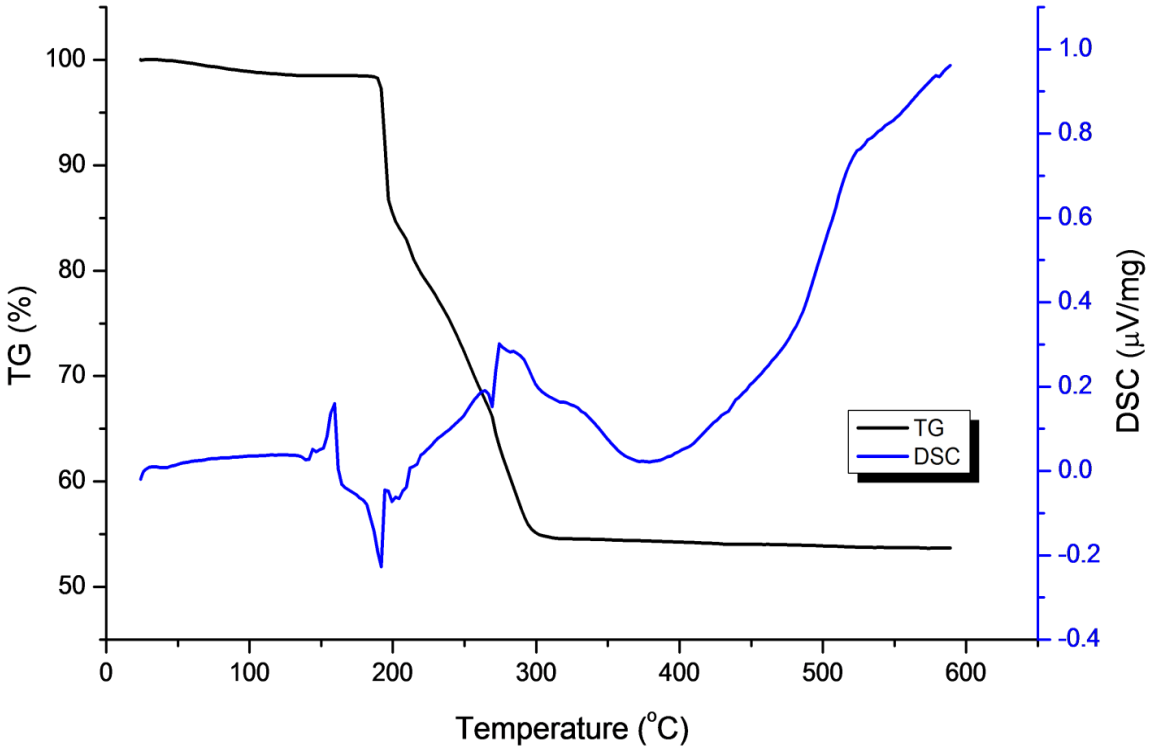

Figure 37: DSC-TGA trace of [Bi(O^{t}Bu)$_3$]. The heating rate was 10 °C min^{-1}.

The TGA data of [Bi(O^{t}Bu)$_3$] showed a negligible weight loss (1.70%) up to 189 °C (Figure 37), with an endotherm observed at approximately 155 °C in the DSC trace assigned as the melt, hence this weight loss is most likely due to volatilisation of the precursor. There then follows a weight loss of 11.0% to 197 °C, which is coincident with an exotherm in the DSC, therefore indicative of partial decomposition. A second weight loss step of 32.8% to 318 °C was also observed, again coincident with exotherms in the DSC, indicative of decomposition. The fraction of weight loss during precursor decomposition was 45% (44% weight loss from a total mass of 98% after accounting for precursor evaporation), which is consistent with the formation of Bi_2O_3 (theoretical mass loss for Bi_2O_3 is 45.7%). The TGA data of [Bi(O^{t}Bu)$_3$] was recently reported by researchers investigating the use of this precursor for ALD.[91] In their analysis, when using similar sealed pans to our experiments, they observed thermal decomposition of the precursor by 270 °C, which is consistent with the data reported here allowing for differences in experimental parameters. Coupled-mass spectrometry data did not reveal any conclusive evidence for the decomposition products or mechanism of [Bi(O^{t}Bu)$_3$], however PXRD of the residue remaining in the pan after the TGA analysis revealed the presence of β-Bi_2O_3 as the sole product of decomposition (Figure 38).

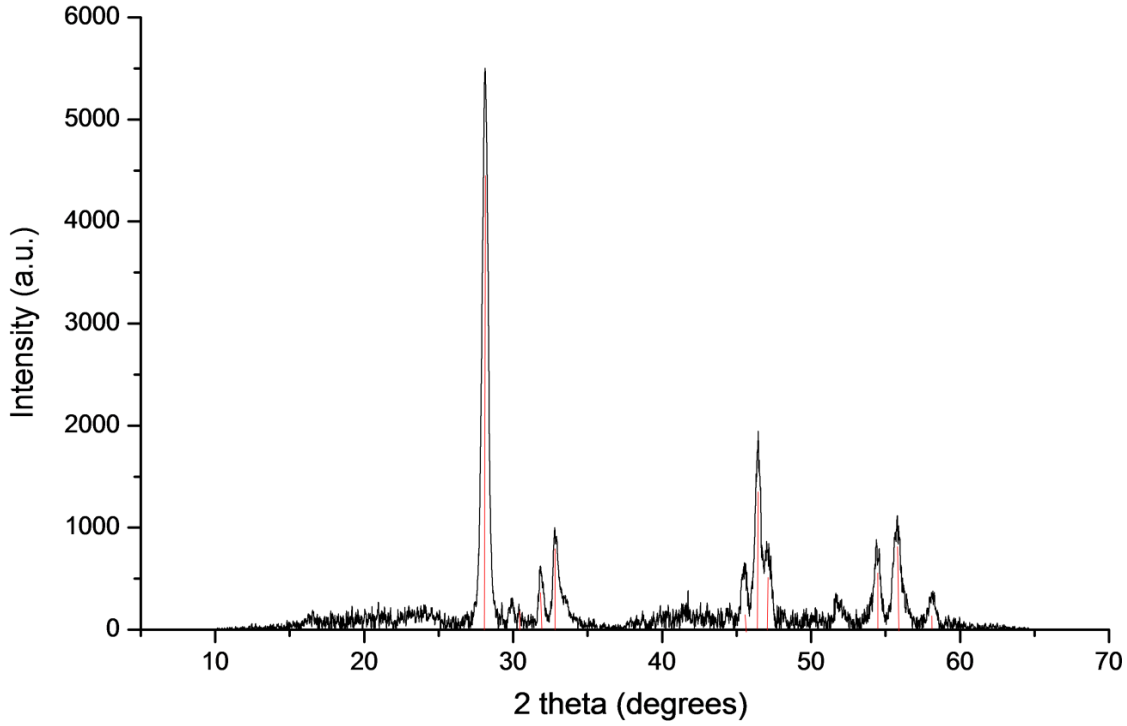

Figure 38: XRD pattern of the residue remaining in the TGA pan from the thermal decomposition of [Bi(O^{t}Bu)$_3$]. Lines in red correspond to the stick pattern of β-Bi_2O_3 (PDF = 027-0050).

3.4.2 DSC-TGA trace of [Bi(mmp)$_3$]

The TGA data of [Bi(mmp)$_3$] (Figure 39) displayed a negligible weight loss (1.1%) up to 129 °C, most likely due to excess solvent molecules remaining after synthesis, and therefore may be ignored. An endotherm was observed in the DSC trace at 130 °C, which was assigned as the melting point of [Bi(mmp)$_3$], and this was followed by the first steep weight loss of 18.3% up to 171 °C which is attributed to volatilisation of the precursor. A subsequent weight loss of 39.8% was observed between 171 and 279 °C, which is coincident with an exotherm in the DSC trace and is therefore attributed to decomposition of the precursor. Between 280 °C and the end of the TGA experiment (600 °C), there was a small weight loss of 7.7%. The fraction of weight loss observed during the decomposition of the precursor is 50% (40% total mass loss from a total mass of 80%, corrected for sample lost during volatilisation), which is somewhat lower than expected for formation of stoichiometric Bi_2O_3 (55.1% mass loss would equate to the formation of Bi_2O_3), although whether this is due to incomplete precursor decomposition or additional precursor evaporation is unclear.

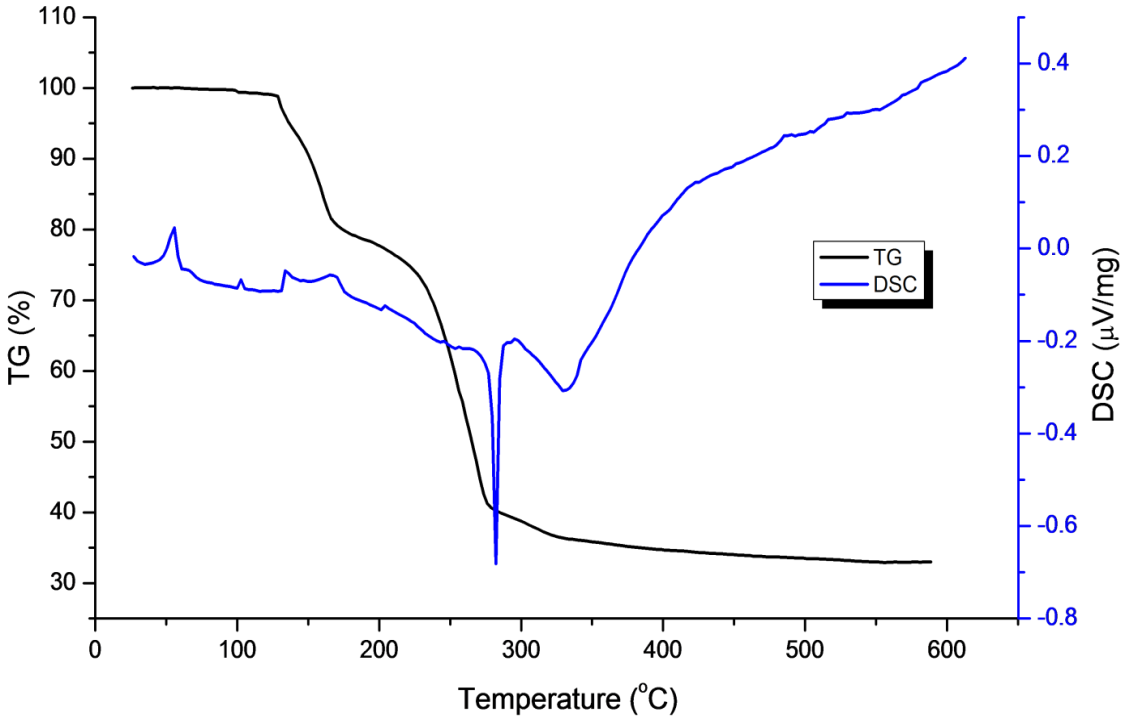

Figure 39: DSC-TGA trace of [Bi(mmp)$_3$]. The heating rate was 10 °C min^{-1}.

3.4.3 DSC-TGA trace of [Bi(thd)$_3$]

The TGA data of [Bi(thd)$_3$] (Figure 40) revealed a negligible weight loss (1.5%) up to 113 °C possibly due to residual moisture or solvent molecules, and may be ignored. Between 113 °C and 195 °C there was loss of 7.5% of mass, which coincides with the observation of an endotherm in the DSC trace at 113 °C (assigned as the melt) and this mass change is therefore ascribed to volatilisation of the precursor. Other groups have ascribed this weight loss to premature decomposition of the precursor and have described this as a significant disadvantage of its use in CVD, although in these reports no further analysis or evidence other than the observed weight loss was presented.[62] Two separate weight loss steps of 26.6% by 246 °C and 46.3% to 600 °C were then observed, which coincide with exotherms in the DSC trace and are therefore due to precursor decomposition. The fraction of weight loss ascribed to precursor decomposition was 80% (73% mass loss from a total mass of 91% after precursor evaporation), which is not consistent with the formation of Bi_2O_3 only, which requires a mass loss of 69.3%; this additional weight loss could be due to decomposition to metallic bismuth or a suboxide, or evaporation through the hole in the lid of the TGA pan.

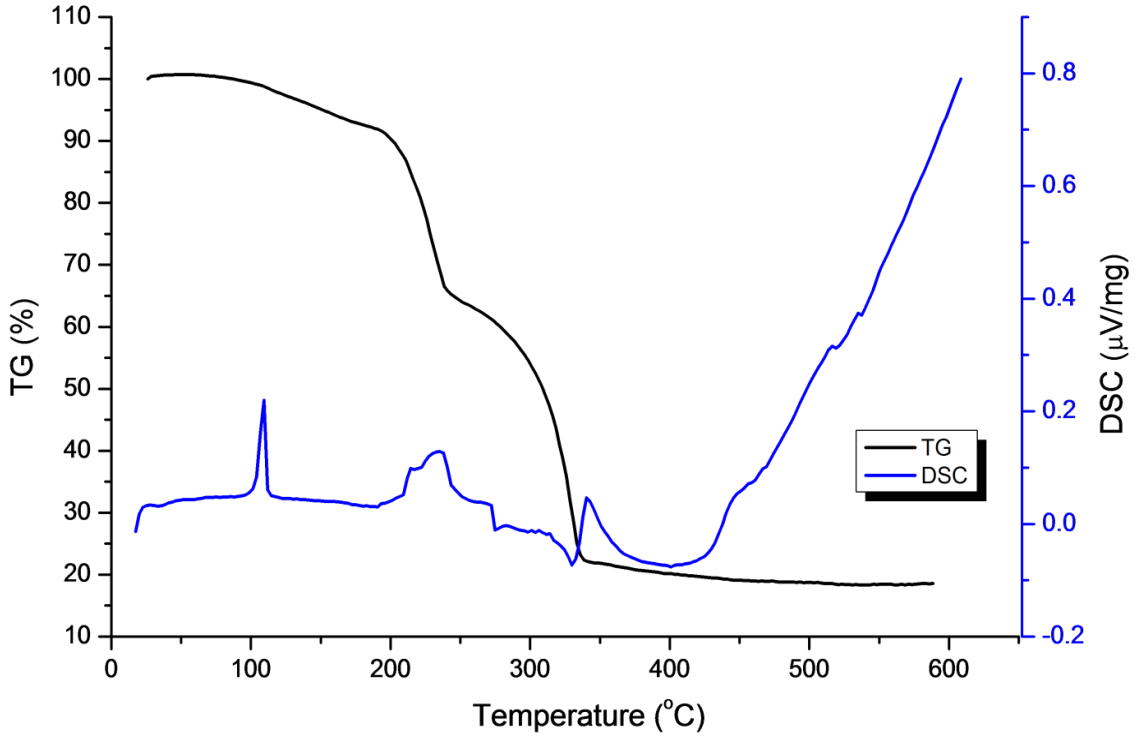

Figure 40: DSC-TGA trace of [Bi(thd)$_3$]. The heating rate was 10 °C min^{-1}.

3.5 Conclusions

The decomposition characteristics of several synthesised homoleptic bismuth(III) *β*-diketonate complexes were investigated *via* DSC-TGA (under a helium atmosphere) in order to assess their potential to serve as single-source CVD precursors to bismuth oxide films. It was observed that the polymeric complex, $[Bi(acac)_3]_n$, decomposed to metallic bismuth and that the observed and calculated mass losses did not match for its decomposition to Bi_2O_3 only. The dimeric complex $[Bi(dbm)_3]_2$ was observed to decompose to β-Bi_2O_3 and its mass loss was consistent with the calculated theoretical mass loss required to form Bi_2O_3. The fluorinated *β*-diketonate complex $[Bi(tfac)_3]$ was found to decompose into α-Bi_2O_3 and, surprisingly, not into BiOF, with the calculated and observed weight losses from TGA analysis consistent with this observation. $[Bi(bzac)_3]$ was found to decompose into a mixture of metallic bismuth and β-Bi_2O_3 during decomposition, however the difference between the theoretical and observed mass loss to form bismuth oxide only was high, indicating it may be unsuitable as a single-source precursor.

A comparison between the decomposition profiles of two volatile precursors, $[Bi(mmp)_3]$ and $[Bi(thd)_3]$, that have been used for deposition of bismuth oxide (and which could be potential single-source precursors to the material) were investigated. In addition, the TGA profile of the volatile alkoxide, $[Bi(O^tBu)_3]$, which has not been employed as a CVD precursor, was investigated. The weight loss of $[Bi(mmp)_3]$ during the analysis appeared to be too low for formation of stoichiometric Bi_2O_3, whilst the weight loss of $[Bi(thd)_3]$ appeared to be too high for formation of Bi_2O_3 only. In both cases the decomposition profiles were complicated due to potential volatilisation coupled with the possibility of premature and/or incomplete decomposition during the experiment.

TGA analysis revealed that the decomposition of $[Bi(O^tBu)_3]$ was consistent with the formation of Bi_2O_3 only, and therefore it could be a suitable single-source precursor for growth of bismuth oxide films using LPCVD.

CVD OF BISMUTH OXIDE FILMS

4 Low pressure CVD of bismuth oxide utilising a single-source precursor

4.1 Introduction

As discussed in the introduction chapter, there are no examples in the literature of the use of single-source precursors to deposit bismuth oxide films. Single-source precursors offer the advantage of containing all the components of the desired thin film within a single molecule, and therefore the energy required for film formation is lower and hence a lower deposition temperature would be required. In this case, the employment and control of an oxidising gas at elevated temperatures could be avoided by using single-source precursors.

This chapter describes the work carried out on the growth of bismuth oxide (Bi_2O_3) films on borosilicate glass substrates *via* low pressure CVD (LPCVD) using bismuth(III) *tert*-butoxide, [$Bi(O^tBu)_3$], as a single-source precursor, without the use of an oxidising gas. The decomposition and mass transport properties of this precursor were compared to previously used and commercially available bismuth precursors [$Bi(thd)_3$] and [$Bi(mmp)_3$]. The films produced were characterised fully and two samples were selected for an investigation into their photocatalytic properties through photo-oxidation of water using a sacrificial solution under low power UV- light irradiation.

4.2 Physical Measurements

All precursors were stored in an MBraun UniLab glovebox under a nitrogen atmosphere. Powder X-ray diffraction (PXRD) was carried out on a Bruker-D8 powder diffractometer equipped with a GADDS Hi-Star area detector using Cu-K_α radiation (λ = 1.54056 Å) in the range 10 – 70° 2 theta (40 kV, 40 mA). Phase information was obtained from the Diffrac^{plus} EVA program suite (Version 2) and ICSD. SEM images were obtained on a Jeol JSM-6301F Field Emission Microscope at 5 kV, after coating samples with an ultrathin layer of gold to prevent charging. WDX measurements were performed on a Philips XL30ESEM Machine operating at 10 kV equipped with an Oxford Instruments INCA detector, after coating samples with a thin layer of carbon to prevent charging. AFM analysis was performed using a Veeco Dimension 3100 machine in intermittent contact mode, where a cantilever with an attached tip oscillates at its resonant frequency. This was scanned across the surface of the film several times to determine the morphology and roughness. Transmission electron microscopy (TEM) images were captured on a JEOL JEM-100CX II machine operating at 100 kV; samples were prepared by deposition on KBr substrates followed by dissolution of the substrate in distilled

water. XPS spectra were obtained using a Kratos AXIS Ultra machine with a delay line detector under a pressure of 10^{-9} torr. A monochromated Al-K_α X-ray source producing a full width at half maximum (FWHM) on the Ag $3d_{5/2}$ peak of 0.48 eV was used. Samples were etched to 5 and 10 nm in depth for 5 and 10 minutes respectively. Raman spectra were acquired using a Renishaw Raman 1000 System using a helium-neon laser wavelength of 514.5 nm at room temperature. UV-Vis spectra were recorded in transmission mode over the range 175 – 2500 nm using a Perkin Elmer Lambda 950 photospectrometer.

4.2.1 LPCVD Apparatus

A schematic diagram of the cold wall LPCVD apparatus that was used is shown in Figure 41. Nitrogen (99.96 %) was obtained from BOC and used as supplied. LPCVD reactions were carried out using a home built, horizontal cold-wall CVD reactor which comprises a stainless steel reaction chamber (100 mm long, 40 mm diameter) housing a resistively heated carbon block substrate holder angled at 15° such that the flow of precursor was aimed directly at the substrate thereon. The carbon block was heated using a Whatman Firerod Cartridge Heater and can hold substrates up to 35 mm^2. The reactor was connected to a resistively heated stainless steel precursor holder (bubbler) with standard Swagelock fittings. A base pressure of 5 x 10^{-2} mbar was achieved using a rotary pump before use, to ensure as far as possible that no air and moisture remained in the system. The CVD pipework (lines) were covered in electrical heater tape, and the temperatures of the graphite block, bubbler lines and bubblers were independently controlled with Pt-Rh thermocouples. The substrate temperature was varied between 425 – 500 °C. The total reactor pressure was maintained at 7 mbar to begin with *via* the use of a mechanical throttle valve, and then later increased to 15, 20 and 45 mbar. The inlet nitrogen gas flow was varied between 12 – 40 cm^3/min and was monitored using a standard BOC flowmeter; no plain flow of nitrogen was used in this study. Each deposition was carried out for 1 hour. Films were deposited on borosilicate glass microscope slides (3 cm x 2 cm) that were cleaned in isopropanol prior to use.

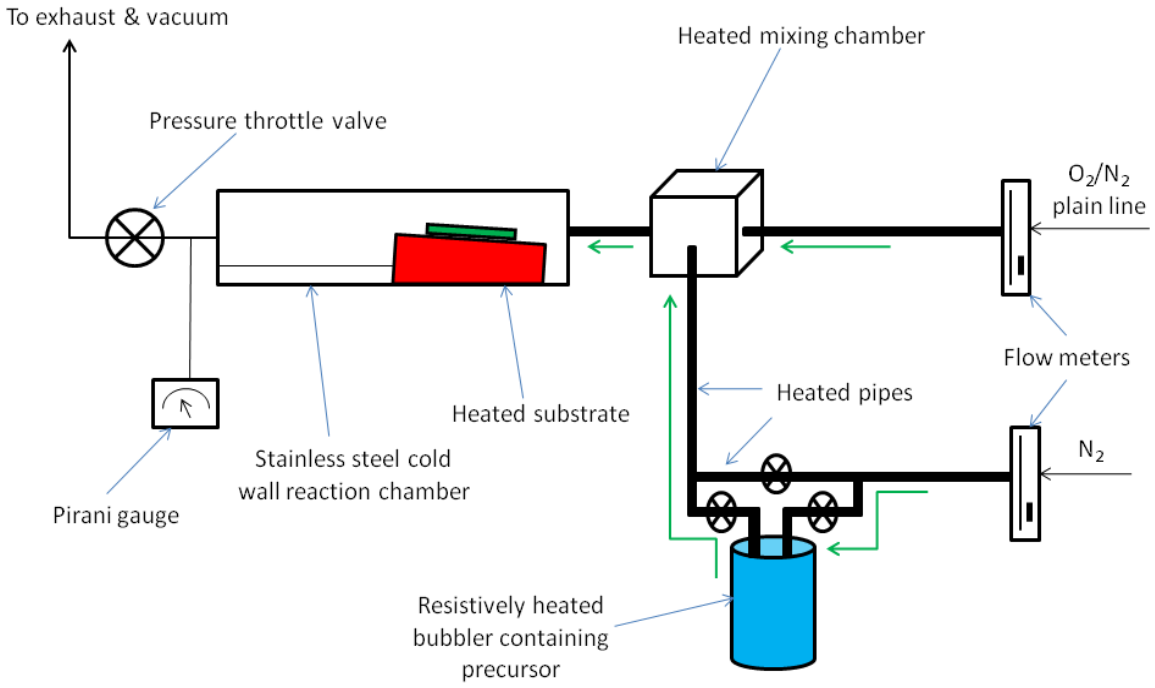

Figure 41: Diagram of the LPCVD setup. Green arrows represent the flow of gas/precursor.

4.2.2 Precursor synthesis

[Bi(thd)$_3$] was synthesised from [Bi(N(SiMe$_3$)$_2$)$_3$] and 2,2-6,6-tetramethylheptanedione *via* a ligand exchange reaction, described in Chapter 2.

[Bi(O^{t}Bu)$_3$]

[Bi(O^{t}Bu)$_3$] was synthesised *via* the metathesis reaction of $BiCl_3$ and three equivalents of NaO^{t}Bu as described in Chapter 2.

Tris (1-methoxy-2-methyl-2-propoxy) bismuth, [Bi(mmp)$_3$]:

[Bi(mmp)$_3$] was synthesised according to the literature *via* an alcohol-amine exchange reaction and is described in Chapter 2.

4.2.3 Vapour pressures

An important property of a good LPCVD precursor is volatility and therefore the vapour pressures of [Bi(O^{t}Bu)$_3$], [Bi(mmp)$_3$] and [Bi(thd)$_3$] were plotted using the following vapour pressure equations obtained from the literature (Figure 42).[163,164]

$[Bi(O^tBu)_3]$: $\log_{10}P$ (mmHg) = 13.11 – 5010/T(K)

$[Bi(mmp)_3]$: $\log_{10}P$ (mmHg) = 8.251 – 2257/T(K)

$[Bi(thd)_3]$: $\log_{10}P$ (mmHg) = 10.27 – 5199/T(K)

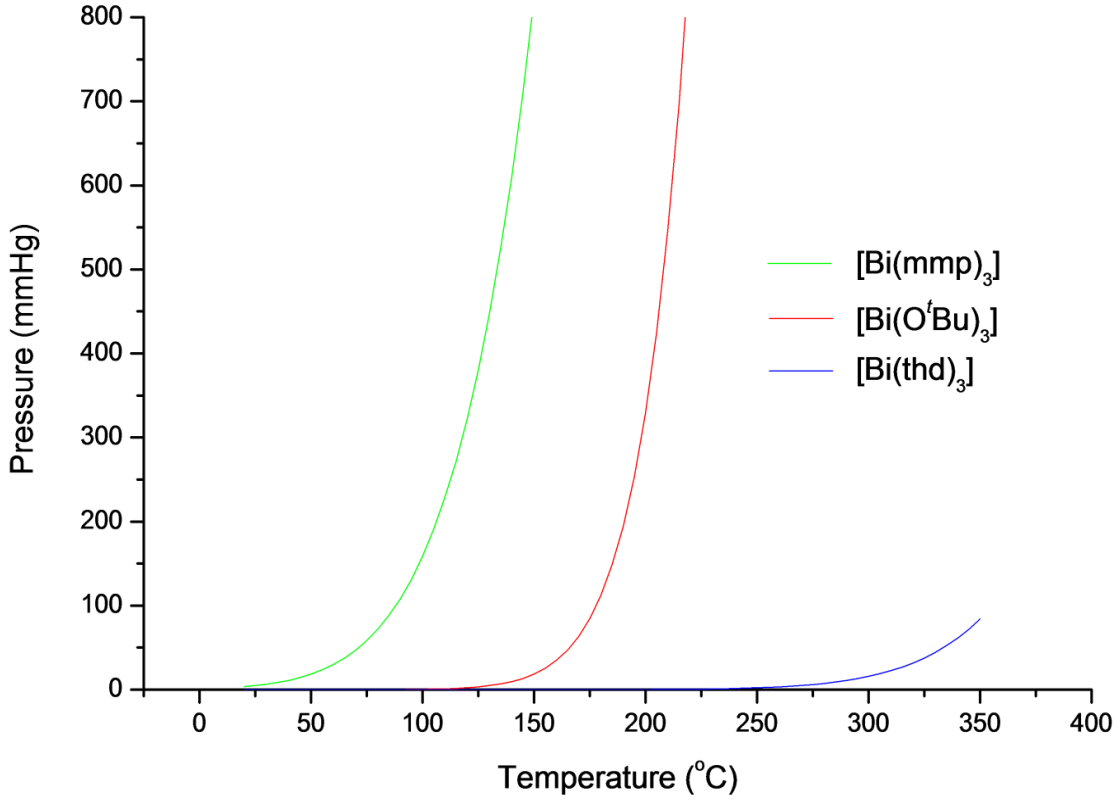

Figure 42: Vapour pressure curves of $[Bi(O^tBu)_3]$, $[Bi(mmp)_3]$ and $[Bi(thd)_3]$.

The TGA of $[Bi(O^tBu)_3]$, $[Bi(mmp)_3]$ and $[Bi(thd)_3]$ are plotted together in Figure 43 to assist with the comparison of their vapour pressures and decomposition. $[Bi(mmp)_3]$ exhibits a relatively high vapour pressure of 158 mmHg at 100 °C and this correlates with the relatively large mass loss of the precursor (c. 18%) observed in the TGA prior to the onset of decomposition, which was ascribed to volatilisation. The vapour pressure of $[Bi(O^tBu)_3]$ at this temperature was 0.48 mmHg, and was negligible (2.15×10^{-4} mmHg) for $[Bi(thd)_3]$, which is somewhat surprising given the observed mass loss of 7.5% for the $[Bi(thd)_3]$ precursor ascribed to evaporation from TGA analysis. However, this early weight loss may also be due to premature decomposition, as previously discussed. Despite its low vapour pressure, $[Bi(thd)_3]$ has been successfully employed as a precursor to Bi_2O_3 films *via* DLI-CVD, a technique which would assist in overcoming the poor volatility and decomposition characteristics of this precursor. On the other hand, $[Bi(O^tBu)_3]$ exhibits an appreciable vapour pressure that is significantly higher than $[Bi(thd)_3]$ and possesses excellent decomposition characteristics for

formation of Bi_2O_3, as assessed using TGA (Chapter 3), and was therefore selected as the precursor of choice for this study.

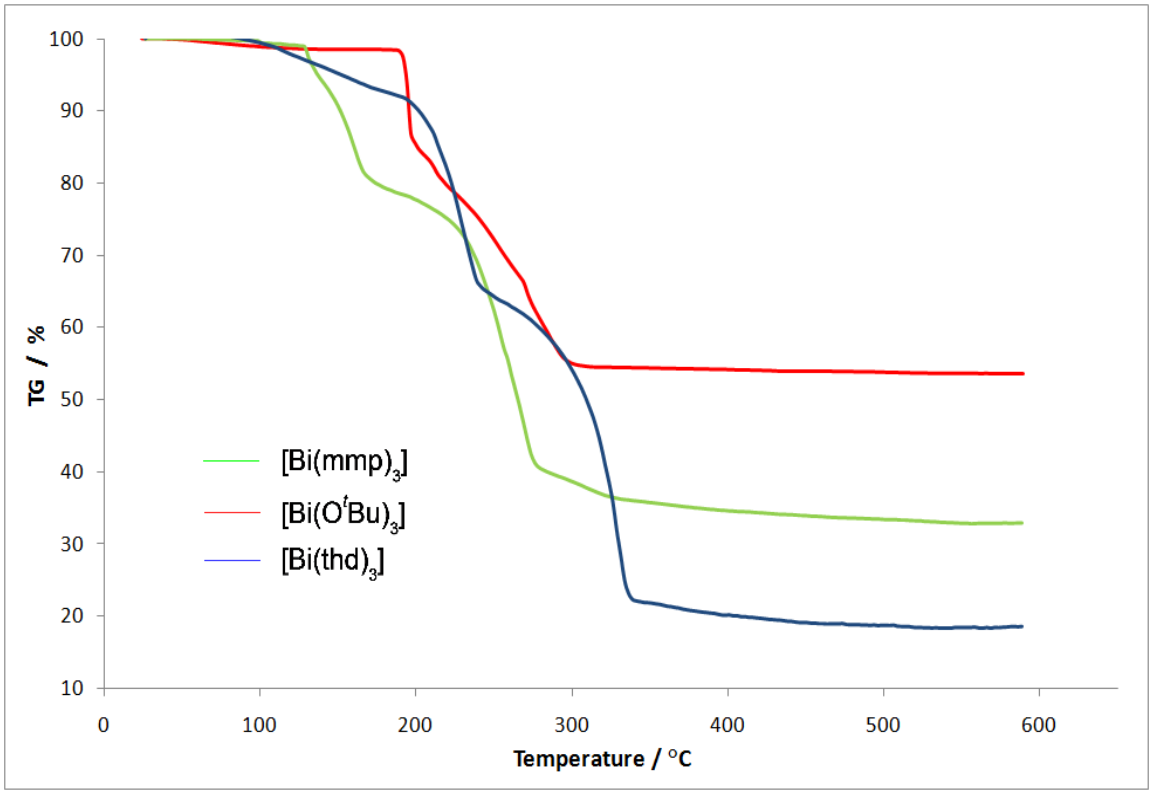

Figure 43: TGA decomposition profiles of $[Bi(O^tBu)_3]$, $[Bi(mmp)_3]$ and $[Bi(thd)_3]$ plotted together. The heating rate was 10 °C min^{-1}.

4.2.4 Decomposition of $[Bi(O^tBu)_3]$

Metal alkoxides, particularly metal *tert*-butoxides, have frequently been employed as single-source precursors to metal oxide thin films.[158,5] However, as such, these precursor molecules do not contain β-hydrogen atoms so their decomposition pathway is open to debate, although it is believed that various hydrolysis mechanisms are involved as with $[Zr(O^tBu)_4]$.[165] Copper(I) *tert*-butoxide, $[Cu(O^tBu)_4]$, has been utilised as a single-source precursor to copper(I) oxide (Cu_2O) films and its decomposition has been studied in detail by Jefferies *et al.* Through the use of *in situ* mass spectrometry the only organic by-products of its decomposition were established as *tert*-butyl alcohol and isobutene, along with, potentially, small amounts of water.[166] The decomposition mechanism of $[Bi(O^tBu)_3]$ is shown in Figure 44 if it were to follow the mechanism proposed by Jefferies.

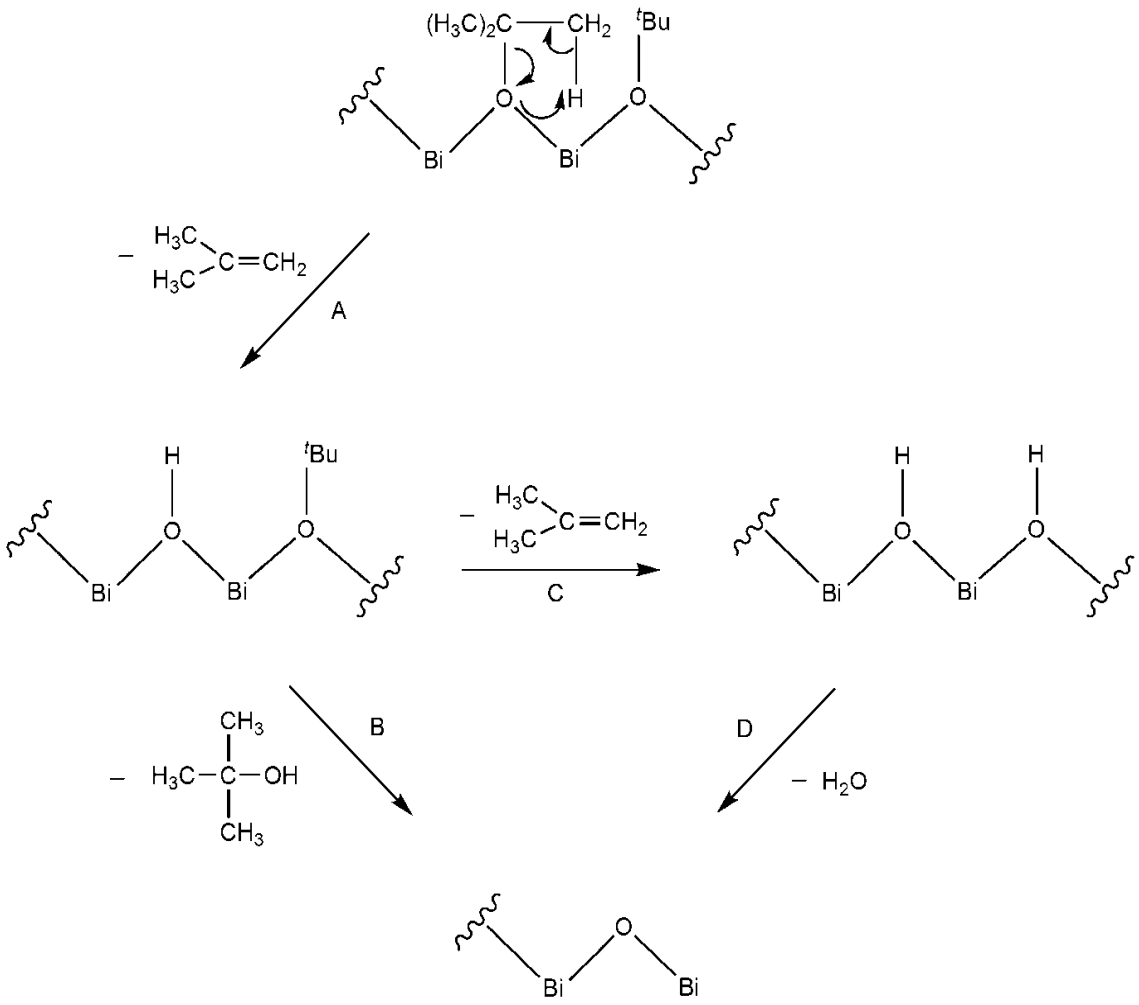

Figure 44: Possible decomposition mechanism of [Bi(O^{t}Bu)$_3$], curvy line represents the rest of the molecule.

The first step in the proposed decomposition pathway (Step A, Figure 44) involves elimination of isobutene from the surface bound tert-butoxide groups via an intramolecular mechanism to yield surface hydroxylated intermediates. A proton transfer then occurs to the neighbouring *tert*-butoxy group, leading to elimination of *tert*-butyl alcohol and formation of metal oxide species (Step B). Alternatively, following the formation of the hydroxyl species from Step A, adjacent *tert*-butoxide groups can eliminate another isobutene fragment (Step C), followed by proton transfer which eliminates water to yield the metal oxide species (Step D). Steps C and D were proposed to be more likely to occur, given the fact that quantitatively, more isobutene compared to *tert*-butanol was measured *via* ^{1}H NMR spectroscopy.

A more likely decomposition mechanism for [Bi(O^{t}Bu)$_3$] is shown in Figure 45.

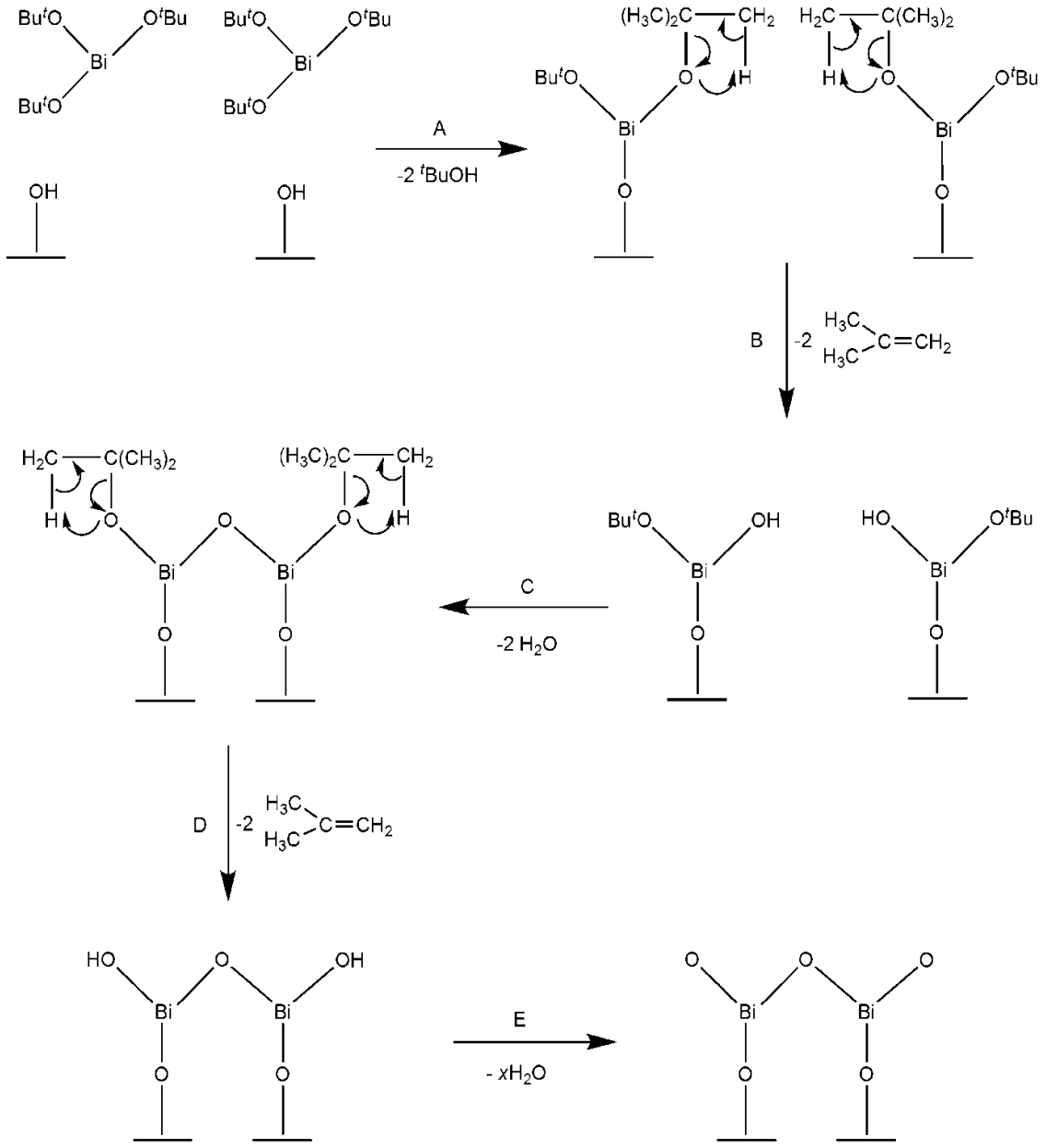

Figure 45: Alternative decomposition pathway proposed for [Bi(O^{t}Bu)$_3$] to form bismuth oxide.

The first step (Step A) involves elimination of *tert*-butanol through a surface reaction with the hydroxyl terminated glass substrate. This is followed by elimination of isobutene (Step B) to leave the hydroxyl terminated bismuth centre with an adjacent *tert*-butoxide group still attached. Elimination of water (Step C) between adjacent hydroxyl groups allows for the formation of a bridging oxygen atom between the bismuth centres. In a similar fashion to Step B, Step D involves additional elimination of isobutene to leave terminal hydroxide groups at the bismuth centre. Finally, elimination of water would result in bismuth oxide species still bound to the substrate *via* the oxygen remaining from the previously hydroxyl terminated glass.

Clearly further investigation of $[Bi(O^tBu)_3]$ is required in order to compare its mode of decomposition with that of $[Cu(O^tBu)_4]$ or $[Zr(O^tBu)_4]$, and the effects this might have on the metal-oxygen ratio and carbon content of the resultant films.

4.3 CVD

The use of $[Bi(O^tBu)_3]$ as a single-source precursor to form transparent gold/yellow crystalline bismuth oxide thin films was studied over a variety of substrate temperatures (no deposition was obtained below 425 °C), system pressures and carrier gas flow rates (no plain line was used). The precursor (150 mg) was weighed out into a vial in a glovebox, sealed with a lid, and then swiftly transferred to the bubbler whilst maintaining a high positive pressure of nitrogen. Despite reported decomposition problems encountered when using this precursor for ALD,[91] no detrimental precursor decomposition was observed when maintaining a bubbler temperature of 110 °C. The amount of precursor remaining in the bubbler after deposition was negligible (< 10 mg material, which had visually decomposed to oxide). All films displayed good substrate coverage and were adherent; all films passed the Scotch tape test but did not survive after treatment with steel wool and were easily scratched. The films did not show any changes in characteristics after prolonged storage in air.

Table 4: Details of the CVD experiments.

Substrate temperature / °C	Nitrogen flow rate / cm^3 min^{-1}	System pressure / mbar	Crystalline phase(s)	Film thickness / nm	Band-gap / eV
425	12	8	β	75	2.4
450	12	8	β, γ	300	2.3
475	12	8	β, minimal γ	330	2.3
500	12	8	γ	520	2.8
450	12	15	β, γ	190	2.5
450	12	20	β, minimal γ	300	2.6
450	12	45	α	525	2.8
450	20	8	γ		2.9
450	25	8	γ		2.7
450	40	8	γ		3.0

4.3.1 X-ray diffraction

The CVD results table (Table 4) demonstrates the effects of varying the substrate temperature, total system pressure and carrier gas flow rate on film properties such as thickness, crystalline phase obtained and band-gap. Film crystallinity was investigated using powder X-ray diffraction. X-ray diffraction patterns revealed the presence of crystalline, mainly mixed phase films, composed of β- and γ-phases. At 500 °C, the γ-phase was the predominant crystalline phase (Figure 46) and this was also the dominant phase upon increasing the carrier gas flow rate from 12 to 40 cm^3/min at a substrate temperature of 450 °C.

Unit cell dimensions of $a = b = c = 10.27$ (3) Å, space group $I23$ obtained for the γ- phase were in agreement with literature values ($a = b = c = 10.25$ Å, PDF = 01-071-0467). At 425 °C (8 mbar), the β-phase was the dominant crystalline species with unit cell dimensions of $a = b = 7.8$ (1) Å, $c = 5.7$ (2) Å, space group $P4\text{-}21c$, for the β- phase in agreement with literature values ($a = b = 7.738$ Å, $c = 5.731$ Å, PDF = 01-073-6885), and films deposited at 450 and 475 °C resulted in mixed β- and γ-phases. There appeared to be a higher amount of amorphous material in this sample as demonstrated by the high background count in the powder X-ray diffraction pattern and penetration of the X-rays to the underlying glass substrate, which may be accounted

for by the very low thickness of this sample (*ca*. 75 nm). Similar variations in crystalline phases obtained *via* MOCVD of Bi_2O_3 films were also observed by Tondello[63] using triphenylbismuth in a dual-source reaction with oxygen, where small variations in the deposition conditions led to changes in the phase deposited, i.e. phase selective deposition.

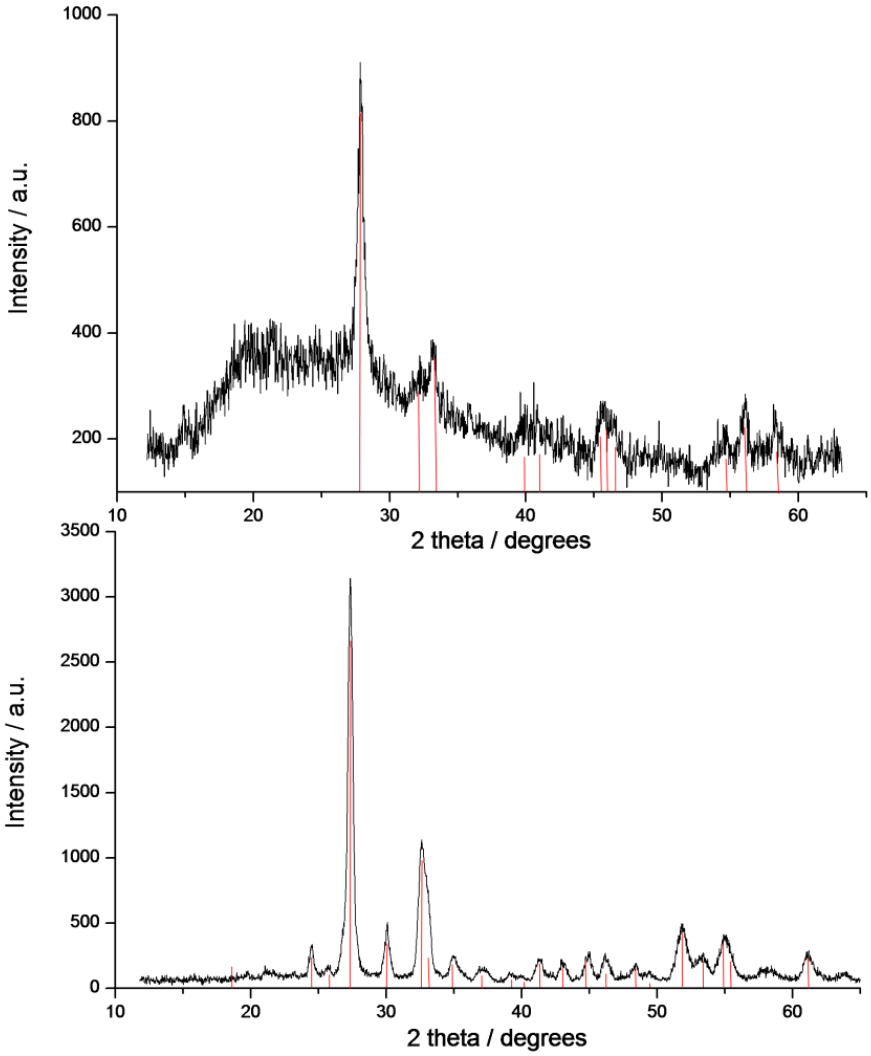

Figure 46: X-ray diffraction patterns of predominantly β-Bi_2O_3 (top) and γ-Bi_2O_3 (bottom).

Somewhat surprisingly, at a total system pressure of 45 mbar and at a substrate temperature of 450 °C, a predominantly α-phase (monoclinic) structure was observed *via* powder X-ray diffraction (Figure 47). Unit cell dimensions of a = 5.83 Å, b = 8.17 Å, c = 7.50 Å were obtained for the α- phase which were in reasonable agreement with literature values (a = 5.83 Å, b = 8.14 Å, c = 7.48 Å, PDF = 01-076-1730). The low temperature, thermodynamically stable α-phase is more commonly found at room temperature, and a possible explanation for its appearance at higher system pressures may be due to the comparatively lower substrate temperature coupled with fewer precursor molecules per unit time in the reactor being transported to the substrate.

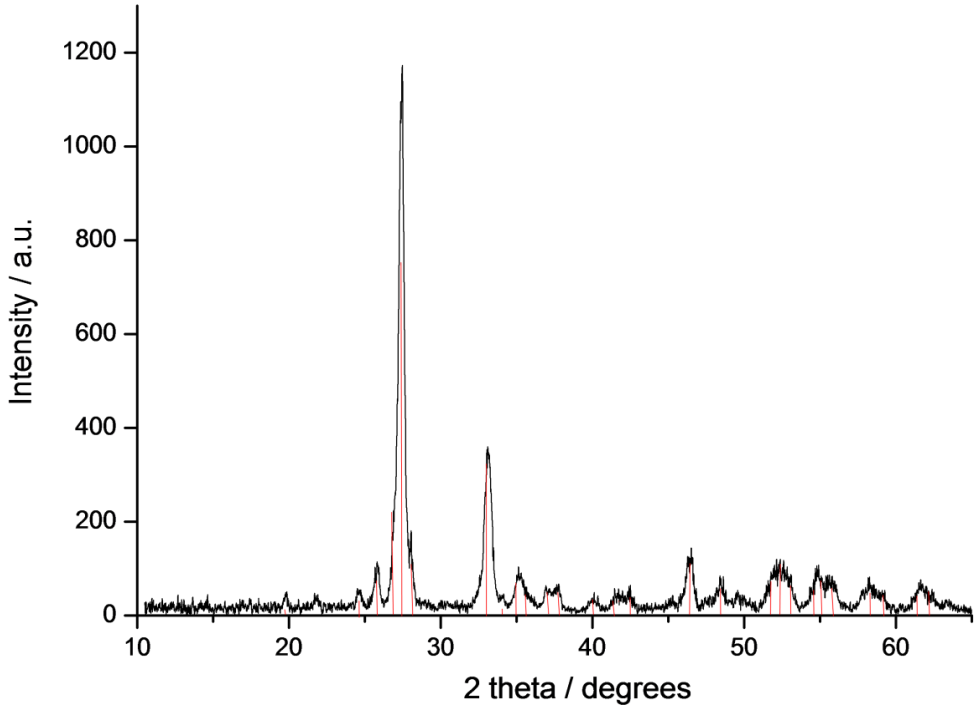

Figure 47: X-ray diffraction pattern of α-Bi_2O_3 formed at a total system pressure of 45 mbar.

4.3.2 Film growth rates

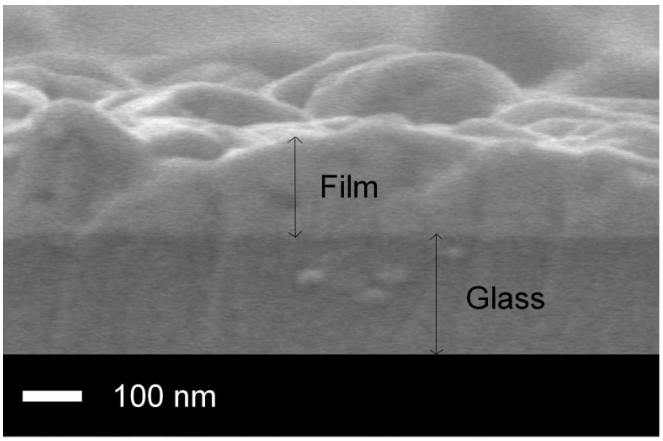

Figure 48: Side on SEM image of a Bi_2O_3 film grown *via* LPCVD on glass.

Film thickness data were obtained using side-on SEM imaging (see Figure 48 for a typical side-on SEM image of a Bi_2O_3 film grown *via* LPCVD). As expected, the film growth rate increased as a function of substrate temperature and also as a function of carrier gas flow rate. In comparison to the use of [$Bi(mmp)_3$] as a bismuth oxide precursor[72] constant/fixed film growth rates, as a function of substrate temperature, were not observed. The film thickness at a substrate temperatures of 425 °C was approximately 75 nm, and at 500 °C approximately 520

nm. The deposition rates were therefore *ca.* 75 nm, 300 nm, 330 nm and 520 nm hr^{-1} at substrate temperatures of 425, 450, 475 and 500 °C, respectively (Figure 49). Typically all deposited films demonstrated good substrate coverage and uniformity.

Film growth rates also varied as a function of total system pressure. The film thickness increased as the system pressure was increased in stages from 8 mbar to 45 mbar, and the deposition rates were therefore *ca*. 75 nm, 190 nm, 300 nm and 525 nm hr^{-1} at system pressures of 8, 15, 20 and 45 mbar, respectively. This increase in film thickness is caused by the increase in reaction rate of the precursor molecules reacting upon the substrate. By increasing the pressure, the concentration per unit volume of precursor molecules in the gas phase is likely to decrease. The higher pressure increases the probability that more molecules in the gas phase would react on the substrate, given that the residence time in the reactor would be longer, therefore resulting in more molecules decomposing on the substrate rather being transported away by the vacuum and carrier gas, leading to an overall increase in film thickness. Nevertheless, by careful tuning of the pressure in the reactor, the thickness of the films produced in this particular process can still be controlled.

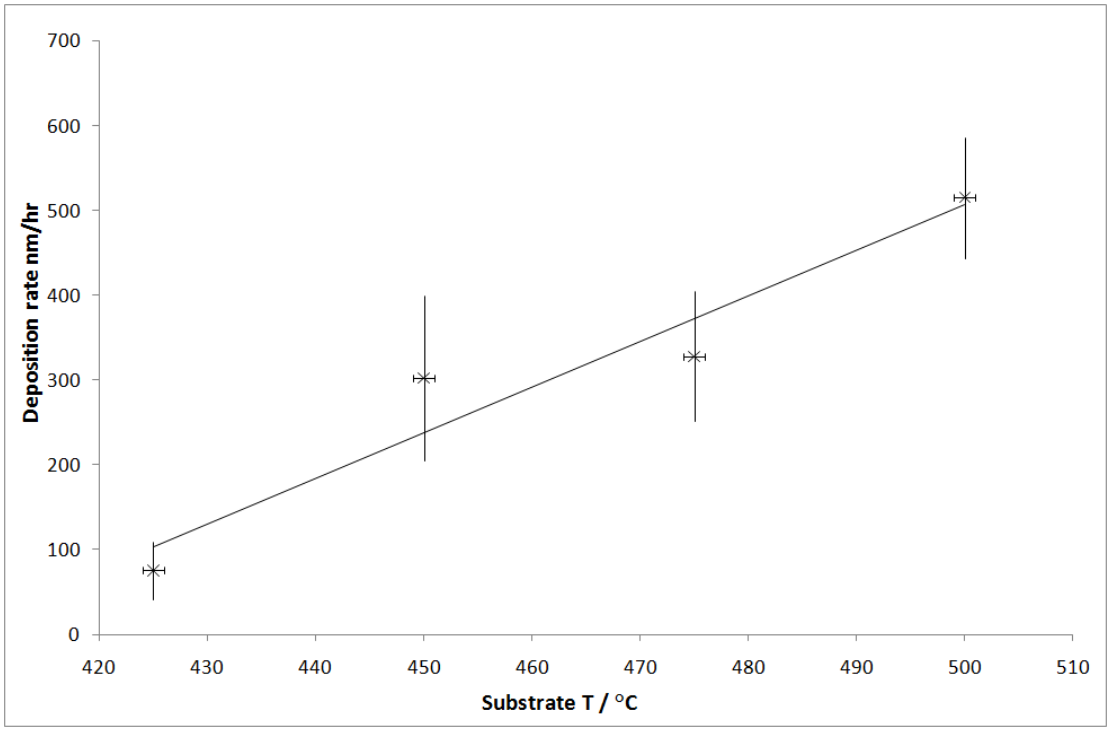

Figure 49: Film growth rates as a function of substrate temperature.

The activation energy for the reaction as a function of substrate temperature was estimated using the Arrhenius equation by plotting the natural logarithm of the growth rate (nm s^{-1}) against the reciprocal of substrate temperature (in Kelvin). The gradient of the slope corresponds to E_a/R, where E_a is the activation energy of the reaction and R is the molar gas constant. A gradient of

13700 nm $s^{-1}K^{-1}$ was obtained, and therefore the activation energy for the reaction was calculated to be 113 kJ mol^{-1}. This is somewhat higher than the activation energy (15 kcal mol^{-1} or 63 kJ mol^{-1}) calculated by Kang[74] for bismuth oxide films grown *via* DLI-CVD from $[Bi(thd)_3]_2$ and an oxygen co-reactant at substrate temperatures between 240- 430 °C, however given the difference in precursor concentrations, experimental setup and much lower growth temperatures, this difference is not unexpected.

4.3.3 Scanning electron microscopy

The morphologies of the as-deposited films were investigated *via* top-down SEM imaging as a function of substrate temperature, system pressure and carrier gas flow rate.

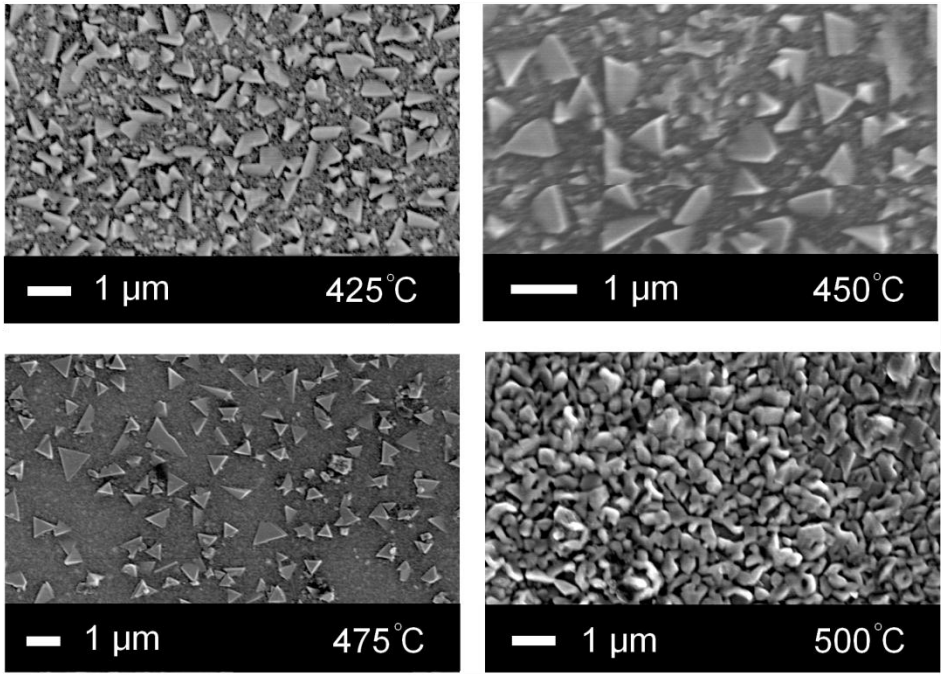

Figure 50: Top-down SEM images of the Bi_2O_3 films formed *via* LPCVD as a function of substrate temperature.

The top-down SEM micrographs of the deposited bismuth oxide films displayed a variety of morphologies according to temperature (Figure 50). Crystallites of varying size (0.4 – 2 µm) were clearly observed in the SEM images, with profound triangular facets apparent in films deposited at 425 °C, 450 C and 475 °C, and these facets were better defined at the higher temperatures. These three samples were determined by powder XRD to be almost entirely composed of β-Bi_2O_3, and it is possible that these triangular shaped crystallites are characteristic of β-Bi_2O_3. As the substrate temperature was increased to 500 °C, these crystallites do not

appear to be present and this is likely to be due to the transformation to the γ-phase, as revealed from powder XRD. The film growth appeared to be non-uniform in most cases, particularly at 475 °C, however the film deposited at 500 °C displayed increased uniformity with the grains appearing to have coalesced together. There does appear to be some material in between and underneath the large crystallites in the film deposited at 475 °C, which could be attributed to the γ-Bi_2O_3 as observed for the film deposited at 500 °C; however powder XRD could not confirm this.

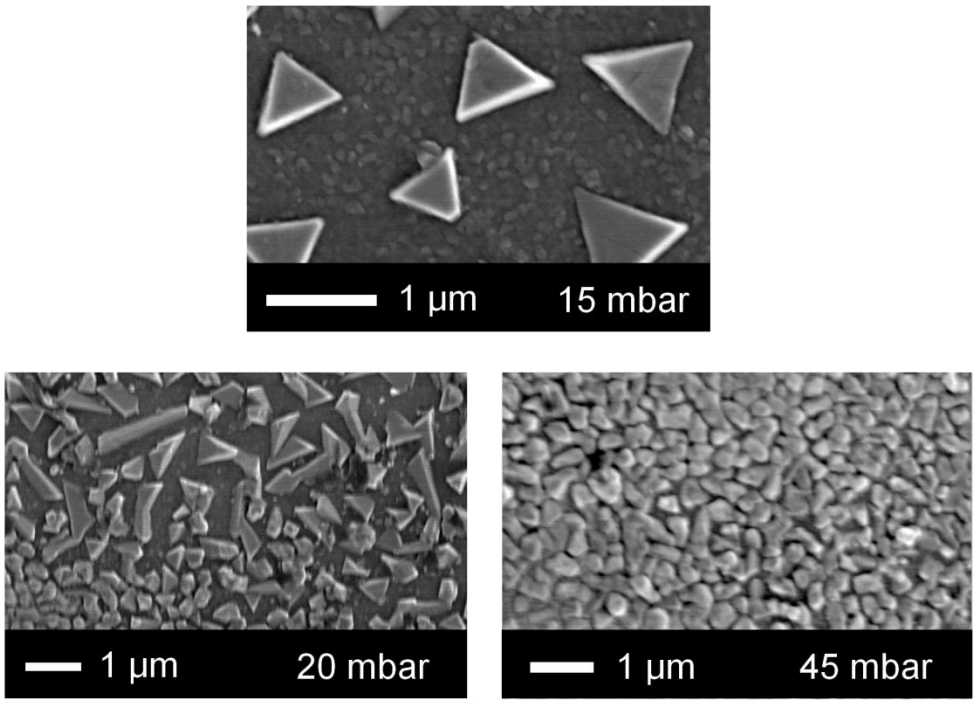

Figure 51: Top-down SEM images of Bi_2O_3 films formed *via* LPCVD as a function of system pressure.

As a function of increasing the total pressure in the CVD reactor we observe a "cluster effect" of unordered agglomeration of particles and crystallites at lower pressures (Figure 51), as the surface reaction rates (adsorption, diffusion, desorption) tend to be greater. There are large crystallites of approximately 1 µm in size observed in the film deposited at 15 mbar and these appear to be three-dimensional, sitting on top of smaller particles, as described earlier with the sample deposited at 475 °C. These large crystallites are evenly spread out and do not provide total coverage; the coverage improves with the sample deposited at 20 mbar although the size of these crystallites is fairly disperse and appears to vary in all three dimensions. At a pressure of 45 mbar, the coverage is particularly uniform with no voids observed and the surface appears to be smoother, and this morphology is somewhat similar to those obtained for Bi_2O_3 films grown via LPCVD[61] and DLI-CVD.[72,74] The Scherrer equation was used to estimate the average particle/crystallite size in the films (Equation 16).[167]

$$D = K \lambda / \beta \cos\theta$$

Equation 16: Debye-Scherrer Equation

Where D corresponds to the particle size (diameter), K is the shape factor which is dependent upon the X-ray instrument (in this case K = 0.9), λ is the X-ray wavelength, θ is the Bragg angle of the peak (half the measured diffraction angle) and β the full width at half maximum (FWHM) in radians of the diffraction peak of the sample corrected by subtracting the peak broadening of a 25mm^2 Al_2O_3 corundum standard (NIST). It was found that the average particle size decreased as the total system pressure increased, and such a correlation is generally observed in the SEM images. The average particle size observed *via* SEM for the film grown at 45 mbar is approximately 300 nm (there appeared to be a range of sizes present between 250 – 450 nm), and the average particle size estimated by use of the Scherrer equation was 420 nm. This variation is perhaps not surprising given the wide particle size distribution observed in this sample and in those deposited at 15 and 20 mbar. Nevertheless, the increase in particle size may be attributed to the greater mobility of incoming reactants and surface diffusion which results in larger crystallites. The increase in reaction rate due to the variation in system pressure has led to the phase transition between mostly β-Bi_2O_3 at low pressures to α-Bi_2O_3 at higher pressures, and this is reflected the morphologies observed in the films.

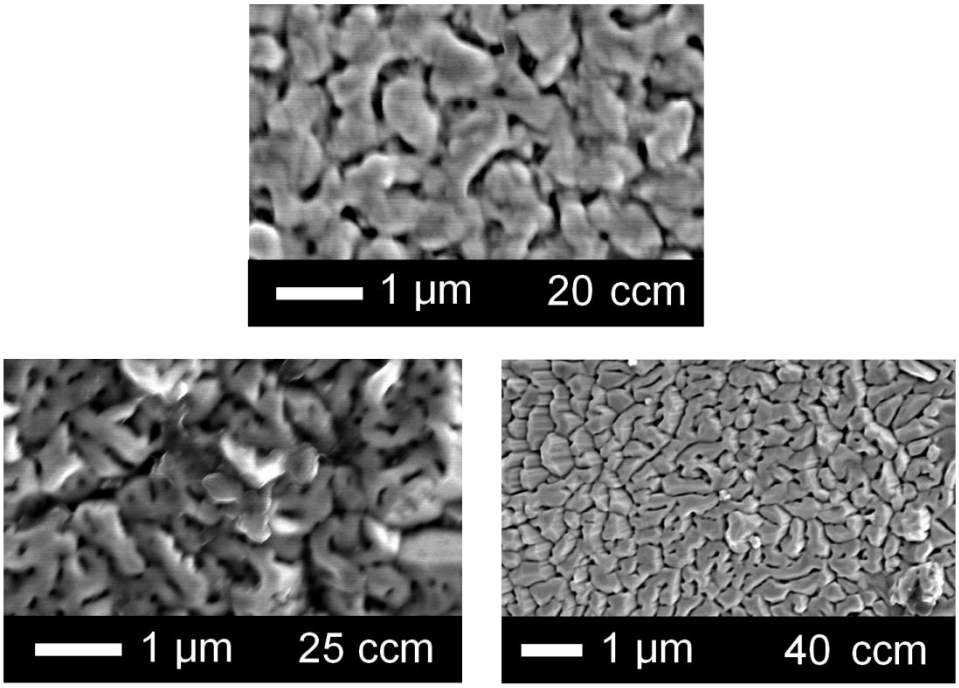

Figure 52: Top-down SEM images of the Bi_2O_3 films formed *via* LPCVD as a function of carrier gas flow rate (ccm = cm^3/min).

Some variation in morphology was observed as a function of varying the carrier gas flow rate (Figure 52). At a flow rate of 20 cm^3/min, the morphology appears to be fairly dense, with clusters of individual particles coalescing together to cover the whole film surface, resulting in very small voids in between. A "cluster effect" of unordered agglomeration of particles and crystallites was observed at higher flow rates, as the surface reaction rates (adsorption, diffusion, desorption) tend to be greater. Limited uniformity and ordering in film growth was seen with the poorly-defined clusters exhibiting random branching out of individual plates and prisms. The edges of the particles are just about visible but estimating their size is difficult given the degree of amalgamation. This is in contrast to the SEM image of Bi_2O_3 deposited at a lower carrier flow rate of 12 cm^3/min at 450 °C, which showed large triangular crystallites closely packed together with very little evidence of particles at the surface fusing together.

Increasing the carrier flow rate slightly to 25 cm^3/min revealed a very similar morphology to that obtained at 20 cm^3/min, albeit now with the loss of detail in the individual particle edges. Apart from some larger particles growing on top of the film surface to the right of the image, the structure was very flat in places and reveals a smoother film surface. There appears to be an increase in the amount of voids on the film surface and the morphology appears more "sintered" than that obtained at 20 cm^3/min.

At a carrier flow rate of 40 cm^3/min, the morphology is very dense, with virtually no voids observed over the surface. The degree of particles coalescing is greatest for this sample, indicating throughout the study that increasing the flow rate, and hence the rate of reaction, leads to more uniform coverage and a higher degree of fusing together of particles. There appears to be no individual grains compared to the other films, as these coalesce to cover the substrate almost entirely. This trend in morphology change appears to match the effect of increasing the substrate temperature and total system pressure described earlier. As a result of peak broadening (and peak overlap) that was observed in the X-ray diffraction patterns, the estimation of particle sizes using the Scherrer equation proved challenging, however the average particle size for the film deposited at 40 cm^3/min was estimated at 90 nm. The comparison with the SEM image of this sample reveals an underestimate in particle size from the Scherrer equation, however, because the degree of particle coalescence was quite high in the SEM image, we may be viewing agglomeration of particles and not individual particles.

4.3.4 Raman spectroscopy

Raman spectra were recorded for all of the bismuth oxide films grown *via* LPCVD of $[Bi(O^tBu)_3]$. The predominantly α- and β-Bi_2O_3 films exhibited few distinguishable features in the Raman spectrum. Broad peaks at 372 cm^{-1} and 580 cm^{-1} were the only two peaks observed

with a relatively large background signal due to breakthrough to the substrate in these thin films. The Raman spectrum of the predominantly γ-Bi_2O_3 film deposited at 500 °C (Figure 53) displayed prominent peaks at 533, 452, 319, 279, 211, 154, 141 and 125 cm^{-1}. These were almost identical to the reported Raman spectra of the metal cation stabilised sillenite structures $Bi_{12}(Bi_{0.53}Mn_{0.47})O_{20}$ and $Bi_{12}SiO_{20}$[168] and $Bi_{12}TiO_{20}$, the structures of which are all body-centred cubic and may be represented parentally by γ-Bi_2O_3 with general structure $Bi_{12}(Bi_{4/5-n/x}M^{n+}_{5x})O_{19.2+nx}$, however the peak highlighted with a * at 185 cm^{-1} (Figure 53) remains unassigned. Due to the laser filter cut-off at around 120 cm^{-1}, any peaks below this figure could not be observed.

Group theory analysis of the sillenite structures has indicated a total of forty Raman active modes – 8A (totally symmetric), 8E (doubly degenerate) and 24F/T (triply degenerate) and 24 IR vibrational modes (only those of F/T symmetry).[168,169] It is difficult to assign exactly each of these individual vibrational modes to the bonds in γ-Bi_2O_3 due to the absence of the stabilising MO_4 tetrahedra (M = Ti, Ge, Mn,Si etc.) found in metal cation-stabilised sillenites. Recent work[64] describing the fluidised-bed CVD growth of Bi_2O_3 films has revealed that the Raman spectra of (not pure) α-Bi_2O_3 closely matches peaks observed in γ-Bi_2O_3 spectra, making comparison of the two phases challenging.

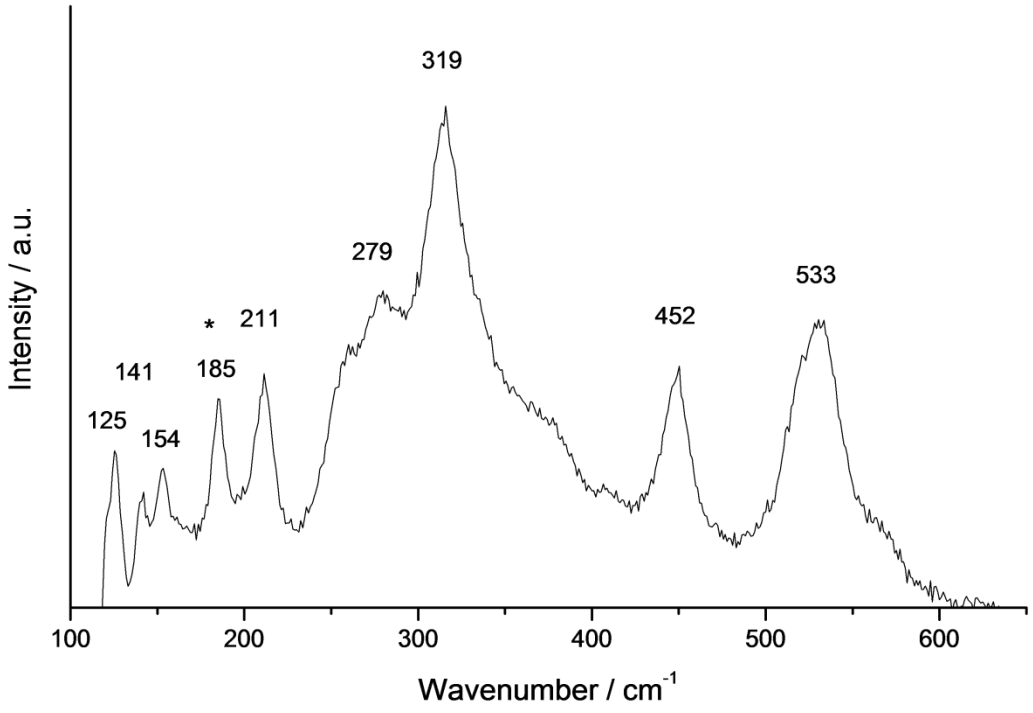

Figure 53: Raman spectrum of the predominantly γ-Bi_2O_3 film grown *via* LPCVD.

4.3.5 X-ray photoelectron spectroscopy

The compositions of the as-deposited films were studied using X-ray photoelectron spectroscopy (XPS). The samples were earthed using copper plates in order to prevent charging, and samples were etched for five minutes and then ten minutes. Full width at half maximum (FHWMs) were constrained between 0.9 – 1.3 for Bi 4f, and its peak position constrained between 153.9 – 168 eV. The high resolution surface scan of the bismuth 4f surface ionisation displayed one principle environment. Figure 54 shows the high resolution XPS spectrum for the bismuth 4f region. The Bi $4f_{7/2}$ peak was observed at 158.8 eV and the Bi $4f_{5/2}$ peak was observed at 164.1 eV for all the films, which is characteristic of Bi_2O_3.[170] Upon etching, distortion of the bismuth 4f peaks was observed due to preferential sputtering of lighter atoms which led to the appearance of metallic bismuth peaks (Bi^0) at 161 eV and 166.5 eV in addition to the aforementioned Bi $4f_{5/2}$ and Bi $4f_{7/2}$ peaks.

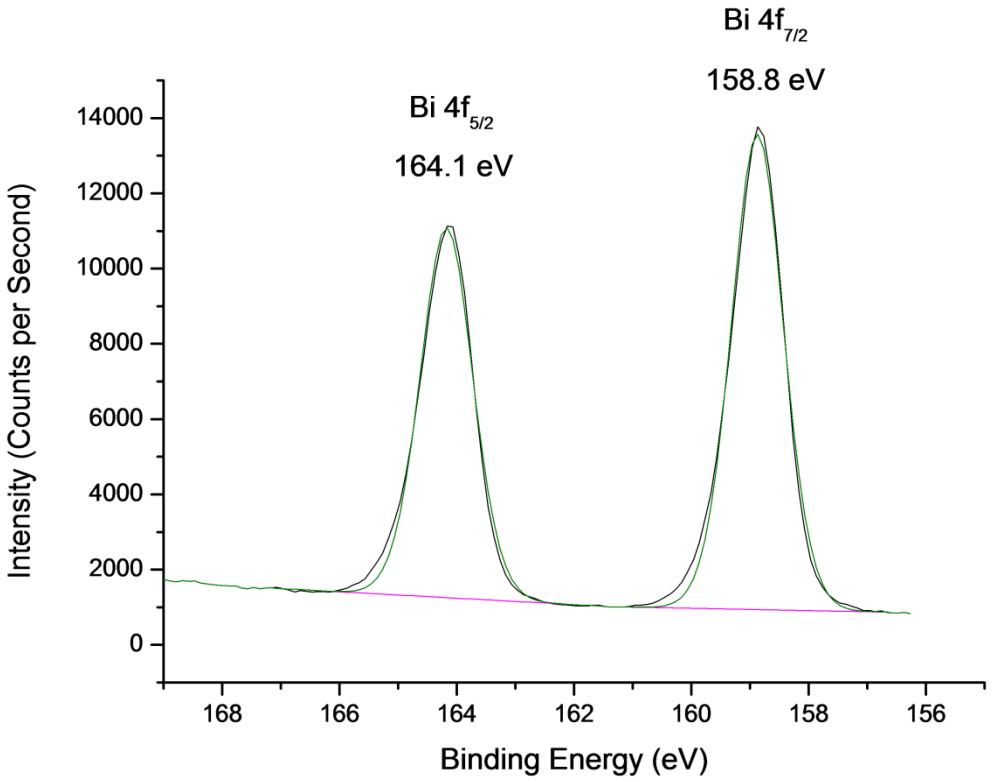

Figure 54: XPS spectrum of the bismuth 4f surface ionisation.

For oxygen 1s (O 1s), the FWHM was constrained between 1.3 – 1.7 and its position limited between 524.7 – 543 eV. The O 1s ionisation was observed between 529.7 – 529.8 eV, a position characteristic of oxygen bound to bismuth in Bi_2O_3,[170] and was composed of one broad asymmetric peak that could be fitted with two individual smaller Gaussian peaks (Figure 55). The presence of a lower binding energy O 1s peak (529.8 eV) is due to metal oxide oxygen

whereas the higher binding energy component (532.3 eV) is due to surface contamination (terminal hydroxyl groups).

By dividing the areas of the bismuth and oxygen peaks by their respective relative sensitivity factors (RSFs) for bismuth (9.14) and oxygen (0.78), and disregarding the contamination peaks, the stoichiometric compositions of the films could be obtained. Bismuth to oxygen ratios close to Bi_2O_3 were observed for all films in the range 1.3 – 1.6 oxygen atoms to bismuth with oxygen deficient stoichiometries found for films deposited at 425 °C (1.4), 450 °C (1.4) and 500 °C (1.3). This is similar to reported XPS data[63] of β-Bi_2O_3 thin films, ascribed to the formation of oxygen-deficient β-Bi_2O_{3-x} as a result of oxygen vacancies found in the lattice. Etching experiments were carried out, however this resulted in preferential sputtering of lighter atoms, and exact bismuth and oxygen compositions could not be determined after etching. Carbon decreased dramatically after etching, suggesting that the carbon on the film surface is due to adventitious carbon contamination; however quantification in the bulk was not possible due to distortion of the peaks after etching. It is, however, expected that the decomposition of [Bi(O^tBu)$_3$] would yield bismuth oxide with minimal carbon contamination if its decomposition pathway is assumed to be comparable to the mechanism shown in Figure 44 and Figure 45.

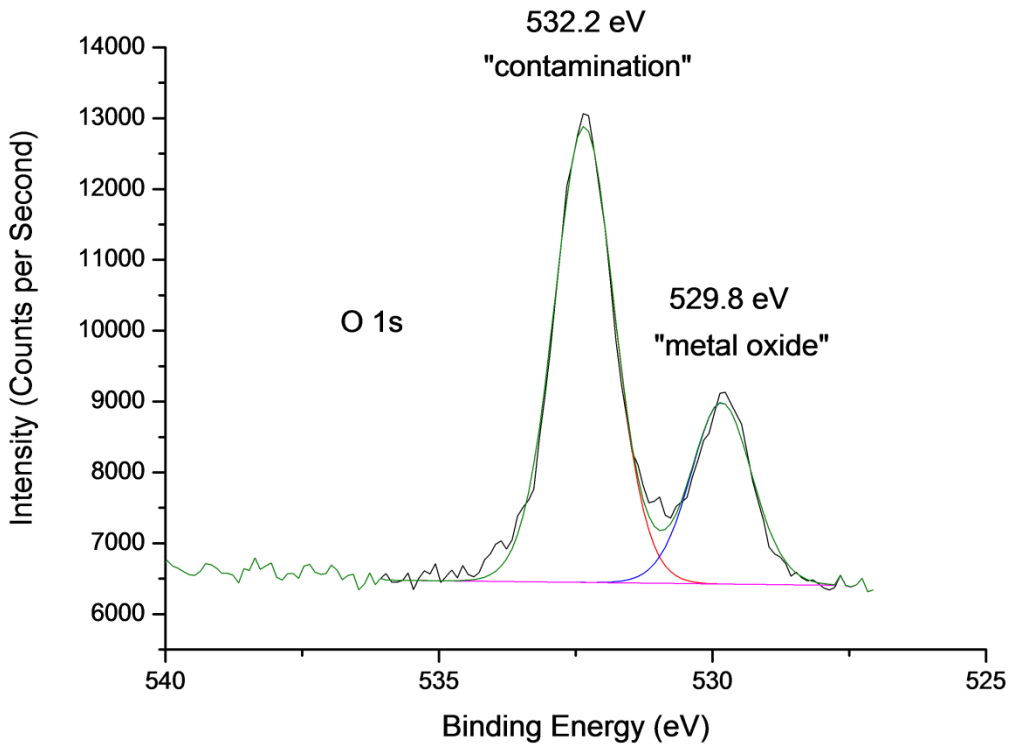

Figure 55: XPS spectrum of the oxygen 1s region.

4.3.6 Atomic force microscopy

The AFM imaging, containing a field size and 3D AFM image (Figure 56), conducted over an area of 5μm^2 area, demonstrates the three-dimensional depth profiling of a Bi_2O_3 film grown at a substrate temperature of 500 °C. Attempts to image a film containing the large triangular crystallites shown in Figure 50 and Figure 51 was not attempted due to the likelihood of tip damage occurring when scanning over such large features. The AFM image shows that the film is mostly composed of globular particles with an average diameter of 200 nm with very few voids visible where no deposition has taken place. This image is similar to the top-down SEM image of the same sample (Figure 50, bottom right) which shows a very dense morphology with a high degree of particle coalescence. It is interesting to note that the SEM image portrays the morphology as quite flat when observing the film from a top-down point of view; in reality the AFM image suggests the structure has some notable roughness and is full of high features (the tallest peak was measured at 53 nm). The root mean squared (rms) roughness of the film was measured at 4.1 nm which is considerably lower than the value obtained (60 nm) for $BiFeO_3$ films grown *via* the LPCVD reaction of $[Fe(O^tBu)_3]_2$ and $[Bi(O^tBu)_3]$ (Chapter 7) and $BiFeO_3$ films grown using $[Fe(acac)_3]$ as the iron source (rms = 30 nm) described in Chapter 6. A value of 4.1 nm is also much lower than the value obtained (97 nm) for β-Bi_2O_3 films grown *via* AACVD from the *β*-diketonate complex $[Bi(dbm)_3]_2$, described in Chapter 5.[171] A roughness value of 4.1 nm is, nevertheless, consistent with roughness measurements carried out on α-Bi_2O_3 films grown *via* DLI-CVD followed by post-deposition annealing (rms of the as-deposited film was 1.72 nm),[74] and similar to the value of 2.0 nm obtained for δ-Bi_2O_3 films grown *via* APCVD.[58] The low roughness value correlates with the dense, almost featureless SEM image, but is perhaps surprisingly low considering some of the high features observed in the AFM image.

The comparatively low roughness value would perhaps be a limiting factor in the use of these films for applications requiring high surface area materials, for example, in catalysis.

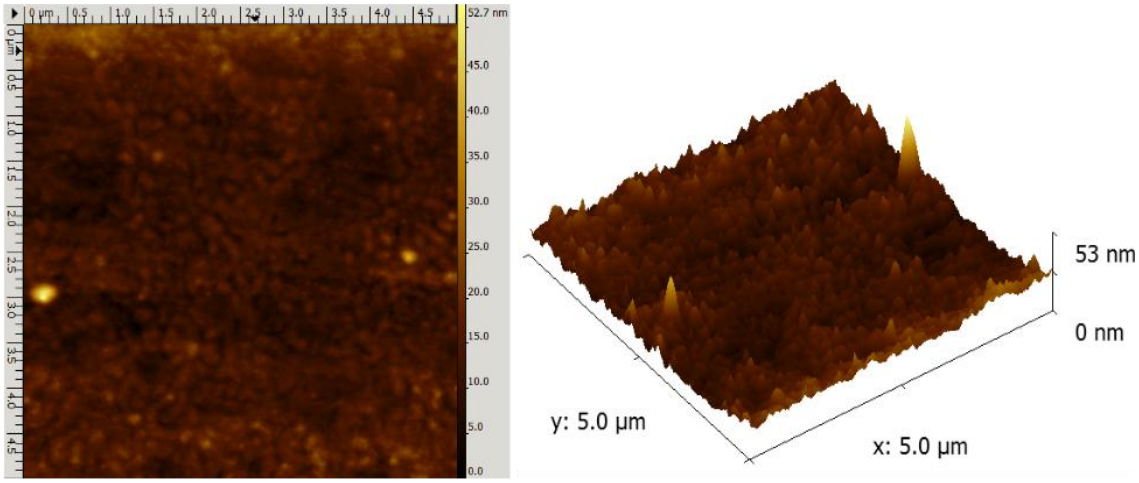

Figure 56: A 5 µm field size (left) and the corresponding 3D AFM image (right) of a Bi_2O_3 film formed *via* LPCVD of [Bi(O^{t}Bu)$_3$] at 500 °C.

4.3.7 UV-Vis spectroscopy

The band-gaps and optical properties of the as-deposited, yellow Bi_2O_3 films were measured using UV-Vis spectroscopy recorded in transmission mode. A spectrum of the borosilicate glass substrate was recorded and then subtracted from the spectra of the combined film and glass. The band-gaps of the films (Table 4) were calculated using Tauc plots[172] and a typical transmission spectrum of two Bi_2O_3 films on glass substrates is shown in Figure 57.

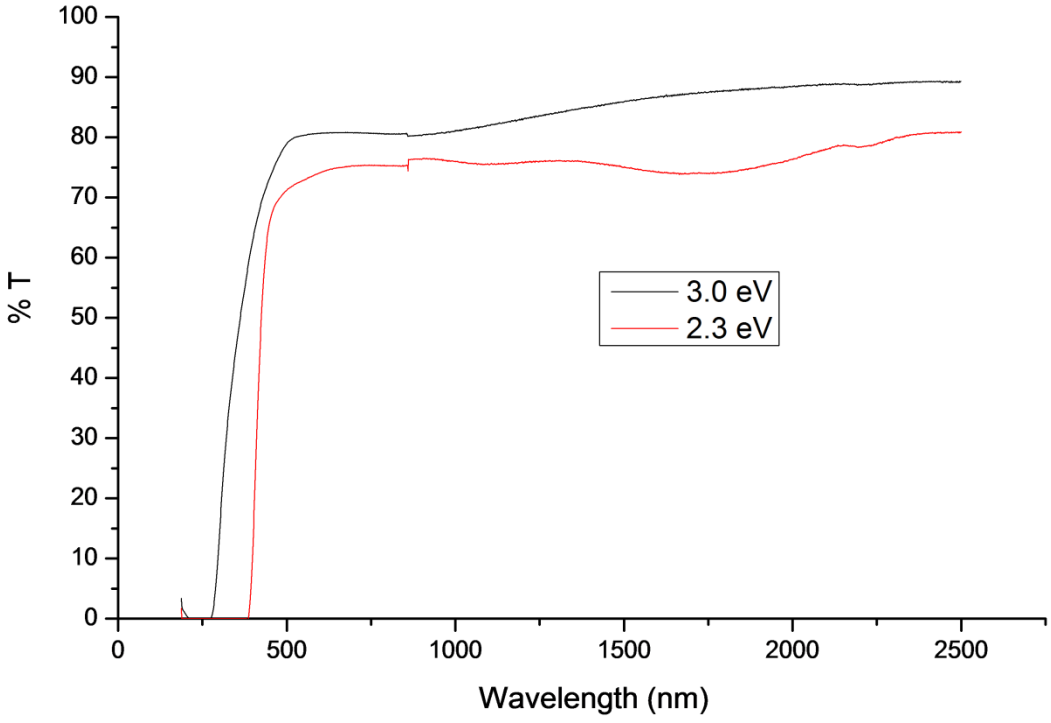

Figure 57: Transmission spectrum of two Bi_2O_3 films with different band-gaps grown *via* LPCVD.

The transmission spectra of two films with differing band-gaps values, shown in Figure 57, show that both films were over 75% transmitting in the 300 – 2500 nm range. Film thicknesses were not obtained *via* the Swanepoel[173] method because of the small number of interference fringes obtained in the spectra for all samples. The small "kink" in the spectrum at approximately 850 nm is caused by the change in the grating inside the machine, but this has no overall effect on the band-gap determination. The cut-off from the borosilicate glass substrate comes into effect below 380 nm, and therefore transmission values between 175 – 380 nm may be ignored. In order to calculate the band-gap of the material, a Tauc plot was constructed by firstly converting the transmission values to absorbance (α) using the Beer-Lambert relationship $\alpha = -\log(\%T_{film} / \%T_{glass})$, where T = transmission value. The general relationship between absorption coefficient and photon energy for fundamental interband electronic transitions is: $\alpha h\nu = A(h\nu - E_g)^n$. Hence by plotting a graph of $(\alpha h\nu)^n$ against $h\nu$, the band-gap may be estimated by extrapolating the linear part of the curve to the intercept on the x-axis.

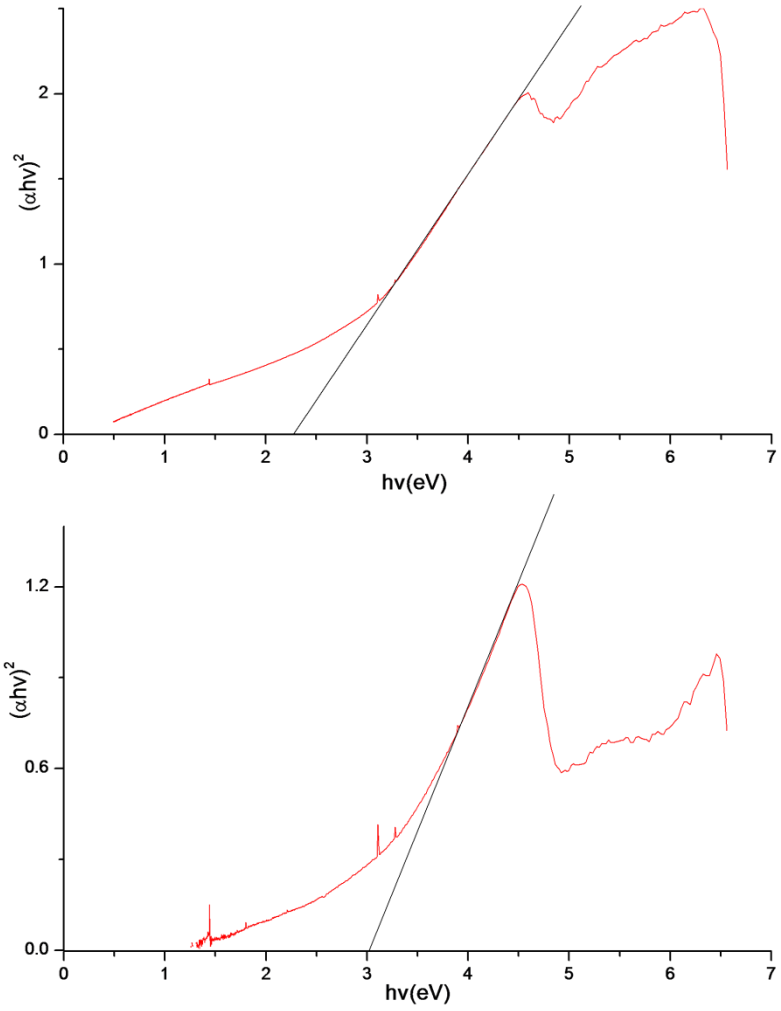

Figure 58: Tauc plot for two Bi_2O_3 films with different band-gaps; 2.3 eV (top), 3.0 eV (bottom).

Figure 58 shows the Tauc plots for two Bi_2O_3 films grown on glass *via* LPCVD. The extrapolation of the linear part of the plot to the x-axis results in band-gap values of 2.3 eV and 3.0 eV for the two films chosen. The same method was used to calculate the band-gap of the other samples. The features in the Tauc plots at energies greater than 4.5 eV are due to the absorption of the glass substrate, and are not used for band-gap determination. The band-gap values were in good agreement with numerous reports containing experimentally derived band-gaps for Bi_2O_3.[174] Indeed, the band-gap value for bismuth oxide appears to depend strongly upon the phase present, with the amorphous phase possessing a band-gap as low as 2.0 eV and γ-Bi_2O_3 having a band-gap of 2.8 eV.[18] Band-gap values for all the films grown here *via* LPCVD were in the range 2.3 – 3.0 eV, with films containing tetragonal β-Bi_2O_3 possessing values in the 2.3 – 2.6 eV range, and the monoclinic α-Bi_2O_3 possessed a band-gap of 2.8 eV. Films containing γ-Bi_2O_3 as the dominant crystalline phase were found to have higher band-gaps in the 2.7 – 3.0 eV range, and therefore we can conclude that not only can the phase be controlled by the deposition conditions, but also the band-gap of the material as this is dependent upon the phase present. This ability to conduct phase-selective depositions and control the band-gap of the material deposited appears to be unique for deposition of bismuth oxide films.

4.4 Photocatalysis

4.4.1 Experimental

As all films possessed band-gaps between 2.3 - 3.0 eV, they lie within the visible range of the electromagnetic spectrum, which is perhaps no surprise given their yellow colour. However, in order to compare the photocatalytic activity of Bi_2O_3 to a common metal oxide photocatalyst (such as TiO_2) that was tested using identical experimental conditions, monochromatic UV-light was used for this photocatalysis experiment.

For this experiment, the ability of Bi_2O_3 films to photo-oxidise water in the presence sacrificial reagents was studied using 365nm UV-light and a Rank Brothers oxygen electrode, which is comprised of a water cooled glass vessel that contains in its base a Clark Cell with a platinum working electrode and a Ag-AgCl counter electrode, separated from the sacrificial solution by a gas permeable, ion impermeable membrane that allows only oxygen to reach the electrode for detection. The oxygen electrode is used to measure the voltage of the solution *via* a potentiostat, whereby the recorded voltage is proportional to the dissolved oxygen content in the solution. The solution was initially purged with air, then N_2 gas, allowing the voltages for purely saturated (maximum oxygenated) and unsaturated (minimum oxygenated) solutions to be

measured.[175] Any increase in voltage (toward saturation) occurs as a direct result of oxygen evolution, and the solubility of O_2 in water is 40 mg l^{-1} at 298 K and 1 atm.[176] The voltage is recorded as a function of time, and the software allows for real-time monitoring of voltage on a computer screen. The potentiostat has an analogue output, so this was converted to digital format by a Pico Technology Picoscope and PicoLog software.

The film(s) were suspended *via* fishing wire into the solution with continuous stirring at room temperature, making sure the film side was facing the light source at all times during the experiment. The sacrificial electron acceptor solution was composed of 0.1M KOH and 0.01M $Na_2S_2O_8$ solution (previously purged with oxygen-free nitrogen), and the sample was enclosed in the chamber and irradiated with 16 W, 365 nm UV-light for 2000 seconds at a distance of 10 cm. The alkalined sodium persulphate undergoes a four-electron reduction, during which the water undergoes a four-electron oxidation to form oxygen gas and four protons (Equation 17).

$$2S_2O_8^{2-} + 4e^- \longrightarrow 4SO_4^{2-}$$

$$2H_2O \longrightarrow O_2 + 4e^- + 4H^+$$

Overall:

$$2S_2O_8^{2-} + 2H_2O \longrightarrow 4SO_4^{2-} + 4H^+ + O_2$$

Equation 17: Equations representing water photo-oxidation from a persulphate sacrificial solution.

The photocatalyst serves to capture photons, generating electron-hole pairs in the semi-conductor; these holes are then used to oxidise water to produce oxygen. The photogenerated electrons in the conduction band are consumed by the oxidising agent (persulphate ion) resulting in enhanced oxygen production. Sacrificial reagents allow an investigation into whether a certain photocatalyst satisfies the kinetic and thermodynamic potentials for photo-oxidation and/or reduction. This process here means that the oxygen evolution can be measured in isolation whilst disregarding hydrogen evolution for the time being (which requires a metal substrate for electron transfer and a hydrogen catalyst such as platinum or rhodium, on the reverse). The generated dissolved oxygen concentration as a function of time was plotted, and therefore the rate of oxygen production was determined from the gradient of these plots.

4.4.2 Photocatalysis Results

Two films were chosen for this investigation - these were the films deposited at 475 °C and 500 °C due to the large variation in their respective band-gaps (2.3 vs. 2.8 eV) in addition to the

difference in thicknesses (330 vs. 520 nm). Monochromatic UV-light was used in order to compare the activity of both films, as using a visible light source would result in differing photon absorption by both samples due to their differing band-gaps, and above all, as stated earlier, due to the scarcity of reports in the literature describing the photo-oxidation of water using bismuth oxide, another objective of the experiment was the comparison of photocatalytic activity between these Bi_2O_3 films and TiO_2 films produced *via* APCVD which had been tested solely under 365 nm light. The Bi_2O_3 films were both cut down to a 1cm x 1cm piece in order to be securely suspended in the catalysis vessel. A graph plotting voltage against time was plotted and is shown in Figure 59.

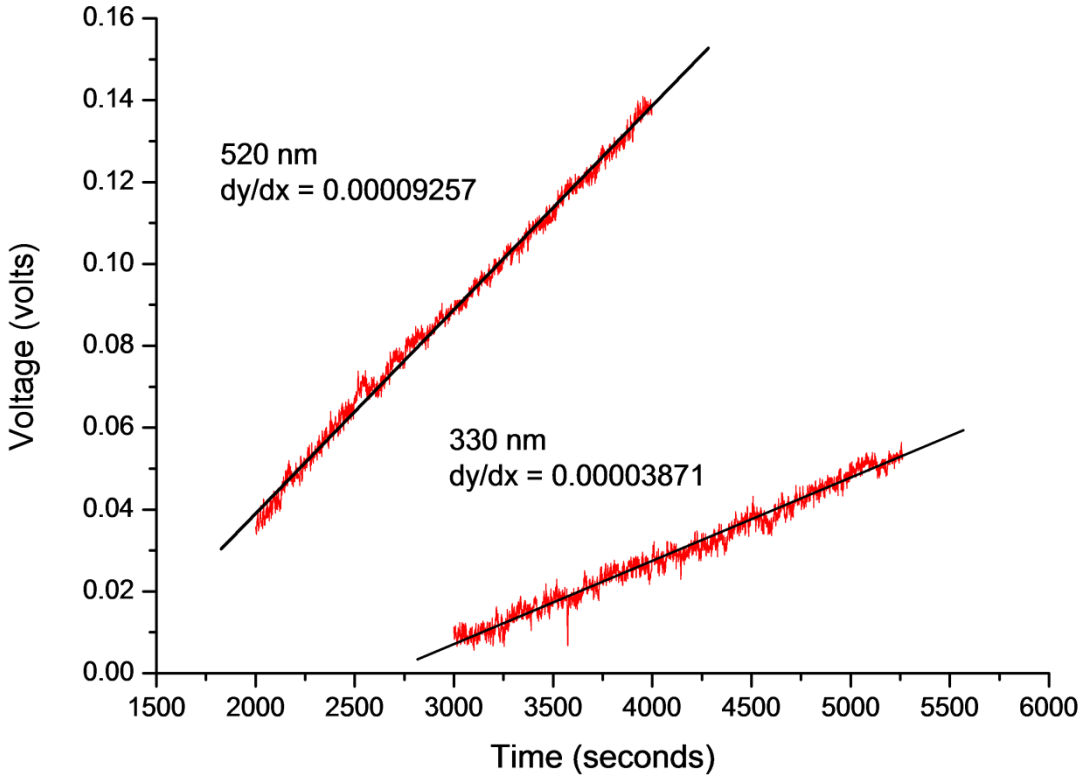

Figure 59: Graphs showing voltage against time measured during the photo-oxidation of water (365 nm light source) for two Bi_2O_3 films of 520 nm (top) and 330 nm (bottom) thicknesses. The gradient of the slopes are used to calculate the amount of oxygen evolution.

The plots of voltage against time for the two chosen Bi_2O_3 films reveal a steady increase in voltage over the time period, however their gradients differ significantly. Appreciable oxygen evolution was observed in both cases in the presence of UV-light, whereas the substrate-only experiment, which acted as a reference, exhibited zero oxygen production as expected. Films deposited at 500 °C, which were predominantly γ-phase, resulted in approximately 2.5 times the rate of oxygen evolution in comparison to films deposited at 475 °C, which were mixed β- and γ-phase, despite the latter sample possessing a narrower band gap of 2.3 eV compared to 2.8 eV.

In order to convert the gradient of the slope, measured in Vs^{-1} (volts per second), to moles of oxygen per second, the first step would be the calculation of the concentration of oxygen in the saturated solution. This was calculated by multiplying the saturated solubility of oxygen in water (40 mg l^{-1} at 298 K, 1 atm) by its fraction of air:

40 mg l^{-1} x 0.2 = 8 mg l^{-1}

Then, the concentration of oxygen in the air purge was calculated by dividing the concentration of oxygen in saturated solution by the molecular mass of oxygen:

8 mg l^{-1} / (32 x1000) = 0.00025 mol dm^{-3}

Next, the number of moles of oxygen in the solution when saturated was calculated by multiplying the concentration of oxygen in the air purge, by the volume of the solution:

0.0025 mol dm^{-3} x 0.03 dm^3 = 0.000075 moles

Finally, the number of moles of oxygen per volt was calculated by dividing the number of moles of oxygen in the solution by the difference in voltage between the air and N_2 purge:

0.000075 moles /2.6028 V = 0.000003 moles/V

Therefore the amount, in moles per second, of oxygen evolution was calculated by multiplying the gradient of the slope (Figure 59) by the number of moles of oxygen per volt:

For the sample of 520 nm thickness, the gradient of the line of best fit = 0.00009257 Vs^{-1}.

Therefore 0.000093 Vs^{-1} x 0.000003 moles/V = 2.92 X 10^{-10} moles s^{-1} = 2.92 x 10^{-4} μmol s^{-1}. Per hour, the rate is **1.1 μmol h^{-1}** (2.92 x 10^{-4} μmol s^{-1} x 3600 s). The photocatalysis results are summarised in Table 5.

Table 5: Summary of the photo-oxidation results for the two Bi_2O_3 films grown *via* LPCVD.

Substrate temperature / °C	Crystalline phase(s)	Film thickness / nm	Band-gap / eV	Rate of O_2 production / μmol hr^{-1}	Rate of O_2 production / μmol h^{-1} m^{-2}	Apparent Quantum Efficiency
475	β, min. γ	330	2.3	0.44	4400	9.8%
500	γ	520	2.8	1.1	10500	25%
Uncoated glass		0	-	0	0	-

In the case of a 1 m^2 sample, the values for the 1 cm^2 samples were multiplied by a factor of 10000 to obtain the rate of oxygen evolution if a 1 m^2 film of bismuth oxide was deposited on glass, making assumptions based on uniform coverage and thickness and reaction rate being the same. The apparent quantum efficiencies of the samples were estimated using the number of incident photons of the light source (1.65 mW cm^{-2}) and the number of molecules of oxygen evolved. In both cases the number of incident photons per second was estimated to be **3 x 10^{15} photons/second**, using the equations $E = hf$ and $f = c / \lambda$, where E = Joules/photon, h = Planck's Constant, and f = frequency in Hertz of the 365 nm light source, and the definition of 1 Watt = 1 Joule per second. Therefore the number of photons per second was calculated by dividing the power (1.65 x 10^{-3} Js^{-1}) by the number of joules per photon of the lamp. The efficiency was calculated as follows:

Quantum efficiency = [No. of O_2 molecules per second/No. of incident photons per second] x 4 (4 electron process) x 100%

It was assumed that each photon from the lamp can promote one electron from the valence to the conduction band and given that the photo-oxidation of water is a four electron process, apparent quantum efficiencies of 9.8% and 24.2% were calculated for the two samples at 365 nm. The use of a low power, monochromatic UV-lamp resulted in fewer incident photons than would be obtained from using a standard, higher powered visible light source producing photons of numerous wavelengths, and therefore in this case a high quantum yield was obtained. A recent study[177] of the photocatalytic activity for organic dye degradation of different polymorphs of Bi_2O_3 under visible light revealed the tetragonal β-phase to possess the highest activity for the phases measured, and the rate followed the order β-Bi_2O_3 > α-Bi_2O_3 > δ-Bi_2O_3, however the activity of the cubic γ-phase was not measured. During our investigation we identified that the γ-phase exhibited more than twice the activity compared to the β-phase, suggesting that this phase could potentially have the highest photocatalytic activity of all the bismuth oxide phases, although this assumption is based upon activity under UV-light.

4.4.2.1 Limitations of quantum efficiency calculations

Due to the fact that the experimental conditions for photocatalysis vary quite significantly between literature sources, the use of units such as μmol hr^{-1} to represent photoactivity for either hydrogen or oxygen production cannot be relied upon. The estimation of a quantum efficiency value for photocatalysis measurements is therefore frequently found in the literature for evaluating the performance of a particular photocatalyst if the evolution of gas is being measured, and is based upon the amount of gas (in this case, oxygen or hydrogen) evolved as a function of the energy invested into the system (photons). The value itself is limited as it is

almost impossible to calculate the number of photons absorbed by the photocatalyst due to light scattering, hence an alternative term used is "apparent quantum efficiency."[152] The use of turnover numbers or turnover rates is even rarer, as they both require an estimation of the number of photocatalytically active sites present.[178] It has been suggested that the use of a model reaction such as the photodegradation of phenol in water could allow for the results of other photocatalyst reactions to be normalized according to phenol.[179] It is also necessary to make an assumption based upon the number of photons required for a reaction. Four photons are required to produce one oxygen molecule in the photo-oxidation of water (a four electron process), however for more complex systems such as the photodegradation of acetic acid in water (which could proceed *via* a radical mechanism), the determination of the exact number of electrons taking part in the reaction is difficult.[180]

The difficulties in comparing photocatalyst activities from different systems led to the publication of an article from IUPAC suggesting specific protocol for calculating quantum efficiencies, caused by the differences in light sources, reactor geometries and solutions used during experiments. The calculation of a relative photonic efficiency (ε) was suggested based upon the oxidation of phenol; however its use within the literature is extremely rare.[181] What is somewhat surprising is that quantum efficiency calculations generally fail to take into account the amount (mass) or volume of photocatalyst used during the experiment, and this is particularly important if comparing the activities of thin film samples to powders. Some normalisation, particularly in the case of powders, in order to quote efficiency as either per gram of catalyst or per unit volume may assist those attempting to compare results. As quantum efficiencies depend upon irradiation wavelength and intensity, calculations should be quoted with both these figures; hence an alternative solution would be to conduct experiments with monochromatic radiation at a fixed intensity to aid comparison between experiments. There are, of course, additional factors as to why photoactivities differ, including, but not limited to: particle size and shape, the hydrophilicity/hydrophobicity of the material when in contact with solution and its surface area.

The high photocatalytic activity for photo-oxidation of water using these Bi_2O_3 films is perhaps not surprising given the relatively positive conduction band level for a typical Bi_2O_3 photocatalyst (Figure 60).[20] It is also interesting to note that the bottom of the conduction band is not sufficiently negative in comparison to the redox potential of H^+/H_2O (0 V *vs*. NHE) and therefore the photo-reduction of water would be thermodynamically impossible for hydrogen production. One should also note that as these photo-oxidation reactions are carried out in highly basic solutions (pH 11), the stability field of water dictates that such a reaction would become more thermodynamically and kinetically favourable.

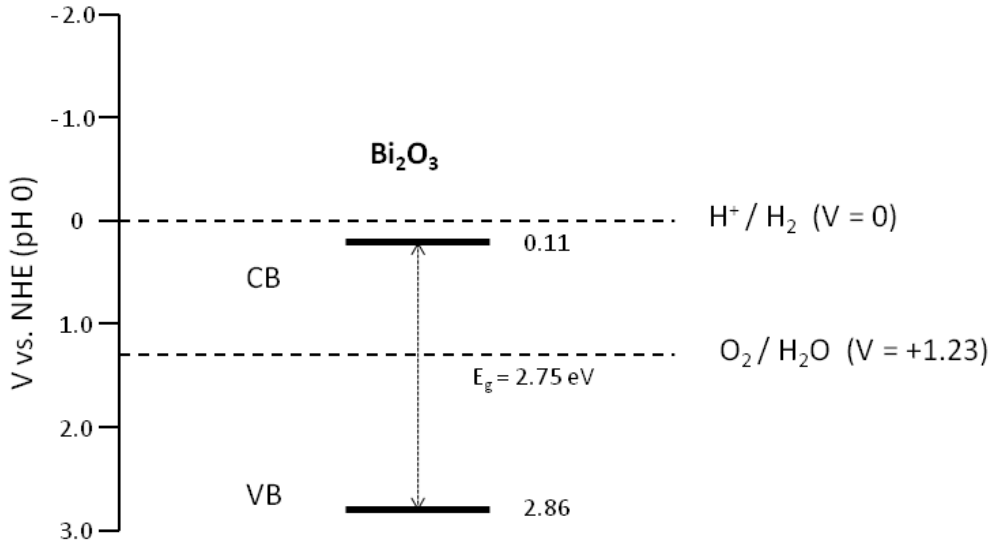

Figure 60: Estimated valence (VB) and conduction band (CB) positions for a Bi_2O_3 sample with a band-gap of 2.75 eV (no particular phase).[20]

As previously stated, the comparison of photocatalytic activity between these and other samples in the literature are notoriously difficult given differences in experimental setup and the assumption that 100% of the photons emitted from the light source reach the photocatalyst. Nevertheless, these efficiencies are clearly high and are comparable to a range of metal oxide catalysts that are photocatalytically active under UV-light.[152] It is slightly more straightforward to compare the photoactivities of these bismuth oxide samples with TiO_2 films (anatase and rutile) grown either *via* APCVD or dip-coating as they were measured using an identical photocatalysis experiment. For optimised anatase films grown on glass *via* APCVD, oxygen evolution rates between 360 - 2800 $\mu molh^{-1}m^{-2}$ were recorded for a variety of samples with different thicknesses; however no direct correlation between photoactivity and film thickness was observed for these samples.[175] For gold and silver incorporated TiO_2 composite films (mixed anatase and rutile phases) grown on glass substrates *via* dip-coating (results for pure TiO_2 were not given), oxygen evolution rates between 1130 - 4540 $\mu molh^{-1}m^{-2}$ were recorded, and an optimum film thickness of 200 nm was observed; however the presence of gold and silver islands was said to improve photocatalytic activity by acting as electron reservoirs to inhibit charge carrier recombination.[176]

To date, this appears to be the only investigation of the photo-oxidation properties of water from undoped Bi_2O_3 films synthesised *via* CVD. Given that the band-gap of bismuth oxide is in the visible region, and the fact that recent work has shown that transition metal ion-doped γ-Bi_2O_3 can split water[18] and Pt-doped bulk α-Bi_2O_3 is able to degrade organic pollutants,[19] both utilising visible light, the potential for Bi_2O_3 films as visible-light photocatalysts is encouraging.

4.5 Conclusions

TGA analysis (Chapter 3) revealed that the decomposition of $[Bi(O^tBu)_3]$ was consistent with the formation of Bi_2O_3 only, and subsequently, a plot of its vapour pressure revealed that it was suitably high for LPCVD purposes, being intermediate between those of the commercially available and commonly used bismuth precursors $[Bi(mmp)_3]$ and $[Bi(thd)_3]$.

$[Bi(O^tBu)_3]$ was therefore utilised as a single source precursor to deposit films of crystalline Bi_2O_3 at a variety of substrate temperatures, carrier gas flow rates and system pressures. Films were characterised fully *via* powder X-ray diffraction, SEM, XPS and Raman spectroscopy. Phase-selective deposition was observed, whereby β-Bi_2O_3 films could be grown at lower substrate temperatures and pressures, whilst γ-Bi_2O_3 films could be grown at higher temperatures and by using higher carrier gas flow rates. Additionally, α-Bi_2O_3 films were grown at the highest system pressure investigated, at 45 mbar.

The band-gaps of the deposited films were measured by constructing Tauc plots from the UV-vis spectra, which indicated that β-Bi_2O_3 films possessed band-gaps between 2.3-2.6 eV, γ-Bi_2O_3 between 2.7-3.0 eV and α-Bi_2O_3 possessed a band-gap of 2.8 eV. Therefore through this phase selective deposition the electronic properties (band-gaps) of the films may be tuned.

Two films were chosen for an investigation into their photocatalytic properties through the photo-oxidation of water using sacrificial reagents under low power near-UV irradiation. The film comprised of predominantly γ-Bi_2O_3 possessed 2.5 times the photoactivity of the film comprised predominantly of β-Bi_2O_3. Comparison of their photoactivities with optimised TiO_2 films investigated using an identical photocatalysis experiment revealed that these Bi_2O_3 films displayed activities of the same order of magnitude as undoped TiO_2. This is caused by the relatively positive location of the conduction band of bismuth oxide with respect to the redox potentials of water, and highlights the high photocatalytic activity of undoped bismuth oxide for photo-oxidation reactions.

5 Aerosol-assisted CVD of platinum incorporated bismuth oxide films

5.1 Introduction

The first part of Chapter 3 described the decomposition characteristics of a variety of novel bismuth *β*-diketonate complexes as potential single-source precursors for deposition of bismuth oxide films. The poor volatilities of these complexes make them unsuitable for film deposition *via* LPCVD; however their appreciable solubility in polar solvents and toluene together with their good stability in solution could make them suitable AACVD precursors. In this chapter, the use of the *β*-diketonate complex, $[Bi(dbm)_3]_2$ (dbm -dibenzoylmethane), as a precursor to thin films of crystalline β-Bi_2O_3 is described, along with the use of hexachloroplatinic acid ($H_2PtCl_6.6H_2O$) as a precursor for deposition of platinum nanoparticles, both deposited *via* Aerosol-Assisted Chemical Vapour Deposition (AACVD). Thin films of platinum nanoparticle incorporated β-Bi_2O_3 films were co-deposited from a mixture of $[Bi(dbm)_3]_2$ and $H_2PtCl_6.6H_2O$. The films were tested for photocatalytic activity *via* the photo-reduction of water using sacrificial reagents under simulated solar irradiation. The introduction of platinum particles into β-Bi_2O_3 causes hydrogen to be evolved during photolysis of water over the composite material; a property not found for Pt particles or β-Bi_2O_3 alone.

5.2 Experimental – General Procedures

$H_2PtCl_6.6H_2O$ and solvents were used without further purification and were procured from Sigma-Aldrich Ltd.

5.2.1 AACVD studies

A schematic diagram of the AACVD apparatus that was used is shown in Figure 61. Nitrogen was used as a carrier gas and the flow rate was monitored using a calibrated flow meter. CVD experiments were performed using a horizontal stainless steel cold wall micro-CVD reactor. The reactor may be opened upwards by removing the lid which screws into the substrate holder. The diameter of the circular reactor chamber is approximately 60 mm and houses a 30 mm x 30 mm square area where the substrate is placed. No top plate is used to direct the flow of precursor; instead the lid of the reactor serves this purpose. The inlet and outlet holes of the reactor are approximately 5 mm in diameter. The substrate was heated using a Whatman Firerod cartridge heater and the temperature was monitored with Pt-Rh thermocouples. A standard BOC flow meter was used to monitor the carrier gas flow and a Vicks ultrasonic

piezoelectric humidifier was used to generate the aerosol. The precursor and solvent were held in a specially built, graduated flat-base borosilicate glass flask whose base is 50% thinner than the walls, which allows for easier generation of the aerosol.

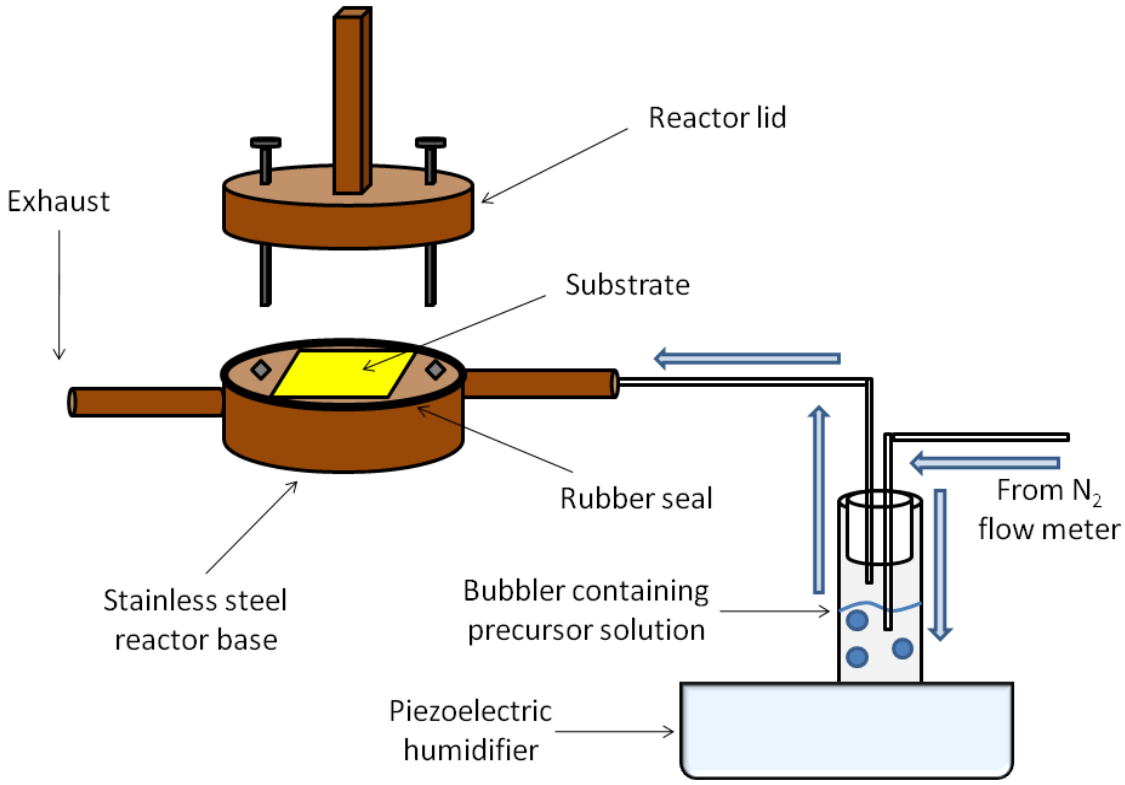

Figure 61: Diagram of the AACVD apparatus, blue arrows indicate direction of precursor/gas flow.

All of the aforementioned *β*-diketonate complexes were investigated for use as single-source precursors to bismuth oxide using the AACVD process, as the problem surrounding their low volatilities may be overcome by their good solubility in solvents such as toluene; this allows them to be transported *via* the use of an aerosol mist to the reaction chamber. Preliminary AACVD studies revealed that only $[Bi(dbm)_3]_2$ was suitable for deposition of bismuth oxide films; the use of $[Bi(acac)_3]_n$, $[Bi(tfac)_3]$ and $[Bi(bzac)_3]$ resulted in no deposition at a variety of substrate temperatures (350 – 600 °C). During these studies, 200 mg of each precursor was weighed in the glovebox and dissolved in toluene (10 cm^3). Nitrogen carrier gas flow rates between 0.2 – 0.6 l/min were used (no oxidising gas was used throughout), however no film deposition occurred on the substrate, but instead a thick powdery layer deposited on the underside of the reactor lid. It is likely that these complexes possess poor thermal stability as evidenced by premature precursor decomposition within the walls and delivery pipe-work of the CVD apparatus, which caused numerous blockages. Films of bismuth oxide were deposited using 200 mg of $[Bi(dbm)_3]_2$ dissolved in toluene (10 cm^3, not dried). The substrate temperature was varied between 410 and 525 °C (no deposition was observed below 410 °C) with

depositions carried out for 1 hr on 25 mm x 25 mm borosilicate glass or stainless steel (316 grade) substrates. For platinum-only films, 20 mg of $H_2PtCl_6.6H_2O$ was dissolved in 10 cm^3 methanol and the substrate temperature was maintained at 410 °C. For deposition of Pt-Bi_2O_3 films, 10 mg of $H_2PtCl_6.6H_2O$ was dissolved in 1 cm^3 methanol (not dried) and was added to 200 mg of $[Bi(dbm)_3]_2$ dissolved in 10 cm^3 of toluene. In all depositions a nitrogen carrier gas flow of 300 cm^3 min^{-1} was maintained.

5.3 CVD of Bi_2O_3 films

As discussed earlier, the DSC-TGA profile of $[Bi(dbm)_3]_2$ is complex, however the residual mass recorded at 600 °C was 32.1%, and the theoretical residual mass required to form Bi_2O_3 only was 26.5%. This resulted in a difference between the calculated and observed values of only 5.6%, and analysis of the residue left in the pan revealed its decomposition to β-Bi_2O_3. Hence $[Bi(dbm)_3]_2$ could well be suitable for use as a bismuth oxide single-source precursor, and for the CVD experiments, 200 mg of this precursor was weighed out into a vial in a glovebox, sealed with a lid, and then swiftly transferred to the bubbler to which the toluene was added. The precursor was completely dissolved in the toluene after 1-2 minutes of stirring. For optimal substrate coverage, a carrier gas flow rate of 0.3 l/min was maintained. The amount of precursor remaining in the bubbler after deposition was negligible. All films displayed good substrate coverage and were adherent; all films passed the Scotch tape test but did not survive after treatment with steel wool and were easily scratched. The films did not show any changes in characteristics after prolonged storage in air. The results for depositions conducted on glass substrates are shown in Table 6.

Table 6: Details of the deposition conditions for deposition of β-Bi_2O_3 films on glass substrates.

Substrate Temp / °C	Thickness / nm	Crystalline phase	Band-gap / eV
410	75	β	2.4
450	280	β	2.2
495	530	β	2.3
525	610	β	2.5

5.3.1 X-ray diffraction

The X-ray diffraction pattern of a Bi_2O_3 film deposited on glass at 450 °C is shown in Figure 62. All peaks can be matched to β-Bi_2O_3, and the tetragonal unit cell parameters are in agreement with literature values[8] ($\alpha = \beta = 7.72(2)$ Å, $\gamma = 5.62(2)$ Å, space group *P*4-21*C*, JCPDS Card No. 027-0050), with similar results found across the temperature range examined.

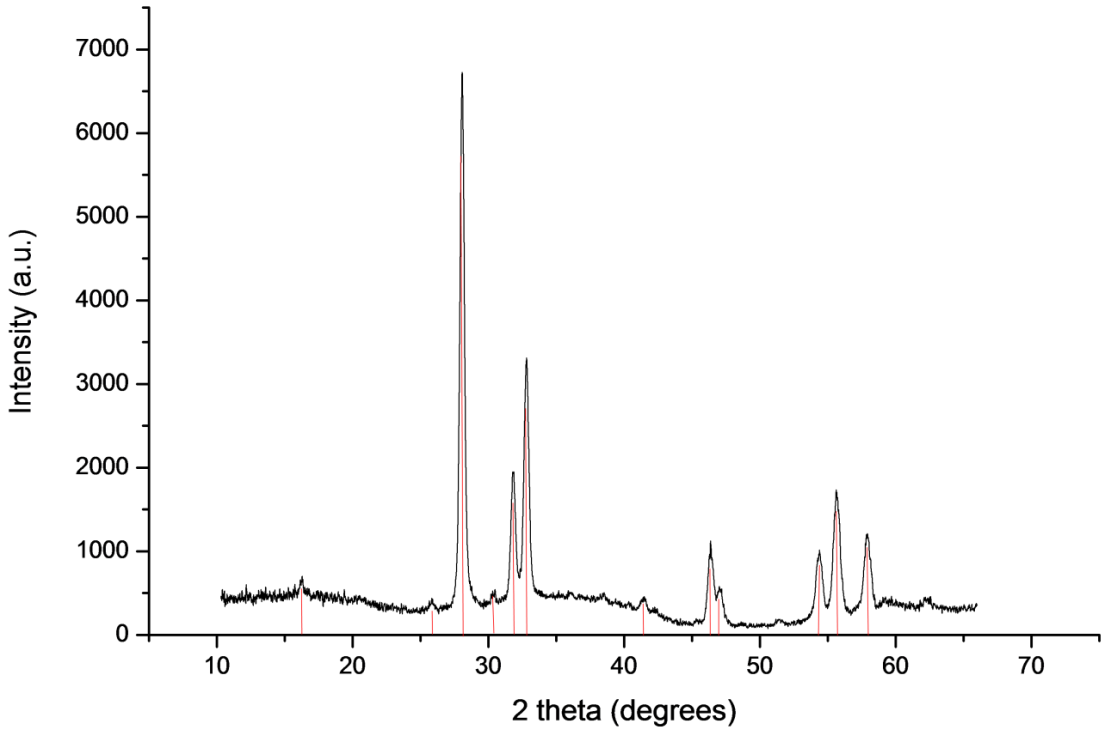

Figure 62: XRD pattern of film deposited at 450 °C on a glass substrate; reflection planes for β-Bi_2O_3 (PDF No. 027-0050) shown.

5.3.2 Scanning electron microscopy

Film composition was measured using wavelength dispersive analysis of X-rays (WDX), however bismuth to oxygen ratios could not be determined due to breakthrough to the glass substrate and the presence of carbon contamination could not be ruled out as the insulating nature of the films required carbon coating before analysis, preventing accurate determination of carbon content. The top-down SEM images of the β-Bi_2O_3 films deposited on glass as a function of substrate temperatures are shown in Figure 63.

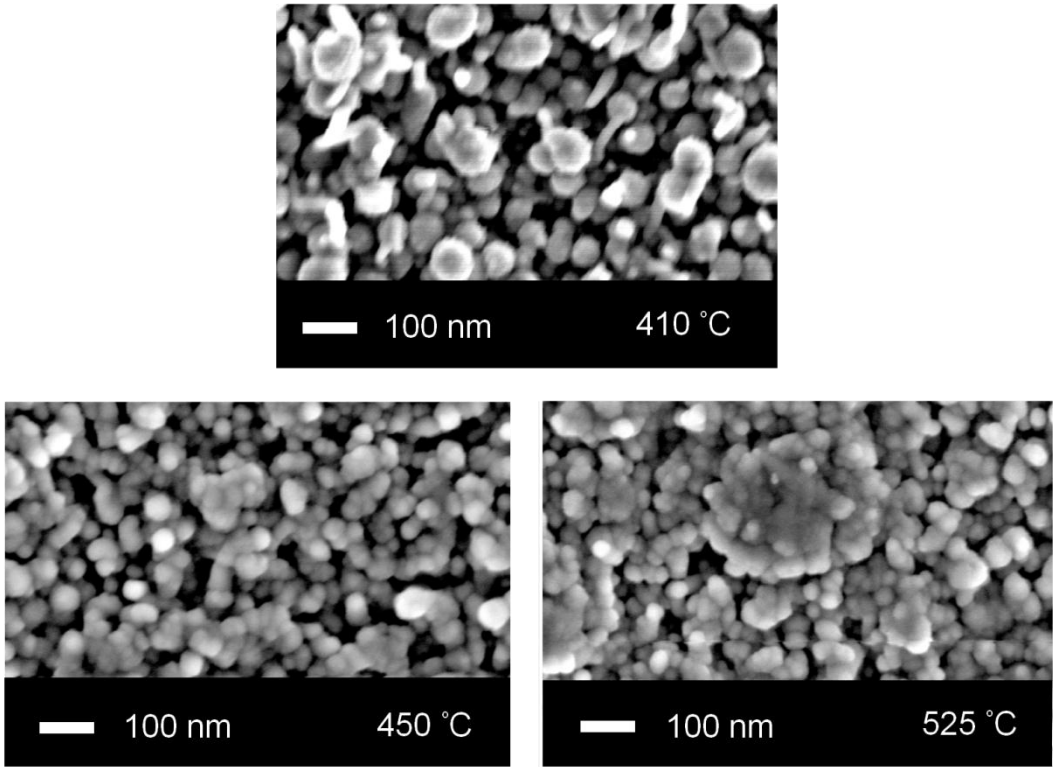

Figure 63: Top-down SEM images of Bi_2O_3 films on glass grown *via* AACVD.

The morphology in all three cases appears to be globular, containing spherical bismuth oxide particles that are approximately 80 nm in diameter. At 410 °C, the coverage is good, but not particularly even, and there are noticeable voids between particles where no deposition has taken place. Upon increasing the temperature to 450 °C, there are fewer voids and some particles have coalesced together in a random manner. By 525 °C, many of the (approx. 60 nm) particles have coalesced, resulting in a dense morphology where one can still see the edges of the particles. This amalgamation of particles has most likely led to increased coverage with very few noticeable voids in comparison to the films deposited at lower temperatures. This morphology is quite different to those observed for β-Bi_2O_3 films obtained *via* LPCVD which had non-uniform grains composed of a range of particle shapes and sizes, most notably triangular crystallites described in Chapter 4,[182] although in general, the morphology seen here does appear consistent with morphologies seen for AACVD deposited indium-gallium oxide thin films.[183] Morphologies of films grown *via* AACVD can vary dramatically depending on the solvent and temperatures used.[184]

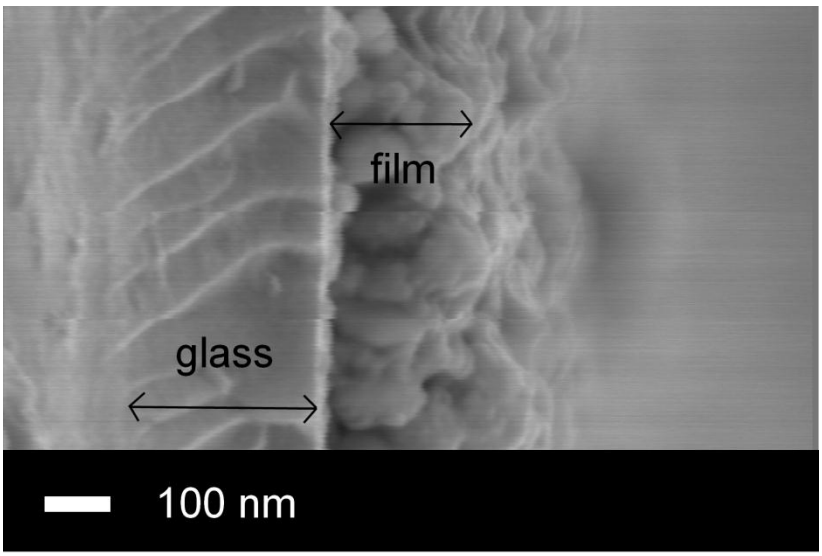

Figure 64: Side-on SEM image of a Bi_2O_3 film on glass grown *via* AACVD at a substrate temperature of 525 °C.

Film thickness was measured *via* side-on SEM imaging (Figure 64), and the film growth rates were *ca*. 75, 280, 530 and 610 nm hr^{-1} at 410, 450, 495 and 525 °C respectively. The activation energy for the reaction was calculated using the Arrhenius equation by plotting the natural logarithm of the growth rate (in nm/s) against 1/T (temperature in Kelvin). In such a case, the gradient of the line is equal to E_a/R, where E_a is the activation energy and R is the molar gas constant.

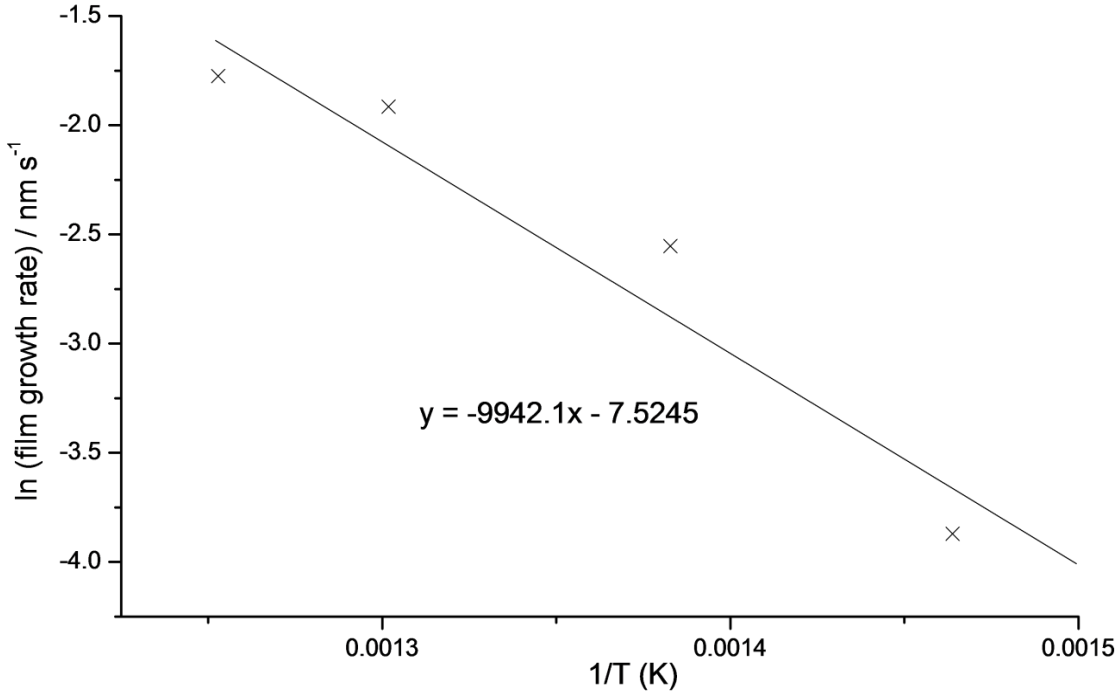

Figure 65: Arrhenius plot for β-Bi_2O_3 films formed *via* AACVD.

From the Arrhenius plot in Figure 65, the growth of β-Bi_2O_3 films formed on glass during this process resulted in a gradient of -9940 nm $s^{-1}K^{-1}$ (4 s.f.) and therefore an apparent activation energy of 82.7 kJ mol^{-1}. This is somewhat higher than the activation energy measured for the deposition of α-Bi_2O_3 films on silicon substrates using $[Bi(thd)_3]_2$ as a precursor (62.8 kJ mol^{-1}) using direct-liquid-injection CVD,[74] however this is not unexpected due to differences in precursor concentration and mass transport in the two systems.

5.3.3 UV-Vis spectroscopy

The band-gaps and optical properties of the as-deposited, yellow β-Bi_2O_3 films were measured using UV-Vis spectroscopy which was recorded in transmission mode. A spectrum of the borosilicate glass substrate was recorded and then subtracted from the spectra of the combined film and glass. The band-gaps of the films were calculated using Tauc plots,[172] and a typical transmission spectrum of a Bi_2O_3 film on glass together with the corresponding Tauc plot is shown in Figure 66.

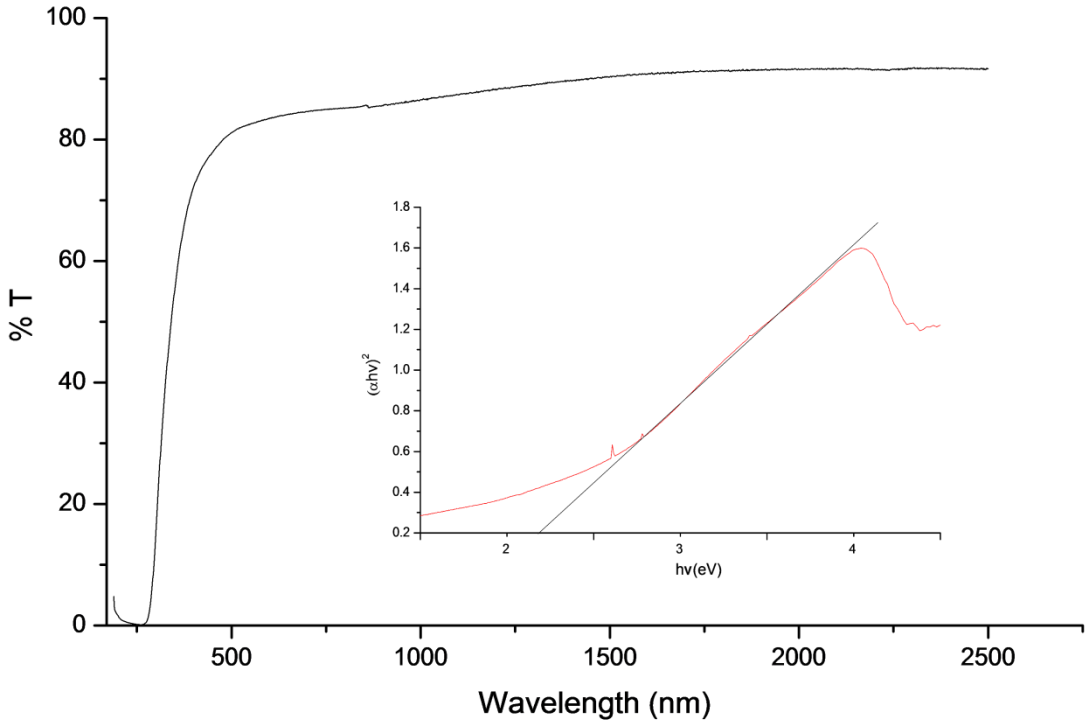

Figure 66: Transmission spectrum and Tauc plot for a β-Bi_2O_3 film deposited on glass at 495 °C.

Films were over 80% transmitting in the 500 – 2500 nm wavelength range for all samples, which is perhaps not surprising given the light yellow colour of the films deposited on glass. The cut-off from the borosilicate glass substrate comes into effect below 380 nm, and therefore

transmission values between 175 – 380 nm may be ignored. The absence of any interference fringes in the spectrum did not allow estimation of film thickness *via* the Swanepoel method.[173] The spectrum of a blank glass substrate was recorded and subtracted from the spectrum of the film + glass. Direct band-gaps were calculated for all samples between 2.3 – 2.5 eV using Tauc plots which are in good agreement with those found in the literature[174] for β-Bi_2O_3 films. As described earlier in Chapter 4, the band-gaps obtained for Bi_2O_3 films are strongly dependent on the phase present, and these results are in agreement with band-gaps found for β-Bi_2O_3 films grown *via* LPCVD of [$Bi(O^tBu)_3$] which possessed values in the 2.3 – 2.6 eV range.

5.4 Growth of platinum films

Using the same AACVD apparatus described for the deposition of Bi_2O_3 films described above, platinum(0) films were grown *via* AACVD of $H_2PtCl_6.6H_2O$ in methanol solvent on borosilicate glass substrates. The nitrogen carrier gas flow rate was varied between 0.2 – 0.6 l/min, however optimum coverage was again obtained at a flow rate of 0.3 l/min. The optimum temperature for deposition of platinum(0) films was found to be 410 °C during a screen of a variety of substrate temperatures. The quality of films deposited above a substrate temperature of 410 °C were very poor and no films were obtained below 350 °C. The reported TGA analysis of the $H_2PtCl_6.6H_2O$ precursor suggested that its decomposition pathway is complex,[185] however the authors suggested formation of $PtCl_2$ between 350 – 410 °C with metallic platinum being formed only above 510 °C. The platinum films deposited were adherent to the substrate, however they could be removed with mild abrasion. WDX analysis revealed chlorine contamination within the films to be negligible (less than 1 at.%).

5.4.1 X-ray diffraction

An X-ray diffraction pattern of a platinum film deposited at 410 °C on glass is shown in Figure 67 and consists of only two, fairly broad peaks, assigned to platinum metal (JCPDS Card No. 004-0802); the low signal to noise ratio and high background between 20 – 30° 2θ is due to the glass substrate.

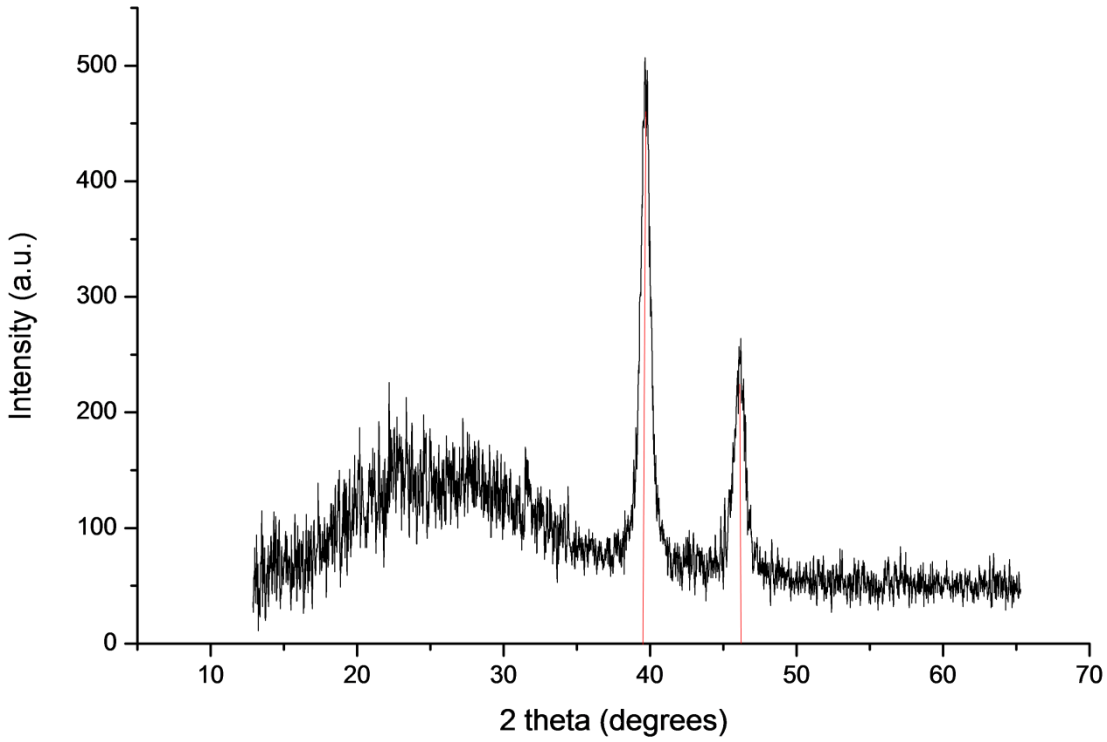

Figure 67: XRD pattern of the Pt film grown on glass *via* AACVD at a substrate temperature of 410 °C.

5.4.2 Scanning electron microscopy

The morphology of the platinum film deposited at 410 °C was investigated *via* SEM imaging (Figure 68). The image reveals a morphology consisting of particles approximately 200 – 400 nm in diameter alongside smaller features roughly 100 nm diameter. Coverage of the substrate appears to be excellent and there are no voids visible where deposition has not taken place, however, there does appear to be a large distribution of particle sizes which could be due to agglomeration.

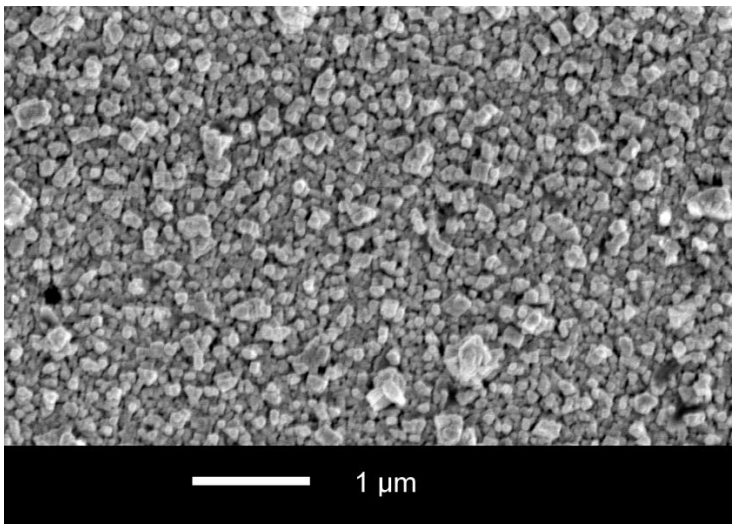

Figure 68: Top-down SEM image of the Pt film grown on glass *via* AACVD at 410 °C.

5.4.3 Transmission electron microscopy

To prepare samples for TEM analysis depositions were performed on KBr substrates that were produced using a 15 tonne press. XRD, SEM and WDX analysis were consistent with results obtained during deposition on glass. Following deposition, the disc was dissolved in distilled water to remove KBr, leaving the platinum behind for imaging. The TEM image (Figure 69) shows individual, well-defined platinum particles of approximately 4-10 nm in size whilst estimation of the particle size from XRD data (Scherrer equation) gave a value of ~ 10 nm. The results obtained from TEM imaging suggest that the variation in particle size observed in the SEM image (Figure 68) is a function of agglomeration.

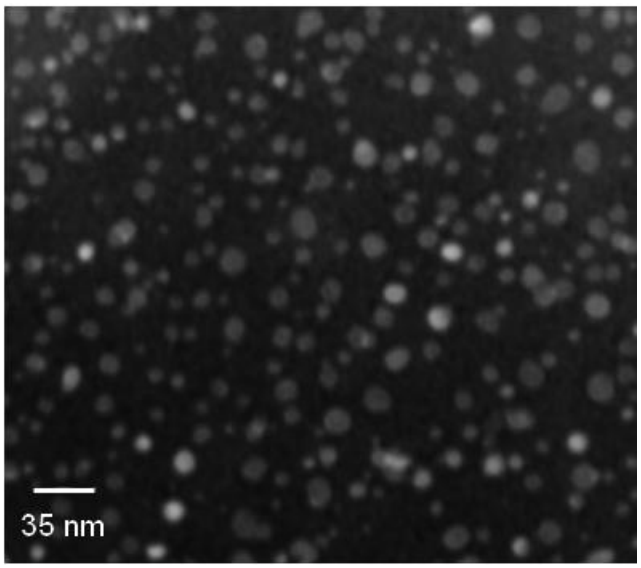

Figure 69: TEM image of platinum nanoparticles deposited at 410 °C on a KBr substrate.

5.5 Co-deposited Platinum and Bismuth Oxide

Platinum-incorporated bismuth oxide films were grown *via* a 'one-pot' method through combining the bismuth oxide precursor $[Bi(dbm)_3]_2$ dissolved in toluene, with the platinum precursor ($H_2PtCl_6.6H_2O$) dissolved in methanol. No reaction between the precursors was observed when they were added together shortly prior to deposition. Depositions were carried out onto borosilicate glass substrates at a variety of substrate temperatures, using a nitrogen carrier gas flow rate of 0.3 l/min. The CVD growth conditions for Pt-Bi_2O_3 films grown on glass substrates are shown in Table 7. Also shown is the platinum atomic percentage (at.%) in the initial precursor solution relative to bismuth only (where a solution of 10 mg $H_2PtCl_6.6H_2O$ and 200 mg $[Bi(dbm)_3]_2$ was used), as well as the Pt at.% in the film relative to Bi, the average film thickness measured *via* side-on SEM and the major band-gap measured *via* Tauc plots using UV-Vis spectroscopy (Figure 72).

Table 7: CVD growth conditions for co-deposition of $H_2PtCl_6.6H_2O$ (10 mg) with $[Bi(dbm)_3]_2$ (200 mg) on glass substrates.

Substrate Temp / °C	at. % Pt relative to Bi only, in precursor solution	at. % Pt relative to Bi only, in film	Average film thickness / nm	Band-gap / eV
410	7.4	1.14	110	2.2
450	7.4	0.76	250	2.1
495	7.4	0.62	440	2.1
525	7.4	0.51	720	2.4

The films were analysed by WDX in order to determine their composition, however breakthrough to the underlying substrate meant quantification of oxygen was not possible. Co-deposition of $[Bi(dbm)_3]_2$ and $H_2PtCl_6.6H_2O$ on glass substrates resulted in Pt-Bi_2O_3 films containing large amounts of chlorine contamination in a slightly substoichiometric ratio of 0.9:1 ratio of chlorine:bismuth. The platinum content present in the films was determined and it was found that the atomic percentage of platinum present in the films decreases with increasing substrate temperature, however this may be attributed to the increased atom efficiency of bismuth deposition at higher temperatures; the film thickness increases approximately seven-fold between 410 and 525 °C but the at. % of Pt decreases by only half, which indicates that the efficiency of platinum deposition must also increase with increasing temperature, but at a slower rate than the increase in bismuth incorporation.

5.5.1 X-ray diffraction

The presence of chlorine was attributed to the formation of a majority BiOCl phase, which was supported by X-ray diffraction analysis (Figure 70) which showed the presence of both BiOCl (JCPDS Card No. 01-085-0861) and minor peaks attributable to γ-Bi_2O_3 (JCPDS Card No. 01-074-1375). The source of this contamination can only be from $H_2PtCl_6.6H_2O$, and given that HCl is one of the suggested products of the decomposition of H_2PtCl_6,[185] the formation of BiOCl can be formulated as shown in Equation 18:

$$Bi_2O_3 + 2\,HCl \longrightarrow 2\,BiOCl + H_2O$$

Equation 18: Formation of BiOCl from Bi_2O_3 and $H_2PtCl_6.6H_2O$.

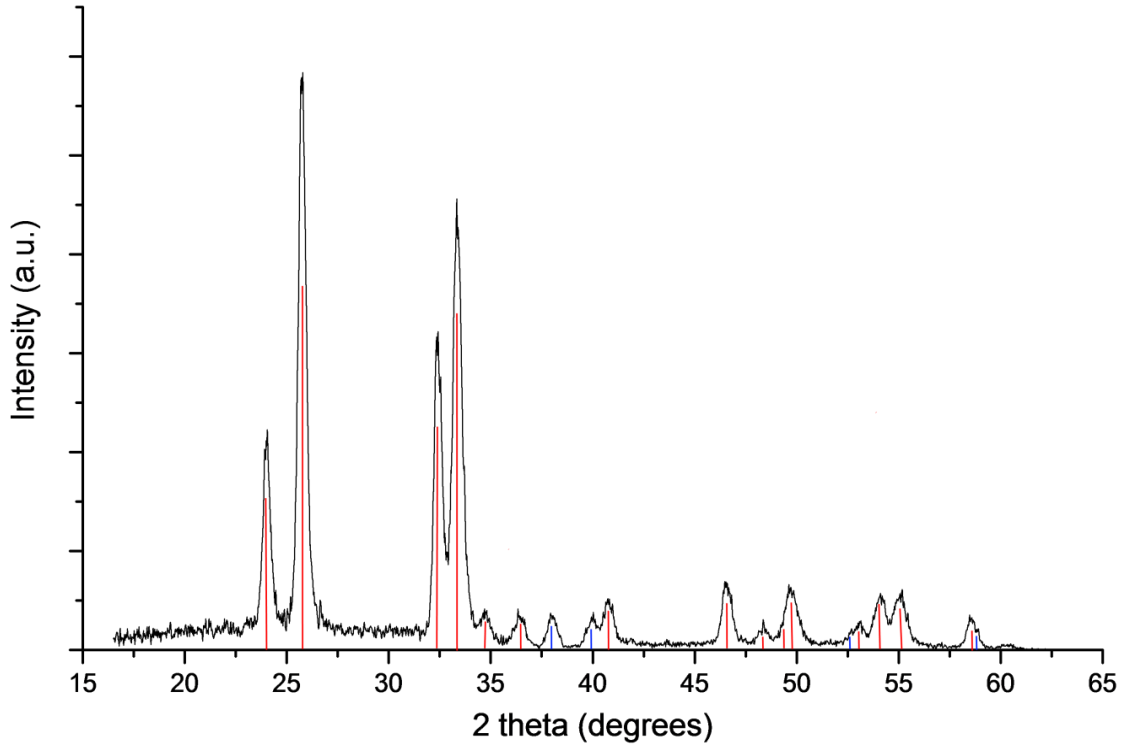

Figure 70: XRD pattern of a Pt-Bi_2O_3 film grown on glass. Blue lines indicate presence of BiOCl and red lines indicate presence of γ-Bi_2O_3.

The amount of contamination was surprising, particularly given the low amount of chlorine contamination found during Pt-only depositions (less than 1 at.%). It is possible that a reaction between $H_2PtCl_6.6H_2O$ and $[Bi(dbm)_3]_2$ in solution would result in a $[Cl_xBi(dbm)_{3-x}]$ compound which may be the source of the contamination, however as mentioned earlier, no obvious reaction between the precursors was observed , and ^1H NMR spectroscopy of the residue

remaining in the flask did not reveal that a reaction had taken place. Film growth rates were *ca.* 110, 250, 440 and 720 nm hr^{-1} at 410, 450, 495 and 525 °C respectively and increased exponentially with increasing temperature, with an apparent activation energy of 72.1 kJ mol^{-1}. This value is lower by approximately 10 kJ mol^{-1} in comparison to the Bi_2O_3 films formed by AACVD of $[Bi(dbm)_3]_2$ without the use of the platinum source described earlier, however the differing values are perhaps not surprising in light of the formation of the impurity phase BiOCl as opposed to Bi_2O_3.

5.5.2 Scanning electron microscopy

The top-down SEM micrographs of the Pt-Bi_2O_3 films deposited on glass substrates are shown in Figure 71. The films displayed a variety of morphologies upon increasing the substrate temperature, most notably at 410 °C where the morphology was composed of randomly oriented needle-like particles of approximately 100 nm thickness but with excellent coverage. Upon increasing the temperature to 450 °C, the morphology is composed of three-dimensional, 60 nm thick plate-like structures of approximately 1 μm length that appear to be interconnected and growing in random orientations. At 495 °C, there is a mixture of these plates along with very small spherical crystallites (approx 50 nm diameter) that are randomly situated over the plates. At 525 °C, the morphology is very dense without the appearance of any needles or interconnecting plates; instead the morphology is composed completely of plate-like structures that are either composed of or have small globular crystallites growing on their surfaces. These morphologies are in contrast to those obtained without the use of hexachloroplatinic acid (described earlier) which were solely globular in appearance, and this difference is attributed to the significant amount of BiOCl found in these samples.

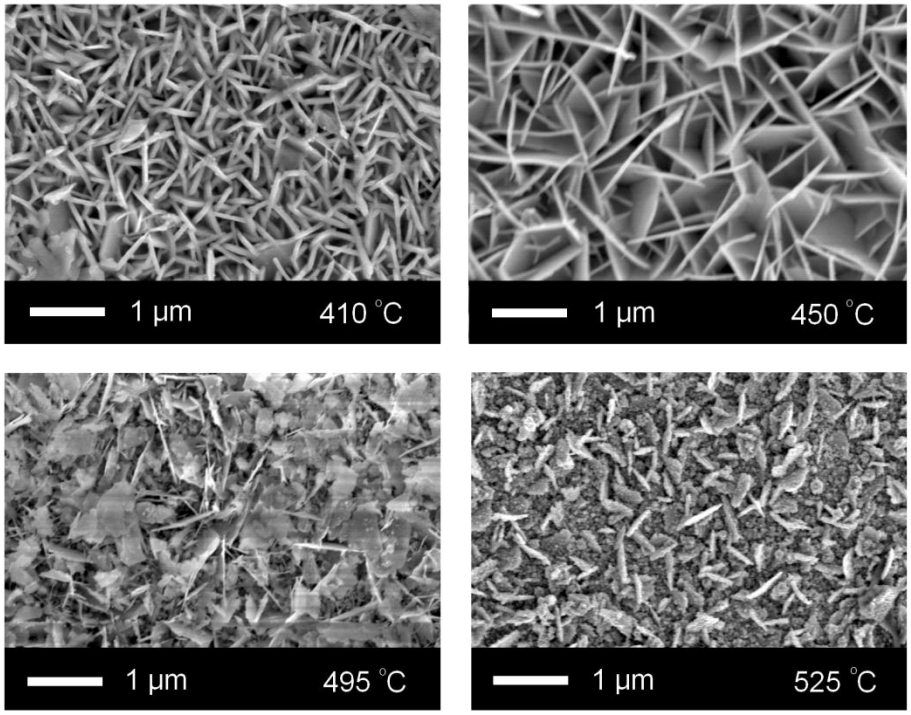

Figure 71: Top-down SEM images of the Bi_2O_3 films deposited on glass containing large amounts of impurity BiOCl.

5.5.3 UV-Vis spectroscopy

The band-gaps of the Pt-Bi_2O_3 films deposited on glass substrates were measured using UV-Vis spectroscopy in transmission mode. A transmission spectrum of a Pt-Bi_2O_3 film is shown in the insert of Figure 72, with no noticeable plasmon peaks for platinum observed, which is not surprising given that platinum nanoparticles are not known to exhibit surface plasmon resonance in the visible region. Although Tauc plots of the UV-Vis data resulted in band-gaps of around 2.2 eV, as expected for β-Bi_2O_3, a second edge was also apparent at higher energies (~ 325 nm). The use of UV-absorbing glass substrates meant it was difficult to assign this edge with confidence, although notionally a value of around 3.6 eV was determined, close to the value expected for BiOCl.[186]

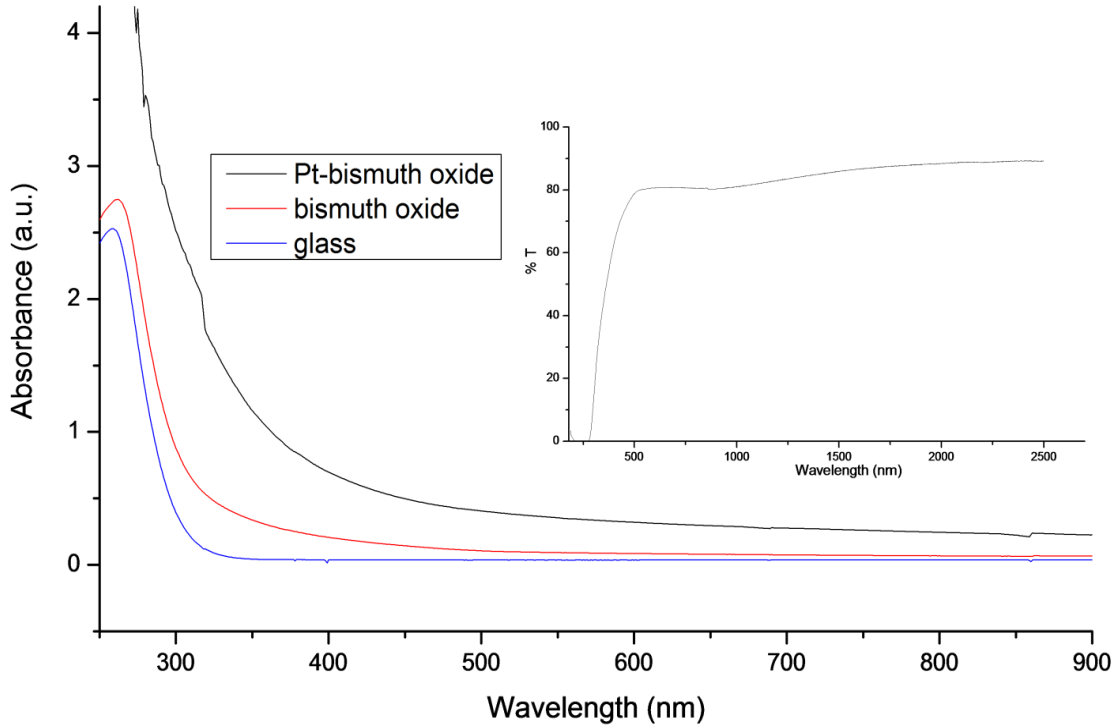

Figure 72: Absorbance spectrum of Pt-Bi_2O_3 and Bi_2O_3 films on glass; the absorbance spectrum of the glass substrate is included for comparison. The insert shows the transmission spectrum of the Pt-Bi_2O_3 film grown on glass.

5.6 Co-deposition of Pt-Bi_2O_3 films on stainless steel substrates

Pt-Bi_2O_3 films were obtained from co-deposition of $[Bi(dbm)_3]_2$ and $H_2PtCl_6.6H_2O$ on stainless steel substrates (316 grade) at 450 °C. Somewhat surprisingly, no impurity BiOCl phase was observed *via* X-ray diffraction (Figure 73), nor was there any noticeable chlorine contamination observed *via* WDX analysis. The cause of this variability is not immediately obvious, particularly given that results for deposition of Bi_2O_3-only thin films were nearly identical irrespective of the substrate used. In fact, WDX analysis showed that the films were slightly oxygen deficient (relative stoichiometry $Bi_2O_{2.8}$) which is similar to β-Bi_2O_3 films found in the literature[182,63] and they contained an average of 0.36 at.% Pt in $Bi_2O_{2.8}$ (0.89 at.% as a fraction of bismuth only), which was slightly higher than the result obtained on glass substrates (0.76 at.% as a fraction of bismuth) at 450 °C.

5.6.1 X-ray diffraction

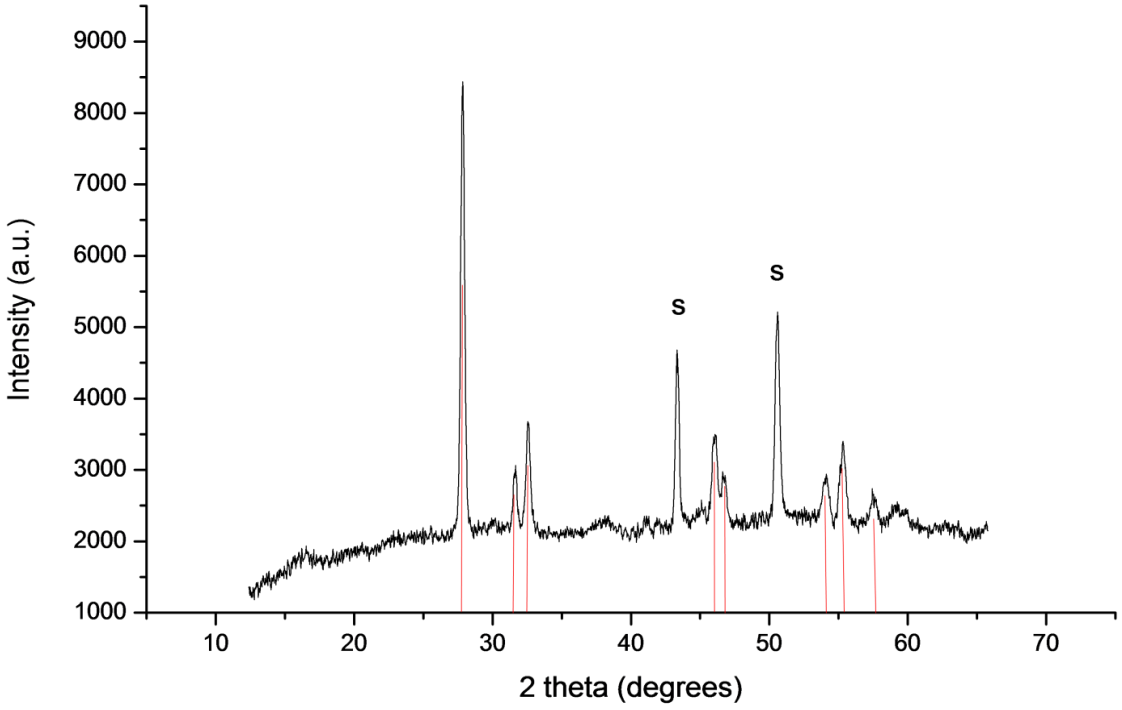

Figure 73: X-ray diffraction pattern of Pt-Bi_2O_3 film deposited at 450 °C on a stainless steel substrate. The red coloured stick pattern refers to β-Bi_2O_3 peaks whereas peaks marked 'S' correspond to the stainless steel substrate.

X-ray diffraction (Figure 73) of the films deposited on stainless steel revealed the presence of β-Bi_2O_3 as the dominant crystalline phase. Unit cell parameters were consistent with the values obtained for deposition of Bi_2O_3-only and are in agreement with literature values {$\alpha = \beta =$ 7.77(2) Å, γ = 5.65(2) Å, JCPDS Card No. 027-0050}.[8] The high, rising background observed in the pattern is due to fluorescence of the iron atoms present in the stainless steel. Substrate peaks were clearly identified in the X-ray patterns, with no secondary phases of bismuth oxide and no peaks corresponding to platinum(0) or BiOCl observed. The lack of peaks for platinum is perhaps not surprising given the relatively low amount of platinum present in these Pt-Bi_2O_3 samples (0.36 at.% based on $Bi_2O_{2.8}$).

5.6.2 Microscopy

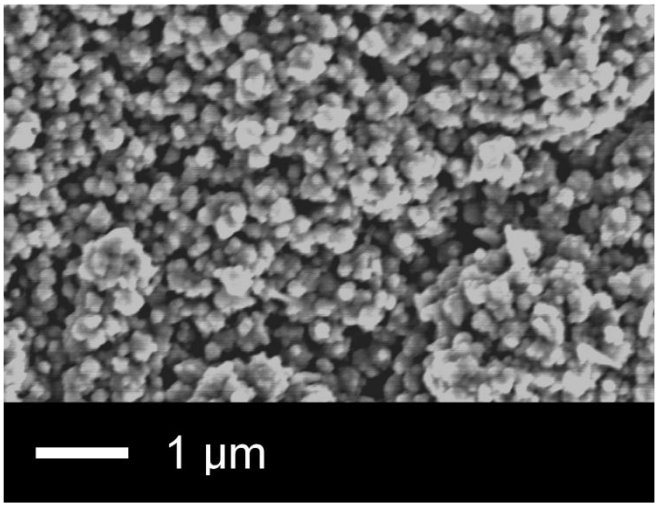

Figure 74: Top-down SEM image of a Pt-Bi_2O_3 film grown on a stainless steel substrate at 450 °C.

The top-down SEM image of the Pt-Bi_2O_3 film grown on stainless steel at 450 °C (Figure 74) shows a morphology very similar to that obtained from deposition of Bi_2O_3 only on glass, composed of globular particles of approximately 80 nm in diameter, and is in contrast to 'BiOCl' films grown on glass substrates which possessed needle-like morphologies. Again, there are very few areas where deposition has not taken place and the coverage throughout the film is complete. There is some agglomeration of particles which is consistent with what was observed in Figure 63, described earlier. Further evidence of the incorporation of platinum nanoparticles into a Bi_2O_3 film was confirmed *via* TEM. TEM images (Figure 75) of Pt-Bi_2O_3 samples deposited on KBr substrates showed individual, disperse nanoparticles, with an average diameter of 5 nm or less. These appeared to be visible on the surface of much larger crystallites, however it is not known whether the larger crystallites formed on KBr are composed of Bi_2O_3 or BiOCl. These nanoparticle features were not observed in TEM images of Bi_2O_3-only samples grown without the use of the platinum precursor, hence we conclude they are Pt nanoparticles.

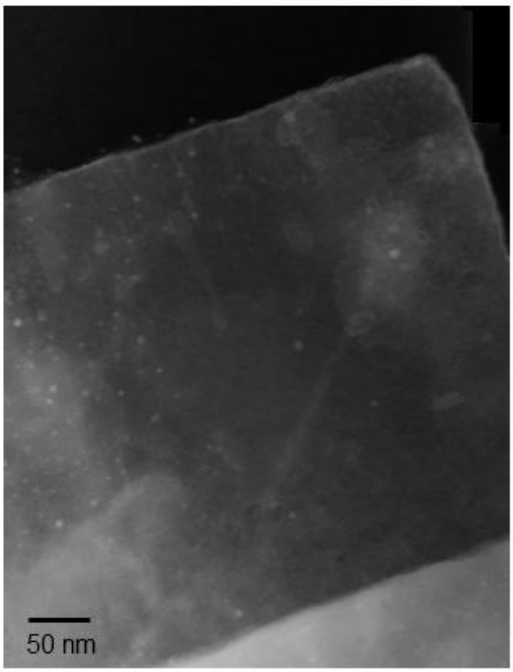

Figure 75: TEM image of platinum nanoparticles on the surface of a bismuth oxide crystallite.

5.6.3 X-ray photoelectron spectroscopy

The composition of a Pt-Bi_2O_3 film deposited at 450 °C on stainless steel was studied using X-ray photoelectron spectroscopy. From the surface scan the bismuth $4f_{7/2}$ ionisation was observed at 159.4 eV, the bismuth $4f_{5/2}$ ionisation at 164.7 eV and the O1s ionisation at 530.1 eV (Figure 76) all of which are characteristic of Bi_2O_3.[170] The ratios of the areas of these peaks were obtained by dividing the peak area by the corresponding relative sensitivity factors (9.14 for bismuth, 0.78 for oxygen) and revealed slightly sub-stoichiometric $Bi_2O_{2.7}$, which is consistent with WDX analysis and is commonly found in β-Bi_2O_3 due to oxygen vacancies in the lattice.[63] This is also in agreement with oxygen deficient β-Bi_2O_3 films formed *via* LPCVD using [$Bi(O^tBu)_3$] as the bismuth source (Chapter 4).

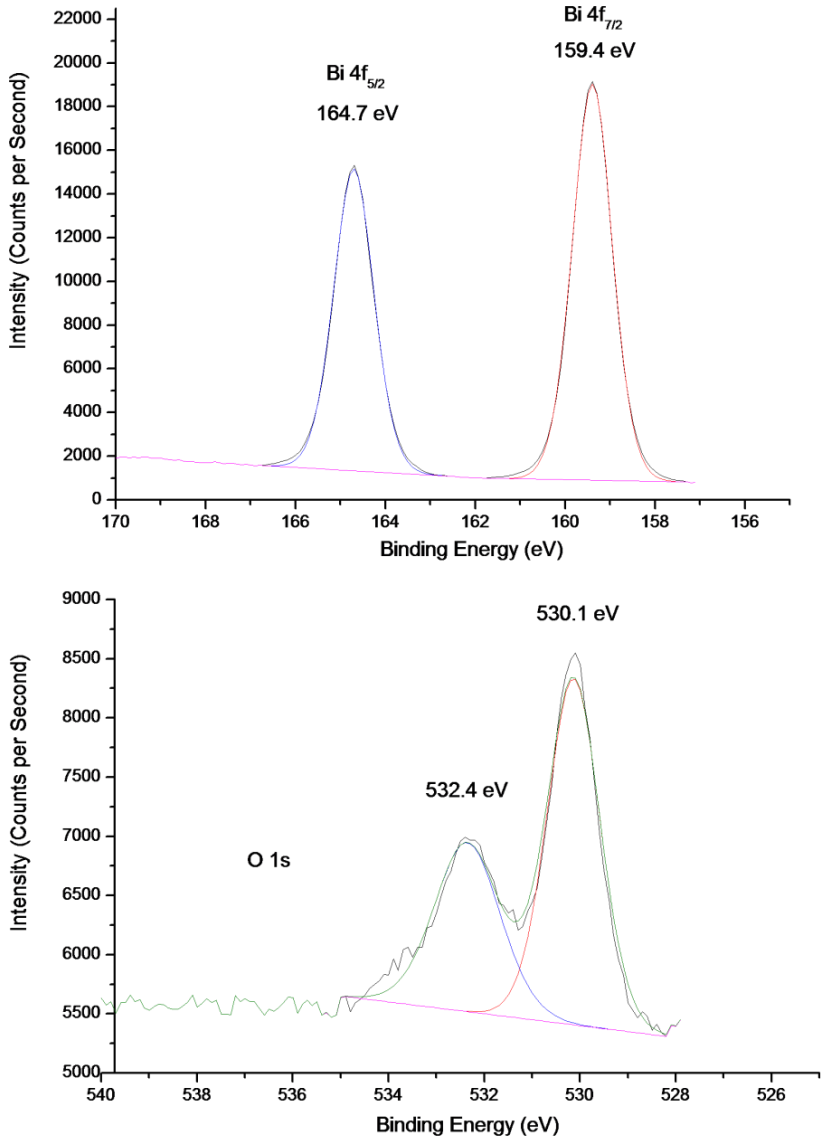

Figure 76: XPS spectra of the bismuth 4f and oxygen 1s regions from the surface scan.

From the XPS spectra of the platinum 4f region (Figure 77), two distinct platinum peaks were observed at 72 eV (Pt $4f_{7/2}$) and 75.3 eV (Pt $4f_{5/2}$) which are characteristic of platinum(0)[187] and rules out formation of $PtCl_2$ or PtO_x.[188] This ionisation is not ascribed to $Pt(OH)_2$ as the Pt $4f_{7/2}$ ionisation would be expected at a significantly higher energy (72.4 eV)[187] and the X-ray diffraction pattern of a Pt-only film deposited at 410 °C (Figure 67) showed the formation of platinum metal. Therefore it is concluded that the platinum present in the Pt-Bi_2O_3 films is as platinum metal.

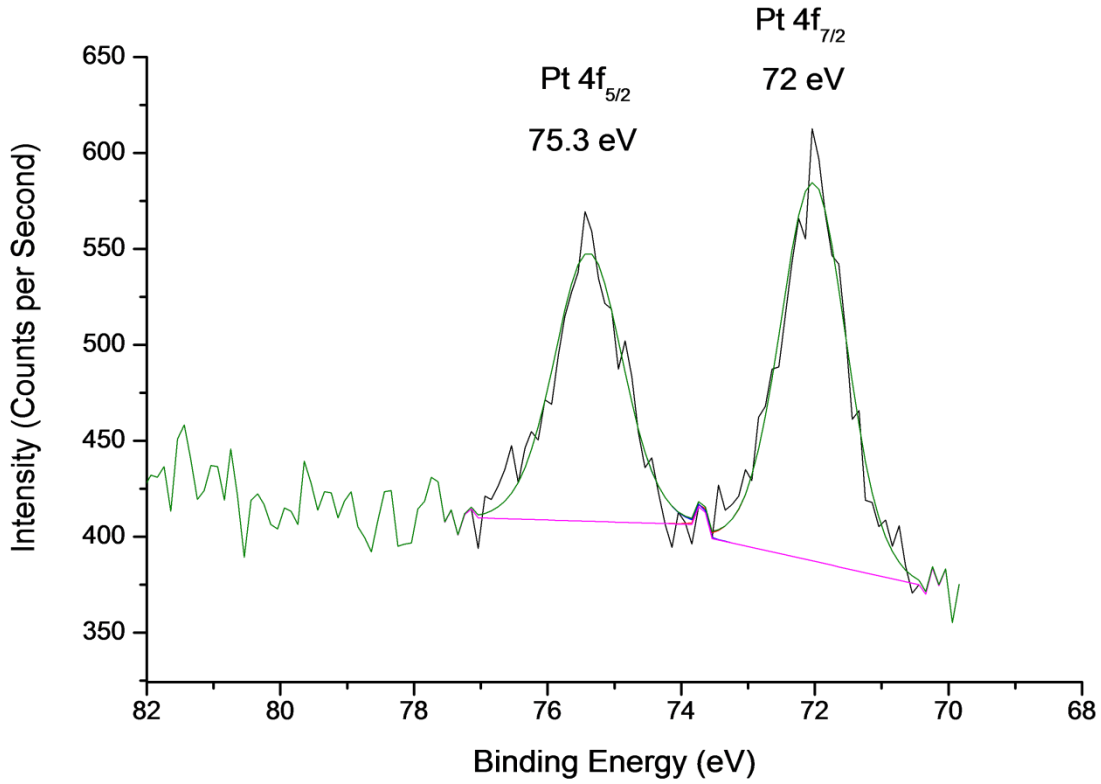

Figure 77: XPS spectrum of the platinum 4f region from the surface scan.

Carbon contamination was significant on the surface (~ 25 at.%) but decreased upon etching (~ 15 at.% after ~ 10 nm), however due to preferential sputtering the quantification becomes unreliable and extensive etching was not performed.

5.6.4 Atomic force microscopy

AFM measurements were carried out on a Pt-Bi_2O_3 sample deposited on a stainless steel substrate at 450 °C (Figure 78). The globular morphology is very distinct albeit with some regions possessing very high features and some areas where deposition is fairly minimal. Unsurprisingly, the morphology is very similar to that observed in the SEM image for the same sample deposited at 450 °C (Figure 74), and coverage is total with no voids visible where deposition has not occurred. The field size image is slightly distorted in one particular area due to the presence of some very high features, where particles have grown on top of each other during the deposition process. AFM gave a value for the root mean squared roughness (rms) at 97 nm. This value is similar to reported rms values of indium-gallium oxide films formed *via* AACVD[183] (94 nm – 1 µm) but much higher than films of β-Bi_2O_3 (rms = 4.1 nm) deposited *via* low-pressure CVD described in Chapter 4.[182] The relatively high surface area obtained *via*

AACVD is expected to be advantageous for catalytic purposes by giving a high contact area with the surrounding medium.

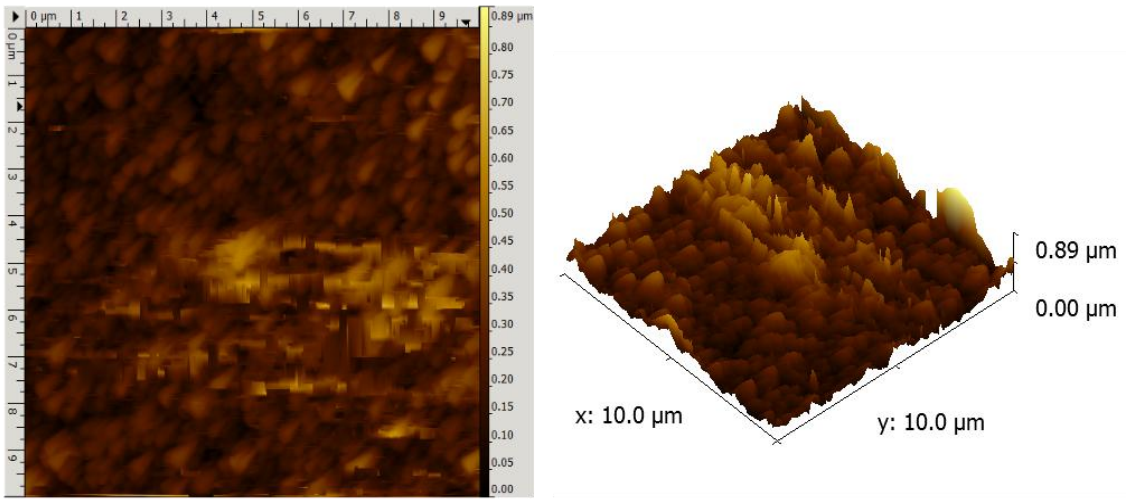

Figure 78: A 10 µm field size (left) and the corresponding 3D (right) AFM image of the Pt-Bi_2O_3 film deposited on a stainless steel substrate at a substrate temperature of 450 °C.

5.6.5 Water photolysis in 1:1 0.1 M HCl : ethanol solutions

The UV-Vis results indicated that the Pt-Bi_2O_3 films possessed band-gaps in the visible region of the electromagnetic spectrum, and that the incorporation of platinum into bismuth oxide appeared to increase the photon absorption in the visible range compared to the undoped sample, although whether this is due to increased haze or thicker films is not known. The high photocatalytic activity of bismuth oxide films for the photo-oxidation of water was described in Chapter 4; however these films were inactive for hydrogen production from a sacrificial electron donor solution. The addition of platinum would therefore be expected to serve as the catalyst to perform the two electron process of reduction of water into hydrogen.

Hydrogen evolution was measured by illuminating thin film samples suspended in a continuously stirred sacrificial solution (40 ml) with simulated solar irradiation (75 W Xenon light source, Photon Technology International, West Sussex, UK).[189,190] The solution, which was contained within a silica vessel surrounded by an outer glass water jacket maintained at 20 °C (Figure 79), was composed of a 1:1 mixture of ethanol (that acted as a hole scavenger) and 0.1 M hydrochloric acid. As conducted in previous work,[190] the lowering of the pH of the solution (measured as pH 1 using a pH meter) by adding hydrochloric acid effectively lowers the levels of the conduction and valence bands of the photocatalyst (they become more negative), making the process thermodynamically more favourable than at neutral pH. Each

sample was suspended using fishing wire from a rubber septum which was used to seal the glass vessel to the outside atmosphere. 250 µL samples of gas were extracted from the headspace of the container hourly *via* a gas syringe and analysed for hydrogen content using gas chromatography (Varian CP-3800 GC). The GC was calibrated before each experiment using a 250 µL sample of pure hydrogen (BOC), allowing the areas of the peaks observed in the chromatographs to be automatically calculated for hydrogen content.

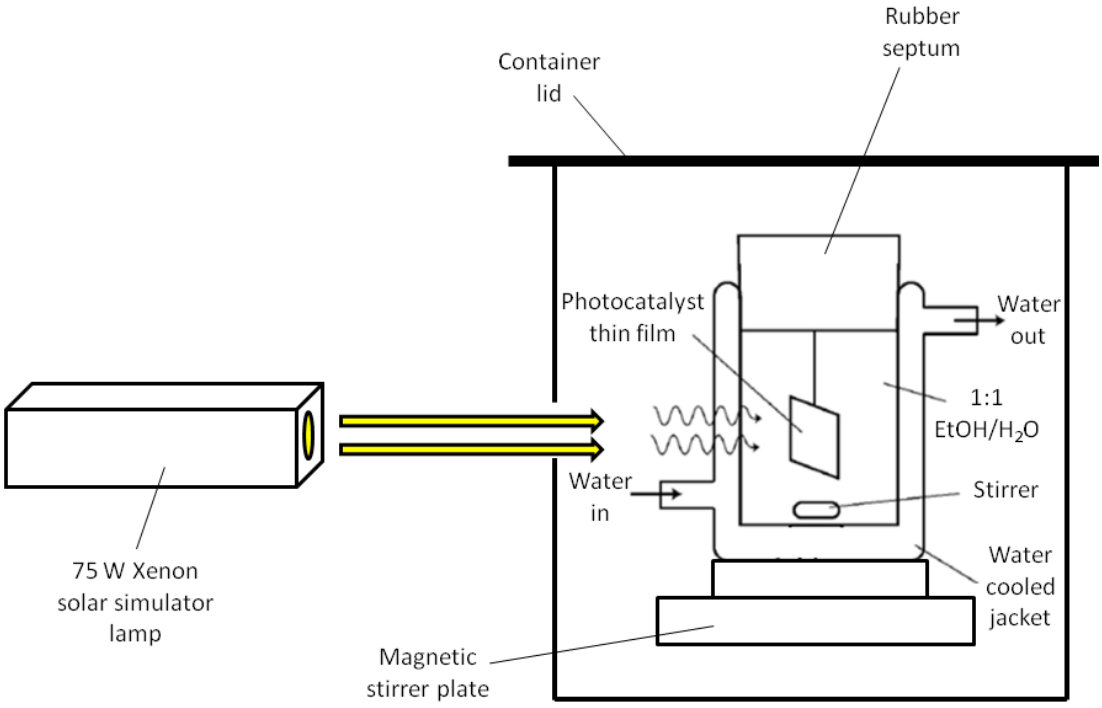

Figure 79: Diagram illustrating the setup used for photocatalytic testing for H_2 production.

The photocatalysis results are shown in Table 8.

Table 8: Results of photocatalytic testing in a 1:1 mixture of ethanol : 0.1 M HCl.

As-deposited Material	Band-gap / eV	Rate of H_2 production / µmol hr^{-1}	Rate of H_2 production / µmol hr^{-1} m^{-2}
β-Bi_2O_3	2.3	0	0
Pt-Bi_2O_3	2.2	2.7×10^{-3}	13.5
TiO_2	3.2	7.4×10^{-3}	37.0

As expected, non-platinised samples on stainless steel substrates produced no hydrogen upon illumination, however Pt-Bi_2O_3 films on stainless steel produced 13.5 µmol H_2 hr^{-1} m^{-2}. For

comparison purposes, in an identical study of APCVD-deposited TiO_2 films that contained no platinum, the rate of hydrogen production was 37 µmol hr^{-1} m^{-2}, and is significant due to the spectral range of the lamp incorporating large amounts of UV-light. The sacrificial solution slowly attacked the bismuth containing films converting the yellow Bi_2O_3 to white BiOCl according to the reaction described earlier in Equation 18 (page 157).

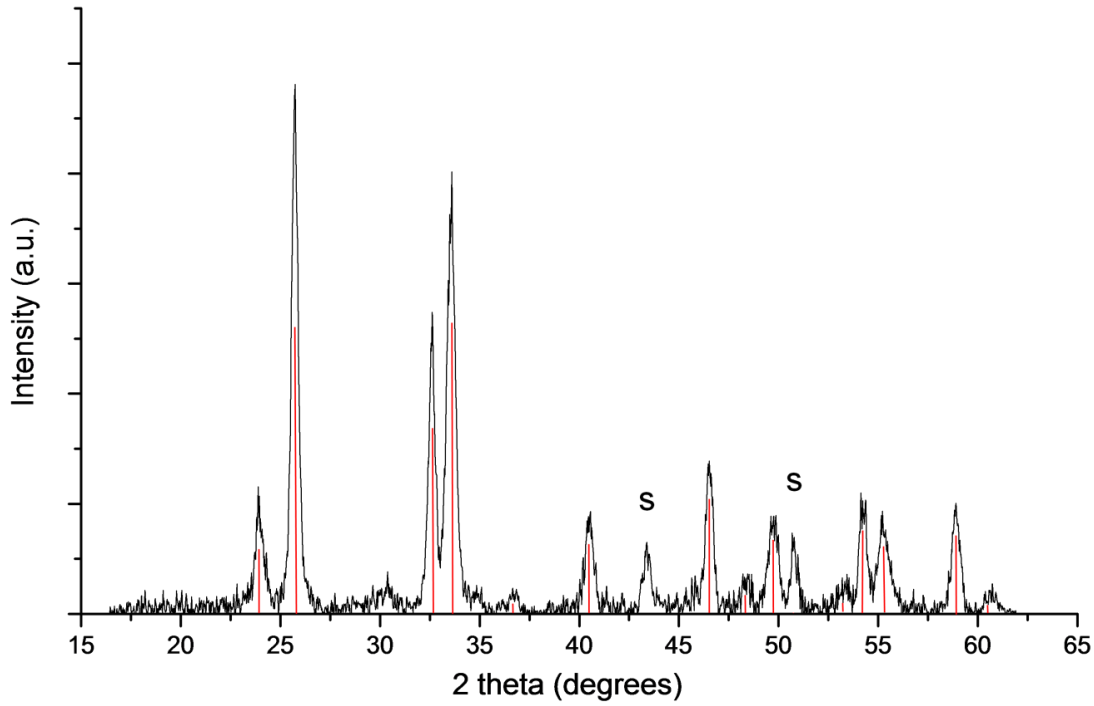

Figure 80: X-ray diffraction pattern of the Pt-Bi_2O_3 on stainless steel after photocatalytic testing. Lines in red correspond to BiOCl phase; peaks marked with 'S' correspond to the stainless steel substrate.

This conversion was confirmed by X-ray diffraction analysis (Figure 80) which showed the presence of solely BiOCl (JCPDS Card No. 073-2060) in samples after photocatalytic testing (only Bi_2O_3 was present before testing). Top-down SEM imaging of the samples after immersion in the 1:1 ethanol/HCl solution revealed a stark change in morphology (Figure 81).

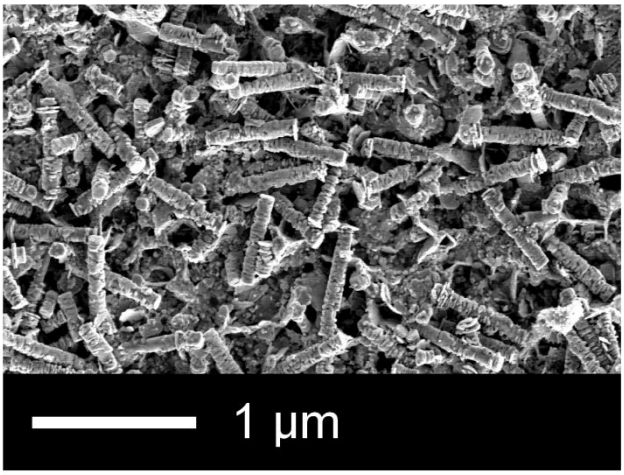

Figure 81: Top-down SEM image of the Pt-Bi_2O_3 deposited on stainless steel after photo illumination in the 1:1 HCl/ethanol solution.

$BiOCl/Bi_2O_3$ has been found to be an active visible light photocatalyst for the oxidation of propan-2-ol and 1,4-terephthalic acid.[186] The mechanism for photo-reduction (hydrogen evolution during water photolysis) for such samples is not obvious, whilst it is thermodynamically favourable for an electron from the valence band in BiOCl to fill a photogenerated hole in the valence band of the Bi_2O_3 (Figure 82), there appears to be no obvious mechanism by which a photogenerated electron in the Bi_2O_3 conduction band could enter the much higher potential conduction band of BiOCl. It should also be noted that this process is driven by visible light irradiation, and that direct excitation of BiOCl cannot occur.

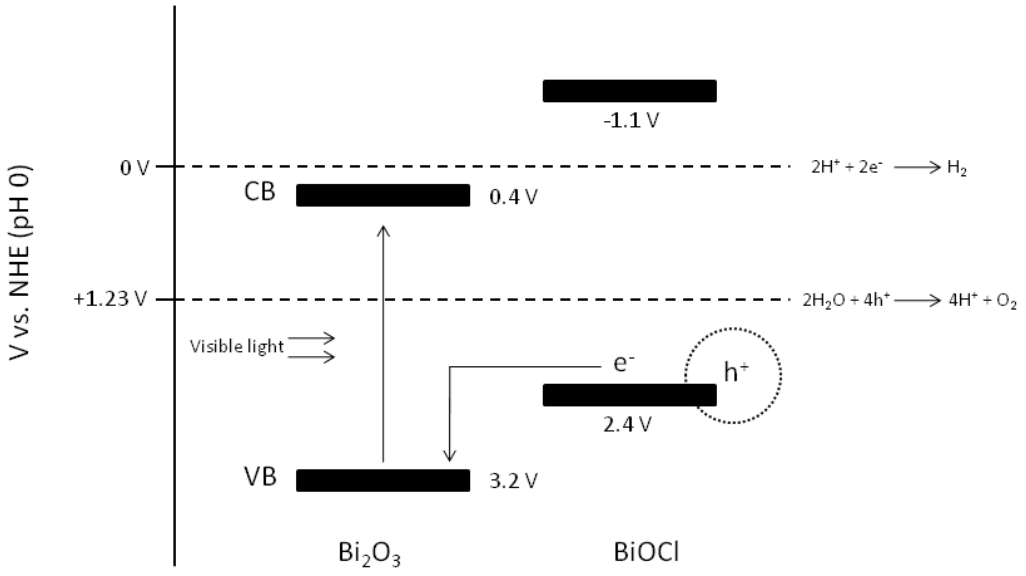

Figure 82: Conduction band potentials of β-Bi_2O_3 and BiOCl, VB = valence band, CB = conduction band.

5.6.6 Water photolysis in 1:1 ethanol:water solution

Given the attack of dilute hydrochloric acid upon bismuth oxide, water photolysis experiments were repeated but instead the sacrificial solution (40 cm^3) was composed of a 1:1 mixture of ethanol (hole scavenger) and distilled water that was stirred continuously. All other parameters such as light source, illumination time and frequency of gas extraction were kept the same. The results are summarised in Table 9.

Table 9: Rates of H_2 evolution on irradiation of samples immersed in 1:1 solution of ethanol and water.

Material	Band-gap / eV	Rate of H_2 production / μmol hr^{-1}	Rate of H_2 production / μmol hr^{-1} m^{-2}
Pt	-	0	0
β-Bi_2O_3	2.3	0	0
Pt-Bi_2O_3	2.2	6.2 x 10^{-4}	3.1
TiO_2	3.2	0	0

As expected non-platinised Bi_2O_3 samples produced no hydrogen upon illumination; it is apparent from Figure 82 that the conduction band of Bi_2O_3 is too low in energy to reduce water to hydrogen at pH 0 and the use of a solution with a near neutral pH is expected to exacerbate this problem. In fact this is the likely reason that no H_2 evolution is observed for the TiO_2 sample, despite the fact that H_2 evolution was observed from the solution containing HCl, with the evolution of H_2 becoming increasing thermodynamically unfavourable with increasing pH. No hydrogen evolution was observed over Pt-only films, however Pt-Bi_2O_3 composite thin films produced an average of 3.1 μmol H_2 hr^{-1} m^{-2}. This represents an apparent quantum efficiency of 0.6% (calculated at 420 nm) and is of the order of those obtained using powdered catalysts CdS-ZnS and Pt-TaON:Pt-WO_3 whose efficiencies were calculated similarly.[152] The comparison of photocatalytic activity of different materials is notoriously difficult due to differences in experimental setup, and although in this case the rate of H_2 evolution is low it should be highlighted these films have not been optimised in terms of film thickness or platinum loading. Instead, the experiment illustrates that the introduction of Pt particles into β-Bi_2O_3 films causes hydrogen to be evolved during photolysis of water over the composite material, a property not found for Pt particles or β-Bi_2O_3 alone.

Previously it has been suggested that β-Bi_2O_3 is unstable to conversion to α-Bi_2O_3 under photo-irradiation,[191] but no visual degradation of any of the Bi_2O_3 or Pt-Bi_2O_3 samples during repeated irradiation in the 1:1 ethanol:water solution was observed. Furthermore, X-ray diffraction

analysis together with SEM imaging of films after photocatalytic testing showed the only phase present was β-Bi_2O_3 with no change in morphology; hence one can conclude that under these conditions β-Bi_2O_3 is photostable.

Neither thin films of platinum nanoparticles or of β-Bi_2O_3 evolved H_2 during water photolysis, therefore the ability of composite Pt-Bi_2O_3 to photo-reduce water is a property not contained by the constituent components. There is currently great interest in plasmon resonance enhancement of semiconductor photocatalytic performance,[192] and recently powdered Pt-Bi_2O_3 has been shown to be a highly active catalyst for photo-oxidation.[19] This has been ascribed to plasmonic enhancement of the photo-reaction, despite the fact that platinum nanoparticles have not previously been reported to have plasmonic properties. Plasmon enhancement causes increased light absorption, i.e. potentially increased quantum efficiency, but would not affect the thermodynamic potential of the Bi_2O_3 conduction band and therefore this effect alone would not be expected to enable photo-reduction of water over Pt-Bi_2O_3. Therefore the mechanism for the evolution of hydrogen must be *via* photon capture in the Bi_2O_3 followed by electron transfer to the Pt particles where they are trapped, this charge accumulates until the Pt particles become reducing.[193]

5.7 Conclusions

The decomposition characteristics of several synthesised homoleptic bismuth(III) *β*-diketonate complexes were investigated *via* DSC-TGA (under a helium atmosphere) in Chapter 3 in order to assess their potential to serve as single-source CVD precursors to bismuth oxide films. The dimeric complex, $[Bi(dbm)_3]_2$, was the only *β*-diketonate complex that decomposed to β-Bi_2O_3 and its mass loss was consistent with the calculated theoretical mass loss required to form stoichiometric Bi_2O_3.

Preliminary AACVD studies revealed that only $[Bi(dbm)_3]_2$ was suitable for deposition of bismuth oxide films; the use of the other synthesised *β*-diketonate complexes $[Bi(acac)_3]_n$, $[Bi(tfac)_3]$ and $[Bi(bzac)_3]$ resulted in no deposition at a variety of substrate temperatures. $[Bi(dbm)_3]_2$, dissolved in toluene, was utilised as a single-source precursor to films of β-Bi_2O_3 on glass substrates at growth temperatures between 410 – 525 °C. Crystalline platinum films were also grown on glass substrates using $H_2PtCl_6.6H_2O$ as the platinum source in methanol solvent. Co-deposited Pt-Bi_2O_3 films were then grown on glass substrates by combining both the precursors in one solution. $[Bi(dbm)_3]_2$ appears to be relatively moisture stable and did not react with the platinum source. Impurity BiOCl phase was incorporated in the films grown on glass due to reaction of Bi_2O_3 with HCl, a by-product of the decomposition of $H_2PtCl_6.6H_2O$. Surprisingly, no BiOCl was observed for films grown on stainless steel substrates.

Hydrogen production from water under visible light (solar) irradiation was observed for the Pt-Bi_2O_3 films grown on stainless steel, however the use of an acidified solution resulted in their degradation to BiOCl. The use of a 1:1 water:ethanol solution resulted in lower hydrogen production, however degradation of the samples was avoided. Hydrogen production was only observed for Pt-Bi_2O_3 composite films and not for the individual Bi_2O_3 or Pt films, and is likely to be due to photon capture by Bi_2O_3 followed by electron transfer to the reducing Pt particles.

CVD OF BISMUTH FERRITE FILMS

6 Low pressure CVD of bismuth ferrite

6.1 Introduction

The introduction chapter highlighted the different precursor combinations that have previously been used to deposit $BiFeO_3$ films *via* a variety of CVD methods. Somewhat surprisingly, the use of the widely commercially available iron precursor [$Fe(acac)_3$] (acac = acetylacetonate) has not been utilised in conjunction with a bismuth source for deposition of $BiFeO_3$ films *via* CVD, despite its relative low cost, good thermal and moisture stability and appreciable volatility. It appears to have been overlooked in the case of $BiFeO_3$ film growth, perhaps due to the fact that $[Bi(acac)_3]_n$ is not volatile and that the use of [$Bi(thd)_3$] as the bismuth source would require the use of [$Fe(thd)_3$] in order to prevent unwanted side reactions in the gas-phase.

This chapter examines the dual-source low pressure CVD (LPCVD) of multiferroic $BiFeO_3$ thin films using [$Bi(O^tBu)_3$] and commercially available [$Fe(acac)_3$] as precursors with air as an oxidising gas. The films were characterised fully and two samples were selected for an investigation into their photocatalytic properties under visible light irradiation.

6.2 Physical Measurements

TGA studies were conducted using a Netzsch 449 C Instrument under a flow of helium gas (50 ccm) with a heating rate of 10 °C min^{-1}. TGA samples were sealed in the glovebox into aluminium pans and pierced with a hole in the lid prior to analysis. X-ray Diffraction was carried out using a Bruker-AXS D8 powder diffractometer equipped with a GADDS Hi-Star area detector, using Cu-K_α radiation (λ = 1.54056 Å) in the range 10 – 65° 2θ. Additionally, X-ray diffraction was carried out using a Bruker-AXS D4 powder diffractometer in reflection geometry using Cu-K_α radiation (λ = 1.54056 Å) on a rotating sample holder in the range 10 – 70° 2θ, 0.05° step size, with 2 s per step. Phase information was obtained from the Diffrac^{plus} EVA program suite (Version 2) and ICSD. SEM images were obtained on a Jeol JSM-6301F Field Emission Microscope at 5 kV, after coating samples with an ultrathin layer of gold to prevent charging. Raman spectra were acquired using a Renishaw Raman 1000 System using a helium-neon laser wavelength of 514.5 nm at room temperature (20 °C) and liquid nitrogen temperature (-195 °C) using a cold stage and temperature controller. AFM analysis was performed using a Veeco Dimension 3100 machine in intermittent contact mode, where a cantilever with an attached tip oscillates at its resonant frequency. This was scanned across the surface of the film several times to determine the morphology and roughness. XPS spectra were

obtained using a Kratos AXIS Ultra machine with a delay line detector under a pressure of 10^{-9} torr. A monochromated Al-K_α X-ray source producing a full width at half maximum (FWHM) on the Ag $3d_{5/2}$ peak of 0.48 eV was used. WDX analysis was performed on a Philips XL30ESEM Machine operating at 10 kV equipped with an Oxford Instruments INCA detector. UV-Vis spectra were recorded in transmission mode over the range 175 – 2500 nm using a Perkin Elmer Lambda 950 photospectrometer. Magnetism measurements (M-H hysteresis and ZFC-FC magnetisation) were conducted at the Royal Institution of Great Britain using a Quantum Design SQUID Vibrating Sample Magnetometer (VSM) with a maximum field setting of 7 Tesla (70000 Oe). Films were mounted on a 4 mm diameter quartz rod using a vinyl phenolic adhesive (code GE7031, stable up to 400 K) and suspended parallel to the magnetic field (in-plane). Ferroelectric measurements (P-E hysteresis) were conducted at the National Physical Laboratory, Teddington, at ambient temperature using a Radiant Technologies (USA) high-voltage ferroelectric characterization system at an applied frequency of 1 kHz.

6.3 Experimental

6.3.1 Dual-source LPCVD

Nitrogen (99.96%) was obtained from BOC and used as supplied. $[Fe(acac)_3]$ (99.9%) was obtained from Sigma-Aldrich Ltd and used as supplied. Bismuth *tert*-butoxide, $[Bi(O^tBu)_3]$, was synthesised according to the literature *via* the metathesis reaction between $BiCl_3$ and three equivalents of NaO^tBu as described in Chapter 2.[67] LPCVD reactions were carried out using an in-house built cold-wall CVD reactor equipped with mass flow controllers (50 sccm max., Brooks Instrument Inc.) and an aluminium block heated using a Whatman Firerod cartridge heater (Figure 83). For each deposition, each precursor was swiftly transferred to the respective bubbler, which was purged with nitrogen before and during its opening. The base pressure was allowed to stabilise to at least 2×10^{-3} mbar before use, to minimise residual air and moisture contamination. The temperatures of the graphite block, mixing chamber, bubbler lines and bubblers were controlled with Pt-Rh thermocouples. The deposition section of the reactor comprised an aluminium block angled at approximately 5° such that the flow of precursor was aimed directly at the substrate thereon. The total reactor pressure was maintained at 7 mmHg (8 mbar) for all depositions *via* the use of a mechanical throttle valve and each deposition was carried out for 1 hour. Films were deposited on borosilicate glass microscope slides (3 cm x 2 cm) and silicon wafers. The silicon wafers were sputtered for 180 seconds with a thin layer of platinum prior to use (for ferroelectric measurements), with deposition directly on to the platinum layer.

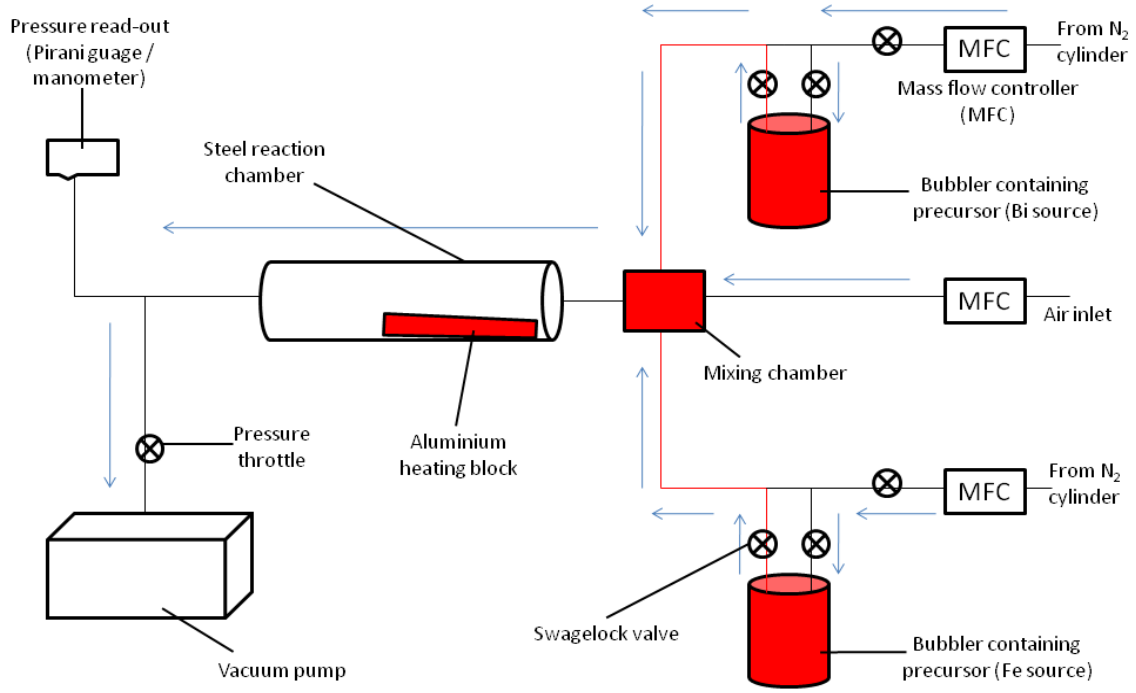

Figure 83: Schematic diagram of the dual-source LPCVD apparatus for deposition of $BiFeO_3$ films. Objects in red indicate those parts that are controllably heated. Arrows indicate the direction of gas flow.

The total system pressure was monitored using a pirani pressure gauge and a mercury manometer connected in series. The manometer enables higher pressures (1 – 100 mmHg) to be easily set and monitored during deposition. Mass flow controllers were used to give accurate flow rates of carrier and reactive gases.

6.3.2 TGA

The decomposition profiles of $[Fe(acac)_3]$ and $[Bi(O^tBu)_3]$ are shown in Figure 84. The decomposition profile of $[Bi(O^tBu)_3]$ has been reported in detail in Chapter 3, and therefore will only be described here in comparison to that of $[Fe(acac)_3]$.

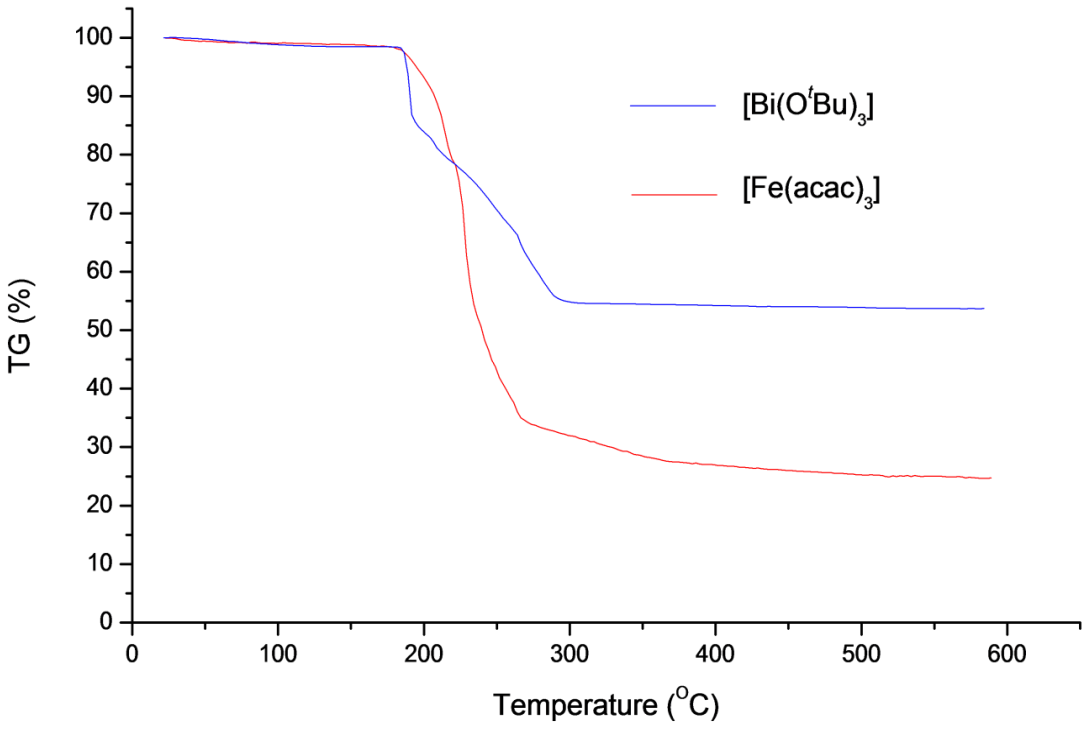

Figure 84: TGA patterns of [Fe(acac)$_3$] and [Bi(O^{t}Bu)$_3$]. The heating rate was 10 °C min^{-1}.

The TGA trace of [Fe(acac)$_3$] reveals a single-step decomposition (Figure 84). The melting temperature was found to be 191 °C from the DSC trace which was run simultaneously (not displayed). The theoretical mass loss required to form Fe_3O_4 would be 78.1%, and the theoretical mass loss required to form Fe_2O_3 would be 77.4%. From the TGA trace, the mass loss of [Fe(acac)$_3$] between 25 °C and 600 °C is in fact 75%. This compares well to the theoretical mass loss required for formation of iron oxide and highlights that [Fe(acac)$_3$] may be a suitable single-source precursor to films of iron oxide, in spite of reports that metal β-diketonates decompose to metallic species in the absence of an oxidising gas.[194,195] The melting temperature of [Bi(O^{t}Bu)$_3$], as described in Chapter 3, was found to be 159 °C, which is somewhat lower than [Fe(acac)$_3$], and its onset of decomposition was observed to be approximately 10 °C lower. The differences in decomposition and melting points between the two precursors suggest that two separate temperature controlled bubblers would be required to vaporise each precursor, as subjecting [Bi(O^{t}Bu)$_3$] to the temperature required for vaporisation of [Fe(acac)$_3$] would almost certainly lead to its premature decomposition.

6.3.3 Vapour pressures

Given that precursor volatility is a fundamental requirement for utilisation in LPCVD, the vapour pressure curves of [Bi(O^{t}Bu)$_3$] and [Fe(acac)$_3$] were plotted using the following vapour pressure equations obtained from the literature (Figure 85).[164,38]

[Bi(O^{t}Bu)$_3$]: $\log_{10}$P (mmHg) = 13.11 – 5010/T(K)

[Fe(acac)$_3$]: $\log_{10}$P (mmHg) = 14.63 – 6510.64/T(K)

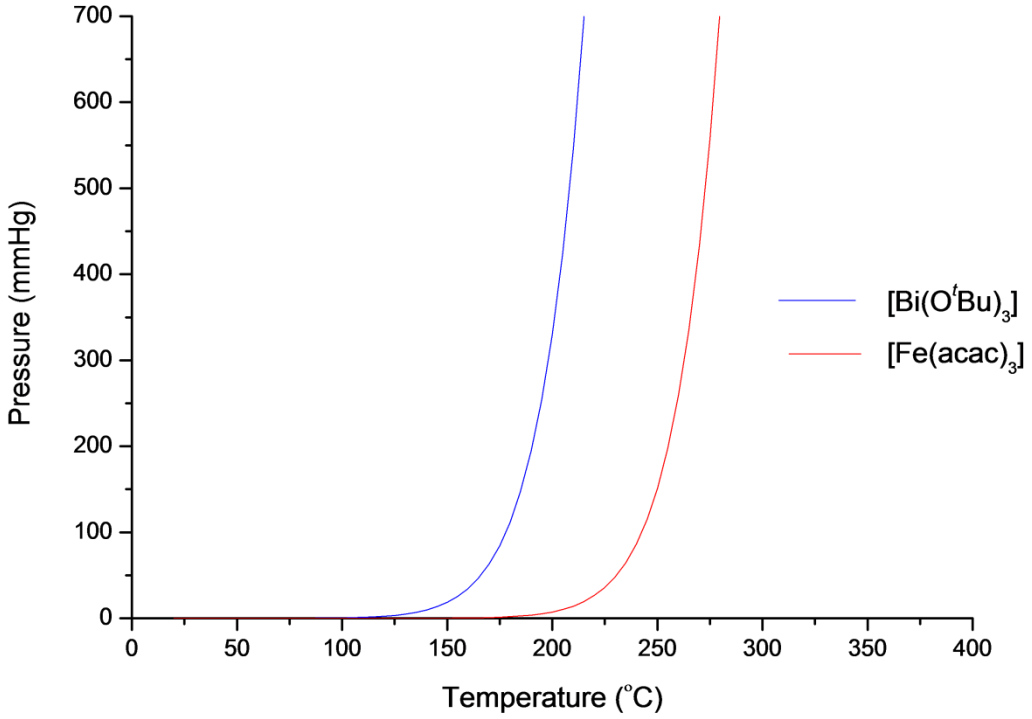

Figure 85: Vapour pressure curves of [Bi(O^{t}Bu)$_3$] and [Fe(acac)$_3$].

The vapour pressure (V_p) curve of [Bi(O^{t}Bu)$_3$] has already been described in Chapter 4. In comparison to [Fe(acac)$_3$], [Bi(O^{t}Bu)$_3$] exhibits a much higher vapour pressure of 0.48 mmHg at 100 °C compared to 1.49 x 10^{-3} mmHg for [Fe(acac)$_3$]. It is not until a temperature of 160 °C is reached that the vapour pressure of [Fe(acac)$_3$] reaches 0.5 mmHg, by which time the vapour pressure of [Bi(O^{t}Bu)$_3$] has increased significantly to 34.6 mmHg. Therefore, due to the fact that [Fe(acac)$_3$] is approximately two orders of magnitude lower in volatility than [Bi(O^{t}Bu)$_3$], a comparatively higher bubbler temperature will be required for evaporation. On examination of the TGA and vapour pressure curves for [Fe(acac)$_3$], and in light of the temperature limits of the bubbler heaters, a bubbler temperature of 160 °C (V_p = 0.39 mmHg) was chosen, whilst for [Bi(O^{t}Bu)$_3$] a temperature of 110 °C (V_p = 1.07 mmHg) was set which is identical to that used for the LPCVD of Bi_2O_3 films described in Chapter 4.

6.4 LPCVD of iron oxide

Initially, [Fe(acac)$_3$] was used as a single-source precursor to deposit thin films of haematite (α-Fe_2O_3) and mixed-phase metallic iron/α-Fe_2O_3 on glass substrates at a variety of substrate temperatures. 100 mg (0.28 mmol) of precursor was loaded into a stainless steel bubbler which was heated to 160 °C, with a carrier gas flow rate of 50 sccm and a total system pressure of 8 mbar. Initially, no oxidising/reactive gas was used. Depositions were carried out for 1 h and the amount of precursor remaining in the bubbler after deposition was negligible (< 10 mg). All films displayed good substrate coverage and were adherent; all films passed the Scotch tape test but did not survive after treatment with steel wool, being scratched. The films did not show any changes in characteristics after prolonged storage in air. The dark red-black films deposited were highly crystalline, however they suffered from high levels of carbon contamination, as revealed from WDX analysis (9-15 at. %). To overcome this, air was used as a reactive gas (50 sccm). The resultant purple-red coloured Fe_2O_3 films were almost free from carbon contamination from the precursor (< 2 at. %) and were highly crystalline. The deposition conditions are summarised in Table 10.

Table 10: Deposition conditions for LPCVD of [Fe(acac)$_3$] with and without the use of air as a reactive gas.

Substrate Temp / °C	Nitrogen carrier gas flow rate / sccm	Air flow rate/ / sccm	Phase(s) obtained *via* XRD	At. % carbon incorporation (from WDX)	Thickness / nm	Band-gap / eV
450	50	0	α-Fe_2O_3	8	260	n/a
475	50	0	α-Fe_2O_3	13	520	n/a
500	50	0	Fe/α-Fe_2O_3	10	650	n/a
550	50	0	α-Fe_2O_3	14	1140	n/a
575	50	0	α-Fe_2O_3	9	330	n/a
450	50	**50**	α-Fe_2O_3/Fe_3O_4	2	350	2.4
475	50	**50**	α-Fe_2O_3	<1	395	2.2
500	50	**50**	α-Fe_2O_3	1.1	640	2.3
550	50	**50**	α-Fe_2O_3	1.6	900	2.1
575	50	**50**	Too thin	<1	120	2.4

No deposition was observed below 450 °C. At 575 °C very little deposition was observed on the substrate and instead, the reactor walls in front of the substrate holder were completely covered, indicating this temperature is high enough to decompose most of the precursor before it reaches the reaction chamber. The decomposition characteristics of $[Fe(acac)_3]$ have been investigated in a number of studies in the literature,[196,197] however a mechanistic pathway for its decomposition is yet to be published. Without the use of an oxidising gas, the CVD reaction of transition metal *β*-diketonates tends to lead to metallic films unless very oxophilic metals are used.[195] The films are also usually heavily contaminated with carbon or oxygen on the surface, which is similar to what was observed here during the CVD reaction of $[Fe(acac)_3]$ without the use of an oxidising gas. Decomposition studies appear to converge on the idea that because the metal-diketonate bond is harder to cleave in comparison to the metal-oxygen bond in metal alkoxides, decomposition of metal *β*-diketonates occurs *via* abstraction, at sufficiently high temperatures, of the complete diketonate ligand to leave metallic species. The process is likely to be more complex given the fact that the ligand is present as an anionic species, $[acac]^-$. Mechanistic studies using mass spectrometry to investigate the decomposition of scandium(III) and aluminium(III) acetylacetonates resulted in the observation of a molecular species $(C_5H_6O)_2$ which was most likely to form as a result of the cyclic dimerisation of two adjacent acetylacetone ligands.[198] Subsequent elimination of ethenone (CH_2CO) from this intermediate led to the formation of the more stable 3,5-dimethylphenol molecule. It is therefore quite clear that most transition metal and less oxophilic metal *β*-diketonates require an oxidising source for thermal decomposition to metal oxides.

Band-gaps for the films were estimated using Tauc plots[172] of UV-Vis spectra recorded in transmission mode and were in good agreement with literature[199] values for α-Fe_2O_3, however films grown without the use of an oxidising gas were too heavily contaminated with carbon and were too dark for meaningful spectra to be recorded.

6.4.1 X-ray diffraction

Powder X-ray diffraction of the resultant films revealed the presence of predominantly haematite (α-Fe_2O_3) at all substrate temperatures when no oxidising gas was used (Figure 86). Upon the introduction of air into the system, haematite films were grown, although a small presence of Fe_3O_4 was observed at 450 °C. The film deposited at 575 °C with air bleed was very thin and phase identification *via* powder X-ray diffraction was not possible. The continued presence of α-Fe_2O_3 in these films matches the results obtained by Veith *et al.* for iron oxide films grown *via* LPCVD using $[Fe(O^tBu)_3]_2$ as a single-source precursor at lower substrate temperatures, however, unlike their study, solely Fe_3O_4 films were not obtained in this study

above 450 °C.[158] The morphologies are also very similar and it is expected that post-deposition annealing would also lead to interconversion between α-Fe_2O_3 and Fe_3O_4.

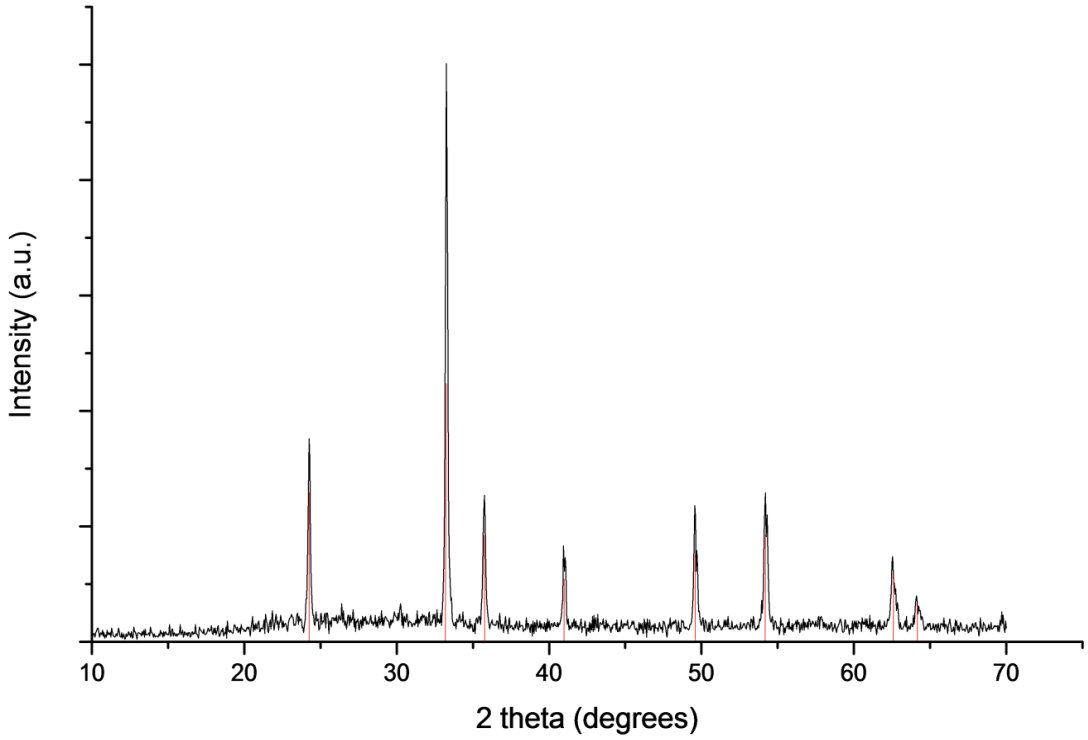

Figure 86: XRD pattern of an α -Fe_2O_3 film formed *via* LPCVD of [$Fe(acac)_3$] and air bleed at 550 °C.

Hexagonal unit cell parameters of $a = b = 5.0272$ (4) Å, $c = 13.7158$ (1) Å, ($\alpha = \beta = 90°$, $\gamma = 120°$, space group *R*3-CH) were obtained *via* unit cell refinement and are in agreement with literature values for bulk Fe_2O_3 ($a = b = 5.03459$ (31) Å, $c = 13.7533$ (13) Å, PDF = 013-0534).[200] The growth of α-Fe_2O_3 films *via* CVD of [$Fe(acac)_3$] at 400 °C, followed by post deposition annealing under a stream of oxygen has already been demonstrated by Dhara.[194] Conversion into the γ-Fe_3O_4 phase was subsequently induced *via* heat treatment under a stream of hydrogen gas.

6.4.2 Scanning electron microscopy

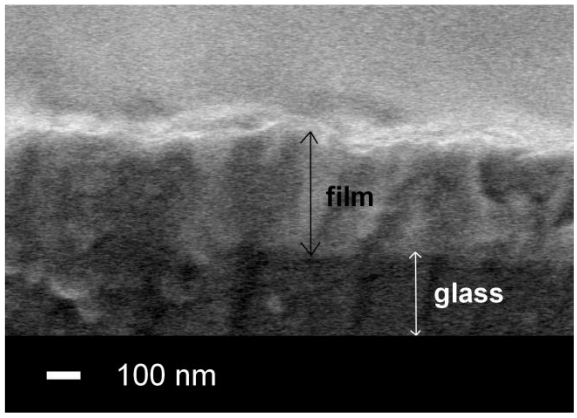

Figure 87: Side-on SEM image of the α-Fe_2O_3 film deposited at 475 °C with air bleed.

Film thickness was obtained *via* side-on SEM imaging (Figure 87), which revealed in general that thickness increased as a function of substrate temperature with and without the use of air as an oxidising gas. Films tended to be thicker at each respective substrate temperature when the air co-reactant was not used; this is however not surprising given the higher level of carbon contamination measured in these films. The only exception were the films deposited at 575 °C which were thinner than expected in light of the trend; however as discussed earlier, this was due to precursor decomposition on the reactor walls at such a high temperature which inhibited complete transport of precursor to the substrate.

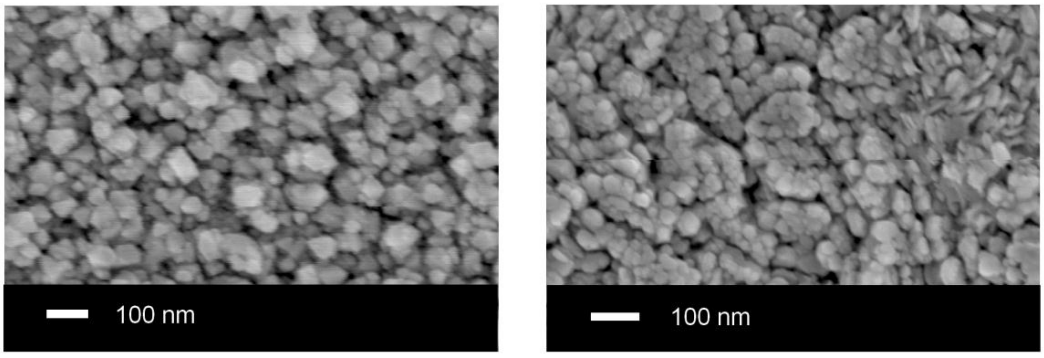

Figure 88: Top-down SEM images of iron oxide films deposited at 450 °C (left) and 550 °C (right) at 8 mbar from the LPCVD reaction of [$Fe(acac)_3$] and air.

The top-down SEM images of the iron oxide films (Figure 88) display a globular morphology composed of individual particles of approximately 100 nm diameter at 450 °C. At 550 °C, these

particles appear to have decreased in size to approximately 50 nm and have coalesced together; the morphology still maintains a globular appearance albeit with a very dense structure. Estimation of the average crystallite size, determined from the broadening of the diffraction peaks (Scherrer Equation) revealed crystallite sizes of 55 nm at 450 °C and 30 nm at 550 °C for both films of α-Fe_2O_3. Nevertheless, coverage appeared to be complete and there are no voids where deposition has not taken place. The morphologies were similar to those obtained by Kuribayashi *et al.* in their mixed phase β-Fe_2O_3 and Fe_3O_4 films grown *via* the CVD reaction of [$Fe(acac)_3$] and oxygen on a variety of substrates.[201]

6.5 CVD of $BiFeO_3$ films

For the deposition of $BiFeO_3$ films, [$Fe(acac)_3$] and [$Bi(O^tBu)_3$] were used as precursors. A slight excess of bismuth precursor was used in order to compensate for bismuth evaporation at high temperatures due to the low melting point of bismuth (271 °C).[202,203] [$Bi(O^tBu)_3$] (150 mg, 0.35 mmol) and [$Fe(acac)_3$] (100 mg, 0.28 mmol) were used for each deposition and the bubbler temperatures were set at 110 °C and 160 °C, respectively. Nitrogen (50 sccm) was used as the carrier gas through both precursors, and depositions were carried out for 1 h onto borosilicate glass substrates and platinised silicon wafers. As expected, without the use of air as a reactive gas, dark, heavily carbon contaminated films were deposited at substrate temperatures between 450 – 550 °C. These films were found to be bismuth deficient from WDX analysis, but were identified *via* powder XRD to be composed predominantly of $Bi_{24}Fe_2O_{39}$ and α-Fe_2O_3. Post-deposition annealing at 550°C resulted in visible removal of carbon contamination but also the evaporation of bismuth which left haematite as the only material observed *via* powder XRD. Indeed, WDX analysis revealed that the annealed films were only composed of iron and oxygen, with no bismuth being present; however the detection of silicon suggested that breakthrough to the underlying glass substrate had taken place and therefore quantification of the Fe:O ratio was not possible. The LPCVD reaction of [$Fe(acac)_3$], [$Bi(O^tBu)_3$] and air (50 sccm) resulted in films of predominantly $BiFeO_3$ at a substrate temperature of 550 °C. Some minor Fe_2O_3 impurity phase was also observed at all temperatures. All films displayed good coverage, and were red-orange in colour, could not be removed *via* tissue or scotch tape but were easily scratched with a steel stylus. The deposition conditions are summarised in Table 11.

Table 11: Deposition conditions for $BiFeO_3$ thin films grown *via* LPCVD of $[Bi(O^tBu)_3]$ and $[Fe(acac)_3]$. The film grown at 550 °C marked with * was chosen for XPS and Raman spectroscopy analysis.

Substrate Temp / °C	Bismuth source carrier gas flow rate / sccm	Iron source carrier gas flow rate / sccm	Air flow rate / sccm	Phase(s) obtained *via* XRD	Thick-ness / nm	Band-gap / eV	At. % Bi:Fe (from WDX)	At. % carbon (from WDX)
450	50	50	**0**	Fe_2O_3	-	-	9:81	6
475	50	50	**0**	$Bi_{24}FeO_{39}$ + Fe_2O_3	-	-	18:82	5
500	50	50	**0**	$Bi_{24}FeO_{39}$ + Fe_2O_3	-	-	28:72	16
550	50	50	**0**	$Bi_{24}FeO_{39}$ + Fe_2O_3	-	-	33:66	14
450	50	50	50	Fe_2O_3	-	1.9	5:95	<1
475	50	50	50	$Bi_{24}FeO_{39}$ + Fe_2O_3	370	2.0	29:71	4
500	50	50	50	$BiFeO_3$ + $Bi_{25}FeO_{40}$	520	2.2	34:66	3
550*	50	50	50	$BiFeO_3$ + Fe_2O_3 + Bi_2O_3	650	2.0	48:52	<1
550	50	50	50	$BiFeO_3$ + Fe_2O_3 + Bi_2O_3	920	2.2	47:53	2
575	50	50	50	$BiFeO_3$ + Fe_2O_3 + Bi_2O_3	860	2.1	44:56	<1
550	50	**40**	50	$BiFeO_3$ + $Bi_2Fe_4O_9$	720	2.3	54:46	<1
550	50	**25**	50	$BiFeO_3$ + $Bi_2Fe_4O_9$	580	2.1	57:43	1.6

6.5.1 Film growth rates

Film thickness, measured *via* side-on SEM imaging, generally increased as a function of substrate temperature. The film growth rates were therefore *ca*. 370 nm, 520 nm, 650 - 920 nm and 860 nm hr^{-1} at substrate temperatures of 475, 500, 550 and 575 °C, respectively. Films deposited at 550 °C in conjunction with air contained $BiFeO_3$ as the major crystalline phase along with some impurity Fe_2O_3, however compositional analysis using WDX revealed close to 50:50 atomic ratios of bismuth to iron in these samples. Very little bismuth incorporation was observed for films deposited at 450 and 475 °C and only minor $BiFeO_3$ phase was observed at 500 °C, which is perhaps due to the insufficient reaction temperature required for growth of $BiFeO_3$.[204] The film growth rates as a function of substrate temperature of iron oxide films, bismuth oxide films and $BiFeO_3$ films grown *via* LPCVD using the same deposition conditions, oxidising gas and individual precursors are shown in Figure 89, and indicates that less bismuth incorporation would be expected at all substrate temperatures below 575 °C, especially 450 °C. The bismuth : iron compositions for bimetallic films deposited at 475 °C and 500 °C in conjunction with air were found to be rich in iron and can therefore be explained by the higher growth rate of iron oxide films (350 and 395 nm hr^{-1}) compared to bismuth oxide films (75 and 305 nm hr^{-1}) at these temperatures. The surprisingly high growth rate of the $BiFeO_3$ film deposited at 575 °C together with the observation by WDX that it was compositionally rich in iron (44:56 at. % Bi:Fe) was unexpected; at 575 °C the growth rate of iron oxide (120 nm hr^{-1}) was found to be significantly lower than that of bismuth oxide (330 nm hr^{-1}) and this is the only temperature where iron oxide growth was lower than both $BiFeO_3$ and bismuth oxide; however one cannot rule out the possibility of bismuth evaporation at this temperature.

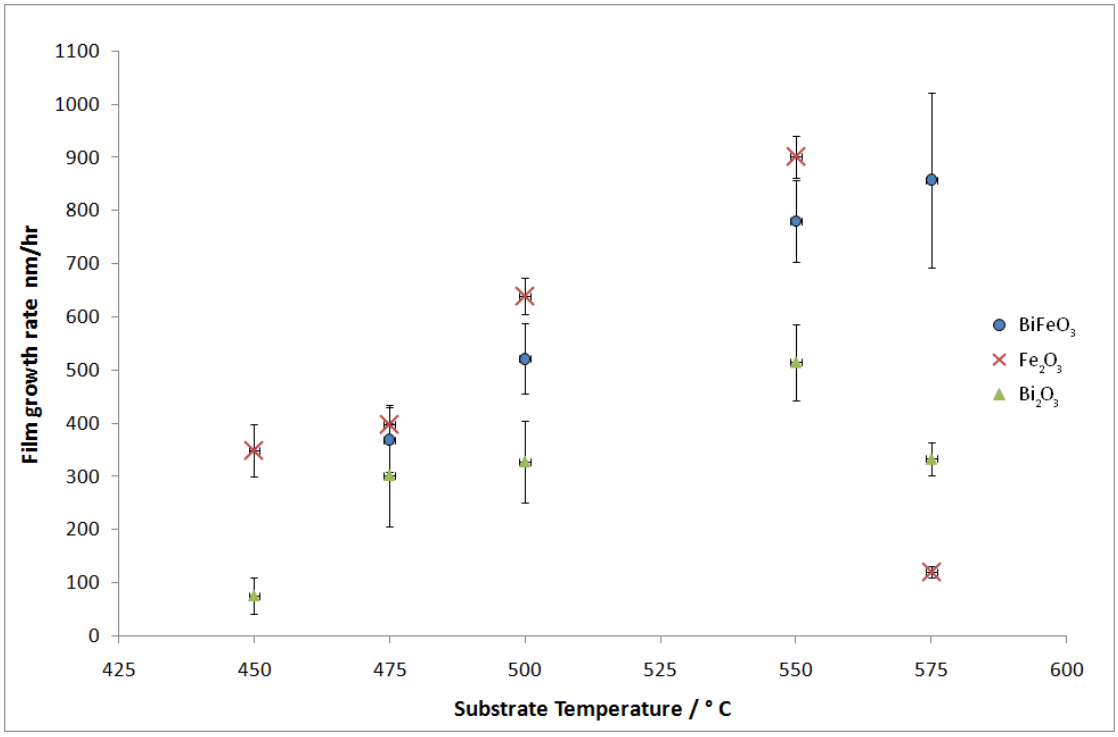

Figure 89: Film growth rates of Bi_2O_3, Fe_2O_3 and $BiFeO_3$ films as a function of substrate temperature, all grown at 8 mbar using air as the oxidising gas (50 sccm).

The film growth rates of $BiFeO_3$ films were significantly higher than those found during preliminary depositions of bismuth oxide films using $[Bi(O^tBu)_3]$ as the bismuth source with air as a reactive gas, but slightly lower than those obtained for iron oxide films grown using $[Fe(acac)_3]$ and air described earlier. At a substrate temperature of 575 °C the film thickness was only slightly higher than that obtained at 550 °C, which is due to premature decomposition of the precursor on the reactor walls in front of the substrate as a result of the high substrate temperature. A large decrease in film thickness was observed when using $[Fe(acac)_3]$ as the iron source for deposition of iron oxide films at 575 °C (Table 10) due to precursor decomposition, and this large decrease was also observed using $[Bi(O^tBu)_3]$ for bismuth oxide film growth at 575 °C. It is therefore worth noting that the $BiFeO_3$ film thickness at this temperature was significantly higher than those seen for bismuth oxide and iron oxide at 575 °C, and this could be due to the combination of three transport gases - air and two nitrogen carriers that together act to transport the precursors to the substrate, minimising the likelihood of premature decomposition, i.e. three transport gases for $BiFeO_3$ films compared to two for Fe_2O_3 and Bi_2O_3 films respectively, leading to a higher total carrier gas flow and reduced residence time.

6.5.2 X-ray diffraction

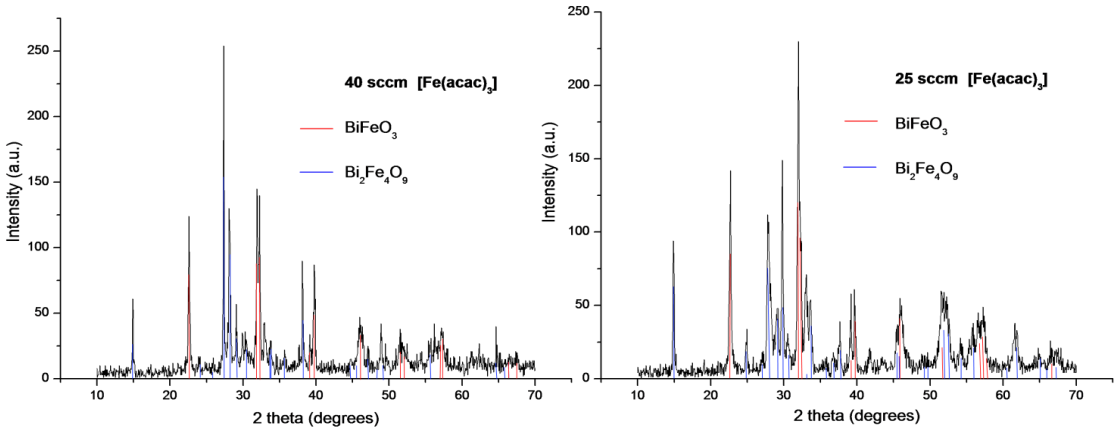

Figure 90: X-ray diffraction patterns of the films obtained by lowering the carrier gas flow rate through the iron source.

In order to decrease the iron oxide content in the films the carrier gas flow rate through the iron source was decreased to 40 and then 25 sccm. This change in iron carrier flow rate to 40 sccm resulted in the disappearance of crystalline Fe_2O_3, but perhaps somewhat surprisingly, the emergence of parasitic $Bi_2Fe_4O_9$ was evident from powder XRD (Figure 90). Compositional analysis from WDX revealed the iron content had decreased, which indicated that the aim of reducing iron in the films was successful. When a carrier gas flow rate of 25 sccm was used the presence of $BiFeO_3$ as well as the impurity $Bi_2Fe_4O_9$ was observed *via* powder XRD. Additionally, this film contained a bismuth to iron ratio of 57:43, clearly demonstrating they were bismuth rich, with powder XRD again revealing it was free from iron oxide phases. Films deposited at 550 °C with both air and carrier gas flow rates of 50 sccm contained bismuth : iron ratios closest to 1. These films were still slightly bismuth deficient (47:53 and 48:52 at. % Bi:Fe), however this can be perhaps explained by the lower film growth rate of bismuth oxide (520 nm hr^{-1}) compared to iron oxide (900 nm hr^{-1}) at this temperature. These films were found to contain some additional α-Fe_2O_3 and a single peak which could be due to γ-Bi_2O_3 (Figure 91).

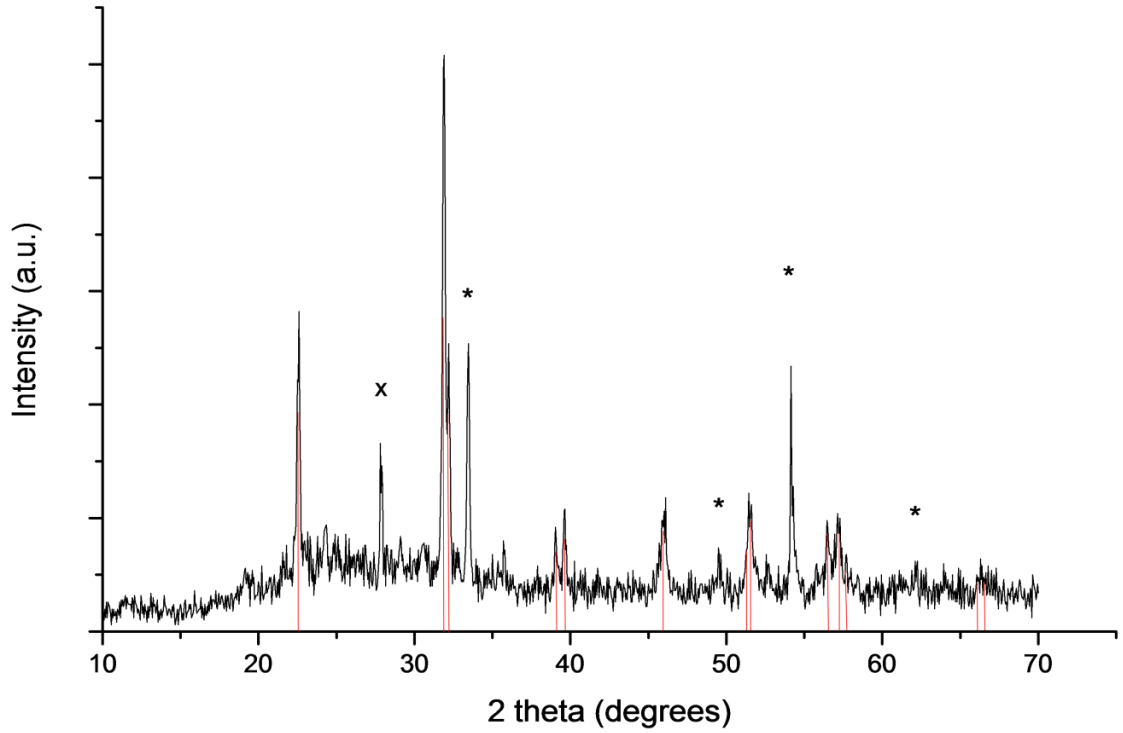

Figure 91: X-ray diffraction pattern of the $BiFeO_3$ film formed *via* LPCVD of [$Bi(O^tBu)_3$], [$Fe(acac)_3$] and air at 550 °C, using a 50 sccm flow rate for all sources. Asterisks (*) correspond to Fe_2O_3 and crosses (x) correspond to γ- Bi_2O_3.

Hexagonal unit cell parameters of $a = b = 5.5680$ (4) Å, $c = 13.841$ (1) Å, ($\alpha = \beta = 90°$, $\gamma = 120°$, space group $R3c$) were obtained *via* unit cell refinement and were in agreement with literature values for bulk $BiFeO_3$ found *via* synchrotron X-ray diffraction ($a = b = 5.57414$ (4) Å, $c = 13.85882$ (12) Å PDF = 014-0181).[205] Both γ-Bi_2O_3 (PDF = 074-1375) and α-Fe_2O_3 (PDF = 013-0534) were observed in the pattern as impurity phases; despite varying the reaction conditions the deposition of phase pure $BiFeO_3$ was unsuccessful. X-ray diffraction patterns for the films grown at 450, 475, 500 and 575 °C are shown in Figure 92.

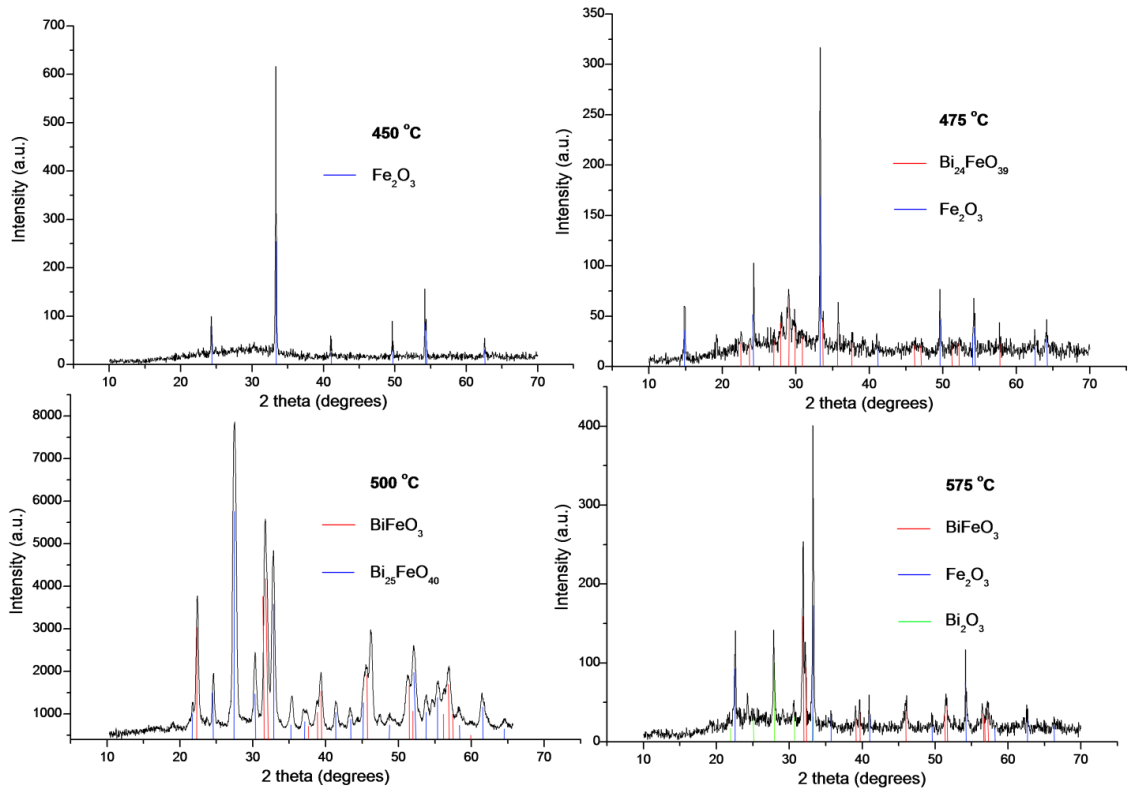

Figure 92: X-ray diffraction patterns of the films deposited *via* LPCVD from [Fe(acac)$_3$], [Bi(O^{t}Bu)$_3$] and air.

6.5.3 X-ray photoelectron spectroscopy

The composition of a $BiFeO_3$ film formed from the LPCVD reaction of [Bi(O^{t}Bu)$_3$], [Fe(acac)$_3$] and air at 550 °C (marked with a * in Table 11) was analysed *via* XPS. The spectra were recorded and analysed after etching for 10 minutes to a depth of 10 nm. The Fe 2p core level was split into $2p_{1/2}$ and $2p_{3/2}$ components. The presence of iron in the 3^+ oxidation state was observed (Figure 93), with the Fe $2p_{1/2}$ region displayed at 723.8 eV. The Fe $2p_{3/2}$ region was represented by a large, broad, slightly asymmetric peak in the 711 eV region, which could be fitted by one peak at 710 eV which is typically observed for iron in Fe_3O_4, in Fe_2O_3 and as iron in $BiFeO_3$ species. It is less likely that the iron in the sample originates from Fe_3O_4 species as one would expect a prominent shoulder or peak at 707 eV.[206] As reported in the literature,[123] the weak Fe^{3+} satellite peak could be observed at 718.1 eV, however the background signal in this region was too high to assign this with certainty, nevertheless this appears to be characteristic of the presence of pure Fe^{3+} in a sample, making the presence of Fe^{2+} species less likely. The small peak at 731 eV is yet to be assigned with confidence, however this peak is likely to correspond to the Fe $2p_{1/2}$ satellite peak, which is in agreement with XPS spectra of synthesised pure α-Fe_2O_3.[207] Furthermore, the Fe 2p region in the XPS spectrum of their pure Fe_3O_4 sample was found to contain no satellite peaks, again indicating that in our samples the presence of Fe_3O_4 is unlikely.

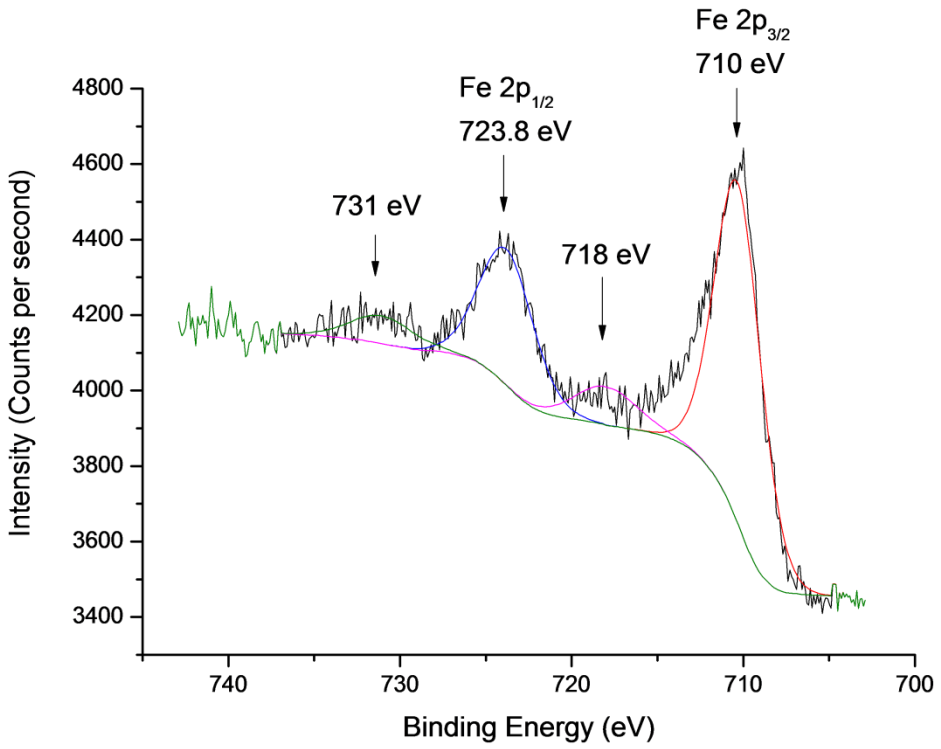

Figure 93: XPS spectrum of the Fe 2p region after etching; satellite peaks are observed at higher binding energies in comparison to the main peaks.

XPS analysis of the surface bismuth 4f spectrum (Figure 94) revealed two peaks corresponding to the Bi $4f_{7/2}$ region at 159.2 eV and the Bi $4f_{5/2}$ region at 164.5 eV, which are both characteristic of Bi^{3+}. The peak shapes in the surface scan had too high a background signal for peak fitting. The spectrum of the etched sample had a much lower background due to the longer data collection time, and the same peaks were observed at 159.2 and 164.5 eV. Further etching revealed the presence of a shoulder attached to both the Bi $4f_{5/2}$ and Bi $4f_{7/2}$ peaks. The Bi^{3+} peaks were shifted to slightly lower binding energies at 158.7 and 164 eV, whilst the shoulders at 159.5 and 164.8 eV were ascribed to formation of metallic bismuth as a result of preferential sputtering during the etching process.[170] For this reason, the results of the extended etch were not used for calculation of film stoichiometry.

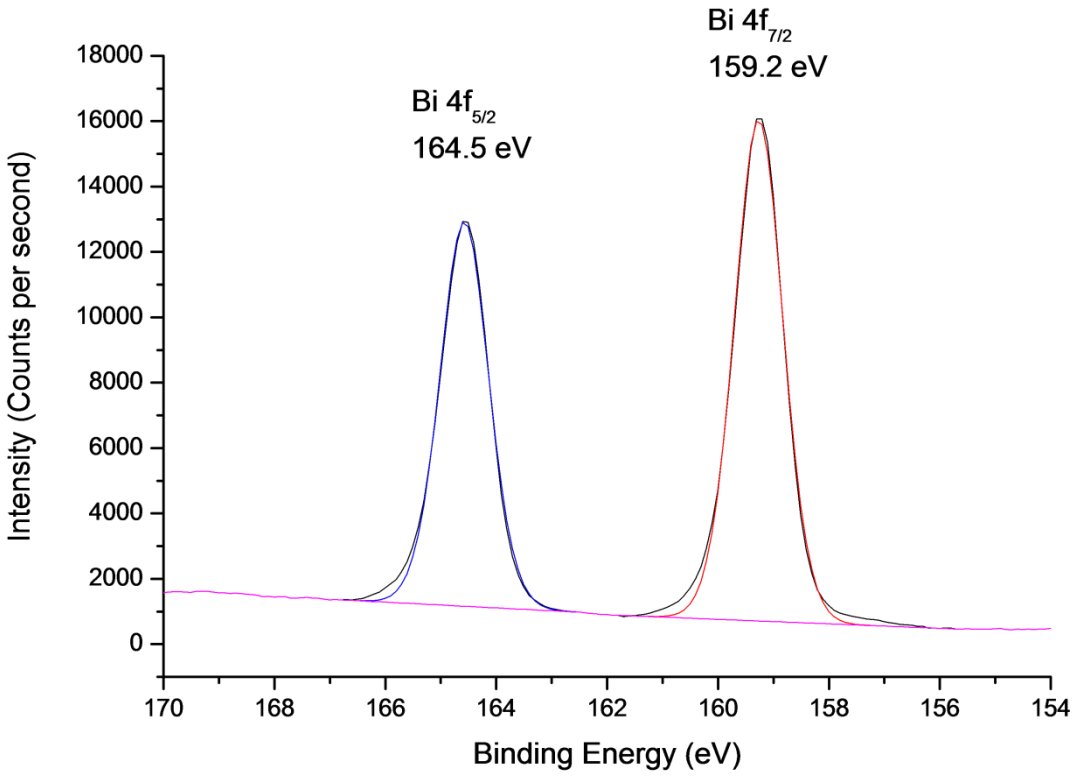

Figure 94: XPS spectrum of the Bi 4f region after etching.

The oxygen O 1s region in the XPS spectrum of the etched sample is shown in Figure 95. There is a broad asymmetric peak which was fitted using two smaller peaks, with one positioned at 530.1 eV, characteristic of metal oxide species, whereas the peak at 532.4 eV is ascribed to either surface-originated hydroxyl species that had penetrated deeper into the film, pin-holes in the film exposing the underlying glass substrate, or some other contamination. Carbon contamination was observed in the surface and etched spectra through the characteristic carbon peak at 284.5 eV, however the etched scans revealed a large decrease in carbon content and therefore it is assumed that the carbon contamination is mainly due to adventitious surface contamination. The summed total of the Bi 4f, Fe 2p and O1s peak areas divided by their relative sensitivity factors (9.14, 2.957 and 0.78 for bismuth, iron and oxygen respectively) revealed the presence of the three elements in the ratio $Bi_{1.3}FeO_{4.1}$. Clearly this indicates that the film is oxygen rich, however the presence of a very small sodium peak at 1072 eV and a silicon peak at 101 eV indicates that either there was some breakthrough to the underlying glass substrate or that these peaks were part of the contamination observed in the XPS spectrum of the O 1s region. Given that the film thickness was approximately 650 nm and that only a light etch was performed, attributing these peaks to the glass substrate is unlikely, however the presence of pin-holes cannot be ruled out despite the conformal coverage observed *via* top-down SEM imaging (Figure 96).

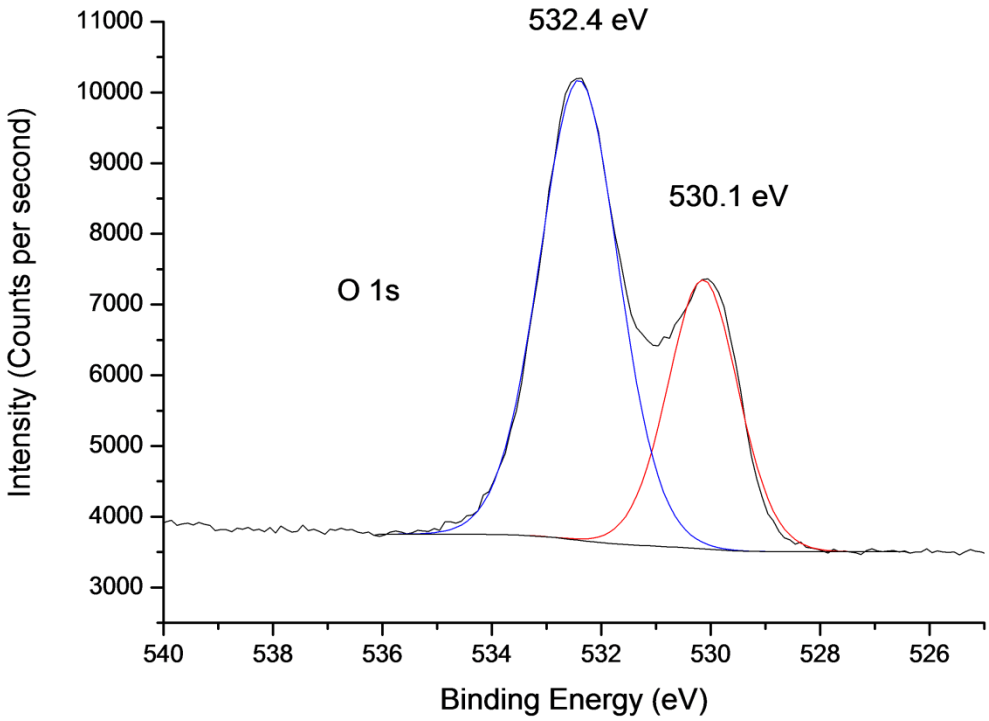

Figure 95: XPS spectrum of the O 1s spectrum after etching.

6.5.4 Scanning electron microscopy

Figure 96 shows the morphologies of the films deposited at 475, 500, 550 and 575 °C. The morphology of the film deposited at 475 °C is primarily composed of distinct plate–shaped crystallites of approximately 100 nm width. The packing of these crystallites is fairly dense and uniform, and there appears to be no voids or areas of zero deposition visible *via* SEM. At 500 °C the crystallites appear to have increased in size to approximately 200 nm in width with a three dimensional structure as shown by the tetrahedral shaped crystals, and again the packing is very dense. At a deposition temperature of 550 °C, a temperature where the most $BiFeO_3$ was obtained amongst other phases, the crystallites appear to have begun to coalesce and it is difficult to pick out individual crystallites, however some edges are still observable. The morphology appears to be intermediate between that obtained at 500 °C and 575 °C. By 575 °C, the morphology displays no individual crystallites; instead the particles have entirely coalesced with few features. The morphology attains a much more globular appearance, somewhat closer to the morphologies obtained for Fe_2O_3 films (Figure 88). Although some of the individual particles appear to be smaller in size (~ 50 nm) than those obtained at the lower temperatures, the fact that they have fused and sintered together makes it difficult to distinguish between them.

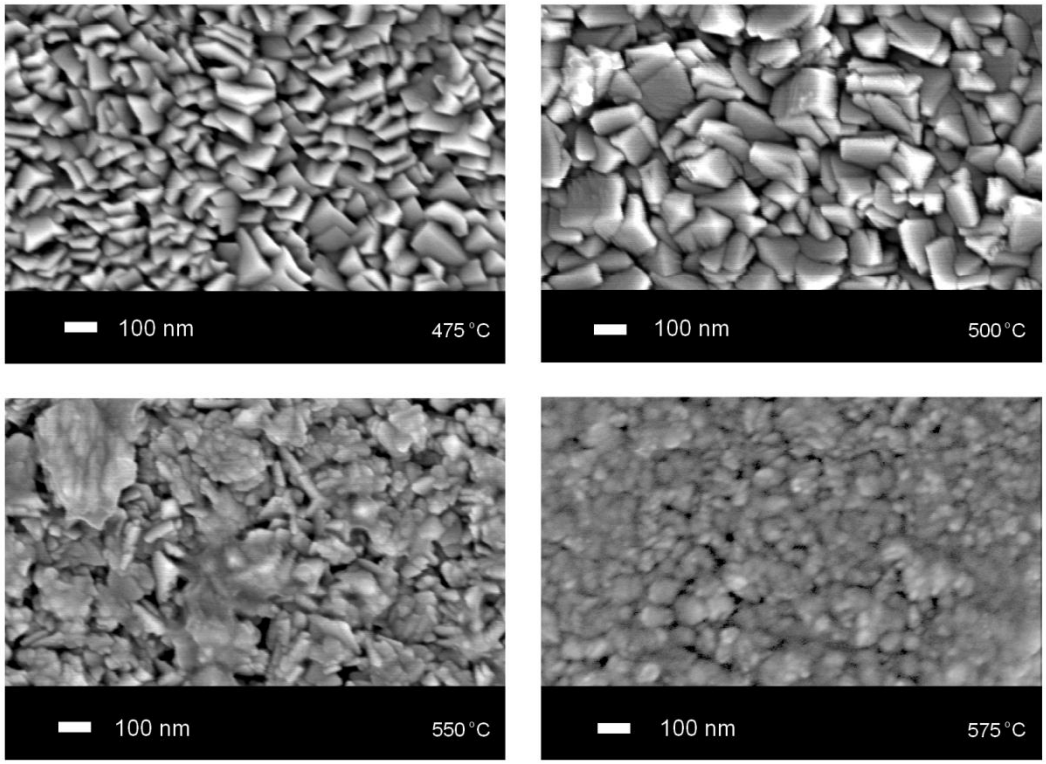

Figure 96: SEM images of $BiFeO_3$ films formed *via* LPCVD of [Fe(acac)$_3$] and [Bi(O^{t}Bu)$_3$] and air at a variety of substrate temperatures.

Nevertheless, the average particle diameters were estimated *via* use of the Scherrer equation from the peak broadening of the X-ray diffraction patterns. The films deposited at 475 °C and 500 °C were found to have particle sizes of 80 and 110 nm respectively, which is much smaller than observed *via* SEM imaging. The films deposited at 550 °C and 575 °C were found to contain average particle sizes of 50 and 30 nm, again smaller than observed *via* SEM, but the overall trend of decreasing particle size (apart from the film deposited at 500 °C) was maintained. It is difficult to ascribe with certainty the change in morphology with temperature as a being a direct result of phase changes. At 475 °C no $BiFeO_3$ was detected *via* powder XRD, and at 500 °C $BiFeO_3$ together with a large amount of $Bi_{25}FeO_{40}$ was present in the film. At a substrate temperature of 550 °C and 575 °C the film is predominantly composed of $BiFeO_3$ and the morphology has changed considerably from the plate-like particles observed at 475 °C and 500 °C, and therefore the change in morphology could be ascribed to the presence of $BiFeO_3$ in the films.

6.5.5 Raman spectroscopy

Raman spectra were collected for the $BiFeO_3$ samples deposited on glass substrates.

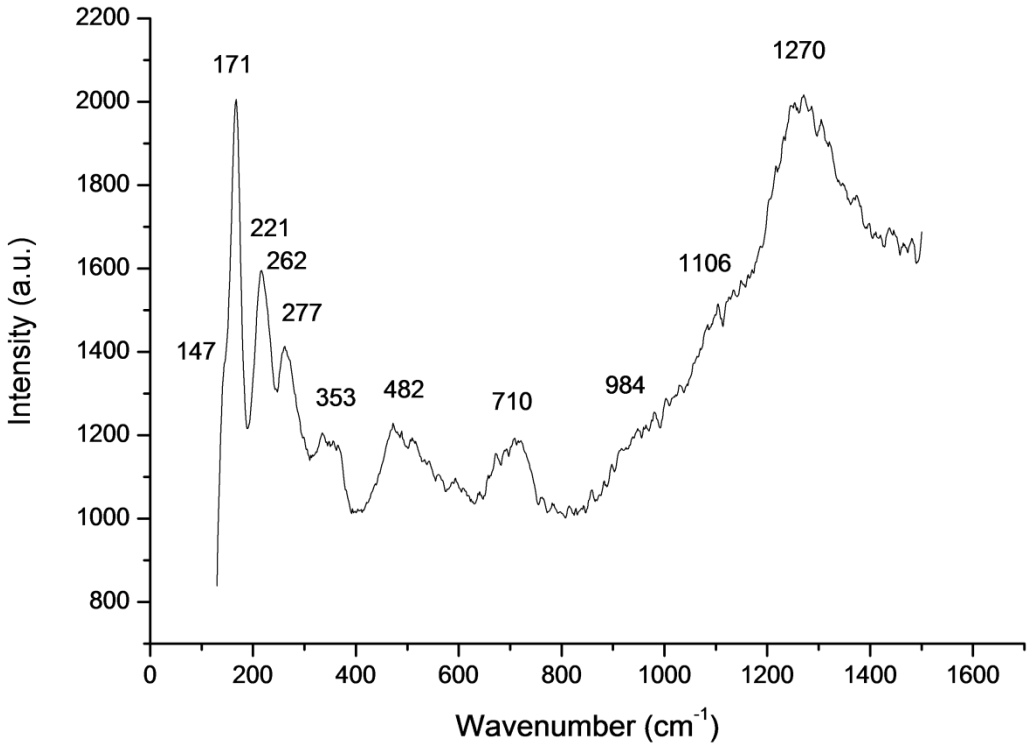

Figure 97: Room temperature Raman spectrum of $BiFeO_3$ film deposited *via* LPCVD of $[Fe(acac)_3]$, $[Bi(O^tBu)_3]$ and air at 550 °C.

The Raman spectrum recorded at room temperature of the film containing predominantly $BiFeO_3$, deposited at a substrate temperature of 550 °C is shown in Figure 97. Amidst the relatively high background count, peaks for $BiFeO_3$ were observed at 147, 171, 221, 262, 277, 353, 482, 984 and 1106 cm^{-1}. The broad peak at 710 cm^{-1} remains unassigned. However, it is unlikely that these peaks are due to γ-Bi_2O_3 impurities as they were not observed in Raman spectra of γ-Bi_2O_3 films that were described in Chapter 4. Figure 98 shows the Raman spectra of the same $BiFeO_3$ film deposited at 550 °C along with a film deposited at 475 °C, which was predominantly composed of α-Fe_2O_3 (Table 11). There appears to be no correlation between the two spectra and peaks at 710, 984 and 1106 cm^{-1}, found in the spectrum of $BiFeO_3$, were not observed in the spectrum of α-Fe_2O_3, hence it is unlikely that these peaks are due to α-Fe_2O_3 impurities in the $BiFeO_3$ film. The expected Raman scattering based on group theory analysis for $BiFeO_3$ is described in more detail in Chapters 7 and 8 from low temperature Raman spectroscopy, as well as in a recent paper by Rout.[208] In a study of Raman spectra of $BiFeO_3$ single crystals conducted in a temperature range between 4 – 1000 K, Fukumura observed the

$4A_1$ and 9E phonon modes of $BiFeO_3$ at 4 K.[209] The spectrum appeared to broaden and "flatten" between 700 – 1100 K which is consistent with T_N and T_C. The A_1 modes were assigned to peaks at 147, 176, 227 and 490 cm^{-1} and these are consistent with the peaks observed in the Raman spectrum of $BiFeO_3$ shown in Figure 97. Likewise, the E phonon modes of single crystal $BiFeO_3$ were observed at 77, 136, 265, 279, 351, 375, 437, 473 and 525 cm^{-1}, of which the peaks at 265, 279 and 353 cm^{-1} are consistent with peaks observed in our $BiFeO_3$ film. It is possible that the other E mode peaks are present however due to the laser filter cut-off at 140 cm^{-1}, the high background and peak broadening, it is impossible to distinguish these. The assignment of the relatively weaker peaks at 984 and 1106 cm^{-1} appear to originate from the two-phonon overtone modes ($2A_4$ and $2E_8$).[210] No peak was observed at ~ 550 cm^{-1} however the peak at 482 cm^{-1} is essentially half the energy value of 984 cm^{-1} (A_4). The very broad peak at 1270 cm^{-1} has been shown to be a result of three different two-phonon Raman overtones $2A_4$, $2A_8$ and $2E_9$. Higher resolution spectra have revealed them to be composed of three individual peaks, however only the original A_4 band at 482cm^{-1} was observed in our spectrum of $BiFeO_3$ recorded at room temperature.[210] These bands were found to disappear upon heating the sample above T_N, however a similar broad peak was observed at 1310 cm^{-1} in the Raman spectrum of Fe_2O_3.

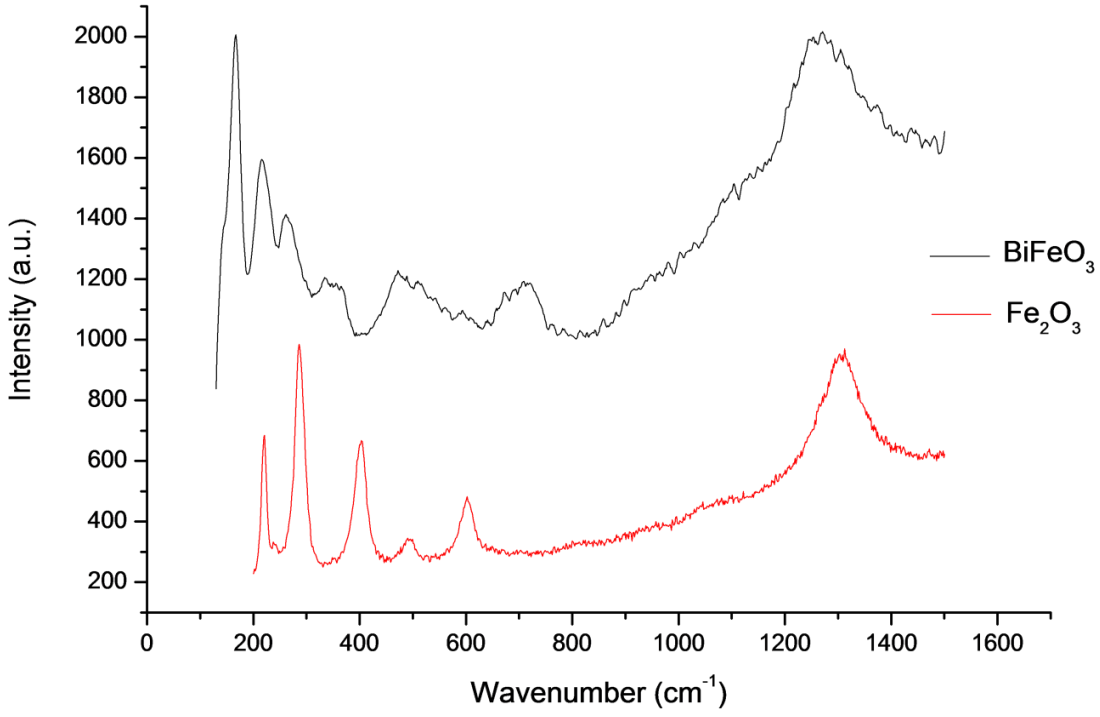

Figure 98: Raman spectra of $BiFeO_3$ and Fe_2O_3 films deposited *via* LPCVD at room temperature.

6.5.6 Atomic force microscopy

A field size and 3D AFM image of the film containing $BiFeO_3$ as the predominant phase is shown in Figure 99. The sample was scanned across the surface of the film for a distance of 3 µm. The morphology appears dense and hierarchical and is composed of small globular particles; however these appear to have coalesced to form larger particles in the higher regions. Similar to the SEM imaging, the coverage is total; however with the amalgamation of particles, the film appears less uniform. The top-down SEM image of this film deposited at 550 °C contained a mixture of plate-like crystallites together with smaller particles, however the edges of those crystallites were not observed in the AFM image. The root mean squares (rms) roughness for the sample was calculated at 30 nm, which is lower than the value obtained for films of $BiFeO_3$ grown *via* the LPCVD reaction of $[Fe(O^tBu)_3]_2$ and $[Bi(O^tBu)_3]$ as described in Chapter 7 (rms = 60 nm); however it is much higher than the roughness of Bi_2O_3 films (rms = 4 nm) grown using $[Bi(O^tBu)_3]$ as a single-source precursor, which is discussed in Chapter 4. It is also lower than the value obtained for $BiFeO_3$ films grown *via* AACVD after annealing (Chapter 8) that possessed a high roughness of 62 nm. One would expect that a lower roughness value for these $BiFeO_3$ films would make them less suitable for high surface area applications such as catalysis, as there would be less catalytic material in contact with the surrounding medium. Conversely, the excellent coverage and crystallinity of the films may be advantageous here as better coverage enables more active sites to participate in catalysis and the increased crystallinity would disfavour charge carrier recombination.

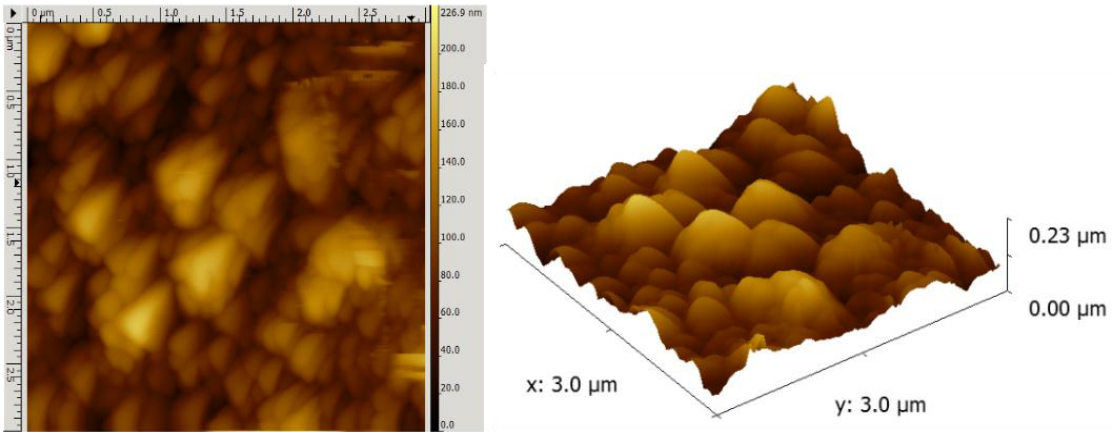

Figure 99: A 3 µm field size (left) and 3D AFM image (right) of the $BiFeO_3$ grown *via* LPCVD of $[Fe(acac)_3]$, $[Bi(O^tBu)_3]$ and air at 550 °C.

6.5.7 Ferroelectric characterisation

A 600 nm film of $BiFeO_3$ was grown *via* the LPCVD reaction of [$Fe(acac)_3$] and [$Bi(O^tBu)_3$] with air bleed at 550 °C directly onto a 1 cm^2 silicon wafer that had been previously sputtered for 2 minutes with a thin layer of platinum (argon pressure 0.1 torr ,current 25 mA). Following deposition of the $BiFeO_3$ film, powder XRD analysis revealed the presence of principally $BiFeO_3$ along with impurity α-Fe_2O_3, (similar to that shown in Figure 91), and side-on SEM imaging revealed the film thickness to be approximately 600 nm. Following deposition, five platinum electrodes were sputtered onto the surface of the film using a 0.5 mm diameter mask in order to serve as conducting top electrodes. The polarisation-electric field (P-E) hysteresis loop was measured at room temperature and is shown in Figure 100. The P-E loop appears quite noisy and this was mainly due to significant electrode damage caused by contacting gold measuring tips to the platinum top electrodes during measurement. The measurement reveals that the films are highly resistive and robust at these electric field strengths; high fields are required because the grains within a sample are split into domains that have random polarisations that cancel each other out, therefore a large field is needed to reorient domains to switch in line with the applied field.

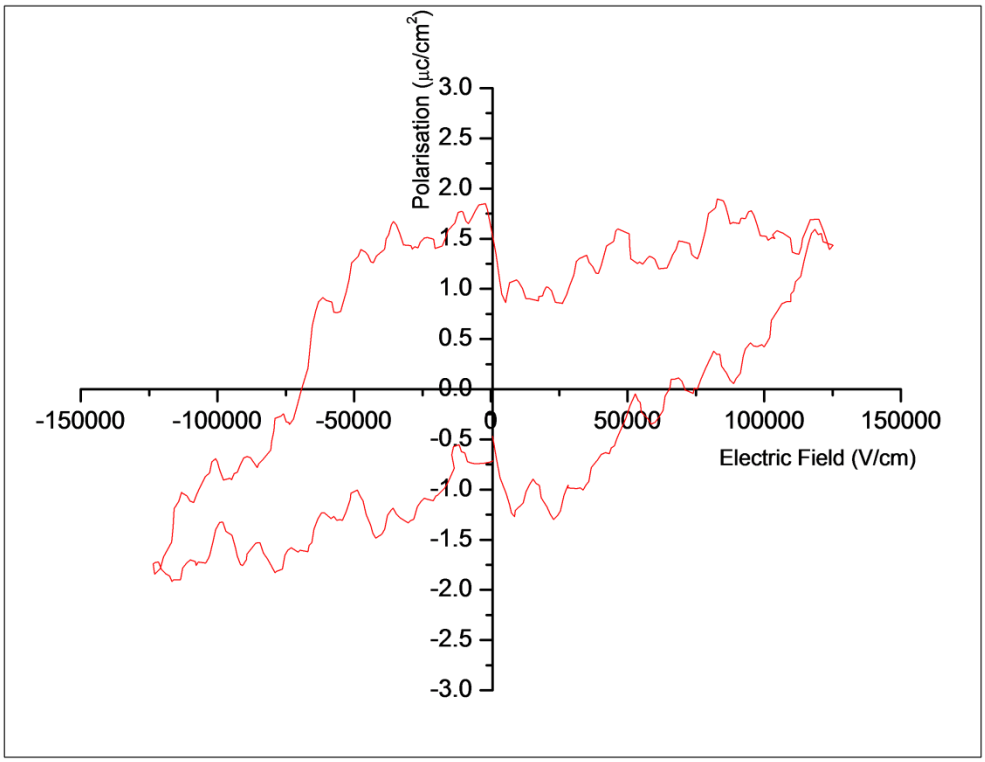

Figure 100: P-E loop measured at room temperature and at 1 kHz for a 600 nm thick $BiFeO_3$ film grown *via* LPCVD onto a Pt/SiO_2/Si substrate.

The hysteresis loop fails to saturate fully, however to prevent breakdown only a comparatively low electric field strength was used for the experiment. Nevertheless, a coercivity of approximately 75 kV/cm was measured, along with a low saturation polarisation (P_s) of approximately 1.5 μC/cm^2. Estimation of the remnant polarisation (P_r) proved challenging as the move to positive voltages caused a shift toward lower polarisation values in the hysteresis loop, however a P_r value of between 1 – 1.5 μC/cm^2 was believed to have been measured. This shift in polarisation is sometimes described as a constricted hysteresis loop. This occurs when defects and internal fields are randomly distributed within the sample, making it appear that the sample has two independant hysteresis loops. One of the greatest challenges for incorporation of $BiFeO_3$ into devices is the high leakage current due to deviation in oxygen stoichiometry, defects and impurity phases. The ferroelectric hysteresis loop of bulk $BiFeO_3$ measured at liquid nitrogen temperature in 1970 revealed a spontaneous polarisation of 6.1 μC/cm^2 in the [100] direction.[105] The polarisation measured by Wang[39] for $BiFeO_3$ with a tetragonal distortion grown on $SrTiO_3$/$SrRuO_3$ substrates *via* PLD revealed much higher values up to 55 μC/cm^2. The polarisation results described here are more closely aligned with those obtained by Nan *et al*.[211] for their pure-phased $BiFeO_3$ film grown *via* sol-gel processing onto platinised silicon substrates, which displayed saturations (P_s) at 0.69 and 1.87 μC/cm^2 coupled with P_r values of 0.36 and 0.88 μC/cm^2 for their 100 and 130 nm thick films. It is also similar to the values obtained by Palkar[212] for PLD-grown $BiFeO_3$ films grown on platinised silicon (P_r = 0.83 μC/cm^2, P_s = 2.2 μC/cm^2). One of the reasons the authors gave for the lower polarisation values was the comparatively lower crystallographic distortion of the $BiFeO_3$ structure when not epitaxially grown onto perovskite substrates such as $SrTiO_3$/$SrRuO_3$, however this has recently been disputed following measurements on high quality samples.[99] Also, the growth of $BiFeO_3$ onto platinised silicon substrates may result in an interface layer (1-3 nm thickness) which reduces strain caused by lattice mismatch between the film and substrate, resulting in a lower polarisation.

Nevertheless, the measurement of a spontaneous polarization indicates that these films fabricated *via* CVD are ferroelectric at room temperature.

6.5.8 Magnetism Measurements

Magnetic measurements were performed using a SQUID-VSM which has a maximum field setting of 7 T (70000 Oe). The film which contained the greatest proportion of $BiFeO_3$ (deposited at 550 °C) was chosen for magnetic measurements. The film was cut to an appropriate size (2mm x 3mm) in order to be mounted on a quartz rod using temperature stable adhesive. The magnetic field was applied parallel to the sample and M-H loops were measured

at 5 K and at 300 K. The corrected magnetic moments were calculated by subtracting the diamagnetic/paramagnetic contribution to the M-H curve (Equation 19).

$$M(H) = M(\text{sample})(H) + \chi * H$$

Equation 19: Magnetism correction applied to M-H data

The susceptibility, χ, is calculated from the linear component of the magnetisation at high fields strengths, typically where the field (H) is larger than 2 T (20000 Oe). From this value, χ*H was subtracted from the whole dataset to leave the corrected moment. The M-H hysteresis loop recorded at 5 K is shown in Figure 101.

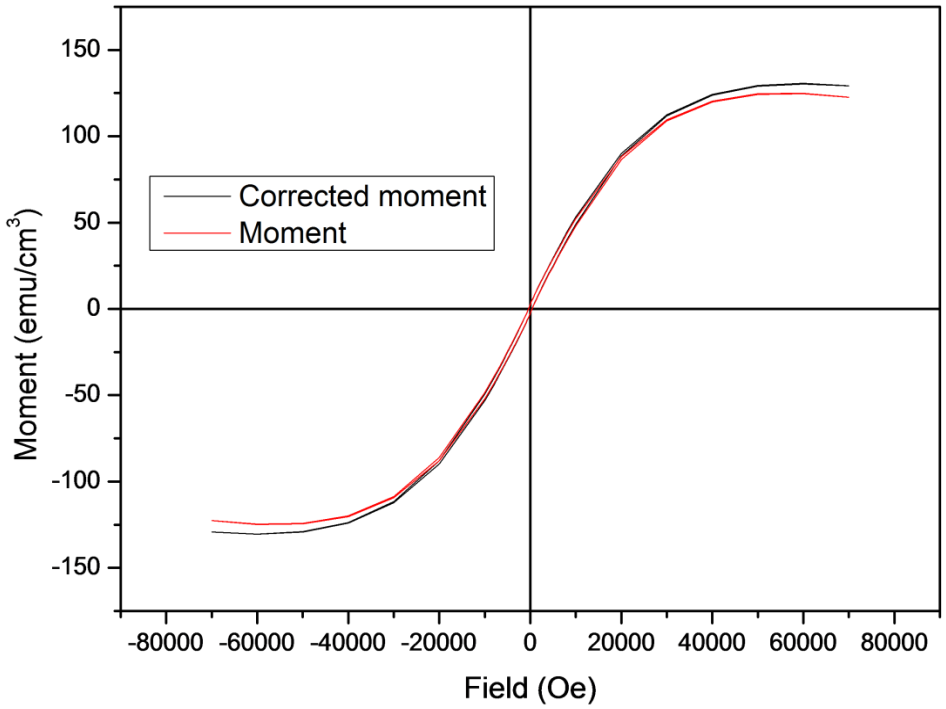

Figure 101: M-H hysteresis loop measured at 5 K for the 650 nm thick, predominantly $BiFeO_3$ film grown *via* LPCVD.

The diamagnetic contribution from the glass substrate appeared to be negligible, however this was still subtracted from the linear component of the recorded moment at high field strengths; this difference was observed above a field strength of 4 T (40000 Oe). The hysteresis loop indicates that at low temperatures, these $BiFeO_3$ films exhibit weak ferromagnetic behaviour. A brief explanation of the various defining characteristics of a magnetic hysteresis loop will now be given. At zero field (H = 0), the moments are aligned in the same direction, however as the domains they are located in are randomly aligned, there is very little induced magnetisation to

begin with. As the applied field increases, more moments align with the field, and domain walls begin to move and grow. At saturation, the moments are all aligned parallel with the field, but gradual removal of the field leads to an instantaneous reversal of some of the moments into their preferred orientation, resulting in the decrease in remnance compared to the value observed at saturation. The domain walls move and reform but can get "stuck" at grain boundaries and defects, resulting in coercivity and contributing to remnance. The loop appears to saturate at 6 T (60000 Oe), and a saturation magnetisation of approximately 130 emu/cm^3 was recorded at 5 K. This value is much higher than that recorded by Thery (70 emu/cm^3) for their 30 nm $BiFeO_3$ film grown on a $SrTiO_3$ substrate *via* the CVD reaction of [Bi(mmp)$_3$], [Fe(thd)$_3$] and oxygen.[123] The expected saturation magnetisation calculated by density functional theory for bulk $BiFeO_3$ is 7 emu/cm^3 or 0.1 μ_B per unit cell,[123,102] however it is unclear what temperatures these calculations were based upon. The high magnetisation is potentially due to the impurity Fe_2O_3 in the film, as observed *via* powder XRD, and does not conform to the trend observed by Wang[39] and co-workers from their epitaxially (PLD) grown $BiFeO_3$ films, where the magnetisation decreased with increasing film thickness; their 75 nm thick film exhibited a saturation magnetisation of 150 emu/cm^3, whilst a 400 nm thick film saturated at ~ 60 emu/cm^3 (thicker films were not grown). In contrast, the $BiFeO_3$ film grown here *via* LPCVD possessed a thickness of 650 nm and saturated at 130 emu/cm^3.

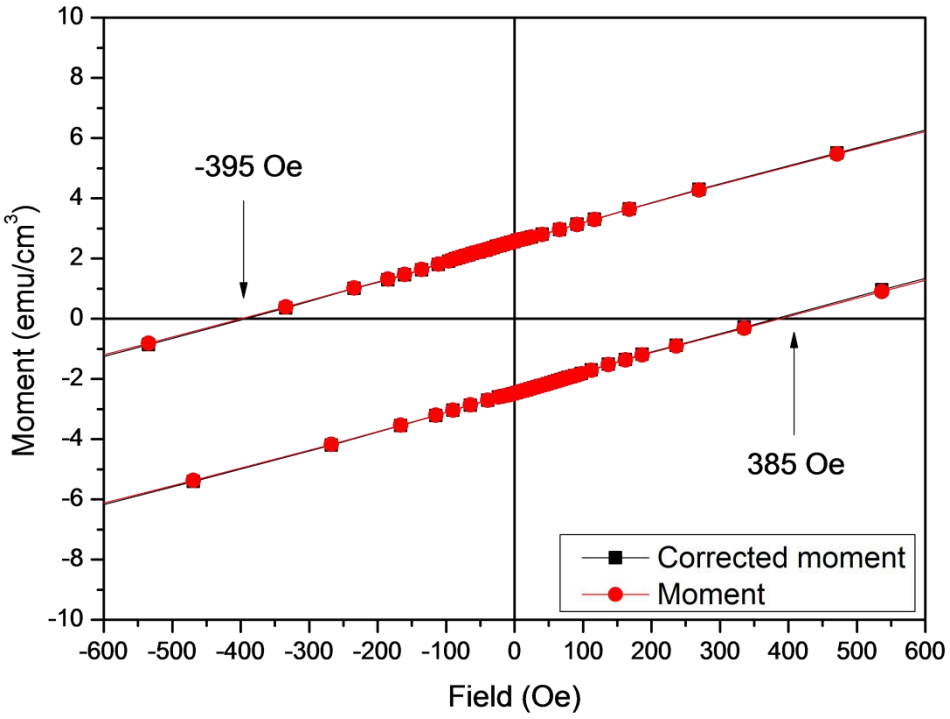

Figure 102: Enlarged coercive field region of the M-H curve of the $BiFeO_3$ film grown *via* LPCVD.

Figure 102 shows the M-H curve for the same $BiFeO_3$ sample, enlarged so that the coercivity may be more easily observed. At these relatively low field strengths the diamagnetic contribution of the substrate to the total moment is shown to be negligible. The coercive field was slightly asymmetric, taking values of -395 and 385 Oe and is high for typical $BiFeO_3$ films, however the presence of Fe^{2+} ions or Fe_2O_3 may have been a contributing factor. The M-H curve was also recorded at room temperature (Figure 103).

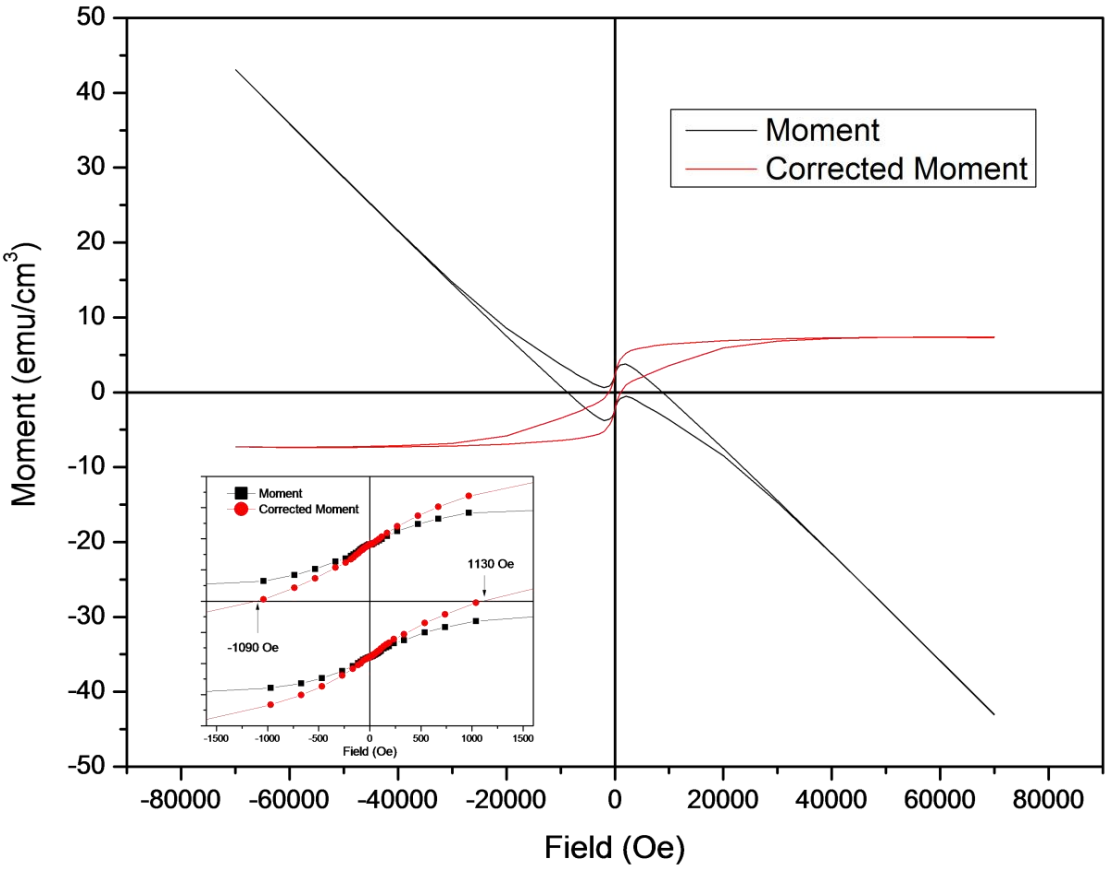

Figure 103: M-H hysteresis loop measure at 300 K for the predominantly $BiFeO_3$ film grown *via* LPCVD. The unset plot shows the M-H curve enlarged to display the coercive field of the sample.

The M-H curve recorded at room temperature (Figure 103) appears to contain a much greater diamagnetic contribution from the substrate, which again had to be subtracted from the total moment. This also had a greater effect on the coercivity compared to the measurement recorded at 5 K. Nevertheless, the magnetisation appeared to fully saturate at a much lower field strength at approximately 3T (30000 Oe) as expected and a saturation magnetisation of 7.3 emu/cm^3 was recorded, which is similar to the calculated 7 emu/cm^3 value for bulk $BiFeO_3$.[102] Surprisingly, the coercive field of the sample appeared to dramatically increase compared to that recorded at 5 K. An asymmetric coercivity of -1080 and 1130 Oe were measured, which is almost three times that recorded for the same sample at the lower temperature. The reasons for this temperature-related behaviour are currently unknown, however these observations are contrary

to the decrease in coercivity observed for CVD-grown $BiFeO_3$ films described in Chapters 7 and 8 as a function of temperature. Barthelemy[213] has recently investigated the influence of impurity phases on the magnetic properties of $BiFeO_3$ and has shown that films containing Fe_2O_3 result in almost perfect ferromagnetic behaviour, leading to higher than expected saturation compared to pure $BiFeO_3$, which itself possesses a low bulk-like magnetic moment. The origin of the variance in the magnetic moment in different $BiFeO_3$ samples has led to much debate over the reproducibility of pure-phased $BiFeO_3$ and the existence of Fe^{2+} states in such samples, as highlighted by Eerenstein *et al*. in 2003.[110,107] Nevertheless, the measurement of ferromagnetic and ferroelectric ordering at room temperature highlights that these $BiFeO_3$ films grown *via* CVD are multiferroic.

6.5.9 UV- Vis spectroscopy

The optical properties of the as-deposited films were measured using UV-Vis spectroscopy in transmission mode (Figure 104). The spectrum of an uncoated glass substrate was also run and was subtracted from the spectra of the film and glass. The film possessing a thickness of 920 nm displayed a sufficient number of interference fringes in its spectrum to allow a calculation of its refractive index, *n*. This was obtained *via* the Swanepoel method[173] by construction of virtual maxima and minima transmittance envelopes from these interference effects. At 900 nm, a refractive index of $n = 2.3$ was calculated, which is in good agreement with measurements by Iakovlev[214] ($n = 2.5$) and Shen[215] ($n = 2.26$-2.28) on $BiFeO_3$ films.

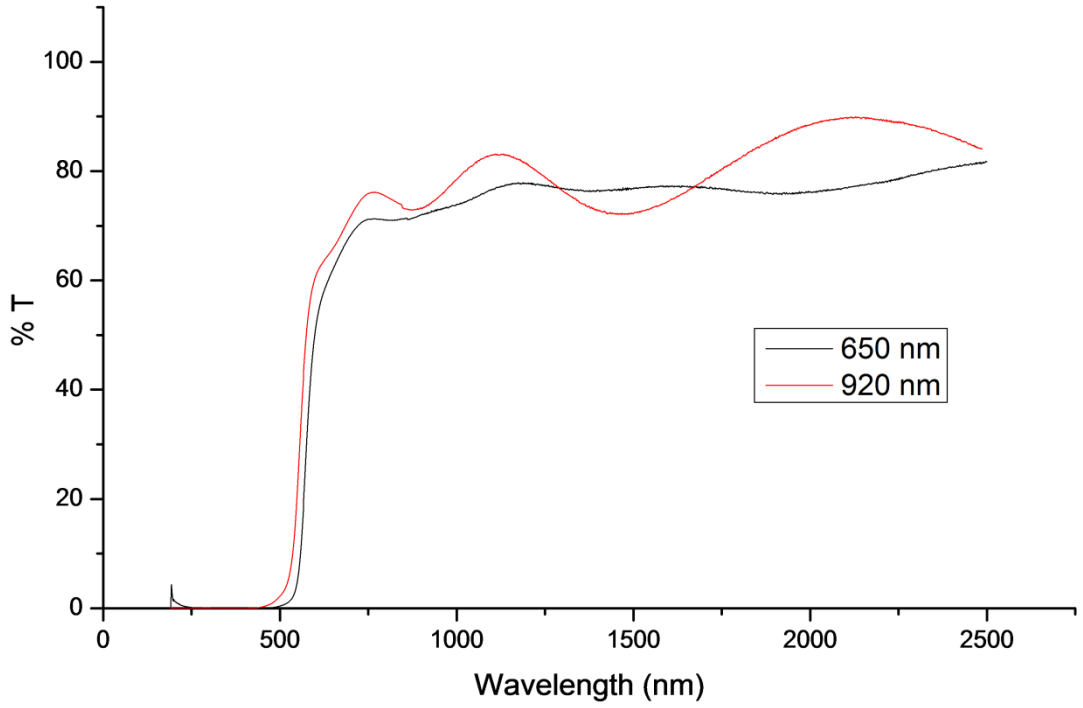

Figure 104: UV-Vis (transmission) spectra of $BiFeO_3$ films deposited *via* LPCVD with different thicknesses.

The direct band-gaps of the films were subsequently calculated *via* a Tauc plot[172] from converting the transmission data into absorbance *via* the Beer-Lambert Law (Figure 105). Band-gaps for all samples were found to be in the range of 1.9 – 2.3 eV. The additional edge for the film of 920 nm thickness could be extrapolated to the *x*-axis at 1.7 eV and could be due to the presence of the (visually darker) Fe_2O_3 phase present. The film deposited at 450 °C was dark purple in appearance due to the sole presence of Fe_2O_3 and therefore this sample absorbed a large percentage of the light and transmitted less through. The band-gap values recorded for the films (containing $BiFeO_3$) were therefore in the range 2.0 – 2.3 eV and are in good agreement with values in the literature, where it has been reported that the thickness of films of $BiFeO_3$ have a considerable effect on the band-gap of the material and appear to differ from the bulk.[216] Indeed, the fact that the band-gap range is in the visible portion of the electromagnetic spectrum, coupled with recent work investigating the photocatalytic behaviour of $BiFeO_3$ powders, the films deposited in this study may offer potential as photocatalysts under visible light irradiation.

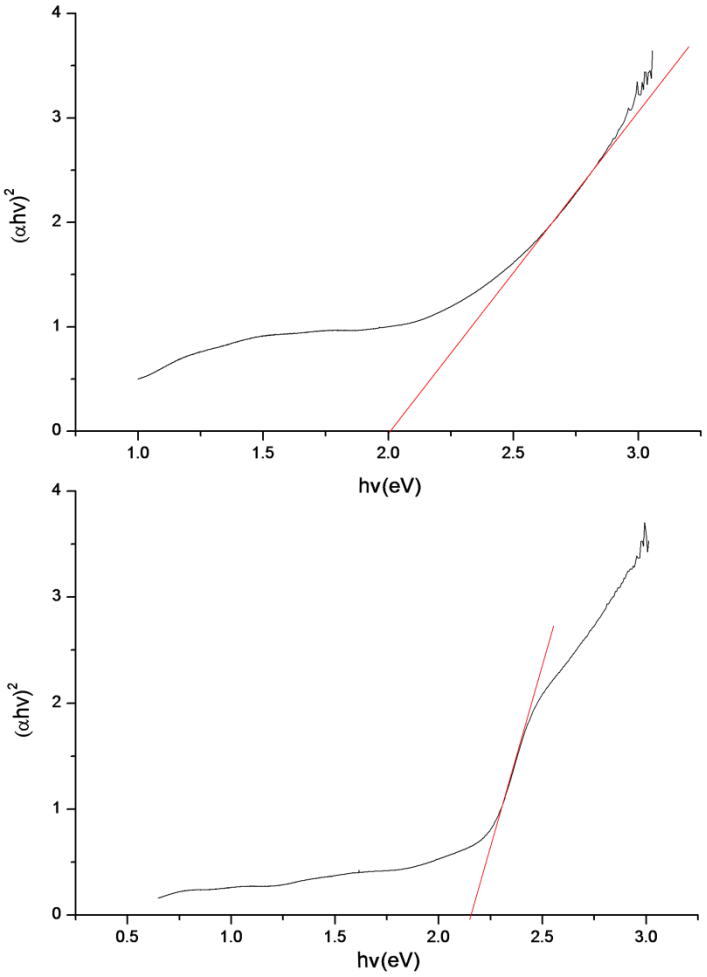

Figure 105: Tauc plot for the two $BiFeO_3$ films with different thicknesses; 650 nm (top), 920 nm (bottom).

6.6 Photocatalysis

The films deposited at 550 °C (Table 11) that were of differing thicknesses (650 nm and 920 nm), which also possessed slightly differing band-gaps (2.0 and 2.2 eV) were selected for an investigation into their photocatalytic properties *via* the photo-oxidation of water, the experimental setup of which was described in more detail in Chapter 4. A sacrificial electron acceptor solution (32 cm^3) composed of 0.1M KOH and 0.01 M $Na_2S_2O_8$ was again used, however a simulated solar light (75 W Xenon lamp, Photon Technology International, UK) with a 420 nm cut-off filter served as the light source. Each film was cut into a square piece measuring approximately 1 cm x 2 cm and suspended from a rubber septum over the solution using a hook. As a control, each sacrificial solution was irradiated with the light source at a distance of 100 mm for 30 minutes prior to insertion of each thin film. As expected, no oxygen evolution was detected by the oxygen electrode for the control sample.

Each film was suspended in the solution and irradiated with the light source for approximately 70 minutes. A graph plotting voltage *vs*. time for the two samples is shown in Figure 106.

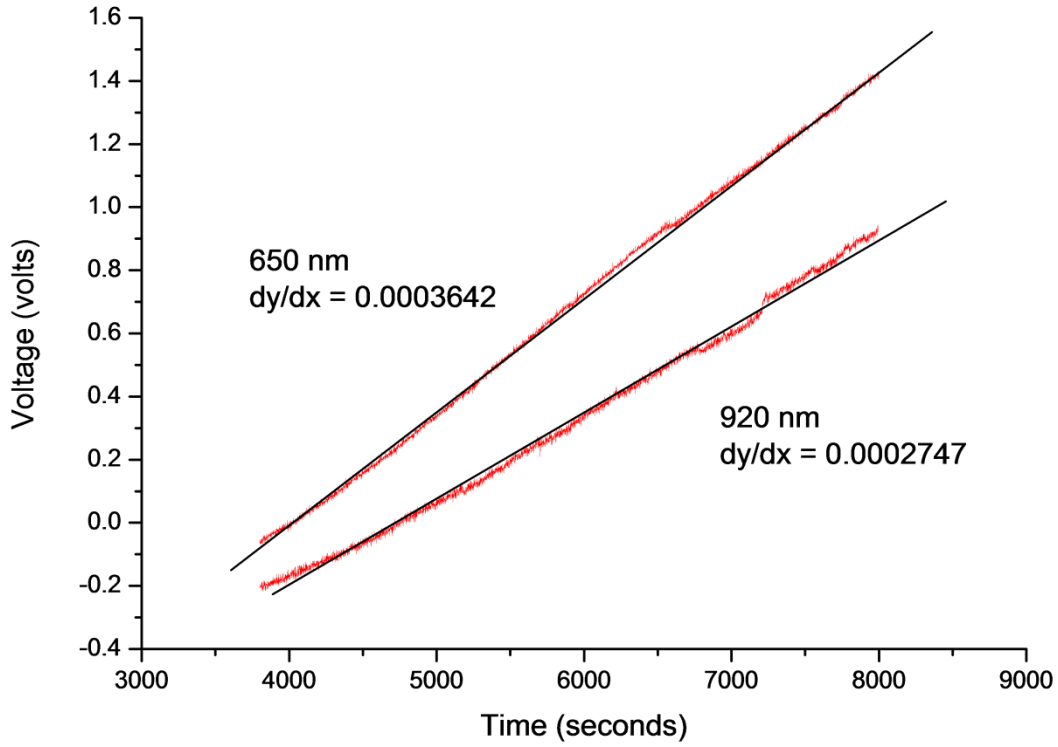

Figure 106: Plots of voltage against time measured during the photo-oxidation of water for two $BiFeO_3$ films of 650 nm and 920 nm thicknesses. The gradient of the slope is used to calculate the amount of oxygen produced.

The photocatalysis results are summarised in Table 12. For a 1 m^2 sample, the results of the 2 cm^2 sample were multiplied by a factor of 5000, which shows the oxygen evolution if one were to assume that we have a 1 m^2 film whose coverage, thickness and reaction rate were the same as those tested. This conversion was performed in order to compare the photoactivity of these films with TiO_2 films of different thickness tested previously using the same photocatalysis experiment, albeit under UV-light.

Table 12: Summary of the individual film properties and the rate of oxygen production for the two films chosen.

Film Thickness / nm	Band-gap / eV	Rate of O_2 production / µmol h^{-1} (for 2 cm^2 sample)	Rate of O_2 production / µmol h^{-1} m^{-2}	No. Of incident photons (420 nm up to band-gap of film)	Molecules of O_2 formed per second (for 2 cm^2 sample)	Quantum efficiency / %
650	2.0	4.13	20700	3.7×10^{17}	8.9×10^{14}	0.96
920	2.2	3.12	15600	2.4×10^{17}	5.2×10^{14}	0.86

The rate of oxygen production observed for the two chosen samples irradiated with solar irradiation and a 420 nm filter were 1-2 orders of magnitude higher than those obtained from the use of anatase films deposited on glass *via* APCVD (360 – 2820 µmol h^{-1} m^{-2}) using a 365 nm UV-light source.[175] They were also of the order of the results obtained for optimised TiO_2 (rutile) films grown on titanium substrates sputtered with platinum metal on the reverse (14400 - 22800 µmol h^{-1} m^{-2}) investigated in the same paper, and similar to optimised silver-gold incorporated mixed phase TiO_2 (anatase and rutile) films grown *via* sol-gel processing onto titanium substrates, sputtered with Pt on the reverse and irradiated with UV-light (highest film activity was ca. 22700 µmol h^{-1} m^{-2}). Recently, optimised rutile films deposited onto titanium substrates *via* AP- and AACVD, sputtered with Pt on the reverse displayed high photoactivities of (ca. 48500 µmol h^{-1} m^{-2} for the best performing sample) using an identical sacrificial solution, but again under UV-light irradiation.[217]

The quantum efficiencies for the two samples were estimated using the number of incident photons of the light source and the number of oxygen molecules evolved for the 2 cm^2 sample. By measuring the spectral output of the lamp, the number of incident photons per second was estimated to be 3.7×10^{17} photons/second using photon energies between 420 – 620 nm, which is dictated by the cut-off filter at 420 nm and the band-gap of the 650 nm thick $BiFeO_3$ film (2.0 eV, 620 nm). Likewise, the film of 920 nm thickness utilised photons in the 420 – 560 nm range, equating to 2.4×10^{17} photons/second. Photons of wavelengths greater than 620 nm or 560 nm do not have sufficient energy to promote an electron from the valence to the conduction band, and were therefore not included in the calculations. Therefore the apparent quantum efficiencies were calculated to be 0.96% and 0.86%, assuming that each photon may promote one electron from the valence to the conduction band and that overall the oxidation of water is a four electron process. For comparison, quantum efficiencies for photo-oxidation of water using Bi_2O_3 films synthesised *via* LPCVD and using an identical sacrificial solution but photo-

irradiated with a 16 W 365 nm UV-light source were in the range of 10 – 25%. The comparatively lower efficiencies calculated in this study are due to the relatively higher photon energies of the solar simulator lamp over the range 420 – 620 nm compared to a monochromatic 16 W 365 nm UV lamp. The calculation of an apparent quantum efficiency is itself not without some limitations, and these were described in Chapter 3. The main limitation is that it fails to take account of sample volume or weight. For our highest oxygen producing sample which has a thickness of 920 nm, its volume is 920 nm x 1 cm x 2 cm, equating to a volume of 1 $x10^{-10}$ m^3. Taking the density of $BiFeO_3$ as 8340 kg m^{-3}, the mass of sample present would be approximately 1.53 μg. Clearly this is a small amount of sample even if the surface area is maximised due to its existence as a thin film. Therefore this makes it difficult to compare quantum efficiencies with those reported in the literature which are almost always given for powder (bulk) samples.[152] It is interesting to note however that the oxygen evolution rate decreases as the film thickness and band-gap increases.

These $BiFeO_3$ films have been demonstrated to possess high visible-light photocatalytic activities for the often difficult four-electron process of photo-oxidation of water, and have not yet, as carried out in other reports for TiO_2,[175,217,176] been optimised for thickness nor been utilised in conjunction with a co-catalyst. The deposition of these $BiFeO_3$ films onto such metal substrates, in conjunction with coating the reverse with Pt could further enhance their photocatalytic activity as the metal barrier would allow electron transfer to Pt layer which would act as an electron sink, promoting charge carrier separation. The high activity for $BiFeO_3$ is perhaps not surprising given the relatively positive valence and conduction band levels of $BiFeO_3$ and its position with respect to the redox potentials of water (Figure 107). Studies using bulk $BiFeO_3$ have also led to the same findings for photo-oxidation of water (lower oxygen production of 0.5 μmol h^{-1}) using an aqueous $FeCl_3$ sacrificial electron acceptor solution,[218] however since these reports utilise bulk material, different sacrificial solutions and light sources, comparison of their photocatalytic data with ours is difficult. Several authors have also used $BiFeO_3$ as a photosensitiser in conjunction with either TiO_2[149] or $SrTiO_3$[142] for enhanced visible light photocatalysis and even for hydrogen production from water.

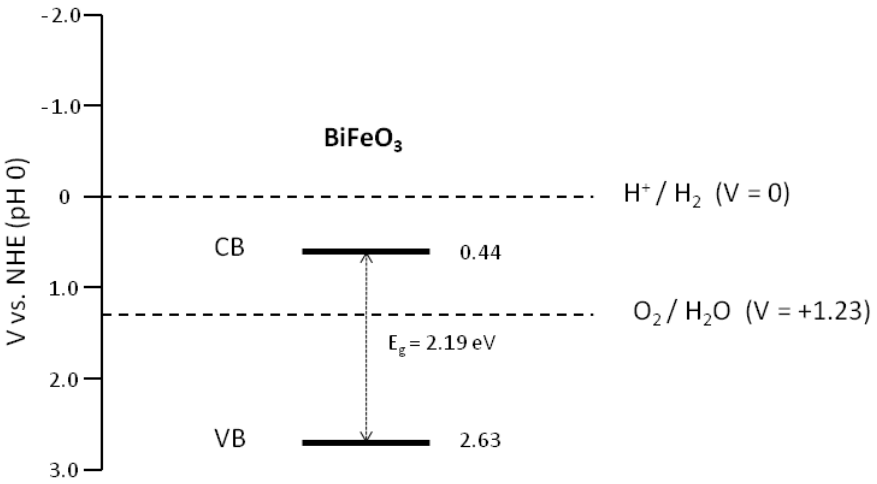

Figure 107: Band diagram of $BiFeO_3$ with respect to the redox potentials of water splitting at pH 0.

6.7 Conclusions

Preliminary studies using $[Fe(acac)_3]$ as a single-source precursor to iron oxide films resulted in dark films due to high levels of carbon contamination from the precursor. The addition of air as an oxidising gas removed the majority of the carbon contamination, resulting in α-Fe_2O_3 films of a purple-red appearance. The use of $[Bi(O^tBu)_3]$ together with the commercially available iron precursor $[Fe(acac)_3]$ resulted in the growth of $BiFeO_3$ films *via* LPCVD, using air as an oxidising gas. The presence of $BiFeO_3$ was confirmed *via* powder X-ray diffraction and Raman spectroscopy, and WDX analysis revealed close to 1:1 stoichiometries of bismuth and iron for optimum samples. The $BiFeO_3$ films all contained various impurity phases, notably α-Fe_2O_3, $Bi_{25}FeO_{40}$ and $Bi_2Fe_4O_9$, however films deposited at a substrate temperature of 550 °C appeared to contain the least amount of α-Fe_2O_3 in addition to $BiFeO_3$.

Magnetism experiments revealed low temperature weak ferromagnetic behaviour coupled with an expected low coercivity, whilst measurements carried out at 300 K revealed low saturation (~7.3 mu/cm^3) in agreement with theoretical values from the literature. In spite of this, an unexpected, significantly higher coercive field was also measured; the reasons for which remain unknown but may be due to the presence of impurity α-Fe_2O_3 in the sample. Ferroelectric polarisation measurements carried out on films deposited on platinised silicon substrates revealed a low spontaneous polarisation of ~ 1.5 $\mu C/cm^2$ and remnance between 1 – 1.5 $\mu C/cm^2$.

A refractive index of 2.3 and direct band-gaps between 2.0 - 2.3 eV were calculated for the $BiFeO_3$ films using transmission spectra, which were in good agreement with literature values. Two films were subsequently chosen for an investigation into their photocatalytic properties for the photo-oxidation of water under visible light irradiation. Due to the relatively positive conduction level of $BiFeO_3$, and for that matter, Fe_2O_3, both films displayed appreciably high oxidation rates that were either higher or of the same order of magnitude as those obtained from optimised TiO_2 films investigated using the same photocatalysis conditions, but under UV excitation.

7 Dual-source low pressure CVD of bismuth ferrite

7.1 Introduction

In the previous chapter $BiFeO_3$ films were grown *via* LPCVD using $[Fe(acac)_3]$, $[Bi(O^tBu)_3]$ and air as precursors and reactive gas respectively. It was found that despite the introduction of an oxidising gas, the resultant films were not phase-pure. This chapter examines the dual-source LPCVD of multiferroic $BiFeO_3$ thin films, using the ligand-matched precursors $[Bi(O^tBu)_3]$ and $[Fe(O^tBu)_3]_2$ without the use of an oxidising gas, on glass and silicon substrates. The excess of oxygen in the coordination sphere in both complexes may be sufficient to not require the use of an oxidising gas for growth of fully oxidised, phase-pure $BiFeO_3$ films. The resultant films were characterised fully and two samples were selected for an investigation into their photocatalytic properties through the photo-oxidation of water under visible light irradiation.

7.1.1 Precursor synthesis

Bismuth(III) *tert*-butoxide, $[Bi(O^tBu)_3]$, was synthesised according to the literature *via* the metathesis reaction of $BiCl_3$ and three equivalents of NaO^tBu as described in Chapter 2.[67]

Iron(III) *tert*-butoxide, $[Fe(O^tBu)_3]_2$, was synthesised using a modified literature preparation *via* the metathesis reaction between anhydrous $FeCl_3$ and three equivalents of NaO^tBu as described in Chapter 2.[158]

7.1.2 TGA

The decomposition characteristics of $[Bi(O^tBu)_3]$ and $[Fe(O^tBu)_3]_2$ were analysed *via* TGA (Figure 108) and are described in order to compare and contrast their decomposition and to identify suitable deposition conditions.

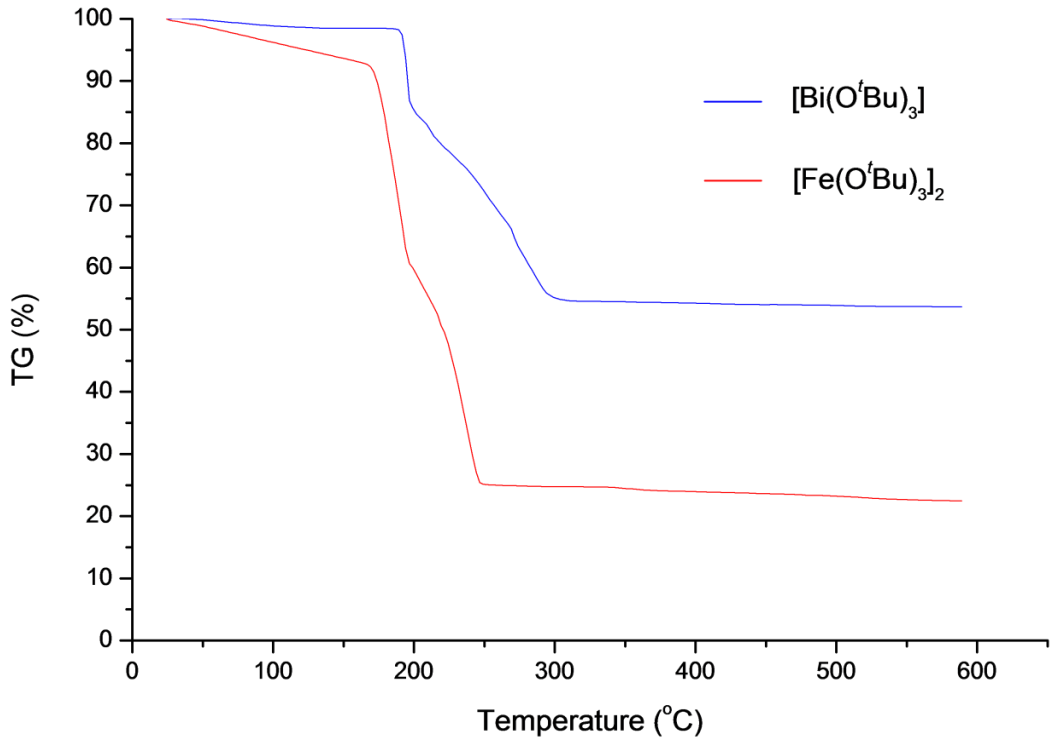

Figure 108: TGA trace of $[Fe(O^tBu)_3]_2$ and $[Bi(O^tBu)_3]$. The heating rate was 10 °C min^{-1}.

The TGA trace of $[Bi(O^tBu)_3]$ represents a two-stage mass loss between approximately 200 – 300 °C, followed by virtually no further mass loss to the end of the experiment at 600 °C. As described in Chapter 3, the melting point, represented by an exotherm in the DSC data, was found to be 159 °C. The first mass loss between 190 – 210 °C was ascribed to precursor evaporation and this was confirmed by the small endotherm in the DSC trace at approximately 200 °C; overall the fraction of weight loss during decomposition after accounting for evaporation was 44%, with the theoretical mass loss required for conversion to Bi_2O_3 being 46%. For $[Fe(O^tBu)_3]_2$, a three stage decomposition profile was obtained, with the mass loss between 160 – 190 °C (32%) most likely to have occurred as a result of evaporation, as evidenced by the small signal in the DSC trace (not shown) that was detected shortly after the melting temperature at 157 °C. Prior to this, a mass loss of 6.5% was believed to be due to premature precursor decomposition. The final mass loss of 37% was attributed to decomposition, and therefore the fraction of weight loss observed during decomposition was 63% (43% mass loss from a total of 68%, corrected for volatilisation). The expected mass loss required to form Fe_2O_3 as the sole product of decomposition is 71%, which is slightly more than the weight loss recorded, however other iron containing species may have been present in the pan after the experiment.

7.1.3 Vapour pressures

An appreciable volatility is an important property of a precursor for LPCVD, and therefore the vapour pressure curves of $[Fe(O^tBu)_3]_2$ and $[Bi(O^tBu)_3]$ were plotted using the following vapour pressure equations:[164]

$[Bi(O^tBu)_3]$: $\log_{10} P$ (mmHg) = 13.11 – 5010/T (K)

$[Fe(O^tBu)_3]_2$: $\log_{10} P$ (Pa) = 18.46 – 5949/T (K)

The vapour pressure data for $[Fe(O^tBu)_3]_2$ was obtained from a 10 g sample sent to SAFC Hitech Ltd, and was plotted in units of mmHg by using the conversion factor 1Pa = 0.0075 mmHg (Figure 109).

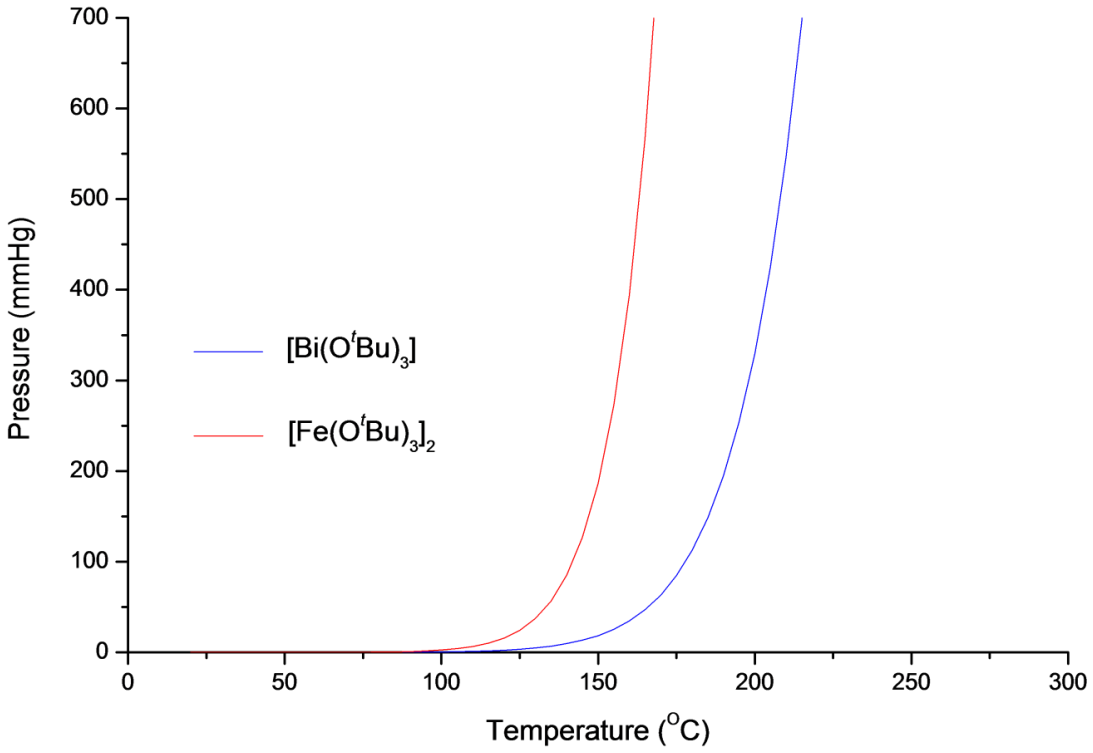

Figure 109: Vapour Pressure curves of $[Fe(O^tBu)_3]_2$ and $[Bi(O^tBu)_3]$.

Analysis of the vapour pressure curve of $[Fe(O^tBu)_3]_2$ reveals a relatively high vapour pressure of 2.43 mmHg at a temperature of 100 °C which could correlate to some part of the mass loss (6.5%) found in the TGA trace prior to the ascribed onset of evaporation and decomposition. For comparison, the vapour pressure of the previously utilised iron β-diketonate precursor, $[Fe(acac)_3]$, was 1.48 x 10^{-3} mmHg at 100 °C (Chapter 6) and therefore possesses a far inferior volatility in comparison to $[Fe(O^tBu)_3]_2$. The vapour pressure of $[Bi(O^tBu)_3]$ at this temperature is lower than $[Fe(O^tBu)_3]_2$ at 0.48 mmHg, however due to the nature of the matching ligands in

both precursors and their known ability to serve as single-source precursors to their respective metal oxides,[158,182] they were chosen as potential precursors to $BiFeO_3$ films without the use of a reactive (oxidising) gas.

7.2 CVD

The low pressure CVD apparatus used for this investigation was identical to that used for the LPCVD of $BiFeO_3$ films, grown using $[Fe(acac)_3]$, $[Bi(O^tBu)_3]$ and air, described in Chapter 6. Nitrogen (99.96%) was obtained from BOC and used as a carrier gas as supplied. A base pressure of 2×10^{-3} mbar was achieved before use, to ensure as far as possible that no air and moisture remained in the system. The total reactor pressure was maintained at 7 mbar to begin with *via* the use of a mechanical throttle valve, and then later increased to 15, 30 and 45 mbar. Each deposition was carried out for 1 hour. Films were deposited on borosilicate glass microscope slides (3 cm x 2 cm) and silicon wafers. For ferroelectric measurements, the silicon wafers were sputtered for 180 seconds with a thin layer of platinum (argon pressure 0.1 torr, current 25 mA) prior to use.

For deposition of $BiFeO_3$ films, a 2:1 molar ratio of Bi:Fe precursor was utilised as $[Fe(O^tBu)_3]_2$ exists as a dimer. 230 mg (0.54 mmol) of $[Bi(O^tBu)_3]$ was used for each deposition and the bubbler temperature was set at 110 °C (V_p = 1.1 mmHg). 150 mg of $[Fe(O^tBu)_3]_2$ (0.27 mmol) was used as the iron source and the bubbler temperature set to 100 °C (V_p = 2.4 mmHg). Nitrogen (50 sccm) was used as the carrier gas through both precursors. No oxidising gas or air was employed; however a plain line flow of nitrogen (50 sccm) was used during all depositions. The LPCVD reaction of $[Fe(O^tBu)_3]_2$ and $[Bi(O^tBu)_3]$ resulted in films of pure-phased, multiferroic $BiFeO_3$ only at a substrate temperature of 550 °C. Impurity phases were observed at lower and higher deposition temperatures, most notably composed of parasitic phases Bi_2O_3, $Bi_{24}Fe_2O_{39}$ and $Bi_2Fe_4O_9$ in addition to the presence of $BiFeO_3$. All films displayed good coverage, and were red-orange in colour and could not be removed *via* tissue or scotch tape, but were scratched with a steel stylus. In contrast to films deposited using $[Bi(O^tBu)_3]$ and $[Fe(acac)_3]$ described in Chapter 6, the films deposited in this investigation were found to be insulating, therefore carbon contamination could not be found *via* WDX as films had to be carbon coated for analysis. The deposition conditions are summarised in Table 13.

.

7.3 Results and discussion

Table 13: Deposition conditions for fabrication of $BiFeO_3$ thin films *via* the LPCVD reaction of $[Bi(O^tBu)_3]$ and $[Fe(O^tBu)_3]_2$ without an oxidising gas.

Substrate Temp / °C	Total Reactor Pressure / mbar	Bismuth source carrier gas flow rate / sccm	Iron source carrier gas flow rate / sccm	N_2 plain line gas flow rate / sccm	Phase(s) obtained *via* XRD	Thick-ness / nm	Band-gap / eV	At. % Bi:Fe (from WDX)
450	8	50	50	50	$Bi_2Fe_4O_9$ + Bi_2O_3	230	-	24:76
475	8	50	50	50	$Bi_2Fe_4O_9$ + $Bi_{24}Fe_2O_{39}$	470	-	16:84
500	8	50	50	50	$BiFeO_3$ + $Bi_{24}Fe_2O_{39}$	600	2.2	34:66
525	8	50	50	50	$BiFeO_3$ + $Bi_{24}Fe_2O_{39}$	640	2.0	39:61
550	8	50	50	50	$BiFeO_3$	880	2.2	47:53
575	8	50	50	50	$BiFeO_3$ + $Bi_{24}Fe_2O_{39}$	210	2.2	45:54
550	**15**	50	50	50	$BiFeO_3$ + $Bi_2Fe_4O_9$	940	2.0	54:45
550	**30**	50	50	50	$BiFeO_3$ + $Bi_2Fe_4O_9$	1200	2.3	58:41
550	**45**	50	50	50	$BiFeO_3$ + $Bi_2Fe_4O_9$	1450	2.3	36:63

Films deposited above 500 °C contained $BiFeO_3$ amongst other impurity phases. Those deposited below this temperature were mainly comprised of $Bi_2Fe_4O_9$ and $Bi_{24}Fe_2O_{39}$ from XRD analysis, however WDX measurements revealed them to be compositionally rich in iron compared to bismuth. Compositional analysis of the film deposited at 500 °C revealed a slight

increase in bismuth incorporation as it contained a bismuth to iron ratio of 34:64 at.%, and the film deposited at 525 °C saw a further increase in bismuth content (39:61 at.% Bi:Fe). The film deposited at 550 °C was found to contain virtually no impurity phases *via* XRD analysis and possessed a Bi:Fe ratio close to 1:1 (47:53 at.% Bi:Fe), close to what one would expect for $BiFeO_3$. The film deposited at 575 °C possessed a similar atomic ratio of the two elements however some impurity $Bi_{24}Fe_2O_{39}$ phase was observed. Its thickness was also much lower, most likely due to premature thermal decomposition of the precursors before arrival onto the substrate. Upon increasing the total system pressure, the presence of $BiFeO_3$ was maintained, although significant impurity $Bi_2Fe_4O_9$ was observed in all films deposited at higher pressures. This observation was not all that surprising given the fact that the complex kinetics of the Fe_2O_3-Bi_2O_3 system can easily lead to co-existence of $Bi_2Fe_4O_9$ and $BiFeO_3$, and that $Bi_2Fe_4O_9$ is a kinetically stable phase.[219,220] Compositional analysis revealed the optimum bismuth to iron ratio of almost 1:1 was incorporated by the film deposited at a pressure of 30 mbar, whereas the film deposited at 45 mbar contained more amorphous material and was compositionally rich in iron (36:63 at.% Bi:Fe ratio), suggesting that higher pressures were either inhibiting formation of (crystalline) $BiFeO_3$ or allowing preferential deposition of iron containing species.

7.3.1 Film growth rates

Film thicknesses, measured *via* side-on SEM imaging, in general increased as a function of substrate temperature, apart from the film deposited at 575 °C which exhibited a large reduction in thickness due to partial decomposition of the precursor(s) on the inner reactor walls. The film growth rates were therefore *ca.* 230 nm, 470 nm, 600 nm, 640 nm, 880 and 210 nm hr^{-1} at substrate temperatures of 450, 475, 500, 525, 550 and 575 °C respectively, and a fixed/constant growth rate over the substrate temperature range was not observed (Figure 110). Upon increasing the total system pressure, film thicknesses increased dramatically from 880 nm at 8 mbar to 1450 nm for the film deposited at 45 mbar. At low pressures the rate of mass transport of gaseous precursors is higher than the surface reaction rate during the deposition (i.e. the process is surface rate limited),[1] but as the pressure increases gas phase reactions become more important and a significant boundary layer is present above the substrate.[221] At higher pressures, as in APCVD, the reaction is mass transport limited.

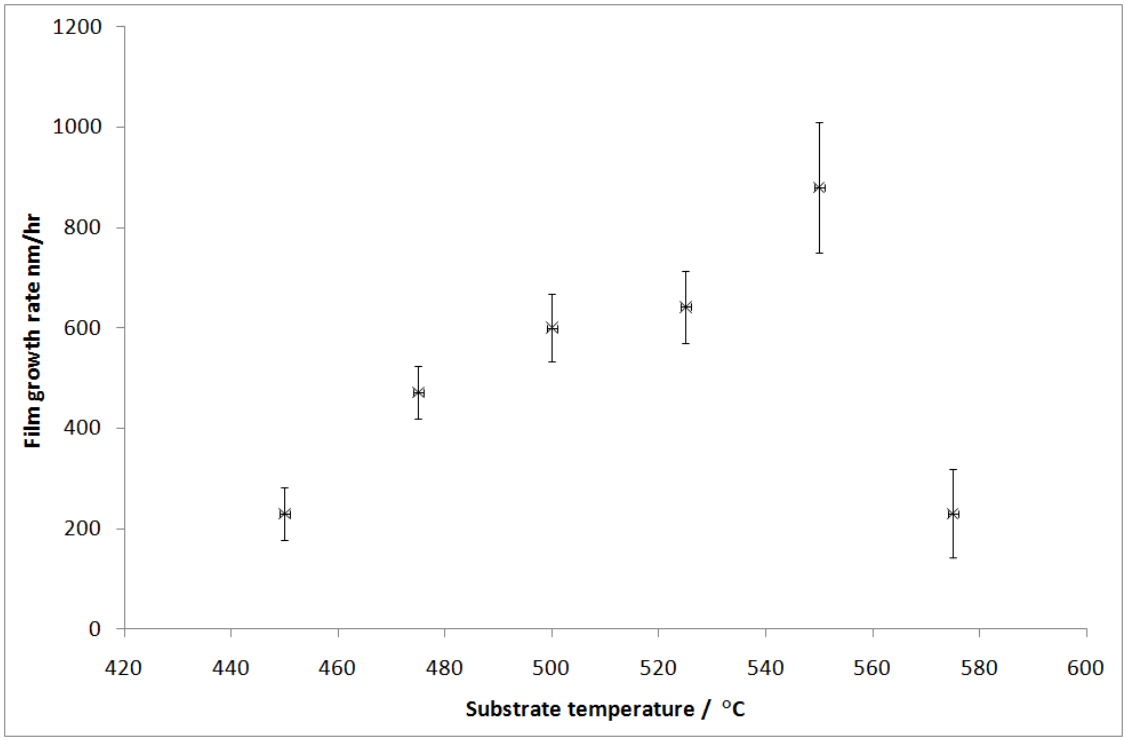

Figure 110: Film growth rates as a function of substrate temperature.

7.3.2 X-ray diffraction

Films deposited at 450 °C and 475 °C mbar contained no crystalline $BiFeO_3$ phase from X-ray diffraction analysis, and instead were found to contain only $Bi_2Fe_4O_9$ and $Bi_{24}Fe_2O_{39}$, with potentially some Bi_2O_3 incorporation in the film deposited at 450 °C (Figure 111). In light of the following discussion on the effect of increasing the reaction temperature on the phase obtained, the substrate temperature in *this* case would appear to be too low for formation of $BiFeO_3$, however fine adjustment of the precursor mixing ratios may be able to permit $BiFeO_3$ growth at this temperature.[222] Increasing the temperature to 500 °C resulted in some evidence of $BiFeO_3$ growth. At 525 °C, some $BiFeO_3$ phase along with impurity $Bi_{24}Fe_2O_{39}$ was observed; however in comparison, the relative peak intensities for the impurity phase have decreased and it is clear that $BiFeO_3$ was the dominant phase. At a substrate temperature of 550 °C, pure $BiFeO_3$ was observed *via* X-ray diffraction and the Bi:Fe ratio found *via* WDX analysis was close to unity (47:53). Again, this suggests that the temperature growth window for formation of $BiFeO_3$ was narrow, but at 550 °C the temperature was high enough to inhibit formation of crystalline impurity phases. This is reinforced by the observation that $BiFeO_3$ is prone to parasitic phases that nucleate at grain boundaries and defects, along with the postulation that $BiFeO_3$ may be metastable in air.[107] The Bi_2O_3-Fe_2O_3 phase diagram has recently been constructed with the addition of parasitic $Bi_{25}FeO_{39}$ (generalised formula) and $Bi_2Fe_4O_9$ phases.[204] At a substrate temperature of 575 °C, $BiFeO_3$ was observed as the dominant

phase albeit with some contamination from $Bi_{24}Fe_2O_{39}$, which was surprising as this would imply that the film was bismuth-rich according to the aforementioned phase diagram. The discrepancy here may be due to the common problem of bismuth evaporation at high temperatures, and compositional analysis from WDX analysis (45:54 at.% Bi:Fe) would agree with this hypothesis.

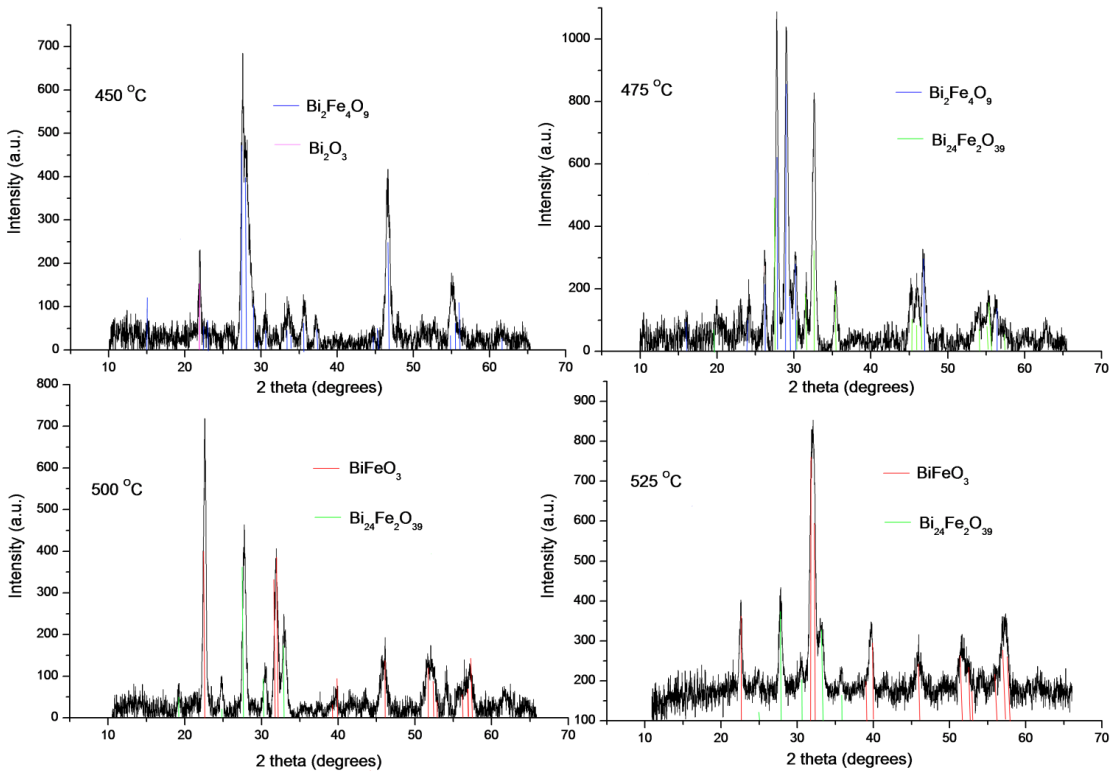

Figure 111: X-ray diffraction patterns of films deposited between 450 - 525 °C.

The presence of $BiFeO_3$ free of Bi_2O_3, Fe_2O_3 or parasitic phases $Bi_{24}Fe_2O_{39}$ and $Bi_2Fe_4O_9$ was confirmed *via* X-ray diffraction for the film deposited at 550 °C and is displayed in Figure 112. Hexagonal unit cell parameters of $a = b = 5.58$ (2) Å, $c = 13.90$ (1) Å, ($\alpha = \beta = 90°$, $\gamma = 120°$, space group $R3c$) were obtained *via* unit cell refinement and are in agreement with literature values for bulk $BiFeO_3$ found *via* synchrotron X-ray diffraction ($a = b = 5.57414$ (4) Å, c = 13.85882 (6) Å, PDF = 014-0181).[205] The presence of other crystalline impurities in the film is unlikely based on X-ray diffraction analysis – if there were any clear phases present then their intensities are too low for any meaningful phase identification.

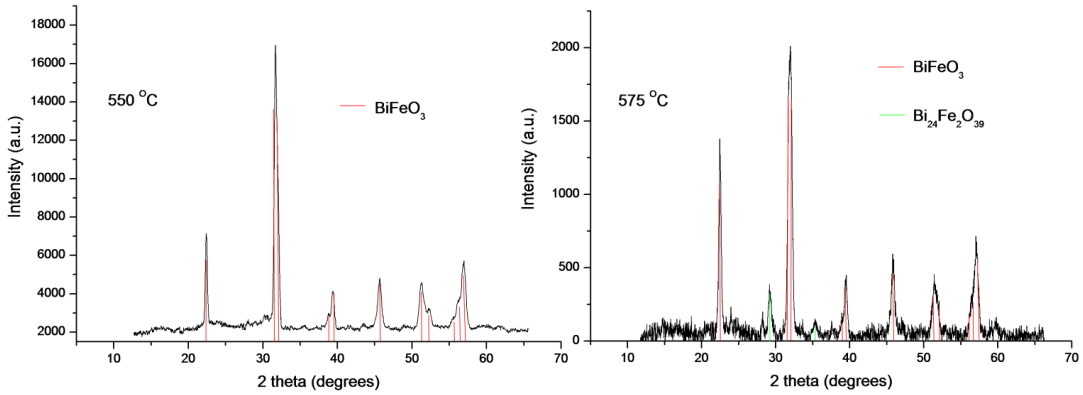

Figure 112: X-ray diffraction patterns of the films deposited at 550 °C and 575 °C at 8 mbar.

Upon increasing the system pressure, films increased in thickness however X-ray diffraction (Figure 113) revealed them to consist of more amorphous material and the peak intensities corresponding to crystalline $BiFeO_3$ appeared to decrease as a function of pressure. It was evident that more impurity $Bi_2Fe_4O_9$ phase was incorporated into the films deposited at higher pressures, therefore the optimum conditions for $BiFeO_3$ in this system would appear to be at a substrate temperature of 550 °C and a system pressure of 8 mbar.

It was found that the growth of $BiFeO_3$ films *via* this dual-source approach only occurred within a limited pressure and temperature range. Tyholdt *et al.* have demonstrated the use of bismuth and iron 2-methoxyethoxides, synthesised by the alcoholysis reaction of the individual metal *tert*-butoxides $[Bi(O^tBu)_3]$ and $[Fe(O^tBu)_3]_2$ with 2-methoxyethanol, for growth of $BiFeO_3$ films *via* chemical solution deposition.[203,223] Phase-pure films were grown following annealing at 500 and 600 °C in air. The authors reiterate the complexity of the phase relationship between $BiFeO_3$ and $Bi_2Fe_4O_9$ and $Bi_{25}FeO_{40}$ ($Bi_{24}Fe_2O_{39}$), whereby the formation of $Bi_{25}FeO_{40}$ occurred at 250 °C and was present up to 500 °C; despite the formation of $BiFeO_3$ at 550 °C not all $Bi_{25}FeO_{40}$ was lost. Additionally, $Bi_2Fe_4O_9$ formation was found to commence at 580 °C. Furthermore, in a much earlier study the activation energies for formation of $BiFeO_3$ and $Bi_2Fe_4O_9$ were found to be very similar (96.6 ± 9 kcal/mol and 99.4 ± 9 kcal/mol, respectively).[224]

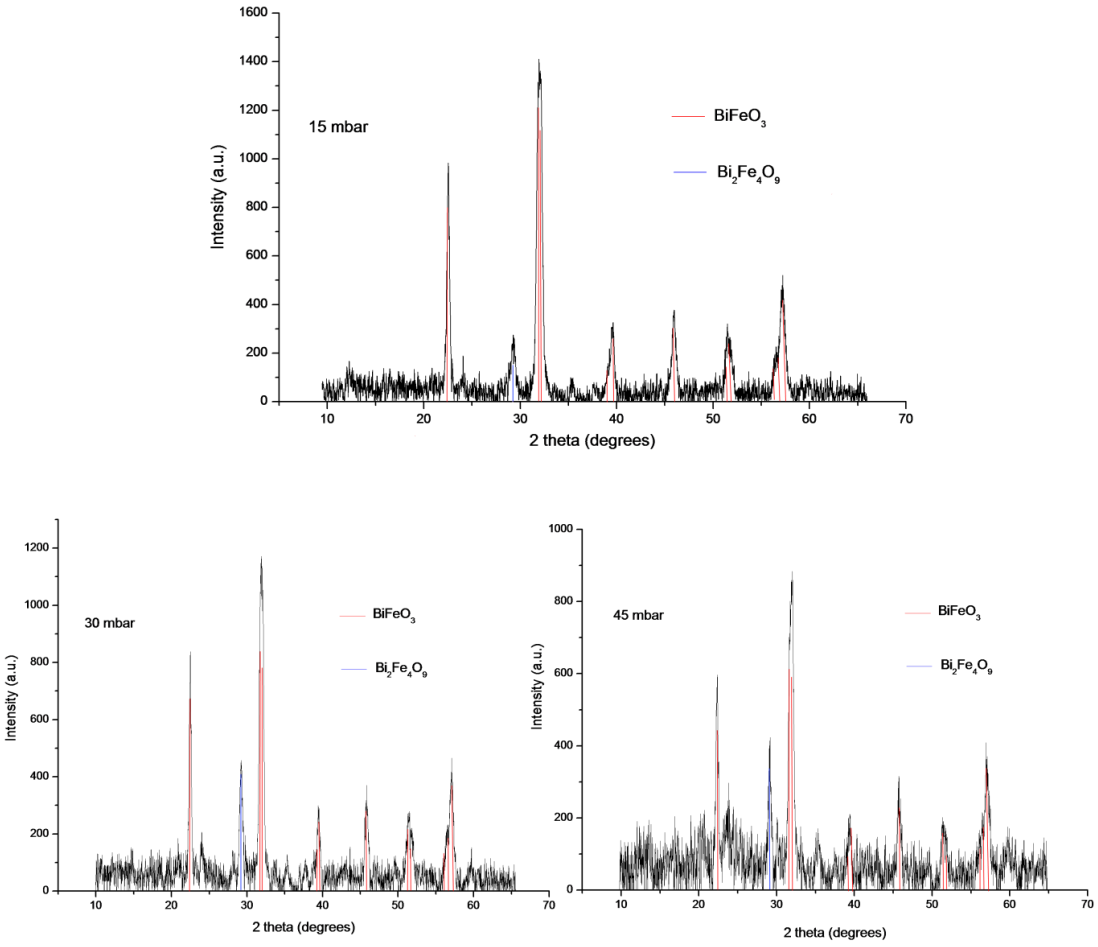

Figure 113: X-ray diffraction patterns of the films deposited at 15 mbar, 30 mbar and 45 mbar.

7.3.3 Scanning electron microscopy

The morphologies of the films were investigated using top-down SEM. Figure 114 shows the morphologies of the as-deposited $BiFeO_3$ films as a function of substrate temperature.

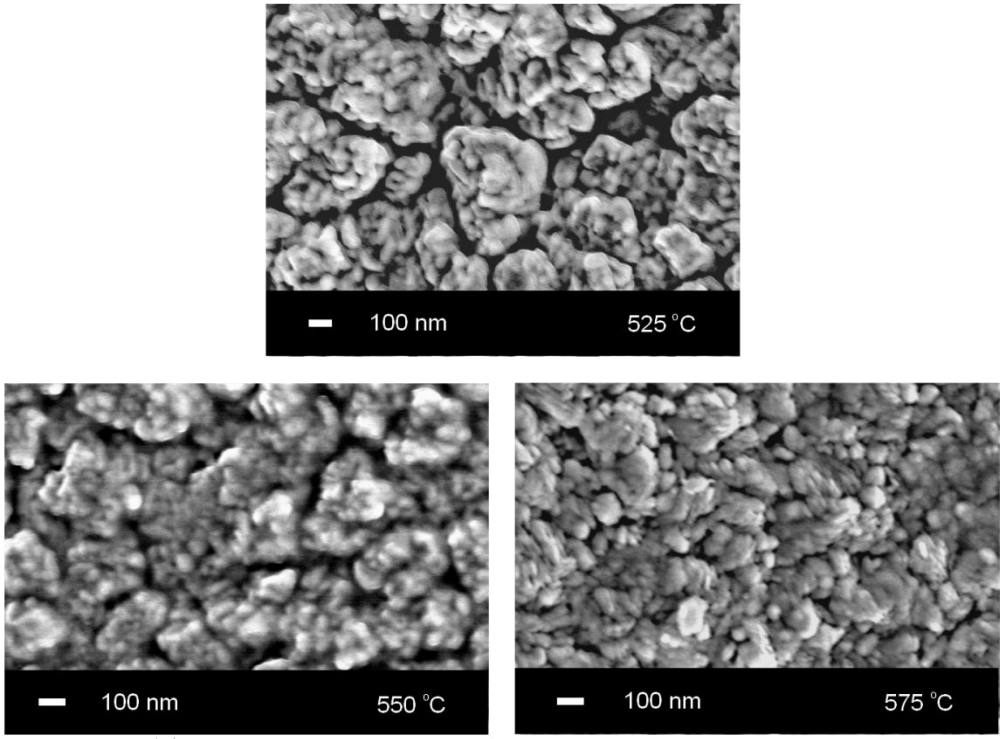

Figure 114: Top-down SEM images of $BiFeO_3$ films deposited from the LPCVD reaction of $[Bi(O^tBu)_3]$ and $[Fe(O^tBu)_3]_2$ as a function of substrate temperature.

Figure 114 shows the morphologies of the films deposited at 525, 550 and 575 °C. The morphologies are slightly globular or cluster-like in appearance with some voids observed at 525 °C; nevertheless the packing of the particles is fairly dense and uniform. Upon increasing the substrate temperature to 550 °C the morphology appeared dense and was consistent with that observed at 525 °C, albeit with fewer features. The morphology of the film deposited at 575 °C appeared more uniform and flatter with fewer voids where there was no deposition, suggesting a higher degree of coalescence or sintering between particles was taking place. It is also easier to see the size of the individual particles which were approximately 50 nm in diameter. It is difficult to distinguish the exact particle size for the (pure) $BiFeO_3$ film deposited at 550 °C *via* microscopy; however estimation of this value was determined from the broadening of the diffraction peaks (Scherrer Equation) which resulted in an average particle diameter of 25 nm. The structure of this film is quite dense with very few features and is somewhat similar in appearance to the top-down SEM image of the $BiFeO_3$ film deposited from $[Fe(acac)_3]$, $[Bi(O^tBu)_3]$ and air at 575 °C described in Chapter 6.

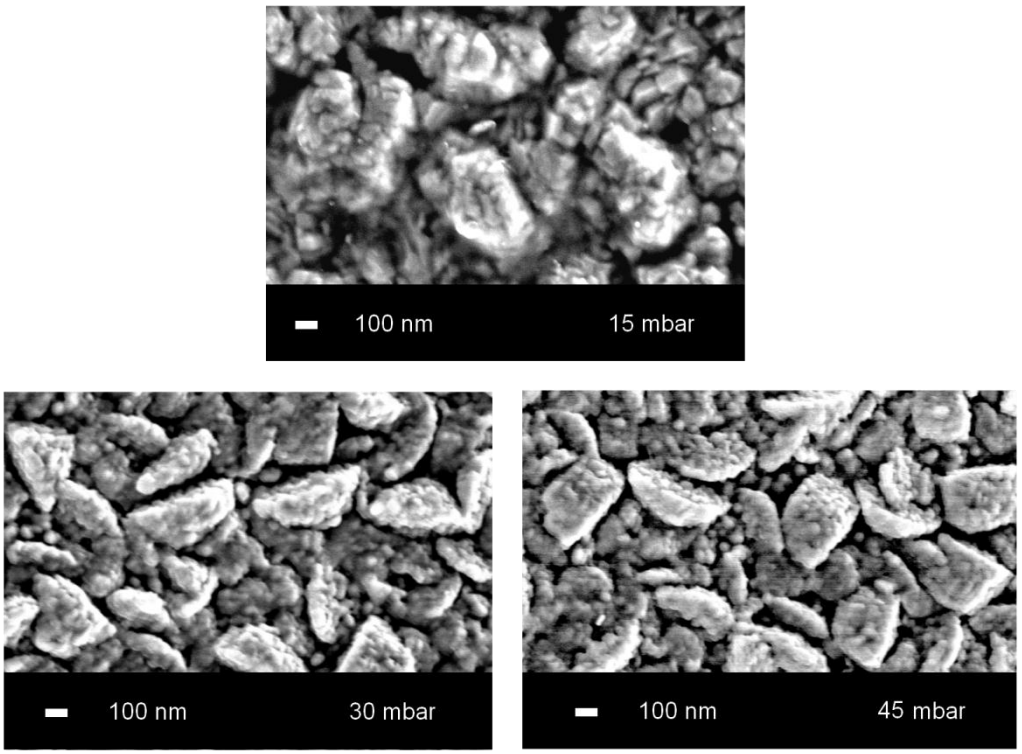

Figure 115: Top-down SEM images of $BiFeO_3$ films deposited from the LPCVD reaction of $[Bi(O^tBu)_3]$ and $[Fe(O^tBu)_3]_2$ at 550 °C as a function of total system pressure.

The morphologies of the $BiFeO_3$ films as a function of total system pressure, all deposited at a substrate temperature of 550 °C, are displayed in Figure 115. At a pressure of 15 mbar the morphology has a dense, globular appearance and is similar to the morphology obtained at a pressure of 8 mbar at 550 °C (Figure 114). Estimation of the average particle size using the Scherrer Equation resulted in particle diameters of 35 nm and 65 nm for films deposited at 15 mbar and 30 mbar, suggesting that the increase in reaction rate results in larger particle sizes. Upon increasing the pressure to 30 mbar, distinct crescent-shaped structures were apparent (Figure 115), which on closer inspection are composed of globular particles of approximately 50 nm diameter. The coverage is total and there are virtually no voids where deposition has not taken place. The large sized structures may be contributing to the thickness of the film, which in this case was 940 nm. Upon increasing the system pressure to 45 mbar, the crescent-shaped morphology was retained along with the small 50 nm sized particles. An increased rate of deposition is expected at higher pressures, which is reflected with the increase in film thickness and particle size, and may explain the difference in the morphologies obtained above 15 mbar. It is, however, also possible that this change in morphology may be due to the existence of increasing levels of impurity $Bi_2Fe_4O_9$ in these samples as indicated by X-ray diffraction in addition to $BiFeO_3$ which might have been caused by the increase in pressure.

7.3.4 Raman spectroscopy

In order to verify the phase purity of the $BiFeO_3$ films, the film assigned as being phase-pure by X-ray diffraction, which was deposited at 8 mbar at a substrate temperature of 550 °C, was characterised by Raman spectroscopy at room temperature (20 °C) and low temperature (-195 °C).

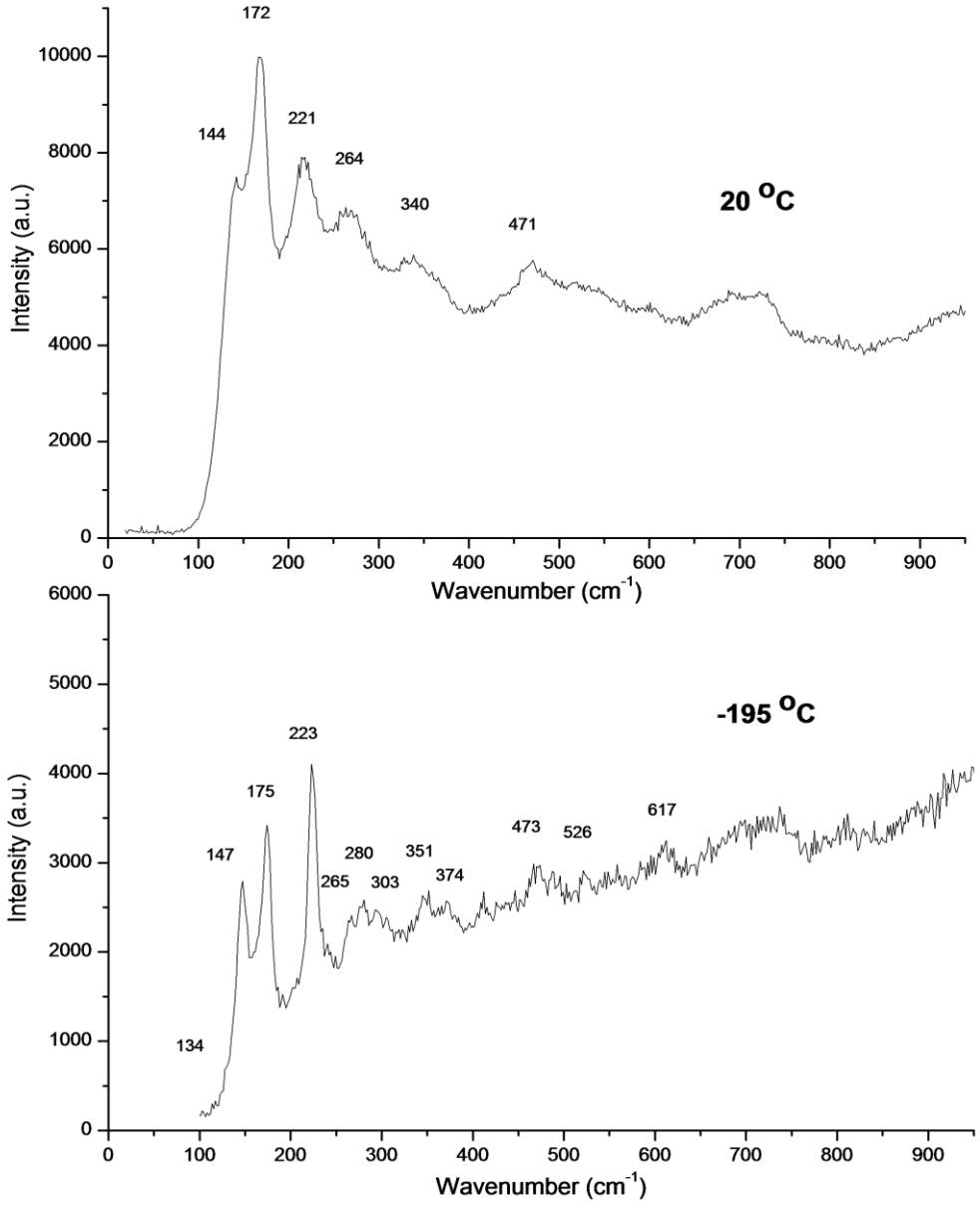

Figure 116: Raman spectra of a $BiFeO_3$ film deposited at 550 °C, 8 mbar, recorded at 20 °C (top) and -195 °C (bottom).

The room temperature Raman spectrum of the pure-phase $BiFeO_3$ film displayed a limited number of very broad peaks. For single crystal $BiFeO_3$, one would expect to observe a total of

13 peaks in the Raman spectrum due to the $4A_1$ and 9E phonon modes.[209] Raman peaks for the $BiFeO_3$ film were observed at 144, 172, 221, 264, 340 and 471 cm^{-1} of which peaks at 144, 172, 221 and 471 may be assigned to A_1 modes (Figure 116). The peak at 351 cm^{-1} was assigned to an E mode. By contrast, the Raman spectrum of the same sample recorded at -195 °C displayed many more peaks. Peaks assigned to the A_1 phonon mode were observed at 147, 175, 223 and 473 cm^{-1}, whilst peaks assigned to the E phonon mode were observed at 134, 265, 280, 351, 374, 473 and 526 cm^{-1}. Fukumura *et al.* observed a very weak E phonon mode vibration at 437 cm^{-1} in their sample, however due to the large background signal in the spectra for these $BiFeO_3$ films it was impossible to see this. Furthermore, the laser filter cut-off at 100 cm^{-1} does not allow the observation of the final E phonon vibration expected at 77 cm^{-1} to be observed. In both samples, the very broad peak at 710 cm^{-1} remained unassigned. Nevertheless peaks for other impurity phases such as Fe_2O_3 (the Raman spectrum of which is shown in Chapter 6) were not observed and the phase purity of $BiFeO_3$ in this sample was confirmed.

7.3.5 X-ray photoelectron spectroscopy

The composition of the $BiFeO_3$ deposited at 550 °C and at 8 mbar was analysed *via* XPS**.** Spectra were recorded and analysed after etching for 10 minutes to a depth of 10 nm. The presence of the carbon peak at 284.5 eV was used to calibrate and fit the spectra.

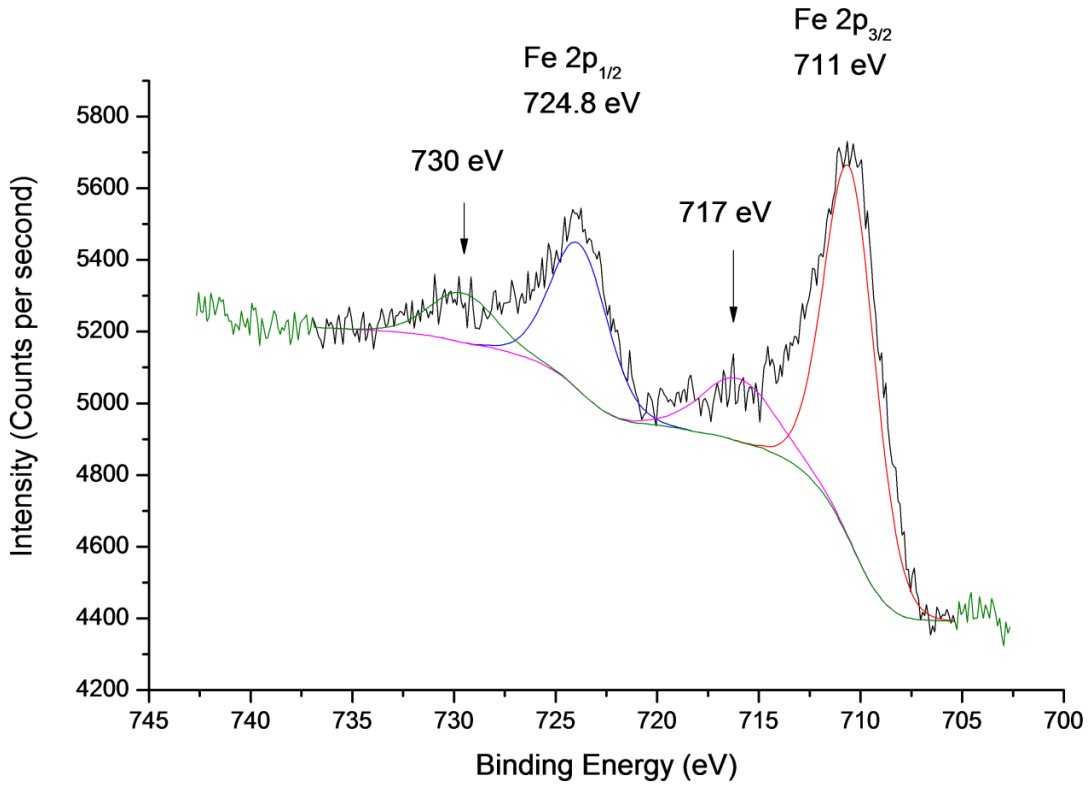

Figure 117: XPS spectrum of the iron 2p region after etching.

The Fe 2p core level is split into the $2p_{1/2}$ and $2p_{3/2}$ components. XPS revealed the presence of iron in the 3^+ oxidation state, represented by the Fe $2p_{1/2}$ peak at 724.8 eV, and the Fe $2p_{3/2}$ region displayed a broad, slightly asymmetric peak that was fitted using one large peak at 711 eV (Figure 117). As stated in Chapter 6, the Fe $2p_{3/2}$ peak at 711 eV is typically observed for iron in Fe_3O_4 and Fe_2O_3 and also as iron in $BiFeO_3$ species, and therefore it is difficult to distinguish with certainty the exact origin of this peak. As reported in the literature,[123] the Fe^{3+} satellite peak tends to be broad and here it was observed at 717 eV as a slight shoulder to the main Fe $2p_{3/2}$ peak, but appears to be characteristic of the presence of pure Fe^{3+} in a sample. It is less likely that the iron in the sample originates from Fe_3O_4 species as one would additionally expect a broad shoulder (at 707 eV) to be attached to the peak at 711 eV.[206] The smaller peak at 730 eV is likely to correspond to the other Fe $2p_{1/2}$ satellite peak, which is in agreement with XPS spectra of pure α-Fe_2O_3,[207] and as spectra for Fe_3O_4 species do not contain these satellite peaks, it is unlikely that there is a mixed valence state of 2^+ and 3^+ for iron in these films.

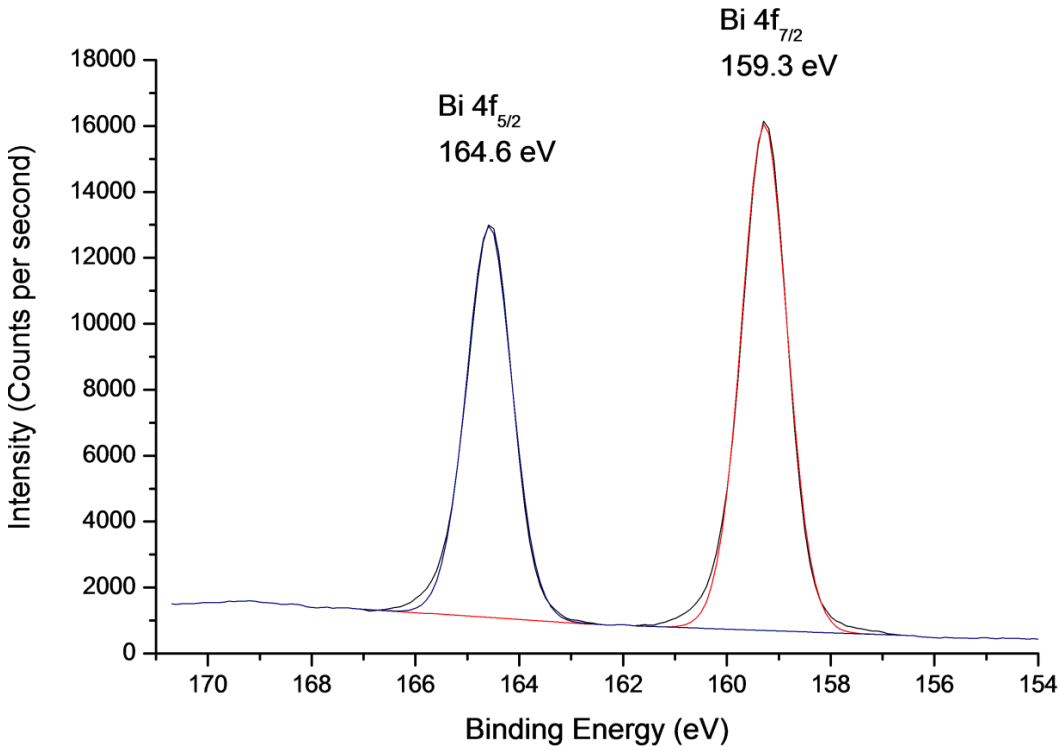

Figure 118: XPS spectrum of the bismuth 4f region after etching.

The bismuth 4f region is represented by two distinct peaks in Figure 118, one corresponding to the $Bi4f_{7/2}$ peak, observed at 159.3 eV, with the other corresponding to the Bi $4f_{5/2}$ peak at 164.6 eV. Both these peaks and their positions are characteristic of the presence of bismuth in the 3^+ oxidation state.[170] The etching process did not appear to lead to preferential sputtering and no additional shoulders were observed that could be assigned to elemental bismuth.

The oxygen 1s region was also analysed *via* XPS. Etching of the sample revealed two broad, slightly asymmetric peaks at 532.4 and 529.7 eV (Figure 119). An additional peak was added at 530.6 eV to account for this peak broadening. The larger peak at 532.4 eV is typically found as a result of surface contamination (hydrocarbon grease) and the smaller peak at 529.7 eV represents oxygen from a metal oxide species. The presence of a silicon peak at 102.5 eV is most likely to be due to the surface contamination (grease etc) and less likely to be a result of breakthrough to the substrate, given that the film had a thickness of 880 nm and the etch depth was only 10 nm. Quantitative analysis using the peak areas for Bi 4f, Fe 2p and O 1s together with the RSFs for bismuth, iron and oxygen (9.14, 2.957 and 0.78 respectively) revealed their presence in a 1.3:1:2 ratio, suggesting that these films were slightly bismuth rich but oxygen deficient, however due to the difficulty in fitting the oxygen metal oxide peak the ratio could not be ascertained with confidence. Nevertheless, the binding energies of the iron and bismuth peaks suggest the presence of both elements in the 3^{+} state.

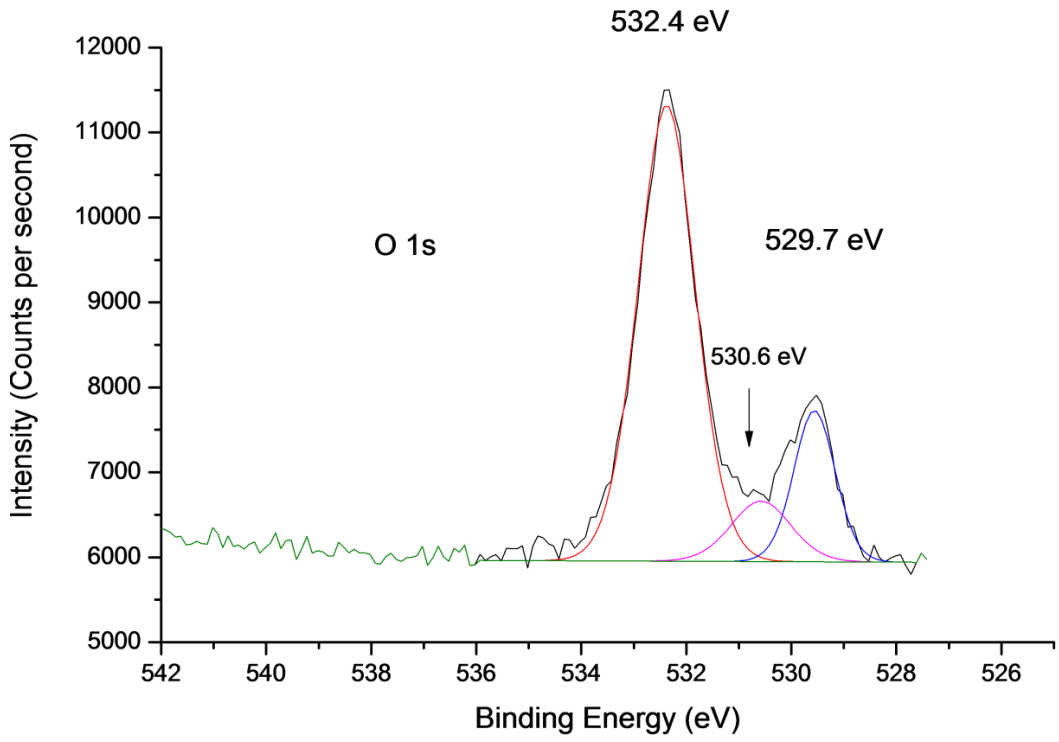

Figure 119: XPS spectrum of the oxygen 1s region.

7.3.6 Atomic force microscopy

Figure 120 displays a typical field size and 3D AFM image of a $BiFeO_3$ film formed *via* LPCVD of $[Bi(O^tBu)_3]$ and $[Fe(O^tBu)_3]_2$ deposited at 550 °C and at 8mbar.

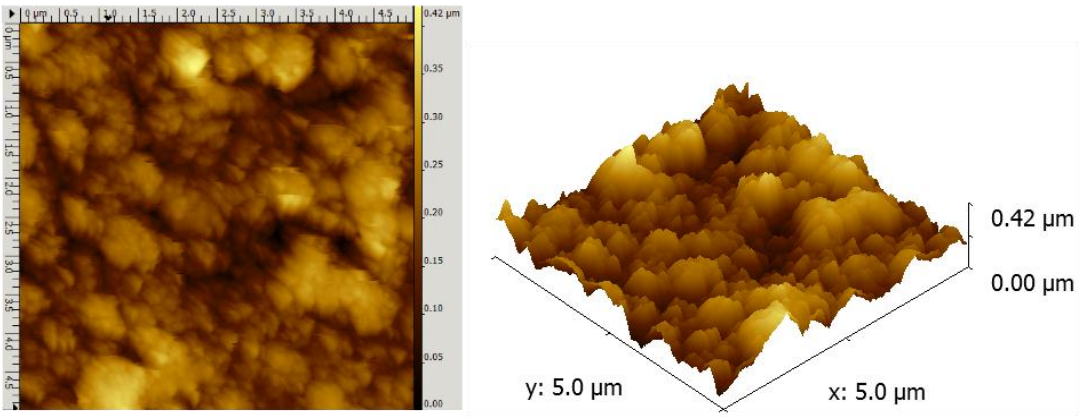

Figure 120: A 5 µm field size (left) and the corresponding 3D AFM image of the $BiFeO_3$ film formed *via* LPCVD of $[Bi(O^tBu)_3]$ and $[Fe(O^tBu)_3]_2$ at 550 °C, 8 mbar.

The AFM imaging demonstrates the three-dimensional depth profile of an LPCVD – grown thin film. A hierarchical structure is shown, composed of slightly globular and spherical particles of approximately 50 nm diameter which have clustered together to form larger aggregates. Although the globular morphology is similar to what is observed in the top-down SEM images, the morphology here appears much rougher with more features. The coverage nevertheless, is continuous over the substrate and there appears to be no voids where deposition has not occurred, which demonstrates the advantages of LPCVD for superior coverage over other film deposition methods. The root mean square (rms) roughness of the sample was calculated at 60 nm which is fairly high for LPCVD, and for that matter, APCVD[225] grown films, but is still lower than values found for films grown *via* AACVD.[183,171] For comparison, $BiFeO_3$ films grown *via* the LPCVD reaction of $[Bi(O^tBu)_3]$ and $[Fe(acac)_3]$ using air as an oxidising gas possessed an rms value of 30 nm (Chapter 6), and Bi_2O_3 films grown *via* LPCVD using $[Bi(O^tBu)_3]$ as a single source precursor possessed an even lower rms of 4 nm (Chapter 4). $BiFeO_3$ films grown *via* AACVD followed by post-deposition annealing resulted in films with an rms of 62 nm (Chapter 8), which is similar to the result obtained in this study of LPCVD grown films. This was somewhat unexpected, but considering that there appears to be no roughness values given for $BiFeO_3$ films grown *via* CVD methods in the literature, comparison with our films in light of this is difficult. Nevertheless, the high roughness is advantageous for applications where a high surface area is required, for example, in catalysis.

7.3.7 Ferroelectric characterisation

Films of $BiFeO_3$ were grown *via* LPCVD directly on to 1 cm^2 silicon wafers. A sputter coater with a platinum target was used to coat the silicon in order to introduce a conducting bottom electrode. After deposition of the $BiFeO_3$ film *via* CVD, circular platinum electrodes were sputtered onto the surface of the film using a 0.5 mm mask to act as conducting top electrodes. The thickness of the deposited $BiFeO_3$ film was found to be 690 nm from side-on SEM imaging.

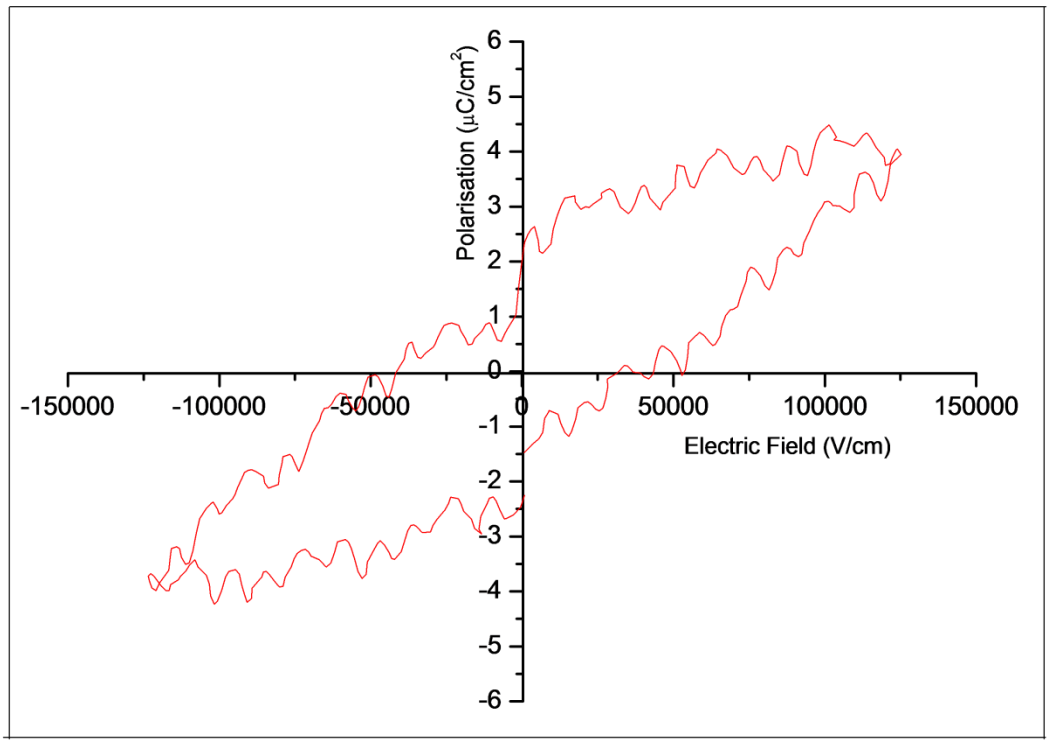

Figure 121: Room temperature P-E hysteresis loop measured at 1 kHz for a 690 nm thick $BiFeO_3$ film deposited on $Pt/SiO_2/Si$ substrate sputtered with Pt top electrodes.

The polarisation-electric field hysteresis loop measured at 1 kHz is shown in Figure 121 for the 690 nm thick film grown *via* LPCVD. The loop has not fully saturated and there appears to be a large amount of background noise through positive and negative field strengths, which makes the estimation of remnant polarisation (P_r) and coercive field difficult. Nevertheless, a P_r value of 2.4 μC/cm^2 and an (almost) saturated polarisation (P_s) of 3.9 μC/cm^2 were measured. A coercive field of approximately 45 kV/cm was measured for the sample. The values are slightly higher than those obtained from $BiFeO_3$ films grown using $[Bi(O^tBu)_3]$, $[Fe(acac)_3]$ and air which contained impurity Fe_2O_3 as described in Chapter 6, and are much higher than those reported by Tasaki *et al.*[122] (P_r ~ 0.2 μC/cm^2, P_s ~ 1.75 μC/cm^2) for their $BiFeO_3$ films grown on platinised silicon substrates *via* liquid-delivery CVD using $[Bi(p\text{-tol})_3]$ and $[Fe(dibm)_3]$ as

precursors (see the Introduction chapter for more details). The polarisation values are more closely aligned to what is expected for bulk $BiFeO_3$; these values are smaller than those obtained for $BiFeO_3$ films grown on $SrTiO_3$ and silicon substrates *via* PLD due to the lower frequency of applied field used here (1 kHz) compared to this literature source (16 kHz).[121] A lower field strength was applied in order to guard against damage to the films during measurement. Some damage to the top electrodes and to the film underneath was observed when the measurement electrode tips made contact with the samples. Epitaxially strained $BiFeO_3$ films grown on $SrRuO_3/SrTiO_3$ substrates have been shown to possess high spontaneous polarisation values of at least 90 $\mu C/cm^2$, which was believed to be due to the extreme sensitivity of the polarisation to small changes in lattice parameter,[39] however measurements on good quality single crystals have since revealed otherwise.[226] Leakage current tends to be high for these films as a result of lower oxygen stoichiometry and defects in the crystal, and this may be reinforced by the oxygen deficiency observed *via* XPS. Nevertheless, the P-E loop demonstrates the films are ferroelectric at room temperature.

7.3.8 Magnetism measurements

The $BiFeO_3$ film grown at a substrate temperature of 550 °C and at a pressure of 8 mbar (thickness of 880 nm) was chosen for magnetic measurements. Magnetic measurements were performed using a SQUID-VSM which has a maximum field setting of 7 T (70000 Oe). The film was cut to an appropriate size (2mm x 3mm) in order to be mounted on a quartz rod using temperature stable adhesive. The magnetic field was applied parallel to the plane of the film and M-H loops were measured at 5 K and at 300 K. The diamagnetic and paramagnetic contribution of the substrate was subtracted from the total moment and is described in Chapter 6. Additionally, a ZFC-FC measurement was performed. The M-H hysteresis loop recorded at 5 K is shown in Figure 122.

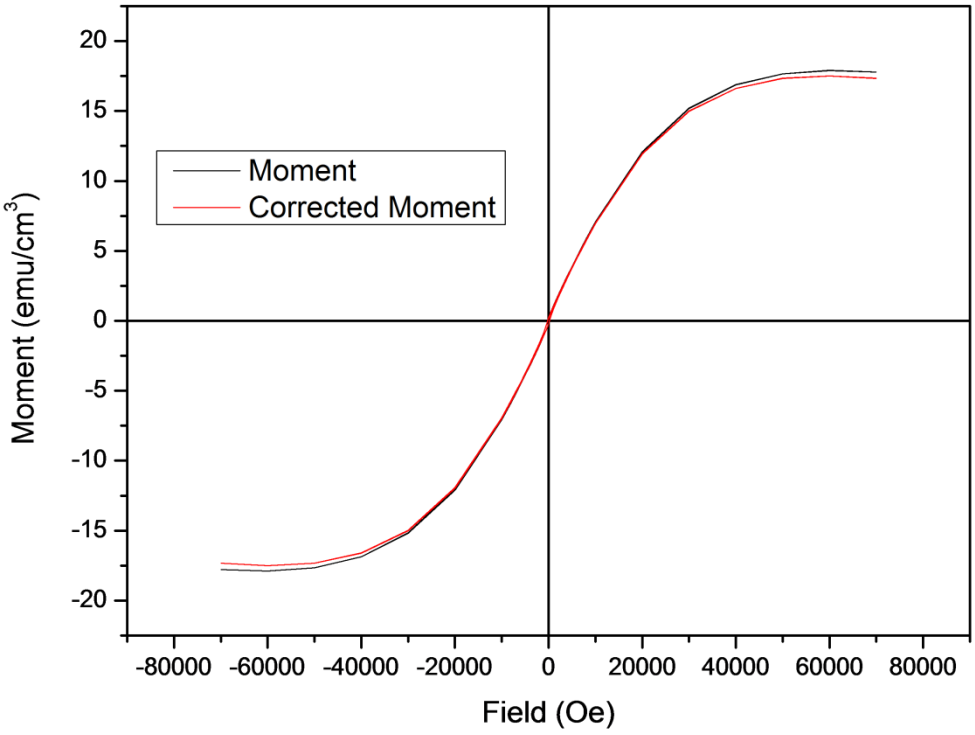

Figure 122: M-H hysteresis loop measured at 5 K for the 880 nm thick $BiFeO_3$ film grown *via* LPCVD at 550 °C, 8 mbar.

The hysteresis loop (Figure 122) indicates that the diamagnetic contribution from the substrate was negligible at low field strengths (<30000 Oe), however above this value there is some deviation between the curves. The loop does saturate by 70000 Oe and as expected, the film displays weak ferromagnetic behavior. The saturation magnetization was found to be 17.5 emu/cm^3 which is slightly larger than that expected for $BiFeO_3$ from DFT calculations.[123,102] A saturation magnetization of 130 emu/cm^3 was recorded at 5 K for $BiFeO_3$ films grown *via* LPCVD using [$Fe(acac)_3$] and [$Bi(O^tBu)_3$] in Chapter 6, however these films were found to contain impurity α-Fe_2O_3 from XRD analysis, which has been demonstrated by other groups to enhance the magnetic properties (coercivity, saturation) of $BiFeO_3$ films.[123,110]

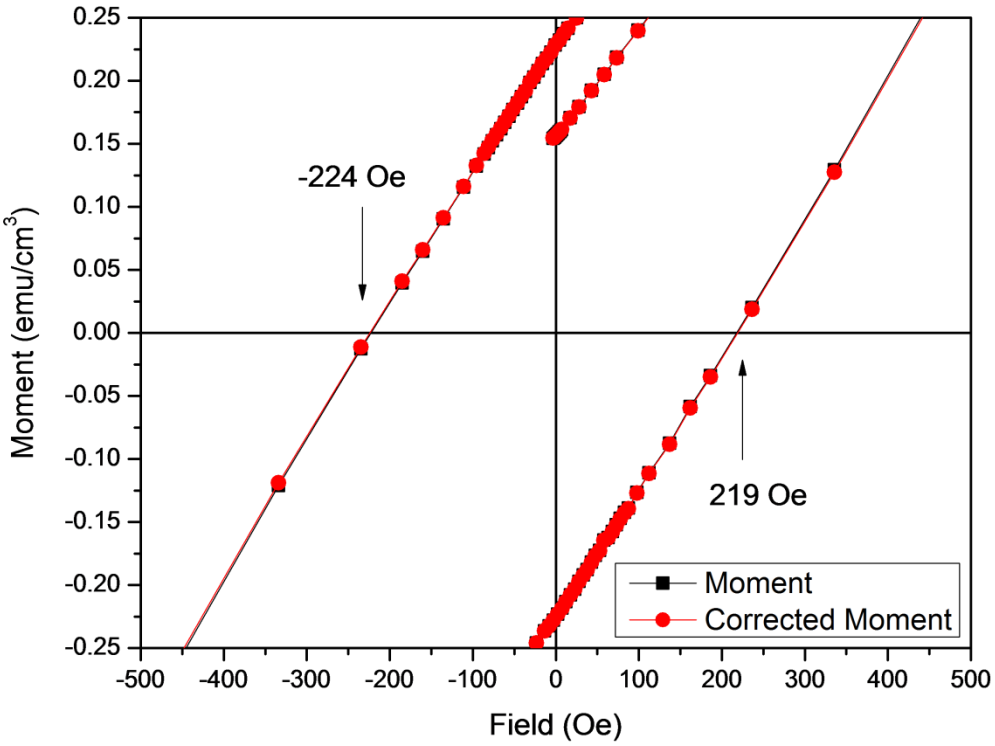

Figure 123: M-H hysteresis loop measured at 5 K enlarged to display the coercivity.

The coercivity of the films at 5 K was estimated to be 219 Oe and -224 Oe and is shown in the enlarged M-H loop in Figure 123. The loop was slightly asymmetric which is usually due to defects, variations in thickness and stress; however a small difference in values is normally obtained. Not surprisingly, these values were approximately 150 Oe lower than those obtained from $BiFeO_3$ films grown by LPCVD that contained Fe_2O_3 impurity described in Chapter 6. As $BiFeO_3$ is considered a room temperature multiferroic, the M-H curve was recorded at 300 K for the same sample (Figure 124).

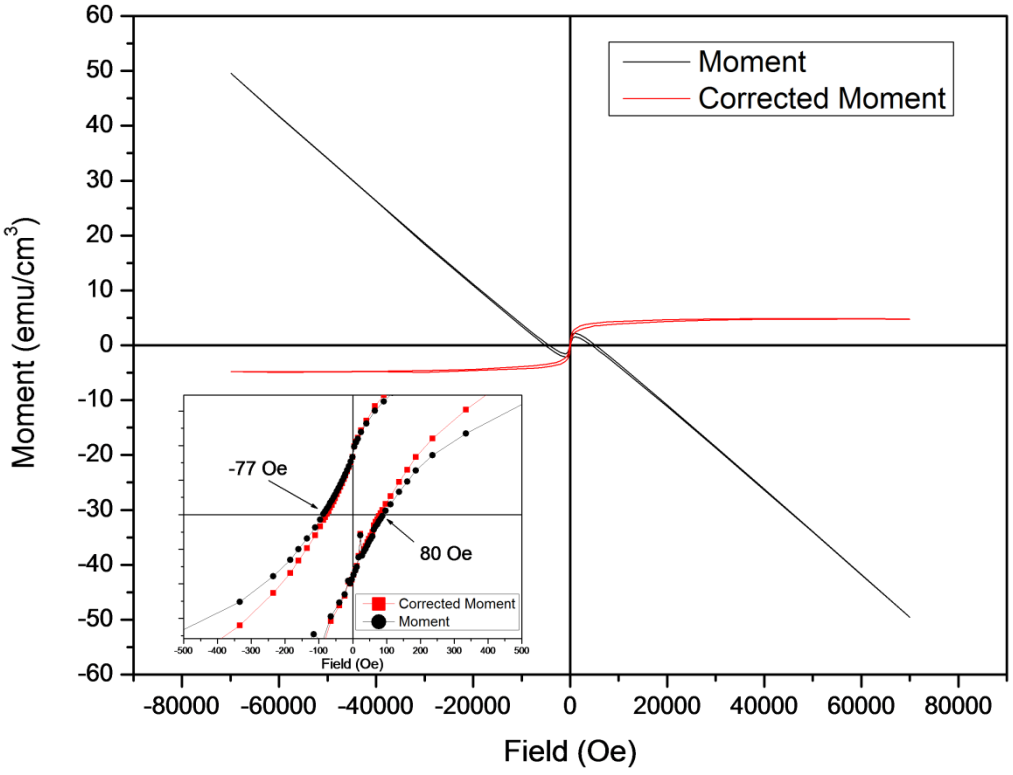

Figure 124: M-H hysteresis loop measured at 300 K for the $BiFeO_3$ film grown *via* LPCVD at 550 °C, 8 mbar. The inset plot shows the M-H curve enlarged to display the coercive field of the sample.

As expected due to increased thermal motion, the (diamagnetic/paramagnetic) contribution of the glass substrate was proportionally higher at 300 K, and was subtracted from the total moment. The increase in temperature resulted in the expected decrease in saturation magnetisation (4.9 emu/cm^3) that occurred at a lower magnetic field strength, along with a decrease in coercivity (-77 and 80 Oe); a trend that was also observed with the $BiFeO_3$ sample grown *via* AACVD in measured in Chapter 8; the result for the film described in Chapter 6 grown *via* LPCVD is thought to have arisen due to an increased presence of impurity Fe_2O_3 in that sample. The saturation point here is more consistent with the expected value for $BiFeO_3$.[138,112] The observation of ferromagnetic behaviour at both 5 K and 300 K may not be solely due to the presence of a mixed Fe^{2+}/Fe^{3+} valence state, but also due to suppression of the cycloidal spin structure of $BiFeO_3$. The wavelength of the spin cycloid is 64 nm[108] and is larger than the average particle size contained within the film (25 nm), possibly giving rise to weak ferromagnetism.[227]

The temperature dependence, displaying the field cooled (FC) and zero field cooled (ZFC) curves for the same $BiFeO_3$ sample is shown in Figure 125. The applied magnetic field was set at 200 Oe and the heating rate was 5 K/min.

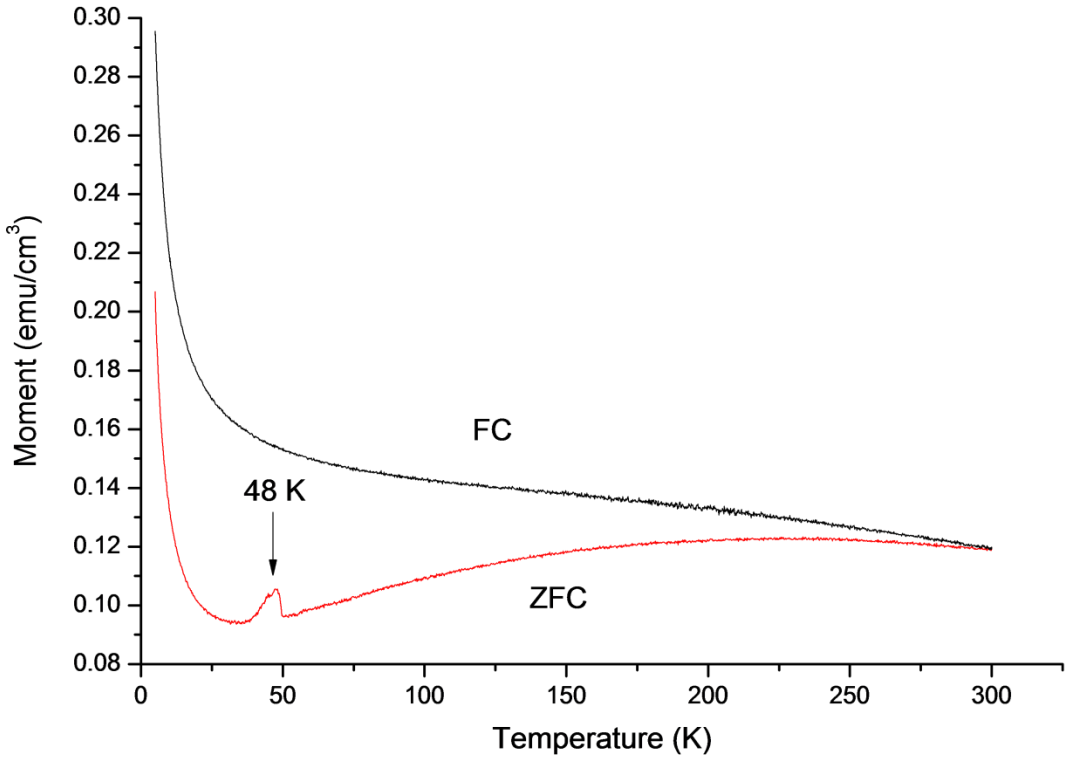

Figure 125: ZFC and FC curves for the 880 nm thick $BiFeO_3$ film formed *via* LPCVD at an applied field of 200 Oe.

The temperature dependence of the magnetisation clearly reveals a sharp cusp at approximately 48 K in the ZFC data, which at first glance, could be a magnetic transition, however the Neel Temperature (T_N) for $BiFeO_3$ is approximately 640 K and therefore cannot be assigned to this cusp. The dramatic increase in magnetisation below ~ 20 K is in agreement with the M-H curve (Figure 122), which demonstrates ferromagnetic behaviour at low temperatures. There is some deviation between the curves below 300 K which is consistent with the M-H hysteresis loops, and their divergence, together with the cusp at ~ 50 K, which have been said to be characteristic of spin-glass behaviour.[107,228] Above 50 K, the ZFC data reveals an increase in magnetisation due to some of the spins becoming aligned with the field, however at high temperatures thermal motion predominates and the spins randomly orientate themselves, resulting in a decrease in magnetisation. This is a disordered state where the moments effectively cancel each other out, and it is expected that a further increase in temperature would lead to zero magnetisation at T_N (640 K).

The cusp could be assigned to the blocking temperature, T_B (or spin glass freezing temperature, (T_f)) of the individual spins and has been observed as a feature of larger $BiFeO_3$ particles (> 95 nm) and the bulk.[126] Top-down SEM imaging did not reveal a conclusive figure for the particle size for these films; the use of the Scherrer Equation resulted in an average particle size of 25

nm for this particular sample. There did appear to be a degree of particle coalescence in all films which could possibly lead to bulk-like magnetic behaviour where the coverage is continuous, as opposed to the studies on discrete, well-defined nanoparticles.[126] Blocking temperature effects are characteristic of superparamagnetic behaviour, affecting particle of small (single domain) sizes. Here, the spins display anisotropy by orienting themselves in a preferred direction, however if given sufficient thermal excitation, can flip direction. The time taken for such a "flip" is known as the Neel relaxation time (τ_N), and the measurement time of the magnetometer is τ_M. Therefore if $\tau_M < \tau_N$, the magnetisation will not "flip" during the measurement and the particle can be viewed in a "blocked" state. Increasing the temperature increases thermal motion of the spins and reduces the energy barrier for "flipping."

These ZFC-FC magnetisation curves are almost identical to those observed by Scott *et al.*[109] from their $BiFeO_3$ single crystals - the splitting of the curves below 250 K is characteristic of spin-glass behaviour; however the peak at ~ 48 K in our data is much sharper than in their observation, but the subsequent decrease in magnetisation as a function of temperature was said to be typical of an antiferromagnetic material. For the ZFC measurement, magnetisation initially decreases with a decrease in temperature, but increases significantly at 10 K which could be a result of uncompensated spins which would give rise to superparamagnetism,[229] but is just as likely to be a consequence of low temperature ferromagnetic behaviour.[109]

7.3.9 UV-Vis spectroscopy

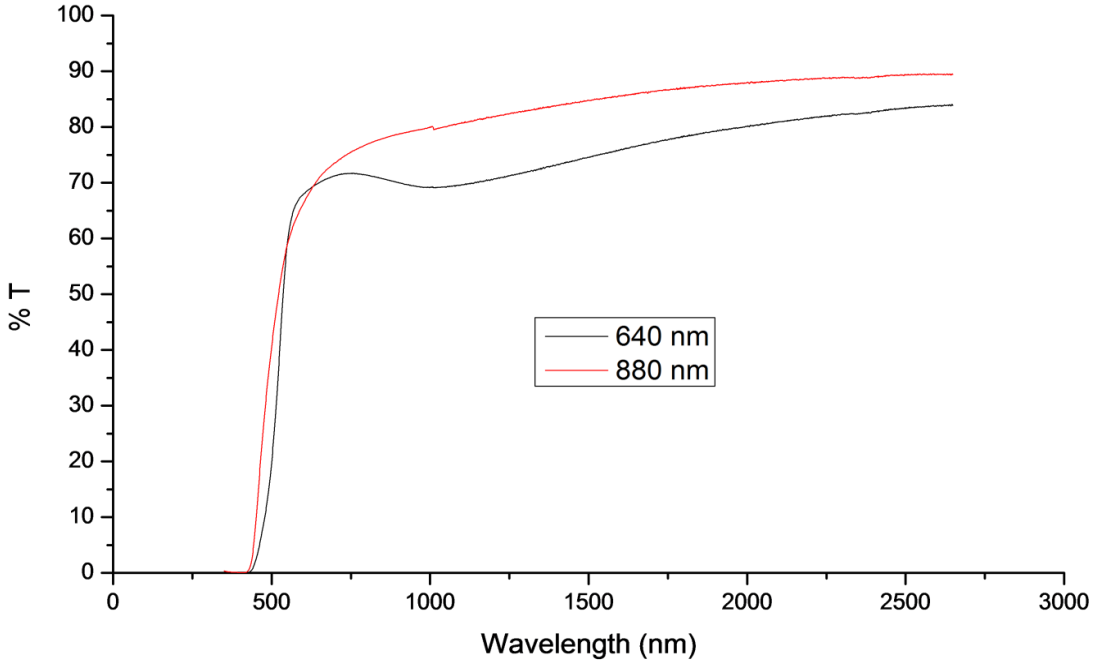

Figure 126: UV-Vis spectra of two $BiFeO_3$ films deposited *via* LPCVD, where the black line corresponds to the film of 640 nm thickness and the red line to the film of 880 nm thickness.

The optical properties of the as-deposited films were measured using UV-Vis spectroscopy recorded in transmission mode. The band-gaps of the films were then calculated *via* a Tauc plot[172] from converting the transmission data into absorbance *via* the Beer-Lambert Law (see Chapters 4 and 5). The transmission spectra of the $BiFeO_3$ films deposited at 525 °C and 550 °C at 8 mbar are shown as example spectra in Figure 126. The films were over 65% transmitting in the 550 – 2500 nm region, however the absence of an adequate number of interference fringes inhibited the use of the Swanepoel[173] method for determination of film thickness.

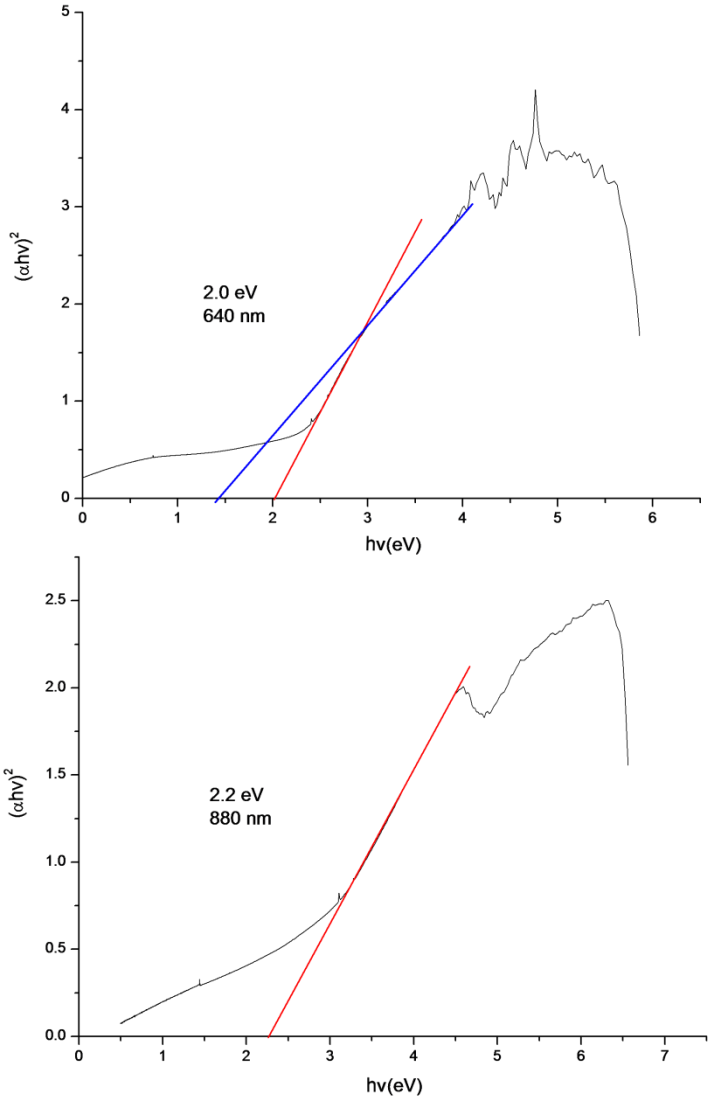

Figure 127: Tauc plots constructed for the $BiFeO_3$ films of 640 nm (top) and 880 nm (bottom) thicknesses that were grown *via* LPCVD at 525 °C and 550 °C respectively at a pressure of 8 mbar. The additional blue line extrapolation at 1.4 eV for the film of 640 nm thickness may be an edge from the presence of $Bi_{24}Fe_2O_9$.

The band-gap of the film deposited at 525 °C was estimated to be 2.0 eV, whereas the film deposited at 550 °C possessed a band-gap of 2.2 eV. Both values are in agreement with reported values for thin film and bulk $BiFeO_3$,[230,142] however the film deposited at 525 °C contained impurity $Bi_{24}Fe_2O_{39}$ in addition to $BiFeO_3$ and this could be the reason for the slight discrepancy in values. The signal at higher energies (> 4.5 eV) in both plots (Figure 127) corresponds to the glass substrate. There is an additional edge (shown in blue) intersecting the *x*-axis at approximately 1.4 eV for the film of 640 nm thickness and could be due to the presence of $Bi_{24}Fe_2O_{39}$, however there appears to be no absorption spectra for this phase reported in the literature which makes this assignment difficult. The band-gap values calculated here are also in agreement with those calculated for $BiFeO_3$ films grown *via* LPCVD (E_g = 2.0 – 2.3 eV) described in Chapter 6.

Values in the visible region of 2-3 eV are common for $BiFeO_3$ and depend on a number of factors including, but not limited to, the purity of sample and whether one is measuring thin films, bulk material or nanoparticles. A band-gap value of 2.18 eV was recently elucidated for $BiFeO_3$ nanoparticles[216] and values of between 2.2 - 2.76 eV were found for thin films of $BiFeO_3$ grown *via* sputtering; values in the higher part of this range were thought to be due to band-gap defect states and oxygen vacancies.[231] The band-gap is evidently in the visible range and literature sources, in addition to work described in the previous chapter, have demonstrated the high visible-light photocatalytic activity of $BiFeO_3$.

7.4 Photocatalysis

The films deposited at 525 °C and 550 °C at 8 mbar and of differing thicknesses were selected for an investigation into their photocatalytic properties *via* the photo-oxidation of water using a sacrificial solution and a simulated solar light source (75 W) with a 420 nm cut-off filter. The experimental procedure was identical to that already described in Chapter 6, and similarly each film was cut into a piece measuring approximately 1 cm x 2 cm. They were suspended from a rubber septum using a hook into a sacrificial solution (32 cm^3) containing a 1:1 mixture of 0.1M $Na_2S_2O_8$ and 0.01M KOH solutions that had been purged with Argon.[190] The oxygen electrode was used to measure the solution voltage over time, which is proportional to the dissolved oxygen concentration. The method for converting the recorded voltage to units of micromoles of oxygen per unit time is already described in Chapter 4 and therefore only the results of the experiment will be discussed here.

Again, as a control, each sacrificial solution was irradiated with the light source for 30 minutes prior to insertion of each thin film. An uncoated substrate was tested, and as expected, no oxygen evolution was detected. Each film was suspended in the solution and irradiated with the light source for approximately 70 minutes. X-ray diffraction analysis of the samples after photocatalytic testing was performed to check for degradation. A graph plotting voltage against time for the two samples is shown in Figure 128.

7.4.1 Results and discussion

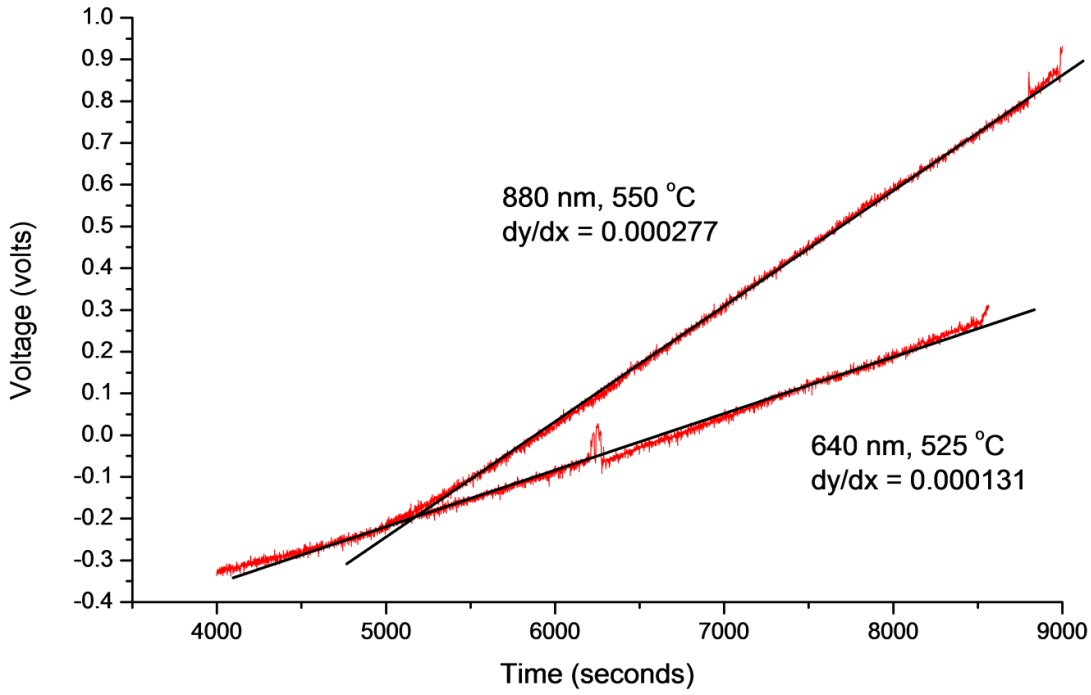

Figure 128: Plots of voltage against time measured during the photo-oxidation of water for two $BiFeO_3$ films of 880 nm and 640 nm thicknesses. The gradient of the slope is used to calculate the rate of oxygen produced.

The photocatalysis results derived from this graph are summarised in Table 14. Both films displayed appreciable photo-activities over the duration of the experiment. The small spike in the data recorded for the 640 nm thick film is due to the very high sensitivity of the oxygen electrode resulting in the detection of a brief, sharp increase in voltage; however this does not affect the overall gradient of the slope. In order to compare these results with the photo-activities of TiO_2 films investigated using an identical experiment, units of oxygen evolution per metre^2 of sample were included by multiplying the results of the 2 cm^2 sample by a factor of 5000, which shows the oxygen evolution if one were to assume that we have a 1 m^2 film whose coverage, thickness and reaction rate were the same as those tested previously.

Table 14: Summary of the individual film properties and the rate of oxygen production for the two films chosen.

Film Thickness / nm	Band-gap / eV	Rate of O_2 production / µmol h^{-1} (for 2 cm^2 sample)	Rate of O_2 production / µmol $h^{-1}m^{-2}$	No. Of incident photons (420 nm - band-gap of film)	Molecules of O_2 formed per second (for 2 cm^2 sample)	Quantum efficiency / %
640	2.0	1.49	7430	3.7×10^{17}	2.5×10^{14}	0.27
880	2.2	3.14	15710	2.4×10^{17}	5.3×10^{14}	0.88

The rate of oxygen production observed for the two chosen samples irradiated with solar irradiation and a 420 nm filter were of the order, albeit slightly lower, than those obtained from LPCVD-grown $BiFeO_3$ films described in Chapter 6, and consequently 1-2 orders of magnitude higher than those obtained from the use of anatase films deposited on glass *via* APCVD (360 – 2820 µmol $h^{-1}m^{-2}$) using a 365 nm UV-light source.[175] The sample possessing a larger band-gap (pure phase $BiFeO_3$ from XRD analysis), grown at 550 °C, displayed a higher water photo-oxidation activity and this would perhaps be expected due its greater thickness, which would result in more photoactive material. The film grown at 525 °C possessed a lower photocatalytic activity that could be due to the presence of impurity $Bi_{24}Fe_2O_{39}$ in addition to $BiFeO_3$ in this sample, which is either not photocatalytically active or serves as a site for charge carrier recombination. Films were analysed *via* X-ray diffraction after photocatalytic testing (Figure 129).

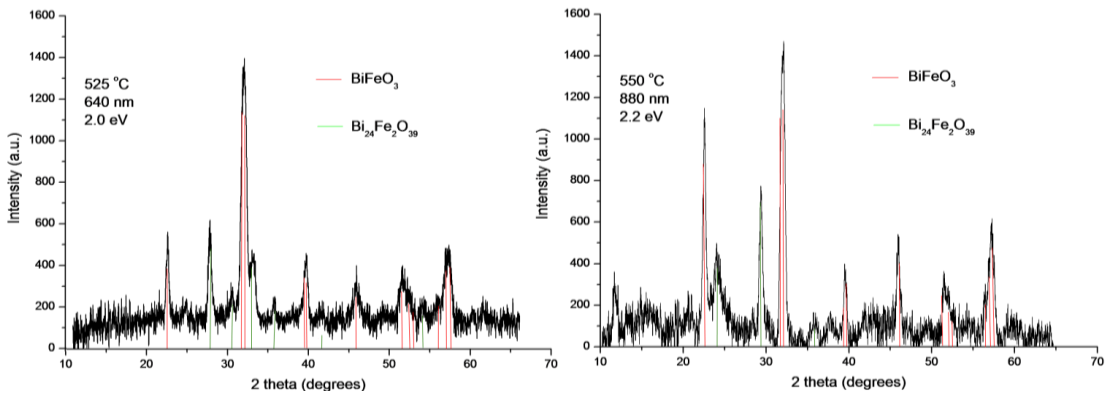

Figure 129: XRD patterns of the two films after the photocatalysis experiment.

There were no distinct changes observed *via* XRD for the film deposited at 525 °C after being submerged in the basic solution and irradiated with the 75 W lamps. The film deposited at 550 °C was found to contain a small amount of $Bi_{24}Fe_2O_{39}$ phase after the experiment which was unexpected, and the peak at 11-12° could not be assigned with certainty. The reason for the apparent low stability in basic solution for this particular sample is unknown; the $Bi_{24}Fe_2O_{39}$ phase is thermodynamically more stable than $BiFeO_3$ and its presence in the sample deposited at 525 °C may stabilise the $BiFeO_3$ phase with respect to degradation.[204] It has recently been reported that following the visible light illumination of $BiFeO_3$ nanoparticles for photocatalytic degradation of Rhodamine B, no changes from XRD data were observed, however XPS revealed significant changes to the chemical state of the Fe cations on the surface, inferring that $BiFeO_3$ may not be photo stable.[232] The explanation for its photo-corrosion appeared to be due to the band positions of $BiFeO_3$ and Rhodamine B, whereby it is possible that positive holes are injected from the Rhodamine B HOMO to the $BiFeO_3$ valence band.

The quantum efficiencies for the two samples were measured to be 0.27% and 0.88% using photon energies between 420 – 620 nm or between 420 – 560 nm as this depended on the band-gap of each film. For example, the film with a band-gap of 2.2 eV would only be excited by photons whose wavelength is lower than approximately 560 nm. As a cut-off filter is being used to remove UV photons, only photon energies between 420 and 560 nm were used for the efficiency calculation for this sample. Likewise, the film with a band-gap of 2.0 eV may only be photo-excited by photons with a wavelength lower than 620 nm. The number of incident photons used for each calculation is also shown in Table 14. Overall, the results show that the thicker sample, composed of phase-pure $BiFeO_3$, displayed a higher photoactivity than the film containing $Bi_{24}Fe_2O_{39}$ as impurity. This is somewhat different to the results obtained for $BiFeO_3$ films described in Chapters 6 and 8, whereby the thicker films displayed a lower activity and efficiency. The reasons for this are unknown, but the quoted difference in film properties makes developing a theory difficult; optimisation of film thickness and composition (and therefore band-gap) would be required in order to test their photocatalytic activity to make any such correlations, but is beyond the scope of the present study.

These results demonstrate the potential of $BiFeO_3$ thin films to act as powerful visible-light photocatalysts for the difficult 4-electron water oxidation reaction. Joshi *et al.* have investigated the potential of $BiFeO_3$ nanocubes to serve as visible-light water oxidation catalysts and found *low* activities in the region of 2.5 µmol O_2 after 12 hours, at a rate of 0.5µmol h^{-1}.[218] The high surface area found in thin films of $BiFeO_3$ is comparable to nanocubes but is significantly higher than bulk material, and so would appear to aid photon capture and electron-hole pair production. The domain structure of $BiFeO_3$ has recently been observed experimentally to inhibit charge-carrier recombination in $TiO_2/BiFeO_3$ heterostructures[149,150] and $SrTiO_3$ coated $BiFeO_3$ powders have been used to photo-reduce water into hydrogen under visible light.[142] The

band-gap of $BiFeO_3$ and its position with respect to the redox potentials of water have already been discussed, and this serves as the primary reason for the strong photo-oxidation power of the material.[143]

7.5 Conclusions

The growth of $BiFeO_3$ films *via* the LPCVD reaction of the matched-ligand precursors $[Bi(O^tBu)_3]$ and $[Fe(O^tBu)_3]_2$ on glass and platinised silicon substrates was demonstrated without the use of an oxidising gas. The substrate temperature and total system pressure were varied in order to investigate their effect upon the films deposited, with phase-pure $BiFeO_3$ films being deposited at 550 °C at a pressure of 8 mbar. The composition of the films was analysed *via* powder X-ray diffraction, WDX, XPS and low temperature Raman spectroscopy. Their morphologies were studied *via* the use of top-down SEM imaging and AFM, the latter revealing a high rms value of 60 nm. Room temperature ferroelectric measurements revealed a spontaneous polarisation of 3.9 $\mu C/cm^2$ and a remnant polarisation of 2.4 $\mu C/cm^2$, whilst M-H hysteresis loops recorded at 5 K revealed low temperature ferromagnetic behaviour with a saturation magnetisation of 130 emu/cm^3. Room temperature M-H curves revealed a much lower magnetisation of ~ 5 emu/cm^3 in agreement with theoretical predictions. A cusp at ~ 50 K detected in the ZFC-FC measurement, ascribed to the freezing or blocking temperature, is said to be characteristic of spin-glass behaviour and is commonly observed for $BiFeO_3$ thin films, nanoparticles and the bulk.

Direct band-gaps of deposited films were measured in the region of 2.0 – 2.3 eV *via* UV-vis spectroscopy and the subsequent generation of Tauc plots. The photocatalytic activities of two films were tested *via* the photo-oxidation of water, using sacrificial reagents and under visible light irradiation. Appreciable photoactivities were recorded, in line with results obtained from LPCVD grown $BiFeO_3$ films tested in Chapter 6, altogether highlighting the potential of $BiFeO_3$ for visible-light photocatalysis applications.

8 Aerosol-assisted CVD of bismuth ferrite

8.1 Introduction

Chapters 6 and 7 described the growth of $BiFeO_3$ films using dual-source LPCVD. The advantages of utilising single-source precursors for film deposition have already been highlighted in the Introduction chapter and also in Chapter 4, where the use of $[Bi(O^tBu)_3]$ for phase—selective deposition of Bi_2O_3 films was demonstrated. There are also many advantages of employing solution-based deposition methods that stem from the simplicity of the process, circumventing the need for vacuum-based deposition and, furthermore, its applicability to different substrates. Therefore employing a bimetallic precursor that contains the correct ratio of metal atoms to those sought in the resultant film would make the deposition process simpler as there would be fewer variables (individual precursors) to control. Using a single-source precursor in a solution-based deposition method would not require vacuum apparatus and could also permit the introduction of dopants, depending on their solubility, *via* a 'one-pot' procedure that was described in Chapter 5 for growth of Pt-Bi_2O_3 films.

This chapter describes the synthesis of multiferroic $BiFeO_3$ thin films onto a variety of substrates *via* aerosol-assisted CVD (AACVD) using the single-source molecular precursor $[\{Cp(CO)_2Fe\}BiCl_2]$. The resultant films were fully characterised and two samples were chosen for an investigation into their visible light photocatalytic activity.

8.1.1 Precursor synthesis

The bimetallic molecular precursor $[\{Cp(CO)_2Fe\}BiCl_2]$ was synthesised according to the literature from the reaction of $[CpFe(CO)_2]_2$ and $BiCl_3$, and is described in Chapter 2.[159]

8.2 Experimental – AACVD

Nitrogen (99.96%) was obtained from BOC and used as supplied. AACVD experiments were initially conducted on SiCO coated float glass substrates (150 mm x 45 mm x 3 mm) supplied by Pilkington Glass Ltd (NSG Group). The glass substrates were cleaned thoroughly in commercial washing up detergent, dried, and then cleaned with isopropanol. They were subsequently dried using a heat gun. In order to anneal films to temperatures greater than 600 °C, depositions were carried out on 20 mm x 20 mm x 2 mm Corning 1737 AMLCD alkaline-earth boro-aluminosilicate transparent glass substrates placed on top of the Pilkington float glass

substrate which was positioned on the graphite block. The Corning substrate, containing the film, was subsequently annealed at the specified temperatures. For ferroelectric measurements the silicon wafers were sputtered for 180 seconds with a thin layer of platinum (argon pressure 0.1 torr, current 25 mA) prior to use, with deposition onto the platinum.

8.2.1 AACVD apparatus

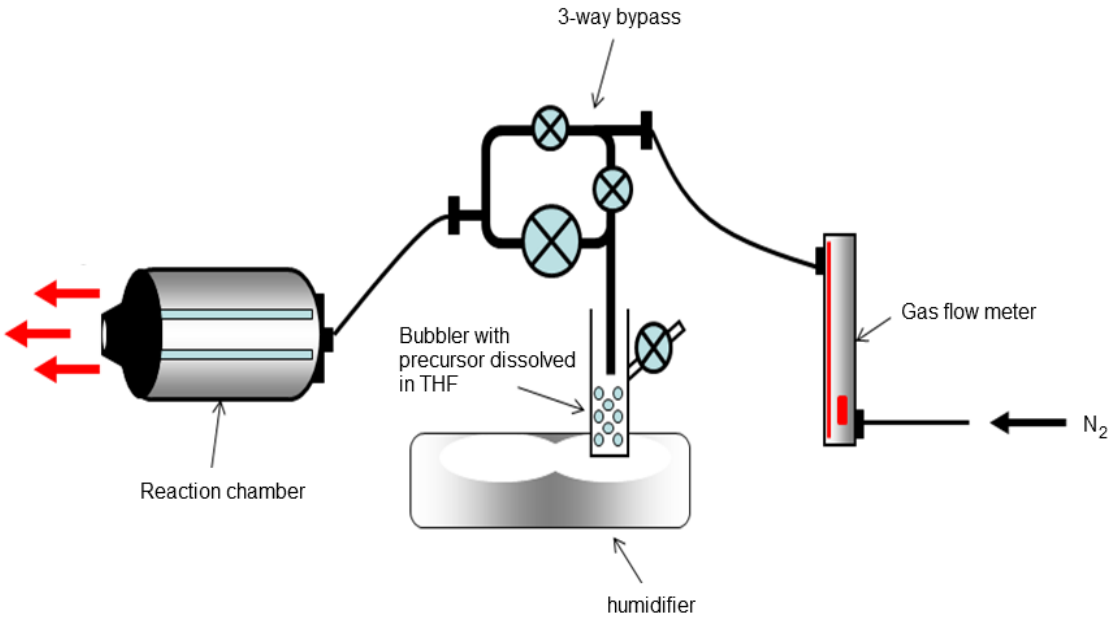

Figure 130: Diagram of the complete AACVD set-up.

AACVD reactions were carried out using an in-house built cold-wall CVD reactor (different to that used and described in Chapter 5) equipped with a graphite block, heated using a Whatman Cartridge Heater controlled with a Pt-Rh thermocouple (Figure 130). The design of the rig is such that the vapour was passed between two glass plates – a "top" plate and a "bottom" plate. The top plate is held in place by steel holders and is suspended above the bottom plate which is sat directly on the graphite block (Figure 131). The rig is designed so that the vapour passes between the two glass plates, whereby the top plate only serves to direct the flow of the vapour across the bottom plate. The temperature of the top plate is generally 50 °C lower than that of the bottom plate (substrate).

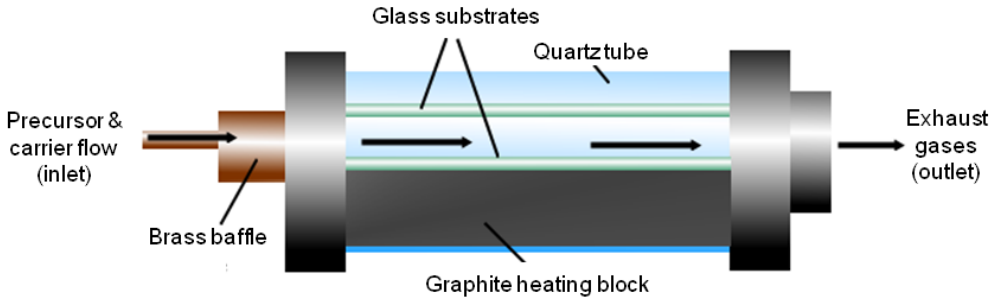

Figure 131: Diagram of the AACVD deposition chamber.

The [{Cp(CO)$_2$Fe}BiCl$_2$] precursor was weighed out in a glove-box into the bubbler. The bubbler itself is comprised of a flat-bottomed Schlenk flask where its thin base allows for facile generation of an aerosol using the piezoelectric humidifier. 150 mg (0.33 mmol) of precursor dissolved in *ca*. 40 cm^3 dry THF was used for each deposition. The precursor is insoluble in toluene, hexane, dichloromethane, diethyl ether and most common organic solvents and requires large volumes of THF or acetone for complete dissolution. This presented a slight problem, because the size of the bubbler flask limited the amount of precursor used and THF is appreciably more volatile than common AACVD solvents such as toluene, therefore some precursor dropped out of solution during the AACVD process due to solvent evaporation. A dense, thick aerosol was maintained during the process to mitigate this problem. The nitrogen gas flow through the precursor was maintained at 0.8 l/min and regulated using a calibrated flow meter.

8.2.2 TGA

The decomposition profile of [{Cp(CO)$_2$Fe}BiCl$_2$] was analysed *via* DSC-TGA (Figure 132). The TGA trace of the [{Cp(CO)$_2$Fe}BiCl$_2$] precursor displays two appreciable mass losses at 200 °C and 490 °C. The first steep mass loss at 200 °C appears just after the appearance of a small peak in the DSC trace at 194 °C and is most likely due to the onset of the melting point of the precursor, which is evidenced by the much sharper peak at 214 °C. The first steep mass loss (17.7%) flattens out by 220 °C, where there then follows a very small mass loss (4.7%) up to 480 °C.

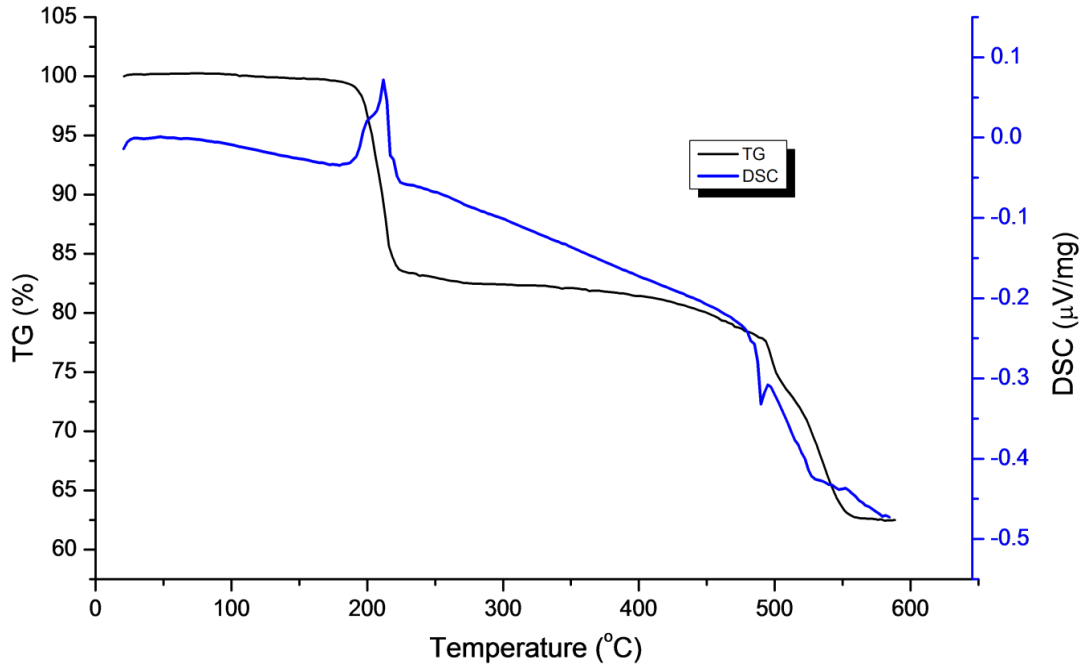

Figure 132: TGA-DSC trace of [{Cp(CO)$_2$Fe}BiCl$_2$]. The heating rate was 10 °C min^{-1}.

The second steep mass loss occurs at 490 °C which is coincident with a peak in the DSC trace present at 494 °C. This second steep mass loss corresponds to a weight loss of 14.9%, after which the TGA curve "flattens" up to the final temperature of the experiment at 600 °C. The first mass loss at 200 °C may be due to volatilisation after melting, however sublimation attempts proved unsuccessful in trying to account for this. It is more likely to be a phase change, possibly to a bismuth-iron oxide phase material, for example, $Bi_{25}FeO_{39}$ that would occur at such low temperatures. The cyclopentadienyl unit, the carbonyl groups and the chlorine atoms are expected to be lost during decomposition. The second mass loss at 490 °C would be due to a secondary phase change as there is a sharp DSC peak at 494 °C which accounts for this. It could be possible that a bismuth-iron oxide phase such as $BiFeO_3$ is being formed here as the temperature is high enough to promote growth of this phase, however powder XRD analysis of the residue remaining in the TGA pan after the experiment (Figure 133) revealed the presence of both metallic bismuth and maghemite (γ-Fe_2O_3).

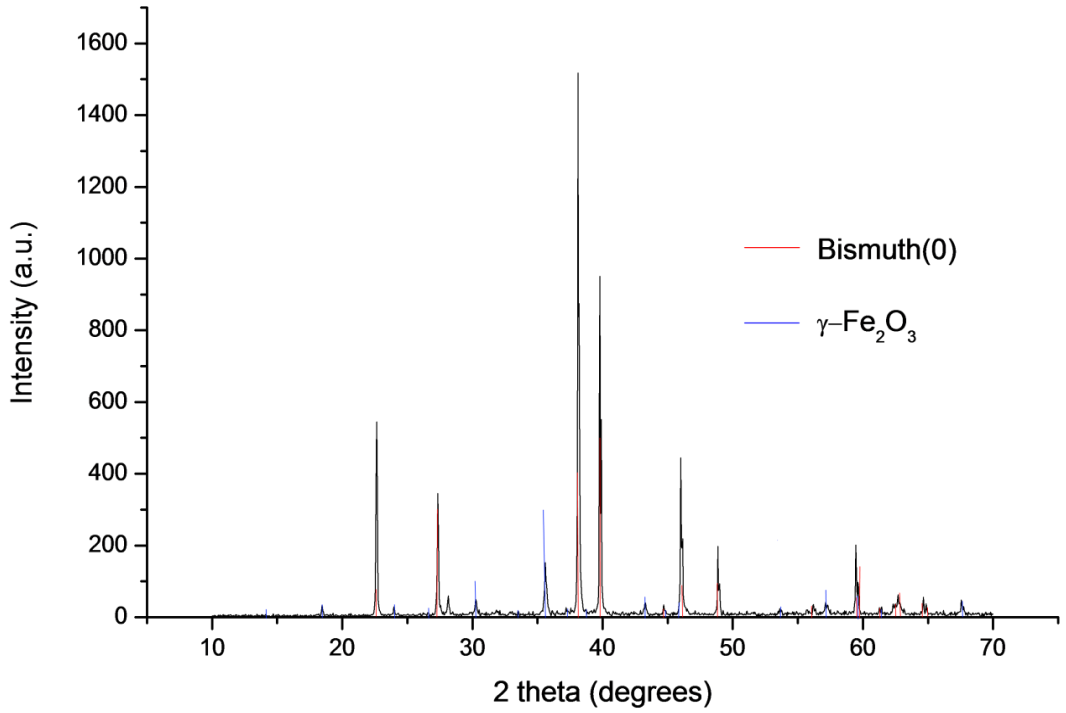

Figure 133: XRD pattern of the residue remaining in the TGA pan from the thermal decomposition of [{Cp(CO)$_2$Fe}BiCl$_2$]. The red stick pattern corresponds to metallic bismuth (PDF = 01-085-1330) and the blue stick pattern corresponds to γ-Fe$_2$O$_3$ (PDF = 039-1346).

8.3 Deposition of $Bi_{24}Fe_2O_{39}$

Films of $Bi_{24}Fe_2O_{39}$ were deposited on float glass substrates *via* AACVD of [{Cp(CO)$_2$Fe}BiCl$_2$] in THF solvent. No oxidising gas was used. Coverage appeared to vary dramatically as a function of substrate temperature, with significantly poor coverage obtained above 350 °C due to premature precursor decomposition within the inlet pipe-work and manifold of the reactor; increasing the carrier flow in an attempt to improve this resulted in minimal coverage on the substrate and was concentrated on an area nearer the exhaust. The best film coverage was observed at a substrate temperature of 300 °C, using a nitrogen carrier gas flow rate of 0.8 l/min; lower temperatures resulted in minimal coverage and poorer film adhesion. A dense mist was maintained at all times to alleviate the problem of any precursor being left behind in the bubbler after the solvent had evaporated, which altogether resulted in a deposition time of approximately twenty minutes. The films deposited at 300 °C had a brown-red appearance and were reasonably adherent – the films passed the scotch tape test but could be rubbed off with prolonged contact with tissue paper. They could all be scratched by steel wool.

8.3.1 X-ray diffraction

The powder X-ray diffraction pattern of a film deposited at 300 °C is shown in Figure 134.

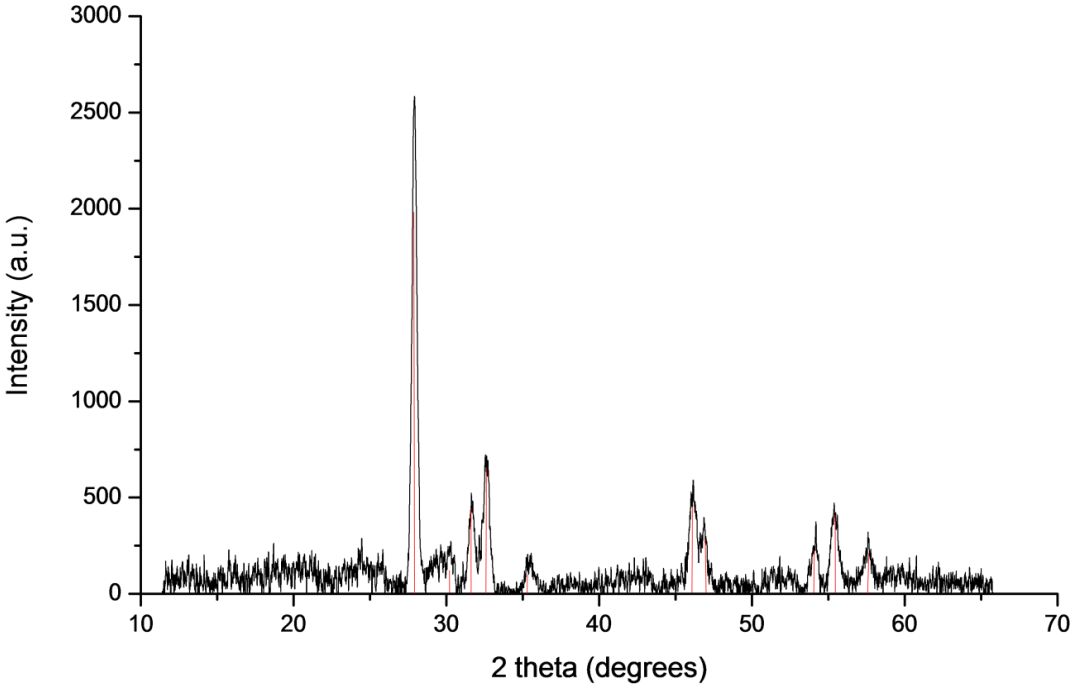

Figure 134: XRD pattern of the film deposited at 300 °C using [{Cp(CO)$_2$Fe}BiCl$_2$] dissolved in THF.

The powder X-ray diffraction pattern displayed in Figure 134 best matches that of the tetragonal structure of $Bi_{24}Fe_2O_{39}$ with unit cell parameters of $a = b = 7.28$ (4) Å, $c = 5.67(2)$ Å, $\alpha = \beta = \gamma = 90°$, space group *P*-421*c* (PDF No. 042-0201) obtained. The pattern displays preferred orientation in the [201] direction from the peak at 28° 2θ, and this preferred growth has also been observed for $Bi_{24}Fe_2O_{39}$ films grown *via* pulsed DC magnetron sputtering followed by annealing in a nitrogen atmosphere.[233] Unsurprisingly, no evidence of $BiFeO_3$ formation at this temperature (300 °C) was observed *via* X-ray diffraction.

8.3.2 Compositional analysis

Compositional analysis *via* WDX revealed that the film deposited as $Bi_{24}Fe_2O_{39}$ at 300 °C contained 53.4 at.% iron, 44.1 at.% bismuth and 2.5 at.% chlorine. Clearly this phase does not match the at.% analysis from WDX measurements, however other non-crystalline iron or bismuth species are likely to be present in the material given the low substrate temperature used. The films were insulating, and were therefore carbon coated to prevent charging during the scans, so quantification of carbon contamination *via* WDX was not possible.

8.3.3 X-ray photoelectron spectroscopy

XPS analysis after etching (Figure 135) revealed the presence of iron solely in the 3^+ oxidation state, with the Fe $2p_{1/2}$ region at 724.5 eV and Fe $2p_{3/2}$ region at 710.9 eV. The Fe^{3+} satellite peak was observed at 717.2 eV, and is characteristic of the presence of pure Fe^{3+} in a sample,[207] however its partnering satellite peak, which would be expected to be present at approximately 730 eV, was difficult to observe due to the high background signal and attempts to model a peak in this region were unsuccessful. Chlorine was also observed in the spectrum at 198.2 eV and 199.8 eV along with a large amount of carbon contamination which decreased slightly upon etching. From the data, the stoichiometry of the bismuth-iron oxide species present in the sample is Bi_2FeO_4 from the XPS data after etching. This would appear to contradict the WDX analysis, where the results had shown that the films were compositionally rich in iron and not bismuth. At present, there appears to be no reported XPS spectra of $Bi_{24}Fe_2O_{39}$ in the literature, so direct comparisons cannot be made. It is not known whether the etched samples used for XPS analysis are more of a true indication of the composition of the material even though it gives information at the surface and also deeper into the sample. However, WDX is usually more reliable for composition analysis as it looks at the bulk; surface layers probed *via* XPS are liable to contain different compositions and the etching process may change the composition.

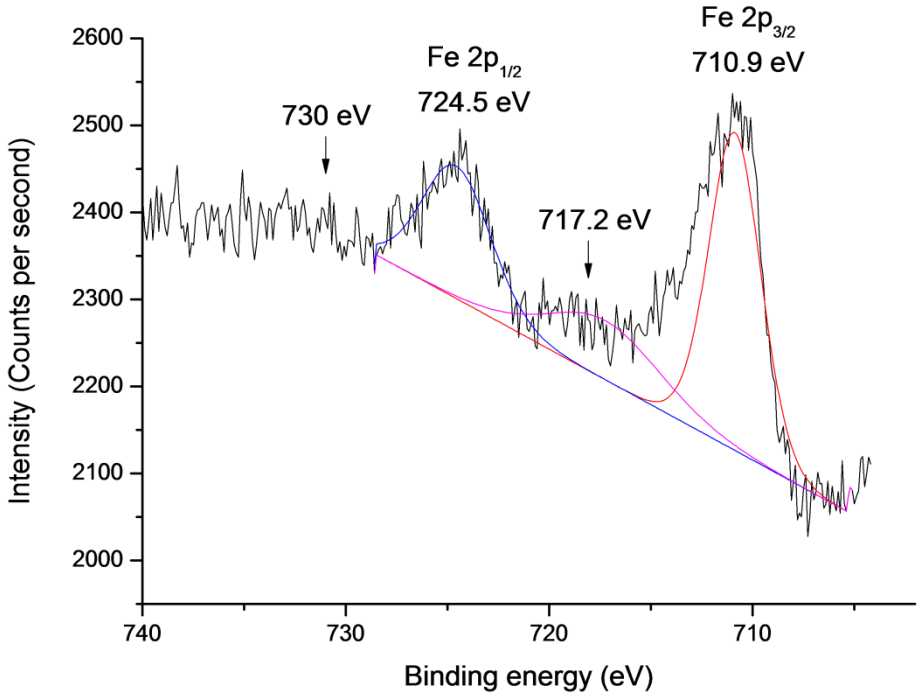

Figure 135: XPS spectrum of Fe 2p region after etching.

8.3.4 Scanning electron microscopy

Scanning electron microscopy was used to view the morphology of the $Bi_{24}Fe_2O_{39}$ film deposited at 300 °C, and is shown in Figure 136. The morphology is comprised of globular particulates, each of approximately 100 nm diameter. The average particle size was estimated *via* the Scherrer equation using the peak broadening from the X-ray diffraction patterns, resulting in a particle size of 130 nm. This is slightly higher than what is observed *via* SEM but this figure may account for some of the coalescence evident in the images, and is within the error associated with the use of the Scherrer equation. Overall, the coverage is excellent as there are virtually no voids where deposition has not taken place. The image on the left has a magnification of 25,000x and the image on the right a magnification of 45,000x. The growth mechanism from both images can easily be regarded as island growth due to the formation of individual spherical particles and clusters indicating strong interactions between the atoms in the film compared to those between the film and the substrate. This is further evidenced by the relatively weak adherence of these films to the substrate.

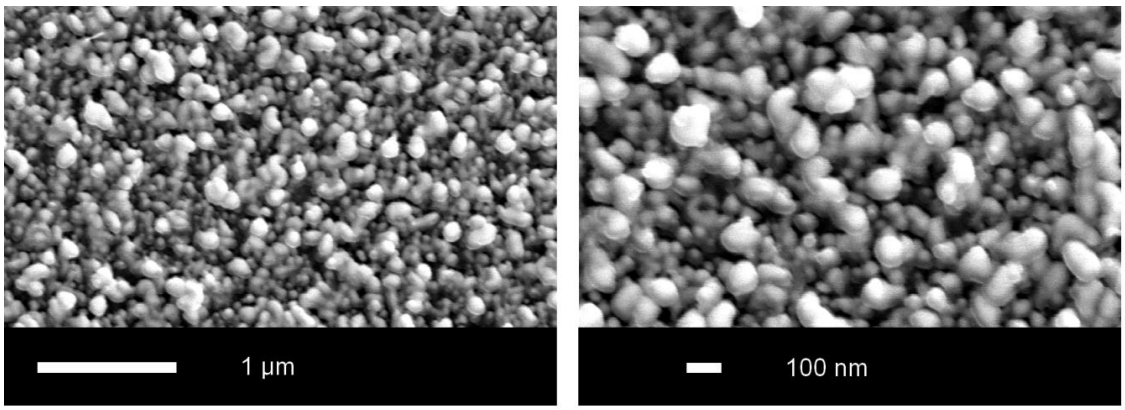

Figure 136: Top-down SEM images of $Bi_{24}Fe_2O_{39}$ film deposited on glass at 300 °C. Image on the left has 25,000x magnification, image on the right has 45,000x magnification.

Thin films of crystalline $Bi_{24}Fe_2O_{39}$, deposited *via* RF magnetron sputtering at room temperature on platinised silicon substrates followed by post-deposition annealing at 450 °C have been shown to possess high dielectric permittivity and low leakage current density, making them suitable for use in high-*k* dielectric applications in integrated circuits.[234] If the sole aim of this study was to deposit films of $Bi_{24}Fe_2O_{39}$, then clearly further work would be required in order to optimise the process of depositing these films *via* this AACVD process, so that the atomic ratios of bismuth and iron in the resultant films accurately reflect the phase observed from XRD analysis. The decomposition pathway of the precursor used in the process is likely to be complex and no evidence for its mechanism was found from TGA analysis.

8.4 AACVD of $BiFeO_3$ films – conversion of $Bi_{24}Fe_2O_{39}$ into $BiFeO_3$

It has been demonstrated that the growth of $BiFeO_3$ films *via* DC sputtering was successful after annealing films in a10% oxygen: 90% nitrogen atmosphere, whereas films annealed solely in a nitrogen atmosphere resulted in the formation of oxygen deficient $Bi_{24}Fe_2O_{39}$.[233]

Following deposition of $Bi_{24}Fe_2O_{39}$ films, it was decided to use post-deposition heat treatment in an attempt to convert these into $BiFeO_3$ films. To our knowledge, $BiFeO_3$ films have not been grown using single-source precursors; pure $BiFeO_3$ powders have been synthesised *via* the decomposition of $[BiFe(CN)_6.4H_2O]$ in air at 600 °C,[136] and $[(CO)_4FeBi(O^tBu)]_n$ has been shown to thermally decompose in a helium atmosphere at 700 °C to form $BiFeO_3$ but with $Bi_{25}FeO_{40}$ impurity.[134] Therefore, a variety of annealing temperatures were used employing Pilkington float glass, Corning AMLCD and polished quartz substrates, depending on the temperature required for heating. For annealing temperatures between 450 – 550 °C, Pilkington float glass was used, and for temperatures between 600 – 700 °C, Corning glass was used, whilst heat treatment at 800 °C and 1000 °C required the use of quartz substrates. Annealing was carried out in air for two hours using a Carbolite furnace at a heating ramp rate of 10 °C/min. For each annealing experiment, a fresh sample (of $Bi_{24}Fe_2O_{39}$) deposited *via* AACVD at a substrate temperature of 300 °C was used. The results are summarised in Table 15.

Table 15: Summary of the AACVD experiments and annealing conditions.

Type of substrate	Annealing Temp / °C	Phase(s) obtained *via* XRD	At.% Bi:Fe (from WDX)	Average film thickness / nm	Band-gap / eV	At.% Cl contamination (from WDX)
Pilkington	**300**	$Bi_{24}Fe_2O_{39}$	54:44	1890	n/a	2.5
Pilkington	**400**	$Bi_2O_{2.33}$ + $Bi_{25}FeO_{40}$	61:39	1580	n/a	1.6
Pilkington	**450**	$Bi_{24}Fe_2O_{39}$ ($Bi_2O_{2.33}$) + $Bi_{25}FeO_{40}$	57:42	1440	n/a	1.4
Pilkington	**500**	$BiFeO_3$ + $Bi_2Fe_4O_9$	58:41	1110	2.0	<1
Pilkington	**550**	$BiFeO_3$ + $Bi_2Fe_4O_9$	55:44	800	1.9	<1
Pilkington	**600**	$BiFeO_3$ + minimal $Bi_2Fe_4O_9$	52:47	680	2.2	0
Corning	**650**	$BiFeO_3$ + $Bi_2Fe_4O_9$	52:48	560	2.1	0
Corning	**700**	$BiFeO_3$	51:49	320	2.1	0
Quartz	**800**	$Bi_4Si_3O_{12}$	n/a	n/a	n/a	0
Quartz	**1000**	Crystobalite SiO_2	n/a	n/a	n/a	0

The as-deposited films (at 300 °C) were characterised as crystalline $Bi_{24}Fe_2O_{39}$ *via* powder X-ray diffraction as described earlier but are likely to contain amorphous iron species due to their higher than expected iron content. Post-deposition annealing using the float glass samples at 400 °C resulted in films that were compositionally rich in bismuth (61:39 at.% Bi:Fe, found *via* WDX) and X-ray diffraction revealed they were composed of $Bi_2O_{2.33}$ and $Bi_{25}FeO_{40}$ phases, whilst annealing at 450 °C resulted in films of mixed phase $Bi_{24}Fe_2O_{39}$ with $Bi_{25}FeO_{40}$, containing a 57:42 at.% Bi:Fe ratio, clearly indicating more iron incorporation in the sample. Annealing at 500 °C resulted in the emergence of the desired $BiFeO_3$ phase in addition to some parasitic $Bi_2Fe_4O_9$, however the Bi:Fe ratio from WDX analysis suggested the film was still

slightly rich in bismuth (58:41 at.% Bi:Fe). This ratio became more iron rich/bismuth deficient (55:44 at.% Bi:Fe) upon increasing the annealing temperature to 550 °C. By raising the annealing temperature to 600 °C and 650 °C and using samples deposited on Corning AMLCD glass, the Bi:Fe ratio became closer to unity, and the XRD peak intensity (abundance) of the parasitic $Bi_2Fe_4O_9$ phase present gradually appeared to decrease. The appearance of the films also gradually changed with temperature; their colour changed from brown to dark orange through to bright orange for the film annealed at 700 °C. Through annealing at 700 °C, pure phase $BiFeO_3$ was observed *via* XRD and the Bi:Fe ratio found *via* WDX (51:49 at.% Bi:Fe) suggested that this film was indeed phase-pure. The decrease in bismuth content as a function of temperature could be due to the appreciable volatility of bismuth and/or bismuth oxide species.[235] Chlorine contamination was high for the as-deposited film and for those annealed at 400 °C (2.5 and 1.6 at.% respectively), however this contamination decreased as a function of annealing temperature (1.4 at. % for the film annealed at 450 °C and less than 1 at.% for films annealed at 500 and 550 °C). Films annealed between 600 – 1000 °C were found to have no chlorine incorporation, suggesting the temperature is high enough to remove all traces of chlorine left over from the precursor.

8.4.1 X-ray diffraction

The as-deposited and annealed films were identified and characterised *via* X-ray diffraction. Samples deposited on polished quartz substrates and annealed at 800 °C in air led to the formation of a pink coloured film, characterised as cubic bismuth silicate $Bi_4Si_3O_{12}$ (Eulytite structure, PDF 076-1726), which may have occurred as a result of a reaction with the substrate at this temperature (Figure 137). Likewise, annealing at 1000 °C only led to the observation of crystalline SiO_2 with the Crystobalite structure (PDF 039-1425), attributed to the substrate.

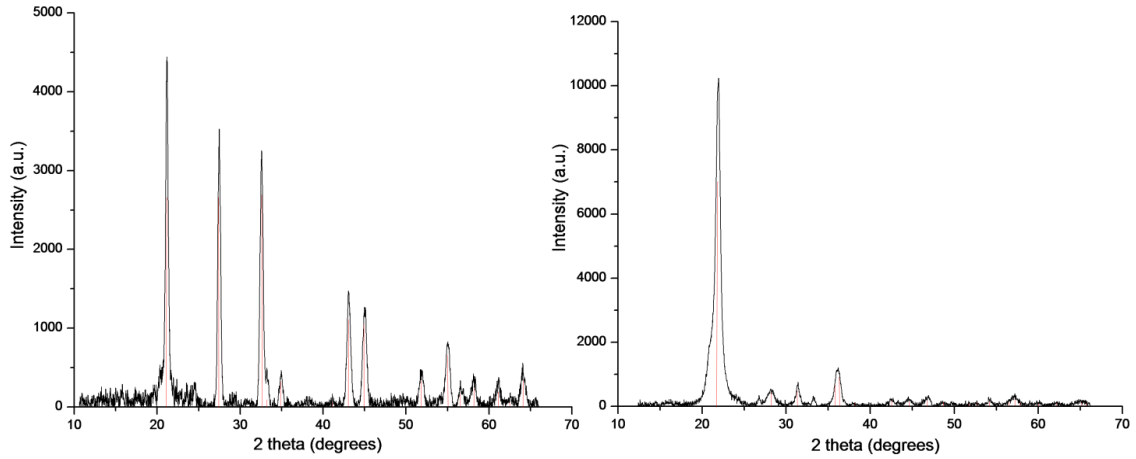

Figure 137: XRD patterns of $Bi_4Si_3O_{12}$ (left) and crystalline SiO_2 (right) after annealing at 800 °C and 1000 °C.

The XRD patterns of samples annealed between 400 – 500 °C are displayed in Figure 138. As previously described, the film annealed at 400 °C contained no crystalline $BiFeO_3$ phase, but instead appeared to contain $Bi_2O_{2.33}$ (PDF 027-0051) and $Bi_{24}Fe_2O_{39}$ (PDF 042-0201). This was also noticed in the film annealed at 450 °C which contained the same species, however the similar crystallographic structures of $Bi_2O_{2.33}$ (β-Bi_2O_3) and $Bi_{25}FeO_{40}$ (PDF 046-0416) made it difficult to distinguish between them from X-ray diffraction patterns. Nevertheless, the observation of these bismuth rich phases is consistent with the high bismuth content measured *via* WDX analysis, however the film must also contain a high proportion of amorphous iron containing species in order to account for the relatively high iron content (Table 15).

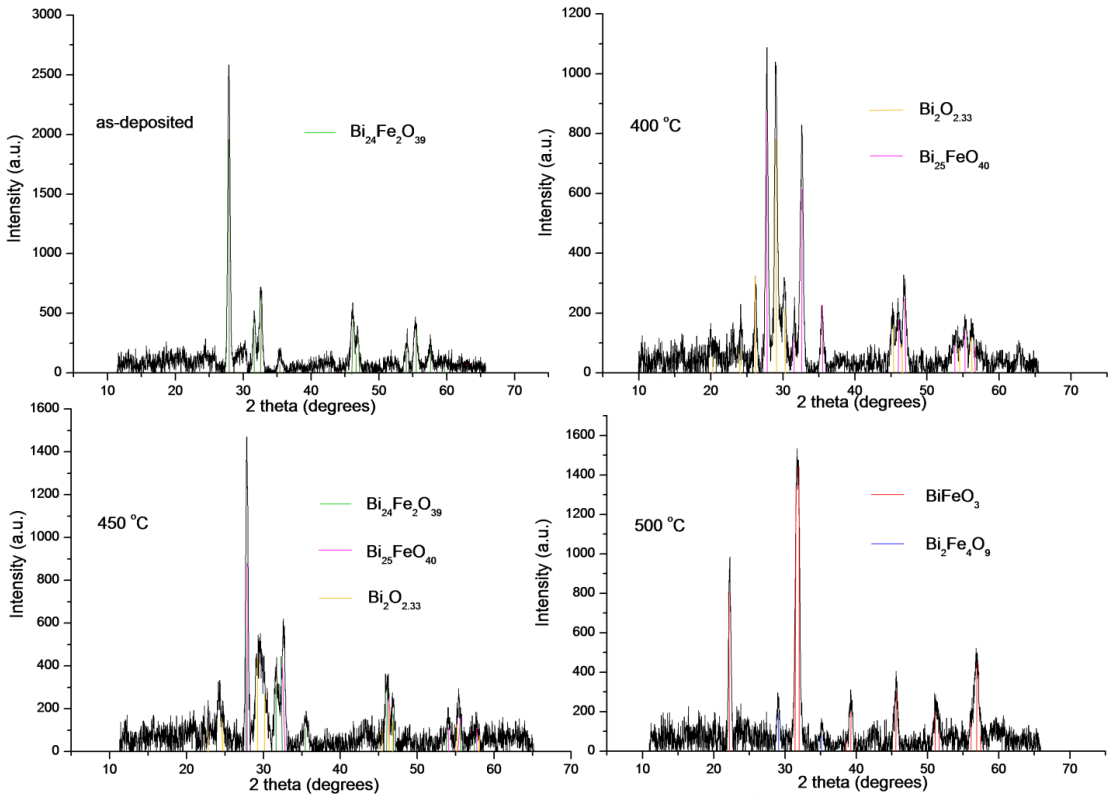

Figure 138: Powder X-ray diffraction patterns of the BFO films annealed between 400 – 500 °C, with a pattern of the as-deposited film included for reference (top left).

The appearance of the hexagonal phase $BiFeO_3$ was observed after annealing at 500 °C, albeit with the parasitic $Bi_2Fe_4O_9$ phase also present. This is encouraging as the previously identified $Bi_{24}Fe_2O_{39}$ and $Bi_{25}FeO_{40}$ phases were no longer seen. Hence there appears to be a phase transition between 450 – 500 °C where growth of $BiFeO_3$ emerges, which is to an extent in agreement with the phase diagram of $BiFeO_3$ constructed by Scott *et al.*[204] (~using Fe_2O_3 and Bi_2O_3 as precursors), whereby $BiFeO_3$ growth emerges at 600 °C based on at least a 1:1 mixing ratio of precursors. Clearly, the difference in precursors and synthetic procedures employed make it difficult to make exact comparisons with their data. The X-ray diffraction patterns of the samples annealed at higher temperatures are shown in Figure 139.

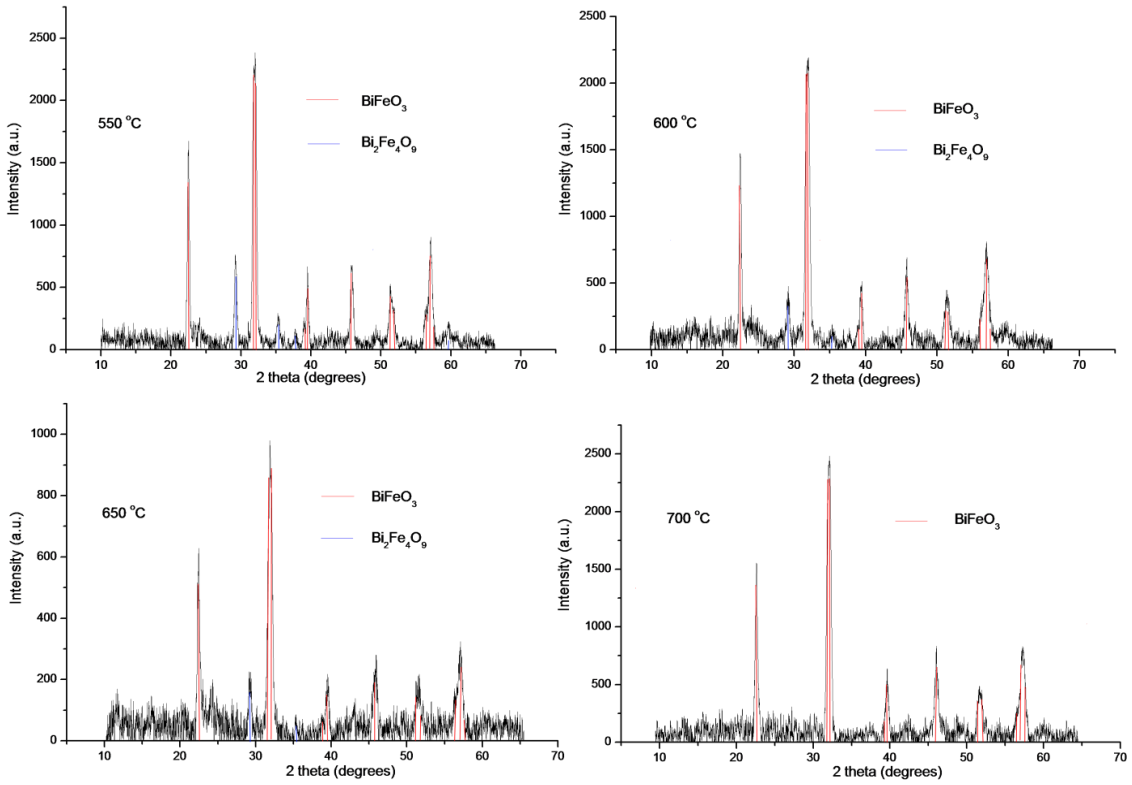

Figure 139: X-ray diffraction patterns of BFO films annealed at temperatures between 550 – 700 °C.

The films still contained various amounts of $Bi_2Fe_4O_9$, in addition to $BiFeO_3$, when annealed between 550 – 650 °C, although the intensity of the $Bi_2Fe_4O_9$ phase at 29° 2θ decreases as a function of temperature and is much lower than those of $BiFeO_3$ at 600 °C and 650 °C. Encouragingly, at 700 °C there is no evidence of parasitic $Bi_2Fe_4O_9$ in the X-ray diffraction data and $BiFeO_3$ is the dominant phase. There may be low intensity peaks that are unassigned at 43° and 49° 2θ, so a longer X-ray scan was obtained using a higher resolution diffractometer in flat-plate geometry equipped with a post-sample monochromator (Figure 140). Films were not annealed at temperatures greater than 700 °C due to the imminent softening point of the substrate (725 °C), and in light of recent work[204] which has shown that $BiFeO_3$ undergoes a phase transition between 820 – 925 °C to an orthorhombic β-phase, followed by a transition to a cubic γ-phase between 925 – 933 °C (leading to collapse of the band-gap); both of which are exhibited in bulk and thin films of the material.

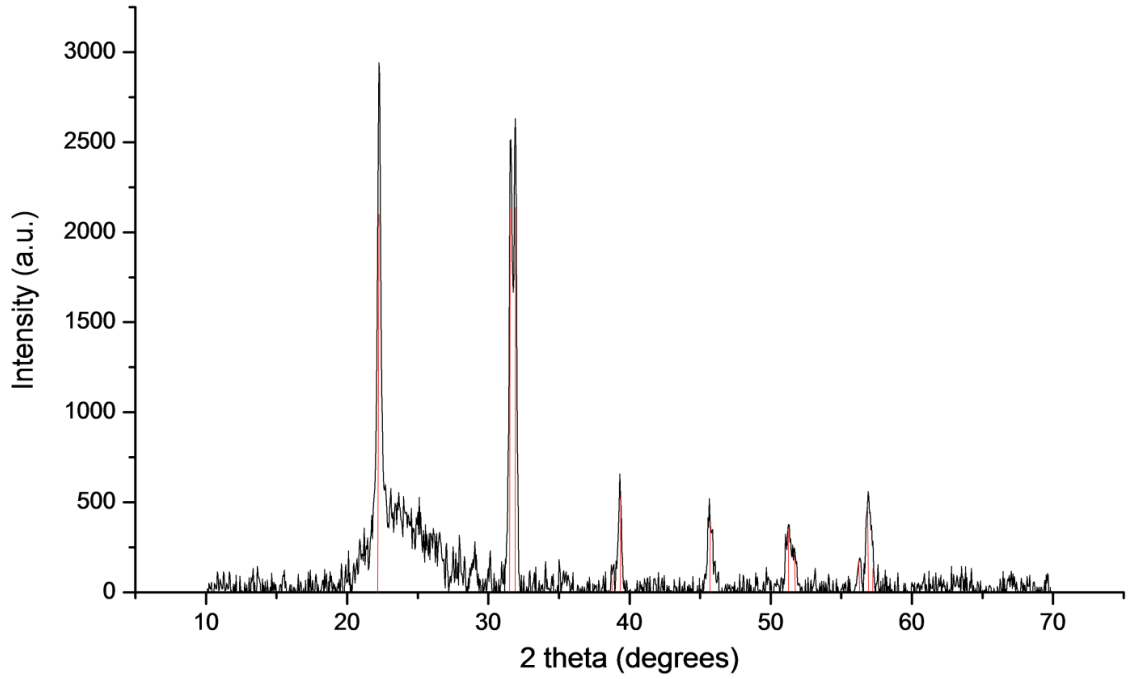

Figure 140: X-ray diffraction pattern of the $BiFeO_3$ film annealed at 700 °C. The red stick pattern corresponds to rhombohedral $BiFeO_3$ (PDF = 014-0181).

Figure 140 shows the X-ray diffraction pattern of the film annealed at 700 °C to be composed of pure $BiFeO_3$ without any evidence of the small peaks at 43° and 49° 2θ obtained from the GADDS-D8 diffractometer. The high background between 20 -30° 2θ is due to the amorphous glass substrate. The splitting of the peak at 32° is now much more apparent after re-collection of this pattern. Hexagonal unit cell parameters of $a = b = 5.588(4)$ Å, $c = 13.913$ (6) Å, ($\alpha = \beta = 90°$, $\gamma = 120°$, space group *R*3*c*) were obtained *via* unit cell refinement and were in agreement with literature values for bulk $BiFeO_3$ found *via* synchrotron X-ray diffraction ($a = b = 5.57414$ (4) Å, $c = 13.85882$ (12) Å, PDF = 014-0181).[205]

8.4.2 Scanning electron microscopy

The morphologies of films annealed at the various temperatures were examined *via* SEM (Figure 141).

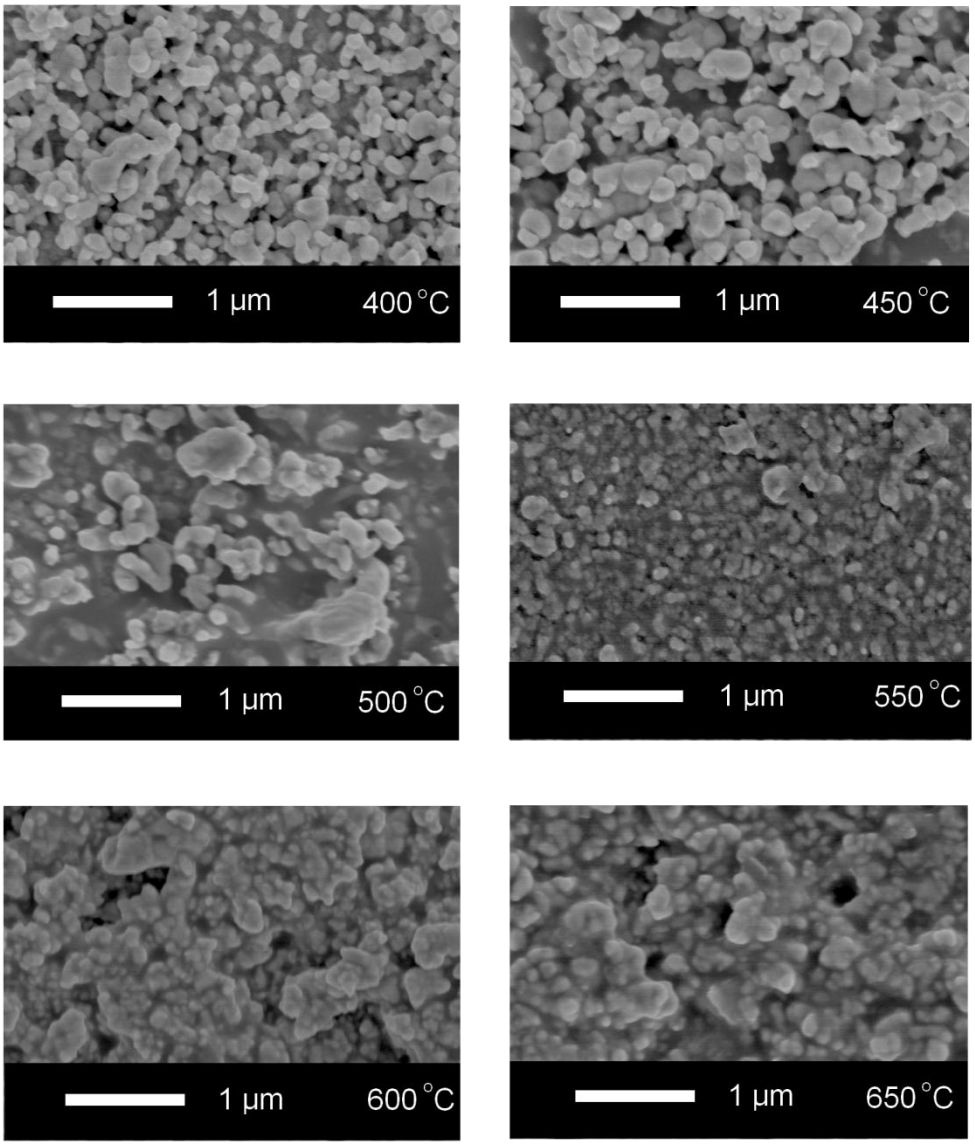

Figure 141: Top-down SEM images of the films annealed at the various temperatures specified within the diagram.

There appears to be a general trend in the morphologies that were observed as the annealing temperature was increased. As described earlier, the as-deposited film (300 °C) possessed a very globular morphology, with average particle diameters of 100 nm, whereas the samples annealed at 400 °C and 450 °C also possess globular morphologies but with some coalescing of the particles. There are more voids visible in the morphology suggesting that the heat treatment has led to diffusion of volatile particles away from the film, which is consistent with the

decrease in film thickness described later. Annealing at 500 °C has led to more coalescing of the particles with some large features observed. Between 550 – 650 °C the degree of coalescing of the particles has increased dramatically and the morphology appears much denser, however individual particles can still be observed. The agglomeration of the particles has led to a "flatter" film with fewer features; a result that is perhaps expected as a consequence of annealing.

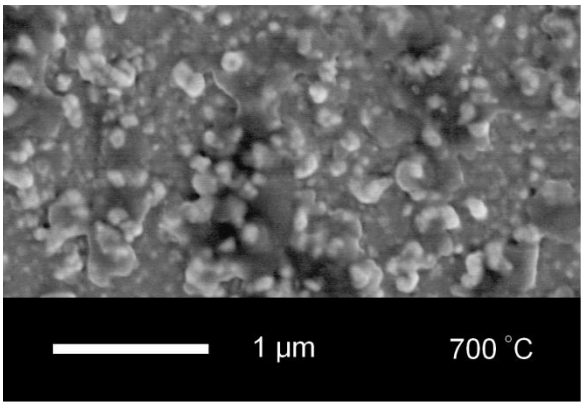

Figure 142: SEM image of the $BiFeO_3$ film formed after annealing at 700 °C.

A similar morphology to those seen at 600 °C and 650 °C was identified for the $BiFeO_3$ film formed through annealing at 700 °C (Figure 142). The agglomeration of some of the particles has led to large outcrops of features, suggesting that heat treatment at this temperature leads to an alteration of the morphology such that the film becomes rougher and less uniform. The average particle sizes in the films were estimated using the broadening of the diffraction peaks (Scherrer Equation) and are shown in Table 16. There appears to be little correlation between annealing temperature and particle size, however particle sizes at the higher end of the temperature range (600 – 700 °C) were almost half the size of those observed between 300 – 550 °C, with the exception of the film annealed at 500 °C. In conventional CVD processes, an increase in particle size is expected as a function of substrate temperature due to the greater mobility and surface diffusion of incoming reactants.

In contrast, the annealing process would result in diffusion away from the film of larger and more volatile species, coupled with surface reactions between the film and the air which would give rise to a change in phase. This is in addition to particle sintering and coalescence, which perhaps reveals why there is little correlation between the annealing temperature and the average crystallite size.

Table 16: Variation in average crystallite size (diameter) as a function of annealing temperature.

Annealing Temperature (°C)	Average crystallite diameter (nm)
300 (as-deposited)	195
400	270
450	210
500	140
550	220
600	90
650	130
700	110

8.4.3 Film thickness

Film thickness was analysed *via* side-on SEM imaging. The $Bi_{24}Fe_2O_{39}$ film deposited at 300 °C possessed a thickness of almost 2 μm (1890 nm) which steadily decreased upon raising the annealing temperature. At 400 °C and 450 °C the average thickness was 1580 nm and 1440 nm respectively, followed by a large decrease to 1110 nm when annealed at 500 °C. The thickness then gradually decreased to 800 nm and 680 nm at 550 °C and 600 °C, followed by an average thickness of 560 nm for the film annealed at 650° C. The film characterised as pure $BiFeO_3$ which was annealed at 700 °C had an average thickness of 320 nm. The large decrease in thickness between films annealed at 450 °C and 500 °C may be due to the removal of volatile parasitic phases $Bi_{24}Fe_2O_{39}$ and $Bi_2O_{2.33}$ along with other non-crystalline impurities, leading to a dramatic reduction in thickness. A typical side-on SEM image of the $BiFeO_3$ annealed at 700 °C is shown in Figure 143. The growth of the film appears fairly uniform and the morphology is quite dense, which is in contrast to the $Bi_{24}Fe_2O_{39}$ film deposited at 300 °C that was very globular in appearance (Figure 136).

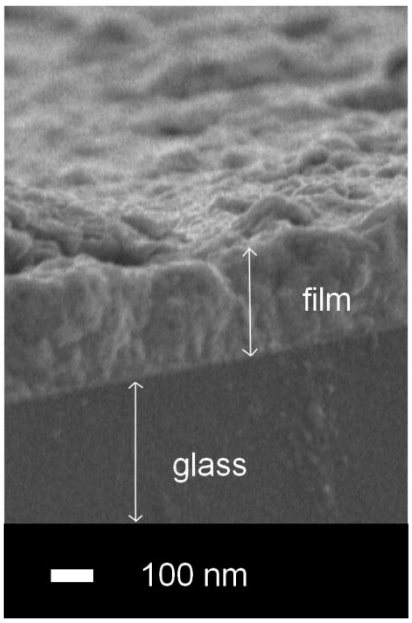

Figure 143: A typical side-on SEM image of the $BiFeO_3$ film formed after annealing at 700 °C.

8.4.4 X-ray photoelectron spectroscopy

The composition of the $BiFeO_3$ film formed after annealing at 700 °C was analysed *via* XPS. Spectra were recorded and analysed after etching for 10 minutes to a depth of 10 nm. As the Fe 2p core level is split into the $2p_{1/2}$ and $2p_{3/2}$ components, analysis revealed the presence of iron in the 3^+ oxidation state, with the Fe $2p_{1/2}$ region at 724.9 eV and the Fe $2p_{3/2}$ region at 711.3 eV (Figure 144). Although the background signal was high, the Fe^{3+} satellite peak could still be observed at 718.9 eV and is characteristic of the presence of pure Fe^{3+} in a sample as reported in the literature.[123] The Fe^{3+} $2p_{3/2}$ peak for pure $BiFeO_3$ is usually found at 711 eV but can shift as a function of introducing dopant transition metal ions into the structure. For example, Kharel *et al.*[236] measured the $2p_{3/2}$ peak for their $BiFeO_3$ films at 711 eV, but doping with Ni^{2+} ions shifted this entire peak to 709 eV, indicating that a proportion of the iron atoms were in the 2^+ state. Broadening of the peak at 711 eV down to 709 eV has been often observed[208] as a result of high sintering temperatures (~ 875 °C) which can induce oxygen non-stoichiometry, leading to a co-existence of Fe^{2+} and Fe^{3+} species, however peak broadening to this extent was not observed in our samples. For the presence of iron in Fe_3O_4 species, one would expect an additional broad shoulder as low as 707 eV which would be attached to the peak at 711 eV.[206]

The expected satellite peak for Fe $2p_{1/2}$ in the 729 eV region was difficult to observe due to the high noise level and the broad nature of the peak at 724.9 eV, which made fitting an extra peak in this region challenging. The signal rises slightly at 732.8 eV and could be due to the influence of the missing Fe $2p_{1/2}$ satellite peak.[207] Kothari *et al.*[237] state that the satellite peak for Fe 2p 3^+ species in undoped $BiFeO_3$ is usually found at approximately 8 eV above the principal

peak, whereas the satellite for Fe 2p 2^{+} is observed at 6 eV above its principal peak, and therefore the former observation is in agreement with our results. No chlorine contamination was detected, and although significant carbon contamination was observed on the surface, this decreased dramatically upon etching, indicating the carbon content to be due to adventitious surface contamination.

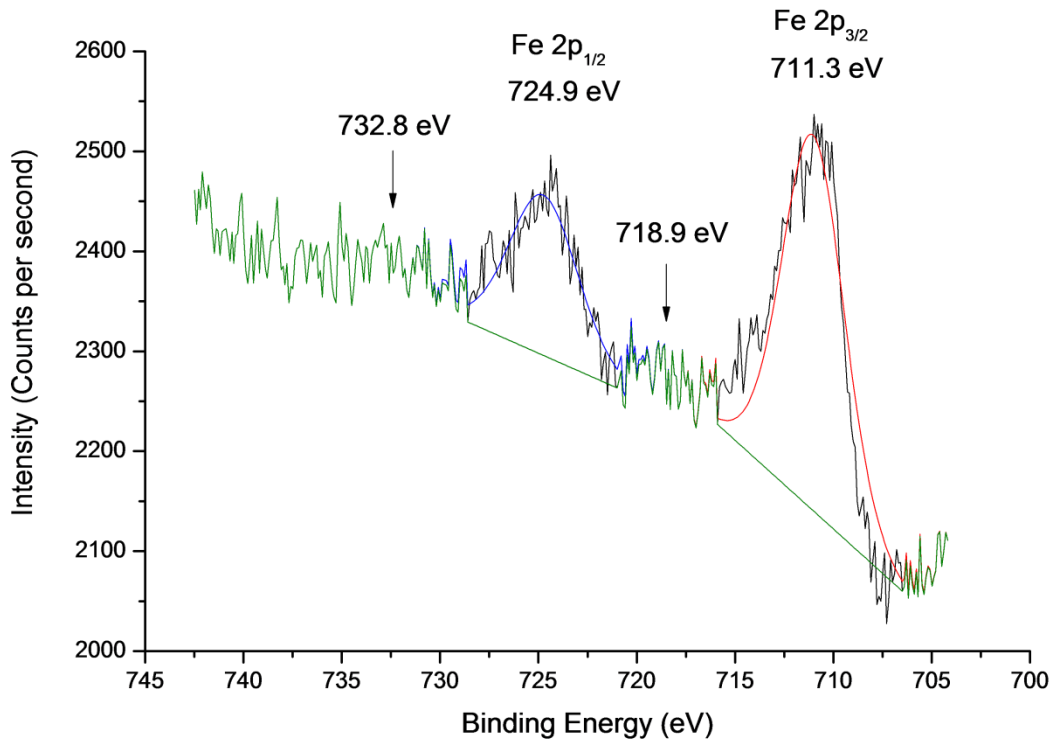

Figure 144: XPS spectrum of the Fe 2p region after etching.

XPS analysis of the bismuth 4f region (Figure 145) revealed two distinct peaks corresponding to the Bi $4f_{7/2}$ region at 159.4 eV and the Bi $4f_{5/2}$ region at 164.7 eV, which are both characteristic of bismuth in the 3^{+} oxidation state, which is expected for $BiFeO_3$.[170] Further etching experiments to greater depths resulted in peak distortion caused by preferential sputtering, which led to the formation of metallic bismuth.

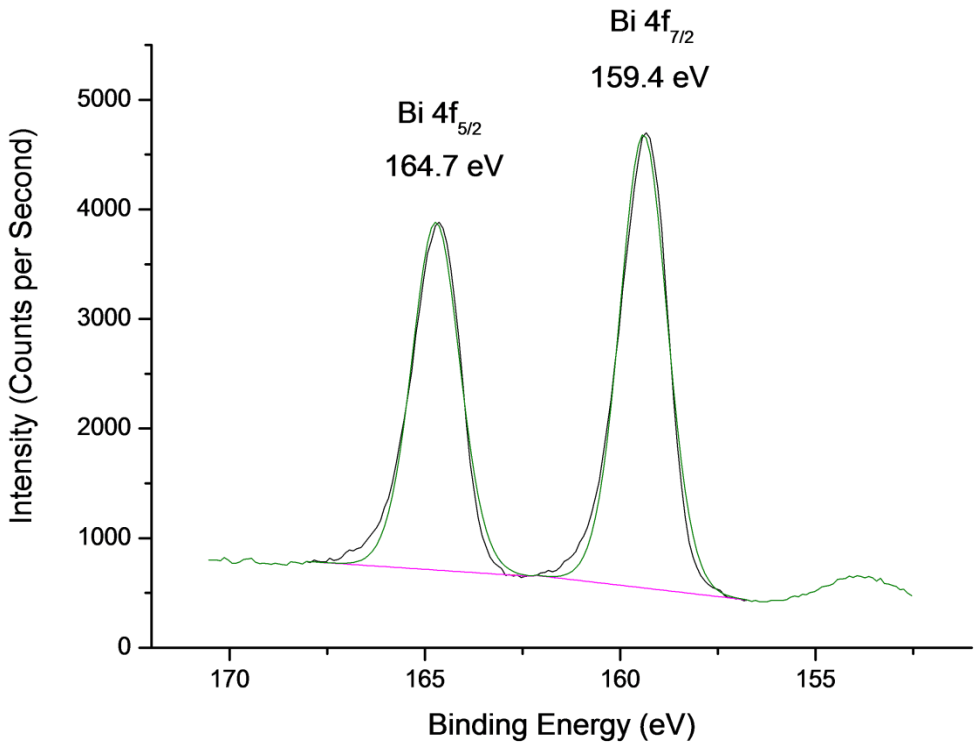

Figure 145: XPS spectrum of the Bi 4f region after etching.

Similarly, XPS analysis of the oxygen 1s region after etching revealed one broad asymmetric peak that could be fitted with 2 smaller individual Gaussian peaks (Figure 146). The lower binding energy O 1s peak is due to metal oxide oxygen species whereas the higher binding energy component is either due to grease contamination (terminal hydroxyl, –OH) or due to some other contamination. Hence the metal oxide oxygen peak is ascribed to the smaller fitted peak at 530.2 eV and the contamination oxygen 1s peak corresponds to the larger fitted peak at 532.3 eV. A silicon peak at 102 eV was observed in the top surface scan and its intensity decreased dramatically during the etching experiments, indicating that the origin of this peak is due to penetration of the surface contamination and not from the glass substrate.

Analysis of the Bi 4f, Fe 2p and O 1s peak areas (after etching) which were divided by their respective relative sensitivity factors (9.14, 2.957 and 0.78 for bismuth, iron and oxygen respectively) indicated the presence of the three components in an approximate 1:1:3 ratio, and this would be expected for stoichiometric $BiFeO_3$.

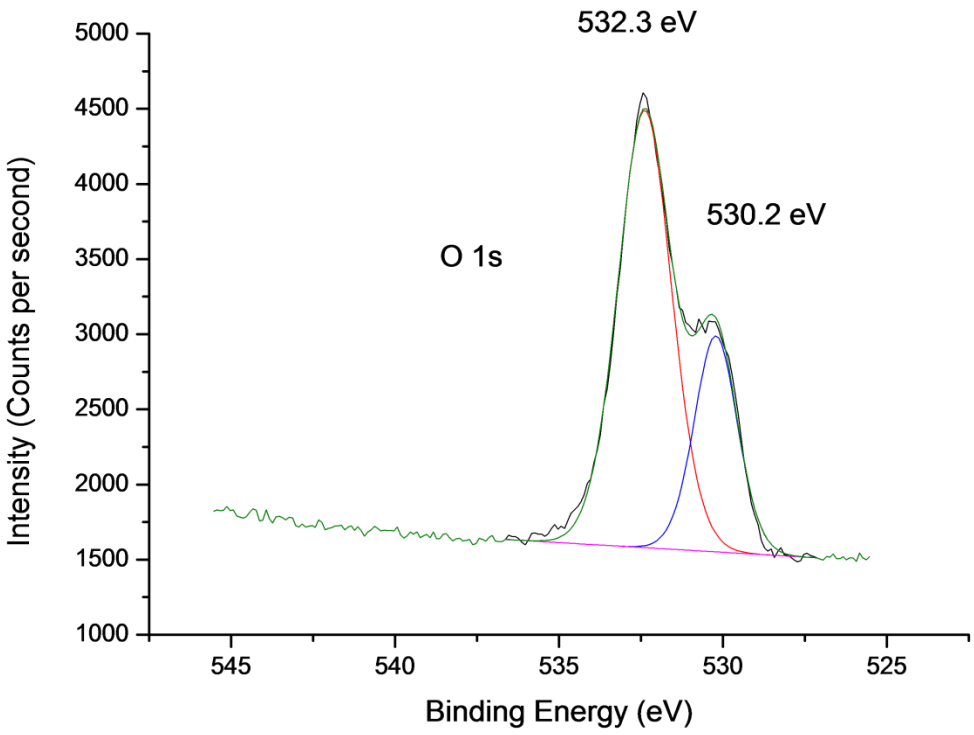

Figure 146: XPS spectrum of the oxygen 1s region after etching.

8.4.5 Raman spectroscopy

Raman spectra were acquired using a helium-neon laser wavelength of 514.5 nm at liquid nitrogen temperature (-195 °C) using a cold stage and temperature controller. The Raman spectrum of the $BiFeO_3$ film formed after annealing at 700 °C and recorded at -195 °C is displayed in Figure 147. As discussed previously, $BiFeO_3$ adopts a highly rhombohedrally distorted perovskite structure (space group *R*3*c*), which indicates that there are 13 Raman active modes[209] – $4A_1$ and 9E vibrations, and as they are doubly degenerate, all modes are both IR and Raman active. Peaks that can be assigned to the A_1 phonon mode were observed at 147, 177, 223 and 475 cm^{-1}. Peaks that could be assigned to the E phonon mode vibration were observed at 265, 282, 301, 354, 374, and 526 cm^{-1}, all of which are almost identical to those observed by Fukumura[209] and Rout[208] in their investigation of the Raman spectra of $BiFeO_3$ single crystals and powders at similar temperatures. The laser filter cut-off at 120 cm^{-1} in our spectra does not allow for identification of the additional E phonon vibrations which are expected to be present at 75 and 81 cm^{-1}. Additional peaks were also observed at 420 cm^{-1} with a broad peak between 650 – 750 cm^{-1} which could not be assigned. The peak at 550 cm^{-1} has previously been assigned to the TO forbidden vibrational mode of the fourth A_1 phonon vibration and the observation of a broad peak around 1100 cm^{-1} suggests it is indeed associated with the 2TO mode.[238] The three broad peaks between 900 – 1400 cm^{-1} are similar to those observed by Ramirez *et al.*[210] for bulk

and thin film $BiFeO_3$ samples, and they assign them to the $2A_4$, $2E_8$ and $2E_9$ modes respectively; they subsequently disappear at the Neel Temperature (T_N ~ 640 K), which they believe indicates a strong spin-two-phonon coupling in the material.

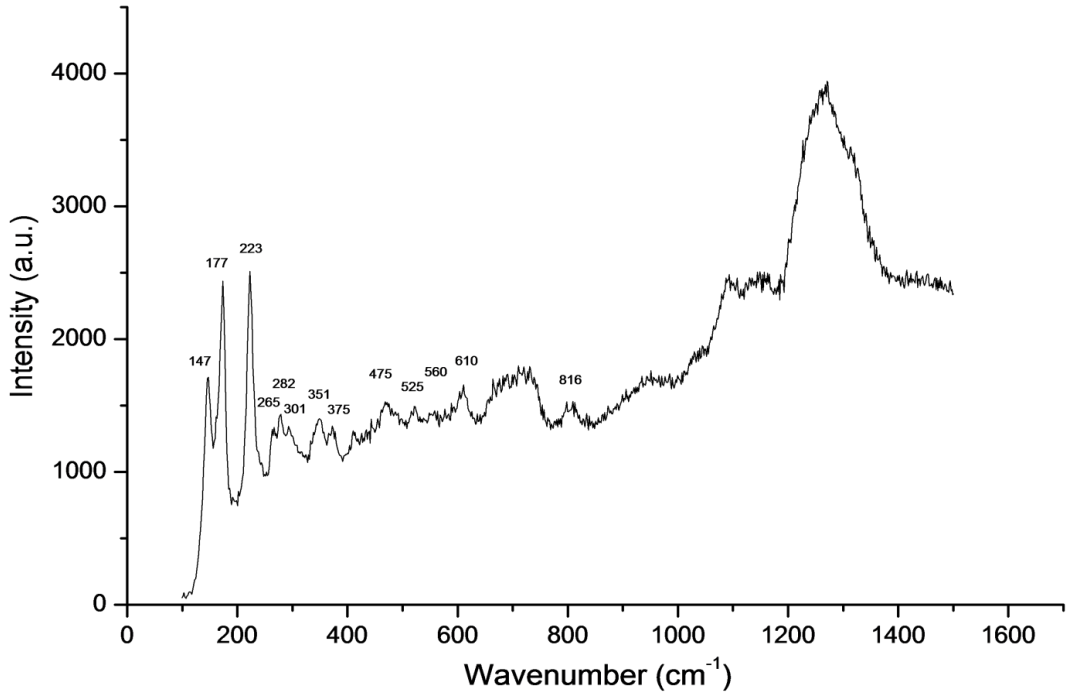

Figure 147: Raman spectrum of the $BiFeO_3$ film formed after annealing at 700 °C, and recorded at - 195 °C.

8.4.6 Atomic force microscopy

A 5 μm field size AFM image and the 3D equivalent image of the $BiFeO_3$ annealed at 700 °C is shown in Figure 148. A hierarchical structure is shown which is comprised of some globular and particles of approximately 50 nm diameter which have clustered together to form larger aggregates. There appears to be no voids where deposition has not taken place and the coverage is excellent and reasonably uniform. Similar to what was observed in the previous chapters when comparing top-down SEM images with the corresponding AFM images, the morphology in both types of imaging still appears globular, however the AFM image appears much rougher with more features. The field size image also reveals good coverage together with high features that have arisen due to "stacking" and sintering of the particles as observed in the SEM image of this film (Figure 142).

The root mean squared roughness (rms) of the sample was calculated at 62 nm, which is almost identical to the value (60 nm) obtained for $BiFeO_3$ films grown *via* LPCVD of $[Fe(O^tBu)_3]_2$ and $[Bi(O^tBu)_3]$ in Chapter 7, but double the value measured for $BiFeO_3$ films grown *via* the LPCVD reaction of $[Bi(O^tBu)_3]$ and $[Fe(acac)_3]$ with air described in Chapter 6. A value of 62

nm here is considerably lower than those obtained from measurements performed on indium-gallium oxide films deposited *via* AACVD followed by post-deposition annealing at 1000 °C, whose roughness values were in the range 94 nm – 1 µm, which were said to be higher than the industry standard of 100 nm.[183] It is also slightly lower than values obtained from measurements of Pt-Bi_2O_3 films grown *via* AACVD, described in Chapter 5, which possessed a roughness of 97 nm but were not subject to post-deposition annealing. Indeed, the annealing process would assist in sintering the particles together and lowering the roughness of the film, however the AFM and top-down SEM images suggest the films still possess high features that would be beneficial for applications requiring high surface area materials, such as catalysis.

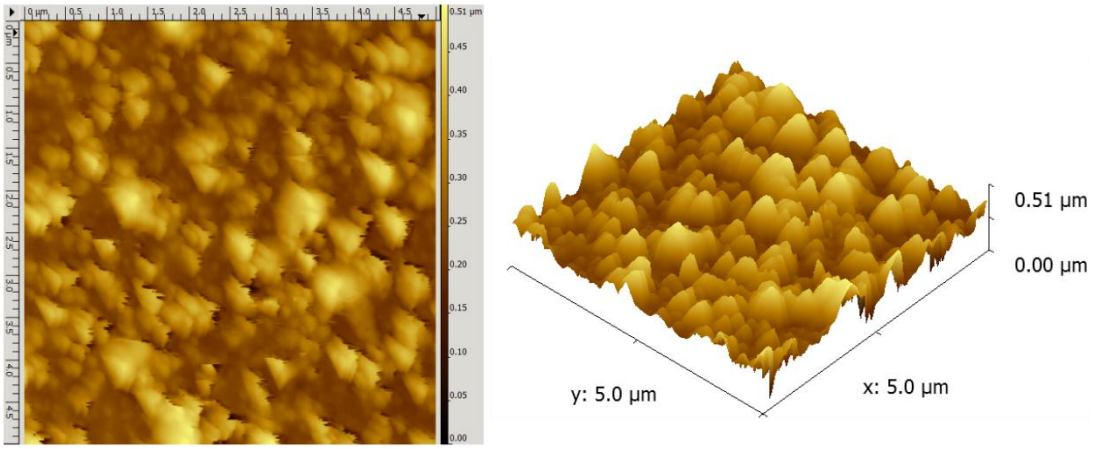

Figure 148: A 5 µm field size (left) and the corresponding 3D (right) AFM image of the $BiFeO_3$ film formed after annealing at 700 °C.

8.4.7 Ferroelectric characterisation

Films of $BiFeO_3$ were grown *via* AACVD of [{$Cp(CO)_2Fe$}$BiCl_2$] followed by annealing at 700 °C, directly on to 1 cm^2 silicon wafers that had been previously sputtered with a thin layer of platinum in order to act as a conducting bottom electrode. Following the heat treatment, circular platinum electrodes were sputtered on to the surface of the film using a 0.5 mm mask to act as conducting top electrodes. The thickness of the $BiFeO_3$ film was determined to be approximately 280 nm through side-on SEM imaging and is consistent (within observational and non-uniformity error) with films deposited on Corning glass substrates followed by heat treatment at 700 °C. The polarisation – electric field (P-E) loop was measured at room temperature and is shown in Figure 149.

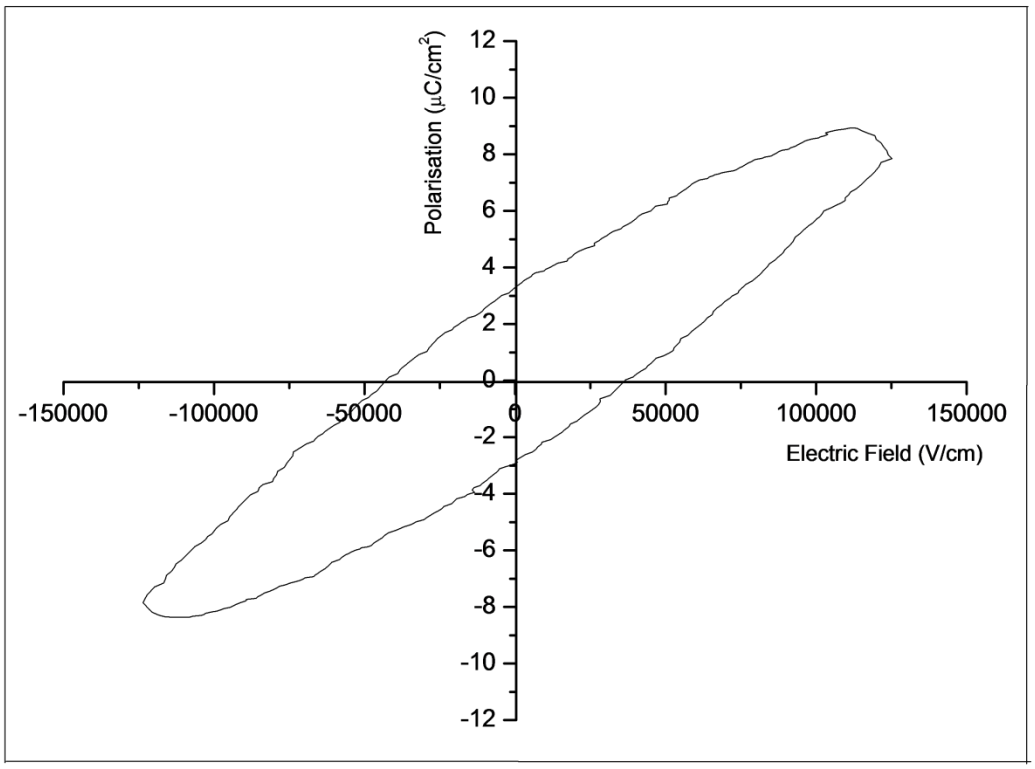

Figure 149: Room temperature P-E hysteresis loop measured at 1 kHz for a 280 nm thick $BiFeO_3$ film grown *via* AACVD and deposited on $Pt/SiO_2/Si$ substrate sputtered with Pt top electrodes.

The P-E hysteresis loop measured at 1 kHz at room temperature for the $BiFeO_3$ film annealed at 700 °C again fails to saturate fully in a similar manner to the $BiFeO_3$ films described in previous chapters. Nevertheless, the spontaneous polarisation confirms the film is ferroelectric at room temperature, albeit with a relatively low (saturation) polarisation (P_s) of 8.7 μC/cm^2 and a low remnant polarisation (P_r) of 3.4 μC/cm^2; P_r tends to be lower than P_s due to internal stress and local electric fields within the sample. Some domains will switch back to their original state as soon as the applied field is removed which can give hysteresis loops a "rugby ball" shape as observed here. A coercivity of approximately +35 kV/cm was measured, but due to the asymmetric shape of the curve, a negative coercivity of -42 kV/cm was also measured. Although some authors have attributed such low values to the absence of epitaxial growth on perovskite substrates (as the polarisation is extremely sensitive to small changes in lattice parameter induced by substrates that have suitable lattice mismatch), high quality non-epitaxially strained films and bulk $BiFeO_3$ have been demonstrated to possess high polarisations of ~100 μC/cm^2, in line with theoretical calculations.[99] The polarisation values are higher than those obtained for $BiFeO_3$ films grown on $Pt/TiO_2/SiO_2/Pt$ substrates *via* sol-gel processing (P_r = 1.8 μC/cm^2)[211] and also higher than those obtained for PLD-grown $BiFeO_3$ films on identical substrates (P_r = 0.83 μC/cm^2).[212] They are also higher than the values measured for $BiFeO_3$

films grown *via* LPCVD described in Chapters 6 and 7, and may be a result of the enhanced film quality from the annealing process resulting in films containing minimal impurity phases. Increasing the applied electric field strength and using a higher frequency during the measurements would encourage higher polarisation values; however damage to the film and a decrease in resistivity is more likely to occur. Electrode damage was also observed when attaching the analyser electrodes to the platinum electrodes sputtered on the film, which made the measurements much more challenging.

8.4.8 Magnetism measurements

The pure-phase $BiFeO_3$ film grown *via* AACVD of [{$Cp(CO)_2Fe$}$BiCl_2$] followed by heat treatment at 700 °C was chosen (due to its purity) for an investigation of its magnetic properties. Magnetic measurements were performed on a SQUID-VSM. The annealed film on Corning glass was cut to an appropriate size (2 mm x 3 mm) piece and was mounted on a quartz rod using adhesive. The magnetic field was applied parallel to the plane of the film and M-H hysteresis loops were recorded at 5 K and at room temperature (300 K). Additionally, a ZFC-FC measurement was performed. The M-H hysteresis loop recorded at 5 K is shown Figure 150.

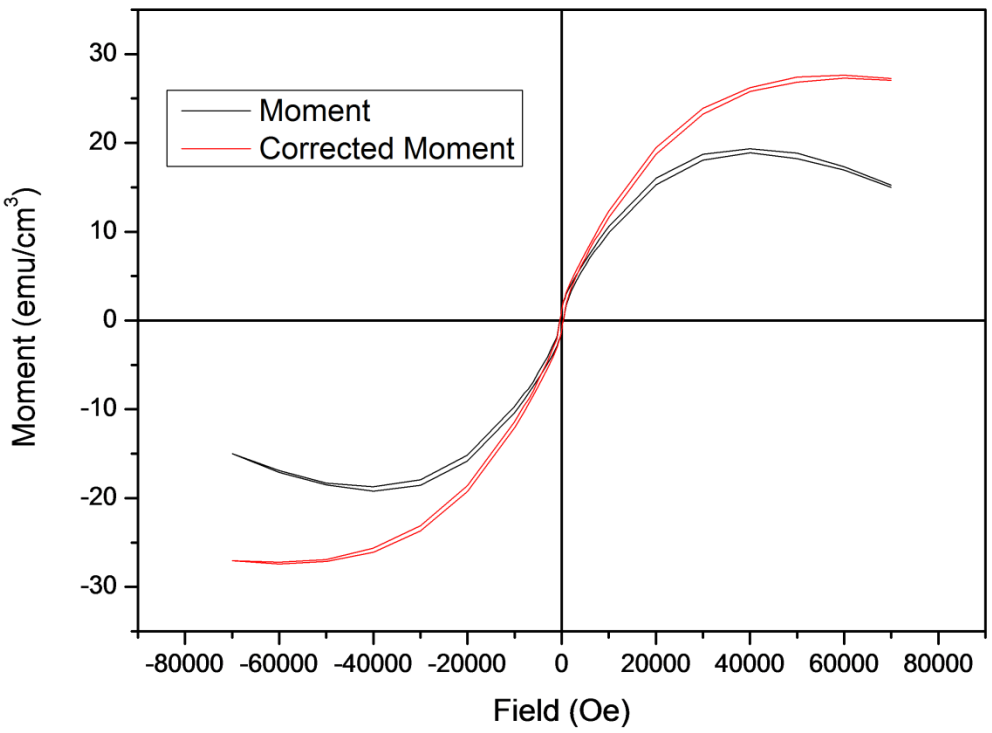

Figure 150: M-H hysteresis loop measured at 5 K for the 320 nm thick $BiFeO_3$ film prepared *via* AACVD and annealed at 700 °C.

Similar to previous reports,[107] these $BiFeO_3$ films show weak ferromagnetic behaviour. The loop displays a reasonable amount of diamagnetic contribution from the purely diamagnetic Corning glass substrate, so this moment was corrected by determining the diamagnetic/paramagnetic contribution to the M-H curve as described in Chapter 6. This was then subtracted from the linear component of the actual recorded magnetic moment at high fields, typically above 2 T (20000 Oe) in this case. The saturation magnetisation was therefore found to be 27.6 emu/cm^3, which was slightly larger than expected for $BiFeO_3$.[102] In comparison, saturation magnetisation values of 130 and 17.5 emu/cm^3 were measured for $BiFeO_3$ films grown *via* LPCVD in Chapters 6 and 7 respectively. The large value of 130 emu/cm^3 was attributed to the increased presence of impurity α-Fe_2O_3 in that sample. The enlarged M-H loop which displays the coercive field is shown in Figure 151.

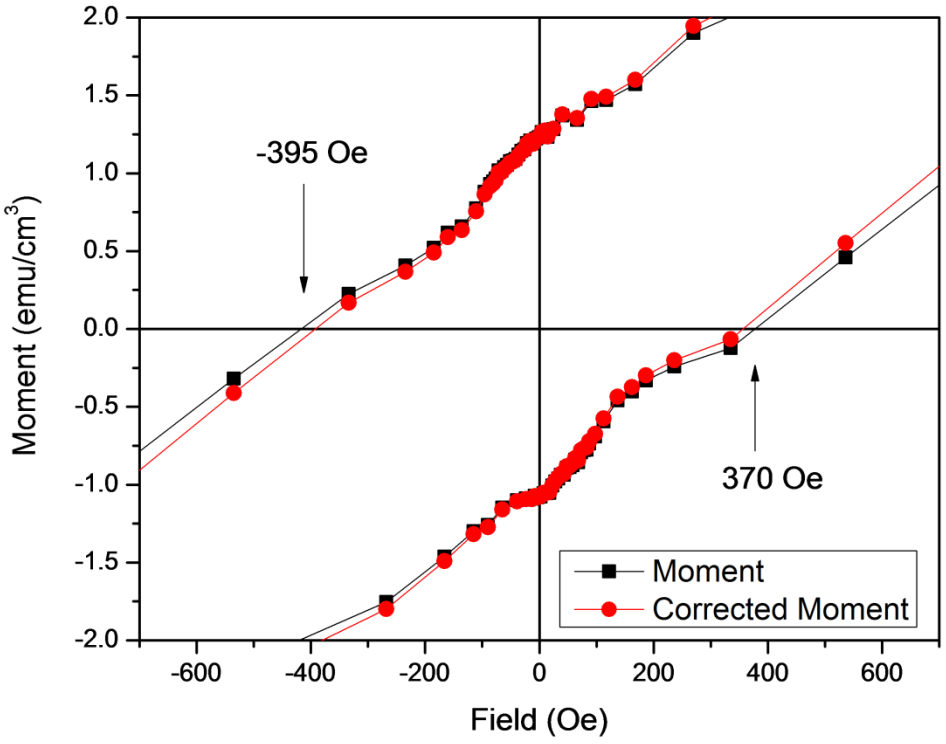

Figure 151: Enlarged section of the M-H loop measured at 5 K of the $BiFeO_3$ film grown *via* AACVD and annealed at 700 °C.

The M-H curve measured at 5 K displays slightly asymmetric coercivities of 350 Oe and –370 Oe before and after applying the diamagnetic corrections. This could suggest a degree of exchange bias is occurring in $BiFeO_3$, whereby the ferromagnetic hysteresis loop is shifted along the field axis by an amount H_e – the exchange field. The bias is a result of interactions between the antiferromagnetic and ferromagnetic domains, resulting in anisotropy when the antiferromagnetic material is cooled below its Neel Temperature T_N.[239] The coercivities here

are slightly lower (approximately 170 Oe lower) than those obtained from $BiFeO_3$ films grown *via* the LPCVD reaction of $[Bi(O^tBu)_3]$ and $[Fe(O^tBu)_3]_2$ described in Chapter 7.

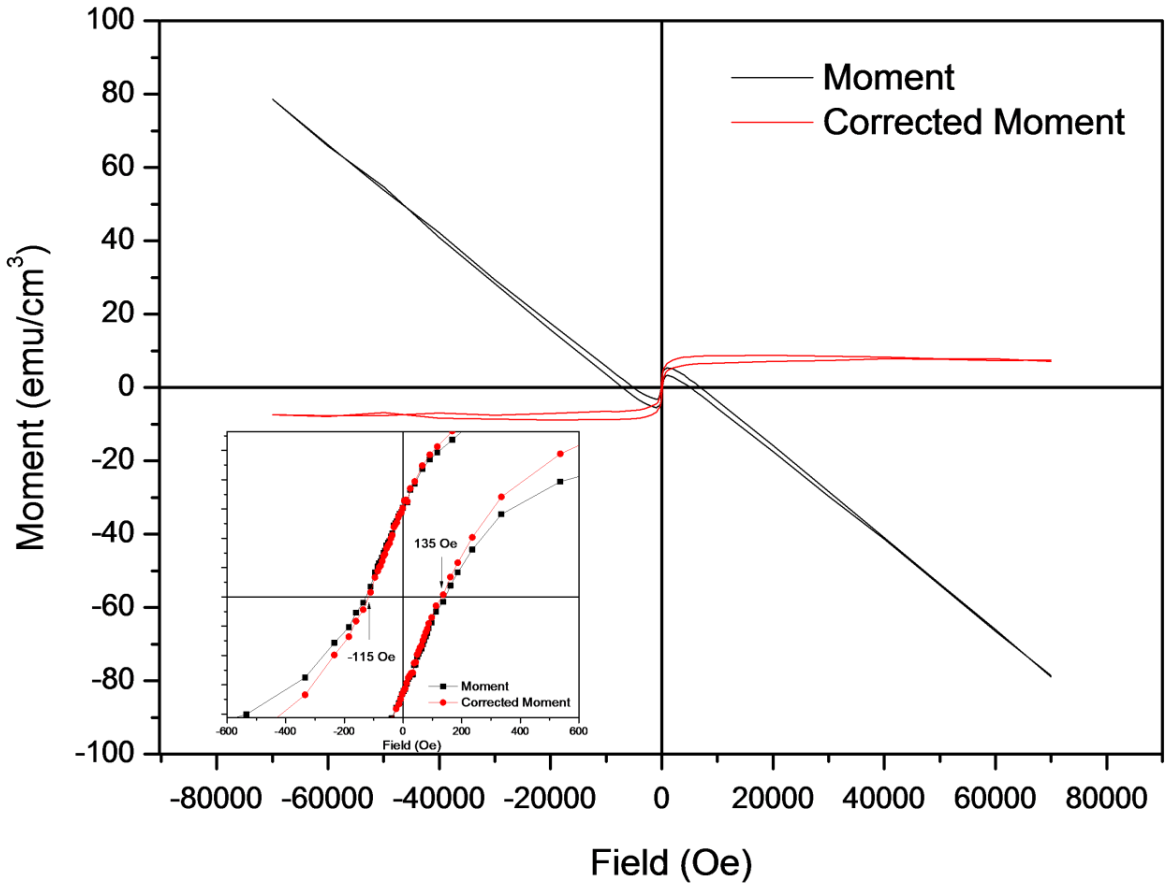

Figure 152: Hysteresis loop measured at 300 K for a 320 nm thick $BiFeO_3$ film grown *via* AACVD and annealed at 700 °C. The inset plot shows the M-H curve enlarged to display the coercive field.

The M-H curve obtained at 300 K is shown in Figure 152. Again the ferromagnetic signal from the sample was found to be lower at ambient temperature, so the diamagnetic contribution from the substrate was calculated and subtracted from the total magnetic moment. The hysteresis loop appears to saturate much faster (at approximately 1 Tesla) compared to the loop obtained at 5 K (approximately 6 Tesla) and the diamagnetic contribution of the substrate is much stronger. The coercive field was measured to be 135 Oe and -115 Oe, which also decreased in comparison to the measurement at 5 K, and the loop appeared to be less asymmetric than the one measured at 5 K. This trend was also observed with LPCVD-grown $BiFeO_3$ films employing $[Fe(O^tBu)_3]_2$ as the iron source described in Chapter 7 and could be a result of superparamagnetism (see later).

The increase in temperature resulted in a decrease in saturation magnetisation (8.9 emu/cm^3) that occurred at a lower magnetic field strength, which is slightly lower than the magnetisation measured for the same sample at 5 K (27 emu/cm^3), but is expected. The saturation point is

more consistent with the expected value for $BiFeO_3$.[102] The coercivity is lower than that observed for the 70 nm thick $BiFeO_3$ film grown by Wang *et al.* using PLD, which exhibited a coercive field of 200 Oe.[39] In this study, the magnetisation decreased from 150 emu/cm^3 for their 70 nm thick film down to 5 emu/cm^3 for their 400 nm thick film. In comparison therefore with the 880 nm thick phase-pure $BiFeO_3$ film grown *via* LPCVD in Chapter 7 that displayed a room temperature magnetisation of ~ 5 emu/cm^3, the 320 nm thick film measured in the present study displayed a room temperature magnetisation of ~ 9 emu/cm^3, and is in agreement with the decrease in magnetisation as a function of film thickness observed by Wang. Wong *et al.* have demonstrated the size-dependent magnetic properties of $BiFeO_3$ nanoparticles, revealing that the coercivity increases as a function of particle diameter but the magnetisation decreases, and furthermore, as these values are a direct result of particle size they are not influenced by epitaxial strain (in thin films) nor oxygen vacancies.[126] Comparing their 95 nm $BiFeO_3$ nanoparticles to our 320 nm thick film, they obtained a high coercivity of 1550 Oe at room temperature, which is considerably larger than the value of 135 Oe obtained for our $BiFeO_3$ film which possessed an average particle diameter of 110 nm (magnetisation values could not be used for comparison due to the different units used). More work would therefore be required in order to form a relationship between film thickness, the average particle size in the film and the magnetic properties in $BiFeO_3$.

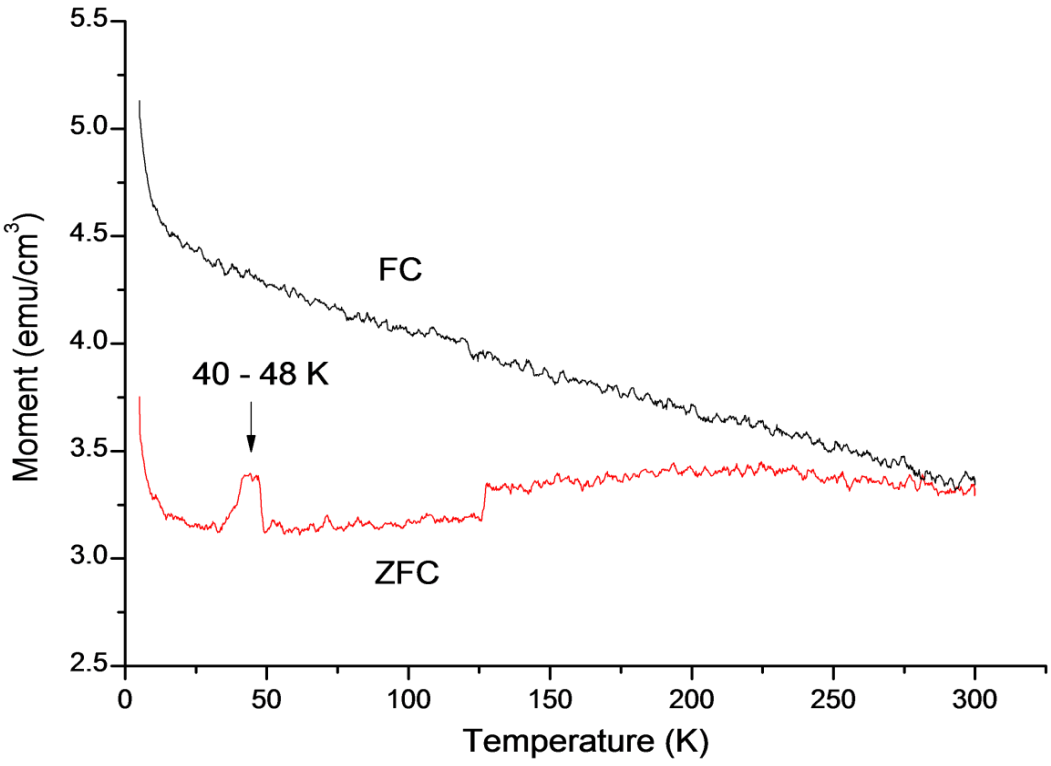

Figure 153: ZFC and FC curves for the 320 nm thick $BiFeO_3$ film formed *via* AACVD, with an applied field of 200 Oe.

The temperature dependence of the magnetisation for a $BiFeO_3$ film, showing the field cooled (FC) and zero field cooled (ZFC) curves are shown in Figure 153. The applied magnetic field was set at 200 Oe and the heating rate set at 5 K/min. The broad peak or "cusp," shown between 40 – 48 K in the ZFC data has been observed before and tends to be a feature of large particles (95 nm and larger) of $BiFeO_3$;[126] even sharper cusps have been obtained for larger particles and the bulk. The cusp may be a result of a magnetic phase transition, but is more likely to be the blocking temperature (or freezing temperature (T_f)) of the individual spins. A similar curve was obtained from LPCVD-grown $BiFeO_3$ films that were described in Chapter 7, together with a description of their potential superparamagetic properties. The film thickness was measured here at 320 nm but the individual particle size is difficult to measure due to the sintering of the particles that takes place during annealing. The particles were estimated to be 110 nm in diameter from the use of the Scherrer Equation, and any coalescence from annealing would most likely increase their overall size to a value approaching the bulk, and hence the appearance of this peak in the ZFC data. Another slight shift in the data is displayed at 132 K and is not commonly observed in ZFC measurements, however Raman spectroscopy has revealed that it may be due to a spin-reorientation transition, usually observed at ~ 140 K.[240]

There is some deviation between the curves below 300 K and this is characteristic of spin-glass behaviour as determined by Scott;[109] the gradual decrease in magnetisation as the temperature increases was said to be typical for antiferromagnetic materials but is usually observed due to random spin orientations that occur from thermal effects. The dramatic increase in magnetisation below ~ 20 K is in agreement with the M-H curve (Figure 150) and suggests ferromagnetic behaviour. The large reduction in coercivity between the experiments run at 5 K and 300 K suggest low temperature superparamagnetic behaviour in $BiFeO_3$ which is in agreement with results from other groups.[109,144,241] This is because superparamagnetic materials behave differently above and below the blocking temperature; below T_B coercivity is observed but above this temperature the material displays paramagnetic properties whereby there is a considerable reduction in coercivity.

8.4.9 UV- Vis spectroscopy

The direct band-gaps and optical properties of the annealed $BiFeO_3$ films were measured using UV-vis spectroscopy recorded in transmission mode. The spectrum of an uncoated glass substrate was also recorded and then subtracted from the spectra of the film and glass. The band-gaps of the films were calculated using Tauc plots[172] from converting the transmission data into absorbance *via* the Beer-Lambert Law, which is described in more detail in Chapters 4 and 5. A typical transmission spectrum of a pure-phase $BiFeO_3$ film and a $BiFeO_3$-$Bi_2Fe_4O_9$ film are shown in Figure 154.

The spectra reveal that the films were over 70% transmitting in the 800 – 2500 nm range with the cut-off from the glass substrate coming into effect below 380 nm. The mixed phase film appears to have two absorption edges, and this is evident in the Tauc plots (Figure 155).

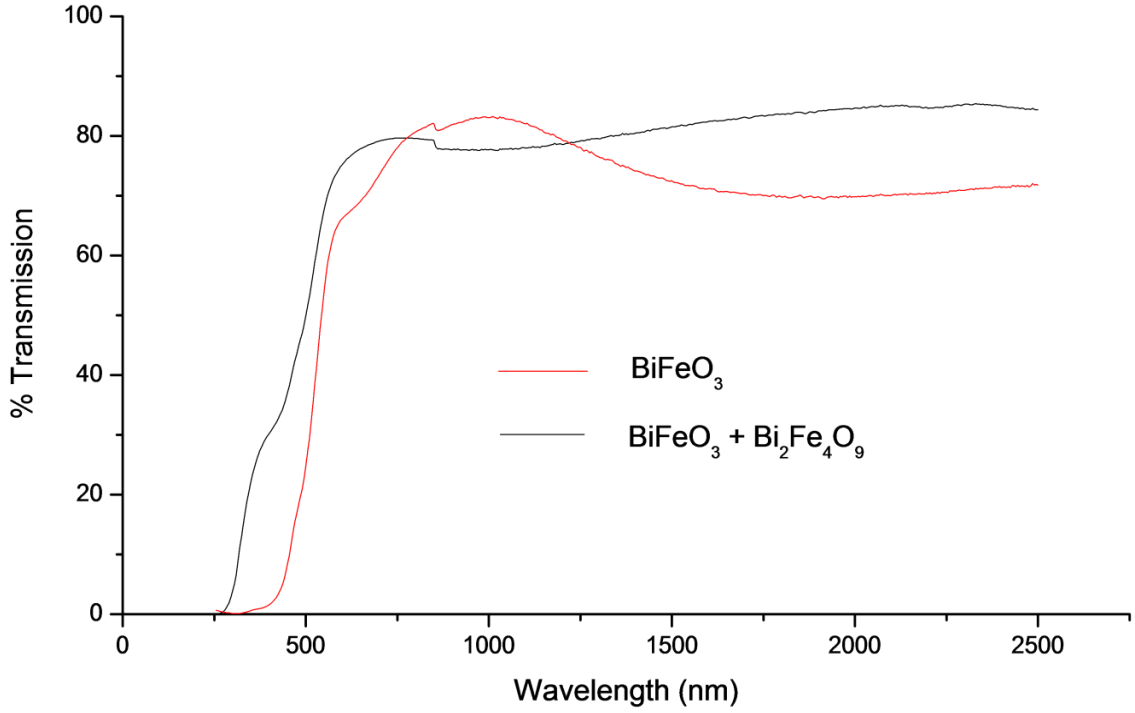

Figure 154: UV-Vis spectra of a $BiFeO_3$ and $BiFeO_3$-$Bi_2Fe_4O_9$ film on a Corning glass substrate.

Figure 155 shows the Tauc plot of the pure-phase $BiFeO_3$ and mixed phase $BiFeO_3$-$Bi_2Fe_4O_9$ film grown on glass *via* AACVD and after post-deposition annealing. Extrapolating the linear part of the plot to the *x*-axis results in an intercept of approximately 2.1 eV, which is in good agreement with many experimentally derived band-gap values for $BiFeO_3$, although some reports have observed band-gaps as high as 2.8 eV.[242] However, it also worth noting that the band-gap of $BiFeO_3$ films generally have no dependence upon the type of substrate used for film growth. A value of 2.1 eV indicates that the band-gap is located in the visible range of the spectrum, which is perhaps not surprising considering the colour of the films in most cases was orange. Band-gaps were estimated for the other films containing $BiFeO_3$ as the major phase using similar calculations based on the construction of Tauc plots for each sample, and the resultant the band-gap values varied between 1.9 – 2.2 eV. Those films with smaller band-gaps (1.9 eV) contained a significant amount of impurity $Bi_2Fe_4O_9$ and therefore these lower values are in line with the expected decrease in band-gap of $Bi_2Fe_4O_9$ compared to $BiFeO_3$.[243,51] From the Tauc plot of the sample containing impurity $Bi_2Fe_4O_9$ phase, one can observe two possible edges that when extrapolated to the *x*-axis yields band-gaps of 1.9 and 2.0 eV, indicating that the lower figure may be due to the impurity phase whilst the higher figure is due to presence of

$BiFeO_3$; however whether these values originate from actual band-edges or interference effects observed in the UV-vis spectrum is not known. The additional edge at ~ 3.5 eV is likely to be due to the glass substrate. Recently, $Bi_2Fe_4O_9$ has been reported to be a photocatalytically active multiband semiconductor possessing band-gaps of 2.05 and 1.53 eV,[220] however the edge at 1.53 eV in our samples was not conclusively identified.

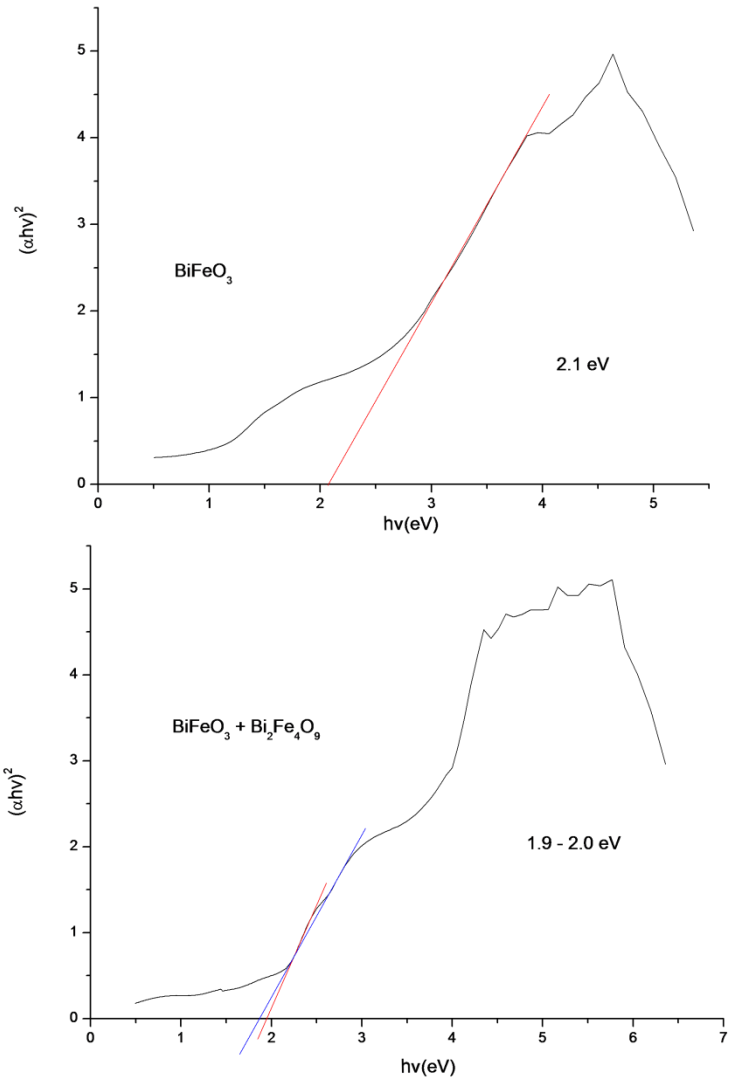

Figure 155: Tauc plots for $BiFeO_3$ films formed *via* AACVD. An additional edge at 1.9 eV (blue line) was obtained from the extrapolation to the x-axis for the film containing impurity $Bi_2Fe_4O_9$ phase.

8.5 Photocatalysis

In order to test the photocatalytic behaviour of these $BiFeO_3$ films, a pure-phase 320 nm thick film and an 850 nm thick film were grown *via* AACVD on glass substrates, followed by annealing at 700 °C. The thicker film was synthesised by means of two separate depositions (on the same Corning glass substrate) of $Bi_{24}Fe_2O_{39}$ films, *via* AACVD of [{$Cp(CO)_2Fe$}$BiCl_2$] in THF, followed by post-deposition annealing at 700 °C. Film thicknesses were measured *via*

side-on SEM imaging. The films were used to photo-oxidise water using sacrificial reagents (alkaline sodium persulphate) under simulated solar irradiation (75 W) equipped with a 420 nm cut-off filter for approximately 2500 seconds. As discussed previously in Chapter 4, a Clark Cell composed of an oxygen electrode was used to measure the voltage of the sacrificial solution *via* a potentiostat, whereby the recorded voltage is proportional to the dissolved oxygen content. The voltage was recorded as a function of time. An uncoated glass substrate was used as a control and as expected, no oxygen evolution was detected when irradiated with the light source.

8.5.1 Results and discussion

A graph plotting voltage against time was plotted for the two films and is shown in Figure 156.

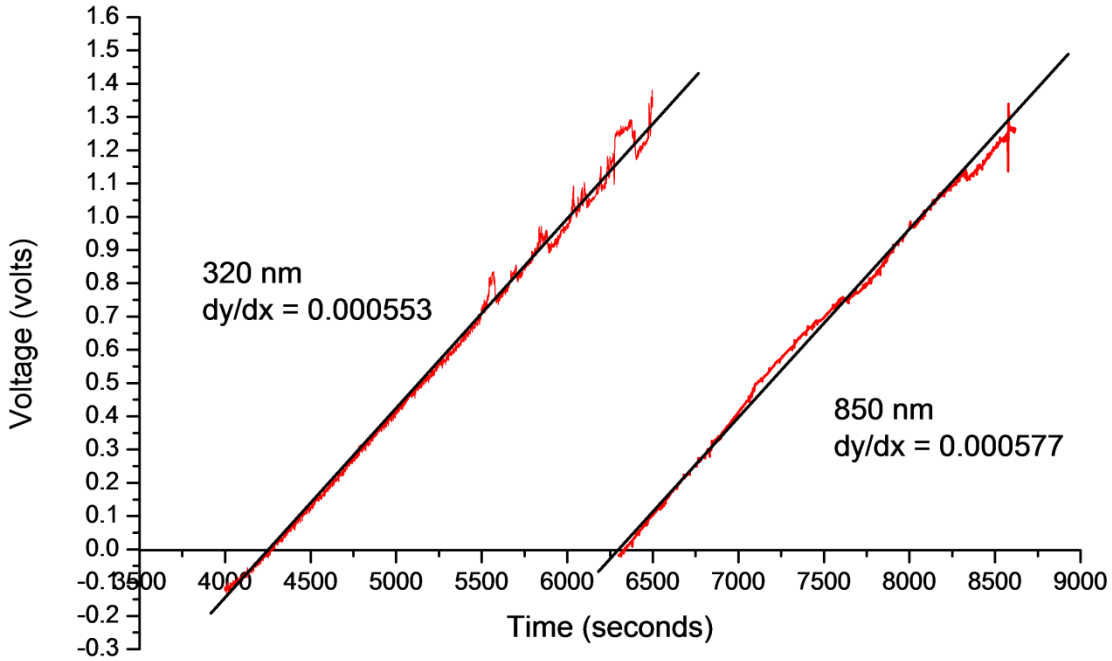

Figure 156: Graph plotting voltage against time measured during the photo-oxidation of water for two $BiFeO_3$ films of 320 nm and 850 nm thicknesses. The gradients of the slopes are used to calculate the oxygen evolution.

The measurements commenced at different times (after 4000 and 6300 seconds) as they were measured on different days and were fitted in with measurements on other samples. The plots of voltage against time for the two chosen $BiFeO_3$ films reveal steady increases in voltage during the 2500 seconds (42 minute) photo-oxidation test, and both appear to have very similar gradients (0.00055 V/s for the 320 nm film, and 0.00058 V/s for the 850 nm film). This would imply that the thickness has little effect on the photocatalytic activity of such films, however to

be sure of this numerous films of different thicknesses would need to be grown and tested. There are some spikes and unevenness in the plots and that appears to be common when this type of oxygen electrode is used due to the high sensitivity of the cell (sudden spikes in oxygen concentration in the solution are hence recorded in the data). X-ray diffraction patterns of the films after testing revealed no change in phase. Details of the conversion between the gradient of the slope (in V/s) and the oxygen production (in μmol h^{-1}) are described in Chapter 4 and will not be discussed here. The overall results for both films are displayed in Table 17.

Table 17: Summary of the photo-oxidation results for the two $BiFeO_3$ films chosen.

Film Thickness / nm	Band-gap / eV	Rate of O_2 production / μmol h^{-1} (for 2 cm^2 sample)	Rate of O_2 production / μmol $h^{-1}m^{-2}$	No. Of incident photons/s (420 nm - band-gap of film)	Molecules of O_2 formed per second (for 2 cm^2 sample)	Apparent quantum efficiency / %
320	2.1	5.73	28650	3.07×10^{17}	9.6×10^{14}	1.25
850	2.1	5.99	29950	3.07×10^{17}	1.0×10^{15}	1.30

The two $BiFeO_3$ samples displayed rates of photo-oxidation between 5.73 – 5.99 μmol h^{-1} which were higher than those obtained from the $BiFeO_3$ films grown *via* LPCVD described in the previous chapters which displayed photoactivities in the range of 1.46 – 4.13 μmol h^{-1}. In this study, one could infer that the thicker film possessed a slightly higher photocatalytic activity, however this may not be the case in light of the errors associated with the measurements. Overall, optimisation of film thickness for photocatalytic activity would be a future aim as the effect of film thickness needs to be thoroughly investigated before making any correlations between thickness and activity. $BiFeO_3$ films grown *via* LPCVD using $[Fe(O^tBu)_3]_2$ as the iron source (Chapter 7) resulted in an increased photoactivity as a function of film thickness, whereas for films grown *via* LPCVD using $[Fe(acac)_3]$ as the iron source, thinner films possessed a higher photoactivity (Chapter 6). It is possible that the presence of impurity α-Fe_2O_3 in films used in the latter study affected their photoactivity. The apparent quantum efficiencies for the two samples in this study were calculated using the number of molecules of oxygen produced per second and the total number of photons produced by the lamp per second.

Quantum efficiency = [No. of O_2 molecules per second/No. of incident photons per second] x 4 (4 electron process) x 100%

Photons with energies lower than the band-gap of $BiFeO_3$ (2.1 eV, 590 nm for both samples) were not used in the calculation as it was assumed that these photons would not possess the required energy to promote an electron between the valence and conduction band. A cut-off filter at 420 nm was used for the experiment and therefore photons with energies below 420 nm were also not used in the calculation. It is notoriously difficult to compare the quantum efficiencies of photocatalysts because of the differences in experimental set-up and differences between bulk and thin film materials. The quantum efficiencies for both samples in this investigation were over 1% which is low in comparison to powdered photocatalysts,[152] however the amount of sample in thin films is comparatively much smaller, and therefore the corresponding efficiencies are expected to be lower.

Continuing with the comparison made between these samples and TiO_2 films described in the literature that utilised the same photocatalysis experiment, the activity of the $BiFeO_3$ films are 1-2 orders of magnitude higher than those obtained from the use of anatase films deposited on glass *via* APCVD (360 – 2820 µmol $h^{-1}m^{-2}$) under 365 nm UV-light irradiation.[175] The results were also of the order of the results obtained for optimised TiO_2 (rutile) films grown on titanium substrates sputtered with platinum metal on the reverse (14400 - 22800 µmol $h^{-1}m^{-2}$) investigated in the same paper, and similar to optimised silver-gold incorporated anatase and rutile films grown *via* sol-gel processing onto titanium substrates, sputtered with Pt on the reverse (to act as an electron sink) and irradiated with UV-light (highest film activity was ~ 22700 µmol $h^{-1}m^{-2}$).[176] Recently, optimised rutile films deposited onto titanium substrates *via* AP- and AACVD and sputtered with Pt on the reverse displayed high photoactivities (*ca.* 48500 µmol $h^{-1}m^{-2}$ for the best performing sample) using an identical sacrificial solution, however they were only active under UV-light irradiation.[217] Clearly the effect of substrate and platinum loading would be interesting to investigate for optimisation of the photoactivity in these $BiFeO_3$ films.

8.6 Conclusions

Pure-phase $BiFeO_3$ films were grown *via* a simple AACVD procedure using the single-source precursor [{$Cp(CO)_2Fe$}$BiCl_2$] dissolved in THF, followed by post-deposition annealing at 700 °C in air. As-deposited films were characterised as crystalline $Bi_{24}Fe_2O_{39}$ *via* X-ray diffraction; in addition, XPS and Raman analysis indicated the purity of the annealed $BiFeO_3$ films whilst compositional analysis *via* WDX revealed close to 1:1 ratios of bismuth to iron. Magnetic hysteresis and ferroelectric polarisation measurements confirmed that the films were multiferroic at room temperature. ZFC-FC measurements revealed low temperature superparamagnetism and spin-glass behaviour, whilst the hysteresis loops confirmed weak ferromagnetic behaviour. Direct band-gaps between 1.9 – 2.2 eV were measured for all films, indicating good visible-light absorption.

The photocatalytic testing confirmed the potential of $BiFeO_3$ as a potent photocatalyst that performs well under visible light irradiation for the often difficult four electron process of the photo-oxidation of water, and is rationalised by its positive valence and conduction band levels with respect to the redox potentials of water.[143] The use of a single-source precursor to grow pure-phase films *via* the AACVD process resulted in higher photoactivities than those obtained from films grown *via* dual-source LPCVD. It is anticipated that $BiFeO_3$ would be a promising candidate for use as a visible light photosensitiser in conjunction with other photocatalysts that are only active under UV irradiation, and any potential coupling of the ferroelectric, magnetic and photochemistry of $BiFeO_3$ could add additional functionality to the material.

9 Conclusions

Results and Chapter Summary

This thesis has investigated the deposition of bismuth oxide and $BiFeO_3$ films using low pressure and aerosol assisted chemical vapour deposition, and their functional testing through either the photo-oxidation or reduction of water. In order to deposit such films, potential single-source precursors to bismuth oxide were synthesised and their decomposition characteristics were studied. Bismuth oxide films were grown either *via* LPCVD or AACVD using single-source precursors, whilst $BiFeO_3$ films were grown using dual-source LPCVD with two different precursor combinations, as well as through AACVD using a single-source precursor.

Several novel bismuth(III) *β*-diketonate complexes were synthesised *via* an alcohol-amine exchange with $[Bi(N(SiMe_3)_2)_3]$. The crystal structure of $[Bi(dbm)_3]_2$ was found to be dimeric, whereas the structure of $[Bi(acac)_3]_n$ was shown to be composed of a 1-D polymer, with the Bi-Bi distance in both complexes being too large to indicate any interaction between the metal centres in each complex. Attempts to sublime the *β*-diketonate complexes in order to test their suitability for LPCVD of bismuth oxide films were unsuccessful. In addition to the *β*-diketonates, the volatile bismuth alkoxides $[Bi(O^tBu)_3]$ and $[Bi(mmp)_3]$ were synthesised either *via* alcoholysis of $[Bi(N(SiMe_3)_2)_3]$ or from the metathesis reaction between $BiCl_3$ and the sodium salt of the alcohol, in order to assess their potential as single-source LPCVD precursors to bismuth oxide. Additionally, $[Fe(O^tBu)_3]_2$ was synthesised in order to be used in conjunction with the ligand-matched bismuth precursor $[Bi(O^tBu)_3]$ for deposition of $BiFeO_3$ films *via* LPCVD. Finally, the bimetallic complex $[\{Cp(CO)_2Fe\}BiCl_2]$ was synthesised for use as a single-source precursor for growth of $BiFeO_3$ films *via* AACVD.

The thermal decomposition characteristics of the novel bismuth *β*-diketonate complexes were investigated using DSC-TGA in order to assess their potential as single-source CVD precursors to bismuth oxide films. Polymeric $[Bi(acac)_3]_n$ appeared to decompose to metallic bismuth, whilst the dimeric complex $[Bi(dbm)_3]_2$ was observed to decompose to β-Bi_2O_3 and its mass loss was consistent with the calculated theoretical mass loss required to form Bi_2O_3. The fluorinated *β*-diketonate complex $[Bi(tfac)_3]$ was found to decompose into α-Bi_2O_3 and, surprisingly, not into BiOF, whilst $[Bi(bzac)_3]$ was found to decompose into a mixture of metallic bismuth and β-Bi_2O_3. It was found, therefore, that the residual masses of $[Bi(dbm)_3]_2$ and $[Bi(tfac)_3]$ were consistent with the formation of bismuth oxide, and PXRD analysis of their residues supported this observation.

A comparison between the decomposition profiles of two volatile precursors, [Bi(mmp)$_3$] and [Bi(thd)$_3$], that have previously been used for deposition of bismuth oxide films using oxygen as a co-reactant, were investigated. The decomposition of the volatile alkoxide [Bi(O^{t}Bu)$_3$] was also studied as it has not yet been employed as a CVD precursor. The resultant weight loss of [Bi(mmp)$_3$] appeared to be too low for formation of stoichiometric Bi_2O_3, whilst that of [Bi(thd)$_3$] appeared to be too high for formation of Bi_2O_3 only. In both cases the decomposition profiles were complicated due to potential volatilisation along with the possibility of premature and/or incomplete decomposition during the experiment. The residual mass of [Bi(O^{t}Bu)$_3$], after taking into account any volatilisation, appeared to be consistent with the formation of Bi_2O_3, and PXRD analysis of the residue revealed decomposition to β-Bi_2O_3, indicating that it may be suitable as a single-source precursor for growth of Bi_2O_3 films *via* LPCVD.

The mass transport characteristics in conjunction with their thermal decomposition of the potential single-source precursors to bismuth oxide [Bi(mmp)$_3$], [Bi(thd)$_3$] and [Bi(O^{t}Bu)$_3$] were investigated for their suitability to be employed as single-source precursors for LPCVD of bismuth oxide. Films of Bi_2O_3 were subsequently grown on glass *via* the LPCVD reaction of [Bi(O^{t}Bu)$_3$] acting as a single source precursor. A variety of substrate temperatures, carrier gas flow rates and system pressures were used, which enabled phase selective deposition to take place – predominantly β-Bi_2O_3 films were grown at lower substrate temperatures and pressures, whilst γ-Bi_2O_3 films were grown at higher temperatures and through increasing the carrier gas flow rate. Additionally, α-Bi_2O_3 films were grown at the highest system pressure of 45 mbar. Band-gaps of the films were measured between 2.3 – 3.0 eV and depended on the phase(s) present. Two films were tested for their photocatalytic potential through the photo-oxidation of water using a low power, near-UV (365 nm) light source and a sacrificial electron acceptor solution. Appreciable oxygen evolution was observed for both films which were of the order of those obtained from the use of optimised, CVD-grown TiO_2 films investigated in a similar study, with the predominantly γ-Bi_2O_3 film exhibiting 2.5 times the photoactivity of the β-Bi_2O_3 sample. This study showed for the first time that crystalline Bi_2O_3 films could be grown from a single-source precursor using conventional thermal CVD apparatus and that the resultant films are powerful photo-catalysts for water oxidation.

All of the novel *β*-diketonate complexes were investigated for use as single-source precursors to bismuth oxide films *via* AACVD. No film growth was obtained from the use of [Bi(acac)$_3$]$_n$, [Bi(tfac)$_3$] and [Bi(bzac)$_3$], however, β-Bi_2O_3 films were grown on glass substrates using [Bi(dbm)$_3$]$_2$ dissolved in toluene, at substrate temperatures between 410 – 525 °C. The complex appeared moisture stable and therefore non-dried toluene could be utilised. Platinum(0) films were grown for the first time *via* CVD using $H_2PtCl_6.6H_2O$ as the precursor dissolved in methanol at 410 °C. Pt-nanoparticle incorporated β-Bi_2O_3 films were grown *via* a "one-pot" AACVD method comprising [Bi(dbm)$_3$]$_2$ and $H_2PtCl_6.6H_2O$ in toluene/methanol solvent onto

steel substrates; the use of glass substrates resulted in deposition of BiOCl in addition to γ-Bi_2O_3. The resultant films were characterised using XRD, UV-Vis, XPS, TEM and AFM. Films were tested for their photocatalytic properties *via* the photo-reduction of water using ethanol as a hole scavenger and a simulated solar lamp. Experiments conducted in a solution comprised of a 1:1 mixture of 0.1 M HCl and ethanol resulted in hydrogen evolution (13.5 μmol hr^{-1} m^{-2}) but also led to chemical degradation of the films to BiOCl as observed from XRD analysis. Testing of the films in a 1:1 ethanol and water solution resulted in comparatively lower hydrogen production (3.1 μmol hr^{-1} m^{-2}) however hydrogen evolution was only observed for the composite Pt-Bi_2O_3 films and not for Bi_2O_3 or Pt films alone. The production of hydrogen was believed to be *via* photon capture in the Bi_2O_3 followed by electron transfer to the Pt particles where they are trapped. This charge accumulates here until the Pt particles become reducing. To summarise, this chapter involved the study of the decomposition characteristics of several novel bismuth *β*-diketonate complexes, the use of one of these complexes as a single-source precursor to crystalline Bi_2O_3 films, the deposition of Pt(0) films and composite Pt-Bi_2O_3 films. Finally, the photo-reduction capabilities of the composite films were studied.

The growth of $BiFeO_3$ films were investigated *via* a multi-source approach, using [$Bi(O^tBu)_3$] and [$Fe(acac)_3$] as precursors and air as an oxidising gas, respectively. However, before the introduction of the bismuth source, a preliminary study using [$Fe(acac)_3$] as a single-source precursor to iron oxide films was carried out. This resulted in dark films due to high levels of carbon contamination from the precursor, however the addition of air as an oxidising gas removed the majority of the carbon contamination to leave α-Fe_2O_3 films. The introduction of [$Bi(O^tBu)_3$] resulted in predominantly $BiFeO_3$ films at a substrate temperature of 550 °C and at a pressure of 8 mbar, albeit with minor impurities α-Fe_2O_3 and γ-Bi_2O_3. Phase-pure $BiFeO_3$ films could not be grown despite reducing the flow rate of the iron precursor; all films contained various impurity phases, notably α-Fe_2O_3, $Bi_{25}FeO_{40}$ and $Bi_2Fe_4O_9$. Film were characterised *via* XRD, UV-Vis, Raman, XPS, AFM, WDX and SEM. Their magnetic properties were also studied M-H hysteresis measurements obtained from Vibrating Sample Magnetometry (VSM) which revealed low temperature weak ferromagnetic behaviour coupled with low coercivity, however at 300 K the observation of an unexpected increase in coercivity was most likely to be due to the high amount of impurity α-Fe_2O_3 in the sample. Ferroelectric hysteresis loops revealed a low polarisation of ~ 1.5 μC/cm^2 at room temperature. The band-gaps of the films measure *via* UV-vis spectroscopy, were in the visible range (2.0 - 2.3 eV). The photoactivities of two films were tested through the photo-oxidation of water under visible-light (> 420 nm) irradiation; both films displayed appreciably high oxidation rates that were either higher or of the same order of magnitude as those obtained from TiO_2 films tested under UV-light, and therefore highlights the potential of $BiFeO_3$ films as strong visible light photocatalysts.

The growth of $BiFeO_3$ films from the LPCVD reaction of the ligand-matched precursors $[Fe(O^tBu)_3]_2$ and $[Bi(O^tBu)_3]$ without an oxidising gas was investigated. The substrate temperature and system pressure were varied, with phase-pure $BiFeO_3$ films being obtained at 550 °C, at 8 mbar. The films were fully characterised, but in addition low temperature Raman spectroscopy confirmed the phase purity of the films. AFM revealed an unusually high roughness of 60 nm for the pure $BiFeO_3$ sample grown *via* this LPCVD method. Magnetism measurements revealed the expected low temperature weak ferromagnetism, whilst the room temperature M-H loop saturated at ~ 5 emu/cm^3, in agreement with theoretical predictions for $BiFeO_3$. ZFC-FC measurements revealed spin-glass behaviour through a sharp cusp at ~ 50 K (T_B), which has previously been observed for both nanoparticle and bulk $BiFeO_3$. The ferroelectric polarisation of the phase-pure film was measured at 3.9 μC/cm^2 with a remnant polarisation of 2.4 μC/cm^2; these were slightly higher than those recorded for the impure sample grown from $[Bi(O^tBu)_3]$ and $[Fe(acac)_3]$. Two films which were chosen for an investigation into their visible-light photocatalytic activity displayed similar photo-oxidation rates to those using the previous route, again highlighting the potential of $BiFeO_3$ as a visible light photo-oxidiser.

The use of the single-source, bimetallic precursor $[\{Cp(CO)_2Fe\}BiCl_2]$ was investigated for deposition of $BiFeO_3$ *via* AACVD. The precursor was dissolved in dry THF and at a substrate temperature of 300 °C, films of $Bi_{24}Fe_2O_{39}$ were deposited, which were characterised *via* XRD. Post-deposition annealing in air of these samples between 400 – 1000 °C resulted in phase-pure $BiFeO_3$ films at 700 °C. The purity was confirmed from WDX analysis and low-temperature Raman spectroscopy, in addition to XRD. The morphologies of the annealed films gradually changed as a function of temperature, from a globular, agglomerated appearance to one of a more coalesced and sintered morphology at 700 °C. Average particle sizes appeared to have little or no correlation with annealing temperature, and the roughness of the film annealed at 700 °C was found to be 60 nm. Saturated M-H hysteresis loops revealed low temperature weak ferromagnetic behaviour and at room temperature, a saturation of 8.9 emu/cm^3 was recorded. The large difference in coercivity between these temperatures could be a result of superparamagnetism. A much broader cusp in the ZFC-FC data at 40 – 48 K was observed in comparison to those in the literature and that observed for films deposited from $[Fe(O^tBu)_3]_2$ and $[Bi(O^tBu)_3]$, which was, nevertheless, an indication of spin-glass behaviour. Additionally, a small feature was observed at ~130 K in the data which has not previously been reported. The photo-oxidation properties of two films were investigated under visible-light irradiation with the highest oxygen evolution obtained for a 850 nm thick film, with both films displaying higher activities than those measured for films deposited using a dual-source approach, resulting in apparent quantum efficiencies of 1.3%. The rates were also higher than those obtained from identical photo-oxidation studies on optimised doped and undoped TiO_2 films deposited on a

variety of substrates (except for rutile films deposited on titanium substrates with a Pt co-catalyst) tested under UV-light.

More work however, is required in order to optimise these $BiFeO_3$ films to improve photocatalytic activity, as well as to take advantage of recent work which has demonstrated the use of $BiFeO_3$ as a visible-light photo-sensitiser over TiO_2 or $SrTiO_3$ for overall water-splitting. Its high activity for photo-oxidation is perhaps not surprising given the relatively positive valence and conduction band levels of $BiFeO_3$ and its position with respect to the redox potentials of water described earlier. Nevertheless, its relative photo-stability and high photo-activity together with the room temperature magnetoelectric coupling, and, more recently, its reported photovoltaic and photodiode properties make it a truly multifunctional material that warrants further investigation.

10 References

1. K. Choy, *Progress in Materials Science*, 2003, **48**, 57–170.

2. A. Cowley and R. A. Jones, *Angewandte Chemie International Edition*, 1989, **28**, 1208–1215.

3. A. Jones, *Chemical Society Reviews*, 1997, **26**, 101–110.

4. W. Herrmann and N. Huber, *Angewandte Chemie International Edition*, 1995, **34**, 2187–2206.

5. A. C. Jones, *Journal of Materials Chemistry*, 2002, **12**, 2576–2590.

6. N. C. Norman, *Chemistry of Arsenic, Antimony and Bismuth, Springer Press*, 1997.

7. A. F. Gualtieri, S. Immovilli, and M. Prudenziati, *Powder Diffraction*, 1997, **12**, 90.

8. H. A. Harwig, *Zeitschrift fur Anorganische und Allgemeine Chemie*, 1978, **444**, 151–166.

9. M. Mehring, *Coordination Chemistry Reviews*, 2007, **251**, 974–1006.

10. N. Cornei, N. Tancret, F. Abraham, and O. Mentre, *Inorganic Chemistry*, 2006, **45**, 4886–4888.

11. R. Mansfield, *Proceedings of the Physical Society. Section B*, 1949, **62**, 476–483.

12. N. M. Sammes, G. A. Tompsett, N. Hafe, and F. Aldinger, *Journal of the European Ceramic Society*, 1999, **19**, 1801–1826.

13. M. J. Verkerk, G. M. H. V. de Velde, and A. J. Burggraaf, *Journal of Physics and Chemistry of Solids*, 1982, **43**, 1129–1136.

14. A. Cabot, A. Marsal, J. Arbiol, and J. R. Morante, *Sensors and Actuators B: Chemical*, 2004, **99**, 74–89.

15. H. Weidong, Q. Wei, W. Xiaohong, D. Xianbo, C. Long, and J. Zhaohua, *Thin Solid Films*, 2007, **515**, 5362–5365.

16. L. Zhou, W. Wang, H. Xu, S. Sun, and M. Shang, *Chemistry - A European Journal*, 2009, **15**, 1776–1782.

17. L. Zhang, W. Wang, J. Yang, Z. Chen, W. Zhang, L. Zhou, and S. Liu, *Applied Catalysis A: General*, 2006, **308**, 105–110.

18. K. Gurunathan, *International Journal of Hydrogen Energy*, 2004, **29**, 933–940.

19. R. Li, W. Chen, H. Kobayashi, and C. Ma, *Green Chemistry*, 2010, **12**, 212–215.

20. X. Lin, J. Xing, W. Wang, Z. Shan, F. Xu, and F. Huang, *Journal of Physical Chemistry C*, 2007, **111**, 18288–18293.

21. S. S. Bhande, R. S. Mane, A. V. Ghule, and S.-H. Han, *Scripta Materialia*, 2011, **65**, 1081–1084.

22. N. Adamian, V. Abovian, and V. M. Aroutiounian, *Sensors and Actuators B: Chemical*, 1996, **36**, 241–243.

23. G. Sarala Devi, *Sensors and Actuators B: Chemical*, 1999, **56**, 98–105.

24. S. S. Sharma, K. Nomura, and Y. Ujihira, *Journal of Applied Physics*, 1992, **71**, 2000–2005.

25. P. Fang, C. Robbins, and B. Aurivillius, *Physical Review*, 1962, **126**, 892.

26. S. E. Cummins and L. E. Cross, *Journal of Applied Physics*, 1968, **39**, 2268–2274.

27. J. F. Dorrian, R. E. Newnham, D. K. Smith, and M. I. Kay, *Ferroelectrics*, 1972, **3**, 17–27.

28. R. L. Withers, J. G. Thompson, and A. D. Rae, *Journal of Solid State Chemistry*, 1991, **417**, 404–417.

29. B. H. Park, B. S. Kang, S. D. Bu, T. W. Noh, J. Lee, and W. Jo, *Nature*, 1999, **401**, 682–684.

30. S. Wei, H. Wang, X. Wu, S. Shang, M. Wang, Z. Li, and W. Lu, *Journal of Crystal Growth*, 2001, **224**, 323–326.

31. C. D. Araujo, J. Cuchiaro, L. McMillan, M. C. Scott, and J. F. Scott, *Nature*, 1995, **374**, 627–629.

32. Y. Noguchi, M. Miyayama, and T. Kudo, *Physical Review B*, 2001, **63**, 1–5.

33. K. Kato, C. Zheng, J. Finder, and S. Dey, *Journal of the American Ceramic Society*, 1998, **75**, 1869–1875.

34. R. Wolfe, R. Newnahm, and M. Kay, *Solid State Communications*, 1969, **7**, 1797–1801.

35. N. McDowell and K. Knight, *Chemistry-A European Journal*, 2006, **12**, 1493–1499.

36. S. C. P. Ayyuba, R. Pinto, and M. S. Multani, *Journal of Materials Research*, 1998, **13**, 1113–1116.

37. E. Turevskaya, V. Bergo, K. Vorotilov, A. Sigov, and D. Benlian, *Journal of Sol-Gel Science and Technology*, 1998, **13**, 889–893.

38. M. K. Singh, Y. Yang, and C. G. Takoudis, *Coordination Chemistry Reviews*, 2009, **253**, 2920–2934.

39. J. Wang, J. B. Neaton, H. Zheng, V. Nagarajan, S. B. Ogale, B. Liu, D. Viehland, V. Vaithyanathan, D. G. Schlom, U. V. Waghmare, N. A. Spaldin, K. M. Rabe, M. Wuttig, and R. Ramesh, *Science*, 2003, **299**, 1719–1722.

40. W. Eerenstein, F. D. Morrison, J. F. Scott, and N. D. Mathur, *Applied Physics Letters*, 2005, **87**, 101906.

41. F. Sugawara, S. Iida, Y. Syono, and S. Akimoto, *Journal of the Physical Society of Japan*, 1968, **25**, 1553–1558.

42. N. A. Hill, P. Bättig, and C. Daul, *Journal of Physical Chemistry B*, 2002, **106**, 3383–3388.

43. H. Maeda, Y. Tanaka, M. Fukutomi, and T. Asano, *Japanese Journal of Applied Physics*, 1988, **27**, 209–210.

44. C. Michel, M. Hervieu, M. M. Borel, A. Grandin, F. Deslandes, J. Provost, and B. Raveau, *Zeitschrift fur Physik B Condensed Matter*, 1987, **68**, 421–423.

45. R. M. Hazen, C. T. Prewitt, R. J. Angel, N. L. Ross, L. W. Finger, C. G. Hadidiacos, D. R. Veblen, P. J. Heaney, P. H. Hor, R. L. Meng, Y. Y. Sun, Y. Q. Wang, Y. Y. Xue, Z. J. Huang, L. Gao, J. Bechtold, and C. W. Chu, *Physical Review Letters*, 1988, **60**, 1174–1177.

46. R. J. Cava, *Journal of the American Ceramic Society*, 2000, **83**, 5–28.

47. T. A. Hanna, *Coordination Chemistry Reviews*, 2004, **248**, 429–440.

48. L. Zhou, W. Wang, and L. Zhang, *Journal of Molecular Catalysis A: Chemical*, 2007, **268**, 195–200.

49. J. Yu and A. Kudo, *Chemistry Letters*, 2005, **34**, 1528–1529.

50. A. Kudo and S. Hijii, *Chemistry Letters*, 1999, **28**, 1103–1104.

51. Q.-J. Ruan and W.-D. Zhang, *The Journal of Physical Chemistry C*, 2009, **113**, 4168–4173.

52. L. Moens, P. Ruiz, B. Delmon, and M. Devillers, *Catalysis Letters*, 1997, **46**, 93–99.

53. L. Moens, P. Ruiz, B. Delmon, and M. Devillers, *Applied Catalysis A: General*, 1999, **180**, 299–315.

54. H. G. Kim, D. W. Hwang, and J. S. Lee, *Journal of the American Chemical Society*, 2004, **126**, 8912–8913.

55. A. Kudo, K. Omori, and H. Kato, *Journal of the American Chemical Society*, 1999, **121**, 11459–11467.

56. S. Tokunaga, H. Kato, and A. Kudo, *Chemistry of Materials*, 2001, **13**, 4624–4628.

57. H. Liu, R. Nakamura, and Y. Nakato, *Chemphyschem*, 2005, **6**, 2499–2502.

58. T. Takeyama, *Journal of Physics and Chemistry of Solids*, 2004, **65**, 1349–1352.

59. M. Schuisky and A. Hårsta, *Chemical Vapor Deposition*, 1996, **2**, 235–238.

60. H. Kim, J. Myung, and S. Shim, *Solid State Communications*, 2006, **137**, 196–198.

61. C. Bedoya, G. G. Condorelli, G. Anastasi, A. Baeri, F. Scerra, I. L. Fragalà, J. G. Lisoni, and D. Wouters, *Chemistry of Materials*, 2004, **16**, 3176–3183.

62. C. Bedoya, G. G. Condorelli, S. T. Finocchiaro, A. Di Mauro, I. L. Fragalà, L. Cattaneo, and S. Carella, *Chemical Vapor Deposition*, 2005, **11**, 261–268.

63. G. Bandoli, D. Barreca, E. Brescacin, G. A. Rizzi, and E. Tondello, *Chemical Vapor Deposition*, 1996, **2**, 238–242.

64. N. Reuge, J. Dexpert-Ghys, and B. Caussat, *Chemical Vapor Deposition*, 2010, **16**, 123–126.

65. R. C. Mehrotra and A. K. Rai, *Indian Journal of Chemistry*, 1966, **4**, 537.

66. M. Matchett, M. Chiang, and W. Buhro, *Inorganic Chemistry*, 1990, **29**, 358–360.

67. M.-C. Massiani, R. Papiernik, L. G. Hubert-Pfalzgraf, and J.-C. Daran, *Polyhedron*, 1991, **10**, 437–445.

68. X. Kou, X. Wang, D. Mendoza-Espinosa, L. N. Zakharov, A. L. Rheingold, W. H. Watson, K. A. Brien, L. K. Jayarathna, and T. A. Hanna, *Inorganic Chemistry*, 2009, **48**, 11002–11016.

69. C. Knispel, C. Limberg, and B. Ziemer, *Inorganic Chemistry*, 2010, **49**, 4313–4318.

70. C. Jones, M. Burkart, and K. Whitmire, *Angewandte Chemie International Edition*, 1992, **31**, 451–452.

71. K. H. Whitmire, S. Hoppe, O. Sydora, J. L. Jolas, and C. M. Jones, *Inorganic Chemistry*, 2000, **39**, 85–97.

72. P. A. Williams, A. C. Jones, M. J. Crosbie, P. J. Wright, J. F. Bickley, A. Steiner, H. O. Davies, T. J. Leedham, and G. W. Critchlow, *Chemical Vapor Deposition*, 2001, **7**, 205–209.

73. W. A. Hermann, N. W. Huber, R. Anwander, and T. Priermeier, *European Journal of Inorganic Chemistry*, 1993, **126**, 1127–1130.

74. S. Kang and S. W. Rhee, *Thin Solid Films*, 2004, **468**, 79–83.

75. L. Armelao, G. Bandoli, M. Casarin, G. Depaoli, E. Tondello, and A. Vittadini, *Inorganica Chimica Acta*, 1997, **276**, 340–348.

76. K. C. Brooks, S. B. Turnipseed, R. M. Barkley, R. E. Sievers, J. V. Tulchinsky, and A. E. Kaloyerosj, *Chemistry of Materials*, 1992, 912–916.

77. E. V. Dikarev, H. Zhang, and B. Li, *Journal of the American Chemical Society*, 2005, **127**, 6156–6157.

78. A. Pisarevsky, in *AIP Conference Proceedings*, 1992, vol. 251, pp. 231–238.

79. L. Armelao, G. Depaoli, and A. Dolmella, *Acta Crystallographica Section C: Crystal Structure Communications*, 2000, **56**, e268–e268.

80. V. Stavila and E. V. Dikarev, *Journal of Organometallic Chemistry*, 2009, **694**, 2956–2964.

81. S. Parola, R. Papiernik, L. G. Hubert-Pfalzgraf, S. Jagner, and M. Hkansson, *Journal of the Chemical Society, Dalton Transactions*, 1997, 4631–4636.

82. A. P. Pisarevsky and L. I. Martynenko, *Russian Journal of Coordination Chemistry*, 1994, **20**, 303–327 (English translation).

83. S. I. Troyanov and A. P. Pisarevsky, *J. Chem. Soc., Chem. Commun.*, 1993, **1**, 335–336.

84. P. C. Andrews, G. B. Deacon, P. C. Junk, I. Kumar, and M. Silberstein, *Dalton Transactions*, 2006, 4852–4858.

85. J. Harjuoja, S. Vayrynen, M. Putkonen, L. Niinisto, and E. Rauhala, *Journal of Crystal Growth*, 2006, **286**, 376–383.

86. M. Schuisky, K. Kukli, M. Ritala, A. Hårsta, and M. Leskelä, *Chemical Vapor Deposition*, 2000, **6**, 139–145.

87. M. Vehkamaki, T. Hatanpaa, M. Ritala, and M. Leskela, *Journal of Materials Chemistry*, 2004, **14**, 3191–3197.

88. J. Harjuoja, T. Hatanpää, M. Vehkamäki, S. Väyrynen, M. Putkonen, L. Niinistö, M. Ritala, M. Leskelä, and E. Rauhala, *Chemical Vapor Deposition*, 2005, **11**, 362–367.

89. S. Paalasmaa, D. Mansfeld, M. Schürmann, and M. Mehring, *Zeitschrift für Anorganische und Allgemeine Chemie*, 2005, **631**, 2433–2438.

90. D. Mansfeld, M. Mehring, and M. Schürmann, *Angewandte Chemie International Edition*, 2004, **44**, 245–249.

91. T. Hatanpää, M. Vehkamäki, M. Ritala, and M. Leskelä, *Dalton Transactions*, 2010, **39**, 3219–3226.

92. R. Ramesh and N. A. Spaldin, *Nature Materials*, 2007, **6**, 21–29.

93. G. Rado and V. Folen, *Physical Review Letters*, 1961, **7**, 310–311.

94. G. T. Rado and V. J. Folen, *Journal of Applied Physics*, 1962, **33**, 1126–1132.

95. R. Hornreich, *Solid State Communications*, 1969, **7**, 1081–1085.

96. E. Ascher, H. Rieder, H. Schmid, and H. Stössel, *Journal of Applied Physics*, 1966, **37**, 1404.

97. L. W. Martin, S. P. Crane, Y.-H. Chu, M. B. Holcomb, M. Gajek, M. Huijben, C.-H. Yang, N. Balke, and R. Ramesh, *Journal of Physics: Condensed Matter*, 2008, **20**, 1–12.

98. I. Ismailzade and R. Yakupov, *physica status solidi (a)*, 1971, **85**, 85–87.

99. L. W. Martin, *Dalton Transactions*, 2010, **39**, 10813–10826.

100. S.-W. Cheong and M. Mostovoy, *Nature Materials*, 2007, **6**, 13–20.

101. R. Seshadri and N. Hill, *Chemistry of Materials*, 2001, **13**, 2892–2899.

102. C. Ederer and N. Spaldin, *Physical Review B*, 2005, **71**, 1–4.

103. N. Hill, *Journal of Physical Chemistry B*, 2000, **104**, 6694–6709.

104. A. Zaslavskii and A. Tutov, *Doklady Akademii Nauk SSSR*, 1960, **135**, 815–819.

105. J. R. Teague, R. Gerson, and W. J. James, *Solid State Communications*, 1970, **8**, 1073–1074.

106. F. Kubel and H. Schmid, *Acta Crystallographica Section B*, 1990, **B46**, 698–702.

107. G. Catalan and J. F. Scott, *Advanced Materials*, 2009, **21**, 2463–2485.

108. D. Lebeugle, D. Colson, A. Forget, M. Viret, A. M. Bataille, and A. Gukasov, *Physical Review Letters*, 2008, **100**, 1–4.

109. M. Singh, W. Prellier, M. Singh, R. Katiyar, and J. Scott, *Physical Review B*, 2008, **77**, 1–5.

110. W. Eerenstein, F. D. Morrison, J. Dho, M. G. Blamire, J. F. Scott, and N. D. Mathur, *Science*, 2005, **307**, 1203a.

111. W. Eerenstein, N. D. Mathur, and J. F. Scott, *Nature*, 2006, **442**, 759–765.

112. J. Wang, J. B. Neaton, H. Zheng, S. Scholl, V. Nagarajan, S. B. Ogale, B. Liu, D. Viehland, V. Vaithyanathan, D. G. Schlom, L. Mohaddes-Ardabili, U. V. Waghmare, N. A. Spaldin, K. M. Rabe, T. Zhao, M. Wuttig, and R. Ramesh, *Science*, 2005, **307**, 1203b–1203b.

113. J. K. Kim, S. S. Kim, W.-J. Kim, A. S. Bhalla, and R. Guo, *Applied Physics Letters*, 2006, **88**, 132901.

114. Y. Wang and C.-W. Nan, *Applied Physics Letters*, 2006, **89**, 052903.

115. H. Liu, Z. Liu, Q. Liu, and K. Yao, *Thin Solid Films*, 2006, **500**, 105–109.

116. Y. Wang and C.-W. Nan, *Thin Solid Films*, 2009, **517**, 4484–4487.

117. S. K. Singh and H. Ishiwara, *Japanese Journal of Applied Physics*, 2005, **44**, L734–L736.

118. H. Zhang, X. Chen, T. Wang, F. Wang, and W. Shi, *Journal of Alloys and Compounds*, 2010, **500**, 46–48.

119. R. R. Das, D. M. Kim, S. H. Baek, C. B. Eom, F. Zavaliche, S. Y. Yang, R. Ramesh, Y. B. Chen, X. Q. Pan, X. Ke, M. S. Rzchowski, and S. K. Streiffer, *Applied Physics Letters*, 2006, **88**, 242904.

120. R. U. Eno, S. O. Kaura, H. F. Unakubo, and K. S. Aito, *Japanese Journal of Applied Physics*, 2005, **44**, 1231–1233.

121. S. Y. Yang, F. Zavaliche, L. Mohaddes-Ardabili, V. Vaithyanathan, D. G. Schlom, Y. J. Lee, Y. H. Chu, M. P. Cruz, Q. Zhan, T. Zhao, and R. Ramesh, *Applied Physics Letters*, 2005, **87**, 102903.

122. Y. Tasaki, T. Kanoko, M. Kabeya, N. Chifu, and S. Yoshizawa, *Integrated Ferroelectrics*, 2006, **81**, 281–288.

123. J. Thery, C. Dubourdieu, T. Baron, C. Ternon, H. Roussel, and F. Pierre, *Chemical Vapor Deposition*, 2007, **13**, 232–238.

124. M. Kartavtseva, O. Gorbenko, and A. Kaul, *Surface and Coatings Technology*, 2007, **201**, 9149–9153.

125. M. Singh, Y. Yang, C. G. Takoudis, A. Tatarenko, and G. Srinivasan, *Electrochemical and Solid State Letters*, 2009, **12**, 161–164.

126. T.-J. Park, G. C. Papaefthymiou, A. J. Viescas, A. R. Moodenbaugh, and S. S. Wong, *Nano Letters*, 2007, **7**, 766–772.

127. L. Martin, Y. Chu, M. Holcomb, and M. Huijben, *Nano Letters*, 2008, **8**, 2050–2055.

128. M. Hunger, C. Limberg, and P. Kircher, *Organometallics*, 2000, **19**, 1044–1050.

129. S. Roggan, C. Limberg, B. Ziemer, and M. Brandt, *Angewandte Chemie International Edition*, 2004, **43**, 2846–2849.

130. J. H. Thurston, A. Kumar, C. Hofmann, and K. H. Whitmire, *Inorganic Chemistry*, 2004, **43**, 8427–8436.

131. J. H. Thurston, T. O. Ely, D. Trahan, and K. H. Whitmire, *Chemistry of Materials*, 2003, **15**, 4407–4416.

132. J. H. Thurston, D. Trahan, T. Ould-Ely, and K. H. Whitmire, *Inorganic Chemistry*, 2004, **43**, 3299–3305.

133. E. V. Dikarev, T. G. Gray, and B. Li, *Angewandte Chemie International Edition*, 2005, **44**, 1721–1724.

134. K. Wójcik, T. Rüffer, H. Lang, A. A. Auer, and M. Mehring, *Journal of Organometallic Chemistry*, 2011, **696**, 1647–1651.

135. S. Farhadi and N. Rashidi, *Polyhedron*, 2010, **29**, 2959–2965.

136. M. C. Navarro, M. C. Lagarrigue, J. M. Paoli, R. E. Carbonio, and M. I. Gómez, *Journal of Thermal Analysis and Calorimetry*, 2009, **102**, 655–660.

137. H. Béa, M. Bibes, S. Cherifi, F. Nolting, B. Warot-Fonrose, S. Fusil, G. Herranz, C. Deranlot, E. Jacquet, K. Bouzehouane, and A. Barthélémy, *Applied Physics Letters*, 2006, **242114**, 3–6.

138. T. Zhao, A. Scholl, F. Zavaliche, K. Lee, M. Barry, A. Doran, M. P. Cruz, Y. H. Chu, C. Ederer, N. A. Spaldin, R. R. Das, D. M. Kim, S. H. Baek, C. B. Eom, and R. Ramesh, *Nature Materials*, 2006, **5**, 823–829.

139. Y.-H. Chu, L. W. Martin, M. B. Holcomb, M. Gajek, S.-J. Han, Q. He, N. Balke, C.-H. Yang, D. Lee, W. Hu, Q. Zhan, P.-L. Yang, A. Fraile-Rodríguez, A. Scholl, S. X. Wang, and R. Ramesh, *Nature Materials*, 2008, **7**, 478–482.

140. T. Choi, S. Lee, Y. Choi, and V. Kiryukhin, *Science*, 2009, **324**, 63–66.

141. S. Y. Yang, J. Seidel, S. J. Byrnes, P. Shafer, C.-H. Yang, M. D. Rossell, P. Yu, Y.-H. Chu, J. F. Scott, J. W. Ager, L. W. Martin, and R. Ramesh, *Nature Nanotechnology*, 2010, **5**, 143–147.

142. J. Luo and P. A. Maggard, *Advanced Materials*, 2006, **18**, 514–517.

143. S. Li, Y.-H. Lin, B.-P. Zhang, J.-F. Li, and C.-W. Nan, *Journal of Applied Physics*, 2009, **105**, 054310.

144. F. Gao, Y. Yuan, K. F. Wang, X. Y. Chen, F. Chen, J.-M. Liu, and Z. F. Ren, *Applied Physics Letters*, 2006, **89**, 102506.

145. U. A. Joshi, J. S. Jang, P. H. Borse, and J. S. Lee, *Applied Physics Letters*, 2008, **92**, 242106.

146. F. Gao, X. Y. Chen, K. B. Yin, S. Dong, Z. F. Ren, F. Yuan, T. Yu, Z. G. Zou, and J.-M. Liu, *Advanced Materials*, 2007, **19**, 2889–2892.

147. S. Li, Y. Lin, B. Zhang, and Y. Wang, *The Journal of Physical Chemistry C*, 2010, **114**, 2903–2908.

148. X. Xu, Y.-H. Lin, P. Li, L. Shu, and C.-W. Nan, *Journal of the American Ceramic Society*, 2011, **94**, 2296–2299.

149. Y. Zhang, A. M. Schultz, P. A. Salvador, and G. S. Rohrer, *Journal of Materials Chemistry*, 2011, **21**, 4168–4174.

150. A. M. Schultz, Y. Zhang, P. A. Salvador, and G. S. Rohrer, *ACS Applied Materials & Interfaces*, 2011, **3**, 1562–1567.

151. A. Fujishima and K. Honda, *Nature*, 1972, **238**, 37–38.

152. A. Kudo and Y. Miseki, *Chemical Society Reviews*, 2009, **38**, 253–278.

153. A. Mills and M. A. Valenzuela, *Journal of Photochemistry and Photobiology A: Chemistry*, 2004, **165**, 25–34.

154. J. K. Cockcroft and P. Barnes, *Powder Diffraction on the Web*, www.pd.chem.ucl.ac.uk.

155. D. Damjanovic, *Reports on Progress in Physics*, 1998, **61**, 1267–1324.

156. M. Stewart and M. G. Cain, *NPL Report CMMT(A)152*, 1999, 1–57.

157. Bruker, *SMART, SAINT and SADABS. Bruker AXS Inc., Madison, Wisconsin, USA*, 2006, **Version 2.**

158. S. Mathur, M. Veith, V. Sivakov, H. Shen, V. Huch, U. Hartmann, and H.-B. Gao, *Chemical Vapor Deposition*, 2002, **8**, 277–283.

159. T. Gröer and M. Scheer, *Journal of the Chemical Society, Dalton Transactions*, 2000, 647–653.

160. C. J. Carmalt, N. A. Compton, R. J. Errington, G. A. Fisher, I. Moenander, and N. Norman, *Inorganic Syntheses*, 1997, **31**, 98.

161. A. Haaland, H. Verne, and H. Volden, *Acta Chemica Scandinavica*, 1993, **47**, 1043–1045.

162. W. A. Herrmann, N. W. Huber, R. Anwander, and T. Priermeier, *Chemische Berichte*, 1993, **126**, 1127–1130.

163. Sigma-Aldrich Fine Chemicals, *Product Catalogue*, 2008, www.safcglobal.com.

164. Y. Kojima, H. Kadokura, Y. Okuhara, M. Matsumoto, and T. Mogi, *Integrated Ferroelectrics*, 1997, **18**, 183–196.

165. D. Bradley, *Chemical Reviews*, 1989, **89**, 1317–1322.

166. P. Jeffries and L. Dubois, *Chemistry of Materials*, 1992, **4**, 1169–1175.

167. S. J. S. Qazi, A. R. Rennie, J. K. Cockcroft, and M. Vickers, *Journal of Colloid and Interface Science*, 2009, **338**, 105–110.

168. B. Mihailova, M. Gospodinov, and L. Konstantinov, *Journal of Physics and Chemistry of Solids*, 1999, **60**, 1821–1827.

169. R. J. Betsch and W. B. White, *Spectrochimica Acta Part A: Molecular Spectroscopy*, 1978, **34**, 505–514.

170. V. S. Dharmadhikari, S. Sainkar, S. Badrinarayan, and A. Goswami, *Journal of Electron Spectroscopy and Related Phenomena*, 1982, **25**, 181–189.

171. S. J. A. Moniz, D. Bhachu, C. S. Blackman, A. J. Cross, S. Elouali, D. Pugh, R. Quesada Cabrera, and S. Vallejos, *Inorganica Chimica Acta*, 2011, **380**, 328–325.

172. J. Tauc, R. Grigorovici, and A. Vancu, *physica status solidi (b)*, 1966, **15**, 627–637.

173. R. Swanepoel, *Journal of the Optical Society of America A*, 1985, **2**, 1339–1342.

174. L. Leontie, *Surface Science*, 2002, **507-510**, 480–485.

175. G. Hyett, J. A. Darr, A. Mills, and I. P. Parkin, *Chemistry - A European Journal*, 2010, **16**, 10546–10552.

176. S. Kundu, A. Kafizas, G. Hyett, A. Mills, J. A. Darr, and I. P. Parkin, *Journal of Materials Chemistry*, 2011, **21**, 6854–6863.

177. H. Cheng, B. Huang, J. Lu, Z. Wang, B. Xu, X. Qin, X. Zhang, and Y. Dai, *Physical Chemistry Chemical Physics*, 2010, **12**, 15468–15475.

178. N. Serpone, A. Salinaro, A. Emiline, and V. Ryabchuk, *Journal of Photochemistry and Photobiology A: Chemistry*, 2000, **130**, 83–94.

179. A. Fujishima, T. Rao, and D. Tryk, *Journal of Photochemistry and Photobiology A: Chemistry*, 2000, **1**, 1–21.

180. B. Ohtani, *Chemistry Letters*, 2008, **37**, 217–229.

181. N. Serpone and A. Salinaro, *Pure and Applied Chemistry*, 1999, **71**, 303–320.

182. S. J. A. Moniz, C. S. Blackman, C. J. Carmalt, and G. Hyett, *Journal of Materials Chemistry*, 2010, **20**, 7881–7886.

183. C. E. Knapp, G. Hyett, I. P. Parkin, and C. J. Carmalt, *Chemistry of Materials*, 2011, **23**, 1719–1726.

184. S. Vallejos, T. Stoycheva, P. Umek, C. Navio, R. Snyders, C. Bittencourt, E. Llobet, C. Blackman, S. Moniz, and X. Correig, *Chemical Communications*, 2011, **47**, 565–567.

185. A. Schweizer and G. Kerr, *Inorganic Chemistry*, 1978, **17**, 2326–2327.

186. S. Y. Chai, Y. J. Kim, M. H. Jung, A. K. Chakraborty, D. Jung, and W. I. Lee, *Journal of Catalysis*, 2009, **262**, 144–149.

187. T. Morikawa, T. Ohwaki, K. Suzuki, S. Moribe, and S. Tero-Kubota, *Applied Catalysis B: Environmental*, 2008, **83**, 56–62.

188. J. Hammond and N. Winograd, *Journal of Electroanalytical Chemistry and Interfacial Electrochemistry*, 1977, **78**, 55–69.

189. G. Hyett, J. A. Darr, A. Mills, and I. P. Parkin, *Chemical Vapor Deposition*, 2010, **16**, 301–304.

190. S. Elouali, A. Mills, I. P. Parkin, E. Bailey, P. F. McMillan, and J. A. Darr, *Journal of Photochemistry and Photobiology A: Chemistry*, 2010, **216**, 110–114.

191. Y. Wang, Y. Wen, H. Ding, and Y. Shan, *Journal of Materials Science*, 2009, **45**, 1385–1392.

192. Z. Liu, W. Hou, P. Pavaskar, M. Aykol, and S. B. Cronin, *Nano Letters*, 2011, **11**, 1111–1116.

193. A. Mills and S. K. Lee, *Platinum Metals Review*, 2003, **47**, 2–12.

194. S. Dhara, G. Malhotra, A. Rastogi, and B. Das, *Thin Solid Films*, 1992, **209**, 116–121.

195. L. G. Hubert-Pfalzgraf, *Applied Organometallic Chemistry*, 1992, **6**, 627–643.

196. M. A. Siddiqi, R. A. Siddiqui, and B. Atakan, *Surface and Coatings Technology*, 2007, **201**, 9055–9059.

197. B. D. Fahlman and A. R. Barron, *Advanced Materials for Optics and Electronics*, 1999, **10**, 223–232.

198. A. Bykov, A. Turgambaeva, and I. Igumenov, *Journal de Physique IV*, 1995, **5**, 191–197.

199. A. A. Akl, *Applied Surface Science*, 2004, **233**, 307–319.

200. N. Pailhé, A. Wattiaux, M. Gaudon, and A. Demourgues, *Journal of Solid State Chemistry*, 2008, **181**, 2697–2704.

201. K. Kuribayashi, *Thin Solid Films*, 1997, **295**, 16–18.

202. S. S. Kim, E. J. Choi, and A. S. Bhalla, *Ferroelectrics Letters Section*, 2007, **34**, 84–94.

203. F. Tyholdt, S. Jørgensen, H. Fjellvåg, and A. E. Gunnaes, *Journal of Materials Research*, 2005, **20**, 2127–2139.

204. R. Palai, R. Katiyar, H. Schmid, P. Tissot, S. Clark, J. Robertson, S. Redfern, G. Catalan, and J. Scott, *Physical Review B*, 2008, **77**, 1–11.

205. A. Reyes, C. Delavega, M. Fuentes, and L. Fuentes, *Journal of the European Ceramic Society*, 2007, **27**, 3709–3711.

206. L. Pan, G. Zhang, C. Fan, H. Qiu, P. Wu, F. Wang, and Y. Zhang, *Thin Solid Films*, 2005, **473**, 63–67.

207. T. Yamashita and P. Hayes, *Applied Surface Science*, 2008, **254**, 2441–2449.

208. D. Rout, K.-S. Moon, and S.-J. L. Kang, *Journal of Raman Spectroscopy*, 2009, **40**, 618–626.

209. H. Fukumura, H. Harima, K. Kisoda, M. Tamada, Y. Noguchi, and M. Miyayama, *Journal of Magnetism and Magnetic Materials*, 2007, **310**, e367–e369.

210. M. O. Ramirez, M. Krishnamurthi, S. Denev, A. Kumar, S.-Y. Yang, Y.-H. Chu, E. Saiz, J. Seidel, A. P. Pyatakov, A. Bush, D. Viehland, J. Orenstein, R. Ramesh, and V. Gopalan, *Applied Physics Letters*, 2008, **92**, 022511.

211. Y. Wang, Q. Jiang, H. He, and C.-W. Nan, *Applied Physics Letters*, 2006, **88**, 142503.

212. V. R. Palkar, J. John, and R. Pinto, *Applied Physics Letters*, 2002, **80**, 1628.

213. H. Béa, M. Bibes, A. Barthélémy, K. Bouzehouane, E. Jacquet, A. Khodan, J.-P. Contour, S. Fusil, F. Wyczisk, A. Forget, D. Lebeugle, D. Colson, and M. Viret, *Applied Physics Letters*, 2005, **87**, 072508.

214. S. Iakovlev, C.-H. Solterbeck, M. Kuhnke, and M. Es-Souni, *Journal of Applied Physics*, 2005, **97**, 094901.

215. Y. Xu and M. Shen, *Materials Letters*, 2008, **62**, 3600–3602.

216. F. Gao, X. Y. Chen, K. B. Yin, S. Dong, Z. F. Ren, F. Yuan, T. Yu, Z. G. Zou, and J.-M. Liu, *Advanced Materials*, 2007, **19**, 2889–2892.

217. C. Edusi, G. Hyett, G. Sankar, and I. P. Parkin, *Chemical Vapor Deposition*, 2011, **17**, 30–36.

218. U. A. Joshi, J. S. Jang, P. H. Borse, and J. S. Lee, *Applied Physics Letters*, 2008, **92**, 242106.

219. J.-T. Han, Y.-H. Huang, X.-J. Wu, C.-L. Wu, W. Wei, B. Peng, W. Huang, and J. B. Goodenough, *Advanced Materials*, 2006, **18**, 2145–2148.

220. Y. Li, Y. Zhang, W. Ye, J. Yu, C. Lu, and L. Xia, *New Journal of Chemistry*, 2012, **36**, 1297–1300.

221. A. C. Jones and M. L. Hitchman, *Chemical Vapour Deposition: Precursors, Processes and Applications*, 2009, **1**, 1–36.

222. J.-H. Xu, H. Ke, D.-C. Jia, W. Wang, and Y. Zhou, *Journal of Alloys and Compounds*, 2009, **472**, 473–477.

223. F. Tyholdt, H. Fjellvag, A. E. Gunnæs, and A. Olsen, *Journal of Applied Physics*, 2007, **102**, 074108.

224. L. Mukherjee and F. Y. Yang, *Journal of the American Ceramic Society*, 1971, **51**, 31–34.

225. D. S. Bhachu, M. R. Waugh, K. Zeissler, W. R. Branford, and I. P. Parkin, *Chemistry - A European Journal*, 2011, **17**, 11613–11621.

226. D. Lebeugle, D. Colson, A. Forget, M. Viret, P. Bonville, J. F. Marucco, and S. Fusil, *Physical Review B*, 2007, **76**, 1–8.

227. J. Zhong, J. J. Heremans, D. Viehland, G. T. Yee, and S. Priya, *Ferroelectrics*, 2010, **400**, 3–7.

228. B. Liu, B. Hu, and Z. Du, *Chemical Communications*, 2011, **47**, 8166–8168.

229. T. Mashino, S. Kimura, D. Shigeoka, T. Hiroki, H. Katayanagi, Y. Moro, and Y. Ichiyanagi, *Journal of Physics: Conference Series*, 2010, **200**, 1–4.

230. S. Li, Y.-H. Lin, B.-P. Zhang, C.-W. Nan, and Y. Wang, *Journal of Applied Physics*, 2009, **105**, 056105.

231. A. J. Hauser, J. Zhang, L. Mier, R. A. Ricciardo, P. M. Woodward, T. L. Gustafson, L. J. Brillson, and F. Y. Yang, *Applied Physics Letters*, 2008, **92**, 222901.

232. C. Hengky, X. Moya, N. D. Mathur, and S. Dunn, *RSC Advances*, 2012, **2**, 11843.

233. C. Ternon, J. Thery, T. Baron, C. Ducros, F. Sanchette, and J. Kreisel, *Thin Solid Films*, 2006, **515**, 481–484.

234. X. H. Zhu, E. Defay, Y. Lee, B. André, M. Aid, J. L. Zhu, D. Q. Xiao, and J. G. Zhu, *Applied Physics Letters*, 2010, **97**, 232903.

235. M. A. Zurbuchen, J. Lettieri, S. J. Fulk, Y. Jia, A. H. Carim, D. G. Schlom, and S. K. Streiffer, *Applied Physics Letters*, 2003, **82**, 4711–4713.

236. P. Kharel, S. Talebi, B. Ramachandran, A. Dixit, V. M. Naik, M. B. Sahana, C. Sudakar, R. Naik, M. S. R. Rao, and G. Lawes, *Journal of Physics: Condensed Matter*, 2009, **21**, 036001.

237. D. Kothari and V. R. Reddy, *Journal of Physics: Condensed Matter*, 2007, **19**, 136202.

238. M. Cazayous, D. Malka, D. Lebeugle, and D. Colson, *Applied Physics Letters*, 2007, **91**, 071910.

239. M. R. Fitzsimmons, P. Yashar, C. Leighton, and I. K. Schuller, *Physical Review Letters*, 2000, **84**, 3986–3989.

240. M. K. Singh, R. S. Katiyar, and J. F. Scott, *Journal of Physics: Condensed Matter*, 2008, **20**, 252203.

241. M. K. Singh, R. S. Katiyar, W. Prellier, and J. F. Scott, *Journal of Physics: Condensed Matter*, 2009, **21**, 042202.

242. J. F. Ihlefeld, N. J. Podraza, Z. K. Liu, R. C. Rai, X. Xu, T. Heeg, Y. B. Chen, J. Li, R. W. Collins, J. L. Musfeldt, X. Q. Pan, J. Schubert, R. Ramesh, and D. G. Schlom, *Applied Physics Letters*, 2008, **92**, 142908.

243. D. Cai, D. Du, S. Yu, and J. Cheng, *Procedia Engineering*, 2012, **27**, 577–582.

11 Appendix

11.1 Crystal data and structure refinement for $[Bi(acac)_3]_n$.

Identification code	2011ncs0195	
Empirical formula	C15 H21 Bi O6	
Formula weight	506.30	
Temperature	100 K	
Wavelength	0.71075 Å	
Crystal system	Monoclinic	
Space group	P21/c	
Unit cell dimensions	a = 10.5937(17) Å	α= 90°.
	b = 7.7238(12) Å	β= 116.875(7)°.
	c = 22.426(3) Å	γ = 90°.
Volume	1636.8(4) $Å^3$	
Z	4	
Density (calculated)	2.055 Mg/m^3	
Absorption coefficient	10.797 mm^{-1}	
F(000)	968	
Crystal size	0.02 x 0.01 x 0.01 mm^3	
Theta range for data collection	3.3 to 27.6°.	
Index ranges	-9<=h<=6, -13<=k<=13, -24<=l<=17	
Reflections collected	8881	
Independent reflections	3720 [R(int) = 0.202]	
Completeness to theta = 27.6°	99.1 %	
Absorption correction	Semi-empirical from equivalents	
Max. and min. transmission	0.8997 and 0.8130	
Refinement method	Full-matrix least-squares on F^2	
Data / restraints / parameters	3720 / 0 / 103	
Goodness-of-fit on F^2	0.941	
Final R indices [I>2sigma(I)]	R1 = 0.0951, wR2 = 0.1555	
R indices (all data)	R1 = 0.2075, wR2 = 0.1982	
Largest diff. peak and hole	2.751 and -2.190 e.$Å^{-3}$	

Atomic coordinates (x 10^4) and equivalent isotropic displacement parameters ($Å^2$x 10^3) for $[Bi(acac)_3]_n$. U(eq) is defined as one third of the trace of the orthogonalized U^{ij} tensor.

	x	y	z	U(eq)
Bi(1)	209(1)	7036(1)	7976(1)	33(1)
O(1)	779(13)	6204(15)	9001(7)	32(2)
O(2)	479(14)	9794(15)	8442(7)	32(2)
O(3)	-1767(13)	7758(14)	8095(6)	32(2)
O(4)	-1197(14)	4413(14)	7785(6)	32(2)
O(5)	1598(14)	4341(14)	8078(6)	32(2)
O(6)	2607(13)	7779(15)	8583(6)	32(2)
C(1)	1820(20)	6110(20)	10186(10)	32(2)
C(2)	1170(20)	7170(30)	9525(11)	34(2)
C(3)	1230(20)	8940(30)	9565(10)	34(3)
C(4)	880(20)	10180(20)	9042(11)	34(2)
C(5)	890(20)	12030(20)	9216(10)	32(2)
C(6)	-3535(19)	8010(20)	8455(10)	32(2)
C(7)	-2670(20)	6990(30)	8224(10)	34(2)
C(8)	-2930(20)	5140(20)	8140(9)	34(3)
C(9)	-2230(20)	3990(30)	7887(11)	34(2)
C(10)	-2680(20)	2170(20)	7832(10)	32(2)
C(11)	3350(20)	2160(20)	8475(10)	32(2)
C(12)	2900(20)	4000(20)	8498(11)	34(2)
C(13)	3850(20)	5120(20)	8967(10)	34(3)
C(14)	3680(20)	6910(30)	9000(10)	34(2)
C(15)	4796(18)	7970(20)	9539(9)	32(2)

Bond lengths [Å] and angles [°] for $[Bi(acac)_3]_n$.

Bi(1)-O(1)	2.193(14)	C(6)-C(7)	1.47(3)
Bi(1)-O(3)	2.296(15)	C(6)-H(6A)	0.9800
Bi(1)-O(2)	2.333(12)	C(6)-H(6B)	0.9800
Bi(1)-O(6)	2.347(12)	C(6)-H(6C)	0.9800
Bi(1)-O(4)	2.436(12)	C(7)-C(8)	1.45(2)
Bi(1)-O(5)	2.499(13)	C(8)-C(9)	1.43(3)
O(1)-C(2)	1.29(2)	C(8)-H(8)	0.9500
O(2)-C(4)	1.25(2)	C(9)-C(10)	1.47(2)
O(3)-C(7)	1.26(2)	C(10)-H(10A)	0.9800
O(4)-C(9)	1.26(3)	C(10)-H(10B)	0.9800
O(5)-C(12)	1.30(2)	C(10)-H(10C)	0.9800
O(6)-C(14)	1.29(2)	C(11)-C(12)	1.51(2)
C(1)-C(2)	1.56(3)	C(11)-H(11A)	0.9800
C(1)-H(1A)	0.9800	C(11)-H(11B)	0.9800
C(1)-H(1B)	0.9800	C(11)-H(11C)	0.9800
C(1)-H(1C)	0.9800	C(12)-C(13)	1.38(2)
C(2)-C(3)	1.37(2)	C(13)-C(14)	1.40(2)
C(3)-C(4)	1.43(3)	C(13)-H(13)	0.9500
C(3)-H(3)	0.9500	C(14)-C(15)	1.49(2)
C(4)-C(5)	1.48(2)	C(15)-H(15A)	0.9800
C(5)-H(5A)	0.9800	C(15)-H(15B)	0.9800
C(5)-H(5B)	0.9800	C(15)-H(15C)	0.9800
C(5)-H(5C)	0.9800		

O(1)-Bi(1)-O(3)	77.4(5)	O(1)-Bi(1)-O(5)	77.8(5)
O(1)-Bi(1)-O(2)	83.0(5)	O(3)-Bi(1)-O(5)	136.2(5)
O(3)-Bi(1)-O(2)	70.1(5)	O(2)-Bi(1)-O(5)	140.5(4)
O(1)-Bi(1)-O(6)	75.5(5)	O(6)-Bi(1)-O(5)	73.3(4)
O(3)-Bi(1)-O(6)	132.7(5)	O(4)-Bi(1)-O(5)	67.1(4)
O(2)-Bi(1)-O(6)	68.6(5)	C(2)-O(1)-Bi(1)	127.4(12)
O(1)-Bi(1)-O(4)	78.3(4)	C(4)-O(2)-Bi(1)	127.8(12)
O(3)-Bi(1)-O(4)	72.8(5)	C(7)-O(3)-Bi(1)	137.4(13)
O(2)-Bi(1)-O(4)	141.2(6)	C(9)-O(4)-Bi(1)	134.3(14)
O(6)-Bi(1)-O(4)	136.1(4)	C(12)-O(5)-Bi(1)	128.6(12)

C(14)-O(6)-Bi(1)	131.7(12)	C(8)-C(9)-C(10)	115(2)
C(2)-C(1)-H(1A)	109.5	C(9)-C(10)-H(10A)	109.5
C(2)-C(1)-H(1B)	109.5	C(9)-C(10)-H(10B)	109.5
H(1A)-C(1)-H(1B)	109.5	H(10A)-C(10)-H(10B)	109.5
C(2)-C(1)-H(1C)	109.5	C(9)-C(10)-H(10C)	109.5
H(1A)-C(1)-H(1C)	109.5	H(10A)-C(10)-H(10C)	109.5
H(1B)-C(1)-H(1C)	109.5	H(10B)-C(10)-H(10C)	109.5
O(1)-C(2)-C(3)	128(2)	C(12)-C(11)-H(11A)	109.5
O(1)-C(2)-C(1)	112.7(17)	C(12)-C(11)-H(11B)	109.5
C(3)-C(2)-C(1)	118.4(19)	H(11A)-C(11)-H(11B)	109.5
C(2)-C(3)-C(4)	129(2)	C(12)-C(11)-H(11C)	109.5
C(2)-C(3)-H(3)	115.5	H(11A)-C(11)-H(11C)	109.5
C(4)-C(3)-H(3)	115.5	H(11B)-C(11)-H(11C)	109.5
O(2)-C(4)-C(3)	124.1(18)	O(5)-C(12)-C(13)	126.4(19)
O(2)-C(4)-C(5)	118.1(18)	O(5)-C(12)-C(11)	114.5(16)
C(3)-C(4)-C(5)	118(2)	C(13)-C(12)-C(11)	119.1(18)
C(4)-C(5)-H(5A)	109.5	C(12)-C(13)-C(14)	126(2)
C(4)-C(5)-H(5B)	109.5	C(12)-C(13)-H(13)	116.8
H(5A)-C(5)-H(5B)	109.5	C(14)-C(13)-H(13)	116.8
C(4)-C(5)-H(5C)	109.5	O(6)-C(14)-C(13)	124.4(18)
H(5A)-C(5)-H(5C)	109.5	O(6)-C(14)-C(15)	114.8(17)
H(5B)-C(5)-H(5C)	109.5	C(13)-C(14)-C(15)	120.8(17)
C(7)-C(6)-H(6A)	109.5	C(14)-C(15)-H(15A)	109.5
C(7)-C(6)-H(6B)	109.5	C(14)-C(15)-H(15B)	109.5
H(6A)-C(6)-H(6B)	109.5	H(15A)-C(15)-H(15B)	109.5
C(7)-C(6)-H(6C)	109.5	C(14)-C(15)-H(15C)	109.5
H(6A)-C(6)-H(6C)	109.5	H(15A)-C(15)-H(15C)	109.5
H(6B)-C(6)-H(6C)	109.5	H(15B)-C(15)-H(15C)	109.5
O(3)-C(7)-C(8)	124(2)		
O(3)-C(7)-C(6)	119.0(19)		
C(8)-C(7)-C(6)	117(2)		
C(9)-C(8)-C(7)	124(2)		
C(9)-C(8)-H(8)	118.0		
C(7)-C(8)-H(8)	118.0		
O(4)-C(9)-C(8)	124.1(19)		
O(4)-C(9)-C(10)	121(2)		

Anisotropic displacement parameters ($Å^2$x 10^3) for $[Bi(acac)_3]_n$. The anisotropic displacement factor exponent takes the form: $-2\pi^2[h^2a^{*2}U^{11} + ... + 2 h k a^* b^* U^{12}]$

	U^{11}	U^{22}	U^{33}	U^{23}	U^{13}	U^{12}
Bi(1)	38(1)	21(1)	37(1)	-1(1)	14(1)	0(1)
O(1)	40(3)	17(3)	30(3)	-1(2)	8(3)	-7(3)
O(2)	40(3)	17(3)	30(3)	-1(2)	8(3)	-7(3)
O(3)	40(3)	17(3)	30(3)	-1(2)	8(3)	-7(3)
O(4)	40(3)	17(3)	30(3)	-1(2)	8(3)	-7(3)
O(5)	40(3)	17(3)	30(3)	-1(2)	8(3)	-7(3)
O(6)	40(3)	17(3)	30(3)	-1(2)	8(3)	-7(3)
C(1)	37(5)	27(4)	38(5)	-6(4)	22(4)	-2(4)
C(2)	36(5)	23(4)	43(6)	-2(4)	19(4)	-3(4)
C(3)	44(8)	25(6)	28(7)	-9(5)	13(6)	-11(6)
C(4)	36(5)	23(4)	43(6)	-2(4)	19(4)	-3(4)
C(5)	37(5)	27(4)	38(5)	-6(4)	22(4)	-2(4)
C(6)	37(5)	27(4)	38(5)	-6(4)	22(4)	-2(4)
C(7)	36(5)	23(4)	43(6)	-2(4)	19(4)	-3(4)
C(8)	44(8)	25(6)	28(7)	-9(5)	13(6)	-11(6)
C(9)	36(5)	23(4)	43(6)	-2(4)	19(4)	-3(4)
C(10)	37(5)	27(4)	38(5)	-6(4)	22(4)	-2(4)
C(11)	37(5)	27(4)	38(5)	-6(4)	22(4)	-2(4)
C(12)	36(5)	23(4)	43(6)	-2(4)	19(4)	-3(4)
C(13)	44(8)	25(6)	28(7)	-9(5)	13(6)	-11(6)
C(14)	36(5)	23(4)	43(6)	-2(4)	19(4)	-3(4)
C(15)	37(5)	27(4)	38(5)	-6(4)	22(4)	-2(4)

11.2 Crystal data and structure refinement for $[Bi(dbm)_3]_2$.

Identification code	str0736	
Empirical formula	C92 H70 Bi2 Cl4 O12	
Formula weight	1927.24	
Temperature	150(2) K	
Wavelength	0.71073 Å	
Crystal system	Triclinic	
Space group	P-1	
Unit cell dimensions	a = 10.350(2) Å	α = 83.891(3)°.
	b = 12.784(3) Å	β = 80.363(4)°.
	c = 15.044(3) Å	γ = 83.159(4)°.
Volume	1940.9(7) $Å^3$	
Z	1	
Density (calculated)	1.649 Mg/m^3	
Absorption coefficient	4.730 mm^{-1}	
F(000)	952	
Crystal size	0.50 x 0.30 x 0.10 mm^3	
Theta range for data collection	2.57 to 28.30°.	
Index ranges	-13<=h<=13, -16<=k<=16, -19<=l<=19	
Reflections collected	16403	
Independent reflections	8744 [R(int) = 0.0220]	
Completeness to theta = 28.30°	90.6 %	
Absorption correction	Semi-empirical from equivalents	
Max. and min. transmission	0.6231 and 0.1928	
Refinement method	Full-matrix least-squares on F^2	
Data / restraints / parameters	8744 / 0 / 497	
Goodness-of-fit on F^2	1.075	
Final R indices [I>2sigma(I)]	R1 = 0.0306, wR2 = 0.0915	
R indices (all data)	R1 = 0.0335, wR2 = 0.0949	
Largest diff. peak and hole	1.868 and -1.238 $e.Å^{-3}$	

Atomic coordinates (x 10^4) and equivalent isotropic displacement parameters ($Å^2$x 10^3) for $[Bi(dbm)_3]_2$. U(eq) is defined as one third of the trace of the orthogonalized U^{ij} tensor.

	x	y	z	U(eq)
Bi(1)	4272(1)	4956(1)	3852(1)	17(1)
O(1)	2710(3)	4685(2)	5147(2)	24(1)
O(2)	2521(3)	5856(2)	3431(2)	22(1)
O(3)	3304(3)	3423(2)	3775(2)	24(1)
O(4)	4897(3)	4570(2)	2341(2)	26(1)
O(5)	5079(3)	6566(2)	3008(2)	24(1)
O(6)	4350(3)	6277(2)	4928(2)	23(1)
C(1)	1125(4)	5163(3)	6394(3)	20(1)
C(2)	-131(4)	5581(4)	6730(3)	26(1)
C(3)	-612(5)	5434(4)	7645(3)	32(1)
C(4)	177(5)	4886(4)	8236(3)	32(1)
C(5)	1444(5)	4456(4)	7898(3)	29(1)
C(6)	1905(4)	4581(3)	6977(3)	25(1)
C(7)	1700(4)	5314(3)	5419(3)	22(1)
C(8)	1131(4)	6136(3)	4848(3)	21(1)
C(9)	1522(4)	6331(3)	3923(3)	20(1)
C(10)	731(4)	7162(3)	3398(3)	22(1)
C(11)	1369(5)	7650(4)	2595(3)	26(1)
C(12)	671(5)	8408(4)	2080(3)	33(1)
C(13)	-672(5)	8668(4)	2364(4)	38(1)
C(14)	-1301(5)	8189(4)	3144(4)	36(1)
C(15)	-606(5)	7439(4)	3676(3)	29(1)
C(16)	2454(4)	1964(3)	3359(3)	23(1)
C(17)	1696(5)	1675(4)	2760(3)	30(1)
C(18)	936(5)	825(4)	2988(4)	36(1)
C(19)	974(5)	239(4)	3822(4)	39(1)

C(20)	1707(5)	525(4)	4423(4)	38(1)
C(21)	2439(5)	1395(4)	4212(3)	30(1)
C(22)	3271(4)	2869(3)	3126(3)	21(1)
C(23)	3939(4)	3014(4)	2242(3)	26(1)
C(24)	4761(4)	3807(3)	1905(3)	21(1)
C(25)	5526(4)	3792(3)	970(3)	23(1)
C(26)	5498(6)	3009(4)	397(3)	38(1)
C(27)	6168(6)	3072(4)	-479(3)	43(1)
C(28)	6902(5)	3912(4)	-800(3)	34(1)
C(29)	6960(5)	4677(4)	-236(3)	31(1)
C(30)	6278(4)	4622(4)	649(3)	28(1)
C(31)	5025(4)	8345(3)	2378(3)	23(1)
C(32)	6152(5)	8176(4)	1745(3)	34(1)
C(33)	6463(5)	8947(5)	1039(4)	41(1)
C(34)	5633(6)	9861(4)	951(3)	39(1)
C(35)	4489(6)	10021(4)	1558(3)	38(1)
C(36)	4190(5)	9276(4)	2280(3)	31(1)
C(37)	4756(4)	7520(3)	3164(3)	24(1)
C(38)	4239(5)	7902(4)	4011(3)	28(1)
C(39)	4145(4)	7289(3)	4834(3)	23(1)
C(40)	3746(4)	7824(3)	5690(3)	22(1)
C(41)	3092(5)	7292(4)	6450(3)	27(1)
C(42)	2724(5)	7756(5)	7251(3)	40(1)
C(43)	3038(6)	8765(5)	7318(4)	42(1)
C(44)	3713(6)	9297(4)	6573(4)	41(1)
C(45)	4058(5)	8841(4)	5764(4)	33(1)
Cl(1)	9545(3)	1206(2)	483(2)	85(1)
Cl(2)	11121(3)	2973(2)	253(1)	76(1)
C(46)	9597(10)	2548(7)	169(8)	96(3)

Bond lengths [Å]and angles [°] for $[Bi(dbm)_3]_2$.

Bi(1)-O(2)	2.177(3)	C(10)-C(15)	1.392(6)
Bi(1)-O(3)	2.326(3)	C(10)-C(11)	1.398(6)
Bi(1)-O(1)	2.337(3)	C(11)-C(12)	1.387(6)
Bi(1)-O(4)	2.345(3)	C(11)-H(11)	0.9500
Bi(1)-O(5)	2.458(3)	C(12)-C(13)	1.396(8)
Bi(1)-O(6)	2.477(3)	C(12)-H(12)	0.9500
Bi(1)-O(6)#1	2.760(3)	C(13)-C(14)	1.365(8)
O(1)-C(7)	1.279(5)	C(13)-H(13)	0.9500
O(2)-C(9)	1.295(5)	C(14)-C(15)	1.393(7)
O(3)-C(22)	1.273(5)	C(14)-H(14)	0.9500
O(4)-C(24)	1.265(5)	C(15)-H(15)	0.9500
O(5)-C(37)	1.263(5)	C(16)-C(17)	1.393(6)
O(6)-C(39)	1.283(5)	C(16)-C(21)	1.405(6)
O(6)-Bi(1)#1	2.760(3)	C(16)-C(22)	1.491(6)
C(1)-C(2)	1.380(6)	C(17)-C(18)	1.397(7)
C(1)-C(6)	1.388(6)	C(17)-H(17)	0.9500
C(1)-C(7)	1.489(6)	C(18)-C(19)	1.396(8)
C(2)-C(3)	1.383(6)	C(18)-H(18)	0.9500
C(2)-H(2)	0.9500	C(19)-C(20)	1.376(8)
C(3)-C(4)	1.387(7)	C(19)-H(19)	0.9500
C(3)-H(3)	0.9500	C(20)-C(21)	1.399(7)
C(4)-C(5)	1.394(7)	C(20)-H(20)	0.9500
C(4)-H(4)	0.9500	C(21)-H(21)	0.9500
C(5)-C(6)	1.387(6)	C(22)-C(23)	1.396(6)
C(5)-H(5)	0.9500	C(23)-C(24)	1.400(6)
C(6)-H(6)	0.9500	C(23)-H(23)	0.9500
C(7)-C(8)	1.420(6)	C(24)-C(25)	1.495(6)
C(8)-C(9)	1.388(6)	C(25)-C(30)	1.389(6)
C(8)-H(8)	0.9500	C(25)-C(26)	1.395(6)
C(9)-C(10)	1.501(6)	C(26)-C(27)	1.380(7)

C(26)-H(26)	0.9500	C(44)-C(45)	1.380(7)
C(27)-C(28)	1.388(8)	C(44)-H(44)	0.9500
C(27)-H(27)	0.9500	C(45)-H(45)	0.9500
C(28)-C(29)	1.374(7)	Cl(1)-C(46)	1.734(9)
C(28)-H(28)	0.9500	Cl(2)-C(46)	1.757(11)
C(29)-C(30)	1.397(6)	C(46)-H(46A)	0.9900
C(29)-H(29)	0.9500	C(46)-H(46B)	0.9900
C(30)-H(30)	0.9500		
C(31)-C(32)	1.388(6)		
C(31)-C(36)	1.394(6)		
C(31)-C(37)	1.511(6)		
C(32)-C(33)	1.393(7)		
C(32)-H(32)	0.9500		
C(33)-C(34)	1.373(8)		
C(33)-H(33)	0.9500		
C(34)-C(35)	1.377(8)		
C(34)-H(34)	0.9500		
C(35)-C(36)	1.386(7)		
C(35)-H(35)	0.9500		
C(36)-H(36)	0.9500		
C(37)-C(38)	1.410(6)		
C(38)-C(39)	1.389(6)		
C(38)-H(38)	0.9500		
C(39)-C(40)	1.495(6)		
C(40)-C(41)	1.383(6)		
C(40)-C(45)	1.396(6)		
C(41)-C(42)	1.377(7)		
C(41)-H(41)	0.9500		
C(42)-C(43)	1.386(8)		
C(42)-H(42)	0.9500		
C(43)-C(44)	1.376(9)		
C(43)-H(43)	0.9500		

O(2)-Bi(1)-O(3)	87.98(11)	C(1)-C(2)-C(3)	120.4(4)
O(2)-Bi(1)-O(1)	78.75(11)	C(1)-C(2)-H(2)	119.8
O(3)-Bi(1)-O(1)	70.73(11)	C(3)-C(2)-H(2)	119.8
O(2)-Bi(1)-O(4)	86.99(11)	C(2)-C(3)-C(4)	120.2(4)
O(3)-Bi(1)-O(4)	75.78(10)	C(2)-C(3)-H(3)	119.9
O(1)-Bi(1)-O(4)	143.86(11)	C(4)-C(3)-H(3)	119.9
O(2)-Bi(1)-O(5)	75.62(11)	C(3)-C(4)-C(5)	119.4(4)
O(3)-Bi(1)-O(5)	145.74(10)	C(3)-C(4)-H(4)	120.3
O(1)-Bi(1)-O(5)	132.47(10)	C(5)-C(4)-H(4)	120.3
O(4)-Bi(1)-O(5)	73.54(10)	C(6)-C(5)-C(4)	119.9(4)
O(2)-Bi(1)-O(6)	89.97(10)	C(6)-C(5)-H(5)	120.0
O(3)-Bi(1)-O(6)	140.23(10)	C(4)-C(5)-H(5)	120.0
O(1)-Bi(1)-O(6)	69.93(10)	C(5)-C(6)-C(1)	120.2(4)
O(4)-Bi(1)-O(6)	143.75(10)	C(5)-C(6)-H(6)	119.9
O(5)-Bi(1)-O(6)	70.73(10)	C(1)-C(6)-H(6)	119.9
O(2)-Bi(1)-O(6)#1	154.02(10)	O(1)-C(7)-C(8)	123.6(4)
O(3)-Bi(1)-O(6)#1	84.60(10)	O(1)-C(7)-C(1)	116.6(4)
O(1)-Bi(1)-O(6)#1	75.29(10)	C(8)-C(7)-C(1)	119.8(4)
O(4)-Bi(1)-O(6)#1	115.02(10)	C(9)-C(8)-C(7)	125.8(4)
O(5)-Bi(1)-O(6)#1	122.27(10)	C(9)-C(8)-H(8)	117.1
O(6)-Bi(1)-O(6)#1	80.15(10)	C(7)-C(8)-H(8)	117.1
C(7)-O(1)-Bi(1)	126.9(3)	O(2)-C(9)-C(8)	126.9(4)
C(9)-O(2)-Bi(1)	128.8(3)	O(2)-C(9)-C(10)	113.9(4)
C(22)-O(3)-Bi(1)	132.6(3)	C(8)-C(9)-C(10)	119.3(4)
C(24)-O(4)-Bi(1)	134.2(3)	C(15)-C(10)-C(11)	119.7(4)
C(37)-O(5)-Bi(1)	129.2(3)	C(15)-C(10)-C(9)	122.2(4)
C(39)-O(6)-Bi(1)	130.1(3)	C(11)-C(10)-C(9)	118.1(4)
C(39)-O(6)-Bi(1)#1	127.7(3)	C(12)-C(11)-C(10)	120.0(4)
Bi(1)-O(6)-Bi(1)#1	99.85(10)	C(12)-C(11)-H(11)	120.0
C(2)-C(1)-C(6)	119.7(4)	C(10)-C(11)-H(11)	120.0
C(2)-C(1)-C(7)	122.6(4)	C(11)-C(12)-C(13)	119.5(5)
C(6)-C(1)-C(7)	117.7(4)	C(11)-C(12)-H(12)	120.3

C(13)-C(12)-H(12)	120.3	C(22)-C(23)-H(23)	117.0
C(14)-C(13)-C(12)	120.7(4)	C(24)-C(23)-H(23)	117.0
C(14)-C(13)-H(13)	119.7	O(4)-C(24)-C(23)	124.0(4)
C(12)-C(13)-H(13)	119.7	O(4)-C(24)-C(25)	116.1(4)
C(13)-C(14)-C(15)	120.4(5)	C(23)-C(24)-C(25)	119.9(4)
C(13)-C(14)-H(14)	119.8	C(30)-C(25)-C(26)	118.4(4)
C(15)-C(14)-H(14)	119.8	C(30)-C(25)-C(24)	117.8(4)
C(10)-C(15)-C(14)	119.7(5)	C(26)-C(25)-C(24)	123.8(4)
C(10)-C(15)-H(15)	120.2	C(27)-C(26)-C(25)	121.0(5)
C(14)-C(15)-H(15)	120.2	C(27)-C(26)-H(26)	119.5
C(17)-C(16)-C(21)	119.2(4)	C(25)-C(26)-H(26)	119.5
C(17)-C(16)-C(22)	122.0(4)	C(26)-C(27)-C(28)	120.3(5)
C(21)-C(16)-C(22)	118.9(4)	C(26)-C(27)-H(27)	119.8
C(16)-C(17)-C(18)	121.2(5)	C(28)-C(27)-H(27)	119.8
C(16)-C(17)-H(17)	119.4	C(29)-C(28)-C(27)	119.3(4)
C(18)-C(17)-H(17)	119.4	C(29)-C(28)-H(28)	120.4
C(19)-C(18)-C(17)	119.0(5)	C(27)-C(28)-H(28)	120.4
C(19)-C(18)-H(18)	120.5	C(28)-C(29)-C(30)	120.8(5)
C(17)-C(18)-H(18)	120.5	C(28)-C(29)-H(29)	119.6
C(20)-C(19)-C(18)	120.2(5)	C(30)-C(29)-H(29)	119.6
C(20)-C(19)-H(19)	119.9	C(25)-C(30)-C(29)	120.2(4)
C(18)-C(19)-H(19)	119.9	C(25)-C(30)-H(30)	119.9
C(19)-C(20)-C(21)	121.2(5)	C(29)-C(30)-H(30)	119.9
C(19)-C(20)-H(20)	119.4	C(32)-C(31)-C(36)	119.3(4)
C(21)-C(20)-H(20)	119.4	C(32)-C(31)-C(37)	118.7(4)
C(20)-C(21)-C(16)	119.2(5)	C(36)-C(31)-C(37)	122.1(4)
C(20)-C(21)-H(21)	120.4	C(31)-C(32)-C(33)	120.0(5)
C(16)-C(21)-H(21)	120.4	C(31)-C(32)-H(32)	120.0
O(3)-C(22)-C(23)	126.6(4)	C(33)-C(32)-H(32)	120.0
O(3)-C(22)-C(16)	115.3(4)	C(34)-C(33)-C(32)	120.1(5)
C(23)-C(22)-C(16)	118.1(4)	C(34)-C(33)-H(33)	119.9
C(22)-C(23)-C(24)	126.1(4)	C(32)-C(33)-H(33)	119.9

C(33)-C(34)-C(35)	120.3(5)	C(45)-C(44)-H(44)	119.6
C(33)-C(34)-H(34)	119.8	C(44)-C(45)-C(40)	120.6(5)
C(35)-C(34)-H(34)	119.8	C(44)-C(45)-H(45)	119.7
C(34)-C(35)-C(36)	120.1(5)	C(40)-C(45)-H(45)	119.7
C(34)-C(35)-H(35)	119.9	Cl(1)-C(46)-Cl(2)	112.3(5)
C(36)-C(35)-H(35)	119.9	Cl(1)-C(46)-H(46A)	109.1
C(35)-C(36)-C(31)	120.1(5)	Cl(2)-C(46)-H(46A)	109.1
C(35)-C(36)-H(36)	120.0	Cl(1)-C(46)-H(46B)	109.1
C(31)-C(36)-H(36)	120.0	Cl(2)-C(46)-H(46B)	109.1
O(5)-C(37)-C(38)	126.6(4)	H(46A)-C(46)-H(46B)	107.9
O(5)-C(37)-C(31)	117.0(4)		
C(38)-C(37)-C(31)	116.3(4)		
C(39)-C(38)-C(37)	124.8(4)		
C(39)-C(38)-H(38)	117.6		
C(37)-C(38)-H(38)	117.6		
O(6)-C(39)-C(38)	125.0(4)		
O(6)-C(39)-C(40)	116.0(4)		
C(38)-C(39)-C(40)	119.0(4)		
C(41)-C(40)-C(45)	118.0(4)		
C(41)-C(40)-C(39)	119.8(4)		
C(45)-C(40)-C(39)	122.1(4)		
C(42)-C(41)-C(40)	121.3(5)		
C(42)-C(41)-H(41)	119.3		
C(40)-C(41)-H(41)	119.3		
C(41)-C(42)-C(43)	120.2(5)		
C(41)-C(42)-H(42)	119.9		
C(43)-C(42)-H(42)	119.9		
C(44)-C(43)-C(42)	119.2(5)		
C(44)-C(43)-H(43)	120.4		
C(42)-C(43)-H(43)	120.4		
C(43)-C(44)-C(45)	120.7(5)		
C(43)-C(44)-H(44)	119.6		

Symmetry transformations used to generate equivalent atoms:

#1 -x+1,-y+1,-z+1

Anisotropic displacement parameters ($Å^2$x 10^3)for $[Bi(dbm)_3]_2$. The anisotropic displacement factor exponent takes the form: $-2\pi^2[h^2a^{*2}U^{11} + ... + 2 h k a^* b^* U^{12}]$

	U^{11}	U^{22}	U^{33}	U^{23}	U^{13}	U^{12}
Bi(1)	21(1)	16(1)	15(1)	-3(1)	-2(1)	2(1)
O(1)	23(1)	24(2)	21(1)	-1(1)	4(1)	3(1)
O(2)	22(1)	26(2)	17(1)	0(1)	-1(1)	2(1)
O(3)	30(2)	23(2)	20(1)	-6(1)	1(1)	-4(1)
O(4)	42(2)	18(1)	17(1)	-4(1)	2(1)	-5(1)
O(5)	25(2)	19(1)	27(2)	-4(1)	-3(1)	1(1)
O(6)	31(2)	16(1)	21(1)	-1(1)	-7(1)	0(1)
C(1)	17(2)	18(2)	24(2)	-4(2)	1(2)	0(1)
C(2)	22(2)	29(2)	23(2)	-2(2)	0(2)	2(2)
C(3)	25(2)	33(2)	30(2)	2(2)	7(2)	7(2)
C(4)	35(2)	33(2)	22(2)	1(2)	3(2)	2(2)
C(5)	33(2)	31(2)	21(2)	0(2)	-6(2)	0(2)
C(6)	23(2)	24(2)	26(2)	-1(2)	-2(2)	0(2)
C(7)	23(2)	20(2)	23(2)	-5(2)	-3(2)	-4(2)
C(8)	22(2)	20(2)	20(2)	-2(2)	2(2)	0(2)
C(9)	18(2)	18(2)	26(2)	-6(2)	-5(2)	-2(2)
C(10)	23(2)	21(2)	24(2)	-5(2)	-7(2)	1(2)
C(11)	32(2)	25(2)	23(2)	-3(2)	-8(2)	-3(2)
C(12)	42(3)	27(2)	30(2)	2(2)	-11(2)	-4(2)
C(13)	44(3)	28(2)	45(3)	2(2)	-24(2)	4(2)
C(14)	27(2)	33(3)	48(3)	-6(2)	-12(2)	9(2)
C(15)	29(2)	28(2)	33(2)	-4(2)	-8(2)	-2(2)
C(16)	23(2)	19(2)	26(2)	-5(2)	2(2)	0(2)
C(17)	29(2)	28(2)	33(2)	-6(2)	-5(2)	-1(2)
C(18)	29(2)	36(3)	45(3)	-11(2)	-5(2)	-7(2)
C(19)	36(3)	30(3)	48(3)	-6(2)	7(2)	-9(2)
C(20)	35(3)	33(3)	38(3)	5(2)	8(2)	-2(2)

C(21)	28(2)	31(2)	29(2)	-2(2)	3(2)	-5(2)
C(22)	19(2)	17(2)	26(2)	-4(2)	-2(2)	1(2)
C(23)	31(2)	25(2)	21(2)	-7(2)	0(2)	-4(2)
C(24)	26(2)	18(2)	17(2)	-3(2)	-3(2)	2(2)
C(25)	29(2)	21(2)	18(2)	-4(2)	-3(2)	1(2)
C(26)	60(3)	28(2)	25(2)	-7(2)	5(2)	-15(2)
C(27)	62(4)	37(3)	25(2)	-15(2)	13(2)	-6(3)
C(28)	43(3)	35(3)	20(2)	-4(2)	7(2)	-4(2)
C(29)	28(2)	31(2)	33(2)	-4(2)	6(2)	-7(2)
C(30)	28(2)	27(2)	27(2)	-4(2)	-1(2)	-5(2)
C(31)	27(2)	24(2)	21(2)	-3(2)	-7(2)	-5(2)
C(32)	30(2)	35(3)	32(2)	2(2)	-1(2)	4(2)
C(33)	35(3)	53(3)	30(3)	6(2)	3(2)	-5(2)
C(34)	59(3)	36(3)	24(2)	4(2)	-10(2)	-13(2)
C(35)	57(3)	23(2)	33(3)	3(2)	-8(2)	0(2)
C(36)	37(3)	26(2)	27(2)	-3(2)	-6(2)	3(2)
C(37)	21(2)	23(2)	29(2)	-1(2)	-8(2)	-1(2)
C(38)	33(2)	18(2)	29(2)	-2(2)	-2(2)	3(2)
C(39)	24(2)	21(2)	25(2)	-6(2)	-6(2)	-1(2)
C(40)	23(2)	21(2)	22(2)	-5(2)	-5(2)	2(2)
C(41)	34(2)	27(2)	22(2)	-8(2)	-5(2)	-3(2)
C(42)	42(3)	48(3)	26(2)	-7(2)	-2(2)	3(2)
C(43)	49(3)	46(3)	33(3)	-25(2)	-9(2)	14(3)
C(44)	50(3)	27(3)	50(3)	-18(2)	-18(3)	4(2)
C(45)	39(3)	20(2)	41(3)	-6(2)	-8(2)	-2(2)
Cl(1)	118(2)	65(1)	69(1)	16(1)	-5(1)	-26(1)
Cl(2)	115(2)	59(1)	59(1)	-7(1)	-22(1)	-14(1)
C(46)	104(7)	51(5)	120(8)	17(5)	-12(6)	8(5)